

**Understanding the mechanistic role of post
translational modifications associated with Tyrosyl-
DNA-phosphodiesterase 1 in response to DNA
damage and anti-cancer agents**

**Thesis Submitted to Jadavpur University
For the Degree of
Doctor of Philosophy (Science)**

by

Srijita Paul Chowdhuri

Index No: 37/17/LifeSc./25



**School of Biological Sciences
Indian Association for the Cultivation of Science
Jadavpur
Kolkata-700032**



INDIAN ASSOCIATION FOR THE CULTIVATION OF SCIENCE

(An Autonomous Institute under DST, GOI and a Deemed to be University)

2A & 2B Raja SC Mullik Road, Jadavpur, Kolkata 700032, India

Prof. Benu Brata Das, *PhD, FAScT, FNASc*

Professor

Head, Laboratory of Molecular Biology

School of Biological Sciences

Phone: +91-33-24734971

Fax: +91-33-2473-6561

Email: pcbbsd@iacs.res.in

benubrata@yahoo.com

CERTIFICATE FROM THE SUPERVISOR

This is to certify that the thesis entitled “**Understanding the mechanistic role of post translational modifications associated with Tyrosyl-DNA-phosphodiesterase 1 in response to DNA damage and anti-cancer agents**” submitted by **Smt. Srijita Paul Chowdhuri**, whose name got registered on **15th May 2017** for the award of Ph.D (Science) degree of Jadavpur University, is absolutely based upon her own work under my supervision and that neither this thesis nor any part of it has been submitted for either any degree/diploma or any other academic award anywhere before.

Date: 12th May 2023

Prof. Benu Brata Das, *PhD, FAScT, FNASc*

(Signature of the supervisor with official seal)

Dedicated to

My

Parents

Acknowledgements

“Scientific knowledge is an enabling power to do either good or bad — but it does not carry instructions on how to use it.”

— **Richard P. Feynman**

This thesis collates the outcomes of an onerous scientific pursuit towards the accomplishment of my PhD degree punctuated with glimpses of success and failures at the Indian Association for the Cultivation of Science (IACS), Kolkata, India. This enriching journey not only strengthened my scientific knowledge but also helped me evolve as a person. As I sit here to write this note of thanks with utmost sincerity and humbleness, I convey my genuine gratitude to the help, co-operation and guidance extended to me by my well-wishers and friends during the tenure of my work.

*First and foremost, I would like to express my deepest gratitude and sincere regards towards my supervisor, **Professor Benu Brata Das**, for his constant motivation and guidance through this exceptionally enlightening yet difficult journey. He gave me the total independence to delve into my endeavor to develop scientific skills, logical thinking and rationale, to accept failures and most importantly the confidence to bounce back with zeal and valor for the future. I sincerely appreciate all the time, and the effort he has contributed in honing my scientific-writing proficiency. Under his supervision have I learnt not only how to carry out scientific research in the methodical, well planned and time bound manner but also the art of presenting my research work. He has provided me with several opportunities to socialize in scientific forums and upgrade my knowledge and skills for personal betterment. The regular lab meetings which apparently seemed tiresome at times were some of the best learning sessions one can hope for. His indomitable enthusiasm and dedication towards science and research has been a constant source of inspiration in motivating me to give my best for my Ph.D. pursuit.*

I am sincerely thankful towards Prof. Ranjan Sen, Director, Indian Association for the Cultivation of Science, for allowing me to pursue my doctoral work in this esteemed Institute. I would also like to express my heartfelt gratitude towards Prof. Hemanta K. Majumder for allowing me to perform my experiments in his laboratory. I would like to express my earnest gratitude towards the scientists of IACS for the help and support during my PhD. I would want to acknowledge all the operators of the CSS facility especially, Chanchal da and Tanojit da for helping me with my experimental procedures. I would like to express my heartfelt regards to Ujjwaladi for her care and concern towards completion of my PhD.

It is aptly said that better than a thousand days of diligent study is one day with a great teacher. I would like to take this opportunity to thank all my teachers right from my school days for making me the way I stand up to the world today. A school is the second home and the school teachers are instrumental in shaping not only a child's academic future but also instilling the right values in the form of discipline, morality, humility which go far beyond our educational degrees. I believe had it not been for my school Bharatiya Vidya Bhavan, I would never have been able to grow as a person beyond books could offer. I would like to thank Rama Ma'am (my first ever teacher) for teaching me how to hold a pencil and scribble the alphabets and numbers. I would like to mention about Shailaja Ma'am (my first ever class teacher), Kabita Ma'am, Rina Ma'am, Kajal Ma'am, Sushmita Ma'am, Gopa Ma'am, Ratna Ma'am and Ranu Ma'am from my primary school for the diligent efforts to equip me to face the greater challenges in life. I am indebted to all of you forever for shaping my character. I would also thank my high school teachers for their immense help towards my educational achievements. I am grateful for the faith they have shown in me and I truly hope I have been able to live up to their expectations. I am ever grateful to my home tutors, Jagadish Sir, Thakur Sir and Kajal Ma'am for your great contributions in teaching me.

I would like to thank all my teachers from Lady Brabourne College for building my interest in the subjects in great depth and detail. I would especially Dr. Shashiprabha Das Gupta for all the help and encouragement she has provided not only during my graduation days but also till this date. I would also like to thank all my teachers from St. Xavier's College for the motivation and encouragement to pursue scientific research.

I would like to express my heartiest regards to Dr. Syamal Roy (IICB, Kolkata), under whose supervision I did my internship for his guidance and co-operation. I would also thank Dr. Sandeep Saxena (NII, New Delhi) for providing me with the opportunity to work in the "DNA Replication and Cell Cycle" field. Working in his laboratory I felt that nothing in this world can be more interesting than molecular and cell biology and this indeed propelled my decision to do an intensive research in the same field for PhD. I express my regards to my mentors Sandipda (Dr. Syamal Roy's lab) and Tanushreedi (Dr. Sandeep Saxena's lab) who taught me the intricacies of research. I am especially indebted to Tanushreedi for teaching me all the techniques with utmost patience (not to mention her caring nature towards me) and having faith in me. I would like to thank Somenathda, Vivek and Sonali for the help in my studies at IICB.

I would like to express my gratitude to all lab members at IACS, Ishitadi, Ayeshadi, Jayasreedi, Soumyadipda, Saritadi, Subhenduda, Arijitda, Sangheeta, Saini, Banhi, Sayan,

Arpan and Abhik for their cordial help during my PhD. During my stay here with you all I have matured as a person and learnt how to be determined and resolute towards the ultimate goal despite all odds. It is truly said that a friend is the one who overlooks your broken fence and admires the flowers in your garden. I feel privileged to have cultivated such friends who have been by me always. I thank my school friends Swagata, Soham and Shiladitya for the help and support whenever I needed. I thank Sayani, Ipsita and Subhadeep for the unconditional love and motivation to complete my PhD. I would thank Neha and Anamika for their constant encouragement and support. I thank all my IACS friends especially Arpana, Parijat and Goutam for the help during the years at IACS. I express my overwhelming gratitude to Subho for the unconditional support and love (for patiently hearing me out without complaining ever) every time my ship was about to sink. I would thank Arnabda for edifying me “the difference between knowing the name of something and knowing something” and whose unparalleled support has been my strength all through my journey.

*There was nothing I could ever have done without the inexpressible support from my **Ma** and **Baba**. Words are just a futile attempt to acknowledge all the love and affection you have shown for me and for all your struggles, tireless efforts and sacrifices you have made to bring a smile to my face. I would like to take this opportunity to express my abyssal gratitude towards all my family members; to my Ma for striking the impressive balance between her office work and household responsibilities. Her rational suggestions, symbolic optimism and unremitting inspirations have compassed every sphere of my life to the right direction. Her collectedness, foresightedness and outstanding ability to mark out the right solutions as well as her active presence in every phase of my life left a permanent indelible impression on my career and my mind. To my Baba, for always encouraging me to do what my heart desires, for patiently waiting for hours outside my tuition classes, for fulfilling all my demands (purchasing every book I have asked), for reposing faith in me at every instance I tripped and for making me feel blessed in all possible ways. I could just go on and on writing about how you both have carved every niche of my existence and still it would not ever end. A very special thanks to my Dida for all the love and care she has showered on me over the years. I also extend my deepest regards to my Mama and Bhai for their care and concern for me.*

Date: 12th May 2023

Srijita Paul Chowdhuri
12.05.2023

(SRIJITA PAUL CHOWDHURI)

Synopsis

Title: Understanding the mechanistic role of post translational modifications associated with TDP1 in response to DNA damage and anti-cancer agents

DNA repair systems provide a critical defense mechanism to safeguard the genome against exogenous and endogenous sources that assault the stability and integrity of our genomes causing various diseases. One of the most common forms of DNA damage that arise in cells are single-strand breaks (SSBs) which can emerge from the abortive activity of DNA topoisomerase 1 (Top1), due to the covalent trapping of Top1 with the 3'-end of the DNA leading to the generation of Top1-linked DNA covalent cleavage complexes (Top1cc). The antitumor activity of camptothecin (CPT) and other non-CPT Top1 poisons that trigger cell death through selective trapping of the Top1cc of the highly proliferating cells exploit the severity of these breaks. However, CPT and its derivatives suffer from dose-limiting toxicity, resulting in severe diarrhoea and neutropenia, rapidly inactivated in plasma because of hydrolysis of lactone E-ring and binding of the ensuing hydroxyl acid to plasma proteins, accumulate resistance in the topoisomerase 1 (Top1) gene and is also found to be a substrate of permeability glycoprotein (Pgp). These limitations press the urgent need for developing newer non-CPT based Top1-targeted drugs which can overcome these shortcomings of CPT or its derivatives.

The key enzyme for the excision of Top1cc is Tyrosyl DNA Phosphodiesterase 1 (TDP1) which hydrolyzes the phosphodiester bond between the Top1-tyrosyl moiety and the DNA 3'-end. TDP1's ability to resolve 3'-phosphotyrosyl linkages is consistent with its role in protecting cells against Top1-induced DNA lesions. Post-translational modifications of TDP1 have been largely implicated in the recruitment, modulation of enzymatic activity, and stability of DNA damage response of TDP1. However, post-translational modifications of TDP1 which regulate the localization of TDP1 during the progression of cell cycle has not been studied so far. The third chapter of the current dissertation work involves the identification of a hitherto unidentified novel phosphorylation of TDP1 by the core mitotic regulatory kinase Cyclin dependent Kinase 1 (CDK1) which regulates the localisation dynamics of TDP1 on the mitotic chromosomes. The phosphorylation of TDP1 initially identified by mass spectrometry was validated using immunoprecipitation and *in vitro* kinase assays of the Wild Type (WT) and the S61A mutant form of TDP1 generated by site-directed

mutagenesis. The fourth chapter deals with the major finding that this phosphorylation plays a key role in temporally regulating the chromosomal association and dissociation of TDP1 during mitotic phase of the cell cycle. We have also shown in the fifth chapter that replication stress induces the enrichment of the phosphorylation mutant TDP1 at the common fragile sites (CFSs) leading to several mitotic defects ultimately culminating into accumulation of 53BP1 nuclear bodies in the G1 phase. Mitotic DNA synthesis (MiDAS) is a break induced repair (BIR) mechanism that resolves late replication intermediates, thereby supporting cell proliferation under replication stress in mitosis. This unusual form of DNA synthesis uses Mus81-Eme1-SLX4, RAD52 and PolD3. This process can be detrimental if hyperactivated and can lead to chromosomal instabilities and segregation defects. The fifth chapter of this dissertation work explores the consequences of unrestrained MiDAS in TDP1 deficient cells overexpressing the phosphomutant TDP1 which could be rescued by MUS81 knockdown. Our findings provide a novel insight into the cell cycle dependent regulation of a primarily S-phase repair protein for safeguarding the genomic instability.

The sixth chapter of the thesis is based on screening of a novel small molecule inhibitor of the DNA Topoisomerase 1 (LdTop1) of the kinetoplastid organism *Leishmania donovani* (*Ld*), the causal organism of Visceral Leishmaniasis (VL) which is a chimeric derivative based on the Pyridine-Imidazo-Quinoline (PIQ) core. The emerging cases of drug resistance against the clinically available antileishmanials and the lack of vaccines for the disease require immediate action and the development of newer drugs with novel pharmacore. The novel derivative was found to inhibit Top1 leading to parasitic killing not only in the wild type *Leishmania donovani* Ag83 strain but also in the antimony resistant strain BHU575. Cytokine profiling studies performed using the murine model of experimental VL showed that the up-regulation of the Th2 cytokines response induced by *Leishmania donovani* infection could be dampened by treating the mice with the PIQ derivative leading to a surge of the Th1 cytokines conferring host protection and parasite clearance.

Abbreviations

ATP	Adenosine triphosphate
BLAST	Basic Local Alignment Search Tool
β -ME	β -mercaptoethanol
BrdU	5-bromo-2'-deoxyuridine
BSA	Bovine serum albumin
CDD	Conserved Domain Database
Ci	Curie
CPT	Camptothecin
CT-DNA	Calf Thymus DNA
DDR	DNA Damage Repair
DMF	Dimethylformamide
DMSO	Dimethyl sulfoxide
DNA	Deoxyribonucleic Acid
DSB	Double Strand Breaks
dNTP	Deoxynucleoside triphosphate
DTT	Dithiothreitol
EDTA	Ethylenediaminetetraacetic acid
EGFP	Enhanced green fluorescence protein
EMSA	Electrophoretic mobility shift assay
EndoG	Endonuclease G

EtBr	Ethidium bromide
FBS	Fetal bovine serum
FITC	Fluorescein isothiocyanate
GSH	Glutathione
h	Hours
HCl	Hydrochloric acid
HEPES	N-[2-hydroxymethyl] piperazine-N'-[2-ethanesulfonic acid]
IPTG	Isopropylthio- β -D-galactoside
Kb	Kilobase
KDa	Kilodalton
KCl	Potassium chloride
kDNA	Kinetoplast DNA
LB	Luria Bertani
Lk	Linking number
M	Molar
M-AMSA	Methanesulfonate
mg	Milligram
MgCl ₂	Magnesium chloride
min	Minutes
MiDAS	Mitotic DNA synthesis
ml	Milliliter

mM	Millimolar
MTT	3-(4,5-Dimethylthiazol-2-yl)-2,5-diphenyltetrazolium bromide
NAC	<i>N</i> -Acetyl-L-cysteine
ng	Nanogram
NM	Nicked Monomer
NTA	Nitrilotriacetic acid
PAGE	Polyacrylamide gel electrophoresis
PARP 1	Poly (ADP-ribose) polymerase 1
PBS	Phosphate buffered saline
PCR	Polymerase chain reaction
PI	Propidium iodide
PMSF	Phenyl methyl sulfonyl fluoride
PSI	Position Specific Iterative
RNA	Ribonucleic acid
RNase	Ribonuclease
ROI	Region of interest
ROS	Reactive Oxygen Species
rpm	Revolution per minute
RPMI	Rosewell Parker Memorial Institute
s	Seconds
SAG	Sodium antimony gluconate

SD	Standard deviation
SDS	Sodium dodecyl sulphate
SM	Supercoiled Monomer
TAE	Tris-Acetic acid-EDTA
TBE	Tris-borate-EDTA
T5PNP	p-nitrophenyl-thymidine-5'-phosphate
TUNEL	Terminal deoxynucleotidyl transferase (TdT) dUTP Nick-End Labeling
μM	Micromolar
UV	Ultra violet
V	Volts
VL	Visceral Leishmaniasis
WHO	World Health Organization

Table of Contents

	<i>Page Number</i>
<i>Chapter 1:</i>	
<i>General Introduction</i>	1- 51
<i>Chapter 2:</i>	
<i>General Materials & Method</i>	52- 57
<i>Chapter 3:</i>	
<i>Identification of TDP1 as a novel substrate of CDK1</i>	58-74
3.1 Introduction	59-61
3.2 Materials and methods	61-64
3.3 Results	64-73
3.4 Discussion	73-74
<i>Chapter 4:</i>	
<i>CDK1 regulates chromosomal localization of TDP1</i>	75-92
4.1 Introduction	76-78
4.2 Materials and methods	78-82
4.3 Results	82-91
4.4 Discussion	92

Chapter 5:

Biological significance of CDK1 mediated

Phosphorylation of TDPI **93 - 113**

5.1 Introduction **94-95**

5.2 Materials and methods **95-99**

5.3 Results **99-111**

5.4 Discussion **111–113**

Chapter 6:

Identification and characterization of a quinoline derivative that posions

Leishmania donovani bisubunit Topoisomerase 1 **114-148**

6.1 Introduction **115-117**

6.2 Materials and methods **117-125**

6.3 Results **125-147**

6.4 Discussion **147-148**

References **149-170**

Publications & Proceedings **171-173**

Chapter 1

General Introduction

1.1 DNA Topoisomerases

“As enzymes, the DNA topoisomerases are magicians among magicians; they open and close gates in DNA without leaving a trace, and they enable two DNA strands or duplexes to pass each other as if the physical laws of spatial exclusion do not exist” – (Wang, 1991)

The enormous size of the double helical structure of the DNA molecules engenders a plethora of topological constraints arising during the DNA metabolic processes involving the relaxing of supercoiled DNA duplexes in the highly compacted nucleus of eukaryotic cells or the nucleoid of bacteria (Capranico et al, 2017). DNA topoisomerases are the highly conserved ubiquitous enzymes which are involved in alleviating the topological crisis of DNA by catalyzing a two-step trans-esterification reaction during DNA transactions like replication, transcription, chromosomal condensation, recombination and segregation in the eukaryotic, prokaryotic, archaeal and certain viral cells (Liu, 1989). The different topological forms of DNA are known to interconvert among themselves for exerting their effective biological functions in cells; these interconversions are catalysed by the DNA topoisomerases through DNA strand cleavage and religation activities (Wang, 1996) which allow topoisomerases to both disentangle as well as decatenate chromosomes. The indispensability of these enzymes coupled with the diverse range of activities performed by them, renders them effective chemotherapeutic targets for anti-cancer therapy, neurological diseases, immune disorders and antimicrobial remedy (Wang, 2002).

1.2 Discovery and coinage of “DNA Topoisomerases”

The discovery of the DNA double helix, the twisted-ladder structure of deoxyribonucleic acid (DNA), by James Watson and Francis Crick in 1953 marked a milestone in the history of science and paved the foundation for modern molecular biology, which is largely concerned with understanding how the DNA metabolic processes operate and how genes control the chemical processes within cells. The early research on unraveling the DNA structure failed to explicitly unearth the molecular mechanism involved in altering the DNA supercoiling; it suggested that the double helical structure posed several topological impediments on processes like replication, transcription, recombination and remodeling. However, the topological stress associated with supercoiled covalently-closed circular DNA molecule cannot be altered without the breakage of the covalent phosphodiester bond of one or both of the backbone strands. The order as well as extent of topological linkage of the two strands of the

DNA double helix is expressed by a numerical invariant known as linking number (Lk) which is a measure of the total number of times each strand of a duplex DNA molecule revolves around the other. It is known that under the normal physiological conditions, the most energetically stable form of a right handed double helix DNA molecule with “ n ” number of base pairs make one full turn after every 10.5 base pairs which consequentially results in a linking number (Lk^0) of $n / 10.5$; wherein the superscript describes the most stable state of the DNA molecule. Furthermore, a deviation of the linking number the Lk of a DNA molecule from its Lk^0 causes a state of strained, supercoiled or contorted (Vinograd et al, 1965) conformation and such DNA molecules which differ only by the virtue of their linking numbers are referred to as topological isomers or topoisomers. DNA topoisomerase occurs in diverse groups of organisms (Table 1.1) including prokaryotic as well as eukaryotic organisms. (Figure 1.1 and 1.2).

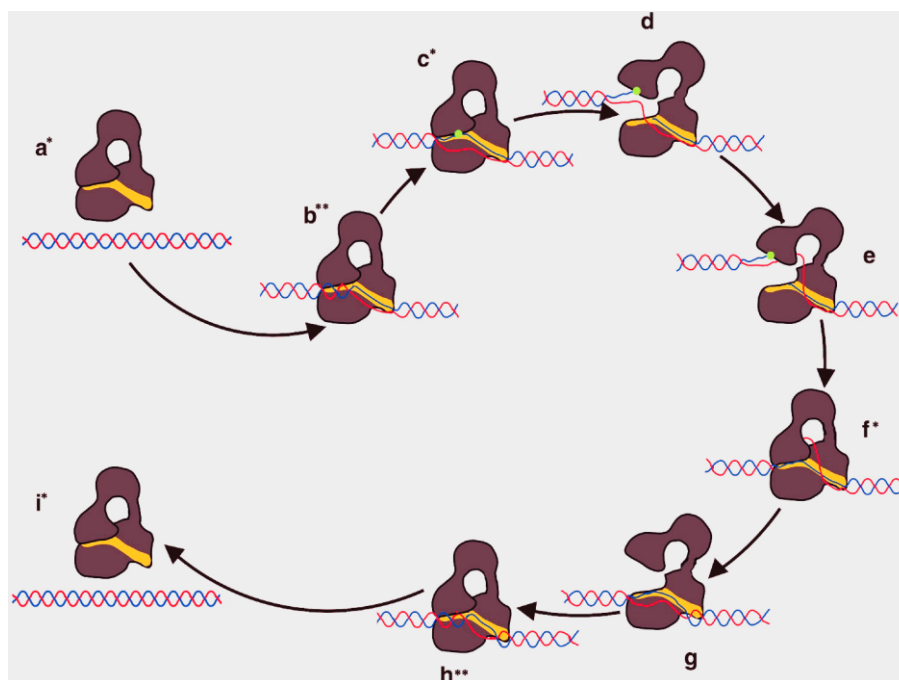


Figure 1.1 Proposed mechanism of relaxation by *E. coli* type IA Topoisomerase I. The proposed mechanism of relaxation of supercoiled DNA by a type IA topoisomerase involves several different transient intermediates involving conformational changes of both the enzyme (brown toroid with a yellow ssDNA binding region) and the DNA (red/blue molecule). The green dot represents the presence of the transient, covalent phosphotyrosine bond between the enzyme and the ssDNA. Single asterisks denote the conformational states where structural information was previously known, while double asterisks refer to the structures described here (a) Enzyme and supercoiled DNA prior to catalysis. The enzyme is in the closed conformation as found in the apo structure of both *E. coli* DNA topoisomerase I (b) The enzyme recognizes a ssDNA region and binds it in the DNA binding groove. This helps position the ssDNA for entry into the active site (c) Further entrance of the ssDNA into the protein triggers a conformational change to create a catalytically competent active site, as observed in the structure of the complex of topoisomerase III with ssDNA, and ssDNA cleavage occurs at the active site, via formation of a covalent bond between the 5'-phosphoryl and the hydroxyl of the active

site tyrosine, whereas the 3' end of the DNA remains noncovalently bound to the enzyme via the DNA binding groove (d) The enzyme opens, bridges the gap between the broken ends of the cleaved DNA, and allows passage of the other strand between the separated ends and into the hole of the toroid.(e) Enzyme-catalyzed strand passage of the second strand of DNA into the central hole of the enzyme. The nature of the conformational change may be illustrated by the structure of the 30 kDa fragment of *E. coli* topoisomerase I. (f) Following strand passage, the enzyme closes, trapping the passing DNA strand inside the toroid. Once the gate is closed, the cleaved strand is religated by the enzyme. The structure of the ssDNA/enzyme complex during religation is illustrated by the structure of the topoisomerase III complex. (g) The cycle is completed by the enzyme opening to release both the religated strand and the one that was passed through the gap. (h) The enzyme returns to a closed conformation after the ssDNA in the hole of the toroid has been released, but the religated strand remains bound to the DNA binding groove, resulting in a partial exit of the DNA. (Adapted from: Perry and Mondragon; Structure 2003)

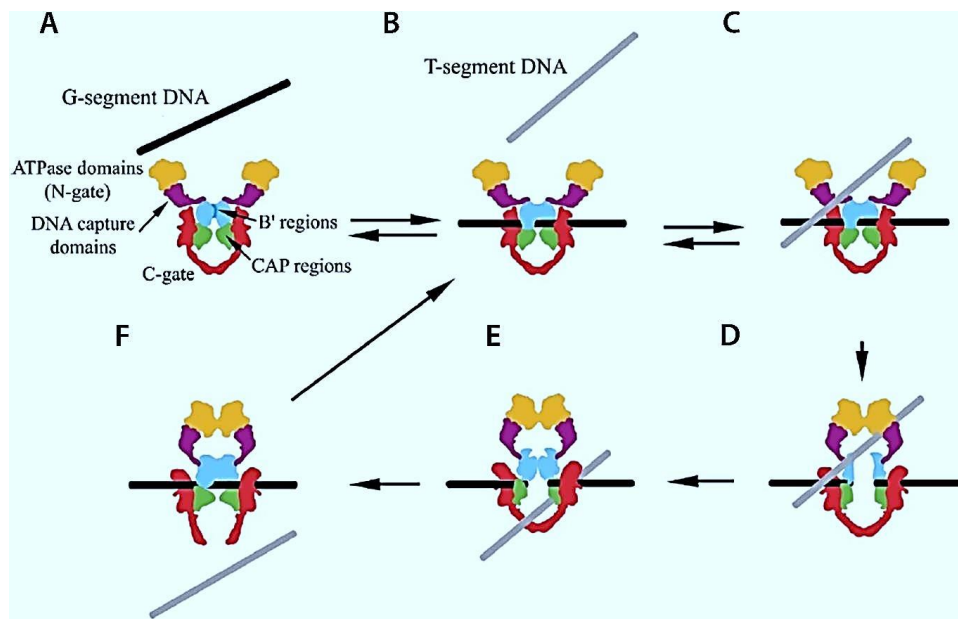


Figure 1.2 Proposed mechanism for DNA transport by type IIA topoisomerases. A schematic model of the type IIA topoisomerase is shown with the following color scheme: ATPase domains, orange; DNA capture domains, purple; B' domains corresponding to the C-terminal half of GyrB, cyan; CAP regions, green; and the remainder of the A' domains, red. The N-gate is shown in the open configuration in panels and is closed in panels **D-F**. The C-gate is closed in panels **A** and is open in panel **F**. The G-segment and T-segment DNAs are shown as black and gray rods, respectively (DNA not drawn to scale). (Image Source: Champoux, 2001).

The 'ω protein' was discovered in 1971 from *E. coli*, which was reported to convert the negatively supercoiled form of λ DNA rings to the relaxed form and catalyzes both the breakage and rejoining of DNA strands (Wang, 1971). Eight years later, the term 'DNA Topoisomerase' was coined to appellate this class of enzymes that catalyze the interconversion of DNA topoisomers (Liu & Wang, 1979). Since the DNA molecules are present mostly in the negatively supercoiled state inside the cell (Bauer, 1978; Vinograd et al, 1965) and harbor the contortions in the form of catenation and knotting (Cozzarelli et al, 1984), topoisomerases are indispensable for various the cellular DNA metabolic processes.

1.3 Types and functions of DNA topoisomerases

The five main subfamilies of DNA topoisomerases can be generally categorised, and each one has a distinctive structure and manner of catalytic action. On the basis of the number of strands they cleave, topoisomerases can be broadly divided into type I (which perform cleavage on single strand) and type II (which cleaves double strand) enzymes. Type I enzymes (Champoux, 2001) can further be classified into three groups, type IA (Wang, 1971), type IB (Champoux & Dulbecco, 1972) and type IC (Forterre et al, 1985), and, type II enzymes can be further classified as type IIA (Gellert et al, 1976) and type IIB (Bergerat et al, 1994). Type I enzymes make a single stranded nick on the duplex DNA while allowing the intact strand to pass through the nicked strand, thereby changing the linking number in steps of one in an ATP independent manner. The type IA enzymes remain associated with the 5' end of phosphate, whereas the type IB and type IC enzymes are known to remain associated with the 3' phosphate end of the Top-DNA intermediate. The type II enzymes hydrolyze ATP for their catalytic cycle which involves the passage of one of the DNA strands through a transient enzyme mediated break in the second duplex of the same DNA strand, thereby altering the linking number in steps of two (Figure 1.2).

In addition to the classifications of topoisomerases as described above, additional subclasses of topoisomerases based on structural dissimilarities of the proteins have been made. The prokaryotic eubacterial topoisomerases I and II, and the α and β forms of the eukaryotic mammalian topoisomerase II and III are considered to be paralogues arising through gene duplication (Champoux, 2001). Based on the isolation, characterization, and mode of action of topoisomerases, these enzymes can be broadly classified into topoisomerase I, topoisomerase II, topoisomerase III, topoisomerase IV, topoisomerase V, gyrase, reverse gyrase etc. (Table 1.1) (Champoux, 2001).

Enzyme	Type	Source	Subunit size (kDa) Composition
Bacterial topoisomerase I (ω protein)	IA	Bacteria (e.g. <i>E. coli</i>)	97 Monomer
Eukaryotic topoisomerase I	IB	Eukaryotes (e.g. human)	91 Monomer
Vaccinia virus topoisomerase I	IB	Vaccinia virus	37 Monomer
Topoisomerase III ^a	IA	Bacteria (e.g. <i>E. coli</i>)	73 Monomer
Reverse gyrase	IA	Thermophilic Archaea (e.g. <i>Sulfolobus acidocaldarius</i>)	143 Monomer
DNA gyrase	IIA	Bacteria (e.g. <i>E. coli</i>)	97 and 90 A ₂ B ₂
T4 topoisomerase	IIA	Bacteriophage T4	58, 51, and 18 2 copies of each subunit
Eukaryotic topoisomerase II	IIA	Eukaryotes (e.g. human topoisomerase II α)	174 Homodimer
Topoisomerase IV ^a	IIA	Bacteria (e.g. <i>E. coli</i>)	84 and 70 C ₂ E ₂
Topoisomerase VI	IIB	Archaea (e.g. <i>Sulfolobus shibatae</i>)	45 and 60 A ₂ B ₂

Table 1.1. DNA topoisomerases are found in viruses, eubacteria, thermophilic archaea, yeast, protozoa, plants and mammalian systems. DNA topoisomerases are named I to VI according to their discovery and are specially named, for example, gyrase (topo II type), reverse gyrase (topo I type), resolvase (topo II type), integrase (topo II type) and so on (Champoux, 2001).

1.4 Eukaryotic DNA topoisomerases

1.4.1 Type I topoisomerase

Eukaryotic topoisomerase through the passage of a single strand of DNA, are known to relax both the positively and negatively supercoiled DNA, changing the linking number associated with the DNA molecule. Topoisomerase I also catalyses the knotting and unknotting of closed single-stranded DNA rings or interwoven closed single-stranded DNA rings with complementary base sequences, in addition to its core role of relaxing supercoiled DNA. The

catalytic functions of DNA topoisomerase I can in general be categorised into several distinct steps which include binding to the DNA, followed by a single stranded cleavage of the duplex DNA, single stranded DNA passage, which is eventually succeeded by the religation and possibly turnover of enzyme (Gellert, 1981; Kirkegaard & Wang, 1978; Liu et al, 1976)(Figure 1.3 A).

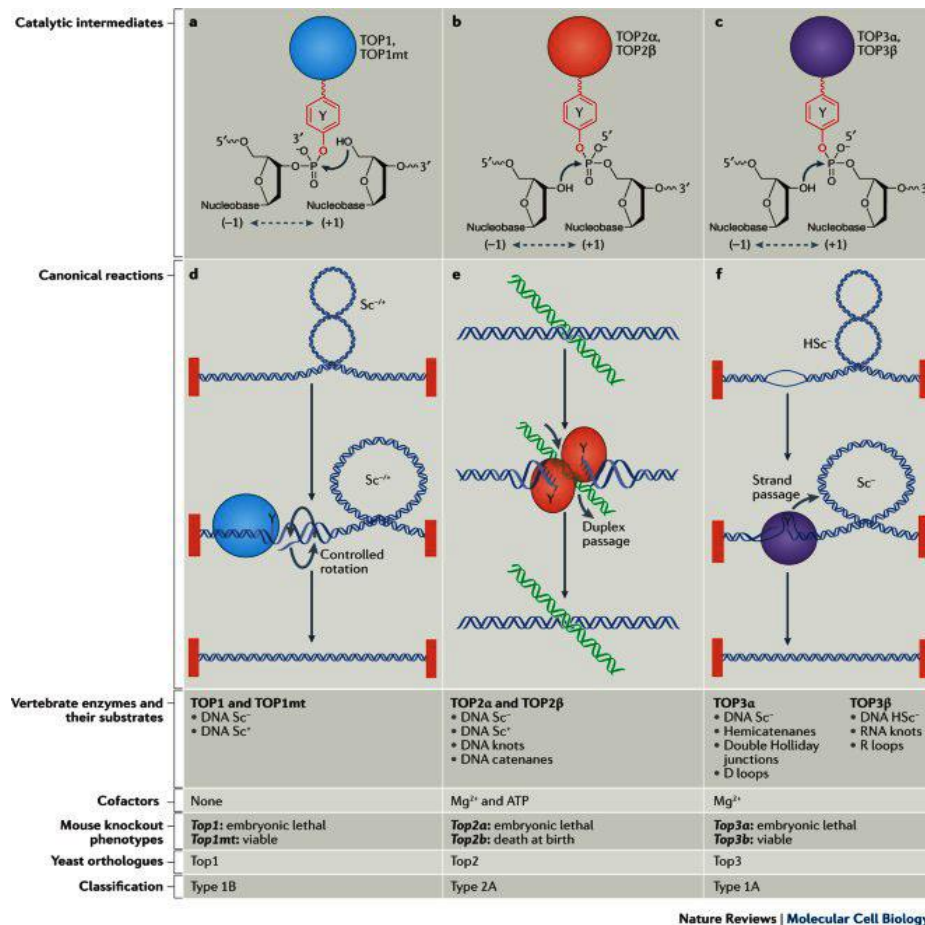


Figure 1.3. Overview of eukaryotic topoisomerases. (a-c) Topoisomerases act by cleaving the DNA phosphodiester backbone and forming transient covalent linkages between a Tyr residue and the DNA 3' end (Top1 enzymes) or 5' end (Top2 and Top3 enzymes). Resealing of the breaks is carried out by nucleophilic attack (arrows) of the 5'-hydroxyl end in the case of Top1 enzymes and the 3'-hydroxyl end in the case of Top2 and Top3 enzymes. Base stacking (dashed double-headed arrows) is crucial for the realignment of the DNA ends (like a molecular zipper) and their religation. **d)** Top1 enzymes relax both negative and positive supercoils (Sc^{-/+}) by nicking one strand and allowing controlled rotation of the broken strand around the intact strand. Top1 enzymes can religate non-homologous ends, thereby acting as DNA recombinases. **e)** Top2 enzymes function as homodimers to relax both negative and positive supercoils and to resolve catenanes and DNA knots, explaining their essential role in cell division, during which supercoiled circles form catenated daughter molecules. They cleave both DNA strands with a four base stagger, thereby directing a second duplex to pass through (duplex passage), and religating the DNA following the passage. They require both Mg²⁺ and ATP hydrolysis for their catalytic cycle. **f)** Top3 enzymes only relax hypernegative supercoiling (HSc⁻) by cleaving one of the two strands of DNA in regions where negative supercoiling promotes their separation and by passing the intact strand through the broken one. Mg²⁺ is a required metal cofactor. Top3β can act as an RNA helicase and resolve R loops. (Image Source: Pommier et al, 2016)

1.4.1A Nuclear DNA Topoisomerase IB

The eukaryotic topoisomerase IB was discovered from a different sources including rat liver, mouse LA9 cells, calf thymus as well as human KB cells (Champoux & McConaughy, 1976; Keller, 1975; Vosberg et al, 1975). The molecular weight of the enzyme was found to range from 60-90 kDa and was reported to catalyze the the relaxation of both positively and negatively supercoiled DNA (Champoux & Dulbecco, 1972; Tang, 1978). Mg^{2+} was found to have a stimulatory effect on the catalytic activity of Top IB, albeit these enzymes remain functional even in the absence of Mg^{2+} (Goto & Wang, 1984). The catalytic activity of type IB topoisomerase depends on its covalent association with the 3' end of DNA followed by DNA cleavage, strand passage/swivelling, religation followed by the turnover of the enzyme (Maxwell & Gellert, 1986; Osheroff, 1989) (Figure 1.3A). The most exhaustively studies type IB topoisomerases is the Human topoisomerase I (HTop1) which is composed of 765 amino acids harboring a relatively disordered and highly charged N-terminal domain (a.a. 1–214) (Stewart et al, 1996) responsible for stimulating the association with DNA (Lisby et al, 2001), a core domain (a.a.215–635) comprising of three major subdomains that wrap around the DNA double helix, a catalytic linker domain (a.a. 636–712) and the C-terminal domain that features the active site catalytic Tyr-723 residue (a.a. 713–765) (Figure 1.4) (Champoux, 2001; Stewart et al, 1998). The N- terminal domain regulates the enzymatic activity of the enzyme through the interactions of the triad of tryptophans (Trp- 203, 205, 206) for the anchoring and the subsequent controlled rotation of bound DNA during the course of the catalytic cycle of the enzyme (Stewart et al, 1998).

1.4.1B Mitochondrial DNA topoisomerase IB

Mitochondrial Topoisomerase I (Top1mt), a type IB topoisomerase is indispensable for the maintenance of mitochondrial integrity, the cellular respiration and energy metabolism. The presence of Top1mt was reported in mammalian cells like, mouse leukemia L cells and human leukemia cells. Top1mt activity demands the presence of divalent metal ions (Ca^{2+} or Mg^{2+}) and alkaline pH (Zhang et al, 2001). The gene encoding the *Top1mt* is located on human chromosome 8q24.3 and has been subsequently characterized from its corresponding polypeptide (Zhang et al, 2001). Similar to its nuclear counterpart Top1, Top1mt also comprises of four domains: N-terminal localization domain, a core domain, a linker domain, and C-terminal catalytic domain containing the tyrosine (Figure 1.4). The N-terminal domain of Top1mt is short (50 amino acid residues) and contains the mitochondrial localization

signal (MTS) (Zhang et al, 2001). The identity scores for the core, linker and C-terminal domains of nuclear Top1 and Top1mt polypeptides are high (73%, 53% and 75%, respectively) (Zhang et al, 2001).

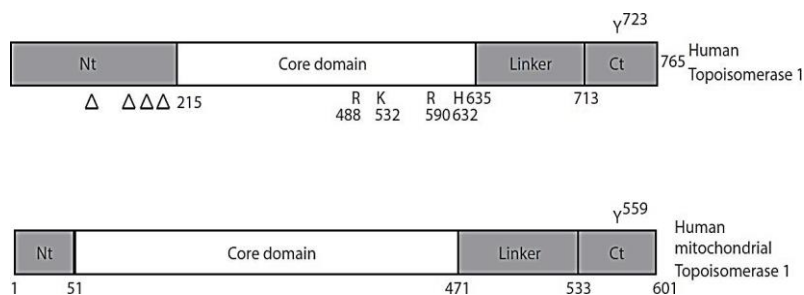


Figure 1.4 Schematic representation of the domain of organization for human monomeric topoisomerase. The alignments of the catalytic residues and nuclear localization signals for both the enzymes are indicated in the figure (Image Adapted from Das et al., 2006).

1.4.1.C Vaccinia topoisomerase I

The topoisomerase enzyme with the lowest molecular weight was isolated from the vaccinia virus which has a molecular size of 36 kDa (314 amino acids). Vaccinia topoisomerase has been classified under type IB subfamily owing to its stark resemblance with cellular Top1 both in terms of sequence homology of amino acids as well as the nature of polarity by which the enzyme remains attached to the DNA-phosphate linking to the cleaved DNA strand. Vaccinia topoisomerase enzymes have the property of recognition site specificity and can resolve Holliday junctions (Sekiguchi et al, 1996) much like tyrosine recombinases. Structurally, the two important units of vaccinia topoisomerase are the N-terminal domain (1-77 amino acids) which is involved in binding of the enzyme with its substrate i.e. the DNA molecule, thereby enhancing the processivity of the enzyme and the C-terminal domain (81-314 amino acids) (Sekiguchi et al, 2000; Sekiguchi et al, 1996).

1.4.1.D Parasite topoisomerase I

The ortholog of the type1B enzyme in kinetoplastid parasites has a unique feature (Figure 1.5). It possesses an unusual bi-subunit structure, completely different from all other eukaryotic type IB enzymes. The enzyme exhibits homology with the N-terminal and central core of other eukaryotic Top 1 while the C terminus is quite variable. Surprisingly, this open reading frame (ORF) is devoid of the SKINYL motif that supplies the catalytic tyrosine (Balaña-Fouce et al, 2014; Balaña-Fouce et al, 2008) in all other eukaryotic Top1. Existence of two such different subunits is evident in both *Leishmania* and *Trypanosoma* (Balaña-Fouce

et al, 2014; Balaña-Fouce et al, 2008; Brata Das et al, 2004; Das et al, 2008; Das et al, 2005; Das et al, 2006b; Das et al, 2006c). Both the subunits are indispensable for the parasite viability [45,46]. In *Leishmania donovani*, genes for large (LdTopIL) and small (LdTopIS) subunits are present on chromosome 34, encoding a 636-amino acid polypeptide with an estimated molecular weight of 73 kDa, and on chromosome 4, encoding a 262-amino acid polypeptide with a molecular weight of 29 kDa (Balaña-Fouce et al, 2014; Balaña-Fouce et al, 2008; Brata Das et al, 2004; Das et al, 2008; Das et al, 2005; Das et al, 2006b; Das et al, 2006c). LdTopIL is closely homologous to the core domain of human Top1. But the short NTD of this subunit is poorly conserved. The small subunit contains the phylogenetically conserved ‘SKXXY’ motif placed at the CTD of all other eukaryotic TopIB. This subunit harbours the conserved catalytic tyrosine residue (Brata Das et al, 2004; Das et al, 2008; Das et al, 2005; Das et al, 2006b; Das et al, 2006c). This Tyr222 residue attacks the phosphate group in the DNA backbone and forms the phosphotyrosine linkage. Along with Tyr, four amino acids (Arg314, Lys352, Arg410, and His453) are also involved in the catalytic activity. Arg410 activates Tyr222 for this nucleophilic attack. Arg314 and Lys352 act as general acids and aid in the transesterification reaction (Brata Das et al, 2004; Das et al, 2008; Das et al, 2005; Das et al, 2006b; Das et al, 2006c). In vitro reconstitution of the two recombinant bi-subunits LdTopIL and LdTopIS gives rise to the active bi-subunit LdTopIB (Brata Das et al, 2004; Chowdhury & Majumder, 2019; Das et al, 2008; Das et al, 2005; Das et al, 2006b; Das et al, 2006c). The binding stoichiometry is 1:1, mediated by protein–protein interaction between LdTopIL and LdTopIS. Deletion of 99 amino acids from the N terminus of LdTopIL disrupts its interaction with LdTopIS (Brata Das et al, 2004). This is probably due to the presence of polar residues in that region necessary for protein–protein interaction. Deletion of the first 39 amino acids from the N-terminus results in a protein with reduced cleavage activity. Interestingly, this mutant enzyme is more resistant to camptothecin (CPT) (Brata Das et al, 2004). This establishes that the NTD of LdTopIL steers both types of interactions (i.e., interaction between two subunits, as well as interaction with DNA by affecting non-covalent DNA binding). Moving on to LdTopIS, this subunit also has a role in controlling the dynamics of the protein. Amino acids 175–180 (RPPVV) of LdTopIS interact with a region (amino acids 525–581) of the LdTopIL and control the CPT sensitivity of the active bi-subunit enzyme (Chowdhury & Majumder, 2019). The most striking property of this unique enzyme is its association with ATP. This is the only type I enzyme discovered to date whose activity is stimulated by ATP (Chowdhury & Majumder, 2019). ATP binds with the arginine residue at the 190 position of LdTopIL and stimulates the rate of strand rotation.

However, ATP is not hydrolysed. This ‘unique’ enzyme is devoid of the clear linker domain otherwise present in the higher eukaryotes. This is compensated by the extended NTD of the LdTopIS. Though the biochemistry of this unique enzyme is well established, its subcellular localisation remains elusive. Reports suggest that multiple nuclear localisation signals (NLSs) exist only in LdTopIL but not in LdTopIS, resulting in the interaction of both the subunits in cytosol to form the active enzyme (Chowdhury & Majumder, 2019). The active enzyme is then trafficked both to nucleus and mitochondria. However, an opposite hypothesis claims that this enzyme localises exclusively to nucleus and two subunits are transported separately by the virtue of NLS sequences separately present in both the subunits; one in LdTopIL and two in LdTopIS (Chowdhury & Majumder, 2019). Similar to *Leishmania*, the large and small subunits of TopIB from *Trypanosoma brucei* are 90 kDa and 36 kDa proteins, respectively (Chowdhury & Majumder, 2019), and interact together to give the active enzyme.

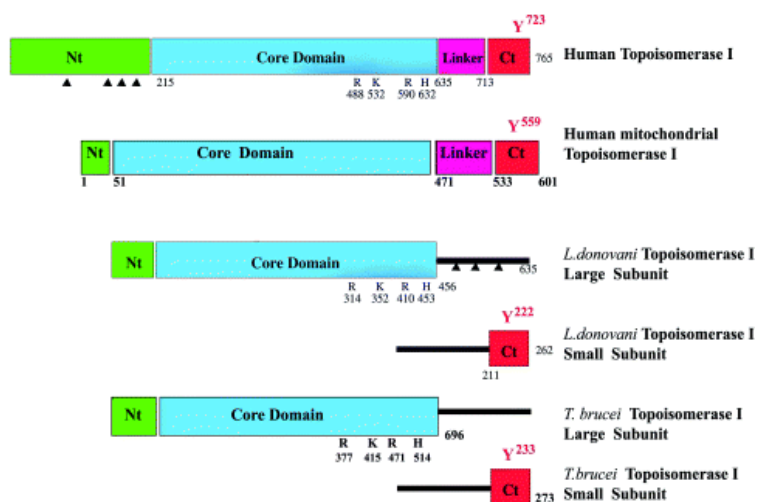


Figure 1.5. Schematic representation of the domain organization of monomeric human and *L. donovani* bisubunit topoisomerase I. The alignments of the catalytic residues and nuclear localization signals for both the enzyme are indicated in this figure. (Source: Das et al, 2006)

1.4.1.E Type IB DNA topoisomerases: Functional mechanism

Topoisomerase IB plays participate in a diverse array of cellular activities by removing the positive supercoils situated ahead or behind the replication fork during DNA replication (Champoux, 2001; Wang, 1996) and allows the smooth functioning of the replication elongation (Kim & Wang, 1989) (Figure 1.3). DNATop1 has been implicated in all stages of the embryonic development in various organisms across the lines of evolution including *Drosophila melanogaster* (Zhang et al, 2000). The occurrence of eukaryotic DNA topoisomerase I in euchromatin regions of active transcription of genome has been extensively documented (Nitiss, 1998; Wang, 1996) and these associations involve the N-terminal region of the type IB DNA topoisomerase enzyme (Shaiu & Hsieh, 1998).

1.4.2 Type II DNA topoisomerases

The type II eukaryotic topoisomerases are known to exert their functions by introducing DSBs in the phosphodiester-backbone of the DNA molecule followed by a complex ATP dependent dsDNA passage mechanism altering the linking number in steps of two (Osheroff, 1989; Vosberg, 1985). This enzyme unique to the eukaryotic organisms can be considered as the homolog of bacterial DNA gyrase and is a single subunit protein which is functionally analogous to the bacterial dimeric counterpart. The N-terminal and C-terminal domains of the protein are homologous to GyrB (ParE) and GyrA (ParC) respectively. DNA cleavage is catalyzed by the GyrA homologue whilst the GyrB homologue is involved in ATP binding. Relaxation of both negatively as well as positively supercoiled DNA can be achieved by the action of this enzyme (Osheroff et al, 1983). Furthermore, this class of enzyme is capable of interconverting various DNA topological forms by catenation in addition to decatenation (Goto & Wang, 1982; Hsieh & Brutlag, 1980) and knotting as well as unknotting of double stranded DNA (Figure 1.6) (Hsieh, 1983; Liu et al, 1980). The existence of two isoforms of topoisomerase II namely TopII α isoform and the TopII β isoform have surfaced from numerous studies on topoisomerase II in vertebrates including human (Drake et al, 1987), mouse (Adachi et al, 1992), rat (Park et al, 1993; Tsutsui et al, 1993) and hamster (Dereuddre et al, 1995).

1.4.2.A Roles of DNA Topoisomerase II α & topoisomerase II β

Human Top II α isoform is a 170 kDa polypeptide which has been isolated and extensively characterized (Tan et al, 1992). Although it is known to bear a high degree of similarity with the Top II β isoform, the two isoforms are genetically distinct and display differential pattern of expression. *In vivo* reports have demonstrated that Top II α is expressed in tissues that are in developing stage (Capranico et al, 1992; Holden et al, 1990); the Top II β is found to be expressed in cells of the somatic tissues (Galante & Muniyappa, 1996); (Juenke & Holden, 1993). Top II β isoform has a molecular weight of 180 kDa (Tsai-Pflugfelder et al, 1988). Cross-species blot hybridization has demonstrated the existence of two Top2 genes in avian cells which are closely related (Tan et al, 1992).

1.4.2.B Type II DNA topoisomerases: Mode of action

DNA topoisomerase II might act as a suitable substitute for DNA topoisomerase I in mitigating the gene transcription related topological problems of DNA. The event of the

convergence of the two replication forks generates distinct topological problems (Figure 1.3 B) when the unreplicated segment of parental DNA becomes increasingly shortened; this calls for a type IIB DNA topoisomerase which can then complete the event of final segregation of the newly replicated pair of DNA. Previous studies in the unicellular eukaryotes *S. cerevisiae* and *S. pombe* advocate that type II DNA topoisomerases are quintessential in chromosome segregation event (Nitiss, 1998); (Wang, 1996). Interestingly, in mitotic yeast cells without type II DNA topoisomerase enzymes, the longer chromosomes appear to be more likely to suffer loss or breakage (Spell & Holm, 1994). Also, the mammalian type II topoisomerase have also been reported to stimulate irregular recombination events in both *in vitro* conditions as well as within the cells.

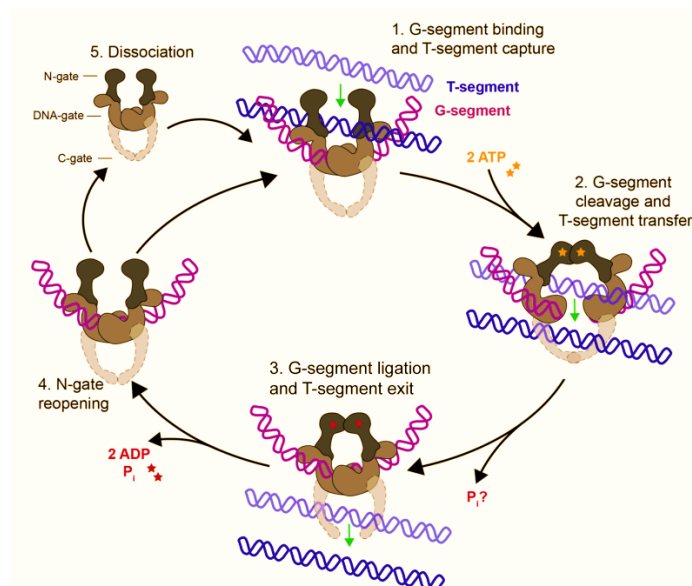


Figure 1.6. Mechanism of strand passage by type II topoisomerases (1) G-segment is bound at the DNA-gate and the T-segment is captured. (2) ATP binding stimulates dimerization of the N-gate, the G-segment is cleaved and the T-segment is passed through the break. (3) The G-segment is re-ligated and the T-segment exits through the C-gate. For type IIB topos, there is no C-gate so once the T-segment passes through the G-segment, it is released from the enzyme. (4) Dissociation of ADP and Pi allows N-gate opening, a scenario where the enzyme either remains bound to the G-segment, ready to capture a successive T-segment, or (5) dissociates from the G-segment. (image source: Adapted from Wikimedia)

1.4.3 Type III DNA topoisomerases

Eukaryotic DNA topoisomerase III (otherwise referred to as Top III) was first isolated and characterized in *S. cerevisiae* as a gene which is essential for the suppression of recombination event within repetitive genes (Wallis *et al.*, 1989). These enzymes are found to occur both in prokaryotes as well as in eukaryotes and are classified as Type IA enzymes due

to their specificity towards single stranded substrates, requirement of Mg^{2+} as a cofactor and formation of a 5'-phosphotyrosyl enzyme intermediate during manifestation of catalytic activity (Figure 1.3). Top III has the ability to cause relaxation of negatively supercoiled DNA without any utilization of ATP. Amongst vertebrate organisms, Top III α in addition to Top III β appear to be the two isoforms of Top III, which are most likely generated by duplication of genes.

1.4.3.A Topoisomerase III α & topoisomerase III β

In humans, Top III α (also referred to as HTop III α) encoded by the *Top IIIA* gene is located within chromosome 17. It harbors two initiation codons for protein subunits which are made up of 1,001 and 976 amino acids (Li & Wang, 1998). HTop III α occurs within both the nucleus as well as the mitochondria while the HTop III β is encoded by the *Top IIIB* gene, which is localized to chromosome 3. Topoisomerase III β consists of 862 amino acids in humans (Tan et al, 1992). Top III β is considered to be a potent candidate for anticancer chemotherapeutic target owing to the different mutations within the *Top IIIB* gene implicated in the development of resistance towards drugs. A previous study has demonstrated that the deletion of mouse topoisomerase III β gene leads to reproductive infertility and shortened lifespan (Kwan et al, 2003).

1.4.3.B Type III topoisomerases: Mode of action

Topoisomerase III is known to facilitate the elongation of nascent DNA chain in a bi-directional manner (Figure 1.3) and helps in decatenation of replicating DNA molecules (Figure 1.3). Additionally, Topoisomerase III also abrogates recombination processes within the wrongly paired single stranded DNA during replication. Furthermore, it can also function as a RNA topoisomerase. Yeast cells express a discrete topoisomerase III enzyme which is encoded by the Top III gene and Top III knockout *S. cerevisiae* cells are characterised by a slow growth rate coupled DNA damage response defects during the S phase of the cell cycle but remain viable plausibly by other compensatory mechanisms (Wallis et al, 1989). On the other hand, Top III $\Delta S. pombe$ are lethal and fail to segregate daughter chromosomes during mitosis phase of cell cycle (Goodwin et al, 1999). Topoisomerase III α directly interacts with the RecQ family of DNA helicase enzymes, which are essential in order to maintain genomic stability. RecQ helicases act in coordination with DNA topoisomerase III α which occurs both in prokaryotes as well as eukaryotes and this interaction recruits topoisomerase III α to its site

of action (Wallis et al, 1989). As mentioned previously, HTop III β functions as a RNA topoisomerase and this is achieved by binding with mRNA translation complex and interacting with a RNA-binding protein, FMRP, in order to facilitate synapse formation processes. The deletion of Top III β gene has been implicated in the incidence of schizophrenia.

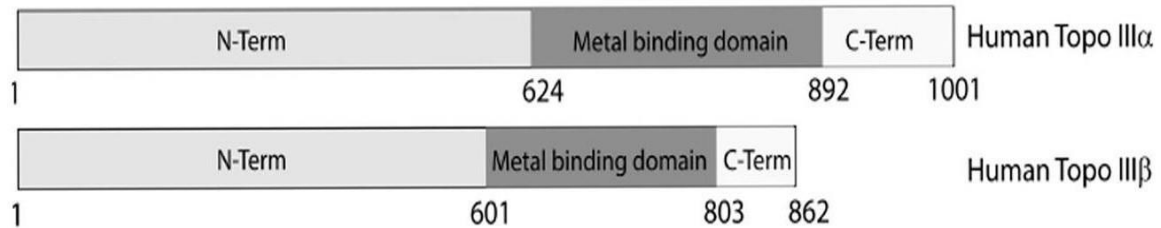


Figure 1.7. Schematic representation of the domain organization of monomeric human topoisomerase III α and β . The alignments of the N-terminal and Zn (III) binding domain and C-terminal for both the enzymes are indicated in the Figure. (Adapted from Champoux 2001)

1.5 Functional regulation of DNA topoisomerase enzymes

1.5.1 Regulation of Topoisomerase at the transcriptional level

DNA topoisomerases are a set of essential enzymes that guarantee cellular viability and uphold essential cellular activities. Therefore, it is crucial to accurately regulate enzymatic activity and maintain these enzymes' optimal functionality. Cellular mechanisms regulate activity at both the transcriptional and post-translational levels to achieve this tight control. In *E. coli* it has been observed that the levels of topoisomerase IA and gyrase within cells are homeostatically regulated in a bid to regulate the mean level of supercoiling of intracellular DNA. Relaxation of intracellular DNA activates transcription of GyrA and GyrB (Menzel & Gellert, 1987). Moreover, a higher level of negative supercoiling is thought to escalate the expression of Top1 gene (Tse-Dinh & Beran, 1988). The prevailing environmental conditions are also known to regulate the expression of these genes as demonstrated in an early experiment wherein cold shock leads to increased synthesis of Gyr A protein, which is possibly mediated by the binding of a cold shock positiveregulator to the gene promoter (Tse-Dinh & Beran, 1988). Furthermore, studies dealing with mammalian DNA topoisomerase have demonstrated that the level of activity of Top II α is correlated with proliferation of cells (Heck & Earnshaw, 1986).

1.5.2 Regulation of Topoisomerase at the post-translational level

Several PTMs have been identified in DNA topoisomerases which includes phosphorylation, SUMOylation, poly (ADP)-ribosylation, and ubiquitination which can occur *in vivo* as well as *in vitro* conditions and are responsible for their controlled regulation of the activity.

1.5.2.A Phosphorylation

Phosphorylation has been implicated in the regulation of DNA topoisomerases (Durban et al, 1983; Durban et al, 1981; Mills et al, 1982; Pommier et al, 1990) both for the expression of DNA topoisomerases as well as for the catalytic activity of the enzyme. The relaxation activity of DNA topoisomerase I has been shown to be increased by phosphorylation on serine and threonine residues and treatment with phosphatase enzymes down tuned the same activity (Durban et al, 1983; Durban et al, 1981; Mills et al, 1982; Pommier et al, 1990). Moreover, phosphorylation of Top 1 mediated by c-Abl-tyrosine kinase appears to be functionally important for activity of Top1 and sensitivity towards chemical agents that can act as Top1 poisons (Yu et al, 2004). Furthermore, phosphorylation of DNA topoisomerase II has also been reported to enhance its enzymatic activity in several earlier *in vitro* studies ((Yu et al, 2004); (Sander et al, 1984) (Ackerman et al, 1985).

1.5.2.B Poly (ADP) ribosylation

Poly(ADP-ribosylation) (PARylation) is mediated by Poly(ADP-ribose) polymerase (PARP) proteins, which are a class of ADP-ribosyl transferase enzymes that transfer ADP-ribose units from donor NAD⁺ molecules onto their target proteins which include topoisomerase enzymes as well. Poly-(ADP) ribosylation of topoisomerases take place both *in vitro* experimental conditions (Das et al, 2016).

1.5.2.C SUMOylation

SUMOylation involves small ubiquitin like modifier proteins commonly referred to as SUMO-1 and have been largely implored in the stabilization event of the topoisomerase I and II during stress either for the purpose of sequestering it from a specific locus or in order to demarcate it for degradation. SUMO1 conjugates to the ϵ -amino group of lysine residues in topoisomerase enzymes and thus regulate its supervisory function either by means of mono- or poly-ubiquitination (Flotho & Melchior, 2013).

1.5.2.D Ubiquitination

Ubiquitination of a protein through the ϵ -amino group of lysine residues within the amino acid sequence enables the marking of the same for proteasomal degradation. However, the conjugation of ubiquitin molecules to topoisomerase I or II not only targets it to degradation but also coordinates other important functions (Mao et al, 2000).

1.6 Targeting DNA topoisomerases for cancer therapy

It has been discovered that DNA topoisomerases are overexpressed in a variety of cancers, making them potential targets for anticancer therapeutics. When a DNA molecule is cleaved, the active site tyrosine residue makes a nucleophilic attack on the phosphodiester bond, which causes the enzyme to bind covalently to the 3' end of the cleaved DNA (in the case of Top1 enzymes) or the 5' end (in the case of other topoisomerases). Different topoisomerases have different mechanisms by which they relax the DNA supercoiling. Under normal physiological conditions, the rate of religation is much more rapid in comparison to the rate of cleavage which underlines the reason for the transient nature of these covalent enzyme-DNA cleavage complexes and their short half-life. As a result, the cells are capable of tolerating them. Nevertheless, an increased lifespan of these breaks can lead to the manifestation of a vast array of harmful side effects, including deletions, mutations, chromosomal aberrations, and insertions (Froelich-Ammon & Osheroff, 1995).

1.6.1 Classification of topoisomerase inhibitors: Topoisomerase poisons and Catalytic inhibitors

There are two broad classes of inhibitors of Topoisomerases which differ by their mechanism of inhibition. The vast majority of therapeutic strategies that specifically target topoisomerases trap the covalent enzyme-DNA complexes (Topcc's). The widely recognized topoisomerase drugs can be categorized into two classes namely, class I and class II (Capranico et al, 1998; Wassermann et al, 1990). The class I drugs include '*topoisomerase poisons*' whilst on the other hand the class II drugs are known as '*catalytic inhibitors*'. The class I '*topoisomerase poison*' drugs exert their function by stabilizing the topoisomerase-DNA covalent complexes and includes alkaloids (Hsiang & Liu, 1988), anthracyclines (Chow et al, 1988); Wassermann *et al.*, 1990), actinomycins, ellipticines (Arguello et al, 1998), epipodophyllotoxins (Chow et al, 1988). Eukaryotic Top1 inhibitor camptothecin and Top2 inhibitors like etoposide, amsacrine, doxorubicin, and teniposide fall in this category.

The class II ‘*catalytic inhibitors*’ drugs, on the other mediate their function by interfering and disrupting DNA topoisomerase catalytic function without actually entrapping the DNA-enzyme covalent complexes (Figure 1.8).

1.6.2 Camptothecins and non camptothecins Top1 inhibitor: recent developments and trends in anticancer therapy

Camptothecin (CPT) and its clinical derivatives have been FDA- approved as Top1-targeted anticancer drugs and mediate their function by selectively binding at the interface of the Top1 and DNA in order to generate a stable ternary complex which in turn reversibly entrap macromolecular complexes and hinder the religation event of the strand-passing reaction. Camptothecin was originally isolated from a Chinese tree known as *Camptotheca acuminata*, and it was characterized by the National Cancer Institute (NCI) at NIH, USA (Pommier, 2013). The vigorous anticancer activity of CPT was known for almost 20 years prior to the actual discovery of its mode of action. Water-soluble semisynthetic derivatives of CPT such as, topotecan and irinotecan which have also been subsequently developed in the years following the discovery of CPT. Topotecan is often recommended for treatment of ovarian cancer and recurrent small cell lung cancer (SCLC). Furthermore, SN-38, an active metabolite of the prodrug irinotecan is widely prescribed in cases of gastrointestinal (colorectal and gastroesophageal) malignancies and also for treatment of primary brain malignancies, cervical cancer, as well as sarcomas (Figure 1.8). However, there are discrete dose limiting toxicities associated with camptothecins like bonemarrow toxicity and severe diarrhoea. Furthermore, all of the CPT derivatives have well- defined disadvantages which results from the rapid inactivation of the drugs due to E-ring opening at physiological pH which involves the spontaneous conversion of α -hydroxylactone to camptothecin carboxylate that has a high serum albumin affinity. In order to overcome the aforementioned limitations of CPT derivatives, these compounds have been coupled with macromolecular core. Eirinotecan pegols (NKTR-102) is one such sort of compound and it is currently in advanced Phase III clinical trials for application in treating ovarian cancer, breast cancer, along with colon cancers. It is not possible to overcome the chemical instability of the camptothecin and its derivatives as the intact α -hydroxylactone E-ring is indispensable for entrapping of Top1 DNA cleavage complex. Non-CPT Top1 inhibitors have the ability to overcome the issue of E-ring instability of camptothecins and are currently in various phases of clinical development (Pommier, 2013). Recently, it was discovered that a group of compounds called

indenoisoquinolines can cause cytotoxicity across as many as 60 diverse cancer cell lines (Pfister et al, 2009). These compounds were discovered through the screening process from the NCI developmental program drug database. Indotecan (LMP400) and indimitecan (LMP776) are two such derivatives which are also currently undergoing clinical trials. In addition to their chemical stability, the indenoisoquinolines confer numerous advantages over the camptothecins as because i) they are capable of targeting at additional genomic sites, ii) their covalent cleavage complexes are far more stable in comparison to camptothecins, iii) they are capable of overcoming multidrug resistance efflux pumps and iv) they also produce a low bone marrow suppression with equivalent antitumor activity (Pommier & Cushman, 2009).

1.6.3 Targeting Topoisomerase 2 for anticancer therapy

Top 2 targeted drugs can also act as by inhibiting the enzyme through disrupting the catalytic activity or by entrapping the Top 2 cleavage complex (Top2cc) through interfacial stacking as well as impeding the religation event. The second class of the inhibitors are referred to a Top2 poisons and are widely recommended for the vast range of efficiency, chemical diversity, sequence selectivity in addition to their ability to entrap concerted Top2 cc, where the two strands of DNA are concurrently cleaved with an overhang of four canonical base pairs. Initially anthracycline daunorubicin (daunomycin) was isolated from soil bacteria *Streptomyces* and for the purpose of treatment of patients with acute leukemia. Doxorubicin (adriamycin) is widely prescribed in cases of first line breast cancers, anaplastic thyroid, and soft tissue sarcomas, in addition to multiple myeloma therapy (Figure 1.8). To overcome the adverse side-effects of doxorubicin an active isomer Epirubicin (4'-epi- doxorubicin) has been developed (and has also been approved by FDA), and it is used for the treatment of breast cancers, esophageal cancers, in addition to gastric cancers. The most selective Top 2 cc-targeted drug, currently in the clinical use, is etoposide. A new derivative of anthracyclines, anthracenedione mitoxantrone (Novantrone), a highly effective intercalator of DNA as well as Top2cc poison has also been developed and has been approved by the FDA for the purpose of treatment of prostate cancer. Voreloxin is currently in phase II of clinical development, and is utilized in combination with cytarabine for the purpose of treatment of patients with refractory acute myeloblastic leukemia. Several other potent and effective anticancer therapeutic agents have been developed such as C-1311 (Symadex) which is an iminodazoacridinone derivative which has DNA interaction property. Catalytic Top2

inhibitor ICRF-187 (Dexrazoxane) is applied as a modulator of anthracyclines. Recent studies have shown that sodium salicylate can act also as a catalytic inhibitor of Top2 (Pommier, 2013).

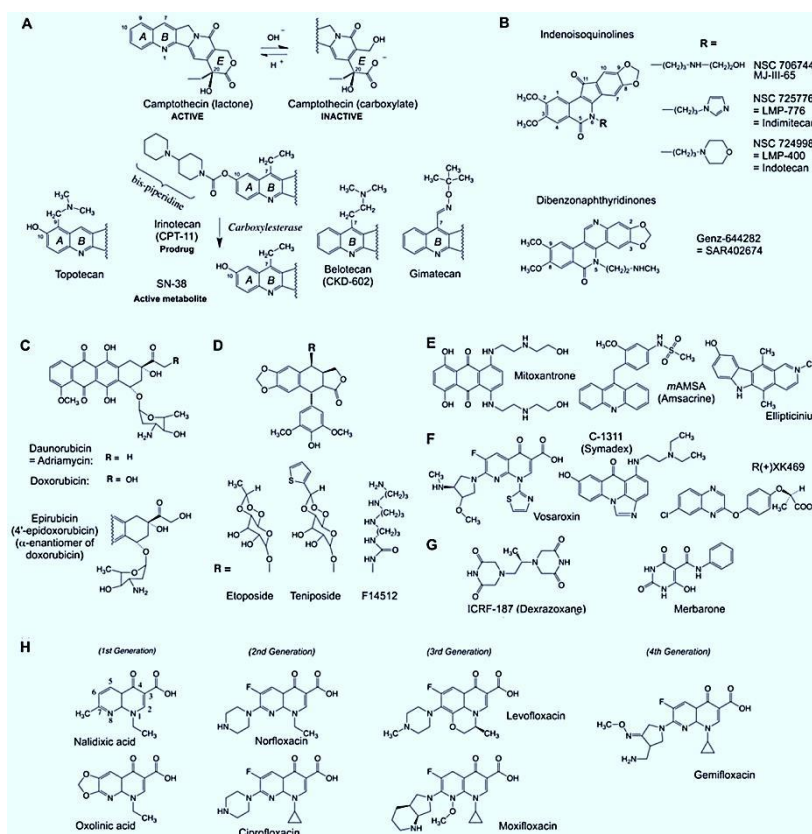


Figure 1.8. Structure of anticancer and antibacterial topoisomerase inhibitors. **A.** Camptothecins. **B.** Non-camptothecin Top1 inhibitors in clinical trials. **C.** Anthracyclines. **D.** Demethylepipodophyllotoxin derivatives, including the clinical trial drug F14512 with its spermine side chain. **E.** Other Top2cc-targeted intercalative drugs. **F.** Three Top2cc-targeted drugs in clinical trials in addition to F14512 shown in panel D. **G.** Top2 catalytic inhibitors. **H.** Quinolone antibacterials (Image Source: Pommier *et. al.*, 2013).

1.7 DNA topoisomerases induce DNA damage

The dynamic and breathing nuclear genome is extremely prone to several types of genomic assaults including, numerous endogenous as well as exogenous damages and base misincorporations (the most commonly occurring damages being oxidative base lesions), DNA nicks and abasic sites (Barnes & Lindahl, 2004; Lindahl, 1993).

1.7.1 Role of trapped Topccs in endogenous or exogenous DNA lesions

The normally short-lived topoisomerase-DNA cleavage complexes (Top1cc and Top2cc) are

often stabilized by binding of interfacial drug molecules at the enzyme–DNA interface causing misalignment of the 3'-hydroxyl DNA ends, thereby preventing the religation event (Pommier, 2013).

1.7.2 Replication events and Topoisomerases

The short-lived transient reversible cleavage complexes that are generated as Topoisomerase reaction intermediates can also be transformed into DNA lesions after processing by DNA as well as RNA polymerases. Inhibition of DNA synthesis takes place within a few minutes after CPT treatment either as result of direct collision of replication forks with Top1 cleavage complexes (Top1cc), or, can also result from indirect arrest of replication by activation of S-phase checkpoint. Stable Top1cc may lead to generation lethal double-strand breaks (DSBs). Camptothecins are also capable of inducing 'replication run-off' of the genome by producing breaks in the DNA double-strand upon collision with the replication or transcription machinery or through irreversible Top1cc adducts. Replication fork reversal at these blocking sites leads to generation of 'chicken foot' (Ray Chaudhuri et al, 2012), which in turn might be resolved by the MUS81–EME1 endonuclease enzymes.

1.7.3 Transcription events and Topoisomerases

The transcription complex machineries are often halted upon collision with stable Top1ccs as Top1 controls initiation of transcription by interacting with TATA binding proteins and additionally activate RNA splicing factors of the SR family. The transcription of both the nucleoplasmic (mRNA) and nucleolar (rRNA) RNA are abrogated by CPT treatment. As mentioned previously, Top1 poisons competently block transcription elongation, which accounts for a significant impact of TOP1cc on long and on frequently transcribed genes (King et al, 2013). Even though inhibition of transcription is significantly contributing towards the anticancer activity of topoisomerase poisons, it may have potential therapeutic applications for neurological disorders and immune diseases, as has been verified in animal model studies in case of Angelman syndrome. In a similar manner, suppression of transcription by Top1 inhibitors has been shown to protect mice against viral as well as bacterial infection by suppressing the fatal over expression of inflammatory immune response genes (Rialdi et al, 2016).

1.8 Repair pathways for Top1-mediated DNA damage

Several mechanisms operate in the cells to repair the Top1-associated DNA damage repair pathways which can be listed as: a) Tyrosyl-DNA phosphodiesterase (TDP1) dependent Top1 excision, b) the endonucleases pathway and c) Reversal of the covalent Top1-DNA complexes by 5'-end religation. Figure 1.9 and 1.10 schematically demonstrates the possible pathways that can mediate the repair of Top1-associated DNA damages.

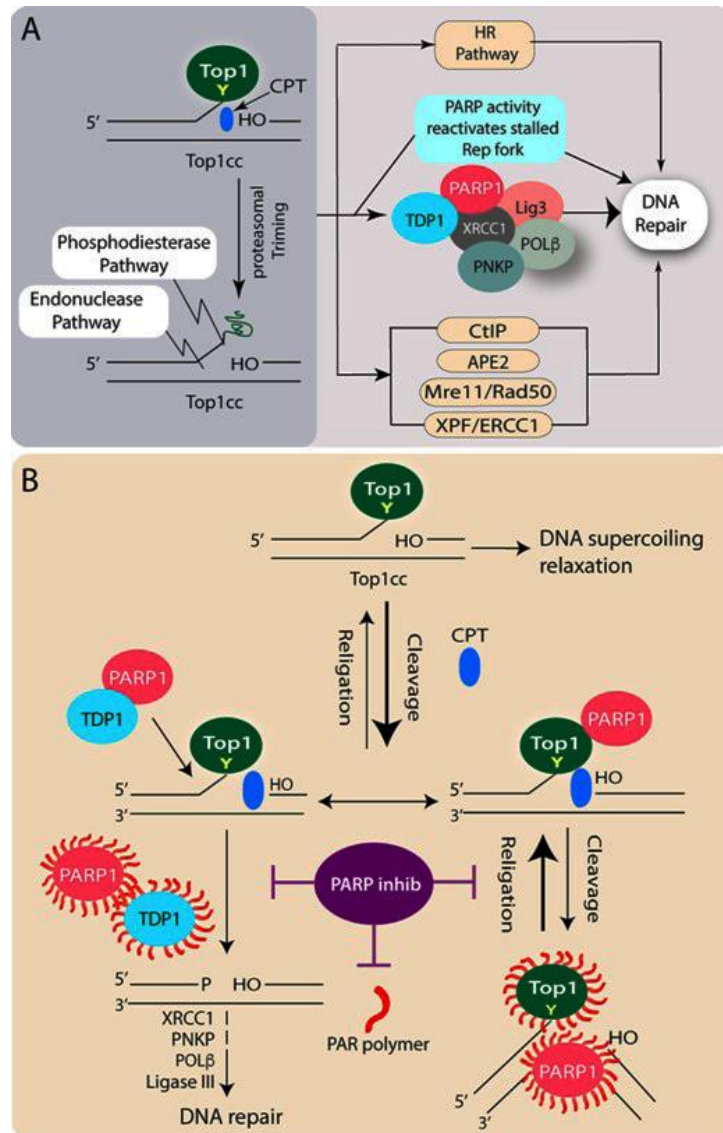


Figure 1.9. Induction of DNA damage with trapped Top1-DNA cleavage complexes (TOP1cc) and repair pathways. (A) Top1 cleaves one strand of duplex DNA via the nucleophilic attack of its active site tyrosine on the DNA phosphodiester backbone to yield a 3'-phosphotyrosyl bond. The short-lived covalent Top1-DNA cleavage complex (Top1cc) is readily trapped by Top1 poisons i.e. Camptothecin (CPT; blue) which binds in the interface of Top1-DNA complexes, stabilizes Top1cc, and inhibits the Top1-religation reaction. Scheme illustrating the repair pathways involved downstream to the proteasomal degradation of trapped Top1cc's, which can be repaired in cells by broadly three pathways: (i) phosphodiesterase pathway: Excision of Top1 by TDP1 which is coupled with PARP1. PARP1 also reactivates stalled replication fork encountered by transient Top1cc; (ii)

Endonuclease pathway: DNA cleavage by 3'-flap endonucleases such as XPF-ERCC1, Mre11/Rad50, CtIP and APE2; (iii) The Top1cc associated DSBs generated by replication run-off, results in a Top1-linked double-stranded end (DSE) which are repaired by homologous recombination repair. (B) PARP inhibits the double-edged sword: Killing Top1 activity and inhibiting TDP1-mediated Top1cc repair. The short-lived covalent Top1-DNA cleavage complex (Top1cc) is readily reversed and facilitates DNA supercoil relaxation. The bold arrow indicates the shift in the cleavage/religation equilibrium in the presence of CPT (blue). PARylation of Top1 helps in the religation of the CPT-induced Top1 cleavage complex (Top1cc). While PARP coupling with TDP1 stimulates the excision of Top1cc by the phosphodiesterase activity of TDP1 and facilitates DNA repair. PARP inhibitors (purple) in combination with CPT abrogate Top1 and TDP1-PARylation, impair the repair of CPT-induced Top1cc, and promoting DSBs and cell death. (Source: *Paul Chowdhuri and Das, NAR Cancer 2021*)

1.8.1 The Tyrosyl-DNA phosphodiesterase (TDP1) enzyme dependent pathway

1.8.1.A Tyrosyl-DNA phosphodiesterase (TDP1) enzyme

Following the observation that the enzymatic activity of selectively hydrolyzed phosphotyrosyl bonds between a tyrosine residue and the 3' end of DNA, tyrosyl-DNA phosphodiesterase (TDP1) was found in yeast *S. cerevisiae* cell extracts in 1996 (Yang et al, 1996). The homozygous mutation in the *Tdp1* gene, which results in a histidine to arginine mutation [H493R] within the active site of *Tdp1*, causes the incredibly rare autosomal recessive neurodegenerative condition known as spinocerebellar ataxia with axonal neuropathy (SCAN1) in humans, which has a physiological significance (Takashima et al, 2002).

i. Structure and function of TDP1:

Human TDP1 is a 68-kDa protein (608 amino acid residues) which consists of two domains (Figure 1.11). Sequence analysis studies of active site composition and conservation of sequence motifs led to the conclusion that *Tdp1* belongs to the phospholipase D superfamily (Interthal et al, 2005; Interthal et al, 2001) which includes a varied collection of enzymes, which cleave phosphodiester bond in biomolecules ranging from phospholipids to DNA. The N-terminus domain regulates protein stability, recruitment in addition to enzymatic activity. On the other hand, the C-terminus catalytic domain harbours two catalytic HKN motifs (H493K495N516 and H263K265N283), a distinct characteristic of phospholipase D (PLD) superfamily of proteins. However, TDP1 significantly differ from the other PLD family members as because the aspartates in the HKD motifs are replaced by asparagines, which can be therefore be referred to as a HKN motif. A mutation in the H263 residue leads to catalytic inactivation of TDP1, whilst mutation of H495 K265, or K497 sites leads to the impairment of enzymatic activity (Interthal et al, 2005; Interthal et al, 2001); (Davies et al, 2002a)).

ii. Mechanism of catalysis of TDP1:

TDP1 catalytic activity is a two-step process which is independent of any metal or nucleotide cofactors. The first step involves a nucleophilic attack by the H263 from N-terminal domain carries on the substrate phosphorous atom and causes cleavage of the phosphodiester bond. Next, the H493 residue of C-terminal HKN motif functions as a general acid. H493 acts as a proton donor to the tyrosine of the peptide-leaving group (Figure 1.12). This leads to the formation of a transiently fleeting covalent phosphoamide bond between H263 and the 3'-end of the DNA (Figure 1.10 B). The second step of the catalytic reaction involves the H493 which acts as a general base to activate a neighbouring water molecule which in turn hydrolyses the phospho-enzyme intermediate (Figure 1.10 C) (Davies et al, 2002b). This step has been further validated by *in vitro* biochemical assays with the SCAN1 H493R mutant, that results in the accumulation of Tdp1-DNA covalent intermediate (Interthal et al, 2005). Thus, the final product after TDP1 enzymatic activity is the DNA molecule which has the 3'-phosphate end (Figure 1.10 D).

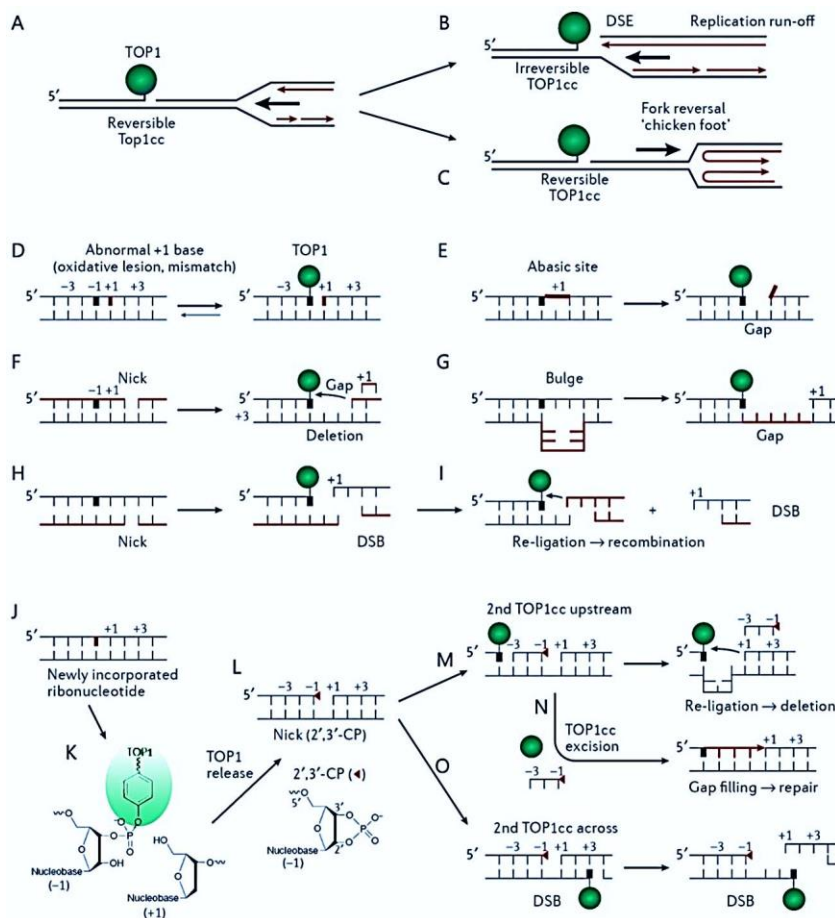


Figure 1.10. Topoisomerases and DNA damage. A-C Collision of a replication fork into a Top1 cleavage complex (Top1cc; part A) produces replication run-off (part B) in which newly replicated

DNA is extended by DNA polymerases up to the 5' end of the broken DNA, thereby generating a double-stranded end (DSE), which is repaired by homologous recombination. Alternatively, replication fork reversal regenerates a reversible Top1cc and produces a 'chicken foot' structure (part C). **D-I.** Processing of Top1cc can produce DNA damage. The -1 base to which Top1 is covalently linked to cleave DNA (Fig. 1.3) is shown as a thick black bar; the red lines represent newly synthesized DNA strands. Efficient re-ligation of Top1cc relies on stacking and hydrogen bonding with the +1 base, which is disrupted by oxidative basedamage and mismatches (part D). The presence of an abasic site at the +1 position interferes with re-ligation by the 5'-hydroxyl end owing to loss of base stacking and hydrogen bonding (part E). A Top1cc 5' end and a pre-existing nick result in loss of the DNA segment between them (gap) and can lead to deletions due to the efficient re-ligation activity of Top1 (part F). Formation of a Top1cc at a bulge or a loop can readily generate a stretch of single-stranded DNA at the gap (part G). A Top1cc opposite to a nick results in a DNA double-stranded break(DSB; part h), which can be resealed by Top1 (part i) with another broken DNA end (red), thereby generating mutations. **J-O.** Following ribonucleotide incorporations into the DNA (shown in red) during replication (part J), a TOP1cc forming at a ribonucleotide site (part k) is reversed by nucleophilic attack of the 2'-ribose hydroxyl, which generates a 2',3'-cyclic phosphate (2',3'-CP) end (indicated by the arrowhead) with the release of catalytically activeTOP1. Sequential cleavage at a nearby nucleobase by the released TOP1 or by another TOP1 can generate a short deletion (part M) when the TOP1 forms a cleavage complex on the same strand, upstream of the 2',3'-CP. Alternatively, endonucleolytic cleavage (not shown) or excision of the TOP1cc by tyrosyl-DNA phosphodiesterase 1 (part N) followed by gap fillingcan repair the DNA while eliminating the ribonucleotide. When the sequential cleavage by a TOP1 is on the opposite strand to the 2',3'-CP, a DSB is formed (part O) (Adapted from Pommier *et al.*, 2016).

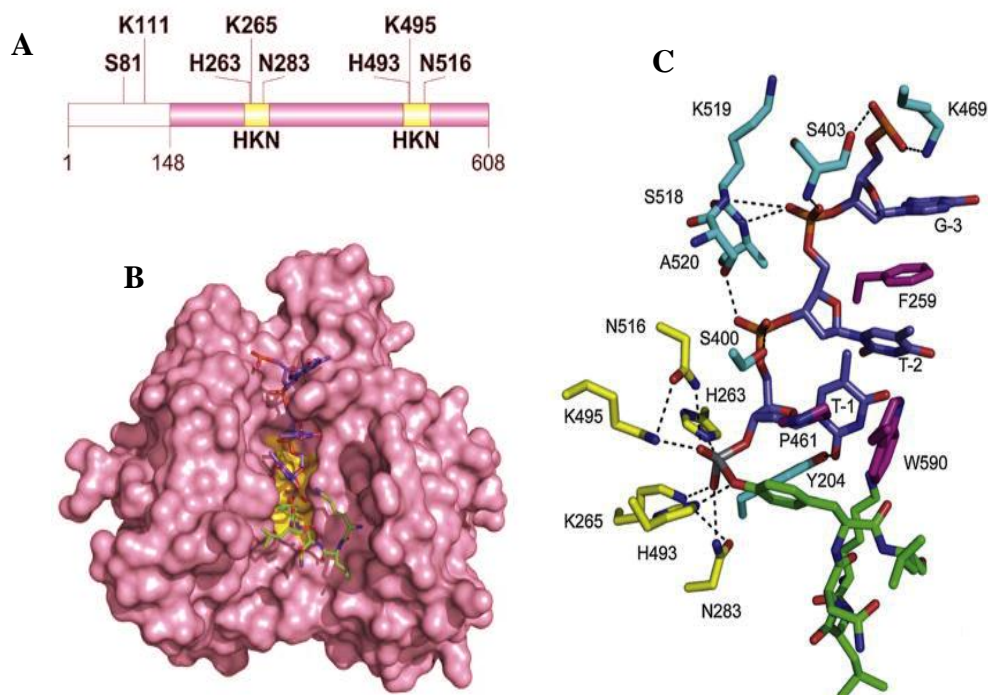


Figure 1.11. Crystal structure of TDP1. A. Ribbon representation of TDP1 polypeptides. N-terminal (white) segments (residues 1–148) for TDP1 are absent in the crystal structures shown below. Conserved catalytic segments are highlighted in yellow. B. Surface representations of the crystal structures for TDP1 (PDB ID 1NOP). Proteins are represented in light pink, catalytic residues in yellow, DNA in blue sticks, peptide in green sticks and both sticks coloured by element (N, blue; O, red; P, orange; Vanadate, grey). C. Detailed contacts between substrates and TDP1 residues in the catalytic site of TDP1. Catalytic residues are represented as yellow sticks; residues involved in polar

interactions are in cyan sticks; residues involved in hydrophobic interactions in magenta sticks. All sticks are coloured by element (N, blue; O, red; P, orange; Vanadate, grey). Dashed lines indicate polar interactions (Adapted from Pommier et. al. 2014)

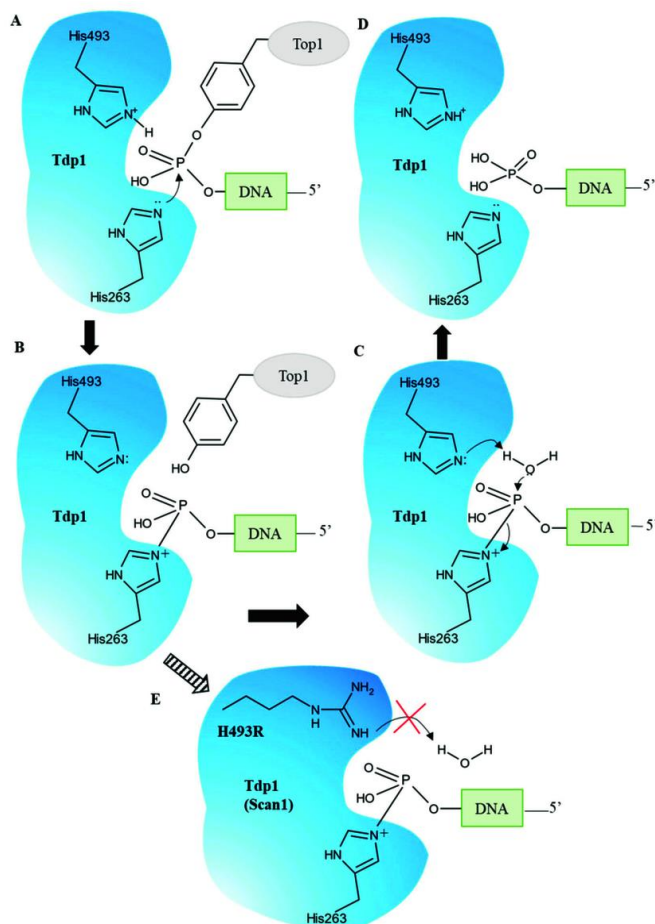


Figure 1.12. TDP1 s catalytic cycle. (A) The nucleophilic attack of the phosphodiester backbone by the imidazole N2 atom of H263. H493 donates a proton to the tyrosyl moiety of the leaving group. (B) The phosphohistidine covalent intermediate. (C) The second nucleophilic attack mediated by a water molecule activated by H493. (D) The emergence of the final 3'-phosphate product and free TDP1. (E) The SCAN1 mutation (H493R) leads to the accumulation of the TDP1-DNA intermediate and a fall in the TDP1 turnover rate.

iii. Substrate preference of TDP1

TDP1 is responsible for the removal of 3'-tyrosine in an extensive array of DNA structures all the while maintaining its inclination for single-stranded DNA. The fragments of DNA that harbour a minimum of 4 nucleotides, double stranded substrates, particularly at gaps and blunt ends are additionally processed by TDP1. Top1 associated DNA cleavage complex (Top1cc) is one of the most appropriate targets for TDP1 (Deb ethune et al, 2002). Furthermore, 5'-phosphotyrosyl bonds can also be processed by TDP1 (Murai et al, 2012). TDP1 activity has been observed against 3'-phosphoglycolate ends and 3'-deoxyribose phosphate ends, which can result from oxidative DNA damage as well as radiomimetic drugs like bleomycin. Concurrently, TDP1 deficient cells are challenged in their ability to repair DNA damages which are caused by oxidative stress. TDP1 also utilizes its nucleosidase activity for the purpose of removal of 3'-terminal deoxyribose as well as ribonucleotides while their 3'-ends

are dephosphorylated. Application of TDP1 nucleosidase activity is observed in anti-viral and anti-cancer chain-terminating nucleoside analogues like, acyclovir (ACV), cytarabine (Ara-C) and zidovudine (AZT). This observation demonstrates the significance of the role of TDP1 in the repair of replication-associated lesions both in the nucleus as well as in the mitochondria (Figure 1.13) (Huang et al, 2013). 3'-deoxyribose lesions that have evolved as a consequence of base alkylation after AP lyase are processed by TDP1, and is important for the purpose of repair of DNA lesions which are caused by ionizing radiations in addition to mono-functional alkylating agents such as methylmethanesulfonate and temozolomide (Pommier et al, 2014). Furthermore, TDP1 also hydrolyses multiple synthetic DNA adducts linked to 3'-phosphate ends like, biotin and numerous types of fluorophores (Figure 1.13), which is extraordinarily useful for the purpose of screening TDP1 inhibitors as well as conducting detailed mechanistic studies.

iv. Repair pathway of Top1-DNA covalent complex mediated by TDP1:

TDP1 produces a nucleotide product which terminates with a 3'-phosphoryl group, that must be hydrolysed to a 3'-hydroxyl group so that further DNA repair can take place. PARP1 is a type of nuclear enzyme that is often termed as a molecular nick sensor, that identifies and binds to single or double strand breaks in a DNA molecule. Recent studies have demonstrated that PARP1-deficient cells are hypersensitive towards CPT treatment and this has been shown to be directly related to a functional defect in TDP1 (Pommier, 2006). This indicates that PARP1 might well be involved in the targeting of BER complex to sites where Top1-mediated DNA damage has occurred.

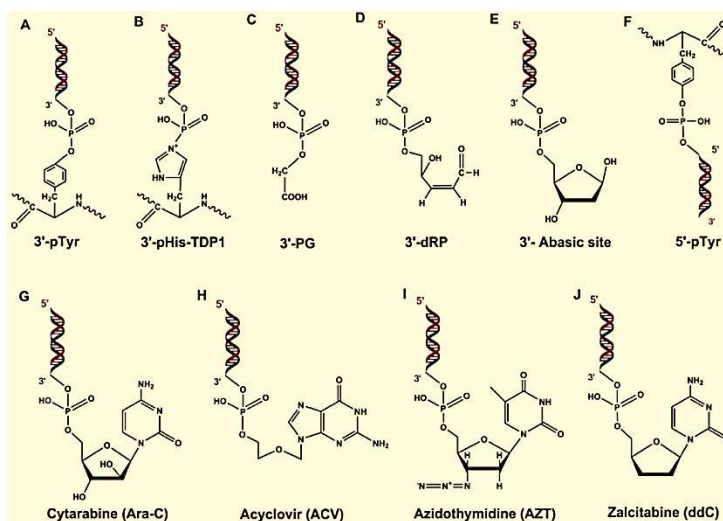


Figure 1.13. TDP1 substrates. **A.** 3'-phosphotyrosyl peptide - canonical substrate of TDP1. **B.** 3'-phosphoamide adducts formed by H493R-mutant TDP1 causing covalent linkage of H263-TDP1 to 3'

'- DNA end. **C.** 3'-phosphoglycolates. **D.** 3'-deoxyribose phosphate and **E.** 3'-basic sites produced because of oxidative DNA damage. **F.** 5'-phosphotyrosyl peptide. **G–J.** Chain terminating nucleoside analogs (Image Source: Kawale and Povirk, 2018).

1.8.1.B PARP1

The sixteen proteins that make up the PARP family are classified based on their similarity to PARP1. Four further subfamilies of the PARP family can be distinguished based on the architecture of their domain. of which PARP1, PARP2 and PARP3 are DNA dependent PARPs while the tankyrase group include tankyrase 1 (also referred to as PARP5A) in addition to tankyrase 2 (also known as PARP5B). PARP7, PARP12, PARP13.1 and PARP13.2 are known to be CCCH (Cys-Cys-Cys-His) PARPs. Additionally, the macro-PARPs includes B-aggressive lymphomaprotein 1 (BAL1; also referred to as PARP9), BAL2 (otherwise known as PARP14 or COAST6 in mice) and BAL3 (also known as PARP15) (Hassa & Hottiger, 2008) Nuclear PARP1 is composed of three domains (Figure 1.14). Amino-terminal includes two zinc finger DNA-binding domains that are crucial for the binding of PARP1 to single-strand as well as double-strand breaks. Third zinc finger has been implicated in coupling damage-induced alterations in the DNA-binding domain to changes in PARP1 catalytic activity (Langelier et al, 2008). The central auto modification domain consists of precise glutamate and lysine residues, which are capable of serving as acceptors of ADP-ribose moieties which imparts PARP1 the property of self-PARylation. Furthermore, BRCA1 carboxy-terminal (BRCT) repeat motifs that are present in this domain raise the likelihood of largely unexplored protein-protein interactions. Finally, C-terminal catalytic domain forms pADPr by successively transferring ADP-ribose subunits to various different protein acceptors from NAD^+ (Figure 1.14). PARP1 is instantly recruited to the sites of DNA damage, which includes nicks and DNA DSBs, and its catalytic activity rapidly increases exponentially by several hundred folds, thus producing protein-conjugated long branched pADPr chains (Hassa & Hottiger, 2008). Recent studies indicate that PARP1 is involved in the recruitment of numerous crucial components of homologous recombination (HR) machinery like, mitotic recombination 11 (MRE11) and ataxia telangiectasia-mutated (ATM) to revive stalled replication forks to DNA DSBs. Along with these different roles in DNA damage responses (DDR), $\text{PARP1}^{-/-}$ mice also exhibit hypersensitivity towards various DNA-damaging agents, chiefly ionizing radiation and alkylating agents (Chowdhuri & Das, 2021).

1.8.1.C XRCC1

In human beings, X-ray repair cross-complementing protein 1 (XRCC1) is encoded by the gene XRCC1. XRCC1 plays a critical role in wide variety of DNA damage repair pathways in human and other mammalian cells including, single-strand break repair (SSB), base excision repair (BER) as well as nucleotide excision repair (NER). XRCC1 has the ability to operate as a scaffolding protein which directly interacts physically with multiple enzymatic components of repair machinery (Figure 1.15). The scaffolding enables these enzymes to achieve their catalytic steps that are required in repairing DNA (Caldecott, 2003). In human beings, XRCC1 interacts with various proteins to form a multiprotein complex with TDP1, PNKP, poly(ADP)ribose polymerase (PARP), Polymerase β and ligase III (El-Khamisy et al, 2005). XRCC1 binds with DNA ligase III and DNA polymerase β through the C terminal and N terminal domains respectively. On the other hand, poly (ADP-ribose) interacts with the central domain of XRCC1 and facilitates its recruitment to the damage site. A recent study demonstrated the association of XRCC1 with aprataxin, which is a 342 amino acid protein whose homozygote mutation produces the condition known as Ataxia-oculomotor Apraxia (AOA1) (Clements et al, 2004)

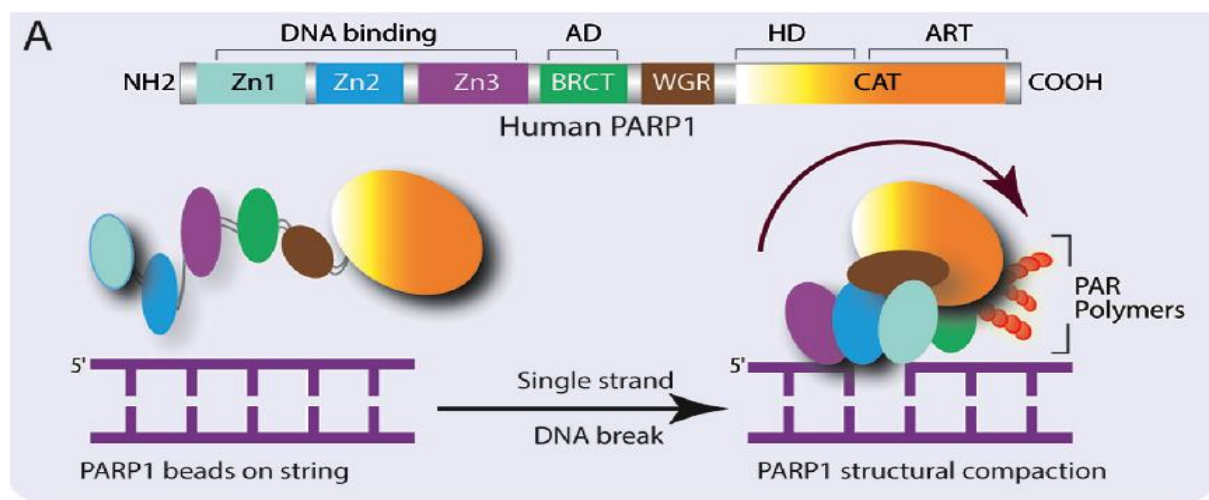
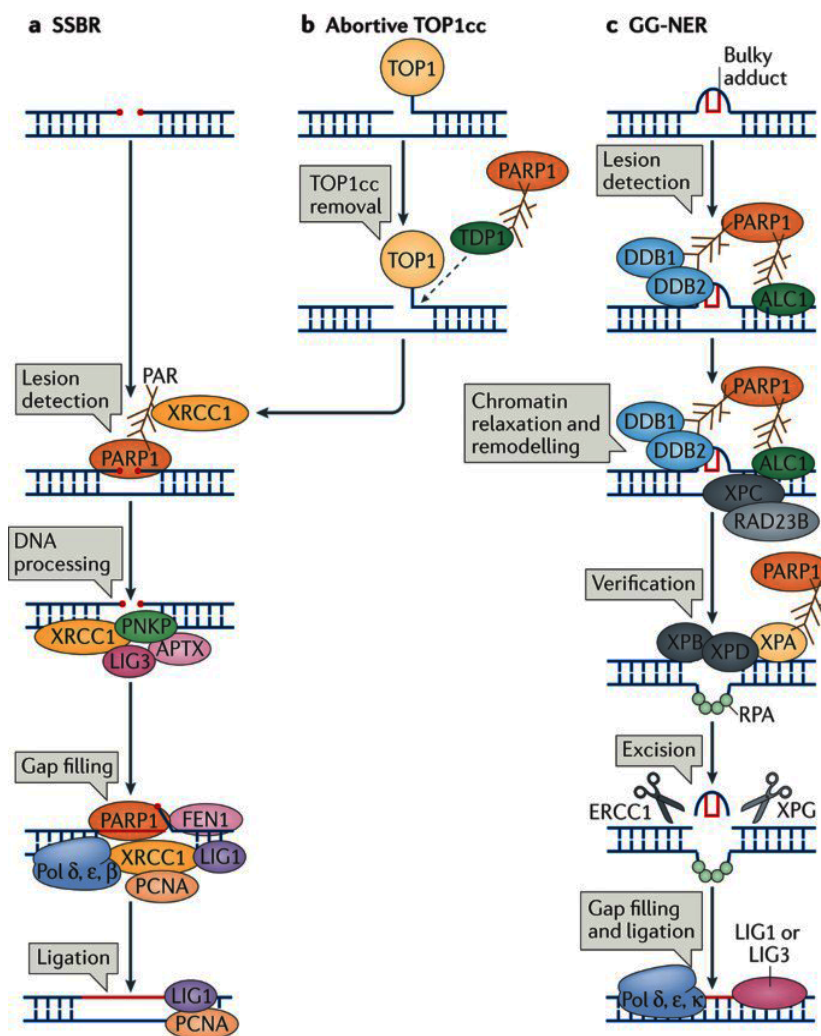


Figure 1.14. PARP1 structural rearrangements facilitate the PARP1 activation at DNA damage sites. Cartoon showing the domain architecture of human PARP1 (top panel) indicating the three DNA binding zinc finger domains (Zn1, Zn2 and Zn3), BRCT (auto modification domain; AD), the WGR domain, and the Catalytic domain (CAT) composed of the helical (HD) and ART (ADP-ribosyl transferase) subdomains. PARP1 inter-domain rearrangements post DNA damage recognition (bottom panel). In absence of DNA damage PARP1 forms loose ‘beads on a string’ conformation (left) which rapidly changes into a collapsed conformation upon recruitment to DNA damage sites (right). The arrow indicates the folding of the ‘beads-on-a-string’ form of PARP1 to the compact conformation.



Nature Reviews | Molecular Cell Biology

Figure 1.15. Structural and functional characteristics of PARP1. The roles of poly(ADP-ribose) polymerase 1 in excision repair. **A.** Poly(ADP-ribose) polymerase 1 (PARP1) activity is required in different steps of single-strand break repair (SSBR). It is essential for the detection of the SSBs and is then required for the recruitment of X-ray repair cross-complementing protein 1 (XRCC1), which acts as a scaffold for the recruitment of polynucleotide kinase 3'-phosphatase (PNKP), aprataxin (APTX) and DNA ligase 3 (LIG3) to process the SSB. This is followed by the gap filling step, which is carried out by DNA polymerase δ (Pol δ), Pol ϵ and Pol β , and also requires PARP1 for stimulating the 5' flap endonuclease activity of flap endonuclease 1 (FEN1). Finally, the DNA is ligated by LIG1. **b** PARP1 is also required for the processing of SSBs at abortive DNA topoisomerase 1 (TOP1) cleavage complexes (TOP1cc). PARP1 recruits and activates tyrosyl-DNA phosphodiesterase 1 (TDP1), which cleaves the TOP1cc from the DNA. The SSB is then repaired by SSBR. **c** | PARP1 is important for the repair of bulky adducts by global genome nucleotide excision repair (GG-NER). In the initial step, lesion detection, the DNA damage-binding protein 1 (DDB1)–DDB2 complex is recruited to autopoly(ADP)ribosylated (autoPARylated) PARP1. This is followed by the recruitment of amplified in liver cancer protein 1 (ALC1), a step that is also mediated by PARP1. This results in chromatin decondensation, the recruitment of xeroderma pigmentosum group C-complementing protein (XPC) and RAD23B, and lesion verification, which involves recruiting XPB and XPD through the interaction of their binding partner XPA with PARP1. Following lesion verification, the bulky adduct is excised by the concerted action of two nucleases, excision repair cross-complementing group 1 protein (ERCC1) and XPG, and the resulting gap is filled by Pol δ , Pol ϵ and Pol κ , and ligated by LIG1 or LIG3. PCNA, proliferating cell nuclear antigen; RPA, replication protein A. (Image Source: Ray Chaudhuri and Nussenzweig, 2017).

1.8.1.D Polynucleotide kinase phosphatase (PNKP)

Polynucleotide kinase phosphatase (PNKP) is one of the many crucial DNA damage repair proteins which functions both in base excision repair (BER) as well as in non-homologous end-joining (NHEJ) pathways. PNKP is considered to be a bi-functional enzyme which has 5'kinase as well as 3'-phosphatase activities, can remove the 3'-phosphate moiety and can also phosphorylate the neighbouring 5'-hydroxyl of TDP1 processed product (Yang et al, 1996). A previous study demonstrated that both TDP1 and PNKP function in the same repair pathway in human cells (Figure 1.15) (El-Khamisy et al, 2005).

1.8.1.E DNA polymerase β and DNA ligase III

DNA polymerase β , also referred to as POLB, is encoded by the gene *POLB* in human beings. DNA polymerase β has been implicated in the stabilization of genome integrity by participating in base excision repair events. It is capable of replacing the missing DNA segment having 3'-hydroxyl and 5'- phosphate moiety for additional processing by the enzyme DNA ligase III (Figure 1.15) (Pommier, 2006).

DNA ligase III much like other DNA ligases joins nicks and breaks in the phosphodiester backbone of DNA molecule which has been generated as a result of DNA damage and its repair during replication and recombination processes, which constitutes indispensable stride towards maintaining genomic integrity. Three different human genes have been identified that encode ATP-dependent DNA ligases and these are LIG1, LIG3 and LIG4. As mentioned previously DNA ends which have been processed by DNA polymerase β are subsequently resealed by DNA ligase III (Figure 1.15) (El-Khamisy et al, 2005).

1.8.2 Top1 excision through endonucleases pathway

The existence of alternate endonuclease pathways for eliminating the Top1 induced DNA damage has been extensively studied in yeasts and has been summarized in the following sections (Pommier, 2006).

1.8.2.A XPF/ERCC1 pathway

Pathways which are parallel and redundant with TDP1 include participation of Rad1/Rad10 and Slx1/Slx4 (Liu et al, 2002). During the process of nucleotide excision repair, Rad1/Rad10, (which are essentially orthologues of the human endonuclease XPF/ERCC1) cleaves DNA 3'

end from the large adduct (Figure 1.9-1.10). TDP1 and Rad1/Rad10 appear to have similar substrate specificity towards a single stranded gap between the 5' -end and the 3'-end of the DNA (Vance & Wilson, 2002).

1.8.2.B Mus81/ Eme1 pathway

Mus81/ Eme1 appear to cleave damaged replication forks in a precise and selective manner with duplex DNA near the 3'-end to be processed (Osman et al, 2003). Recent reports have demonstrated Mus81 and Rad50-deficient yeasts are hypersensitive towards CPT (Osman et al, 2003).

1.8.2.C MRN complex associated pathway

The Mre11/Rad50/Xrs2 complex (widely referred to as the MRX) (the human orthologs are Mre11/Rad50/Nbs1 [MRN]) operate in an independent manner from the TDP1 pathway (Figure 1.9-1.10) (Liu et al, 2002). This is also true for Mus81/Mms4 and Rad27 (Liu et al, 2002). Two separate but redundant pathways involved in repairing Top1-mediated DNA damage are a) TDP1-dependent pathway and b) TDP1-independent checkpoint dependent pathway which involves BRCA1, 53BP1 as well as MDC1 in the checkpoint response and consequent removal of the damage by three parallel functioning endonucleases (Figure 1.9-1.10) (Zhou & Elledge, 2000). TDP1 becomes the foremost enzyme responsible for the removal of Top1-associated DNA damage in case there has been inactivation of cancer-related checkpoint.

1.8.3 Top1-DNA complexes reversal by means of 5' end religation

Removal of Top1 induced damaged complexes can be also accomplished by the process of 5' end religation. Religation event can be associated with the transcription and replication induced DNA damage repair through regression of replication or transcription complex ("pull-back") (Rao et al, 2005). Regression of replication fork could result in generation of "chicken foot" like structure. Additionally, Holliday junctions are topologically similar to this structure.

1.9.1 TDP1 Post-translational modification (PTM) regulations

Technological advancements have unraveled a diverse array of more than 200 variants of post-translational modifications that are extremely dynamic in nature (Deribe et al, 2010). The fine tuning of the equilibrium between the modified and unmodified forms of the protein is

essential since it may alter the function of the protein. This equilibrium is established by striking a balance between the opposing catalytic activities of the enzyme that attaches and enzyme that detaches the modification. Some of the most prevalent post-translational modifications include phosphorylation, PARylation, NEDDylation, acetylation, ubiquitination, SUMOylation and methylation (Beltrao et al, 2013; Deribe et al, 2010). The regulation of cellular TDP1 occurs mainly at the post-translational level.

1.9.1A. SUMOylation

Another study demonstrated that TDP1 is a suitable substrate for modification by the small ubiquitin-like modifier SUMO (Hudson et al, 2012). In this study SUMOylated TDP1 was isolated and purified from mammalian cells and the SUMOylation site was identified to the amino acid residue at lysine 111 (Figure 1.11) (Hudson et al, 2012). Even though SUMOylation exerts no quantifiable or observable impact on catalytic activity of TDP1, the study demonstrated that it promotes the accumulation of TDP1 at sites of DNA damage (Hudson et al, 2012). Additionally, SUMOylation-deficient TDP1 mutants demonstrated a significant reduction in the rate of repair of chromosomal single-strand breaks which originated from transcription-associated topoisomerase 1 activity or oxidative stress. These data identified a role for SUMOylation during single-strand break repair (Hudson et al, 2012).

1.9.1B. PARylation

As mentioned previously TDP1 is responsible for the hydrolysis of the phosphodiester bond between the DNA 3'-end and the Top1 tyrosyl moiety. On the other hand, alternative repair pathways for Top1cc involve endonuclease cleavage (Figure 1.9-1.10) (Das et al, 2014). PARP1 plays a critical role in the process of determining the choice between TDP1 and the endonuclease repair pathways (Das et al, 2014). A previous study demonstrated that TDP1 and PARP1 are epistatic for the repair of Top1cc, by producing TDP1 and PARP1 double-knockout lymphoma chicken DT40 cells (Das et al, 2014). This study showed that N-terminal domain of TDP1 directly binds with the C-terminal domain of PARP1, and thus TDP1 gets PARylated by PARP1. PARylation leads to stabilization TDP1 coupled with SUMOylation of TDP1. TDP1-PARylation leads to elevated recruitment of TDP1 to sites of DNA damage without any interference in TDP1 catalytic activity. Subsequently TDP1-PARP1 complexes, sequentially recruit XRCC1. Genetic experiments in the same study established that PARP1 and TDP1 are epistatic for the repair of Top1-associated DNA breaks (Das et al, 2014).

1.9.1C. Ubiquitination

TDP1 is regulated by ubiquitination and identified UCHL3 as the deubiquitylase that regulates proteostasis of TDP1 (Liao et al, 2018). The study also demonstrated that the depletion of UCHL3 results in an increase of TDP1 ubiquitination in addition to elevated turnover rate and additionally sensitizes cells to Top1 poison treatment (Liao et al, 2018). The study suggested that overexpression of TDP1 in the topoisomerase therapy-resistant rhabdomyosarcoma is mediated by overexpression of UCHL3. Furthermore, the study also found that UCHL3 is downregulated in SCAN1, resulting in elevated levels of TDP1 ubiquitination and increased rate of turnover (Liao et al, 2018). This study established UCHL3 as a modulator of TDP1 proteostasis and, therefore, a regulator for protein-linked DNA damage repair (Liao et al, 2018).

1.9.1D. Arginine methylation

Top1-induced replication-mediated DNA damage induces TDP1 arginine methylation, enhancing its 3'-phosphodiesterase activity. TDP1 arginine methylation also increases XRCC1 association with TDP1 in response to CPT, and the recruitment of XRCC1 to Top1cc DNA damage foci (Rehman et al, 2018).

1.9.1E. Phosphorylation

A previous study demonstrated that Top1-associated DNA double-stranded breaks (DSBs) induce the phosphorylation of TDP1 at S81 site of the protein (Das et al, 2009). This phosphorylation event is mediated by the participation of two protein kinases namely, DNA-dependent protein kinase (DNA-PK) and ataxia-telangiectasia-mutated (ATM) (Das et al, 2009). The phosphorylated TDP1 subsequently forms nuclear foci that subsequently co-localizes with those of phosphorylated histone H2AX (also referred to as γ H2AX). Both Top1-induced replication as well as transcription-mediated DNA damages can result in the induction of phosphorylation event in TDP1 (Das et al, 2009). Moreover, this study demonstrated S81 phosphorylation led to stabilization of TDP1. This induces the formation of XRCC1 (X-ray cross-complementing group 1)-TDP1 complexes and augments the movement of TDP1 towards DNA damage sites. Additionally, phosphorylation event at TDP1-S81 also promotes survival of cell and DNA damage repair in response to CPT-induced double strand breaks (Das et al, 2009). In this study, we have identified a novel phosphorylation of TDP1 at Serine 61 residue by the core mitotic kinase CDK1. This phosphorylation helps in the maintenance of

the cell cycle dependent association and dissociation of TDP1 from the chromosomal DNA during mitosis. It becomes evident from our work that this CDK1 mediated phosphorylation of TDP1 helps to safeguard the genome against chromosomal instabilities arising from the mis-segregation of chromosomes during mitosis.

2. DNA repair in mitotic phase of the cell cycle:

Chromosome instability (CIN) can result from improperly repaired DNA double-strand breaks (DSBs), which are extremely toxic DNA lesions (Bakhoun et al, 2017). When cells undergo the difficult process of equal and error-free chromosomal segregation into daughter cells during the mitotic phase of the cell cycle, DSBs pose a significant problem. DSBs cause DNA damage response (DDR) to be elicited in cells, which allows the cells to stop the cell cycle until the breaks are fixed before entering mitosis (Bakhoun et al, 2017). The completion of cell division takes precedence over DNA damage repair when cells encounter DSBs during mitosis, however, and they no longer arrest (Bakhoun et al, 2017). The mechanisms by which mitotic cells can delay DSB repair without building up significant CIN are still poorly understood, and it is still unknown what potential physiological effects failed DSB responses in mitosis might have (Blackford & Stucki, 2020). The majority of human cell-based DDR studies have been conducted on asynchronous cell populations, and any effects of the cell cycle have typically been examined by contrasting how cells react to DNA damage (Figure 1.16) at different stages of interphase (G1, S, and G2) (Blackford & Stucki, 2020). The process of tolerating genotoxic stress during mitosis, when chromatin dramatically condenses, the nuclear envelope (NE) separating the nucleus and cytoplasm breaks down, and cells are coordinating the complex process of equal chromosome segregation into daughter cells is far and away very poorly understood (Blackford & Stucki, 2020). The lack of understanding is in part due to the difficulties of studying a highly dynamic process that can be completed in less than an hour with only a small percentage of cells in an asynchronous population at any one time attempting it (Figure 1.16) (Bakhoun et al, 2017; Groelly et al, 2022; Petsalaki & Zachos, 2020).

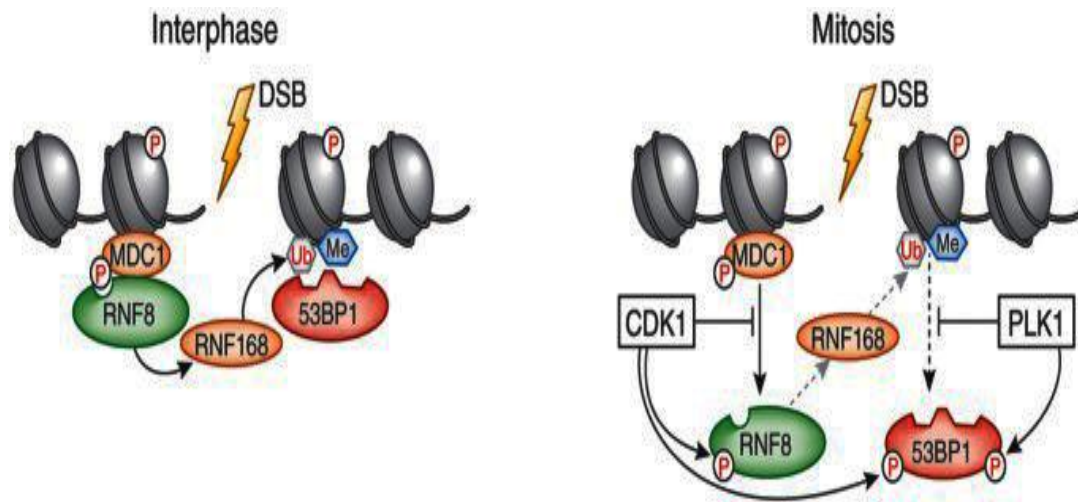


Figure 1.16 Inhibition of recruitment of RNF8 and 53BP1 to DSBs during mitosis. During interphase, phosphorylation of MDC1 on Thr752 recruits the E3 ubiquitin ligase RNF8 to DSBs. RNF8 promotes the recruitment of RNF168, another E3 ubiquitin ligase that ubiquitinates H2A on residues K13 and/or K15. 53BP1 is recruited to nucleosomes containing ubiquitinated H2A and dimethylated H4. In mitotic cells, CDK1 phosphorylates RNF8 on Thr198, and this inhibits RNF8 recognition of MDC1. CDK1 and PLK1 phosphorylate 53BP1 on Thr1609 and Ser1618, respectively, and this suppresses the association of 53BP1 with nucleosomes. P, phosphate; Ub, ubiquitin; Me, methyl. (Source: Denchi and Li, NSMB 2014)

2.1. DNA Damage Checkpoint Signaling in Interphase and Mitosis

DNA DSBs owing to their high toxicity can be particularly challenging for cells to repair accurately without causing CIN especially if left unrepaired when cells attempt chromosomal segregation during mitosis (Bakhom et al, 2017; Groelly et al, 2022; Petsalaki & Zachos, 2020). The DDR is initiated by three structurally related protein kinases: ATM, ATR, and DNA-PKcs. ATM and DNA-PKcs are primarily activated by DSBs, whereas ATR is activated by DNA replication stress or lesions that are processed to produce single-stranded DNA (ssDNA) (Gomez Godinez et al, 2020). The primary role of DNA-PKcs is probably limited to DSB repair in the vicinity of the lesion, whereas ATR and ATM activate both local and global cellular responses to DNA damage, in part by phosphorylating and activating other kinases such as CHK1 and CHK2, respectively (Orthwein et al, 2014). However, it is important to note that ATM, ATR, and DNA-PKcs have a range of overlapping substrates and can substitute for each other to some extent (Bakhom et al, 2017; Blackford & Stucki, 2020; Orthwein et al, 2014). All three DDR kinases are recruited and activated by a discrete set of cofactors: ATM is recruited and activated by the MRE11-RAD50-NBS1 (MRN) complex, which can recognize and bridge broken double-stranded DNA (dsDNA) ends; DNA-PKcs is recruited and activated at dsDNA ends by Ku, a heterodimeric complex

comprising two subunits, Ku70 and Ku80; and ATR has a stable binding partner, ATRIP, which binds to the heterotrimeric RPA complex when it is bound to ssDNA. ATM and DNA-PKcs are activated by binding to their cofactors at DSB ends, but ATR requires additional stimulation by either TOPBP1 or ETAA1, which both contain an ATR-activation domain (Bakhoun et al, 2017; Blackford & Stucki, 2020; Orthwein et al, 2014). ETAA1 is recruited directly to RPA-coated ssDNA where it can activate ATR kinase activity, whereas the factors and mechanisms controlling TOPBP1 recruitment are not yet clear but may involve multiple, possibly redundant mechanisms (Bakhoun et al, 2017; Blackford & Stucki, 2020; Orthwein et al, 2014). In response to DNA damage, ATM and ATR activate cell-cycle checkpoints to arrest cells at the G1/S or G2/M boundaries. By contrast, S phase checkpoint signaling limits DNA replication origin firing, stabilizes stalled replication forks, and increases nucleotide supply to slow S phase progression and maintain the fidelity of DNA replication rather than causing cell-cycle arrest (Bakhoun et al, 2017; Blackford & Stucki, 2020; Orthwein et al, 2014). While there are differences in how these checkpoints are activated, they all share essentially the same output; that is, inhibition of the cyclin-dependent kinase (CDK) activity that drives cell-cycle progression. This is achieved rapidly by ATM/ATR-dependent activation of checkpoint kinases that inactivate the CDC25 family of phosphatases, which counteract inhibitory phosphorylation of CDKs by the WEE1 kinase. Slower, transcription-dependent inhibition of CDKs by p21 is also activated by ATM- and ATR-dependent phosphorylation of p53, which is particularly important for the G1/S checkpoint (Bakhoun et al, 2017; Blackford & Stucki, 2020; Orthwein et al, 2014).

Once cells have moved beyond prophase, there is no DNA damage checkpoint until daughter cells re-enter G1 in the next cell cycle. While high levels of DNA damage can delay the metaphase-to-anaphase transition, this is due to defects in microtubule attachment to kinetochores and an active spindle assembly checkpoint rather than direct signaling from DNA lesions. It is therefore clear that cells, at some point, become committed to mitosis and prioritize completion of cell division over repair of DNA damage. There are several mechanisms that prevent inhibition of CDK1 by DNA damage signaling in mitosis (Bakhoun et al, 2017; Blackford & Stucki, 2020; Orthwein et al, 2014). First, little or no transcription occurs during mitosis except possibly at specific genes and regions such as centromeres, so mechanisms such as p21 induction and subsequent inhibition of CDKs are disabled. Another major mechanism involves ubiquitylation and proteasomal degradation of key cell-cycle and DNA damage checkpoint mediators (Enserink & Kolodner, 2010). WEE1 is phosphorylated

by CDK1 and PLK1 at the onset of mitosis, which creates phosphodegrons that are recognized by the SCF- β TrCP ubiquitin ligase, resulting in WEE1 degradation (Ghelli Luserna di Rorà et al, 2020). Claspin, a protein required for CHK1 activation, is also phosphorylated by PLK1 and degraded by SCF- β TrCP. Finally, CHK2 is phosphorylated and inhibited by PLK1 on mitotic entry, which prevents CHK2 activation rather than promoting its degradation. ATM-dependent phosphorylation of CHK2 is also reduced during mitosis, which may further limit CHK2 kinase activity (Mailand et al, 2006). This may be required because aberrant ATM-CHK2 signaling during mitosis can result in stabilization of kinetochore–microtubule attachments to chromosomes, thereby increasing the frequency of lagging chromosomes during anaphase (Blackford & Stucki, 2020). Taking these findings together, CDK1-cyclin B activity is thus maximized at the end of prophase through multiple mechanisms and can no longer be inhibited by ATM or ATR signaling until mitosis is complete (Blackford & Stucki, 2020).

2.2 DSB repair in mitosis

The absence of 53BP1 recruitment to sites of DSBs in mitosis removes a major DNA-end resection roadblock that could allow hyper-resection in mitosis. However, this phenomenon is not observed in mitotic cells probably owing to the high degree of compaction and condensation of chromosomes to be substrates of enzymes involved in long-range resection to overcome (Bakhoun et al, 2017; Blackford & Stucki, 2020; Denchi & Li, 2014; Orthwein et al, 2014). In addition to lack of DNA-end resection, key HR factors such as BRCA1 and RAD51 are also not recruited to mitotic DSB sites. The bulk of evidence therefore suggests that DSB repair by HR is inactivated in mitosis (Bakhoun et al, 2017; Blackford & Stucki, 2020; Denchi & Li, 2014; Orthwein et al, 2014). A lack of RPA-coated ssDNA in mitosis might also explain why ATR is not recruited to DSBs during mitosis, although ATR could be activated in this cell-cycle phase by other mechanisms. The situation is less clear for NHEJ: while early studies suggested that DSB repair is universally inhibited during mitosis and therefore that DSBs are also not repaired by NHEJ until the subsequent G1 phase, the absence of NHEJ during mitosis has never been demonstrated directly. There is circumstantial evidence arguing that although chromatin responses are attenuated during mitosis, the DSB repair machinery itself may remain active to some extent (Bakhoun et al, 2017; Blackford & Stucki, 2020; Denchi & Li, 2014; Orthwein et al, 2014). For example, Ku foci still form on mitotic chromatin, although it is unclear whether they are resolved during

mitosis or in the following G1 (Bakhoun et al, 2017; Blackford & Stucki, 2020; Denchi & Li, 2014; Orthwein et al, 2014). Given that the expression of 53BP1 mutants that cannot be phosphorylated by mitotic kinases promotes sister-telomere fusions, it seems likely that at least some NHEJ activity is present in mitotic cells. However, there is evidence that XRCC4 is phosphorylated by mitotic kinases and that this attenuates its localization at DSB sites (Bakhoun et al, 2017; Blackford & Stucki, 2020; Denchi & Li, 2014; Orthwein et al, 2014). Thus, it remains unclear to what extent the core NHEJ machinery is inhibited during mitosis. Regardless, in the absence of efficient DSB repair, broken chromosomes represent a major threat for mitotic cells since broken chromatid fragments lacking a centromere (so-called acentric fragments) would be unable to segregate properly without the existence of compensatory mechanisms. A simple such mechanism would be the tethering of broken chromosome ends until they can be repaired in the following G1 phase. Recent evidence suggests that tethering of acentric chromatid fragments during mitosis may at least exist in mammalian cells. As described above, the chromatin response to DSBs is only partially disrupted in mitosis, such that the upstream events including H2AX phosphorylation and MDC1 recruitment still occur, and the kinase activities of ATM and DNA-PKcs are important for cell survival in response to mitotic DNA breaks (Bakhoun et al, 2017; Blackford & Stucki, 2020; Denchi & Li, 2014; Orthwein et al, 2014). It was recently shown that a major role of the chromatin response to DSBs during mitosis is the recruitment of the mediator protein TOPBP1. TOPBP1 is a versatile protein with multiple roles in DNA replication, DNA repair, and transcription. In interphase cells, TOPBP1 is recruited to DSBs via interaction with 53BP1 and other factors, but in mitosis it is recruited to sites of DSBs via direct phosphorylation-dependent interaction with MDC1 (Bakhoun et al, 2017; Blackford & Stucki, 2020; Denchi & Li, 2014; Orthwein et al, 2014).

2.3 Consequences of Defective Responses to DNA Breaks during Mitosis

When a mitotic DSB fails to be repaired or tethered, the affected chromosome breaks into two pieces: an acentric chromosome fragment and a centric chromosome fragment, each containing a telomere on one end and free DNA end on the other (Bakhoun et al, 2017; Blackford & Stucki, 2020; Denchi & Li, 2014; Orthwein et al, 2014). Since the acentric fragment is not able to interact with the mitotic spindle, it lingers near the equatorial plate during anaphase. These acentric fragments usually randomly segregate into the cytoplasm of one of the daughter cells and are converted into micronuclei. The centric fragment, by

contrast, can attach to the spindle and thus be properly segregated into one of the daughter cells, but its free DNA end can potentially fuse to another centric fragment from a different chromosome or to an intact chromosome with a deprotected telomere in the subsequent G1, leading to the formation of a dicentric chromosome (Bakhoun et al, 2017; Blackford & Stucki, 2020; Denchi & Li, 2014; Orthwein et al, 2014). These dicentric chromosomes are sources of so-called breakage-fusion-breakage (BFB) cycles, first described by Barbara McClintock in 1941. BFB cycles are a major source of chromosomal instability in cancer. Micronuclei, by contrast, are associated with heavily deregulated DNA metabolism and can thus give rise to a unique form of chromosomal instability termed chromothripsis (Shorokhova et al, 2021), where large numbers of clustered chromosomal rearrangements occur in a confined genomic region typically on only one chromosome. Chromothripsis can occur when a micronucleus is reincorporated into the nucleus in a subsequent mitosis. Thus, failed responses to DSBs in mitosis can critically contribute to the formation of the kind of chromosomal instability frequently observed in cancers (Shorokhova et al, 2021). It is well established that genotoxic stress leads to inflammatory responses. For example, exposure of cells to DSB-inducing agents leads to the expression of type I interferons, which activates p53 and induces senescence. It was originally suggested that DNA fragments leaking from the site of DNA damage in the nucleus into the cytosol are recognized by cGMP-AMP synthase (cGAS), an important sensor of cytosolic DNA that activates innate immunity by engaging the stimulator of interferon genes (STING) cascade (Uhlorn et al, 2020). However, two recent studies identified micronuclei as the main source of immune stimulatory cytosolic DNA (Krupina et al, 2021). Although micronuclei are structurally comparable with primary nuclei, their NE is unstable resulting in frequent NE breakdown, which leads to the exposure of fragmented DNA from within the micronuclei to cGAS and activates an inflammatory response (Levine & Holland, 2018). Thus, a failed response to DNA breaks in mitosis may have physiological consequences beyond the accumulation of chromosomal instability and may contribute to shape the immune microenvironment of tumors (Bakhoun & Cantley, 2018).

2.4 Under-replicated DNA as an Endogenous Source of Mitotic DSBs

Due to the relative amount of time cells spend in mitosis compared with interphase, the majority of DSBs that cells acquire from exogenous sources would be expected to occur and be repaired in interphase (Bertolin & Hoffmann, 2020). However, mitosis-specific DSB

responses exist and are apparently conserved from some single-celled organisms to human beings suggest that DSBs must occur to a significant extent during cell division and be recognized for the maintenance of genome stability (Bakhoun & Cantley, 2018; Bakhoun et al, 2017; Bertolin & Hoffmann, 2020; Blackford & Stucki, 2020; Denchi & Li, 2014; Orthwein et al, 2014). Some of the DSBs that occur during mitosis are introduced deliberately by cells as a result of unfinished DNA replication in the previous S phase (Bakhoun & Cantley, 2018; Bakhoun et al, 2017; Bertolin & Hoffmann, 2020; Blackford & Stucki, 2020; Denchi & Li, 2014; Orthwein et al, 2014). These under-replicated DNA often arise from specific regions of the genome called common fragile sites (CFSs), which are replicated late in S phase and are sensitive to breakage under conditions of replication stress such as aphidicolin treatment (when CFSs are said to be ‘expressed’). CFS expression is an active process promoted by RAD52 and a large protein complex containing the SLX1-SLX4, MUS81-ERCC1, and XPF-ERCC1 (SMX) nucleases (Bakhoun & Cantley, 2018; Bakhoun et al, 2017; Bertolin & Hoffmann, 2020; Blackford & Stucki, 2020; Denchi & Li, 2014; Orthwein et al, 2014). Under-replicated regions that have been processed by SMX can still be replicated even though cells have passed through S phase, via a break-induced conservative DNA replication pathway (Bhowmick et al, 2016; Minocherhomji et al, 2015) called MiDAS (mitotic DNA synthesis) that requires TOPBP1, POLD3 (a noncatalytic subunit of DNA polymerase δ), and prior disassembly of the S phase replisome by the ubiquitin ligase TRAP (Bakhoun & Cantley, 2018; Bakhoun et al, 2017; Bertolin & Hoffmann, 2020; Blackford & Stucki, 2020; Denchi & Li, 2014; Orthwein et al, 2014).

2.5 Cyclin dependent kinases (CDKs)

In eukaryotic cells, the cell cycle is controlled by cyclin dependent kinases (CDKs) (Brown et al, 2015; Diril et al, 2012; Enserink & Kolodner, 2010; Holt et al, 2009; Lau et al, 2021; Li & He, 2020; Satyanarayana et al, 2008). Six conserved CDKs exist in the budding yeast *S. cerevisiae*: Cdk1 (also known as Cdc28), Pho85 (similar to mammalian Cdk5), Kin28 (similar to mammalian Cdk7), Ssn3 (similar to mammalian Cdk8), and Ctk1 and the more recently identified Bur1 (both of which correspond to mammalian Cdk9). A single CDK, Cdk1, is necessary and sufficient to drive the cell cycle in budding yeast, but many of its functions, especially in the earlier phases of the cell cycle, are supported by the non-essential CDK Pho85, and there exists significant cross-talk between these kinases in regulation of e.g. cell morphology (Brown et al, 2015; Diril et al, 2012; Enserink &

Kolodner, 2010; Holt et al, 2009; Lau et al, 2021; Li & He, 2020; Satyanarayana et al, 2008). The other CDKs are thought to function mainly in the process of transcription. In addition to the six classical CDKs, *S. cerevisiae* has a distant, highly diverged CDK family member, Cak1, which is involved in activation of several CDKs. Budding yeast Cdk1 was first identified in a landmark genetic screen for genes that control the cell cycle performed by Hartwell. It is a proline-directed kinase that preferentially phosphorylates the consensus sequence S/T-P-x-K/R (where x is any amino acid), although it also phosphorylates the minimal consensus sequence S/T-P, and recent work indicates that at least *in vitro* Cdk1 can also phosphorylate non-SP/TP sites (Brown et al, 2015; Diril et al, 2012; Enserink & Kolodner, 2010; Holt et al, 2009; Lau et al, 2021; Li & He, 2020; Satyanarayana et al, 2008). Cdk1 substrates frequently contain multiple phosphorylation sites that are clustered in regions of intrinsic disorder, and their exact position in the protein is often poorly conserved in evolution, indicating that precise positioning of phosphorylation is not required for regulation of the substrate (Brown et al, 2015; Enserink & Kolodner, 2010; Holt et al, 2009). Cdk1 interacts with nine different cyclins throughout the cell cycle (Brown et al, 2015; Diril et al, 2012; Enserink & Kolodner, 2010; Holt et al, 2009; Lau et al, 2021; Li & He, 2020; Satyanarayana et al, 2008). The interaction with cyclins is important for activation of its kinase activity and also for recruitment and selection of substrates. For example, several cyclins contain a hydrophobic patch that binds the RXL (also known as Cy) motif in Cdk1 substrates (Brown et al, 2015; Enserink & Kolodner, 2010; Holt et al, 2009). This hydrophobic patch is important for substrate selection of some cyclin-Cdk1 complexes, like e.g. Clb5-Cdk1, while for other cyclins it helps determine the cellular localization of the cyclin-Cdk1 complex, like e.g. Clb2-Cdk1. However, robust cell cycle progression depends on the orderly expression of cyclins, indicating that different cyclin-Cdk1 complexes are important for phosphorylation of the right proteins at the right time (Brown et al, 2015; Enserink & Kolodner, 2010; Holt et al, 2009). The fact that aberrant CDK activity underpins proliferation of tumor cells makes it a highly significant research subject. Approximately 75 *bona fide in vivo* Cdk1 targets have been identified thus far. However, this number is likely to be an underestimate, because a recent study that combined specific chemical inhibition of Cdk1 with quantitative mass spectrometry identified over 300 potential Cdk1 targets (Brown et al, 2015; Enserink & Kolodner, 2010; Holt et al, 2009).

2.6 Role of CDK1 in mitotic DDR

Durocher and colleagues have shown that mitotic kinases (CDK1 and PLK1) phosphorylate RNF8 and 53BP1, which inhibit their recruitment to sites of DNA damage (Belotserkovskaya & Jackson, 2014; Escribano-Díaz et al, 2013). Their recent study identified a CDK1-dependent mitosis specific phosphorylation site on RNF8 (Thr198) which prevents the recruitment of RNF8 to sites of DNA damage (Figure 1.17). Restoring RNF8 recruitment in mitosis allows recruitment of the downstream factors RNF168 and BRCA1 but not 53BP1 suggestive of the existence of an additional step by which mitotic cells inhibit 53BP1 recruitment (Escribano-Díaz et al, 2013; Orthwein et al, 2014). Indeed, recruitment of 53BP1 requires the RNF168-mediated ubiquitination of histone H2A and access to K20-dimethylated histone H4. 53BP1 recognizes K15-ubiquitinated H2A via its ubiquitination-dependent recruitment motif and K20-dimethylated H4 via its Tudor domain. Two amino acids of 53BP1, Thr1609 and Ser1618 located in the ubiquitination-dependent recruitment region, are phosphorylated by CDK1 and PLK1 during mitosis (Escribano-Díaz et al, 2013; Orthwein et al, 2014). It was found that 53BP1 allele bearing phosphomimetic substitutions of these two residues is no longer recruited to DSBs, whereas the corresponding alanine substitutions (53BP1 TASA) generate a nonphosphorylated 53BP1 protein that can be recruited to mitotic DSBs. Indeed, these findings raise the possibility that cancer cells with deregulated PLK1 or CDK1 activity might have impaired DNA-repair capacity due to inhibition of RNF8 or 53BP1 (Escribano-Díaz et al, 2013; Orthwein et al, 2014). This would provide a new explanation for the genome instability displayed by these types of cancer cells and would launch an interesting avenue for cancer therapy.

In the context of the aforementioned discussion, the current study has aimed to elucidate the novel association of CDK1 with TDP1 with following specific objectives:

- Identification of TDP1 as a novel substrate of CDK1
- Investigating the role of CDK1 mediated cell cycle dependent phosphorylation in regulating TDP1 dislodging from the mitotic chromosome.
- Elucidating the biological significance of the CDK1 mediated phosphorylation of TDP1

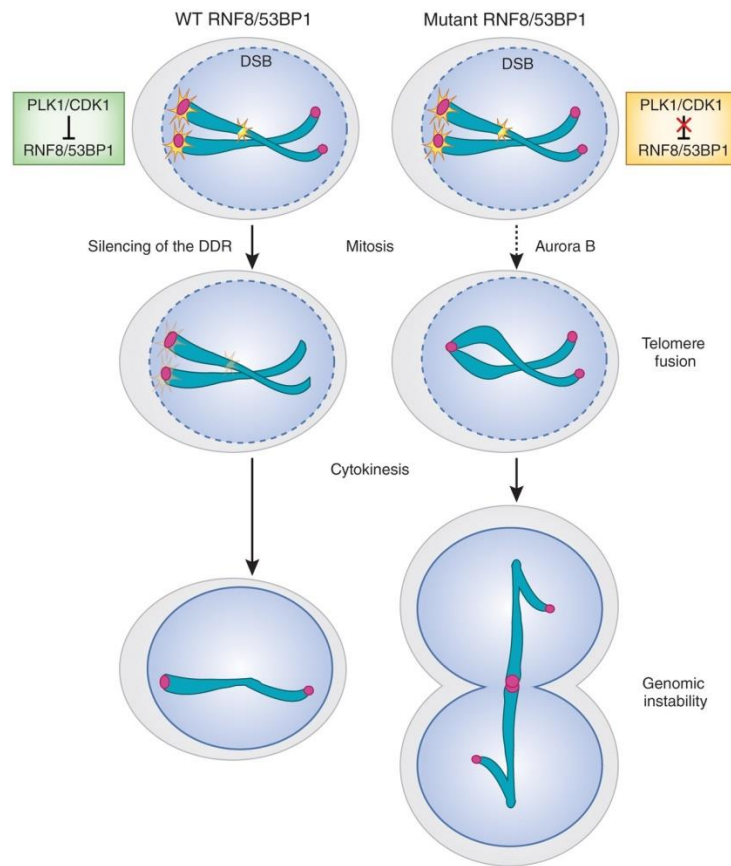


Figure 1.17 Mitotic kinases regulate DDR in mitosis. In wild-type (WT) cells, PLK1 and CDK1 inhibit recruitment of RNF8 and 53BP1 (RNF8/53BP1) to DSBs during mitosis.

This leads to silencing of the downstream DDR and normal cytokinesis. In cells expressing mutant RNF8 (T198A) and mutant 53BP1 (TASA), loss of inhibition by CDK1 and PLK1 restores the downstream DSB repair and paradoxically results in genomic instability. A major consequence of mitotic DSB repair is the formation of Aurora B-dependent telomere fusions.

3. Leishmaniasis

The term “leishmaniasis”, refers to a group of vector borne infectious disease caused by intracellular obligate, protozoan parasite *Leishmania* which are transmitted through the *phlebotomine* sand flies (Altamura et al; Chappuis et al, 2007; Desjeux, 2001; Kaye & Scott, 2011; Mann et al, 2021). Leishmaniasis arises due to different parasites affecting various populations and each can be related to a characteristic vector and animal reservoirs host. The problem is not only complex but also cosmopolitan. Until about 60 years ago leishmaniasis was thought to be endemic only in India, China, the Middle East, Southern Europe and parts of southern America (Altamura et al; Chappuis et al, 2007; Desjeux, 2001; Kaye & Scott, 2011; Mann et al, 2021). Currently, all continents except Australia and Antarctica have been recognised to be at risk. Visceral Leishmaniasis (VL), also known as “Kala azar” (a synonym in Hindi), which means black fever due to the hyperpigmentation on the hands and forehead, is the most severe form of the disease which proves to be fatal if left untreated. Epidemiological data shows that leishmaniasis at present is the most fatal parasitic disease affecting more than 16 million people and putting 600 million at risk second only to malaria (WHO, 2000) (Altamura et al; Chappuis et al, 2007; Desjeux, 2001; Kaye & Scott, 2011; Mann et al, 2021). Coinfection of Leishmaniasis infected patients with human

immunodeficiency virus (HIV) infections are increasing and approximately every third of the patients die during their first VL episode. In the developing countries like India, Bangladesh, Afghanistan, Brazil, Bolivia, Iran, Peru, Saudi Arabia and Syria the situations are deplorable (Altamura et al; Chappuis et al, 2007; Desjeux, 2001; Kaye & Scott, 2011; Mann et al, 2021). In fact, only 6 lakh cases of the 2 million actual occurrences are officially recorded per year. For the last 50 years Kala azar or VL has remained as one of the major health concerns in India. Survey report during 1991 suggests that VL affected more than 2.5 million people with 75,000 mortality, across 6 different states. In Bihar alone, 44 million people of 28 districts and about 3.5 million people of West Bengal are at risk (WHO, 1993) (Altamura et al; Chappuis et al, 2007; Desjeux, 2001; Kaye & Scott, 2011; Mann et al, 2021).

3.1 Classification of *Leishmania* and disease epidemiology

The systematic position of the pathogenic protozoan *Leishmania* is as follows:

KINGDOM : Protista

PHYLUM : Protozoa

SUBPHYLUM : Sarcomastigophora

SUPERCLASS : Mastigophora

CLASS : Zoomastigophora

ORDER : Kinetoplastida

SUBORDER : Trypanosomatida

FAMILY : Trypanosomatidae

GENUS : *Leishmania*

3.2 *Leishmania*

Leishmania has a digenetic life cycle. Although the initial infection of the mammalian host is initiated by promastigotes through the bite of an infected sand fly, this form of *Leishmania* has been rarely observed inside the mammalian host. Upon entry into host macrophage, the flagellated motile promastigote transforms into a round, non-flagellated, non-motile amastigote form (Figure 1.18). It is known that transformation to amastigotes within macrophages take place within 12-24 hours of internalization by macrophages (Kaye & Scott, 2011; Mann et al, 2021). Amastigotes are spherical in shape, only about 2.5-5 μm in diameter

(Figure 1.18B) and are contained within parasitophorous vacuoles within a macrophage and possess a prominent nucleus and kinetoplast, the cytoplasm is vacuolated and contains lysosomes (Kaye & Scott, 2011; Mann et al, 2021). The outer membrane is composed of a polysaccharide component but there is no cell surface coat. Amastigotes of different species of *Leishmania* in mammalian hosts bear morphological similarity albeit the general characteristics of amastigotes vary between species to species (Kaye & Scott, 2011; Mann et al, 2021; Olivier et al, 2005). In the sand fly midgut, *Leishmania* exists as an elongated, flagellated, motile promastigotes form which are usually 12 μm and sometimes as short as 5 μm in size (Figure 1.18A). The kinetoplast is anterior in position and free flagellum measures upto 15 μm in length. Very small, unattached promastigotes found in the proboscis of sand flies are believed to be the infective form introduced into the mammals (and & Kamhawi, 2001; Kaye & Scott, 2011; Mann et al, 2021; Olivier et al, 2005; Pearson et al, 1983). flagellate promastigotes form. Then promastigotes move to the alimentary tract for multiplication by binary fission. After 4-5 days of feeding, the promastigotes migrate to the oesophagus and the salivary glands of the fly (Kaye & Scott, 2011; Mann et al, 2021; Olivier et al, 2005; Pearson et al, 1983). The *Leishmania* promastigotes are transferred to the mammalian host along with the saliva when the infected insect feed on a mammalian host. After that the promastigotes gets readily converted to the amastigote inside the mamalian host (Kaye & Scott, 2011; Mann et al, 2021; Olivier et al, 2005; Pearson et al, 1983).

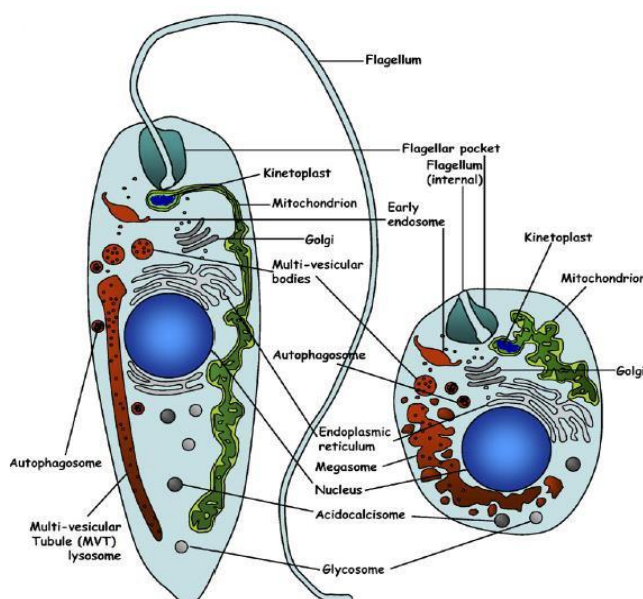


Figure 1.18. (A) Ultrastructure of *Leishmania* promastigote. (B) Ultrastructure of *Leishmania* amastigote

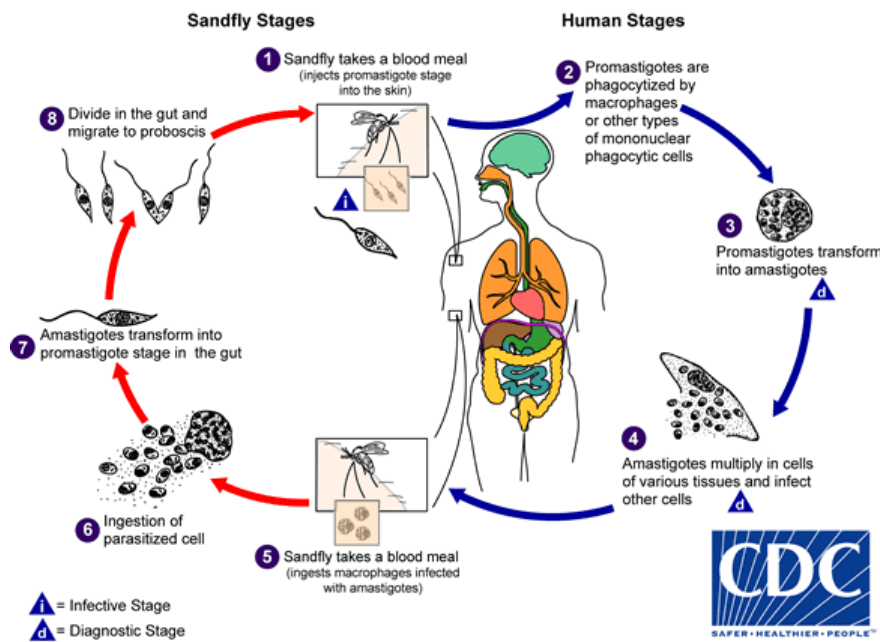


Figure 1.19. Life cycle of *Leishmania* spp., involving the motile promastigote stage in the gut of sand fly vector and the non-motile amastigote stage in the macrophage phagolysosome inside human host. Source: <https://www.cdc.gov/parasites/leishmaniasis/biology.html>

Leishmania are capable of resisting the microbicidal action of the acid hydrolases. Hence, they can survive and multiply inside the macrophages and subsequent lysis of the macrophages occurs. Again to continue the cycle, additional macrophages occupy the released amastigotes. Finally, all the organs especially, the spleen, liver and bone marrow are infected by the parasite containing macrophages and phagocytes (Kaye & Scott, 2011; Mann et al, 2021; Olivier et al, 2005; Pearson et al, 1983).

3.3 Unique features of *Leishmania*

3.3.1A Kinetoplast: A unique mitochondrion

Flagellated protozoans of the class kinetoplastida have a single large mitochondrion called the kinetoplast. It comprises of disc shaped mass of DNA network comprising maxicircles and catenated minicircle and is adjacent to the organism's basal body (Kaye & Scott, 2011; Mann et al, 2021; Olivier et al, 2005; Pearson et al, 1983).

3.3.1B kDNA (Maxicircles and Minicircles)

The most remarkable characteristics of the kinetoplastids is the presence of kinetoplast DNA (kDNA). Electron microscopy has revealed that within the mitochondrial matrix of each cell is a DNA network condensed into a disc like structure (Shapiro & Englund, 1995). kDNA exist as a network with high AT-content and molecular weight of 4×10^{10} to constitute upto 25% of total cellular DNA (Borst & Hoeijmakers, 1979) Two types of DNA molecules:

maxicircles, present in few dozen copies and minicircles, present in several thousand copies that make up the complex kDNA network (Figure 1.20).

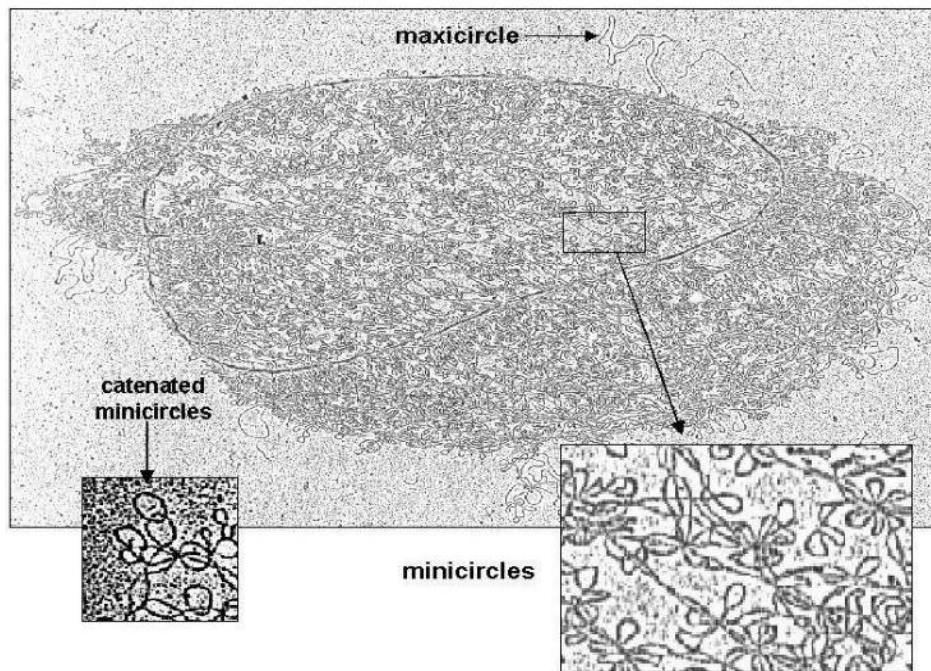


Figure 1.20. Electron micrograph of Kinetoplast DNA (kDNA) network, maxicircles and minicircles. (Source: https://kdna.net/para site_course-old/kDNA/subchapters/kdna1.htm)

Minicircles are covalently closed, relaxed DNA molecules that comprise 90% of the kDNA network. Thousands of minicircles, usually homogenous in size (0.5-2 kb) but heterogenous in sequence exist within a network (Figure 1.20). In *Leishmania*, they are about 830 bp in size. Each minicircle is catenated to an average of three neighbours (Borst & Hoeijmakers, 1979) which is again linked to the maxicircles. Minicircles do not code for any protein but they produce guide RNA's which are involved in RNA editing (Cooper et al, 2022; Simpson et al, 2000). The maxicircle has functional similarity to conventional mitochondrial DNA of higher eukaryotes (Cavalcanti & de Souza, 2018). The size ranges from 20-40 kb and their transcripts include rRNAs and mRNAs for several subunits of respiratory complexes (Figure 1.20). Maxicircles do not encode tRNAs, therefore cytoplasmic tRNAs are imported into the mitochondrion (Cavalcanti & de Souza, 2018). Transcripts derived from maxicircles undergo post-transcriptional uridine insertion and deletion to create functional open reading frames which is termed as RNA editing (Cavalcanti & de Souza, 2018).

3.3.1C kDNA Replication:

Replication of kDNA causes a special topological problem because of its massive inter-catenated network structure. kDNA replication occurs synchronously with nuclear DNA

synthesis (Borst & Hoeijmakers, 1979) and every minicircle or maxicircle replicates only once per generation (Borst & Hoeijmakers, 1979). Minicircles are decatenated from the network by a topoisomerase to its covalently closed form. Free minicircle replication starts at the universal minicircle sequence 5'-GGGGTTGGTGTA-3' (Borst & Hoeijmakers, 1979). Gaps generated in the lagging strand due to discontinuous replication helps in differentiating already replicated minicircles from those that are going to be replicated (Borst & Hoeijmakers, 1979). Thereafter gaps are filled and the networks segregate into developing daughter cells (Figure 1.21).

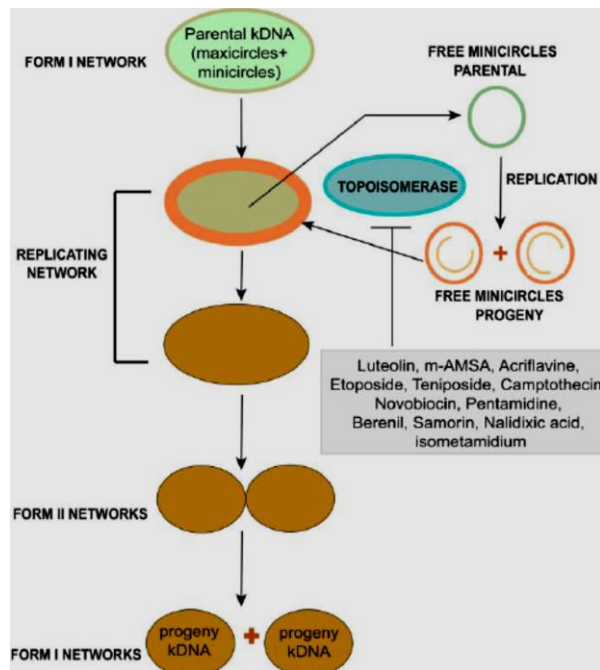


Figure 1.21. A putative model showing the involvement of topoisomerase during replication of kDNA and some potential inhibitors against the enzyme. During kDNA replication the DNA content of the network doubles and the progeny networks partition into two daughter cells (Source: Englund and Marini, 1980).

RNA Editing: The addition or modification of RNA sequences by substitutions, deletions, base modification and insertions are termed as 'RNA editing'. Rewriting or editing RNA transcripts result in major effects including over half of the nucleotides in some transcripts of kinetoplastid protozoa (Hajduk & Ochsenreiter, 2010). Post-transcriptional insertion and occasional deletion of Uridine (U) residues within the coding regions edited the transcripts of the maxicircle protein coding genes and corrected frame shifts and generate translatable mRNAs. gRNAs, the tiny RNA transcripts, guide the editing machinery, are encoded by minicircles (Hajduk & Ochsenreiter, 2010). gRNAs behave like mini-templates to guide the addition and deletion of Us from the pre-edited mRNA. For complete editing of a gene several overlapping gRNAs are required. Each gRNA begins with a 5' anchor region and terminates with a 3'-poly (U) tail that may be involved in the initial interaction of gRNA and mRNA through RNA-RNA and RNA-protein interaction (Hajduk & Ochsenreiter, 2010).

3.4 Search for new molecular targets

Development of new intervention strategies to control public health impact of parasitic diseases is the main object of current biomedical research. Recently, the remarkable advances in molecular and cell biology open up new opportunities for inventing and evaluating targets for drug designing. Several studies confirm the antifolate chemotherapy in *Leishmania* to target both pteridine reductase (PTR-1) and dihydrofolate reductase (DHFR) simultaneously (Chakravarty & Sundar, 2010; Mohapatra, 2014). Various unusual facets of *Leishmania* organisms might be exploited for drug design and novel drug targets are investigated from the parasite genome sequence data. In conjunction with the fact that DNA topoisomerases are proven targets for clinically useful anti-tumor and anti-leishmanial drugs (Chowdhury et al, 2012; Chowdhury et al, 2017; Das et al, 2008; Das et al, 2006a; Das et al, 2006b), the unique bi-subunit topoisomerase I of the kinetoplastid parasites (Brata Das et al, 2004; Chowdhury et al, 2012; Chowdhury et al, 2017; Das et al, 2008; Das et al, 2006a; Das et al, 2005; Das et al, 2006b), have also been found to be good target for anti-parasitic drug discovery. Besides, these targets could be used as potential candidates for vaccine development, which would help to fight against the leishmaniasis menace (Chowdhuri et al, 2023). Topoisomerase I inhibitors generate single-(SSB) or double stranded breaks (DSB), which cause fragmentation of the genome and cell death (Brata Das et al, 2004; Chowdhury et al, 2012; Chowdhury et al, 2017; Das et al, 2008; Das et al, 2006a; Das et al, 2005; Das et al, 2006b). Therefore, efficiency of these drugs, which target topoisomerases directly or indirectly, depends heavily on the ability of DNA repair machinery to restore the basic cellular functions (Pommier, 2006; Pommier, 2013) of the parasites. The key mechanism for chemotherapeutic resistance is to recognize DNA damage and initiate repair. DNA repair enzymes are considered to be attractive targets to enhance the cytotoxicity of the DNA damaging agents towards cancer cells. Understanding the DNA repair pathway of the unicellular protozoan parasites is vital as it may influence the effectiveness of widely used parasitic drugs which exert their cytotoxic effect by stabilizing topo I-DNA covalent complexes (Chowdhuri et al, 2023).

3.5 Targeting parasitic Topoisomerases

The currently available potent and therapeutically used anti-leishmanial drugs are urea-stibamine and sodium stibogluconate (SAG) (Haldar et al, 2011). Camptothecin inhibits DNA topoisomerase I from both *Leishmania* and *Trypanosoma*. The EC₅₀ values for *T. brucei*, *T. cruzi* and *L. donovani* are 1.5, 1.6 and 3.2 μ M respectively (Bodley & Shapiro,

1995). Anilinoacridines have recently been found to possess anti-parasitic activity towards *Leishmania*, *Trypanosoma* and *Plasmodium* species. A biologically active synthetic compound, indolyl quinoline acts as a dual inhibitor of *L. donovani* TopI and II (Chowdhuri et al, 2023; Chowdhury et al, 2012; Chowdhury et al, 2017). 3,3'-di-indolylmethane (DIM) and its derivatives like diphenyl DIM can acts as LdTOPIB poison and is more potent than (Roy et al, 2008). DIM may induce oxidative stress in *Leishmania* cells and leads to fragmentation of genomic DNA. Niranthin, a lignan (diphenyl propanoids) compound, isolated from the plant *Phyllanthus amarus* exhibits as a potent antileishmanial agent and triggers apoptosis by activation of cellular nucleases. Further, niranthin shows effectivity against *Leishmania* parasites with antimony-resistant and low cytotoxicity to the host cells (Chowdhury et al, 2012). Recently, chemically synthesized isobenzofuranone compounds, 3,5-bis(4-chlorophenyl)-7-hydroxyiso-benzofuran-1(3H)- one (JVPH3) and (4-bromo)-3-hydroxy-5-(4-bromo-phenyl)-benzophenone (JVPH4) inhibit *L. donovani* topoisomerase II (LdTOP2) mediated decatenation of the kinetoplast DNA network and exhibit potent antileishmanial activity against both antimony sensitive and resistant parasites (Mishra et al, 2014). Interestingly, these compounds do not inhibit LdTOPIB and are selective for LdTOP2. All the above mentioned compounds have promising anti-leishmanial activities and are important leads for future anti-parasitic drug development. The sixth chapter of this dissertation work is based on the identification and characterisation of a novel pyrido[2',1':2,3]imidazo[4,5-c]quinoline derivative which selectively poisons *Leishmania donovani* bi-subunit Topoisomerase 1 to inhibit the antimony-resistant *Leishmania* infection *in vivo*(Chowdhuri et al, 2023).

Chapter 2

General Materials & Methods

2.1 General Materials: Chemicals and Reagents; Biological Chemicals and Reagents

2.1.1 Chemicals and Reagents; Biological Chemicals and Reagents

All chemicals and reagents used for this study were of ultrapure grade, reagent grade or equivalent. Agarose (A6013) was procured from Sigma Chemicals (St. Louis, MO, USA). Camptothecin (CPT), Thymidine, Aphidicolin (Aph), Hydroxyurea (HU), RO3306 (CDK1 inhibitor) was procured from Sigma (St. Louis, MO, USA) and dissolved in 100% DMSO at a final concentration of 20 mM and stored at -20⁰C. Colcemid (Karyomax) was purchased from Roche. 3-(4,5-dimethylthiazol-2-yl)-2,5-diphenylterazolium bromide (MTT) was procured from Sigma Chemicals (St. Louis, MO, USA). Anti-TDP1 and anti-Mus81 antibodies were purchased from abcam. Anti-β actin antibody was purchased from Santa cruz and Invitrogen. Anti-MPM2, anti-pHH3 and anti-γH2A.x antibodies were purchased from Merck-millipore. Anti-Histone H3 and anti-CDK1 antibody was purchased from Cell Signalling technologies. Anti-FLAG (M2) antibody was purchased from Sigma. Mouse monoclonal anti-human Top1 (C21) antibody, rabbit polyclonal PARP1 antibody and secondary antibodies: horseradish peroxidase conjugated anti-rabbit IgG or anti-mouse IgG were procured from Invitrogen and Novus technologies respectively. Restriction enzymes, T4 DNA ligase, Polynucleotide kinase, Taq DNA polymerase, Expand Hi-fidelity Taq DNA polymerase were purchased from Roche Biochemicals. TOPO-TA cloning vector was purchased from Invitrogen. [³²P] ATP was purchased from Amersham International, (U.K). Ampicillin, kanamycin, chloramphenicol and tetracycline were purchased from Sigma Chemicals. Site directed mutagenesis kit was purchase from Agilent.

Markers: DNA markers used in this study includes λ DNA / Hind III (λ DNA cleaved with Hind III;0.12-23.1 kb), GeneRuler 1kb DNA Ladder was purchased from Fermentas. Prestained Protein Molecular Weight marker (19-240 kDa) was from Puregene.

Bacterial strains: E. coli DH5α was widely used for general transformation and BL21 (DE3) pLysS strain was used as expression host. Cells were grown in LB media in presence or absence of antibiotics.

Leishmania strains: *Leishmania donovani* (Ag83 and BHU575) was used for most studies by growing in M199 medium.

2.1.2 Biological Growth Media

DMEM: DMEM was purchased from Invitrogen. Fetal bovine serum (Invitrogen) was added to final concentration of 10% v/v. Penicillin and streptomycin were added to a final concentration of 100 U/ml and 100 µg/ml respectively.

M199: 11 gm dry powdered medium and 0.35 gm sodium bicarbonate were dissolved in 1 liter water containing 20 mM HEPES and pH adjusted to 7.2 with 1 N NaOH. Heat inactivated fetal calf serum was added to a final concentration of 10% v/v. Penicillin and streptomycin were added to final concentrations of 100 U/ml and 100 µg/ml respectively.

RPMI-1640: RPMI was purchased from Invitrogen. Fetal bovine serum (Invitrogen) was added to final concentration of 10% v/v. Penicillin and streptomycin were added to a final concentration of 100 U/ml and 100 µg/ml respectively.

LB Media: Bacto tryptone (1% w/v), Yeast extract (0.5% w/v), NaCl (1% w/v); and pH adjusted to 7.5.

Liquid culture media: M199 powder (Sigma) 1.1%, HEPES buffer (pH7.5) 20 mM. Buffered media was filter sterilized by passing through 0.22 µm pore sized filter (Nalgene) and then heat inactivated fetal calf serum 10% (GIBCO), Penicillin 100 U/ml and Streptomycin 100 µg/ml were added. This media was used for liquid culture of *Leishmania* promastigotes.

Drug Solutions: Camptothecin (CPT), Aphidicolin, Nocodazole, Thymidine, MK1775, RO3306 and Colcemid were dissolved in 100% DMSO. Drug solutions were kept in aliquots at -200C. The final concentration of DMSO was kept at 4% and 0.5% for the in vitro studies and cellular experiments respectively.

Materials for Column Chromatography:

Ni²⁺-NTA agarose was purchased from Qiagen.

2.1.3 Solutions and Buffers

Lysis/Equilibration Buffer: 50 mM NaH₂PO₄; 300 mM NaCl; 10 mM Imidazole;
1 mM DTT; 1mM PMSF (pH 7.5-7.8).

Wash Buffer:	50 mM NaH ₂ PO ₄ ; 300 mM NaCl; 40 mM Imidazole; 1 mM DTT; 1mM PMSF (pH 7.5-7.8).
Elution Buffer:	100 mM Tris-HCl, pH 7.5; 300 mM NaCl; 300 mM Imidazole; 15% glycerol; 1 mM DTT; 1 mM PMSF.
TAE Buffer:	40 mM Tris-HCl, pH 7.5; 40 mM acetic acid; 2 mM EDTA, pH 8.0.
TBE Buffer:	89 mM Tris-HCl, pH 7.5; 89 mM boric acid; 2 mM EDTA, pH 8.0.
TE Buffer:	10 mM Tris-HCl, pH 7.5; 1 mM EDTA, pH 8.0.
Annealing Buffer:	20 mM Tris-HCl, pH 7.5; 150 mM NaCl.
STE Buffer:	10 mM NaCl, 10 mM Tris-HCl pH 7.9 and 1 mM EDTA. Phosphate Buffered Saline: 20 mM phosphate buffer (pH 7.4), 150 mM NaCl. (PBS)
DNA gel loading Buffer:	0.25% (w/v) bromophenol blue, 0.25% (w/v) xylene cyanol, 30% glycerol (v/v) and 10 mM Tris-HCl, pH 8.
Protein gel loading:	100 mM Tris-HCl (pH 6.8), 200 mM DTT, 4% SDS, Buffer (2X) 0.2% bromophenol blue and 20% glycerol.
STE:	20 mM Tris-HCl, pH 7.5; 300 mM NaCl; 1 mM EDTA.
Solution I:	50 mM glucose, 10 mM EDTA, 25 mM Tris-HCl (pH 8.0).
Solution II:	0.2N NaOH, 0.1% SDS.
Solution III:	3M potassium acetate buffer (pH 5.2).

2.2 General Methods

2.2.1 Cell culture and maintenance of cell lines

Human cancerous cell lines like MCF7, HeLa, HCT116, NIH: OVCAR-3 and HEK293 were obtained from the Developmental Therapeutics Program as generous gift from Dr. Yves

Pommier (NIH/NCI/USA), TDP1^{+/+} and TDP1^{-/-} primary MEF cells were kind gift from Dr Cornelius F Boerkoel (University of British Columbia, Canada) were cultured and were maintained at 37°C under 5% CO₂ in Dulbecco's modified Eagle's medium containing 10% fetal bovine serum (Life Technologies). Cells were treated with different concentrations of CPT as described previously (Das *et al.*, 2009; Das *et al.*, 2014).

2.2.2 Preparation of plasmid DNA

Plasmid DNA preparation was carried out according to the methods described previously (Brinboim and Doly, 1979) with some modifications. *E. coli* host cells (DH5α) containing plasmid was grown in 250 ml LB media containing ampicillin at a concentration of 100 µg/ ml at 37⁰ C for 16 h (overnight). The cells were harvested by centrifugation at 6000 rpm for 10 min at 4⁰ C. The pellet was washed thoroughly with ice-cold STE buffer and subsequently suspended in 2.5 ml Solution I containing 50 µg/ ml lysozyme. The suspended cells were kept at 4⁰ C for 15 min and lysed by addition of freshly prepared 5 ml Solution II with gentle shaking. To the lysate 3.75 ml ice cold Solution III was added mixed and kept on ice for 15 min. Cell debris was pelleted at 12,000 rpm for 20 min at 4⁰ C (Heraeus Biofuge Primo R Centrifuge; Rotor number 7593). The supernatant was precipitated by addition of volume of isopropanol, followed by centrifugation at 12,000 rpm for 20 min at room temperature, washed with 70% ethanol, dried and resuspended in 500 µl TE buffer. RNA was digested with 100 µg/ml RNase A for 3h at 37⁰ C and RNase was inactivated by Proteinase K in the presence of 0.1% SDS. The mixture was extracted with equal volume of phenol: chloroform (1:1) and chloroform and aqueous phase was precipitated with ethanol. The DNA pellet was dried and resuspended in 500µl TE buffer.

2.2.3 Agarose Gel Electrophoresis

Agarose gel electrophoresis was carried out for the separation of DNA. Usually electrophoresis is carried out at 0.8-1.2% agarose gel in 1X TAE or TBE buffer at a constant voltage of 5-6 V/cm for 2- 8 hrs. DNA was stained by soaking in 0.5 µg / ml of ethidium bromide solution, visualized in U.V. transilluminator and photographed.

2.2.4 Construction of recombinant plasmids, expression, site directed mutagenesis and purification of recombinant proteins

All the recombinant constructs, over expression and purification procedures of the recombinant proteins, enzymatic analysis with the recombinant proteins and other specific procedures are described in the Materials and Methods section of individual chapters.

Chapter 3

Identification of TDP1 as a novel substrate of CDK1

3.1 Introduction:

DNA topoisomerase 1 (Top1) has been attributed indispensable for the maintenance of DNA torsional stress generated during nucleic acid metabolic processes like replication, transcription and chromatin remodelling (Champoux, 2001; Pommier, 2006). Supercoiling relaxation demands the reversal of Top1-linked DNA single-strand breaks (SSBs) (Top1 cleavage complexes), which are usually transient but can be selectively trapped by the Top1 interfacial inhibitors like camptothecin (CPT) and its clinical derivatives topotecan and irinotecan (Das et al, 2018; Pommier, 2006; Pommier et al, 2016). Top1cc also accumulate under physiological conditions when Top1 acts on altered DNA structures (mismatches, abasic sites, oxidized and adducted bases) (Pommier, 2006; Pommier et al, 2016). The trapping of Top1cc results in DNA double-strand breaks (DSBs) upon replication and transcription collisions (Pommier et al, 2016), associated with concomitant cell cycle arrest and cell death. Hence, repairing irreversibly trapped Top1cc is an absolute necessity for DNA metabolism, genome maintenance and is relevant to resistance of tumours to Top1 inhibitors (Ashour et al, 2015; Das et al, 2016; Pommier et al, 2014; Pommier et al, 2016). Tyrosyl-DNA phosphodiesterase (TDP1), is the key enzyme for the repair of trapped Top1cc and hydrolyses the phosphodiester bond between the catalytic tyrosine of Top1 and the 3'-end of DNA nicked by Top1 (Pommier et al, 2014). It has been previously described that the genetic inactivation of TDP1 results in heightened susceptibility to CPT (Das et al, 2009; Hirano et al, 2007; Katyal et al, 2007; Murai et al, 2012; Pommier et al, 2014). Homozygous mutation of TDP1 is also responsible for the neurodegenerative syndrome, spinocerebellar ataxia with axonal neuropathy SCAN1, which results from elevated levels of Top1cc in post-mitotic neurons (Caldecott, 2003; Caldecott, 2008; El-Khamisy et al, 2005; Interthal et al, 2005; Katyal et al, 2007; Takashima et al, 2002). TDP1 is not only implicated in Top1cc repair, it also repairs blocking DNA lesions at the 3'-end of DNA breaks, including abasic sites, phosphoglycolate, and alkylated bases at the 3'-end of DNA breaks (Caldecott, 2008) resulting from oxidative DNA damage produced by radiomimetic drugs such as bleomycin, alkylating agents and nucleoside analogues (Das et al, 2010; Hirano et al, 2007; Murai et al, 2012; Pommier et al, 2014). Additionally, TDP1 harbors nucleosidase activity towards 3'-deoxyriboses, 3'-ribonucleotides and 3'-chain terminating anticancer and antiviral nucleosides (cytarabine, acyclovir, AZT and abacavir) and even 5'-phosphodiesterase activity for topoisomerase II cleavage complexes (Das et al, 2010; Hirano et al, 2007; Huang et al, 2011; Huang et al, 2013; Murai et al, 2012; Nitiss, 1998; Pommier et al, 2014) and acts both in the

cell nucleus and mitochondria (Das et al, 2010; Murai et al, 2012).

The regulation of cellular TDP1 has been studied widely and occurs mostly at the post-translational level (Das et al, 2009; Pommier et al, 2014). ATM-and/or DNA dependent protein kinase (DNA-PK)-mediated S81 phosphorylation has been reported to stabilize TDP1 (Das et al, 2009) and fosters the recruitment and activity of TDP1 for repairing Top1cc and ionizing radiation (IR)-induced DSBs (Ashour *et al.*, 2015; Das *et al.*, 2009; Chiang *et al.*, 2010; McKinnon, 2012; Shiloh *et al.*, 2015). Poly(ADPribose)ylation of TDP1 by poly(ADPribose) polymerase-1 (PARP1) also enhances the stability of TDP1 and its interaction with X-ray cross-complementing group 1 (XRCC1) and facilitates the recruitment of TDP1 to Top1cc damage sites (Das et al, 2014). Additionally, SUMOylation of TDP1 at lysine 111 has been reported to recruit TDP1 at transcription-associated Top1cc damage sites (Hudson et al, 2012). Recently it has been reported that the arginine methyl transferase PRMT5 acts as a molecular determinant for Top1cc repair and that TDP1 is dimethylated at R361 and R586 by PRMT5 (Bhattacharjee et al, 2022; Rehman et al, 2018) which modulates TDP1 catalytic activity.

Previous studies using live cell microscopic imaging with GFP tagged constructs of TDP1 and Top1 have shown that there is a markedly distinct chromosomal localisation pattern of these proteins during the different phases of cell cycle, in as much as GFP-TDP1 does not associate with the chromosomes in mitosis until late telophase (late mitosis), whereas GFP-Top1 remains DNA-bound during the entire mitotic cycle (Barthelmes et al, 2004). However, a PTM or any other regulation of TDP1 responsible for this differential temporal (cell cycle dependent) association of TDP1 with the chromatin has never been studied. In the current study, we report a novel phosphorylation of TDP1 at S61, that was detected through Mass Spectrometry. We show that the mitotic archetypical kinase Cyclin dependent kinase 1 (CDK1) phosphorylates TDP1 at Serine 61 (S61) in the early mitotic stage independent of replication stress. CDK1 mediated phosphorylation stimulates TDP1 dissociation from chromatin, and it is required for the proper chromosomal segregation in mitosis. Complementation of a phosphodeficient mutation of TDP1 at S61A in TDP1^{-/-} MEFs results in chromosomal aberrations and accumulation of extensive genome instability. Therefore, our results represent the first demonstration of a cell cycle dependent regulatory phosphorylation of TDP1 in human cells which is not involved in the recruitment of TDP1 at DNA damage sites or in enforcing the stability of the protein in response to DNA damage (Bhattacharjee et

al, 2022; Das et al, 2009; Rehman et al, 2018). Cell cycle dependent phosphorylation of TDP1 at S61 regulates the chromosomal association and dissociation of TDP1 and also acts as a switching tool for its role in the canonical base excision repair (BER) pathway coupled with PARP1, XRCC1, Ligase III, PNKP and Polymerase Beta (Pommier et al, 2014) during the S-phase and the alternative break induced repair (BIR) pathway known as mitotic DNA synthesis (MiDAS) during the mitosis (Minocherhomji et al, 2015).

3.2 Materials and methods

3.2.1 Mass spectrometry analysis of TDP1

Ectopic FLAG-TDP1 complexes were immunoprecipitated with anti-FLAG antibody as described above. To induce DNA damage cells expressing FLAG-TDP1 were treated with CPT (5 μ M/3 h) prior to anti-FLAG immunoprecipitation and were subjected to tryptic digestion at 37⁰C, overnight, followed by lyophilisation, reconstitution, and fractionation applying strong cation exchange (SCX) liquid chromatography (LC) and mass spectrometry analysis as previously described (Rehman et al, 2018).

3.2.2 Drugs

DNA replication inhibitor aphidicolin (APH) (Sigma-Aldrich) was used at 0.4 μ M (low dose) or 1.5 μ M (intermediate dose), Hydroxyurea (Sigma-Aldrich) was used at 2 mM, Camptothecin (Sigma-Aldrich) was used as per experimental requirements as indicated in the experiment, CDK1 inhibitor (RO-3306, Sigma-Aldrich) at 9 μ M. Nocodazole (Sigma-Aldrich) was used at 200ng/ml and Thymidine (Sigma-Aldrich) at 2 mM. 5-Bromo-2'-Deoxyuridine (BrdU, Thermo-fisher) was used at 1X working concentration.

3.2.2 Antibodies

Rabbit polyclonal anti-phospho-Histone H3 (06-570), anti- MPM2 (05-368), anti-Top1cc (MABE1084) and mouse monoclonal anti- γ H2AX (05-636) antibodies were purchased from Millipore, USA. Rabbit polyclonal TDP1 (Ab4166) and GAPDH (Ab9485), mouse monoclonal anti-XRCC1 (Ab1838), anti-MUS81 antibody (Ab14387) and Histone H3 (Ab24834) antibodies were purchased from Abcam (Cambridge, MA, USA). Mouse monoclonal anti-flag (M2) (F3165), rabbit polyclonal anti-FLAG (F7425) antibodies were purchased from Sigma (St Louis, MO, USA). The anti-CDK1 (9116), mouse monoclonal

antibody was from Cell Signalling Technologies. Rabbit polyclonal anti-GFP (A-11122) antibody was from Invitrogen. Rabbit polyclonal PARP1 antibody and anti-actin (sc-47778) antibody secondary antibodies: Horseradish peroxidase (HRP)-conjugated anti-rabbit IgG or anti-mouse IgG were obtained from Santa Cruz Biotechnology (Santa Cruz, CA, USA).

3.2.3 Expression constructs and site-directed mutagenesis

Human flag-tagged full-length TDP1 (FLAG-TDP1^{WT}), His-tagged and green fluorescent protein (GFP)-tagged TDP1 constructs were described previously (Das *et al.*, 2009; Das *et al.*, 2014). The HA-CDK1 fusion construct was a kind gift from Dr Sorab Dalal (Tata Memorial Centre Advanced Centre for Treatment, Research and Education in Cancer, India). The point mutations: TDP1^{S61A} in FLAG as well as His-TDP1^{S61A} were created using the ‘QuickChange’ protocol (Stratagene, La Jolla, CA, USA). All PCR-generated constructs were confirmed by DNA sequencing.

3.2.4 Cell culture, treatment and transfections

Cell cultures were maintained at 37°C under 5% CO₂ in Dulbecco’s modified Eagle’s medium containing 10% fetal calf serum (Life Technologies, Rockville, MD, USA). The cervical carcinoma cell line (HeLa), human kidney origin (HEK293) and human breast cancer (MCF7) was obtained from the Developmental Therapeutics Program (NCI, NIH/ USA). TDP1^{+/+} and TDP1^{-/-} primary MEF cells were a kind gift from Dr Cornelius F Boerkoel (University of British Columbia, Vancouver, British Columbia, Canada). Cells were treated with the indicated concentrations of CPT. Plasmid DNAs and Si RNAs were transfected with Lipofectamine 2000 (Invitrogen) according to the manufacturer’s protocol. TDP1^{-/-} MEF cells were transfected with the FLAG-TDP1 constructs using X-tremeGENE HP DNA transfection reagent (Roche) according to the manufacturer’s protocol.

3.2.5 siRNA transfection

Transfections were performed as described previously (Das *et al.*, 2009). In brief, cells (1.5×10^5) were transfected with control siRNA or 25 nM CDK1, Mus81 or TDP1 siRNA (GE Dharmacon, SiRNA- SMARTpool) using lipofectamine (Invitrogen) according to the manufacturer’s protocol. Time course experiments revealed a maximum suppression of CDK1 or TDP1 protein at day 3 after transfection, as analysed by Western blotting.

3.2.6 Cell extracts, immunoblotting, and immunoprecipitation

Preparation of whole cell extracts, immunoprecipitation, and immunoblotting were carried out as described previously (Das *et al.*, 2009; Das *et al.*, 2010 a; Das *et al.*, 2014). Briefly, cells were lysed in a lysis buffer (10 mM Tris–HCl (pH 8), 150 mM NaCl, 0.1% SDS, 1% NP40, 0.5% Na-deoxycholate supplemented with complete protease inhibitors) (Roche Diagnostics, Indianapolis, IN) and phosphatase inhibitors (Phosphatase Inhibitor Cocktail 1 from Sigma). After thorough mixing and incubation at 4⁰C for 2 h, lysates were centrifuged at 12 000 g at 4⁰C for 20 min. Supernatants were collected, aliquoted, and stored at –80⁰C. For immunoprecipitation, cells were lysed in a lysis buffer (50 mM Tris–HCl (pH 7.4), 300 mM NaCl, 0.4% NP40, 10 mM MgCl₂, 0.5 mM dithiothreitol supplemented with protease and phosphatase inhibitors). Supernatants of cell lysates were obtained by centrifugation at 15 000 g at 4⁰C for 20 min and pre-cleared with 50 µl of protein A/G-PLUS agarose beads (Santa Cruz, CA, USA). About 5 mg of precleared lysate was incubated overnight at 4⁰C with indicated antibodies (2–5 µg/ml) and 50 µl of protein A/G-PLUS agarose beads. Isolated immunocomplexes were recovered by centrifugation, washed thrice with lysis buffer, and were subjected to electrophoresis on 10% Tris–glycine gels and immunoblot analysis. Immunoblottings were carried out following standard procedures, and immunoreactivity was detected using ECL chemiluminescence reaction (Amersham) under ChemiDoc™ MP System (Bio-Rad, USA). Densitometric analyses of immunoblots were performed using Image J software.

3.2.7 Immunocytochemistry and confocal microscopy

Immunofluorescence staining and confocal microscopy were performed as described previously (Das *et al.*, 2009; Das *et al.*, 2010 a; Das *et al.*, 2014). Briefly, cells were grown and drug treated on chamber slides (Thermo Scientific™ Nunc™ Lab-Tek™ II Chamber slides) followed by fixation with 4% paraformaldehyde for 10 min at room temperature. Primary antibodies against FLAG, γH2AX, anti-BrdU and Top1cc were detected using anti-rabbit or anti-mouse IgG secondary antibodies labelled with Alexa 488/568 (Invitrogen). Cells were mounted in anti-fade solution with 4',6-diamidino-2-phenylindole (DAPI) (Vector Laboratories, Burlingame, CA, USA) and examined under Leica TCS SP8 confocal laser-scanning microscope (Germany) with a 63×/1.4 NA oil objective. Images were collected and processed using the Leica software and sized in Adobe Photoshop 7.0. The γH2AX or Top1cc or BrdU intensity per nucleus was determined with Adobe Photoshop 7.0 by

measuring the fluorescence intensities normalized to the number of cell count (Das *et al.*, 2009; Das *et al.*, 2010 a; Das *et al.*, 2014).

3.2.8 *In vitro* kinase assays

Purified His-TDP1 (WT and S61A) protein (1 μ g) was incubated with immunoprecipitated HA-CDK1 kinase, 0.05 mM ATP and in 1X kinase assay buffer (25 mM Tris-HCl (pH 7.5), 5 mM beta-glycerophosphate, 2 mM dithiothreitol (DTT), 0.1 mM Na₃VO₄, 10 mM MgCl₂.) buffer for 30 min at 37 °C. Reactions were stopped by adding 2x Laemmli sample buffer and heating at 95 °C for 5 min. Samples were loaded onto a 10% SDS-PAGE gel and run at 25 mA for 2 hr. Phosphorylation reaction products were separated by SDS-PAGE, transferred on to PVDF membrane and analyzed by Western blotting using anti-phosphoTDP1 (peptide antibody) and anti-TDP1 antibodies.

3.2.9 Flow cytometry based cell cycle analysis

For cell cycle profile analysis, cell samples are harvested by scraping or trypsinisation followed by pelleting the cells at 1500 rpm. The cell pellets are washed with 1X PBS before fixation with 70% ethanol. On the day of the flow cytometry, the cell suspension in 70% ethanol is pelleted and washed using 1X PBS. All fixative should be removed from cells before proceeding with cell staining. Next, the flow cytometry samples each containing $\sim 1 \times 10^6$ cells in suspension are prepared. The samples are centrifuged and the supernatant is decanted, leaving a pellet of cells in each sample tube. 0.5 mL of FxCycle™ PI/RNase Staining Solution stain is added to each flow cytometry sample, mixed well. The samples are incubated for 15–30 minutes at room temperature, protected from light. The samples are analyzed the samples without washing, using 488-nm, 532-nm, or similar excitation, and collect emission using a 585/42 bandpass filter or equivalent.

3.3 Results

3.3.1 TDP1 is phosphorylated at Serine 61 during mitosis

To investigate new post translational modifications of TDP1, we pulled down ectopic FLAG-TDP1 both in the presence and absence of CPT and were examined using mass spectrometry (MS) as described previously (Rehman *et al.*, 2018). MS analysis of FLAG-TDP1 immunoprecipitation complex detected S61 as a phosphorylated serine residue on TDP1

located at the N-terminal end of TDP1 (Figure 3.1A-B). MSdata also revealed that TDP1-S61 phosphorylation was detected independently of DNA damage. S61 residue of human TDP1 located at the N-terminal domain is phylogenetically conserved across vertebrate species as a proline directed phosphorylation site (Figure 3.1B), and lies within a conserved motif, which is the preferred substrate for Cyclin dependent kinase 1 (CDK1) (Holt et al, 2009). We used phosphoNET (Kinexus) and the kinase predictor scansite algorithm, both of which predicted CDK1 as the proline-directed serine/threonine kinases to phosphorylate S61 (<http://www.phosphonet.ca/>). Further, we also mined the cBioPortal Cancer Genomics database and the BioMuta-single-nucleotide variations (SNVs) in cancer for any cancer relevant variants associated with S61, which identified serine-to-leucine (S61L) melanoma and oral-cavity cancer variants (<https://portal.gdc.cancer.gov/genes/>) imperative to the physiological significance of this residue.

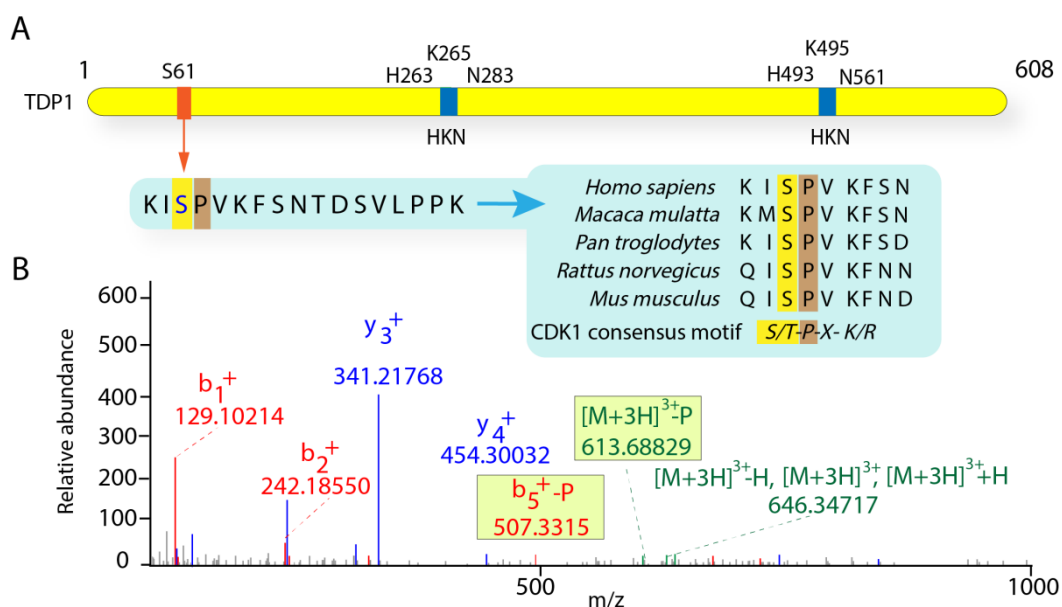


Figure 3.1 (A) Schematic representation of human TDP1 showing the serine phosphorylation site (S61) and the catalytic residues (HKN motifs). The sequence alignment of amino acids of TDP1 in the region flanking the S61 phosphorylation site (a conserved CDK1 substrate phosphorylation site S/T-P-X-K/R highlighted in blue) from human (*Homo sapiens*), monkey (*Macaca mulatta*), chimpanzee (*Pan troglodytes*), rat (*Rattus norvegicus*), mouse (*Mus musculus*) demonstrates the phylogenetic conservation of the residue. Sequence alignment was performed using ClustalW2 (<http://www.ebi.ac.uk/Tools/msa/clustalw2>). (B) MS/MS spectrum of the TDP1 phospho-peptide harbouring S61 residue.

In order to validate TDP1-S61 phosphorylation as a mitotic event we had generated a non-phosphorylatable mutant variant of TDP1 at S61 (FLAG-TDP1^{S61A}) by site directed mutagenesis and performed the co-immunoprecipitation of FLAG-TDP1^{WT} or FLAG-TDP1^{S61A} with anti-FLAG antibody ectopically expressed in TDP1^{-/-} MEFs cells, left in an

asynchronous state or synchronized to G2/M by treatment with nocodazole (noc) as outlined in the protocol (Figure 3.2A). Following immunoprecipitation and Western blotting with anti-MPM2 antibody that recognizes epitopes in proteins phosphorylated during mitosis, we found that the FLAG-TDP1^{WT} indeed interacts with the MPM2 specific antibody only in the G2/M arrested cells while the phosphorylation signal on TDP1 was abrogated in the phosphorylation mutant variant FLAG-TDP1^{S61A} indicating S61 as the residue for the mitotic phosphorylation (Figure 3.2B; phosphorylated TDP1). Further, to confirm TDP1-S61 phosphorylation, we also generated a phospho-specific peptide antibody that recognizes the epitope HKRKI(S*)PVKFSN (the asterisk denotes phosphorylation) spanning S61 residue of TDP1. This antibody also recognized a single band with molecular weight similar to that of TDP1 (pS61-TDP1) in the G2/M arrested cells expressing FLAG-TDP1^{WT} while cells expressing the phosphomutant FLAG-TDP1^{S61A}, were completely defective in detecting the pS61-TDP1 signal in both asynchronous and noc arrested cells (Figure 3.2B; pS61-TDP1), confirming that the antibody detected mitosis specific TDP1 phosphorylation at S61 residue (TDP1-pS61).

In order to monitor the temporal kinetics of TDP1 phosphorylation at S61, we synchronized TDP1^{-/-} MEFs expressing FLAG-TDP1^{WT} to the G2/M border using noc, and monitored the phosphorylation of this site at stages after release from the arrest at indicated time points in G2/M (0 h), late mitotic (1 h) and G1 (5 h) phases (see FACS profile; Figure 3.2C) using both the anti-MPM2 antibody and also the TDP1-pS61-phospho-specific antibody (Figure 3.2D). We found that the S61-phosphorylation peaked upon release from early mitosis before declining in telophase to return to near asynchronous basal levels in G1 (Figure 3.2D) which exactly mirrored the CDK1 kinase activity (Brown et al, 2015; Diril et al, 2012; Enserink & Kolodner, 2010; Holt et al, 2009; Li & He, 2020; Satyanarayana et al, 2008) congruent with our assumption that CDK1 might be the kinase responsible for phosphorylating TDP1 at S61. The flow cytometry analysis of the FLAG-TDP1^{WT} and FLAG-TDP1^{S61A} transfected TDP1^{-/-} MEFs further confirmed that the overexpression of the phospho-mutant did not perturb the cell cycle progression of the MEFs (Figure 3.2C).

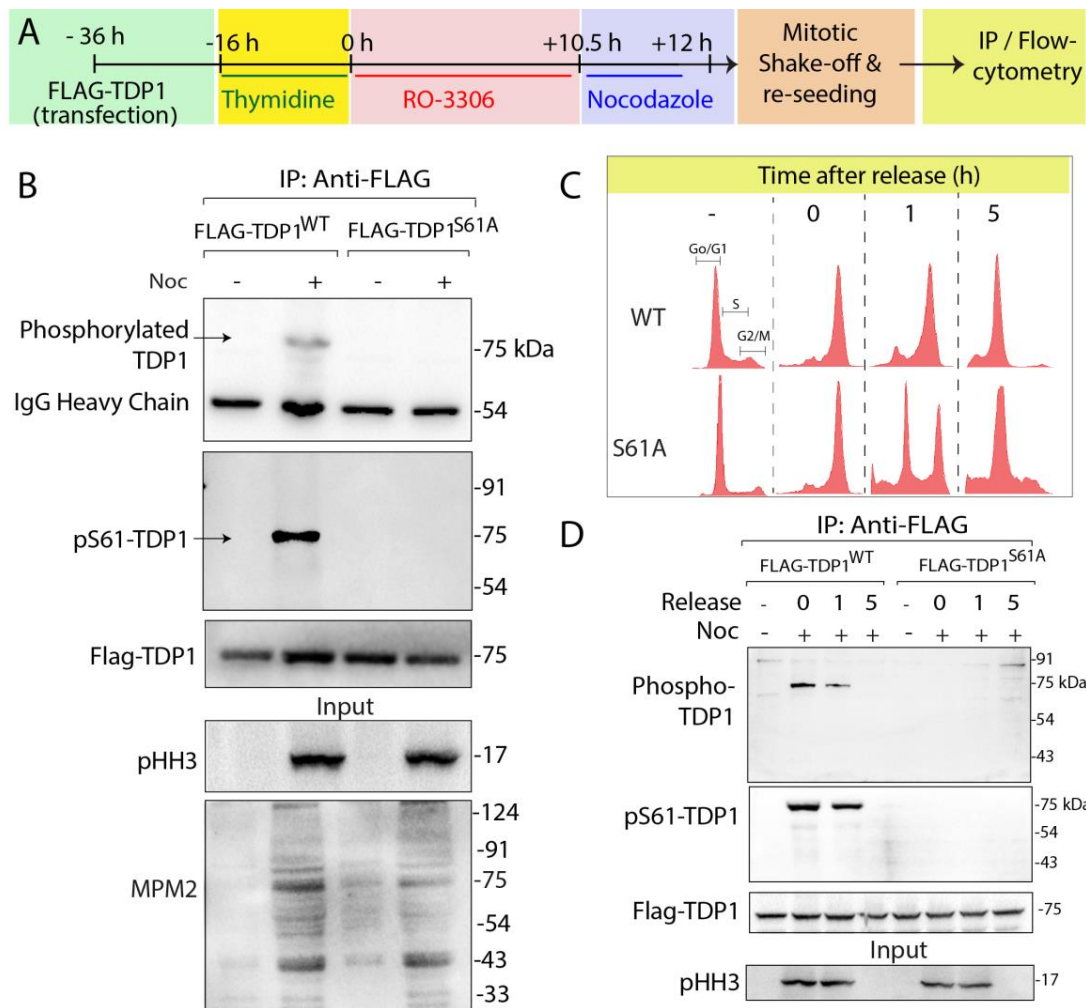


Figure 3.2 Human TDP1 is phosphorylated at S61 during early mitosis. (A) Schematic representation of the protocol followed for synchronisation of TDP1^{-/-} MEFs transfected with FLAG-TDP1 (WT or S61A) variants to mitotic phase for immunoprecipitation or flow cytometry analysis. (B) TDP1^{-/-} MEFs ectopically expressing FLAG-TDP1^{WT} or FLAG-TDP1^{S61A} were left asynchronous or synchronised to G2/M phase as per the above protocol, following immunoprecipitation with anti-FLAG antibody the immune complexes were analysed by Western blotting. The anti-MPM2 antibody recognizes a single band (phosphorylated TDP1) with molecular weight corresponding to TDP1 in the MEFs transfected with FLAG-TDP1^{WT} which have been synchronised at G2/M phase. The phospho-specific antibody also recognizes a single band (pS61-TDP1) with molecular weight corresponding to TDP1 in FLAG-TDP1^{WT} expressing MEFs synchronised at G2/M. This blot was stripped and re-probed with anti-FLAG antibody (FLAG-TDP1) to confirm equal levels of immunoprecipitation for each condition. Aliquots (10%) of the input show the level of proteins phosphorylated in the mitotic phase for each panel (anti-MPM2) and phospho-histone H3 at Ser10 (anti-pHH3) indicates mitotic state prior to immunoprecipitation. (C) Flow cytometry profile of the TDP1^{-/-} MEFs ectopically expressing FLAG-TDP1^{WT} and FLAG-TDP1^{S61A}, synchronised to G2/M phase and harvested at indicated time points after release. (D) Detection of the temporal kinetics of phosphorylation on TDP1-S61 using the anti-MPM2 and phospho-specific antibody generated for the S61-epitope. FLAG-TDP1^{WT} and FLAG-TDP1^{S61A} were ectopically expressed in TDP1^{-/-} MEFs. Following G2/M synchronisation as per the protocol, FLAG-TDP1 variants were immunoprecipitated at the indicated time points (0, 1 and 5 hours post noc release) using anti-FLAG antibody and immune complexes were blotted with the anti-MPM2 and anti-pS61-TDP1 antibody. The same blot was stripped and re-probed with anti-FLAG antibody. Phospho-histone H3 (anti-pHH3) indicates mitotic state prior to immunoprecipitation in the aliquots (10%) of the input.

We also confirmed that the phosphorylation of TDP1 at S61 is a mitotic event by immunocytochemistry using the phosphopeptide antibody (TDP1-pS61) in MCF7 cells at interphase or arrested at mitosis in presence or absence of CPT or aphidicolin (Aph) following the protocol outlined in Figure 3.3A. Coherent with our previous results we found the phosphopeptide antibody (TDP1-pS61) detected phosphorylation mark on endogenous TDP1 in mitotic cells but failed to detect any phosphorylation in interphase cells (Figure 3.3B) consistent with the previous literature that CDK1 remains inactive during S-phase. Moreover the phosphorylation was detected independent of DNA damage or replication stress induced by CPT (corroborating with the MS data) or aphidicolin respectively (Figure 3.3B-C). Interestingly we observed that the phosphorylated TDP1 (pS61-TDP1) remains extruded from the mitotic chromosomes and shows cytosolic localization pattern (Figure 3.3B) in M-phase.

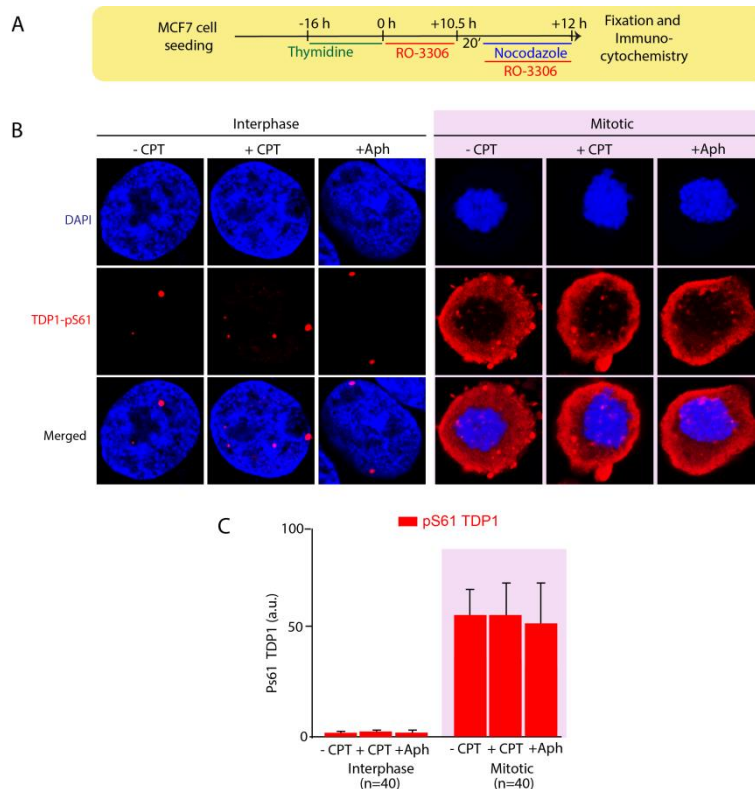


Figure 3.3 Phosphorylation at TDP1-S61 residue is a mitotic event. (A) Schematic of the protocol to study the cell cycle dependent S61 phosphorylation status of endogenous TDP1 in MCF7 cells. (B) MCF7 cells were treated with or without CPT or aphidicolin and left asynchronous or fixed after release from nocodazole arrest and stained with anti-pS61-TDP1 (phosphopeptide antibody which detects TDP1-S61 phosphorylation). Cells at interphase and mitosis were tallied on the basis of their chromatin morphology, as indicated by DAPI staining. The phosphorylated TDP1-S61 (pS61) is stained in red. (C) Bar graph showing the levels of the phosphorylated TDP1 (pS61) for interphase and mitotic cells as indicated for untreated cells or following replication stress with CPT or Aph. Staining intensities from 40 nuclei per stage (indicated in the parenthesis) were expressed as mean \pm s.d. a.u: arbitrary unit.

3.3.2 CDK1 physically interacts with TDP1

CDK1 is the core mitotic regulatory kinase whose activity oscillates during each cell cycle peaking at the G2/M phase and remaining low at G1/S phase (Brown et al, 2015; Diril et al, 2012; Enserink & Kolodner, 2010; Holt et al, 2009; Li & He, 2020; Satyanarayana et al, 2008) which led us to investigate if the phosphorylation of TDP1 at S61 is regulated by CDK1 during the progression of cell cycle. CDK1 has been exhaustively studied to play a key role in the regulation of the mitotic DNA damage response proteins and pathways (Brown et al, 2015; Diril et al, 2012; Enserink & Kolodner, 2010; Holt et al, 2009; Li & He, 2020; Satyanarayana et al, 2008). This prompted an investigation into the possible role of CDK1 in the repair of Top1cc repair by a cell cycle dependent S61-TDP1 phosphorylation in the M-phase. Since TDP1 is the key repair protein for the efficient repair of trapped Top1ccs, TDP1-CDK1 interaction was examined directly using immunoprecipitation. We ectopically expressed FLAG-TDP1 in HEK293 cells and immuno-precipitated enriched TDP1 using anti-FLAG antibody to test TDP1-CDK1 association. Co-immunoprecipitation (co-IP) of ectopically expressed TDP1 pulled down endogenous CDK1 (Figure 3.4A) both in the presence as well as in the absence of CPT, indicating TDP1-CDK1 binding is independent of DNA damage. To test whether CDK1 directly interacts with TDP1, we performed co-IP with FLAG-TDP1 in the presence of the benzonase nuclease. We found that the TDP1-CDK1 association was resistant to benzonase, indicating a direct protein - protein interaction, not mediated through DNA or RNA. We further established the presence of TDP1 in the CDK1-complex using reverse co-IP in cells ectopically expressing HA-CDK1 (Figure 3.4B). We also found that the treatment with CDK1 inhibitor RO3306 does not disrupt the interaction between CDK1 and TDP1 suggesting the physical interaction between the two proteins is not dependent on the catalytic activity of CDK1.

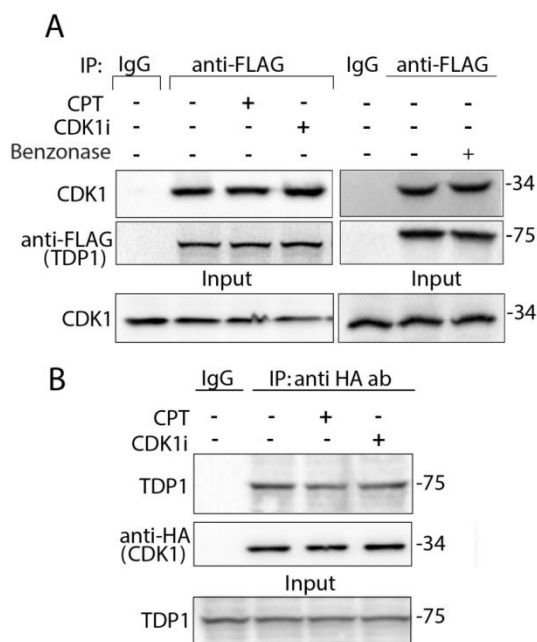


Figure 3.4 CDK1 physically interacts with TDP1. (A) HEK293 cells ectopically expressing FLAG-TDP1 treated with or without CPT (5 μ M, 3 h), and CDK1i (9 μ M, 16 h) were immunoprecipitated using anti-FLAG antibody. Immune complexes were blotted with anti-CDK1 antibody. The same blot was stripped and reprobed with anti-FLAG antibody to show the expression of the FLAG-TDP1. Aliquots (10%) of the input show the level of CDK1 prior to immunoprecipitation. To examine direct protein-protein interaction between CDK1 and TDP1, cell lysates were pretreated with benzonase prior to co-IP as indicated. Blots were subsequently stripped and probed with anti-FLAG antibody to show the expression of the FLAG-TDP1 variants. Aliquots (10%) of the input show the level of CDK1 prior to immunoprecipitation. (B) MCF7 cells ectopically expressing HA-CDK1 were treated with or without CPT (5 μ M, 3 h) and CDK1i (9 μ M, 16 h) and immune-precipitated using anti-HA antibody. The immune complexes were blotted with anti-TDP1 antibody. The same blot was stripped and reprobed with anti-HA antibody. Aliquots (10%) of the input show the level of TDP1 prior to immunoprecipitation. Migration of protein molecular weight markers (kDa) is indicated at right.

3.3.3 CDK1 phosphorylates TDP1 at S61 both *in vitro* and *in vivo* at G2/M phase

The observation that CDK1 physically interacts with TDP1 led us to further confirm whether CDK1 is indeed the kinase responsible for TDP1-S61 phosphorylation. To explore the possibility, we ectopically expressed FLAG-TDP1^{WT} in CDK1-knockdown cells using small interfering RNA (siRNA). Figure 3.5A shows that CDK1 depletion resulted in a marked decrease in pS61-TDP1, showing that TDP1 not only physically interacts with CDK1 (Figure 3.4A-B) but is also phosphorylated at S61 *in vivo* by CDK1. Next, we performed the *in vitro* kinase assay to substantiate the CDK1 mediated TDP1 phosphorylation at S61. . Recombinant 6X-His-TDP1 (WT and S61A) protein variants were used as substrates for immune-precipitated HA-CDK1 in the *in vitro* kinase assay. The phospho-peptide antibody detected phosphorylation of TDP1^{WT} by CDK1, but not of TDP1^{S61A} (Figures 3.5B), which

indicates that CDK1 phosphorylates TDP1 *in vitro* at S61. Taken together, these results confirm a CDK1 mediated novel mitotic phosphorylation on TDP1 at S61 residue.

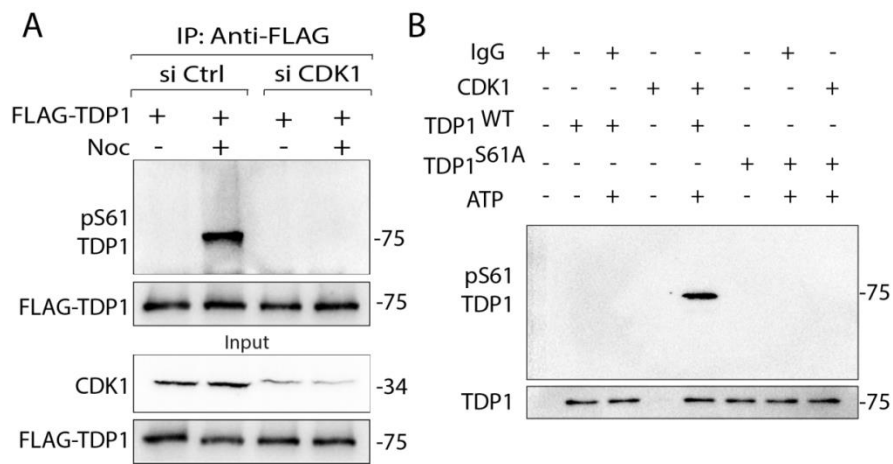


Figure 3.5 CDK1 depletion abrogates the mitotic phosphorylation of S61 residue on TDP1. (A) MCF7 cells were transfected with siCDK1 or siCtrl, then transfected 24 h later with a FLAG-tagged human TDP1 construct (FLAG-TDP1). Following nocodazole treatment (200 ng/ml for 8 hours), ectopic FLAG-TDP1 was immunoprecipitated using anti-FLAG antibody and the immune complexes were blotted with a phospho-S61 specific peptide antibody. The same blot was stripped and re-probed with anti-FLAG antibody. Aliquots (10%) of the input show the level of CDK1 knockdown and FLAG-TDP1 prior to immunoprecipitation. Electrophoretic migration of protein molecular weight markers (kDa) is indicated at right. (B) *In vitro* kinase assays with overexpressed HA-CDK1 immunoprecipitated from MCF7 cells. The substrates were recombinant 6XHis-tagged TDP1 variants purified from bacterial expression system: wild type (WT) and phospho-mutant (S61A). Input denotes the western blotting against anti-TDP1 antibody showing the amount of substrate in each reaction.

3.3.4 TDP1-S61 phosphorylation is dispensable for the catalytic activity of the enzyme

Next, in order to delineate whether this phosphorylation of TDP1 at S61 residue by CDK1 might regulate the catalytic activity of TDP1 we used real-time fluorescence-based assays (Bhattacharjee et al, 2022; Bhattacharjee et al, 2023; Flett et al, 2018). We employed an *ex vivo* approach with immune-precipitated FLAG-TDP1 variants (WT and S61A) as the source of the enzyme to test the impact of S61 phosphorylation on TDP1 catalytic activity as illustrated in Figure 3.6A (Bhattacharjee et al, 2022; Bhattacharjee et al, 2023; Flett et al, 2018). FRET-based TDP1 assays were performed using a double-stranded DNA hairpin (dsDNA) containing 15 base pairs (Figure 3.6B). Each substrate had a 5' fluorophore and a 3' quencher that ablates fluorescence, as described previously (Flett et al, 2018). Cleavage of the 3' quencher by TDP1 abolishes FRET, giving

rise to fluorescence that can be detected in real time. Figure 3.6B shows that the 3' cleavage efficiency of the phosphorylation mutant TDP1 (S61A) was comparable with the wild-type protein (WT) suggesting that TDP1 phosphorylation at S61 is dispensable for its catalytic activity. We also tested the activities of recombinant TDP1 mutant variants (WT and S61A) purified from bacterial system and obtained similar results (Figure 3.6B). Additionally, we also performed *in vitro* kinase assay on the bacterially purified recombinant WT and S61A mutant enzymes using immune-precipitated HA-CDK1 (from mammalian cells) as the kinase and used these *in vitro* phosphorylated mutants (TDP1-pS61 and TDP1-S61A) in the FRET-based cleavage assays which also showed no significant differences between the two variants (Figure 3.6B). These results further confirm that the enzymatic activity of TDP1 is independent of the phosphorylation of TDP1 at the S61 residue by CDK1 coherent with previous studies showing N-terminal deletion mutants of TDP1 are known to have complete catalytically active (Interthal et al, 2001).

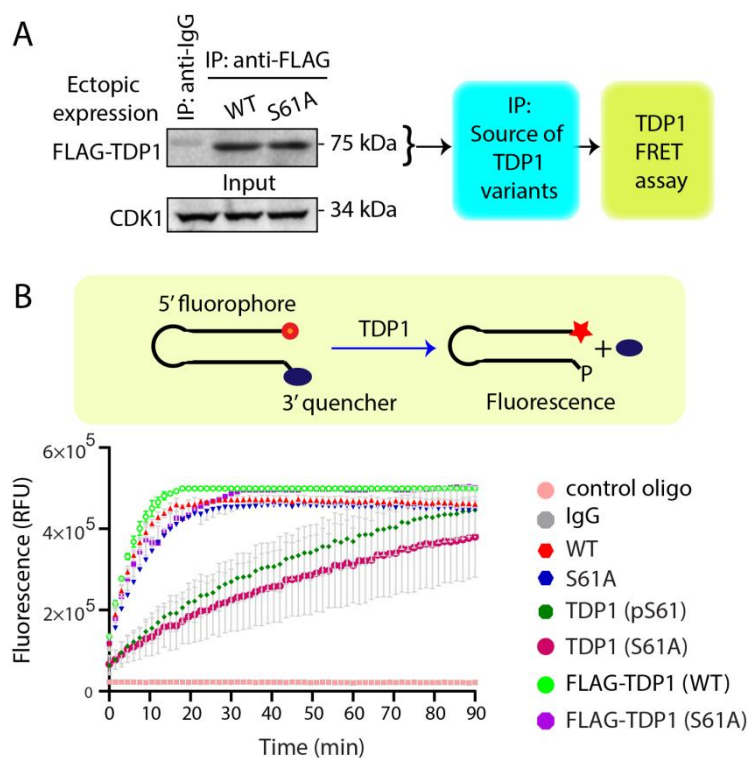


Figure 3.6 TDP1-S61 phosphorylation is dispensable for the catalytic activity of the enzyme (A) Representative Western blot showing equal levels of immunoprecipitated FLAG-tagged TDP1 variants (FLAG-TDP1^{WT} and FLAG-TDP1^{S61A}) in the immune complexes used as the source of TDP1 variants for time-dependent FRET-based real time TDP1 Cleavage assays. (B) Schematic representation of activity assays using a 15-bp hairpin double-stranded fluorescence quencher DNA (dsDNA). Cleavage of the 3' quencher (blue ellipse) by TDP1 increases the fluorescence of 5' fluorophore (orange dot) (lower). (C) Graph for the time-dependent FRET-based real time TDP1 Cleavage assays. Immunoprecipitated FLAG-tagged TDP1 variants (FLAG-TDP1^{WT} and FLAG-TDP1^{S61A}) were used for the assay. Also recombinant TDP1 (WT and S61A) purified from bacterial expression system were used as the source of enzyme for the cleavage assay. These recombinant

proteins were phosphorylated by *in vitro* kinase assay using immune-precipitated HA-CDK1 as the source of kinase and the phosphorylated proteins (TDP1 (pS61) and TDP1 (S61A)) were also used for the cleavage assay. Substrate cleavage by WT and S61A TDP1 was measured by fluorescence intensity, in relative fluorescence units (RFU), and plotted as a function of time (min). Error bars represent mean \pm SEM (n = 3).

3.3.5 TDP1-association with XRCC1-PARP1 is independent of TDP1-S61 phosphorylation.

It has been previously reported that TDP1 is a part of the base excision repair complex comprising of XRCC1, PARP1, PNKP, Pol β , LigIII α (Pommier et al, 2014), we tested whether phosphorylation of TDP1 at S61 affected its interaction with XRCC1 or PARP1. Immunoprecipitation of ectopic FLAG-TDP1^{WT} or FLAG-TDP1^{S61A} showed that the phosphomutant TDP1S61A was equally efficient in pulling down XRCC1 from untreated and CPT-treated cell extracts (Figure 3.7). Thus, S61 phosphorylation seems to have no role in governing the association of TDP with PARP1 or XRCC1. This data further provide evidence that coupling of TDP1-XRCC1-PARP1 for Top1cc repair is independent Mitotic-phase specific TDP1-S61 phosphorylation.

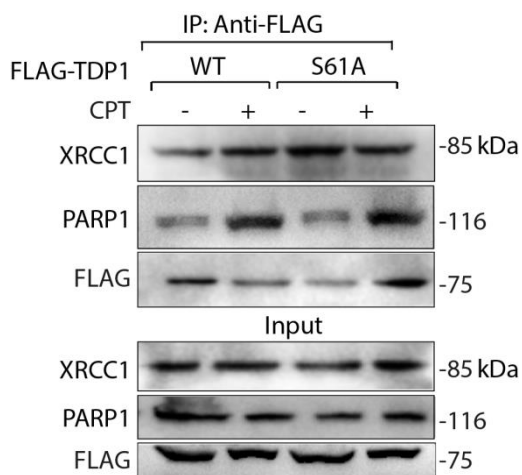


Figure 3.7 TDP1-association with XRCC1-PARP1 is independent of TDP1-S61 phosphorylation.. FLAG-TDP1^{WT} and FLAG-TDP1^{S61A} were ectopically expressed in TDP1^{-/-} MEFs. After CPT treatment (5 μ M, 3 h), ectopic FLAG-TDP1 was immunoprecipitated using anti-flag antibody and the immune complexes were blotted with anti-XRCC1 antibody. The same blot was stripped and reprobed with anti-FLAG antibody to show equal loading and further blotted with anti-PARP1 antibody. Aliquots (10%) of the input show the similar level of XRCC1, PARP1 and FLAG-TDP1 prior to immunoprecipitation. Migration of protein molecular weight markers (kDa) is indicated at right.

3.4 Discussion

The present study reveals that TDP1 is a novel substrate of the archetypical mitotic kinase CDK1. CDK1 catalyzes phosphorylation on a wide spread target proteins (Enserink & Kolodner, 2010) is commonly activated in cancers (Li & He, 2020). Genetic inactivation of CDK1 in mice is early embryonic lethal (Satyanarayana et al, 2008), while CDK1 depletion

causes cell proliferation defects (Lau et al, 2021). CDK1 directly binds to TDP1 and catalyzes phosphorylation of TDP1 at S61 residue both *in vitro* and *in vivo*. Till date studies involving the PTMs associated with TDP1 are restricted to the interphase (Bhattacharjee et al, 2022; Das et al, 2009; Das et al, 2014; Rehman et al, 2018) and have been reported to regulate TDP1 recruitment and stability at the sites of DNA damage (Bhattacharjee et al, 2022; Das et al, 2009; Das et al, 2014; Rehman et al, 2018). PTMs play key roles in ensuring efficient segregation of the mitotic chromosomes to allow accurate transmission of genetic material to the daughter cells (Shoaib et al, 2020). While CDK1 mediated phosphorylation of several mitotic proteins is an established key regulator for the accurate mitotic propagation (Enserink & Kolodner, 2010) and cell proliferation (Diril et al, 2012) and also for proper mitotic DNA damage repair, its emerging role in coordinating the localization and delocalization of the DDR proteins to and from the condensed mitotic chromosomes are gaining interest in the recent past (Brown et al, 2015).

Our findings unveil a novel physical and functional association between CDK1 and TDP1 (Figure 3.4), whose role in the repair of Top1cc-associated DNA damage and genome maintenance will be explored in the subsequent chapters of this dissertation work. CDK1 mediated phosphorylation at S61 residue of TDP1 was detected in mitosis (Figures 3.2 and 3.3). Interestingly it was observed that the phosphorylated TDP1 (pS61-TDP1) was extruded from the mitotic chromosomes and showed a cytosolic localization pattern (Figure 3.3, Mitotic); which has been investigated in the fourth chapter of this thesis. The abrogation of this phosphorylation by site directed mutagenesis into the nonphosphorylatable alanine residue (S61A) neither altered the catalytic activity of TDP1 (Figure 3.6) nor disrupt the interaction of the phosphomutant with the BER partner proteins of TDP1 (Figure 3.7) suggesting a role of this phosphorylation beyond the canonical repair functions known for TDP1 so far. In conclusion, the present study reveals a novel interaction between CDK1 and TDP1 for the post translational phosphorylation of TDP1. Further studies are warranted to determine the potential relevance of CDK1 mediated TDP1 phosphorylation for the repair of Top1cc (Pommier et al, 2014) which will be addressed in the following chapters of the present dissertation.

Chapter 4

CDK1 regulates chromosomal localization of TDP1

4.1 Introduction:

An intriguing example of how cells regulate DNA damage response (DDR) machinery occurs during the mitotic phase of the cell cycle (Clay & Fox, 2021). Double strand break (DSB) accumulation in this phase of the cell cycle does not evoke a full DDR causing the mitotic cells challenged with DNA damage bypass any arrest to facilitate DNA repair and directly transit to the next cellular cycle for the repair to commence at the G1 phase in the daughter cells (Denchi & Li, 2014). Although early DDR markers such as the phosphorylations of ataxia telangiectasia mutated (ATM) and histone H2A.x (H2AX) can be readily detected, the ionizing radiation-induced foci (IRIF) formation of late DDR markers such as breast cancer type 1 susceptibility protein (BRCA1) and p53-binding protein 1 (53BP1) are absent until the telophase/cytokinesis stage (Blackford & Stucki, 2020). Incompletely replicated, or unresolved, chromosomes from S-phase can often persist into mitosis, where they present a potential threat to the faithful segregation of sister chromatids (Mankouri et al, 2013). Indeed, it is becoming increasingly apparent that the transition from S-phase to M-phase perhaps encounters a less stringent checkpoint, and cells frequently enter mitosis with under-replicated or unrepaired chromosomes (Mankouri et al, 2013). The expression of common fragile sites (CFS) on metaphase chromosomes suggests that these sites also fail to complete DNA replication in the S-phase and G2-phase or suffer breakages that are carried over to mitosis (Li & Wu, 2020). Mitotic DNA synthesis (MiDAS) is a recently discovered break induced repair (BIR) mechanism that operates in early mitosis for the resolution of late replication intermediates to allow disjunction of sister chromatids in anaphase and involves POLD3, RAD52, MUS81 as a key players (Minocherhomji et al, 2015). Interestingly, Top1 has been reported to assist RNA Polymerase II (RNAPII) during mitotic transcription (Baranello et al, 2016; Wiegard et al, 2021). This Top1-RNAPII interaction allows completion of transcription during prometaphase and reloading of RNAPII at promoters during mitotic exit, facilitating the progression into G1 (Wiegard et al, 2021). Interfering with Top1-RNAPII interaction affects the transcriptional program of the cell and the progression through cell cycle (Baranello et al, 2016; Wiegard et al, 2021). Top1 undergoes a cell-cycle specific phosphorylation which regulates its activity during mitotic transcription to remove supercoiling that would otherwise impair RNAPII elongation and clearance before the re-initiation of transcription in mid-mitosis (Baranello et al, 2016). Top1 has also been implicated in CFS instability and the depletion of Top1 significantly increases CFS breakage (Tuduri et al, 2009). FANCD2 is a key DNA repair protein from the Fanconi Anemia

pathway that localizes to CFSs in G2 and mitosis to ensure their efficient replication. Top1 enrichment at CFS loci in G2/M phase has been reported in a study conducted using Orbitrap Mass Spectrometry (MS) in combination with chromatin immunoprecipitation (ChIP) of FANCD2, to map the proteins that are recruited to CFSs when challenged (Pladevall-Morera et al, 2019). In the previous chapter we discovered a novel post-translational regulation that CDK1 phosphorylates on the N-terminal region of TDP1 at Serine 61 (S61) in the early mitotic stage independent of replication stress. TDP1 is found to be overexpressed in several cancers types including non-small cell lung cancers (Liu et al, 2007), Dukes C colorectal cancers (Yu et al, 2005), breast cancer cell lines (Dean et al, 2014), and some rhabdomyosarcomas (RMS) (Fam et al, 2013). It has also been reported that high levels of chromosomal instability (CIN) in RMS cell lines could be partially rescued by TDP1 downregulation (Duffy et al, 2016), implying the role of TDP1 for the CIN phenotype in these cells (Duffy et al, 2016). Further, in yeast, high levels of yTdp1^{WT} results in sensitivity to a broad spectrum of adduct-forming agents and DNA damaging agents like CPT, hydroxyurea (HU), methyl methane sulphonate (MMS) and bleomycin (Duffy et al, 2016). Synthetic dosage lethal (SDL) partner screens in yeast to identify a set of genes that when deleted specifically kill cells with high levels of TDP1 revealed that TDP1 overexpressing yeast cells could not grow in the absence of several DNA repair factors especially endonucleases like Rad27, Slx4, and Mus81 (Duffy et al, 2016). Moreover, the overexpression of the yTdp1H432R mutant (ortholog of SCAN1 in humans) had similar CIN levels and sensitivity profiles compared with the overexpression of wild type, despite the reduced activity and increased adduct-forming ability of the mutant (Duffy et al, 2016). It is therefore possible that overexpression of TDP1 leads to the accumulation of nonspecific TDP1-DNA adducts, in a manner similar to Top1-DNA adducts, which may lead to DNA double-strand breaks resulting from the collision of the replication fork with the protein-DNA adducts, increasing DNA damage and CIN (Duffy et al, 2016). Also, it has been previously evidenced that, during interphase TDP1 is homogeneously distributed in the entire nuclear space, while it is not bound to the chromosomes at early mitosis until late telophase (Barthelmes et al, 2004). We therefore hypothesized if this CDK1 mediated phosphorylation at the TDP1-S61 residue controls the dynamics of the occlusion of TDP1 from the condensed mitotic chromosomes. The current chapter of this dissertation work deals with the physiological implications of this mitotic phosphorylation of TDP1 at S61 residue by CDK1 and explores into the role of this PTM of a fundamental base excision repair (BER) protein in repairing Top1ccs beyond interphase. Since TDP1 has been implicated in the repair of

Top1cc associated DNA breaks, we rationalised whether this mitotic phosphorylation of TDP1 at S61 residue by CDK1 which aids in the ousting of this repair protein from the condensed mitotic DNA, has a role in maintaining the stability of the common fragile sites (CFS) under mild replication stress (RS).

4.2 Materials and Methods

4.2.1 Drugs

DNA replication inhibitor aphidicolin (APH) (Sigma-Aldrich) was used at 0.4 μ M (low dose) or 1.5 μ M (intermediate dose), Hydroxyurea (Sigma-Aldrich) was used at 2 mM, Camptothecin (Sigma-Aldrich) was used as per experimental requirements as indicated, CDK1 inhibitor (RO-3306, Sigma-Aldrich) at 9 μ M. Nocodazole (Sigma-Aldrich) was used at 200ng/ml and Thymidine (Sigma-Aldrich) at 2 mM. 5-Bromo-2'-Deoxyuridine (BrdU, Thermo-fisher) was used at 1X.

4.2.2 Antibodies

Rabbit polyclonal anti-phospho-Histone H3 (06-570), anti-MPM2 (05-368), anti-Top1cc (MABE1084) and mouse monoclonal anti- γ H2AX (05-636) antibodies were purchased from Millipore, USA. Rabbit polyclonal TDP1 (Ab4166) and GAPDH (Ab9485), mouse monoclonal XRCC1 (Ab1838), anti-MUS81 antibody (Ab14387) and Histone H3 (Ab24834) antibodies were purchased from Abcam (Cambridge, MA, USA). Mouse monoclonal anti-flag (M2) (F3165), rabbit polyclonal anti-FLAG (F7425) antibodies were purchased from Sigma (St Louis, MO, USA). The anti-CDK1 (9116), mouse monoclonal antibody was from Cell Signalling Technologies. Rabbit polyclonal anti-GFP (A-11122) antibody was from Invitrogen. Rabbit polyclonal PARP1 antibody and anti-actin (sc-47778) antibody secondary antibodies: Horseradish peroxidase (HRP)-conjugated anti-rabbit IgG or anti-mouse IgG were obtained from Santa Cruz Biotechnology (Santa Cruz, CA, USA).

4.2.3 Expression constructs and site-directed mutagenesis

Human flag-tagged full-length TDP1 (FLAG-TDP1^{WT}), His-tagged and green fluorescent protein (GFP)-tagged TDP1 constructs were described previously (Das et al, 2009; Das et al, 2014). The HA-CDK1 fusion construct was a kind gift from Dr Sorab Dalal (Tata Memorial Centre Advanced Centre for Treatment, Research and Education in Cancer, India). The point

mutations: TDP1^{S61A} in FLAG as well as His-TDP1^{S61A} were created using the ‘QuickChange’ protocol (Stratagene, La Jolla, CA, USA). All PCR-generated constructs were confirmed by DNA sequencing.

4.2.4 Cell culture, treatment and transfections

Cell cultures were maintained at 37⁰C under 5% CO₂ in Dulbecco’s modified Eagle’s medium containing 10% fetal calf serum (Life Technologies, Rockville, MD, USA). The cervical carcinoma cell line (HeLa), human kidney origin (HEK293) and human breast cancer (MCF7) was obtained from the Developmental Therapeutics Program (NCI, NIH/ USA). TDP1^{+/+} and TDP1^{-/-} primary MEF cells were a kind gift from Dr Cornelius F Boerkoel (University of British Columbia, Vancouver, British Columbia, Canada). Cells were treated with the indicated concentrations of CPT. Plasmid DNAs were transfected with Lipofectamine 2000 (Invitrogen) according to the manufacturer’s protocol. TDP1^{-/-} MEF cells were transfected with the FLAG-TDP1 constructs using X-tremeGENE HP DNA transfection reagent (Roche) according to the manufacturer’s protocol.

4.2.5 siRNA transfection

Transfections were performed as described previously (Das *et al.*, 2009). In brief, cells (1.5 × 10⁵) were transfected with control siRNA or 25 nM CDK1 or TDP1 siRNA (GE Dharmacon, SiRNA- SMARTpool) using oligofectamine (Invitrogen) according to the manufacturer’s protocol. Time course experiments revealed a maximum suppression of CDK1 or TDP1 protein at day 3 after transfection, as analysed by Western blotting.

4.2.6 Cell extracts, immunoblotting, and immunoprecipitation

Preparation of whole cell extracts, immunoprecipitation, and immunoblotting were carried out as described previously (Das *et al.*, 2009; Das *et al.*, 2014). Briefly, cells were lysed in a lysis buffer (10 mM Tris-HCl (pH 8), 150 mM NaCl, 0.1% SDS, 1% NP40, 0.5% Na-deoxycholate supplemented with complete protease inhibitors) (Roche Diagnostics, Indianapolis, IN) and phosphatase inhibitors (Phosphatase Inhibitor Cocktail 1 from Sigma). After thorough mixing and incubation at 4⁰C for 2 h, lysates were centrifuged at 12 000 g at 4⁰C for 20 min. Supernatants were collected, aliquoted, and stored at -80⁰C. For immunoprecipitation, cells were lysed in a lysis buffer (50 mM Tris-HCl (pH 7.4), 300 mM NaCl, 0.4% NP40, 10 mM MgCl₂, 0.5 mM dithiothreitol supplemented with protease and

phosphatase inhibitors). Supernatants of cell lysates were obtained by centrifugation at 15 000 g at 4⁰C for 20 min and pre-cleared with 50 µl of protein A/G-PLUS agarose beads (Santa Cruz, CA, USA). About 5 mg of pre-cleared lysate was incubated overnight at 4⁰C with indicated antibodies (2–5 µg/ml) and 50 µl of protein A/G-PLUS agarose beads. Isolated immunocomplexes were recovered by centrifugation, washed thrice with lysis buffer, and were subjected to electrophoresis on 10% Tris–glycine gels and immunoblot analysis. Immunoblottings were carried out following standard procedures, and immunoreactivity was detected using ECL chemiluminescence reaction (Amersham) under ChemiDoc™ MP System (Bio-Rad, USA). Densitometric analyses of immunoblots were performed using Image J software.

4.2.7 Immunocytochemistry and confocal microscopy

Immunofluorescence staining and confocal microscopy were performed as described previously (Das et al, 2009; Das et al, 2010; Das et al, 2014). Briefly, cells were grown and drug treated on chamber slides (Thermo Scientific™ Nunc™ Lab-Tek™ II Chamber slides) followed by fixation with 4% paraformaldehyde for 10 min at room temperature. Primary antibodies against FLAG, γH2AX, anti-BrdU and Top1cc were detected using anti-rabbit or anti-mouse IgG secondary antibodies labelled with Alexa 488/568 (Invitrogen). Cells were mounted in anti-fade solution with 4',6-diamidino-2-phenylindole (DAPI) (Vector Laboratories, Burlingame, CA, USA) and examined under Leica TCS SP8 confocal laser-scanning microscope (Germany) with a 63×/1.4 NA oil objective. Images were collected and processed using the Leica software and sized in Adobe Photoshop 7.0. The γH2AX or Top1cc or BrdU intensity per nucleus was determined with Adobe Photoshop 7.0 by measuring the fluorescence intensities normalized to the number of cell count (Das et al, 2009; Das et al, 2010; Das et al, 2014).

4.2.8 Cell fractionation and isolation of chromatin bound protein

For cell fractionation and isolation of chromatin bound proteins (Wu & Wang, 2021), cells were washed with 1× PBS followed by washing with hypotonic buffer containing 20 mM HEPES, pH 7.5, 20 mM NaCl, 5 mM MgCl₂ and suspended in hypotonic buffer (10 ml). Post 10 min incubation on ice, cells were lysed to free nuclei by 45 strokes of a dounce homogenizer and were centrifuged at 1500 g at 4⁰C for 5 min to isolate the supernatant from the nuclear pellet. Nuclei were further suspended in extraction buffer containing 50 mM

HEPES, pH 7.5, 100mMKCl, 0.25% Triton X-100, 2.5mM MgCl₂, 1mM dithiothreitol, aprotinine (1 μM), leupeptine (50 μM), 4-(2-aminoethyl)-benzenesulfonylfluoride/HCl (1 mM) and NaF (10 mM) followed by centrifugation at 600 g at 4⁰C for 3 min. Nuclei were further suspended thrice in extraction buffer for complete lysis of the nuclear envelope and full extraction. Supernatants were pooled to yield nucleosolic proteins and the residual pellet contained all DNA and structure bound proteins (chromatin fraction).

4.2.9 Chromatin immunoprecipitation (ChIP)

Cells were cultured overnight at a density of 1×10^7 per 100 mm petri dish and subjected to transfections or treatments as indicated in the experimental protocol outlines. Chromatin and proteins were cross-linked by incubating cells in 1% formaldehyde for 15 min at room temperature and the reaction was stopped by 10 min incubation with 125 mM glycine. Cells were collected and washed sequentially with solution A (10 mM HEPES [pH7.5], 10 mM EDTA, 0.5 mM EGTA, 0.75% Triton X-100) and solution B (10 mM HEPES [pH7.5], 200 mM NaCl, 1 mM EDTA, 0.5 mM EGTA). The cell pellets were resuspended in 1 ml lysis buffer (25 mM Tris-HCl [pH7.5], 150 mM NaCl, 0.1% SDS, 1% Triton X-100, 0.5% deoxycholate freshly supplemented with protease inhibitor cocktail (Roche) and sonicated on ice by 10s pulses at 25% of maximal power on a sonicator. After centrifugation at 13 000 rpm for 15 min to remove any debris, the supernatant was pre-cleared with protein-G-sepharose/salmon sperm DNA beads at 4°C for 1h. For each immunoprecipitation, 600μl of the pre-cleared chromatin was incubated overnight at 4°C with 6 μg of antibodies specific for TDPI, FLAG, Top1, Mus81 and γH2AX. A reaction containing an equivalent amount of Goat/rabbit IgG was included as the background control. 10% of the pre-cleared chromatin was taken as input control. Antibody-chromatin complexes were pulled down by adding 50 μl of protein-G-sepharose/salmon sperm DNA beads and incubated for 4 h at 4°C. The beads were washed for 10 min each with the lysis buffer followed by high-salt wash buffer (0.1% SDS, 1% Triton X-100, 2 mM EDTA, 20 mM Tris-HCl [pH 8.1], 500 mM NaCl), LiCl wash buffer (250 mM LiCl, 1% NP-40, 1% deoxycholate, 1 mM EDTA, 10 mM Tris-HCl [pH 8.0]), and TE buffer (10 mM Tris-HCl [pH 8.0], 1 mM EDTA). Finally, DNA was eluted with elution buffer (1% SDS, 100 mM NaHCO₃). Elutes were incubated at 65°C for overnight with the addition of 5 M NaCl to a final concentration of 200 mM to reverse the formaldehyde cross-linking and digested at 55°C for 3 h with proteinase K at a final concentration of 50 μg per ml. Following phenol/chloroform extraction and ethanol

precipitation, sheared DNA fragments served as template in semi-quantitative PCR analysis.

The sequences of the PCR primers are as follows:

FCR Forward-5'-TGTTGGAATGTAACTCTATCCCAT-3';

FCR Reverse 5'-ATATCTCATCAAGACCGCTG-CA-3';

FDR Forward- 5'-CAATGGCTTAAGCAGACATGGT-3';

FDR Reverse- 5'-AGTGAATGGCATGGCTGGAATG-3';

FRA16D Forward- 5'-TCCTGTGGAAGGGATATTTA-3';

FRA16D Reverse-5'-CCCCTCATATTCTGCTTCTA-3';

β -actin Forward-5'-GACGCAGGA-TGGCATGGG-3';

β -actin Reverse- 5'-ACGCCTCTGGCCGTACCAC-3'.

4.3 Results

4.3.1 S61-phosphorylation of TDP1 by CDK1 facilitates TDP1's dissociation from mitotic chromosomes.

In order to investigate the role of the CDK1-mediated phosphorylation of S61 residue of TDP1 in the chromosomal recruitment and or dissociation during mitosis, we knocked down CDK1 by siRNA in MCF7 cells ectopically expressing FLAG-TDP1, synchronised the cells to mitotic phase with nocodazole (noc) treatment, followed by chromatin fractionation. A 60-70% knockdown of CDK1 was aimed to allow cells to progress into mitosis because CDK1 deficiency prevents mitotic entry (Diril et al, 2012). Figure 4.1A shows that the phosphopeptide antibody raised to span the TDP1-S61 epitope detected a phosphorylation mark on TDP1 in the control (siCtrl) which was markedly reduced upon CDK1 knockdown. We also noted pS61-TDP1 was detected only in the mitotically enriched cellular lysates (cytosolic fraction) and was not detected in the chromatin fraction for both CDK1 proficient and deficient conditions during interphase or mitosis. We also observed that pS61-TDP1 had an inverse correlation with the chromosomal enrichment of FLAG-TDP1. In the whole cell lysates, FLAG-TDP1 was not found to be in the chromatin fraction in CDK1 proficient cells. In contrast we detected a marked increase in the FLAG-TDP1 in the chromatin fraction (~ 3-4 fold; Figure 4.1B) in CDK1 knockdown cells which led to abrogation of the phosphorylation at S61 (Figure 4.1). Next we confirmed the enrichment of endogenous TDP1

on mitotic chromosomes upon CDK1 knockdown (Figure 4.1C). Figure 4.1C shows phosphorylated TDP1 (pS61) in mitosis in control cells which was abrogated upon CDK1 knockdown. This decrease in the phosphorylation was associated with a concomitant increase in the chromatin fraction of endogenous TDP1 (~ 4 fold; Figure 4.1D). Taken together, our data provide new evidence that CDK1-dependent TDP1 phosphorylation at S61 promotes its dissociation from mitotic chromosomes

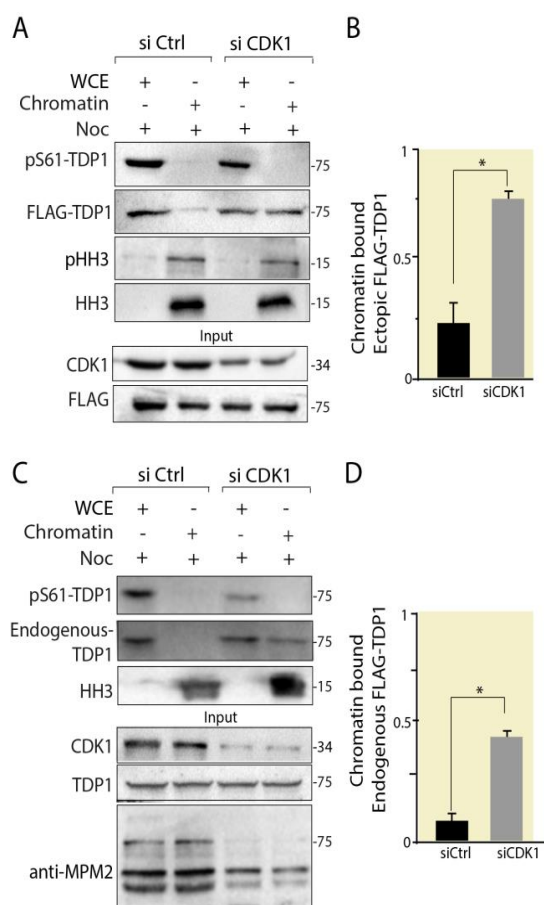


Figure 4.1 TDP1 phosphorylation at S61 by CDK1 abrogates chromosomal enrichment of TDP1 during mitosis. (A) Knocking down CDK1 reduced TDP1 phosphorylation at S61 (pS61-TDP1) and accentuated chromatin loading of FLAG-TDP1^{WT} in TDP1^{-/-} MEFs ectopically expressing FLAG-TDP1^{WT}. TDP1^{-/-} MEFs were co-transfected with FLAG-TDP1^{WT} and CDK1 or control (ctrl) siRNA. Chromatin fraction were prepared and used for Western blotting against anti-FLAG antibody and the phospho-peptide antibody raised against TDP1-S61 epitope (TDP1-pS61). Protein levels of CDK1 and FLAG-TDP1^{WT} were analysed to ensure equal levels of both the proteins in the whole cell lysates of all the samples assessed before chromatin fractionation. (B) Bar graphs showing quantifications of relative chromatin enrichment of FLAG-TDP1 in mitotic cells upon CDK1 knockdown. (C) MCF7 cells were transfected with CDK1 or control (ctrl) siRNA. Chromatin fraction were prepared and used for Western blotting against anti-TDP1 antibody and the phospho-peptide antibody raised against TDP1-S61 epitope (TDP1-pS61). Protein levels of CDK1 and endogenous TDP1 were analysed to ensure equal levels of both proteins in the whole cell lysates of all the samples assessed before chromatin fractionation. Electrophoretic migration of protein molecular weight markers (kDa) is indicated at right. (D) Bar graphs showing quantifications of relative chromatin enrichment of endogenous TDP1 in mitotic cells upon CDK1 knockdown. Asterisks denote statistically significant difference (*P < 0.01; t test).

4.3.2 Inhibition of CDK1 causes enrichment of endogenous TDP1 on mitotic chromosomes.

There is a marked difference in the cell cycle dependent chromosomal localisation of TDP1 (Barthelmes et al, 2004). During interphase, TDP1 is homogeneously distributed in the entire nuclear space, while it is not chromosome-bound at early mitosis and does not associate with the chromatin until late telophase (Barthelmes et al, 2004). Because the CDK1-mediated

phosphorylation of TDP1 at S61 exactly mirrors the delocalization pattern of TDP1 from the chromosome observed in M-phase, we tested if phosphorylation at the S61 residue was responsible for controlling the dynamics of TDP1 occlusion from condensed mitotic chromosomes. In order to delineate the effect of the CDK1 mediated phosphorylation on the chromosomal recruitment kinetics of endogenous TDP1 in the different stages of cell cycle, we left the cells asynchronous or synchronized the MCF7 cells to the mitosis as per the schematic protocol (Figure 4.2A). We then treated the cells with or without CDK1 inhibitor (RO3306) at interphase/mitosis to monitor the effect of phosphorylation of this site at interphase and the distinct stages of mitosis (Figure 4.2B-C). The cells at the indicated stages of mitosis were selected on the basis of their chromatin morphology indicated by DAPI staining. Treatment with RO3306 resulted in a markedly distinct pattern of chromosomal localisation of TDP1 during mitosis. It is known that CDK1 remains inactive during S-phase due to inhibitory phosphorylations at T14 and Y15 by Myt1 and Wee1 kinases and is activated at the late G2/M transition by the action of cdc25 phosphatases (Barthelme et al, 2004). We noted that the RO3306 untreated and treated interphase cells showed similar TDP1 chromatin localisation which can be correlated with the absence of CDK1 activity in S-phase under normal physiological conditions mimicking the effect of RO3306 administration. However, the loss of chromosomal enrichment of endogenous TDP1 was observed in the mitotic cells with functional CDK1 (-RO3306). However a stark change in the localisation pattern was seen with RO3306 treatment (+RO3306) with a significant TDP1 association with chromosomes from prophase to telophase (Figure 4.2B-C). This chromosomal enrichment of the endogenous TDP1 in mitosis corroborated with our results discussed in the previous chapter where it was observed that CDK1 inhibition during mitosis resulted in occlusion of phospho-TDP1 from both the interphase and mitotic chromosomes (Figure 3.3A-C) thereby strengthening our hypothesis that this phosphorylation plays a key role in ousting TDP1 from chromosomes in mitosis.

4.3.3 TDP1^{S61A} mutant shows cell cycle independent chromosomal recruitment

The non-phosphorylatable mutant of FLAG-TDP1 was generated by site directed mutagenesis (FLAG-TDP1^{S61A}) to investigate the effect of TDP1-S61 phosphorylation on chromosomal localisation. We complemented TDP1^{-/-} MEFs either with FLAG-TDP1^{WT} or with FLAG-TDP1^{S61A}, synchronized to the mitosis as per the schematic protocol in presence and absence of a low dose of CPT (15 nM) which generates replication stress, and the effect

of TDP1-S61 phosphorylation during interphase and the distinct stages of mitosis (Figure 4.3A and C) was monitored. The cells at the indicated stages of mitosis were selected on the basis of their chromatin morphology indicated by DAPI staining (Figure 4.3B and D). Using anti-FLAG antibody, we detected a markedly different pattern of chromosomal localisation of the TDP1^{WT} and the phosphomutant TDP1^{S61A} (Figure 4.3B and D).

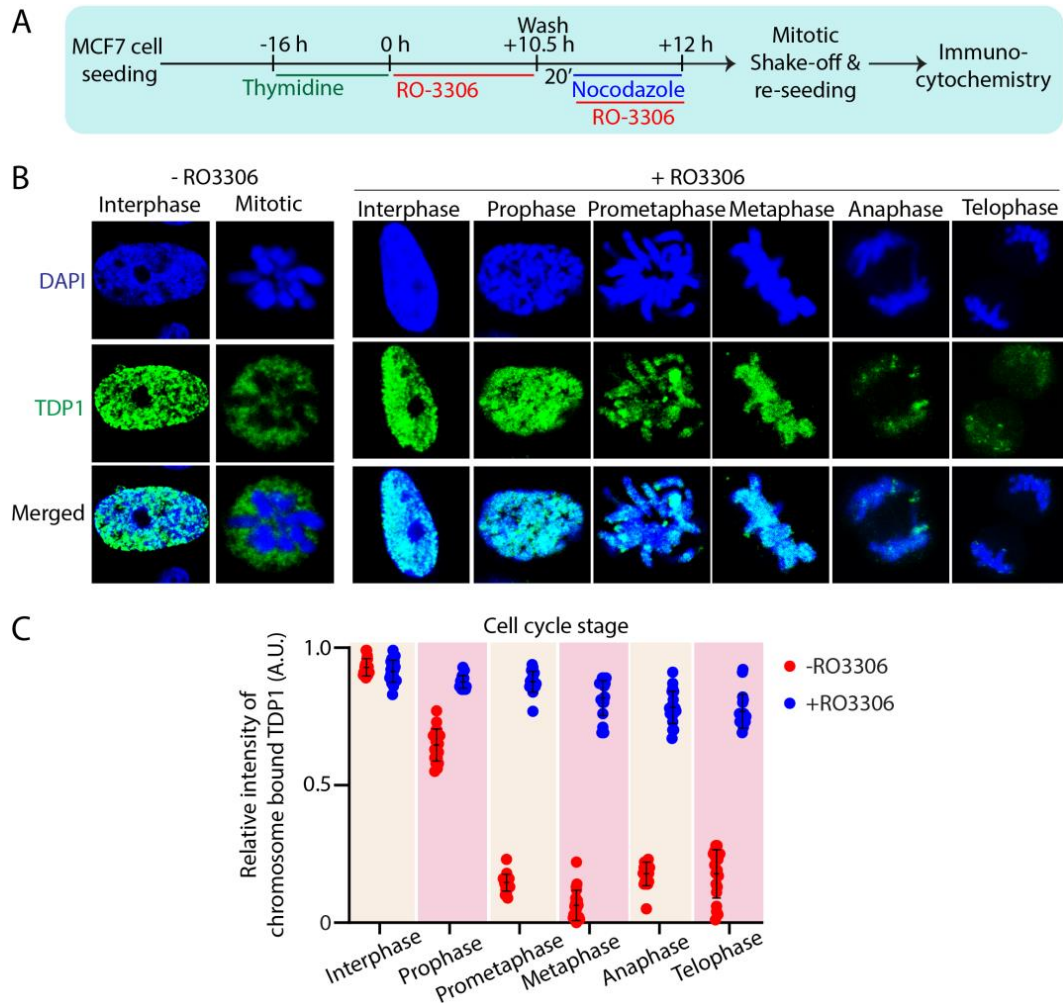


Figure 4.2 CDK1 mediated phosphorylation of TDP1 at S61 helps to dislodge TDP1 from mitotic chromosomes. (A) Schematic representation of the protocol followed to study the cell cycle stage dependent co-localisation of endogenous TDP1 with the chromosomes in presence and absence of CDK1 inhibitor (RO3306) as indicated. (B) MCF7 cells were fixed at different time intervals after release from G2/M arrest as outlined in the protocol and stained with anti-TDP1 antibody to detect endogenous TDP1 (green). Cells at interphase and the indicated distinct stages of mitotic propagation were tallied on the basis of their chromatin morphology, as indicated by DAPI staining. (C) Fluorescence intensity of co-localised TDP1 variant over the region of interest (on DNA) was quantified. Staining intensities from 20-30 nuclei per stage were expressed as mean \pm s.d. a.u: arbitrary unit.

Although the chromatin localisation pattern of the two variants bear similarity in the interphase cell, TDP1^{WT} shows a relatively low chromosomal

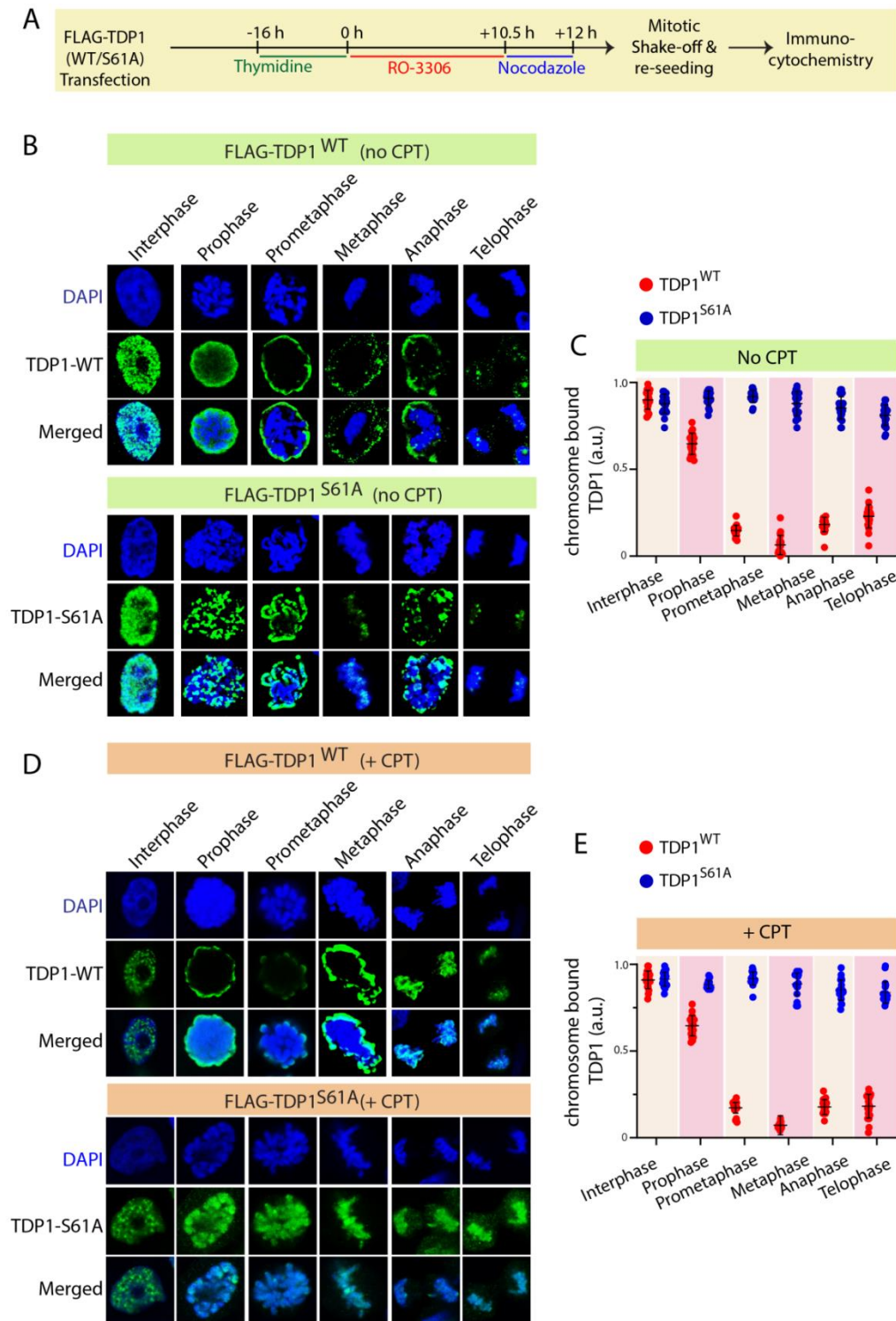


Figure 4.3 Abrogation of S61 phosphorylation accumulates TDP1 on mitotic chromosomes. (A and C) Schematic of the protocol followed to study the cell cycle stage dependent co-localisation of FLAG-TDP1 variants *viz.* wild type (WT) and non-phosphorylatable mutant (S61A) with the chromosomes in presence and absence of CPT as indicated. (B and D) TDP1^{-/-} MFEs transiently overexpressing the FLAG-TDP1 variants were fixed after release from G2/M arrest and stained with anti-FLAG antibody. Cells at interphase and the indicated distinct stages of mitotic propagation were tallied on the basis of their chromatin morphology, as indicated by DAPI staining. (E and F)

Fluorescence intensity of co-localised TDP1 variant over the region of interest (on DNA) was quantified. Staining intensities from 20-30 nuclei per stage were expressed as mean \pm s.d. a.u: arbitrary unit.

enrichment in the early to mid-mitotic phases (prophase to metaphase) with a slight increase in chromosomal association in the anaphase/telophase. However, the TDP1^{S61A} shows relatively steady chromosomal enrichment during prophase to metaphase, before dropping to the same level as that of TDP1^{WT}, during the late stages of mitosis (Figure 4.3B and D). Interestingly the intensity of chromatin enrichment of the S61A mutant was not significantly altered when the TDP1^{-/-} MEFs were subjected to CPT as compared to the untreated cells (Figure 4.3E and F).

4.3.4 TDP1^{S61A} is enriched at CFS loci in G2/M-phase during CFS expression

The presence of phospho-mutant TDP1-S61A on mitotic chromosomes prompted us to investigate the location of TDP1 recruitment on mitotic chromosomes. Chromosomal fragile sites are specific regions of the genome that exhibit gaps or breaks on metaphase chromosomes under conditions that partially inhibit DNA replication (Li & Wu, 2020). These sites often co-localize with regions deleted, amplified, or rearranged in cancer (Li & Wu, 2020). We tested the enrichment of endogenous Top1 and TDP1 at three CFS loci located on mitotic chromosome at three CFSs, FRA3B (FDR and FCR regions) and FRA16D (Figure 4.4B-C) following the protocol illustrated in Figure 4.4A using chromatin immunoprecipitation (chIP). To create conditions of mild RS that mimic those of oncogenic transformation causing CFS instability, the MCF7 cells were exposed to low dose of CPT (15 nM) for 24 h then synchronized to G2/M by 8 h noc (400 ng/ml) treatment. These conditions are known to increase the number of challenged CFSs in G2/M (Li & Wu, 2020; Pladevall-Morera et al, 2019) and are typically used to study the mechanisms and proteins that resolve CFS aberrations (Li & Wu, 2020; Pladevall-Morera et al, 2019). We found endogenous Top1 but not endogenous TDP1 to be enriched at the fragile sites (Figure 4.4D-F) which showed significant increase following CPT treatment. Immunoprecipitation of FLAD-TDP1 variants confirmed similar levels of interactions between Top1 and TDP1 variants (WT or S61A) in Western blotting suggesting that the abrogation of the

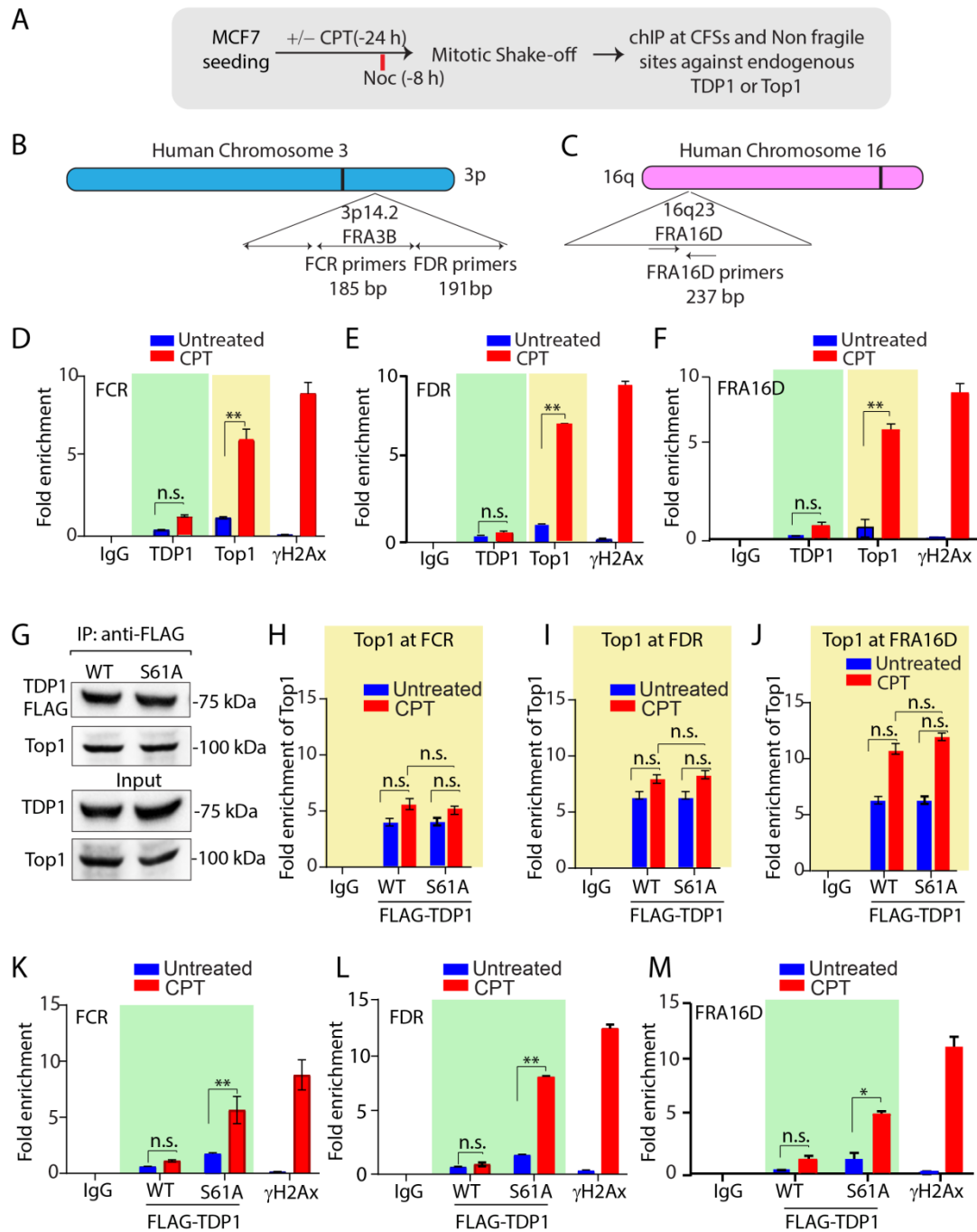


Figure 4.4 Phosphomutant TDP1 is enriched at the CFS (A) A schematic representation for the protocol followed for the chromatin immunoprecipitation (chIP). (B-C) Genomic organization of the common fragile sites FRA3B and FRA16D region along with the primer sets of distal (FDR) and central (FCR) region within the FRA3B locus; FRA16D locus is designated. (D-F) Endogenous Top1 but not TDP1 preferentially localizes to Common Fragile Sites (CFSs) upon low dose CPT treatment during mitosis. Quantification of cross-linked FRA3B-FCR, FRA3B-FDR and FRA16D loci chromatin-immunoprecipitated from MCF7 cells using the specified antibodies (Top1 and TDP1). γ H2A.x antibody was used as a positive control for FRA3B and FRA16D enrichment post CPT treatment. Fold enrichment over goat IgG was determined and is shown for each primer pair for the ChIP. (G) MCF7 cells ectopically expressing FLAG-TDP1 variants (WT and S61A) were immunoprecipitated using anti-FLAG antibody. Immune complexes were blotted with anti-Top1 antibody. The same blot was stripped and reprobed with anti-FLAG antibody to ensure equal pull down events for WT and S61A. Aliquots (10%) of the input show the level of Top1 and TDP1 prior

to immunoprecipitation. (H-J) Quantification of cross-linked FRA3B-FCR, FRA3B-FDR and FRA16D loci chromatin-immunoprecipitated from MCF7 cells transfected with FLAG-TDP1 (WT or S61A) using the specified antibodies (endogenous Top1). γ H2A.x antibody was used as a positive control for FRA3B and FRA16D enrichment post CPT treatment. Fold enrichment over goat IgG was determined and is shown for each primer pair for the ChIP. (K-M) Quantification of cross-linked FRA3B-FCR, FRA3B-FDR and FRA16D loci chromatin-immunoprecipitated from MCF7 cells overexpressing the FLAG-TDP1 variants (WT and S61A) using the specified antibodies with or without low dose CPT treatment. γ H2A.x antibody was used as a positive control for FRA3B and FRA16D enrichment post CPT treatment. Fold enrichment over goat IgG was determined and is shown for each primer pair for the ChIP. All the results are expressed as mean \pm SD for at least three independent experiments. Asterisks denote statistically significant difference (*P < 0.01, **P < 0.001, ***P < 0.0001; t test).

phosphorylation at S61 residue does not impact TDP1-Top1 interaction (Figure 4.4G). ChIP assay confirmed that ectopic expression of the FLAG-TDP1 variants (FLAG-TDP1^{WT} and FLAG-TDP1^{S61A}) had no effect on the Top1 enrichment at the CFSs which could be rationalised by the hierarchical involvement of TDP1 after Top1 trapping (Figure 4.4H-J). CPT treatment preferentially enhanced enrichment of the Top1 to the CFSs congruent with the increased occupancy of Top1cc's on stalled replication forks at CFS loci (Pladevall-Morera et al, 2019). Additionally, replication stress was also induced by the low dose treatment with aphidicolin and the role of abrogating the CDK1 mediated phosphorylation on TDP1 occupancy at CFSs in MCF7 cells was monitored. ChIP assay showed that CPT treatment preferentially enhanced binding of the TDP1^{S61A} with respect to the TDP1^{WT} to the CFSs as compared to aphidicolin induced replication stress (data not shown). The observation can be correlated with to the more direct involvement of TDP1 in repair of trapped Top1ccs which are significantly more in CPT treated cells as compared to aphidicolin. Previous studies also provide compelling evidence for the involvement of DNA topoisomerase in CFS breakage (Arlt & Glover, 2010). Interestingly it was also noted that treatment with neither CPT nor Aphidicolin led to the enrichment of TDP1 (WT or S61A) to the β -actin locus, coherent with the hypothesis that this loci may be different from the replication stress induced CFSs in that they map to genomic regions replicating in the early S-phase, which are close to early-firing replication origins, are highly transcribed, and may display R-loop-forming potential (Arlt & Glover, 2010; Li & Wu, 2020; Pladevall-Morera et al, 2019). Our data suggest that the lack of extrusion of the TDP1-S61A mutant is perhaps at the late replicating regions of the genome at CFS loci.

4.3.5 TDP1 is not involved in the repair of Top1cc's in mitosis

Our data and previous studies (Barthelmes et al, 2004) show the extrusion of TDP1 from the mitotic chromosomes during the cell cycle progression. Therefore, we reasoned how Top1cc's are repaired during mitosis. To test the possibility, we complemented the TDP1^{-/-} MEFs ectopically expressing empty vector (EV), FLAG-TDP1 variants (WT or S61A) and the cells were arrested in mitosis and treated with CPT during mitotic progression (Figure 4.5A). No significant differences in the γ H2AX levels were observed for the FLAG-TDP1^{WT} or FLAG-TDP1^{S61A} or the empty vector (EV) expressing TDP1^{-/-} MEFs (Figure 4.5B-C) suggesting the involvement of alternate pathways for the repair of Top1ccs in mitosis (Wu & Wang, 2021). Intriguingly it was found that when the TDP1^{-/-} MEFs were subjected to CPT induced replication stress during the indicated times in S-phase (Figure 4.5D-F), Top1cc's levels were greatly reduced for the FLAG-TDP1^{WT} or FLAG-TDP1^{S61A} transfected cells as compared to EV confirming the similar catalytic potentials of both the TDP1 variants (Figure 4.5G and H) Moreover, the CPT treatment during early and late S-phase showed a difference in γ H2AX levels on mitotic chromosomes. It was found that the CPT treatment in late S/G2 phase led to accumulation of mitotic DNA breaks, while the mitotic γ H2AX levels was significantly reduced in early S-phase CPT treated TDP1^{-/-} MEFs (Figure 4.5J). In the TDP1^{-/-} MEFs expressing the EV, the reduction in γ H2AX levels on mitotic chromosomes could be attributed to the repair of trapped Top1cc's by a functional homologous recombination in S-phase in absence of TDP1 (Wu & Wang, 2021). However, it was observed that despite similar reduction in the Top1cc levels for the two variants, the γ H2AX levels were significantly more in the FLAG-TDP1^{S61A} expressing cells and was almost comparable to the TDP1^{-/-} MEFs expressing the EV (Figure 4.5G-I). Figures 4.6J-K shows quantification of the γ H2ax and Top1cc levels in S and M phases of the cell cycle in the TDP1^{-/-} MEFs expressing either EV or the FLAG-TDP1 variants. Our data suggest that a source of DNA breaks manifested in mitotic chromosomes which entirely distinct from the Top1cc mediated DSBs in the FLAG-TDP1^{S61A} expressing TDP1^{-/-} MEFs. Therefore, we conclude that mitotic DNA breaks are generated by endonucleases, which are required for the clearance of the trapped TDP1-S61A mutant on mitotic chromosomes (Figure 4.5) (Wu & Wang, 2021).

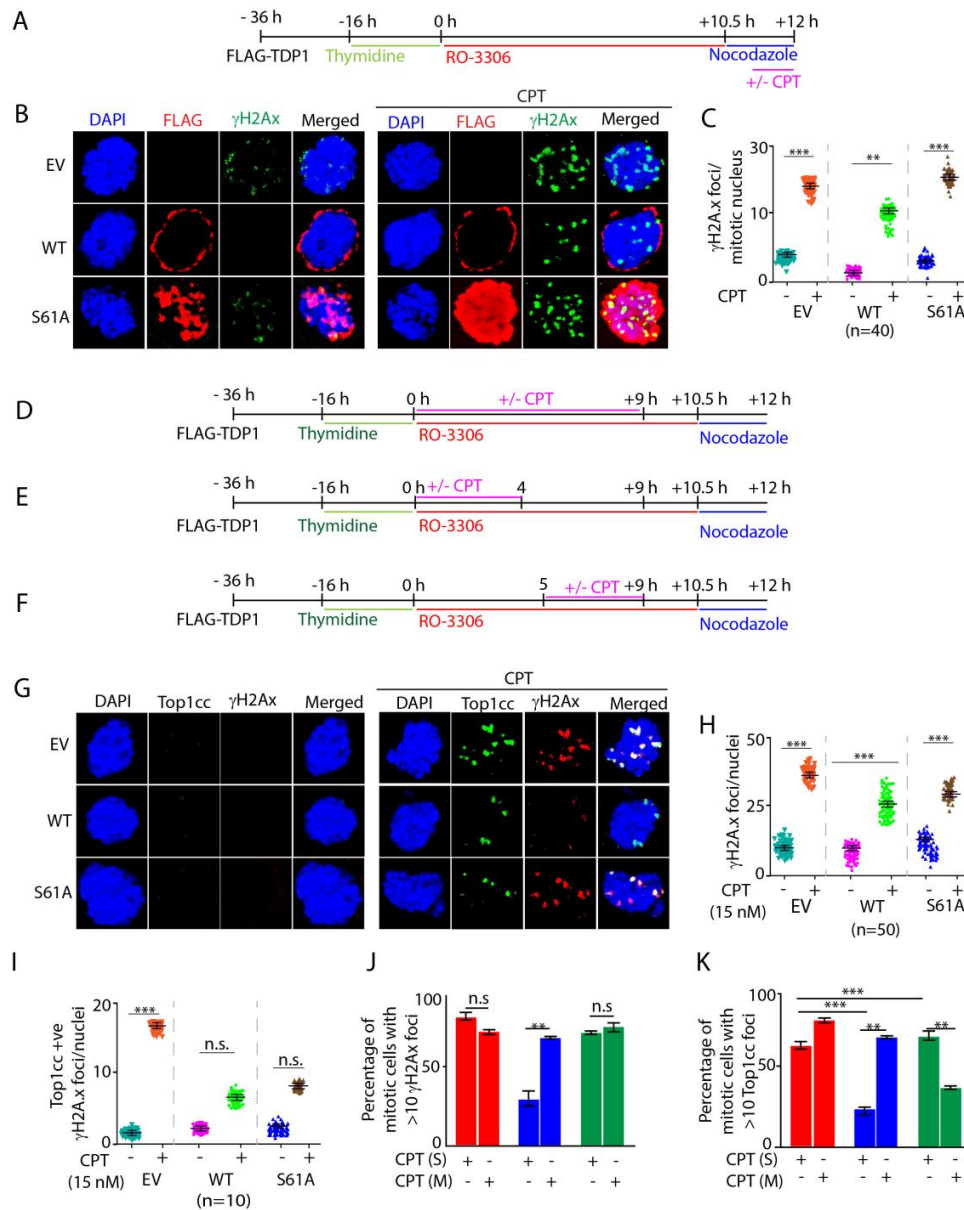


Figure 4.5 CPT induced Top1cc's are not repaired by TDP1 during mitosis. (A) Schematic for the protocol followed to study the repair of Top1ccs induced by CPT treatment during mitotic propagation. (B) TDP1^{-/-} MEFs ectopically expressing FLAG-TDP1 variants (WT and S61A) were synchronised in G2/M phase and treated with or without CPT (10 μ M, 1 h) in presence of nocodazole followed by immunocytochemistry with anti-FLAG (red) and anti- γ H2Ax (green) antibody. (C) Quantification for the number of γ H2Ax foci per mitotic nucleus calculated for 40 nuclei. (mean \pm S.E.M.) (D- F) Schematic for the protocol followed to study the repair of Top1cc's induced by CPT treatment in early and late S-phases. (G) TDP1^{-/-} MEFs ectopically expressing FLAG-TDP1 variants (WT and S61A) were treated with very low dose (15 nM) CPT for 9 hours in S-phase as indicated, synchronised in G2/M phase followed by immunocytochemistry with anti- γ H2AX (red) and anti-Top1cc (green) antibody. (H & I) Quantifications for the number γ H2AX foci and Top1cc positive γ H2AX foci per mitotic nucleus of cells treated with CPT as per the protocol in detailed in scheme (D) respectively. (J) Bar diagram showing the quantifications of percentages of mitotic nuclei with >10 γ H2Ax upon treatment with 15 nM CPT following protocols detailed in schemes: early CPT (E) and late CPT (F) respectively. (K) Bar diagram showing the quantifications of percentages of mitotic nuclei with >10 Top1cc's upon CPT treatment during S or M phases calculated for 20–25 cells (mean \pm S.E.M.). Asterisks denote statistically significant difference (**P < 0.001, ***P < 0.0001; t test). n.s. non-significant.

4.4 Discussion:

The current study deals with the functional characterization of a novel CDK1 mediated phosphorylation of TDP1 at S61 residue which is responsible for regulating the temporal chromosomal association-dissociation kinetics of TDP1 through the cell cycle progression. CDK1 depletion by knockdown was found to reduce the level of phosphorylated TDP1 (pS61-TDP1) with a concomitant enrichment in the levels of TDP1 in the chromatin fraction at mitotic phase implying that the phosphorylation is responsible for the dissociation of TDP1 from the chromosomes. The phosphorylation was found to be a mitotic event and the abrogation of the phosphorylation occludes the dissociation of TDP1 from the condensed mitotic chromosomes (Figure 4.2 and 4.3) which is associated with accumulation of mitotic DNA breaks (Figure 4.5) upon replication stress by treatment with Top1 poison CPT. Our study clearly shows the dispensability of TDP1 in the repair of Top1ccs generated in exclusively in mitosis (Figure 4.6A-C) coherent with the observation that TDP1 remains extruded from the chromosomes in the mitotic phase (Figure 4.2 and 4.3). The study also emphasizes on the need of the phosphorylation of TDP1 at S61 residue to prevent accumulation of mitotic DSBs resulting from the formation of non-specific TDP1-DNA adducts. Conclusively, the study reveals a novel cell cycle specific post translational phosphorylation on TDP1 at S61 residue which governs the chromosomal localization dynamics of TDP1.

Chapter 5

Biological significance of CDK1 mediated phosphorylation of TDP1

5.1 Introduction:

The primary function of mitosis is the faithful segregation of the genome into two copies that are equally shared among daughter cells. Mitotic cells are exquisitely sensitive to DNA DSBs (Bakhoum et al, 2017) to which they can only mount a partial response that stops short of activating downstream DNA damage repair pathways (Blackford & Stucki, 2020). While the compact architecture of mitotic chromatin is thought to confer a protective role, mitotic cells can still encounter DSBs as a result of persistent pre-mitotic errors (Orthwein et al, 2014) or due to the direct exposure to DNA-damaging agents (Petsalaki & Zachos, 2020). The consequences of such damage have remained elusive. Mounting evidence suggests that untimely activation of the DDR and DSB repair induces severe chromosome segregation defects (Bakhoum et al, 2017). These intricacies between the response to DNA damage during mitosis and interphase have important implications not only for normal biology, but also for cancer cells, which are frequently exposed to mitotic DNA damage either through unrepaired pre-mitotic errors or exogenous therapies (Bakhoum et al, 2017). Top1 relax topological stress generated during DNA metabolic processes by temporarily forming a reversible Top1-DNA cleavage complex (Top1cc) nicking one strand and allowing controlled rotation of the broken strand around the intact strand (Pommier, 2006; Pommier, 2013). CPT and its clinical derivatives trap Top1cc's forming protein-DNA crosslinks blocking DNA replication fork progression and ongoing transcription (Pommier, 2006; Pommier, 2013). Replication forks colliding with the stabilized Top1ccs induce replication-associated DNA double-strand breaks (DSBs). These are replication associated DNA double stranded ends (DSE's) caused by either replication run-off or cleavage of stalled replication forks by Mus81 (Groelly et al, 2022; Regairaz et al, 2011). Poisoning of Top1 by CPT also induces accumulation of unscheduled R-loop, a three-stranded structure formed during transcription, which contain DNA-RNA hybrids and single-stranded displaced non-template DNA (Groelly et al, 2022). R-loops induced by stalled Top1ccs lead to generation of transcription-dependent DSBs (Cristini et al, 2019). R-loop-impeded replication forks can be sensed and cleaved by Mus81 leading to DSBs (Matos et al, 2020). Two major pathways, homologous recombination (HR) and nonhomologous end joining (NHEJ) are involved in DSBs repair (Chowdhuri & Das, 2021). Compared to DSB's, the DSE's lack another DNA end to be ligated to for end joining, and thus are preferentially repaired by HR (Rodgers & McVey, 2016). In budding yeast, it has been established that DSEs undergo break-induced replication (BIR), a type of HR process that involves extensive 5' to 3'-end resection to

generate a 3'-single- stranded DNA (ssDNA) end that is bound by RPA, RAD52-mediated strand invasion and formation of displacement loop (D- loop) intermediates and POLD3-dependent DNA synthesis (Wu & Wang, 2021). In human cells, Mus81-mediated cleavage of collapsed replication forks at common fragile sites (CFS) initiates mitotic DNA synthesis (MiDAS) via BIR mechanism that depends on RAD52 and POLD3 but not on RAD51 (Kramara et al, 2018). BIR also occurs in response to oncogene overexpression (Stivison et al, 2020), re-replication, or telomere erosion (Kramara et al, 2018). Although HR is indicated as a high-fidelity repair mechanism, BIR is a mutagenic mechanism that leads to chromosome rearrangements. The mechanism of resection to generate 3'-ssDNA and regulation of BIR has been extensively studied in yeast but still remains poorly understood in mammalian cells (Wu & Wang, 2021). In the absence of TDP1 we found an enrichment of SLX4/MUS81 on damaged chromatin which promotes MiDAS for the Top1cc repair (Zhang et al, 2022). However we found that abrogation of the CDK1 mediated phosphorylation of TDP1 at S61 residue leads to several fold higher DNA end resection at CPT-induced DSE's sites by promoting excess of SLX4/MUS81 chromatin loading and subsequent cleavage of replication-associated DSBs. DNA ends of cleaved replication-associated DSBs are further processed by MRE11 endonuclease, CTIP, and DNA2/BLM nucleases, generating excessive ssDNA that leads to MiDAS via BIR mechanism and chromosome aberrations. Our results demonstrate a novel role of CDK1 mediated phosphorylation of TDP1 at S61 residue in ousting of TDP1 from chromosomes in mitotic phase which otherwise forms non-specific DNA adducts, hyperactivating MiDAS culminating in genome instability.

5.2 Materials and Methods

5.2.1 Drugs

DNA replication inhibitor aphidicolin (APH) (Sigma-Aldrich) was used at 0.4 μ M (low dose) or 1.5 μ M (intermediate dose), Hydroxyurea (Sigma-Aldrich) was used at 2 mM, Camptothecin (Sigma-Aldrich) was used as per experimental requirements as indicated, CDK1 inhibitor (RO-3306, Sigma-Aldrich) at 9 μ M. Nocodazole (Sigma-Aldrich) was used at 200ng/ml and Thymidine (Sigma-Aldrich) at 2 mM. 5-Bromo-2'-Deoxyuridine (BrdU, Thermo-fisher) was used at 1X.

5.2.2 Antibodies

Rabbit polyclonal anti-phospho-Histone H3 (06-570), anti-MPM2 (05-368), anti-Top1cc (MABE1084) and mouse monoclonal anti- γ H2AX (05-636) antibodies were purchased from Millipore, USA. Rabbit polyclonal TDP1 (Ab4166) and GAPDH (Ab9485), mouse monoclonal XRCC1 (Ab1838), anti-MUS81 antibody (Ab14387) and Histone H3 (Ab24834) antibodies were purchased from Abcam (Cambridge, MA, USA). Mouse monoclonal anti-flag (M2) (F3165), rabbit polyclonal anti-FLAG (F7425) antibodies were purchased from Sigma (St Louis, MO, USA). The anti-CDK1 (9116), mouse monoclonal antibody was from Cell Signalling Technologies. Rabbit polyclonal anti-GFP (A-11122) antibody was from Invitrogen. Rabbit polyclonal PARP1 antibody and anti-actin (sc-47778) antibody secondary antibodies: Horseradish peroxidase (HRP)-conjugated anti-rabbit IgG or anti-mouse IgG were obtained from Santa Cruz Biotechnology (Santa Cruz, CA, USA).

5.2.3 Cell culture, treatment and transfections

Cell cultures were maintained at 37⁰C under 5% CO₂ in Dulbecco's modified Eagle's medium containing 10% fetal calf serum (Life Technologies, Rockville, MD, USA). The cervical carcinoma cell line (HeLa), human kidney origin (HEK293) and human breast cancer (MCF7) was obtained from the Developmental Therapeutics Program (NCI, NIH/ USA). TDP1^{+/+} and TDP1^{-/-} primary MEF cells were a kind gift from Dr Cornelius F Boerkoel (University of British Columbia, Vancouver, British Columbia, Canada). Cells were treated with the indicated concentrations of CPT. Plasmid DNAs were transfected with Lipofectamine 2000 (Invitrogen) according to the manufacturer's protocol. TDP1^{-/-} MEF cells were transfected with the FLAG-TDP1 constructs using X-tremeGENE HP DNA transfection reagent (Roche) according to the manufacturer's protocol.

5.2.4 siRNA transfection

Transfections were performed as described previously (Das et al, 2009; Das et al, 2010; Das et al, 2014). In brief, cells (1.5×10^5) were transfected with control siRNA or 25 nM CDK1 or TDP1 siRNA (GE Dharmacon, SiRNA- SMARTpool) using oligofectamine (Invitrogen) according to the manufacturer's protocol. Time course experiments revealed a maximum suppression of CDK1 or TDP1 protein at day 3 after transfection, as analysed by Western blotting.

5.2.5 Cell extracts, immunoblotting, and immunoprecipitation

Preparation of whole cell extracts, immunoprecipitation, and immunoblotting were carried out as described previously in chapter IV.

5.2.6 Immunocytochemistry and confocal microscopy

Immunofluorescence staining and confocal microscopy were performed as described previously (Das et al, 2009; Das et al, 2010; Das et al, 2014). Briefly, cells were grown and drug treated on chamber slides (Thermo Scientific™ Nunc™ Lab-Tek™ II Chamber slides) followed by fixation with 4% paraformaldehyde for 10 min at room temperature. Primary antibodies against FLAG, γ H2AX, anti-BrdU and Top1cc were detected using anti-rabbit or anti-mouse IgG secondary antibodies labelled with Alexa 488/568 (Invitrogen). Cells were mounted in anti-fade solution with 4',6-diamidino-2-phenylindole (DAPI) (Vector Laboratories, Burlingame, CA, USA) and examined under Leica TCS SP8 confocal laser-scanning microscope (Germany) with a 63 \times /1.4 NA oil objective. Images were collected and processed using the Leica software and sized in Adobe Photoshop 7.0. The γ H2AX or Top1cc or BrdU intensity per nucleus was determined with Adobe Photoshop 7.0 by measuring the fluorescence intensities normalized to the number of cell count (Das et al, 2009; Das et al, 2010; Das et al, 2014).

5.2.7 Neutral COMET assays

To compare the levels of DNA damage in TDP1 depleted cells transfected with the different TDP1 variants, samples were subjected to neutral comet assays according to the manufacturer's instructions (Trevigen, Gaithersburg, MD) as described previously (Das et al, 2009; Das et al, 2010; Das et al, 2014). Briefly, after treatment with 30 nM CPT and mitotic arrest by nocodazole treatment, cells were collected and mixed with low melting agarose. Slides were immersed in lysis solution at 4⁰C for 1 h. After a rinse with deionized water, slides were immersed in a 4⁰C electrophoresis solution (50 mM NaOH, 1 mM EDTA, and 1% dimethyl sulfoxide) for 1 h. Electrophoresis was carried out at a constant voltage of 25 V for 30 min at 4⁰C. After electrophoresis, slides were neutralized in 0.4 M Tris-HCl (pH 7.5), dehydrated in ice-cold 70% ethanol for 5 min, and air-dried. DNA was stained with ethidium bromide (EtBr) purchased from Sigma (USA). The relative length and intensity of EtBr-stained DNA, tails to heads, is proportional to the amount of DNA damage present in the individual nucleus. Comet length was measured using the TriTek Comet Score software (TriTek Corp,

Sumerduck, VA) and was scored for at least 50 cells. Distributions of comet lengths were compared using the Student t-test.

5.2.8 Cell survival assays

Cells (6×10^3) were transfected with control or CDK1 siRNA (25 nM) as described above and seeded in 96-well plates (BD Biosciences, USA). After 24 h, cells were treated with CPT at the indicated concentrations and kept further for 48 h. In a related experiment the TDP1^{+/+} and TDP1^{-/-} MEFs were ectopically expressed with FLAG-TDP1 variants and treated with 30 nM CPT for 24 hours. The cells were arrested at G2/M phase by treatment with 200 ng/mL nocodazole for the last 8 hours of CPT treatment. The cells were allowed to grow for additional 24 hours in drug free medium. Cell survival was then assessed by 3-(4,5-dimethylthiazol-2-yl)-2,5-diphenyltetrazolium bromide (MTT) purchased from Sigma, USA as described previously (Rehman et al, 2018). Plates were analysed on Molecular Devices SpectraMax M2 Microplate Reader at 570 nm. The percent inhibition of viability for each concentration of CPT was calculated with respect to the control. Data represent mean values \pm S.D. for three independent experiments.

5.2.9 Cell fractionation and isolation of chromatin bound protein

Cell fractionation and isolation of chromatin bound proteins was performed previously as described in chapter IV (Rehman et al, 2018; Wu & Wang, 2021).

5.2.10 Chromatin immunoprecipitation (ChIP)

ChIP was performed following protocol described in chapter IV.

5.2.11 Metaphase spread

For metaphase spreads, cells were transfected as per experimental requirements treated with or without low dose of CPT and later incubated with 1 g/ml colcemid for the last 4 h. Cells were then harvested and treated with hypotonic solution (75 mM KCl) for 12 min, washed with chilled fixative (methanol/acetic acid 1:1), and left overnight at 4°C. Cells were later dropped onto a chilled glass slide, air-dried and stained with 5% aqueous Giemsa. For each case, 50 metaphase plates were scored.

5.2.12 Detection of mitotic BrdU foci (Mitotic DNA synthesis)

For detection of mitotic BrdU foci in MEFs, cells were transfected as detailed in experimental protocol, synchronized at the G1/S transition with 1.5 mM thymidine (Sigma-Aldrich) for 16 hours, washed three times with PBS, released in fresh medium containing 6 μ M RO-3306 (Sigma-Aldrich) for 10.5 hours (in the absence of aphidicolin) or for 17.5 hours (in the presence of 15 nM CPT alone or combined with 1 μ M aphidicolin (Sigma-Aldrich)) and treated as indicated. Cells were then washed three times with warm medium and released in medium containing 100 ng/mL nocodazole (Sigma-Aldrich) and 1X BrdU (ThermoFisher) for 60-90 min before being processed. Cells were fixed and permeabilized with 4% paraformaldehyde, 20mMHEPES, 10mMEGTA, 0.2%Triton X-100, 1mMMgCl₂ for 20 min at room temperature. Coverslips were washed three times with PBS and then BD Pharmingen™ BrdU Flow Kits was used for the immunofluorescence staining of the incorporated BrdU in mitosis. Coverslips were washed once with PBS, incubated with DAPI (0.5 mg/mL, ThermoFisher) in PBS for 10 min at room temperature, washed three times with PBS and rinsed in distilled water before being mounted on slides using ProLong Gold Antifade Mountant (ThermoFisher) mounting media. Microscopy was done on LeicaTCSSP8 confocal laser-scanning microscope(Germany) with 633/1.4NAoil objective. Leica software was used for image processing which was later sized in AdobePhotoshop7.0. The γ H2AX or BrdU foci/intensity per nucleus was measured by the fluorescence intensities normalized to the number of cell counts in Adobe Photoshop 7.0. Images were also analyzed with ImageJ/FIJI software (National Healthcare Institute, USA; (Schindelin et al., 2012).

5.3 Results

5.3.1 Top1cc's are repaired independent of TDP1 in mitosis through mitotic DNA synthesis (MiDAS)

Trapped Top1cc's, which can be repaired in cells broadly by phosphodiesterase pathway that primarily includes TDP1, which is coupled with PARP1 and are restricted to the "S"-phase of the cell cycle; while alternative endonuclease pathways that include Mus81-EME1, XPF-ERCC1, etc are known to operate independent "S-phase" of the cell cycle (Wu & Wang, 2021) for Top1cc repair in mitotic phase. Therefore, we tested the role TDP1 as well as alternative endonuclease pathways pathway in the repair of trapped Top1cc's during mitosis. During early mitosis the nuclease activity of the structure specific endonuclease Mus81-

Eme1 complex promotes a RAD52-mediated break-induced replication process using POLD3 at mitotic break sites (Bhowmick et al, 2016), which might serve to minimize chromosome mis-segregation and non-disjunction under conditions of replication stress. Although homologous recombination (HR) is indicated as a high-fidelity repair mechanism, the break-induced replication (BIR) or MiDAS, classified as a subtype of HR, is a mutagenic error-prone mechanism that leads to chromosome rearrangements and chromosomal instabilities (Wu & Wang, 2021). It remains poorly understood how cells suppress mutagenic BIR. CPT-induced trapped Top1cc can be transformed into induce replication-associated DNA double-strand breaks (DSBs). These are replication associated DNA double stranded ends (DSE's) caused by either replication run-off or cleavage of stalled replication forks or transcriptional machinery. To test the repair of such unrepaired premitotic Top1cc linkeds DSE's by MiDAS, we looked into BrdU incorporation on prophase DNA to mark the newly replicating cells. The TDP1^{-/-} MEFs used in this study were transfected with empty vector or FLAG-TDP1 variants (WT or S61A), synchronized at the G1/S transition using a single thymidine block and released them in media containing the CDK1 inhibitor RO-3306 (Figure 5.1A). This treatment caused cell-cycle arrest in G2, reflected by the lack of histone H3 phosphorylation at Ser10 in FACS analyses (data not shown). After 10.5-h incubation with RO-3306, we released the cells into mitosis in the presence of nocodazole and BrdU (Figure 5.1A). Entry into mitosis was demonstrated by FACS analyses of histone H3 Ser10 phosphorylation (data not shown), while BrdU incorporation was used to monitor MiDAS. Because labeling with BrdU takes 20–30 min, any BrdU found in mitotic cells was assumed to have been incorporated into the genome in G2. The use of the CDK1 inhibitor, RO3306 (Vassilev, 2006), to arrest cells at the G2/M boundary allowed us to separate G2 from M-phase, and therefore to add BrdU only after cells had entered the prophase of mitosis. Under these circumstances, we could detect BrdU on metaphase chromosomes and demonstrate that DNA synthesis was still occurring in early mitosis. Also, to exclusively capture DNA synthesis in mitosis, we inhibited S/G2 replication with hydroxyurea, as previously described (Macheret et al., 2020). BrdU-labeled DNA was isolated from mitotic “shake-off” cells and analyzed by immunofluorescence microscopy. We detected no BrdU

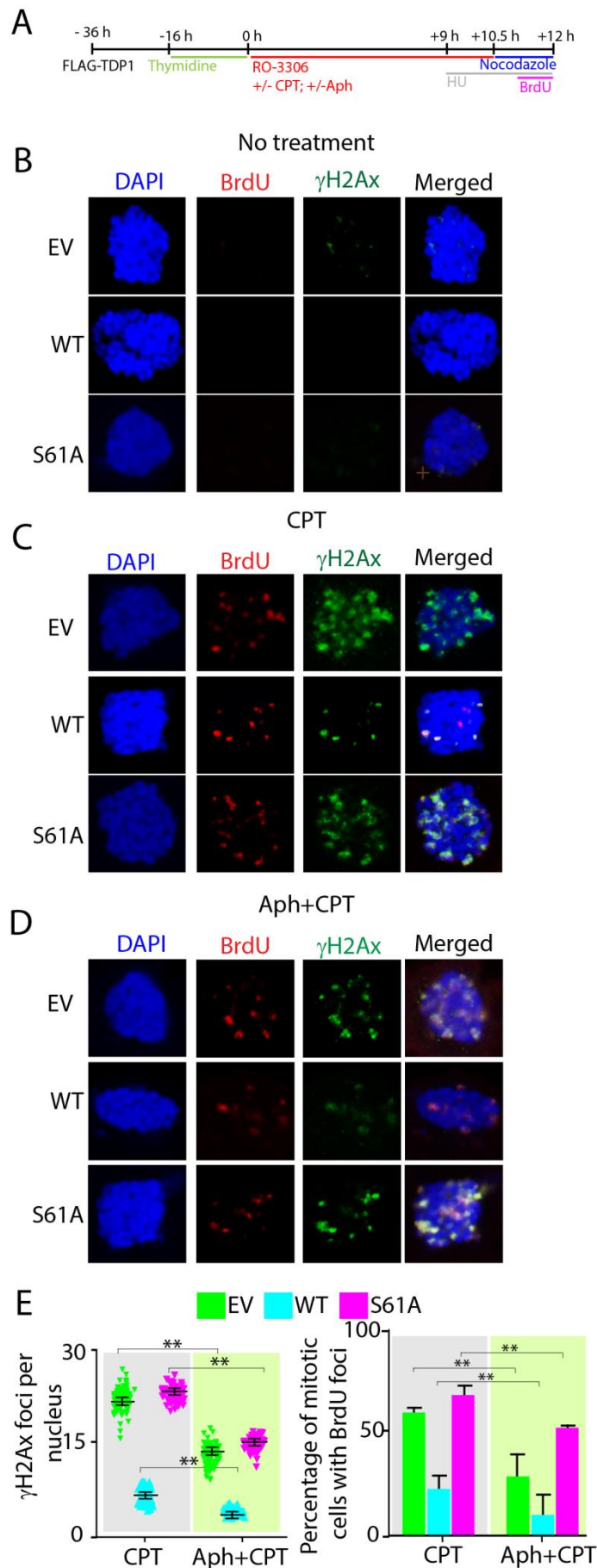


Figure 5.1: Mitotic Top1cc's resulting from replication collisions are repaired by the error prone mitotic DNA synthesis (MiDAS). (A) Schematic representation showing protocol followed to study Top1cc repair by MiDAS in mitosis. (B) γ H2AX and BrdU foci as observed in mitotic chromosomes. TDP1^{-/-} MEF cells were transfected with the empty vector (EV) or FLAG-TDP1 variants (WT or S61A). Cells were enriched at M phase as detailed in schematic protocol. Cells were counterstained with DAPI to visualize nuclei (blue). (C) γ H2AX and BrdU foci as observed in mitotic chromosomes upon replication stress induced by low dose CPT (15 nM). TDP1^{-/-} MEF cells were transfected with the empty vector (EV) or FLAG-TDP1 variants (WT or S61A). Twenty four hours after transfection, cells were treated with CPT (15 nM, 24 h) and were enriched at M phase as detailed in schematic protocol. Representative images shows break induced repair with newly synthesised mitotic DNA marked by BrdU foci (red). γ H2AX foci signifying the strand breaks are shown in green. Cells were counterstained with DAPI to visualize nuclei (blue). (D) BrdU foci were observed on mitotic chromosomes upon replication stress induced by CPT when replication process is inhibited by Aphidicolin (Aph) treatment as detailed in the schematic protocol. (E) Quantification of γ H2AX intensity per nucleus obtained from immunofluorescence confocal microscopy was calculated for 20–25 cells (mean \pm S.E.M.). Asterisks denote statistically significant difference (**P < 0.001; t test). ((left). Quantification of the percentage of BrdU positive mitotic nucleus obtained from immunofluorescence confocal microscopy was calculated for 20–25 cells (mean \pm S.E.M.) (right). Asterisks denote statistically significant difference (**P < 0.001; t test).

or γ H2AX foci in control untreated cells (Figure 5.1B) which were markedly increased after CPT treatment (Figure 5.1C). TDP1^{-/-} MEFs expressing the FLAG-TDP1^{WT} were found to accumulate significantly low γ H2AX (green) levels (Figure 5.1C) confirming our previous data (Figure 4.5), BrdU foci (red) were found to colocalise with the γ H2AX foci indicating the involvement of MiDAS in the repair of these Top1cc-associated breaks (Figure 5.1C). TDP1^{-/-} MEFs expressing the EV or FLAG-TDP1^{S61A} showed marked increase in the levels and simultaneous colocalization of BrdU and γ H2AX foci upon CPT treatment (Figure 5.1C) confirming that this BIR operates in cells to repair Top1cc's independent of TDP1. We also co-treated the cells with Aph and CPT and observed a reduction in the levels of BrdU and γ H2AX foci suggesting replication conflicts as a potential source of these Top1cc induced DNA breaks (Figure 5.1D). Figure 5.1E shows CPT treatment results in marked increase in γ H2AX foci due to concomitant increase of MiDAS in the TDP1^{-/-} transfected with FLAG-TDP1^{S61A} both compared to the EV or FLAG-TDP1^{WT} overexpressing MEFs which could be partly diminished by the co-treatment with the replication inhibitor aphidicolin.

5.3.2 Abrogation of CDK1-mediated phosphorylation of TDP1 at Serine 61 promotes MiDAS by escalating chromatin enrichment of Mus81

MiDAS requires the structure specific endonuclease Mus81-Eme1, Rad52 and a non-catalytic subunit of the Pol-delta complex, POLD3 and is correlated with diminished chromosome missegregation and nondisjunction (Minocherhomji et al, 2015) if tightly regulated. Unrestrained Mus81 mediated resection and hyperactivated MiDAS can be potentially dangerous to the cells translating into chromosomal instabilities (Wu & Wang, 2021). Cells overexpressing yeast TDP1 (yTDP1) are found to be excessively dependent on DNA repair enzymes especially endonucleases like Rad27, Slx4, and Mus81 (Duffy et al, 2016) which suggests the non-specific adduct forming tendencies of yTDP1 which might be processed and removed by the endonucleases (Duffy et al, 2016). Mus81 overloading on the mitotic chromatin was observed in TDP1^{-/-} MEFs which leads to increased resection as marked by increased γ H2AX foci (Figure 5.2B) under CPT treated conditions. Mus81 is involved in the cleavage of Top1cc-stalled replication forks and R-loop-impeded replication forks (Wu & Wang, 2021). We found that chromatin-bound Mus81 level was even higher in CPT treated TDP1^{-/-} MEFs complemented with FLAG-TDP1^{S61A} as compared to that of the TDP1^{-/-} MEFs expressing EV and negligible Mus81 chromatin loading was observed upon FLAG-TDP1^{WT} complementation (Figure 5.2B). Quantification of the IF staining of chromatin-

bound Mus81 for cells pre-extracted with Triton X-100 before fixation showed enriched Mus81 intensity in FLAG-TDP1^{S61A} cells upon CPT treatment (Figure 5.2D, left) compared to TDP1^{-/-} MEFs complemented with EV or FLAG-TDP1^{S61A}. Chromatin fractionation followed by Western blot analysis also showed that Mus81 loading on chromatin was greater in FLAG-TDP1^{S61A} complemented TDP1^{-/-} MEFs (Figure 5.3B-C) as compared to FLAG-TDP1^{WT}. We also tested whether Mus81 overloading results in uncontrolled Mus81-mediated cleavage leading to increased DSBs. DNA breaks were analysed using γ H2AX as a DSB marker; we found that the number of γ H2AX foci significantly increased in TDP1^{-/-} MEFs complemented with TDP1^{S61A} compared to TDP1^{WT} transfected MEFs treated with CPT. Importantly, knocking down Mus81 using siRNA largely reduced elevated γ H2AX in TDP1^{-/-} MEFs complemented with either EV, FLAG-TDP1^{WT} or FLAG-TDP1^{S61A} and treated with CPT, indicating that the extensive resection culminating in the process of break induced replication (MiDAS) of CPT-induced collapsed replication forks in mitosis cells depends on MUS81 independent of TDP1 (Figure 5.2C and E). Thus, complementation of TDP1^{-/-} MEFs with FLAG-TDP1^{S61A} results in uncontrolled Mus81-mediated cleavage, leading to increase DSBs that are subjected to subsequent DNA end resection and processing for the break induced replication (BIR).

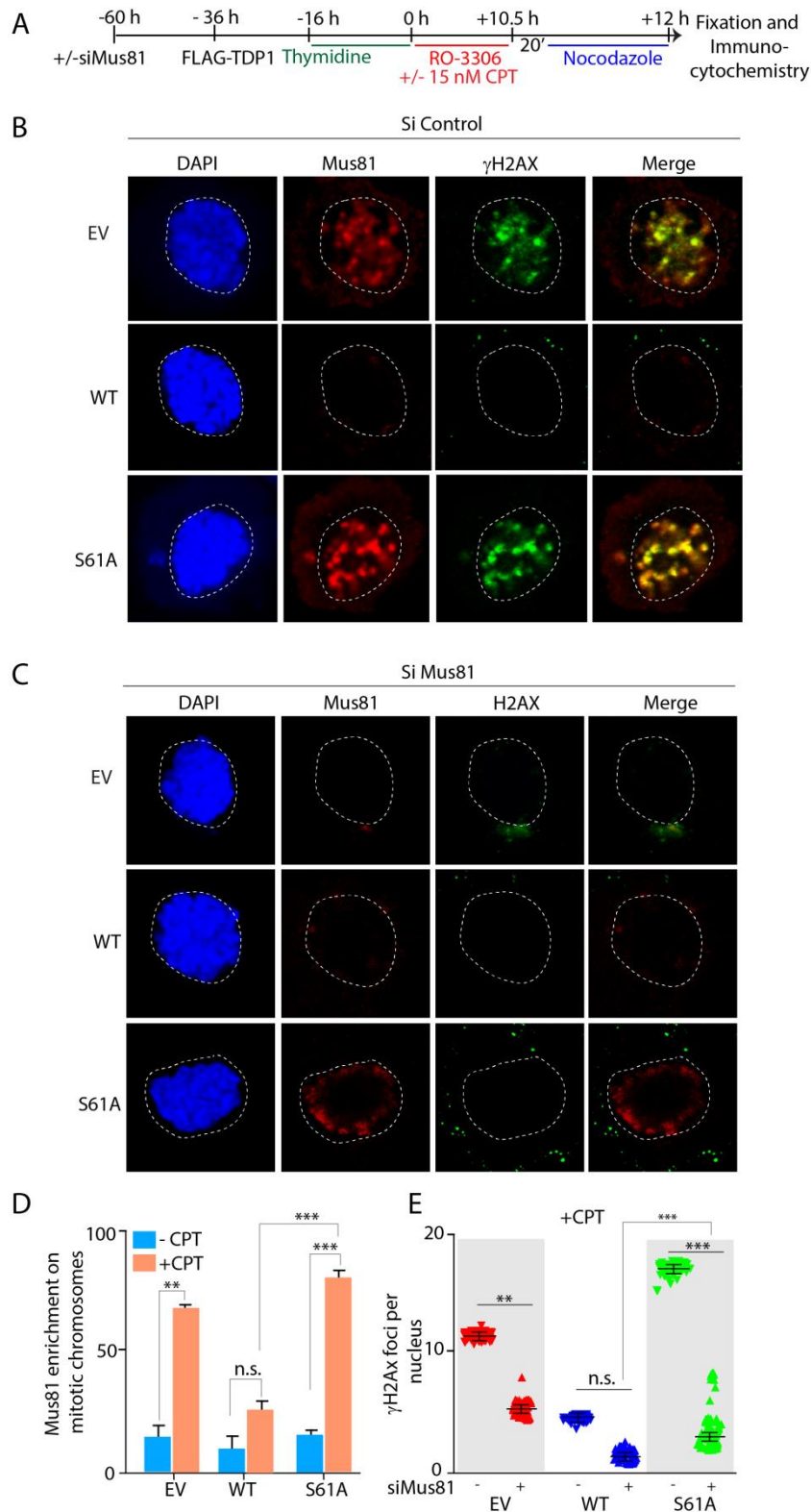


Figure 5.2 Abrogation of CDK1-mediated phosphorylation of TDP1 at Serine 61 promotes MiDAS by escalating chromatin enrichment of Mus81 (A) Schematic representation of the protocol followed for the scoring of mitotic DNA breaks by γ H2AX staining in Mus81 proficient and deficient TDP1^{-/-} MEFs. (B and C) Representative images showing the γ H2AX (green) and Mus81 (red) levels observed in the TDP1^{-/-} MEFs co-transfected with SiCtrl (B) or siRNA against Mus81 endonuclease (C) and FLAG-TDP1 variants (WT and S61) or empty vector (EV) following replication stress (15 nM CPT, 24 h) as shown in protocol. (D) Quantifications of the enrichment of

Mus81 on the mitotic chromosomes scored for 50 mitotic nuclei (each category) as depicted by the corresponding bar diagram. (E) Quantifications for the percentage of γ H2Ax foci on mitotic nuclei after CPT treatment upon Mus81 knockdown calculated for 50 cells (mean \pm S.E.M.). Asterisks denote statistically significant difference (**P < 0.001; ***P < 0.0001; t test). n.s. non significant

5.3.3 Mus81 is enriched at CFS loci in G2/M-phase during CFS expression in MCF7 cells overexpressing FLAG-TDP1^{S61A}

Chromosomal common fragile sites are specific regions of the genome that exhibit gaps or breaks on metaphase chromosomes under conditions that partially inhibit DNA replication (Li & Wu, 2020)). These sites often co-localize with regions deleted, amplified, or rearranged in cancer (Li & Wu, 2020). In the previous chapter of our dissertation we had looked into the enrichment of the ectopically expressed FLAG-TDP1 variants (FLAG-TDP1^{WT} and FLAG-TDP1^{S61A}) at three CFSs using ChIP assay which confirmed CPT treatment preferentially enhanced binding of the TDP1^{S61A} with respect to the TDP1^{WT} to the CFSs as compared to aphidicolin induced replication stress (Figure 4.5A-D). In the chapter, we performed chIP against endogenous Mus81 at CFSs in MCF cells overexpressing FLAG-TDP1^{WT} or FLAG-TDP1^{S61A}. Corroborating with our previous results that chromatin loading of Mus81 is increased in the FLAG-TDP1^{S61A} expressing TDP1^{-/-} MEFs in both the immunofluorescence and chromatin fractionation (Figure 5.2 and 5.3A-C), chIP analysis confirmed an enrichment of endogenous Mus81 at the CFSs cells overexpressing the phosphomutant TDP1 (S61A) after CPT treatment which could be rationalised to be due to the role of the structure specific endonuclease in the removal of trapped TDP1^{S61A} from the mitotic chromosomes (Figure 4.5A-D). These data also strengthens our hypothesis that the lack of extrusion of the TDP1-S61A mutant results in the formation of non-specific TDP1-DNA adducts which could be plausibly be processed by the Mus81 endonuclease. In the CPT treated TDP1^{-/-} MEFs expressing EV or FLAG-TDP1^{WT}, Mus81 seems to be involved in the repair of the Top1ccs.

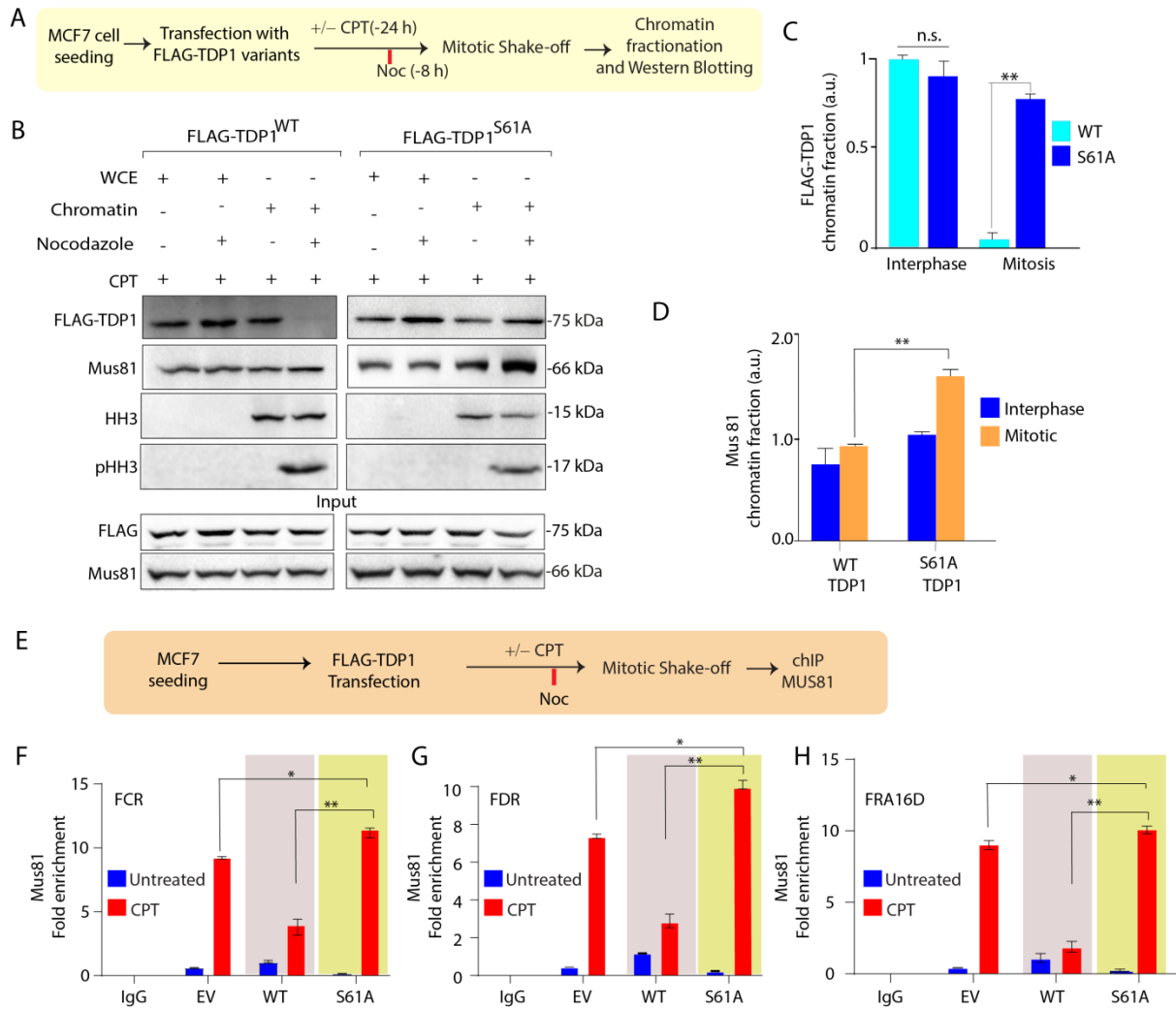


Figure 5.3 Mus81 is enriched at CFS loci in G2/M-phase during CFS expression in MCF7 cells overexpressing FLAG-TDP1^{S61A} (A) Schematic representation showing the protocol followed for the chromatin fractionation of the MCF7 cells transfected with FLAG-TDP1^{WT} or FLAG-TDP1^{S61A} to study the mitotic chromosomal enrichment of Mus81 and the TDP1 variants. (B) MCF7 cells were transfected with FLAG-TDP1^{WT} or FLAG-TDP1^{S61A} and the chromatin fractions were prepared to be used for Western blotting performed against anti-FLAG and anti-Mus81 antibodies. Histone H3 (anti-HH3) and phospho-Histone H3 (anti-pHH3) were used as chromosomal and mitotic markers. Protein levels of Mus81, FLAG-TDP1^{WT} and FLAG-TDP1^{S61A} were analysed in the whole cell lysates to ensure equal levels of protein before chromatin fractionation. (C) Quantification showing the relative chromosomal enrichment of FLAG-TDP1 variants (FLAG-TDP1^{WT} or FLAG-TDP1^{S61A}) in interphases (Asn) and Mitotic (M) chromosome. (D) Quantification showing the relative enrichment of Mus81 on mitotic chromosomes in interphases (Asn) and Mitosis (M) for the FLAG-TDP1^{WT} or FLAG-TDP1^{S61A} expressing MCF7 cells following replication stress with low dose CPT (15 nM, 24 hours). (E) A schematic representation for the protocol followed for the chromatin immunoprecipitation (ChIP) of endogenous Mus81 at the CFSs loci in mitosis upon replication stress induces by low dose of CPT. (F-H) Quantification of cross-linked FRA3B-FCR, FRA3B-FDR and FRA16D loci chromatin-immunoprecipitated from MCF7 cells transfected with empty vector (EV) and FLAG-TDP1 variants (WT or S61A) using the specified antibodies (endogenous Mus81). Fold enrichment over goat IgG was determined and is shown for each primer pair for the ChIP. Asterisks denote statistically significant difference (**P < 0.001; *P < 0.01; t test). n.s. non significant.

However in the FLAG-TDP1^{S61A} complemented TDP1^{-/-} MEFs, the endonuclease has a bipartite function where it not only removes the trapped Top1cc's from the mitotic chromosomes but also participate in the removal of trapped TDP1-DNA adducts as indicated by concomitant increase of DNA breaks (Figure 5.2D-E).

5.3.4 Mitotic phosphorylation of TDP1 at Serine 61 prevent genome instability

Earlier studies show that the overexpression of TDP1 induces CIN resulting in accumulation of chromosomal breaks and fusions as a consequence of non-specific TDP1-DNA adduct formation which might lead to the poor resolution of replication/recombination intermediates prior to mitosis (Duffy et al, 2016). Our data suggest that the abrogation CDK1 mediated S61 phosphorylation of TDP1 leads to the formation of non-specific TDP1 adducts on the DNA which might plausibly be involved in defective mitotic progression and accumulation of chromosomal aberrations. Hence, metaphase spreading was performed and we analysed the micronuclei (MN) formation, presence of bulky anaphase bridges (AB), chromatid breaks (CB) and several other mitotic defects in TDP1^{-/-} MEFs expressing the EV or the FLAG-TDP1 variants (WT or S61A) exposed or not to a low-dose CPT (30 nM for 24 hours) (Figure 5.4A). TDP1 depleted cells and the cells expressing the TDP1^{WT} and TDP1^{S61A} had comparable levels of MN formation under non-CPT treated condition (data not shown). However, CPT treatment was found to greatly augment the micronuclei formation in the TDP1 depleted and TDP1^{S61A} complemented MEFs compared to the TDP1^{WT} complemented MEFs (Figure 5.4B). In CPT-treated cells, the percentage of anaphases with bulky chromatin bridges was similar among cell lines, except those expressing the phosphomutant TDP1S61A, which showed significant increase in anaphase bridges (Figure 5.4B). Taken together our results provide evidence for the role of S61 phosphorylation of TDP1 during mitosis in the maintenance of genomic stability.

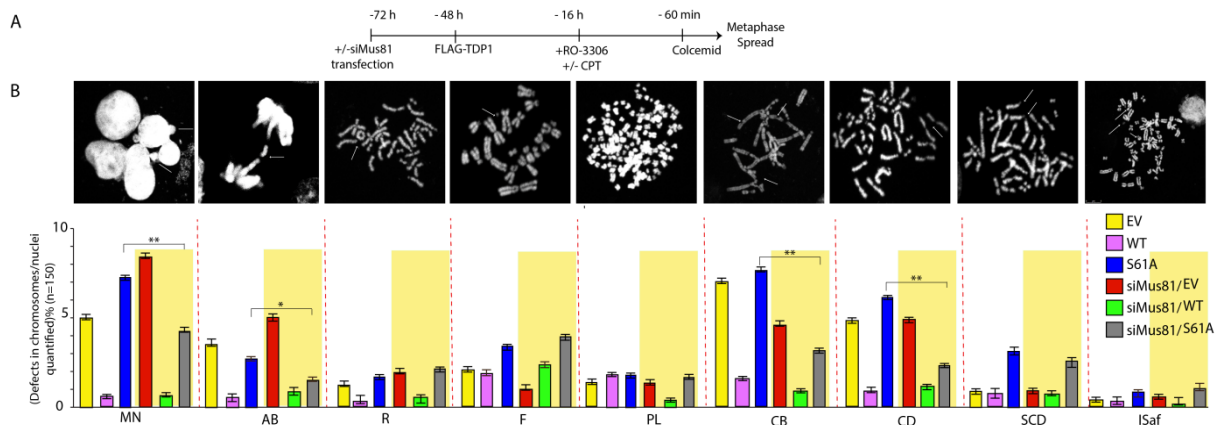


Figure 5.4 (A) Schematic representation of the protocol followed for the scoring of mitotic defects on metaphase chromosomes using metaphase spreading. (B) Representative images showing the different

mitotic defects observed in the metaphase spreads of TDP1^{-/-} MEFs co-transfected with Si Ctrl or siRNA against Mus81 endonuclease and FLAG-TDP1 variants (WT and S61) or empty vector (EV) following replication stress (15 nM CPT, 24 h). The percentage of such defects scored for 150 metaphase spreads (each category) as depicted by the corresponding bar diagram quantification. Asterisks denote statistically significant difference (**P < 0.001; *P < 0.01 t test). MN, micronuclei; AB, anaphase bridges; R, ringed chromosome; F, fragmentation; PL, polyploidy; CB, chromatid breaks; CD, cohesion defect; SCD, single chromatid decomposition; ISaf, iso-arm fragmentation.

5.3.5 53BP1 nuclear bodies accumulate upon FLAG-TDP1^{S61A} overexpression following replication stress

53BP1 nuclear bodies are induced by DNA or chromatin damage, increase after replication stress, and are largely confined to G1 (Fernandez-Vidal et al, 2017). A fraction of under-replicated chromosomes often escape the G2 checkpoint and 53BP1 nuclear bodies could arise after such loci become converted to DNA lesions during mitosis (Harrigan et al, 2011). To test whether the non-specific trapping of the TDP1^{S61A} phosphomutant on the mitotic chromosomes can lead to the replication-stress-induced formation of 53BP1 nuclear bodies in the subsequent G1 phase, which can be correlated with the presence of DNA DSBs at the M-phase (Figure 5.5A-C), TDP1^{-/-} MEFs overexpressing FLAG-TDP1^{WT} or FLAG-TDP1^{S61A} were left untreated or exposed to a low dose of CPT followed by synchronisation to the next G1 phase of the cell cycle. Immunostaining of 53BP1 was performed which revealed the detectable accumulation of G1 phase 53BP1 nuclear bodies in the FLAG-TDP1^{S61A} transfected cells as compared to the TDP1^{-/-} and the FLAG-TDP1^{WT} transfected TDP1^{-/-} MEFs, indicating that the abrogation of the CDK1 mediated phosphorylation of TDP1 at S61 contributes to the genesis of these structures (Figure 5.5B and C). Next, we also used neutral comet assays to compare the CPT-associated DNA strand breaks (Cortés-Gutiérrez et al, 2012) in TDP1^{-/-} cells. We measured the level of DNA double strand breaks following 24 h incubations with 30 nM CPT and Figure 5.5D shows that CPT-treated TDP1^{-/-} MEFs accumulate ~4-fold more DSBs as compared to the TDP1^{-/-} cells complemented with FLAG-TDP1^{WT} while the FLAG-TDP1^{S61A} complemented MEFs showed ~5 fold more DNA DSBs. Interestingly Mus81 knockdown resulted in a marked reduction of the mean comet length (Figure 5.5, siMus81) in these cells indicative of lesser number of DNA breaks generated in cells in absence of Mus81 endonuclease.

5.3.6 Mus81 knockdown rescue the survival of TDP1^{-/-} MEFs complemented with FLAG-TDP1^{S61A} following replication stress

To further establish the role of the CDK1 mediated phosphorylation of TDP1 at S61 in response to Top1cc repair, we performed survival assays. Figure 5.5E shows that TDP1 proficient MCF7 cells do not showed increased the cytotoxicity towards CPT when Mus81 is knocked down which could be primarily because TDP1 is the main repair protein responsible for CPT induced Top1cc's and Mus81 endonuclease pathway might just be a backup pathway functioning in absence of TDP1. However, when the survival assays were performed in TDP1^{-/-} MEFs transfected with empty vector (EV), FLAG-TDP1^{WT} or FLAG-TDP1^{S61A}, CPT treatment rendered the EV and FLAG-TDP1^{S61A} transfected cells hypersensitive but the FLAG-TDP1^{WT} complemented cells were protected against CPT (Figure 5.5F) treatment. Importantly it was also observed that the TDP1^{-/-} MEFs in which Mus81 has been additionally depleted using siRNA, the MEFs were significantly hypersensitive to CPT suggesting that the TDP1 dependent phosphodiesterase pathway and the endonuclease pathways distinctly operate in repair of Top1ccs (Figure 5.5F). The additional hypersensitivity to CPT in these TDP1^{-/-} MEFs caused by Mus81 depletion could be rescued by complementation with FLAG-TDP1^{WT} further substantiating the role of TDP1 in Top1cc repair. However, when TDP1^{-/-} MEFs were transfected with FLAG-TDP1^{S61A} the cells were simultaneously Mus81 depleted, the MEFs showed a better survival phenotype when challenged with CPT (Figure 5.5F) which further validates our previous results that excessive Mus81 loading on the chromatin in TDP1^{S61A} overexpressing cells leads to unrestrained end

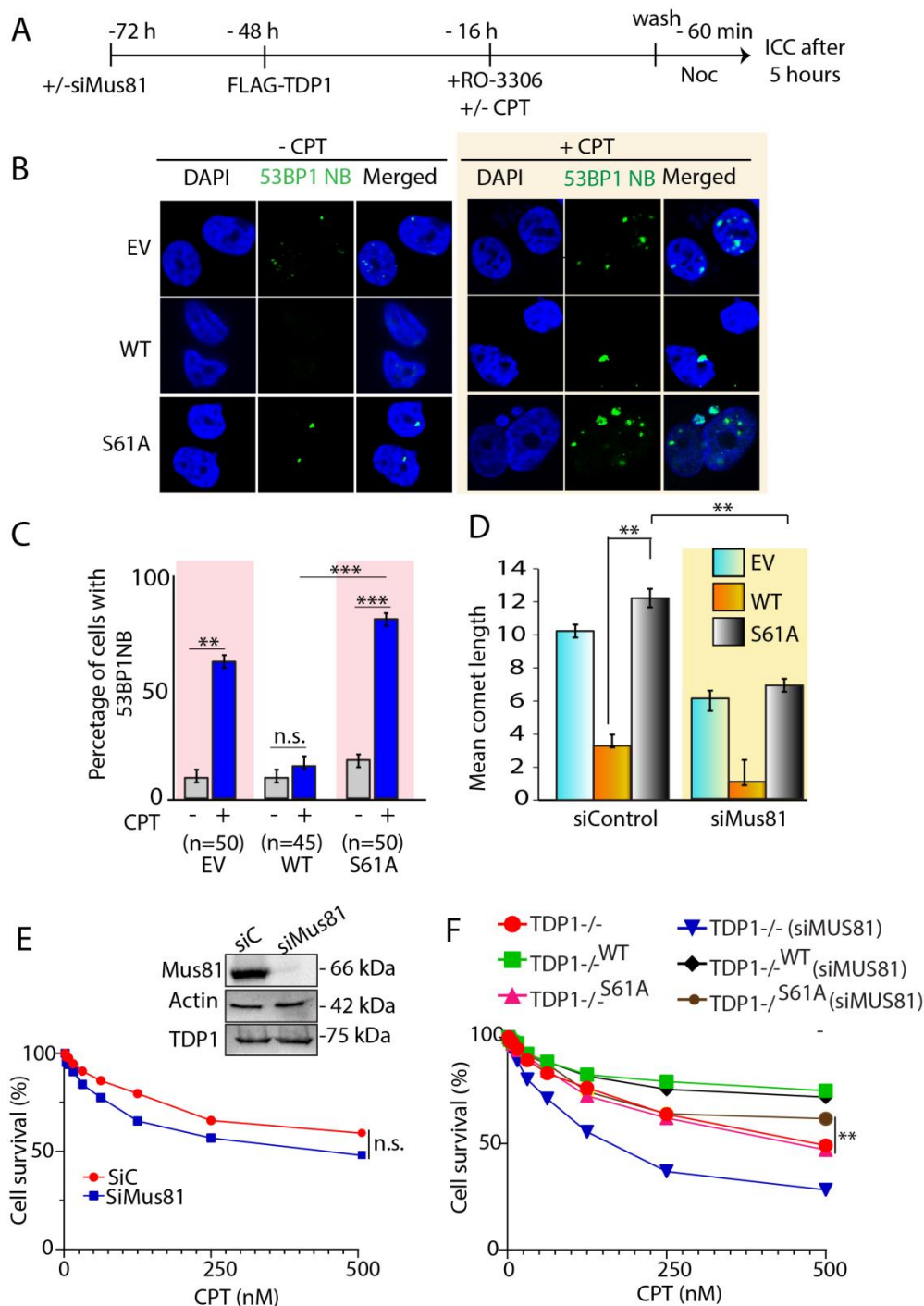


Figure 5.5 Mus81 knockdown rescue the survival of TDP1^{-/-} MEFs complemented with FLAG-TDP1S61A following replication stress (A) Schematic showing the workflow to study the 53BP1 nuclear body formation in G1 daughter nuclei post CPT induced replication stress after Mus81 knockdown in TDP1^{-/-} MEFs ectopically expressing empty vector (EV) or FLAG-TDP1 variants (WT and S61A). (B) TDP1^{-/-} MEFs transfected with SiCtrl or SiMus81, ectopically expressing empty vector, FLAG-TDP1 (WT or S61A) were subjected to CPT (15nM, 16 h) followed by G2/M arrest with 200ng/mL nocodazole during the last 8 hours. Mitotic cells were harvested by shake-off and re-seeded, 5 hours after release cells were fixed and stained with 53BP1 antibody (green). (C) Quantifications showing the number of cells having 53BP1 nuclear bodies upon CPT treatment in G1 phase calculated for 45–50 cells (mean ± S.E.M.). (D) Quantification of CPT-induced DNA strand breaks measured by neutral comet assays in TDP1^{-/-} MEF cells expressing empty vector or FLAG-TDP1 variants (WT or S61A) arrested in G2/M phase with 200 ng/mL nocodazole added during the

last 8 h of CPT treatment. CPT-induced DNA strand breaks were calculated for 50 cells (mean \pm S.E.M.). (E) Survival of MCF7 cells expressing SiCtr or SiMus81 in presence of CPT for 72 hours. Percentage survival was normalized to the CPT untreated cells \pm S.E.M. Western blots showing the levels of Mus81 knockdown and the corresponding TDP1 levels in the MCF7 cells. Actin was used as loading control. (F) Survival of TDP1^{-/-} MEF cells expressing SiCtr or SiMus81 and ectopically expressing empty vector (EV), FLAG-TDP1^{WT} or FLAG-TDP1^{S61A} following replication stress. The cells were released from the arrest and allowed to grow for an additional 48 hours. Percent survival was normalized to the CPT untreated cells \pm S.E.M. Asterisks denote statistically significant difference (**P < 0.01, ***P < 0.001, ****P < 0.0001; t test). N.s non-significant.

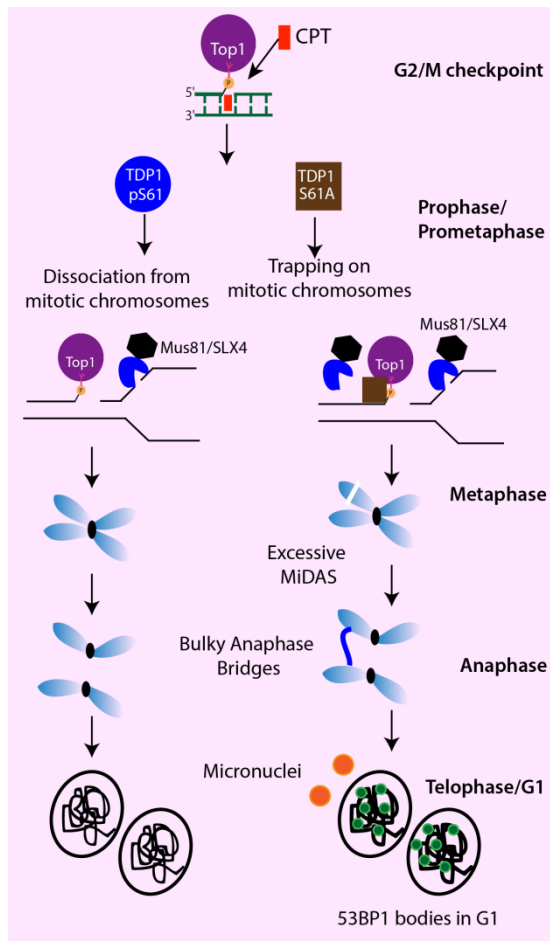


Figure 5.6 Model depicting how TDP1^{S61A} trapping on mitotic chromosomes leads to hyperactivation of mitotic DNA synthesis (MiDAS) causing excessive Mus81-Eme1 endonuclease mediated DNA resection and breaks on the mitotic DNA. These breaks manifest as bulky anaphase bridges followed by chromosomal segregation defects leading to formation of micronuclei and accumulation of 53BP1 nuclear bodies in G1 daughter cells. CDK1 mediated phosphorylation of TDP1 at S61 residue promotes its extrusion from the mitotic chromosome to safeguard genomic stability.

5.4 Discussion:

The current study identifies a unique CDK1-mediated serine (S61) phosphorylation of TDP1 as a key regulator of genomic stability during mitosis following replication stress. The results of this work show that S61 phosphorylation of TDP1 facilitates its dissociation from condensed chromosomes at the start of mitosis, promoting normal chromosome segregation and preventing non-disjunction and other chromosomal defects. We further show that phosphomutant-TDP1 (TDP1^{S61A}) are trapped on mitotic DNA causes DSBs that can be significantly decreased by the replication inhibitor aphidicolin, implying that pre-mitotic

replication conflicts are a potential source of these mitotic breaks (Figure 5.1). Moreover, the additional mitotic DNA breaks in the FLAG-TDP1^{S61A} complemented TDP1^{-/-} MEFs as compared to the empty vector or the FLAG-TDP1^{WT} complemented TDP1^{-/-} MEFs indicate the removal of trapped TDP1^{S61A} on the mitotic chromosomes activates an end-resection mediated repair pathways (break induced replication). This is further justified by excessive chromatin loading of the structure specific endonuclease Mus81 was seen in cells overexpressing FLAG-TDP1^{S61A}, which is likely responsible for the elevated H2AX in these cells. (Figure 5.2). Furthermore, increased Mus81 enrichment on mitotic chromosomes is associated with hyperactive MiDAS (Figure 5.1), which causes chromosomal defects (Figure 5.3) that can be rescued by Mus81 knockdown (Figure 5.1), confirming hyperactive unrestrained MiDAS as a potential source of the observed chromosomal instabilities. Mus81-mediated Top1cc repair functions as a backup route in TDP1 competent cells, as evidenced by the minimal sensitivity to CPT in TDP1 competent cells in which Mus81 has been knocked down by SiRNA (Figure 5.5E). TDP1^{-/-} MEFs with concomitant Mus81 knockdown, on the other hand, displayed increased sensitivity to CPT, which was rescued by FLAG-TDP1^{WT} complementation (Figure 5.5F). Interestingly, CPT treated TDP1^{-/-} MEFs complemented with FLAG-TDP1^{S61A} showed better survival upon Mus81 knockdown, further confirming the occurrence of unrestrained Mus81 dependent MiDAS responsible for abnormal chromosomal segregation and mitotic defects (Figure 5.3). Our findings provide novel mechanistic and functional insights into CDK1-mediated phosphorylation of TDP1 at S61 during mitosis, which confers a protective function in maintaining genomic stability (Figure 5.6 and 5.7).

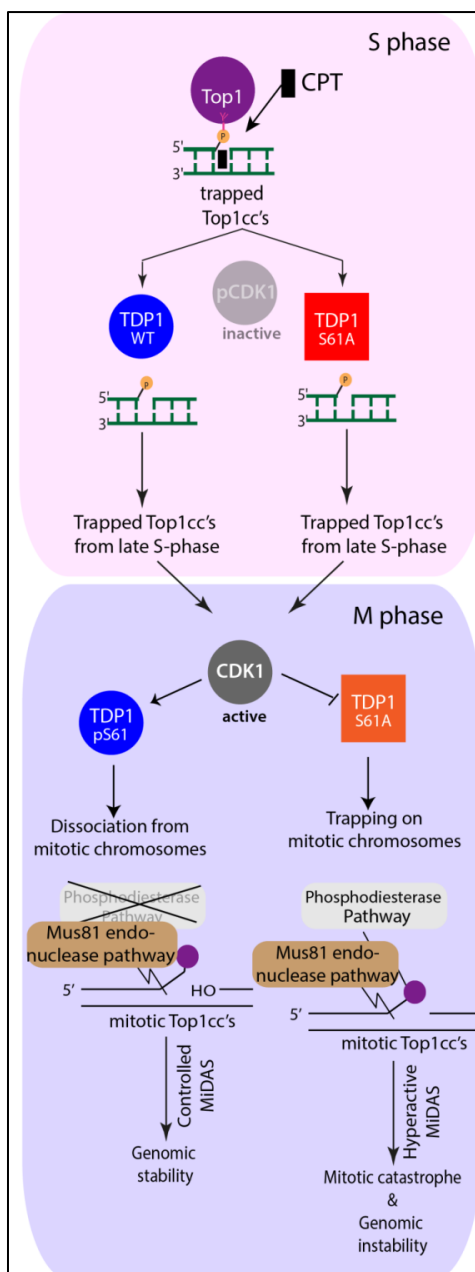


Figure 5.7 Hypothetical model for the proposed mechanism of CDK1 mediated phosphorylation of TDP1 at S61 residue for the repair of pre-mitotic Top1cc's and preventing chromosomal instabilities. In S-phase CDK1 remains inactivated by dual phosphorylations on its Threonine 14 and Tyrosine 15 residues by Myt1 and Wee1 kinases respectively. TDP1-S61 phosphorylation is thus prevented during S-phase which allows TDP1 to get recruited on the chromatin and participate in the base excision repair (BER) for the removal of Top1cc's. At the G2/M phase of the cell cycle, CDK1 is activated by the action of the CDC25 phosphatases which dephosphorylate CDK1 (T14, Y15 residues). CDK1 then mediates phosphorylation of TDP1 at S61 residue which promotes extrusion of TDP1 from the mitotic chromosomes at early mitosis. Pre-mitotic Top1cc's are removed in mitosis by the alternate pathways (Mus81-Eme1 mediated) independent of TDP1. Abrogation of TDP1-S61 phosphorylation (TDP1^{S61A}) leads to the formation of nonspecific TDP1-DNA adducts which are processed by the structure specific endonuclease Mus81-Eme1 by a break induced repair (BIR) mechanism operating in mitosis (mitotic DNA synthesis) which leads to unrestrained end resection and accumulation of DNA breaks. These DNA breaks lead to bulky anaphase bridge formation which leads to non-disjunction and chromosomal segregation defects culminating in micronuclei formation and accumulation of 53BP1 nuclear bodies in the G1 daughter cells.

Chapter 6

Identification and characterization of a quinoline derivative that poisons *Leishmania donovani* bisubunit Topoisomerase I

6.1 Introduction:

Leishmania donovani is an obligate intracellular protozoan parasite that contributes to an annual estimate of 50,000 to 90,000 new cases of kala-azar or Visceral leishmaniasis (VL), worldwide in 98 countries with 350 million people at risk of infection (Desjeux, 2001; Torres-Guerrero et al, 2017). *Leishmania* propels an immune-suppressive infection in the host by colonizing within macrophages followed by trans-differentiation from the extracellular insect gut form promastigotes to intracellular amastigote stage (and & Kamhawi, 2001; Kaye & Scott, 2011). The broad spectrum of clinical manifestations (Torres-Guerrero et al, 2017) includes localized cutaneous leishmaniasis characterized by ulcerative skin lesions, damaging mucosal inflammation, and disseminated systemic visceral infection (Mann et al, 2021). Pentavalent antimonials or sodium stibogluconate are no longer recommended owing to their toxicity and high levels of resistance in the Indian subcontinent (Altamura et al; Bi et al, 2018; Chappuis et al, 2007; Mohapatra, 2014; Sundar & Chakravarty, 2010). Alternatively, other drugs like the orally active polyene antibiotic miltefosine (hexadecyl phosphocholine) shows clinical limitations that include potential fetotoxicity, nausea, vomiting and other adverse side effects while the currently used liposomal formulation of an anti-fungal agent amphotericin B is restricted by severe nephrotoxicity which raise serious concerns for their future applications (Sundar & Chakravarty, 2010). The lack of effective drugs, vaccines against any form of human leishmaniasis, and emerging cases of drug-resistant strains call for immediate identification of new molecular targets for anti-leishmanial therapy (Altamura et al; Chakravarty & Sundar, 2010; Mann et al, 2021; Mohapatra, 2014).

DNA topoisomerases are essential enzymes that regulate DNA topology by catalyzing the nicking and resealing of DNA strands to facilitate relaxation of supercoiling generated during the DNA metabolic processes (Capranico et al, 2017; Champoux, 2001). Unlike other type IB eukaryotic topoisomerases, *Leishmania* topoisomerase IB (LdTop1) is a heterodimeric enzyme (Figure 6.3.1A) with the core DNA binding domain 'VAILCNH' located on the large subunit (LdTOP1L, 635 amino acids) and catalytic domain harboring the consensus catalytic 'SKXXY' motif on the small subunit (LdTOP1S, 262 amino acids) (Brata Das et al, 2004; Das et al, 2006a; Das et al, 2006b; Das et al, 2006c). The two subunits are encoded by two different genes, which associate with each other through protein-protein interactions to form an active heterodimeric Top1 (LdTop1) within the parasite (Das et al, 2005). Therefore,

LdTop1 bi-subunit could be exploited as a novel drug target for the treatment of leishmaniasis, which is starkly distinct from the mono-subunit human counterpart (Das et al, 2006a; Das et al, 2006c). Camptothecin (CPT), the human Top1B poison has already been reported to inhibit LdTop1B *in vitro* and induce cytotoxicity in *Leishmania donovani* promastigotes and amastigotes leading to apoptosis (Sen et al, 2004b). CPT promotes the formation of protein-DNA adducts both with the nuclear as well as kinetoplast DNA of *Leishmania* and *Trypanosoma* parasites (Balaña-Fouce et al, 2014; Das et al, 2006b; Sen et al, 2004b). However, there are several limitations associated with CPT including the chemical instability of the CPT alpha-hydroxy-lactone ring and loss of efficacy due to the drug efflux-mediated resistance generation (Das et al, 2018; Kundu et al, 2019; Kundu et al, 2020; Pommier, 2013) as well as its dose-limiting cytotoxicity (Pommier, 2013).

Non-camptothecin compounds like pyridine derivatives have a broad range of pharmaceutical properties that strengthen their medicinal application as antileishmanial, antiviral, antimalarial, and anticancer agents (de Mello et al, 2004; Kishbaugh, 2016). Pyridine derivatives have also been reported to target the Top1 enzyme (Zhao et al, 2004). The quinoline core structure is shared by CPT and its clinically approved derivatives like topotecan and irinotecan which have anticancer activities (Chowdhuri & Das, 2021; Das et al, 2021a; Kundu et al, 2019; Kundu et al, 2020; Pommier, 2006). Moreover, imidazole groups represent broad non-CPT based Top1 inhibitors like indotecan, indimitecan, and other indenoisoquinolines (Beck et al, 2014; Pommier & Cushman, 2009; Song et al, 2010) derivatives which are in clinical trials as anticancer agents (Kundu et al, 2019; Kundu et al, 2020; Pommier, 2006). Therefore, we rationalized that a pyrido[2',1':2,3]imidazo[4,5-*c*]quinoline (PIQ) derivative harboring the pyridine, imidazole, and quinoline scaffolds could potentially target the unique heterodimeric bi-subunit Top1 enzyme of the *Leishmania donovani*.

In the present study, we report the characterization and validation of a novel class of chimeric compounds based on the pyrido[2',1':2,3]imidazo[4,5-*c*]quinoline (PIQ) core identified through the structural features of known ligands (Figure 6.3.1B) and tested their potential role in the inhibition of *Leishmania* Top1 activity. The structure-activity relationships (SAR) of the twenty compounds resulting from the parental structure of the PIQ core suggested that compound C17 is the most potent LdTop1 inhibitor both in the *in vitro* and *ex vivo* DNA relaxations assays (Table 6.2). C17 inhibits the growth of both the antimony-resistant field

isolate of *Leishmania* (BHU575) which is also known to be less susceptible towards the clinically used anti-leishmanials like sodium stibo-gluconate (SSG), miltefosine, paromomycin and amphotericin B (Ghosh et al, 2021) as well as the wild-type drug-responsive strain (Ag83) by targeting LdTop1. C17 did not inhibit the activity of human monomeric Top1 which further exalts its promise as a selective anti-leishmanial drug candidate. C17 poisons LdTop1-DNA covalent complex's (LdTop1cc) formation in the parasites leading to the accumulation of apoptotic DNA breaks that was evidenced by *in vitro* biochemical assays coupled with microscopic examination and *in vivo* studies. Furthermore, administration of C17 by intraperitoneal route results in marked reduction of the *Leishmania* amastigotes burden from the wildtype and antimony-resistant BHU575 parasite-infected spleen and liver of BALB/c mice implicating a new drug candidate against drug-resistant leishmaniasis.

6.2 Materials and Methods

6.2.1 Chemicals

3-(4,5-Dimethyl-2-thiazolyl)-2,5-diphenyl-2H-tetrazolium-bromide (MTT), dimethyl sulfoxide (DMSO), isopropyl- β -D-thiogalactoside (IPTG), camptothecin (CPT), amphotericin B, penicillin and streptomycin were purchased from Sigma Aldrich (St. Louis, MO, USA). CPT and C17 were dissolved in 100% DMSO (Sigma) at a concentration of 10 mM and stored at -20°C.

6.2.2 Parasite maintenance and culture

The *Leishmania donovani* cells were cultured in M199 containing 10% (v/v) heat-inactivated fetal bovine serum (FBS) supplemented with 100 IU/ml of penicillin and 100 mg/ml of streptomycin at 22 °C. Promastigotes were obtained from amastigotes of the spleens of infected hamsters and were cultured in 10% (v/v) heat-inactivated FBS for 3-5 days at 22°C. The antimony-resistant field isolates MHOM/IN/2009/BHU575/0 (BHU-575) strains of *Leishmania donovani* cells were cultured as discussed previously and utilized for the experiments (Chowdhury et al, 2012; Chowdhury et al, 2017).

6.2.3 Cell extracts

Cellular extracts from Ag83 or BHU575 cells were prepared as described previously (Chowdhury et al, 2012; Chowdhury et al, 2017). Briefly, cells were lysed in buffer (10mM Tris-HCl, pH 7.5, 0.1mM EGTA, 1mM EDTA, 1mM PMSF, 5mM DTT and 1mM Benzamidine hydrochloride), homogenized and was centrifuged at 10,000 rpm for 10 min at 4°C. The lysate was utilized as the source of the endogenous LdTop1 enzyme for plasmid DNA relaxation assays.

6.2.4 Purification of recombinant *Leishmania* bi-subunit Top1 (LdTop1)

The large (LdTOP1L, 73 kDa) and the small (LdTOP1S, 29 kDa) subunits of LdTop1 were cloned in pET16b separately (Brata Das et al, 2004; Chowdhury et al, 2012; Chowdhury et al, 2017). *Escherichia coli* BL21(DE3)/pLysS cells harbouring pET16b-LdTOP1L and pET16b-LdTOP1S were separately induced at an optical density of 0.6 at 600 nm with 0.5 mM IPTG (isopropyl- β -D-thiogalactoside) at 22 °C for 12 h. Cells were separately lysed by lysozyme and then sonicated. The proteins were purified through Ni-NTA column (Qiagen, Hilden, Germany) followed by a phosphocellulose column (P11 cellulose; Whatman, Maidstone, Kent, United Kingdom). Both the subunits were mixed at a molar ratio of 1:1 at a total protein concentration of 0.5 mg/ml in reconstitution buffer and dialyzed overnight at 4°C as described (Brata Das et al, 2004; Chowdhury et al, 2012; Chowdhury et al, 2017).

6.2.5 Recombinant Human Top1 purification

The recombinant human Top1 was purified from Sf-9 insect cells which were infected with the recombinant baculovirus (a kind gift from Prof. James J. Champoux) as described previously (Das et al, 2018; Kundu et al, 2019; Kundu et al, 2020; Majumdar et al, 2015).

6.2.6 Plasmid DNA relaxation assay

DNA topoisomerases were assayed by decreased mobility of the relaxed isomers of supercoiled pBluescript SK(+) [pBS SK(+)] DNA at 37°C for 30 min in 1% agarose gel (Das et al, 2018; Kundu et al, 2019; Kundu et al, 2020; Majumdar et al, 2015). LdTop1 was diluted in the relaxation buffer (25 mM Tris-HCl [pH 7.5], 5% glycerol, 0.5 mM DTT, 10 mM MgCl₂, 50 mM KCl, 25 mM EDTA, and 150 μ g/ml bovine serum albumin [BSA]) and supercoiled plasmid pBS SK(+) DNA (85 to 95% were negatively supercoiled, with the

remaining being nicked circles). For recombinant human Top1, the relaxation assay was carried out as described elsewhere (Das et al, 2018; Kundu et al, 2019; Kundu et al, 2020; Majumdar et al, 2015). *Ex vivo* relaxation assays were carried out with whole-cell extracts obtained from indicated cells as described (Das et al, 2018; Kundu et al, 2019). Briefly, the equivalent amount of whole-cell extracts from indicated cells was incubated with supercoiled pBS SK(+) DNA (200 ng) in the relaxation buffer (25 mM Tris-HCl [pH 7.5], 10 mM MgCl₂, 5% glycerol, 50 mM KCl, 0.5 mM DTT, 25 mM EDTA, and 150 mg/ml bovine serum albumin [BSA]) at 37⁰C for 30 min and products from relaxation assay were analyzed by agarose gel electrophoresis as discussed before.

6.2.7 Plasmid DNA cleavage assay

For cleavage assay, 50 fmol of pBS SK(+) supercoiled DNA and 100 fmol of reconstituted LScO or recombinant human Top1 were incubated in a standard reaction mixture (50 µl) containing 50 mM Tris-HCl (pH 7.5), 100 mM KCl, 10 mM MgCl₂, 0.5 mM DTT, 0.5 mM EDTA, and 30 µg/ml BSA (Chowdhury et al, 2012; Chowdhury et al, 2017) at 37⁰C for 30 min. The reactions were terminated by adding 1% SDS and 150 µg/ml proteinase K, and the mixtures were further incubated for 1 h at 37⁰C. DNA samples were electrophoresed in 1% agarose gel containing 0.5 µg/ml EtBr to resolve more slowly migrating nicked product (form II) from the supercoiled molecules (form I).

6.2.8 Oligonucleotide Cleavage Assay

Equilibrium cleavage assays with a 25-mer duplex of an oligonucleotide containing a Top1 binding motif were labeled and annealed as described previously (Kundu et al, 2019). Samples were analyzed by 12% sequencing gel electrophoresis, dried, exposed on PhosphorImager screens, and imaged with Typhoon FLA 7000 (GE Healthcare, UK).

6.2.9 Analysis of Compound 17–DNA Intercalation

The ability of the drug to intercalate into plasmid DNA was determined by the Top1 unwinding assay (Das et al, 2018; Kundu et al, 2019). Assays were performed with 50 fmol of pBluscript (SK+) DNA in the presence or absence of C17, m-AMSA, and etoposide. Relaxed DNA was prepared by treatment of the supercoiled plasmid DNA with an excess of LdTop1, followed by proteinase K digestion at 37 °C, phenol/chloroform extraction, and ethanol precipitation. After incubation at 37 °C for 15 min, reactions were terminated and

electrophoresed onto 1% agarose gel as described above (Das et al, 2018; Kundu et al, 2019). The DNA band was stained with 0.5 µg/mL of EtBr and visualized by UV light as described above. Second, an ethidium displacement fluorescence assay (Das et al, 2018; Kundu et al, 2019) was employed to determine whether compound 17 binds in the minor groove of DNA. Fluorescence emission spectra ($\lambda_{\text{max}} = 590$ nm, excitation wavelength 510 nm) were obtained at 25 °C. The assays contained 1 µM EtBr, 0–300 mM compound 28, and 5 nM CT DNA in 2 mL of fluorescence buffer.

6.2.10 Cell cycle analysis

DNA synthesis or replication was measured by flow cytometry analysis (FACS). *L. donovani* promastigote (2.5×10^6 cells) were treated with camptothecin or C17 (5µM) for the indicated time, harvested, and washed several times with PBS (1X). Fixation and staining of cells were performed and were analyzed via flow cytometry as discussed previously (Chowdhury et al, 2012). Detection of cells in individual G1, S, and G2/M phases of the cell cycle was carried out using a Becton Dickson flow cytometer and further data were processed by BD FACS Scan Software (San Diego, CA).

6.2.11 DNA laddering experiment

Fragmentation of DNA into oligonucleosomal bands, as a function of apoptotic cell death, was studied by DNA laddering assay as described before (Shadab et al, 2017). Briefly, the treated and untreated cells were suspended in 500 µl of extraction buffer followed by incubation on ice for 30 min and centrifuged at 15000 x g for 5 min. Isolated DNA aliquots were electrophoresed on 1.5% agarose gel containing ethidium bromide (0.5µg/ml), using Tris- acetate-EDTA (pH 8.0) running buffer, and then observed and photographed under UV illumination in a BioRad gel documentation system (Bio-Rad Laboratories, Inc., Hercules, CA, USA).

6.2.12 SDS-KCl precipitation assay

For C17-induced protein-DNA complex determination, *L. donovani* promastigotes were labeled with 1X BrdU for 24 h and exposed to different concentrations of CPT, C17, and Top1 catalytic inhibitor (HR8) for 30 minutes. Cells were pelleted and permeabilized by incubation at 60°C for 10 min in the presence of 2.5% (wt/vol) SDS, 0.8 mg/ml salmon sperm DNA, and 10 mM EDTA. After the addition of 65 mM KCl, the reaction mixture was

incubated on ice for 60 min. The pellet was resuspended in 100 mM KCl (10 minutes at 65 degrees) followed by the repetition of the washing step. The resulting pellet was resuspended in anti-BrdU (Alexa-488 conjugated) antibody for 2 hours followed by 1X PBS wash and spectrophotometric reading at 488 nm.

6.2.13 Measurement of cell viability

The viability of the *Leishmania donovani* promastigotes was measured by MTT assay (Bhattacharjee et al, 2022; Chowdhury et al, 2012; Chowdhury et al, 2017). All EC₅₀ values were calculated by using the non-linear variable slope model for finding EC₅₀ in Prism (ver. 5.0; GraphPad Software, USA).

6.2.14 Terminal deoxyribonucleotide transferase (TdT)-mediated dUTP nick-end labelling (TUNEL) assay

TUNEL assay was performed according to the manufacturer's instructions (ApoDirect™ Kit, BD Biosciences, Cat. 556381). Briefly, CPT/C17 treated and untreated promastigotes were harvested by centrifugation and fixed by adding 5 ml of fresh, prechilled 1% paraformaldehyde/PBS. The cell suspension is centrifuged for 5 minutes at 300xg and the pellets resuspended in 0.5 ml of PBS were then permeabilized by adding 5 ml of 70% ice-cold ethanol and incubated at -20°C for at least 24 h before staining. The cells were then resuspended in 80 µl of equilibration buffer and incubated at room temperature for 5 min. The cells were washed with PBS and resuspended in 50 µl of TdT incubation buffer and incubated at 37°C in a water bath for 60 min followed by the addition of 20 mM EDTA to terminate the reaction, and mixed by gentle vortexing. The cells were pelleted down by centrifugation and resuspended in 1 ml of 0.1% Triton X-100/BSA/PBS. The cells were then resuspended gently in 0.5 ml of PI/RNase/ PBS to stain with PI following incubation at room temperature in the dark for 15±30 min and spread on poly-lysine coated glass slides. They were analyzed by confocal microscopy.

6.2.15 Double staining with annexin V and PI

The externalization of phosphatidyl-serine of indicated promastigotes with or without treatment of C17 or CPT was measured by attachment of FITC-annexin V and PI by an annexin V-FITC staining kit (Invitrogen Incorporation Ltd). Flow cytometry was also performed for treated and untreated parasites. The gating was fixed in such a way that the

mean intensity of FITC-annexin V and the mean intensity of PI were depicted by FL-1 and FL-2 channels, respectively. The data presented are the mean of three independent experiments (Chowdhury et al, 2012).

6.2.16 *In vitro* macrophage infection

Macrophages were isolated from Balb/c mice 36–48 h post-injection (intraperitoneal) with 2% (w/v) hydrolyzed starch by peritoneal lavage with ice-cold phosphate-buffered saline. *In vitro* infection with promastigotes was carried out as described previously (Chowdhury et al, 2012). C17 was added to infected macrophages and left for another 48-96 h period. Cells were then fixed in methanol and stained with Propidium Iodide (PI). Percentages of infected cells and the total number of intracellular parasites were determined by manual counting in at least 200 cells using a fluorescent microscope.

6.2.17 *In vivo* studies

For experimental visceral infections, female BALB/c mice (4 weeks old and 20–25 g each) were divided into the following groups: (i) uninfected control group (ii) infection control group infected with Ag83 and BHU575 separately and (ii) two treatment groups for each infection group viz. 5 and 10 mg C17/kg body weight, respectively. Each group consisted of 5 animals. The animals were injected via the intracardiac route with 2×10^7 hamster spleen-transformed *L. donovani* promastigotes (suspended in 200 ml of 0.02 M PBS per mouse) (Chowdhury et al, 2012). Three weeks post-infection, C17 was administered to infected animals via intraperitoneal routes separately twice a week for 3 weeks. Visceral infection was determined by Giemsa-stained impression smears of spleen and liver from 6-week infected mice and reported as Leishman Donovan Units (LDU), calculated as the number of parasites per 1000 nucleated cells \times organ weight in mg (Das et al, 2020; Das et al, 2021b) as well as by Limiting Dilution Assay (Das et al, 2020; Das et al, 2021b). For LDA calculation, a 1 mg/ml (w/v) organ suspension (spleen or liver) prepared in Schneider drosophila media was serially diluted and cultured at 22°C for 2 weeks. Parasite burden was expressed as a 10-fold logarithm scale of the highest dilution containing viable parasites, and the mean values of five mice per group were represented. All the animals were euthanized by carbon dioxide exposure.

6.2.18 RT-PCR for mRNA expression of cytokines

Total RNA was isolated from 1 mg organ (in presence of liquid nitrogen) of different control and treatment groups of Balb/c mice used for the study, using TriZOL method (15596018, Invitrogen) which includes deoxyribonuclease (AMPD1; Sigma-Aldrich) treatment for each sample. The RNA pellet obtained was dissolved in di-ethyl pyrocarbonate (DEPC) treated water and the concentration was measured using a UV-Visible spectrophotometer. An aliquot of 2 µg of RNA was reverse-transcribed using a reverse transcription kit (4368814, Applied Biosystems). For RT-PCR, 2 µl cDNA, 0.5 µl 25 nM primer pairs of the respective gene as well as internal control, 5 µl SYBR green master mix (A25742, Applied Biosystems), and nuclease free water were added in 10 µl reaction mixture and PCR was performed in ABI 7500 thermocycler (Applied Biosystems) software and fold change was calculated using the following formula:

$$\text{Fold change} = 2^{-\Delta\Delta\text{Ct}}; \Delta\Delta\text{Ct} = (\Delta\text{Ct}_{\text{experiment}} - \Delta\text{Ct}_{\text{control}}); (\Delta\text{Ct} = \Delta\text{Ct}_{\text{gene}} - \Delta\text{Ct}_{\text{Actin}})$$

All the experiments were performed in triplicates and mouse β -actin was used as a reference gene.. A negative control containing all reaction components except the reverse transcriptase enzyme was included and subjected to RT-PCR to confirm the absence of DNA contamination in RNA. The primers used for the experiment have been enlisted Table 6.1.

6.2.19 DNA isolation from blood and parasites

Blood samples were collected in heparinized tubes. DNA extraction was performed using QIAamp DNA Blood mini kits (Qiagen, Germany) from whole blood or organs according to the manufacturer's instructions. DNA was isolated from 400 µl of sample and eluted in 25 µl elution buffer. A stock solution of *L. donovani* DNA was also obtained by extraction (QIAamp DNA mini kit, Qiagen, Germany) from 2.5×10^6 promastigotes. After eluting in 25 µl elution buffer, assuming the extraction was nearly 100% efficient, the DNA concentration corresponded to 10^5 parasites/µl. All the DNAs were stored at -20°C until use.

6.2.20 qPCR assay for the estimation of parasite burden in mice

SYBR Green-based real-time PCR was applied for quantification of the *Leishmania* parasites in mice blood. For accurate sensitivity, *L. donovani*-specific kinetoplast DNA was chosen as the target region. The PCR was performed in a final volume of 20 µl containing 10 µl of

SYBR Green master mixture, 3 µl of MiliQ water, 5 µl of DNA template and 1 µl (50 pmol/µl) of forward and reverse primers, 5'-CTTTTCTGGTCCTCCGGGTAGG-3' and 5'-CCACCCGGCCCTATTTTACACCAA-3' respectively. To construct the standard curve ten-fold serially diluted *L. donovani* DNA stocks corresponding to 10⁵, 10⁴, 10³, 10², 10,1 parasite/µl were included in the assay. The thermal cycling conditions included an initial incubation at 50°C for 2 min, followed by a 10 min denaturation at 95°C and 40 cycles at 95°C for 15 s and 60°C for 1 min each. Each sample was tested in triplicate. Negative controls with no template were included in each plate to deal with contamination issues. For all the real-time PCR reactions we used specific primers for the constitutively expressed GAPDH gene as a quality control to verify the integrity of the DNA samples. Threshold cycle values (Ct) were calculated by determining the point at which the fluorescence exceeded the threshold limit plotted against known concentrations of parasite DNA, and the parasite load of Balb/c mice was then determined using the standard curve.

Table 6.1: List of the primers

S. No	Name of primer	Sequence
1	Mouse GAPDH (F)	GCATCTTCTTGTGCAGTGCC
2	Mouse GAPDH (R)	TACGGCCAAATCCGTTTACA
3	Mouse IL-10 (F)	GTACAGCCGGGAAGACAATAAC
4	Mouse IL-10 (R)	CTCCACTGCCTTGCTCTTATTT
5	Mouse TGF-β (F)	ACGGAATACAGGGCTTTTCGATT
6	Mouse TGF-β (R)	CGGGTTGTGTTGGTTGTAGAG
7	Mouse IL-4 (F)	AGATGGATGTGCCAAACGTCCTCA
8	Mouse IL-4 (R)	AATATGCGAAGCACCTTGAAGCC
9	Mouse IFN-γ (F)	GGCCATCAGCAACAACATAAGCGT
10	Mouse IFN- γ (R)	TGGGTTGTTGACCTCAAACCTTGGC
11	Mouse TNF- α (F)	GCCTCTTCTCATTCCTGCTTG
12	Mouse TNF- α (R)	CTGATGAGAGGGAGGCCATT
13	Mouse IL-12a (F)	ACGAGAGTTGCCTGGCTACTAG
14	Mouse IL-12a (R)	CCTCATAGATGCTACCAAGGCAC
15	Mouse IL-2 (F)	GCGGCATGTTCTGGATTTGACTC
16	Mouse IL-2 (R)	CCACCACAGTTGCTGACTCATC
17	kDNA (F)	CTTTTCTGGTCCTCCGGGTAGG
18	kDNA (R)	CCACCCGGCCCTATTTTACACCAA

6.2.21 Statistical calculations

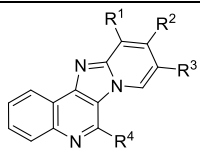
Results are reported as mean SEM and statistical significance was determined with the unpaired t-test with Welch's or Mann–Whitney correction test by GraphPad Software, LLC.

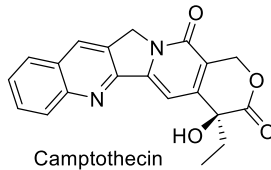
6.3 Results and Discussion

6.3.1 C17 inhibits the *Leishmania* Top1 relaxation activity

To test the inhibitory effect of the synthetic library of pyrido[2',1':2,3]imidazo[4,5-c]quinoline compounds on LdTop1 activity, we performed the *in vitro* and *ex vivo* plasmid DNA relaxation assays in standard assay conditions using either recombinant LdTop1 or the Ag83 lysates as the source of endogenous LdTop1. Table 6.2 shows inhibitory patterns of the LdTop1 mediated relaxation of supercoiled plasmid DNA with the different derivatives of the PIQ compounds (C1-C21) with relative efficiencies of LdTop1 inhibition as a measure of their effective drug concentrations (IC₅₀ value), indicating the highest activity for the selected PIQ derivative compound C17.

Table 6.2. Half maximal inhibitory concentrations (IC₅₀) of screened PIQ derivatives (C1-C21) on the *Leishmania donovani* Top1 mediated plasmid DNA relaxation inhibition.

Compound					Top1 inhibition IC ₅₀ (μM)		Activity index ^a
					<i>In vitro</i>	<i>Ex vivo</i>	
							
	R¹	R²	R³	R⁴			
C1	H	H	H	H	>10	NT ^b	+
C2	H	CH ₃	H	H	>10	NT ^b	+
C3	H	H	CH ₃	H	>10	NT ^b	+
C4	H	H	Br	H	>10	NT ^b	+
C5	H	H	Cl	H	>10	NT ^b	+
C6	H	H	H	C ₆ H ₅	>10	NT ^b	+
C7	CH ₃	H	H	C ₆ H ₅	6.75 ± 0.211	12.75 ± 0.117	++

C8	CH ₃	H	H	4-MeC ₆ H ₄	7.25 ± 0.018	15.06 ± 0.811	++
C9	CH ₃	H	H	4-ClC ₆ H ₄	5.5 ± 0.022	12.5 ± 0.314	++
C10	CH ₃	H	H	2-thienyl	7.25 ± 0.078	14.9 ± 0.036	++
C11	CH ₃	H	H	2-pyridyl	>10	NT ^b	+
C12	H	CH ₃	H	C ₆ H ₅	>10	NT ^b	+
C13	H	CH ₃	H	4-MeC ₆ H ₄	>10	NT ^b	+
C14	H	CH ₃	H	4-MeOC ₆ H ₄	>10	NT ^b	+
C15	H	H	H	4-MeC ₆ H ₄	>10	NT ^b	+
C16	H	H	H	4-ClC ₆ H ₄	8.52 ± 0.014	NT ^b	++
C17	H	H	H	3,4,5-(MeO) ₃ C ₆ H ₂	3.75 ± 0.122	6.5 ± 0.34	+++
C18	H	H	H	4-NO ₂ C ₆ H ₄	>10	NT ^b	+
C19	H	H	H	3-NO ₂ C ₆ H ₄	>10	NT ^b	+
C20	H	H	H	2-NO ₂ C ₆ H ₄	>10	NT ^b	+
C21	H	H	H	3,4-(MeO) ₂ C ₆ H ₃	5.25 ± 0.261	11.95 ± 0.611	++
 Camptothecin					9.2 ± 0.148	21.91 ± 0.125	++

^aCompound-induced *in vitro* inhibition of Top1 with scores given according to the following system based on the activity of camptothecin: + = IC₅₀ > 10 μM; ++ = IC₅₀ in between 5 μM and 10 μM; +++ = IC₅₀ in between 2 μM and 5 μM; ^bNT = not tested.

6.3.2 C17 poisons the *Leishmania* Top1-DNA cleavage complexes without intercalating with DNA.

To evaluate the inhibitory activity of C17 towards the bi-subunit LdTop1, we performed the plasmid DNA relaxation assays using both the recombinant LdTop1 enzyme (Figure 6.3.1D) and endogenous LdTop1 from the whole-cell extracts of *Leishmania donovani* Ag83 strain (Figure 6.3.1F). When LdTop1 and C17 were added simultaneously to the plasmid DNA in the relaxation assays, C17 inhibited the plasmid DNA relaxation activity of LdTop1 in a dose-dependent manner (Figure 6.3.1D, lanes 5–10), with 85-90% inhibition of Top1 achieved at 5 μM concentration of C17 (Figure 6.3.1D, lane 8, see the quantification in 1E). Accordingly, the *ex vivo* plasmid DNA relaxation assay using Ag83 cellular lysate as a source of endogenous LdTop1 (Figure 6.3.1F) was inhibited to ~85% at 10 μM concentration

of C17 (Figure 6.3.1F, lane 8 and see the quantification in 1G). Additionally, to investigate whether C17 interacts with the free enzyme, we pre-incubated C17 with recombinant or endogenous LdTop1 for 5 min. at 37 °C before the addition of substrate plasmid DNA. We observed no significant increment in the inhibition pattern of LdTop1 in the pre-incubation as compared to

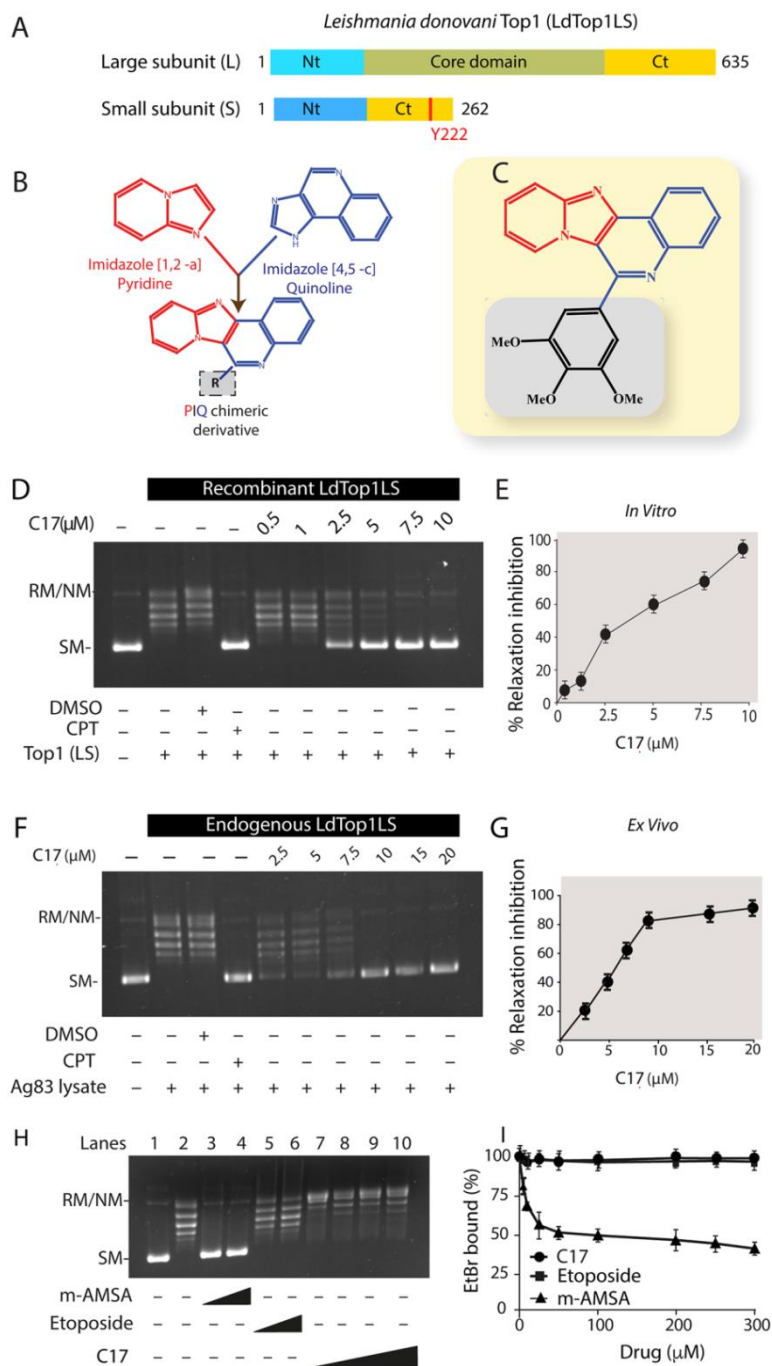


Figure 6.3.1: Inhibition of *Leishmania donovani* Top1-induced plasmid DNA relaxation activity by C17. (A) Schematic representation of the large and small subunits of the *Leishmania donovani* heterodimeric bi-subunit Top1 (LdTop1LS) enzyme. The catalytic residue (Y222) in the small subunit is indicated. (B) Design for the synthesis of the chimeric PIQ derivatives from the parental

imidazo[1,2-*a*]pyridine and imidazo[4,5-*c*]quinoline molecules with different substitutions in the “R” group. **(C)** Structure of the “R” group for the most active compound C17. **(D)** Relaxation assays of supercoiled plasmid DNA using recombinant LdTop1LS at 3:1 molar ratio. Lane 1, pBS (SK+) DNA (90 fmol); lane 2, same as lane 1 but incubated with 30 fmol of recombinant LdTop1LS; lane 3, same as lane 2, additionally Top1 was incubated with 2% DMSO as the solvent control; lane 4, same as lane 2 but incubated simultaneously with 50 μ M CPT; lanes 5–10, same as lane 2 but incubated with increasing concentrations of C17 as indicated, at 37 °C for 30 minutes. Positions of supercoiled monomer (SM) and nicked and relaxed monomer (RM) are indicated. **(E)** Quantitative representation of inhibition (%) of recombinant LdTop1 at variable concentrations of C17 in plasmid DNA relaxation assays. The experiments were performed in triplicate and expressed as the mean \pm SD. **(F)** Relaxation of supercoiled pBS (SK+) DNA by endogenous Top1 from the *Leishmania* Ag83 cellular extract (each reaction volume contains 0.1 μ g protein). Lane 1, pBS (SK+) DNA (0.3 μ g); lane 2, same as lane 1, but DNA was incubated with Ag83 cell lysates; lane 3, same as lane 2 but incubated with 2% DMSO; lanes 4–10, same as lane 2, but Ag83 whole cell lysates were incubated simultaneously with 50 μ M CPT or with increasing concentrations of C17 (as indicated) together with plasmid DNA at 37 °C for 30 minutes. **(G)** Quantitative representation of endogenous Top1 DNA relaxation inhibition (%) at variable concentrations of C17. The experiments were performed in triplicate and expressed as the mean \pm SD. **(H)** C17-DNA interaction as investigated by agarose gel electrophoresis in Top1 relaxation assays. Lane 1, 50 fmol of pBS (SK+) DNA. Lane 2, relaxed pBS (SK+) DNA generated by incubation with a molar excess of Top1. Lanes 3–4, same as lane 2 but incubated with 25 and 50 μ M m-amsacrine (AMSA); Lanes 5–6, same as lane 2 but incubated with 100 and 200 μ M etoposide; Lanes 7–10, same as lane 2 but incubated with 20, 50, 100, and 200 μ M of C17 as indicated. **(I)** Fluorescence-based ethidium bromide (EtBr) displacement assay. All samples contained 1 μ M EtBr and 5 nM calf thymus (CT) DNA in the presence or absence of the indicated drugs. Graphical representation of the percentage of bound EtBr with increasing concentration (0–300 μ M) of C17, m-AMSA, and etoposide. EtBr fluorescence was monitored with an excitation wavelength of 510 nm and an emission wavelength of 590 nm.

simultaneous incubation of C17 with LdTop1 in the plasmid DNA relaxation inhibition assays (Figure 6.3.2A-D), suggesting C17 might not interact with the free enzyme (Chowdhury et al, 2012; Chowdhury et al, 2017). Notably, C17 was ~2.5 fold more potent in inhibiting LdTop1-mediated DNA relaxation activities when compared with CPT (Figure 6.3.2E; Table 6.2). Further, C17 failed to inhibit the plasmid DNA relaxation activities (Figure 6.3.2F-G, lanes 4-8) and stabilize the cleavage complexes (Figure 6.3.2H-I) with recombinant human Top1 even at 10-fold molar excess of C17. Consequently, the relative extent of C17-mediated LdTop1 inhibition was increased by ~2.5 fold (IC_{50} value 3.75 μ M) in comparison with CPT (IC_{50} value 9.2 μ M) (see Table 6.2), implying C17 is a specific inhibitor for LdTop1 as it failed to inhibit human Top1 both in the plasmid DNA cleavage and relaxation assays (Figure 6.3.2).

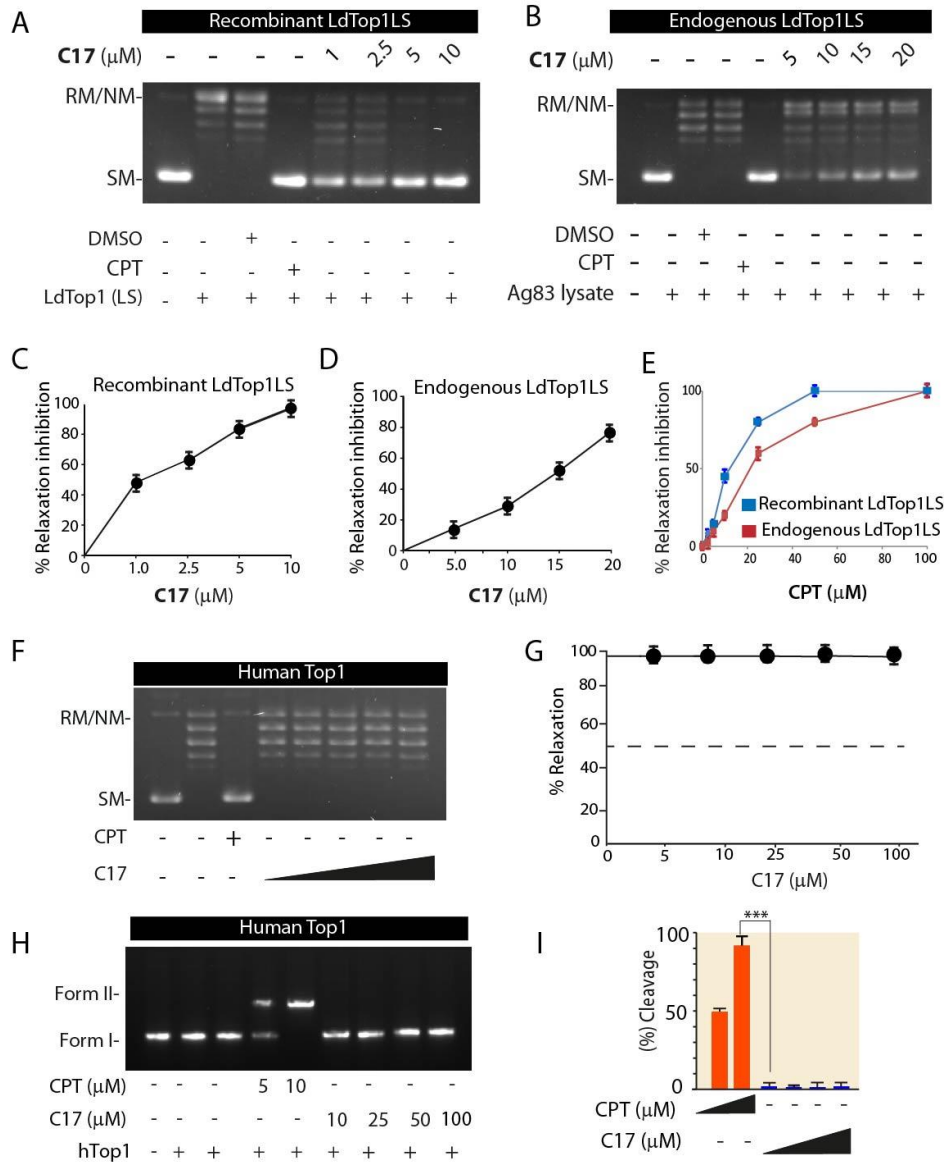


Figure 6.3.2: C17 binds to the LdTop1-DNA complex but not to the free LdTop1 enzyme (A) Relaxation assay of supercoiled plasmid DNA using recombinant *Leishmania* bi-subunit Top1 (LdTop1LS) at 3:1 molar ratio under pre-incubated conditions. Lane 1, pBS (SK+) DNA (90 fmol); lane 2, pBS (SK+) DNA (90 fmol) incubated with 30 fmol of recombinant LdTop1LS; lane 3, same as lane 2, additionally Top1 was incubated with 2% DMSO as the solvent control; lane 4, same as lane 2 but Top1 was pre-incubated for 5 minutes with 50 μM CPT before addition of the DNA substrate; lanes 5–8, same as lane 2 but Top1 was pre-incubated with increasing concentrations of C17 as indicated for 5 minutes before addition of DNA substrate. After addition of DNA to the preincubated Top1-drug reaction mix, the total reaction volume was additionally incubated at 37 °C for 30 min. Positions of supercoiled monomer (SM) and nicked and relaxed monomer (RM) are indicated. **(B)** Relaxation of supercoiled pBS (SK+) DNA by Top1 activity from the Ag83 cellular extract (each reaction volume contains 0.1 μg protein). Lane 1, pBS (SK+) DNA (0.3 μg); lane 2, same as lane 1, but pBS (SK+) DNA (0.3 μg) was incubated with Ag83 cell lysates; lane 3, same as lane 2 but incubated with 2% DMSO; lanes 4–8, same as lane 2, but Ag83 whole cell lysates were pre-incubated with 50 μM CPT or with increasing concentrations of C17 (as indicated) for five minutes followed by addition of the plasmid DNA substrate and an additional incubation at 37 °C for 30 min. Positions of supercoiled monomer (SM) and nicked and relaxed monomer (RM) are indicated. **(C)** Quantitative representation of recombinant LdTop1LS mediated DNA relaxation inhibition (%) at variable concentrations of C17 as indicated. The experiments were performed in triplicate and expressed as the mean ±SD. **(D)** Quantitative representation of endogenous LdTop1 DNA relaxation inhibition (%) at

variable concentrations of C17. The experiments were performed in triplicate and expressed as the mean \pm SD. **(E)** Quantitative representation of recombinant LdTop1LS (*in vitro*) and endogenous Top1 from *Leishmania donovani* Ag83 lysates (*ex vivo*) mediated plasmid DNA relaxation inhibition (%) at variable concentrations of CPT as indicated. The experiments were performed in triplicate and expressed as the mean \pm SD. **(F)** Relaxation assay of supercoiled plasmid DNA using recombinant human Top1 at 3:1 molar ratio. Lane 1, pBS (SK+) DNA (90 fmol); lane 2, pBS (SK+) DNA (90 fmol) incubated with 30 fmol of recombinant human Top1; lane 3, same as lane 2, additionally human Top1 was incubated simultaneously with 10 μ M CPT; lanes 4–8, same as lane 2 but incubated with increasing concentrations of C17 as indicated, at 37 °C for 30 min. Positions of supercoiled monomer (SM) and nicked and relaxed monomer (RM) are indicated. **(G)** Quantitative representation of recombinant human Top1 DNA relaxation inhibition (%) at variable concentrations of C17 as indicated. The experiments were performed in triplicate and expressed as the mean \pm SD. **(H)** Representative gel showing plasmid DNA cleavage mediated by recombinant human Top1 in the presence of CPT or C17. Lane 1, 50 fmol of pBS (SK+) DNA; lane 2, with 150 fmol recombinant hTop1; lane 3, same as lane 2, but with SDS–proteinase K treatment; lanes 4 and 5, same as lane 3, but in the presence of 5 and 10 μ M CPT, respectively, as control; lanes 6–9, same as lane 3, but in the presence of 10, 25, 50 and 100 μ M of C17, respectively. Positions of the supercoiled substrate (form I) and nicked monomers (form II) are indicated. **(I)** Quantitative measurement of hTop1cc (%) formation induced by CPT or C17 by recombinant hTop1.

Next, to test the DNA intercalating property of C17 as a mechanism of LdTop1 inhibition, we used both gel-based Top1 unwinding assays and fluorescence-based Ethidium Bromide (EtBr) displacement assays. Topoisomerase unwinding assay exploits the ability of the intercalating compounds to unwind the DNA duplex and thereby change the DNA twist inducing net negative supercoiling. It was found that in the presence of a strong DNA intercalator such as m-AMSA, net negative supercoiling of the relaxed substrate DNA was induced at 50 and 200 μ M concentration (Figure 6.3.1H, lanes 3 and 4), while non-intercalative compounds such as Etoposide failed to show any such effect at 50 and 200 μ M concentrations (Figure 6.3.1H, lanes 5 and 6). C17 also rendered no effect on the substrate DNA topology leading to its complete relaxation at the indicated concentrations (Figure 6.3.1H, lanes 7–10), ruling out the possibility of C17 acting as a DNA intercalator. To further substantiate this observation, we carried out the EtBr displacement assays. The DNA intercalator mAMSA (50 μ M) dislodges the already bound fluorophore (EtBr) from the plasmid DNA while (Figure 6.3.1I), C17 was unable to induce any EtBr displacement even at a high concentration (200 μ M) confirming that C17 is not a DNA intercalator.

To further investigate the ability of C17-mediated stabilization of LdTop1 cleavage complex, we performed *in vitro* DNA cleavage reactions under equilibrium conditions by reacting LdTop1 with plasmid DNA in the presence of C17 or CPT. Covalently closed circular DNA (Form I) are converted to nicked circular DNA (Form II) by Top1 which are trapped in the presence of Top1 poisons and are referred to as “cleavage complex; Top1cc”. C17 acts as a

poison to stabilize Top1cc in plasmid DNA cleavage assays both with recombinant LdTop1 (Figure 6.3.3A), and with endogenous Top1 from Ag83 lysate (Figure 6.3.3C) like CPT.

Next, we confirmed the C17-induced stabilization of Top1cc in single turnover equilibrium cleavage assays by using recombinant LdTop1 and 25-mer duplex oligonucleotides harboring Top1 cleavage sites (Figures 2E and F). The quantification of LdTop1-mediated cleavage assays (Figure 6.3.3B, 2D, and 2G) indicates that the extent of Top1-DNA cleavage complex formation (% cleavage) with C17 was increased by ~2-3 fold when compared with CPT at indicated concentrations, which is in keeping with C17-mediated increased inhibition of LdTop1 in the plasmid DNA relaxation assays (Table 6.2).

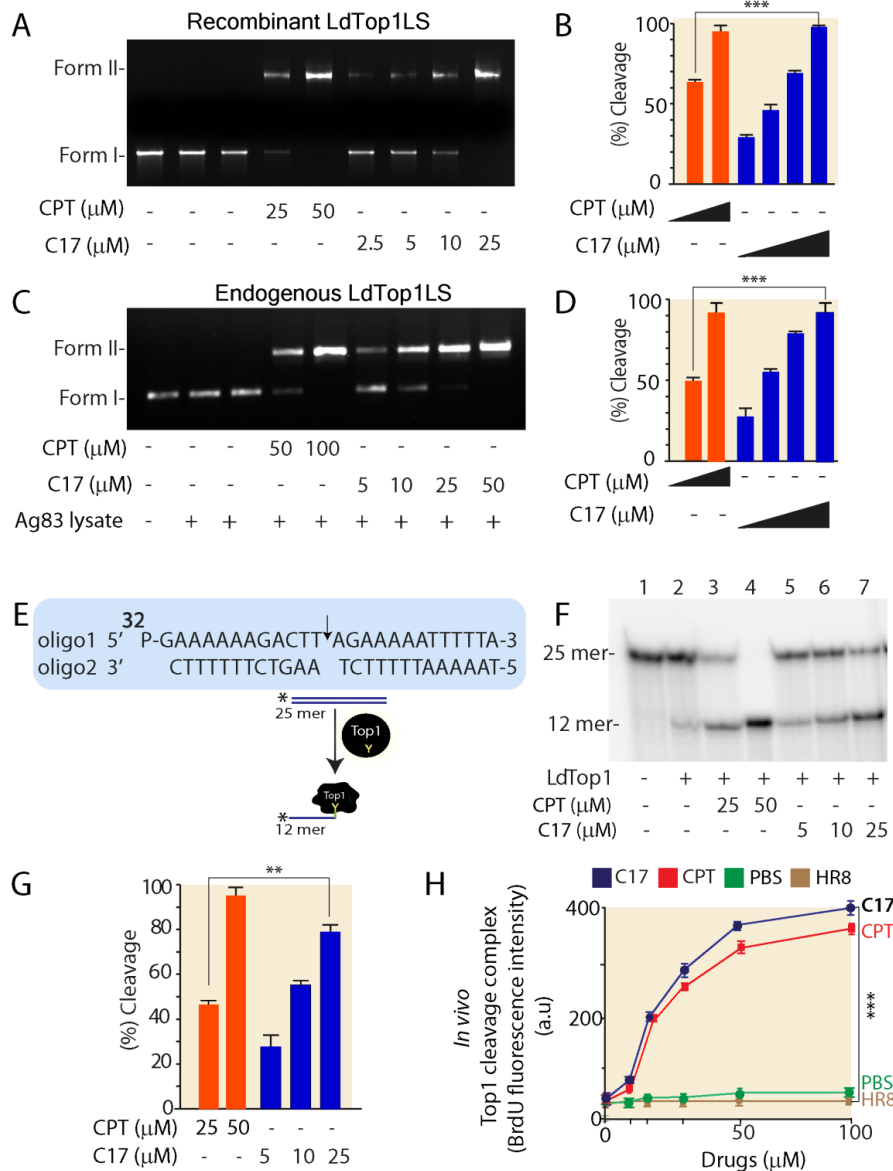


Figure 6.3.3: C17-mediated trapping of Top1-DNA cleavage complexes. (A) Representative gel showing plasmid DNA cleavage mediated by recombinant LdTop1LS in the presence of CPT or C17. Lane 1, 50 fmol of pBS (SK+) DNA; lane 2, with 150 fmol LdTop1LS; lane 3, same as lane 2, but

with SDS–proteinase K treatment; lanes 4 and 5, same as lane 3, but in the presence of 25 and 50 μM CPT, respectively, as control; lanes 6–9, same as lane 3, but in the presence of 2.5, 5, 10 and 25 μM of C17, respectively. Positions of the supercoiled substrate (form I) and nicked monomers (form II) are indicated. **(B)** Quantitative measurement of LdTop1cc (%) formation induced by CPT and C17 by recombinant LdTop1LS. **(C)** Representative gel showing plasmid DNA cleavage mediated by endogenous LdTop1 from Ag83 lysate in the presence of CPT or C17. Lane 1, 0.2 μg of pBS (SK+) DNA; lane 2, with 0.6 μg lysate; lane 3, same as lane 2, but with SDS–proteinase K treatment; lanes 4 and 5, same as lane 3, but in the presence of 50 and 100 μM CPT, respectively, as control; lanes 6–9, same as lane 3, but in the presence of 5, 10, 25 and 50 μM of C17, respectively. Positions of the supercoiled substrate (form I) and nicked monomers (form II) are indicated. **(D)** Quantitative measurement of LdTop1cc (%) induced by CPT and C17 using endogenous LdTop1 from Ag83 lysate. All the experiments were performed three times and expressed as the mean \pm SD. * $p < 0.05$, ** $p < 0.01$ (Student's t-test). *** Indicates a significant difference between CPT and C17 treatments ($p < 0.001$). **(E)** Schematic representation of the formation of LdTop1cc with 5'-32P-end-labeled oligonucleotide substrates in the presence of Top1 poison. **(F)** Representative gel showing Top1-mediated 25-mer duplex oligonucleotide cleavage in the presence of CPT and C17. Lane 1, 15 nM 5'-32P-end-labeled 25-mer duplex oligo as indicated above. Lane 2, same as lane 1 but incubated with recombinant LS (0.2 μM). Lanes 3–4, same as lane 2 but incubated with an indicated concentration of CPT. Lanes 5–7, same as lane 2 but incubated with an indicated concentration of C17. Positions of uncleaved oligonucleotide (25-mer) and the cleavage product (12-mer oligonucleotide complexed with residual Top1) are indicated. **(G)** Quantitative measurement of cleavage complex (Top1cc) formation (%) by CPT and C17 by oligo cleavage assay. All the experiments were performed three times and expressed as the mean \pm SD. * $p < 0.05$, ** $p < 0.01$ (Student's t-test). ** Indicates a significant difference between CPT and C17 treatments ($p < 0.01$). **(H)** Exponentially growing *L. donovani* promastigotes (5×10^6 cells/ml) were labelled with BrdU at 22 $^{\circ}\text{C}$ for 24 hours and then treated with different concentrations of CPT, C17, and a catalytic inhibitor of Top1 as indicated. SDS-K+ precipitable complexes were measured as described in Materials and Methods. All the experiments were performed three times and representative data from one set of experiments are expressed as mean \pm SD. Variations among different sets of experiments were $< 10\%$. * $p < 0.05$, ** $p < 0.01$ (Student's t-test). *** Indicates a significant difference between catalytic inhibitor control and C17 treatments ($p < 0.001$).

We further tested the ability of C17 to induce Top1-linked DNA complexes in the *L. donovani* promastigotes by using modified KCl-SDS precipitation assays (Chowdhury et al, 2012). BrdU-labeled promastigotes were treated with various concentrations of C17 as well as CPT and a catalytic inhibitor of Top1 (compound 8 or HR8) as controls (Das et al, 2018). Treatment of promastigotes with different concentrations of C17 markedly increased the SDS-KCl precipitable complex compared with the untreated control cells as detected by anti-BrdU staining (Figure 6.3.3H), which was similar to that obtained by treatment with different concentrations of CPT for 24 hours. These results show that the formation of SDS-KCl precipitable complexes is due to the formation of protein-linked DNA complexes following treatment with C17. Together, we conclude that C17 selectively stabilizes the LdTop1 cleavable complex and acts as poison inside the *Leishmania* parasites. Cumulatively, our data suggest that C17 selectively poisons LdTop1 cleavage complexes abrogating the religation activity.

6.3.3 C17 treatment inhibits cell cycle progression, accumulates DNA breaks, and triggers apoptosis-like death in Ag83 promastigotes.

Trapped LdTop1cc generates toxic DNA lesions which result in DNA double-strand breaks (DSBs) upon collision with ongoing replication forks and/or transcription machinery leading to cell cycle arrest and killing of the parasites (Das et al, 2008). To test such a possibility, we examined the cell cycle profile of the parasites after treatment with C17 using the flow-cytometric analysis (Figure 6.3.4A). In the absence of C17 treatment *Leishmania* promastigotes exhibited regular cell cycle distribution in G1, S, and G2/M phases (G1: 65.1%, S: 18.1%, and G2/M: 15.1%), while, after treatment with 5 μ M C17 led to a time-dependent arrest at the S/G2-M phase and concomitantly inhibited entry into the next cell cycle phase as evident from a declining G1 phase promastigote population at 6 h (55.3%), 12 h (40.7%) and 24 h (31.5%) post C17 treatment compared to untreated control parasites. Also, continuous exposure to C17 led to S/G2-M phase arrest with 41.3% at 6 h, 57.6% at 12 h, and 65.7% after 24 h after treatment, suggesting C17-induced disruption of the parasite replication cycle.

Next, we performed TUNEL staining that detects C17-induced DNAs breaks inside the parasites by labelling their DNA-free ends with dUTP. This assay utilizes a reaction catalyzed by exogenous terminal deoxynucleotidyl transferase for labelling DNA breaks with fluorophore tagged-dUTP in a template-independent addition to the 3'-hydroxyl (OH) termini of double- and single-stranded DNA (Chowdhury et al, 2012; Shadab et al, 2017). C17 significantly increased TUNEL positive (+ve) cells in a time-dependent manner compared to the untreated control parasites (Figure 6.3.4B; see the quantification). The representative confocal microscopic images show TUNEL +ve cells induced by 5 μ M of C17 treatment for 24 h compared to the untreated control (Figure 6.3.4B) and also suggested that C17 might trap LdTop1cc's both in the nucleus as well as the kinetoplast as reflected in the accumulation of DNA breaks in both compartments. (Chowdhury et al, 2012; Shadab et al, 2017) We confirmed that DNA breaks in the *Leishmania* promastigotes was detected as early as 15 min post treatment with C17 using TUNEL assays (blue). Under similar condition we failed to detect, significant increase in apoptotic *Leishmania* promastigotes (Annexin V-FITC +staining cells) Figure 6.3.7E, suggesting C17-inuced LdTop1cc generates DNA breaks in the parasites (Figure 6.3.3). In the later time point of C17 treatment, we detected significant increase in the apoptotic cells 1.5 h post treatment (Figure 6.3.4B-D and S3E). Further, we

also confirmed the extent of DNA fragmentation in the *Leishmania* Ag83 promastigotes after treatment with C17 using DNA laddering assays (Chowdhury et al, 2012; Shadab et al, 2017). Consistent with TUNEL staining (Figure 6.3.4B), C17-induced apoptotic DNA breaks in the promastigotes were also confirmed by a marked increase in genomic DNA fragmentation when promastigotes were treated with C17 post 6h treatment (Figure 6.3.4C). Further, we confirmed that C17-induced DNA fragmentation triggers apoptotic-like cell death in *Leishmania* promastigotes using fluorescein isothiocyanate (FITC)-annexin V and propidium iodide (PI) staining (Chowdhury et al, 2012; Shadab et al, 2017). Externalization of phosphatidyl serine (stained by annexin V) and the presence of impermeant cell membrane (negative PI staining) are hallmarks of apoptosis or programmed cell death (PCD) (Sen et al, 2006; Sen et al, 2004a; Sen et al, 2004b). Figure 6.3.4D confirmed that C17 treatment leads to an increment of the late apoptotic population in a time-dependent manner compared to the untreated control. Next, we tested whether C17 treatment promotes cell cycle arrest and cell death in human cells. CPT treatment impairs the cell cycle progression of human MCF7 cells with a decrease in G1-sub population leading to apoptosis-like cell death (Figure 6.3.5A and S2B; CPT). Unlike CPT, C17 neither affects the progression of the human MCF7 cell cycle (Figure 6.3.5A; C17) nor causes any apoptotic-like cell death in human MCF7 cells (Figure 6.3.5B).

Accordingly, in the cell viability assays, IC_{50} of C17 treated cancerous MCF7 cell lines (Figure 6.3.5C) and the non-cancerous HEK293 cell lines (Figure 6.3.5D) were significantly high (~90 fold) as compared to CPT. These data are in agreement that C17 is not an inhibitor of human Top1 (Figure 6.3.2F-I), implying the specificity of C17- induced DNA breaks, inhibition of cell cycle progression, and apoptosis-like cell death in the parasites is due to trapping of LdTop1cc in the promastigotes.

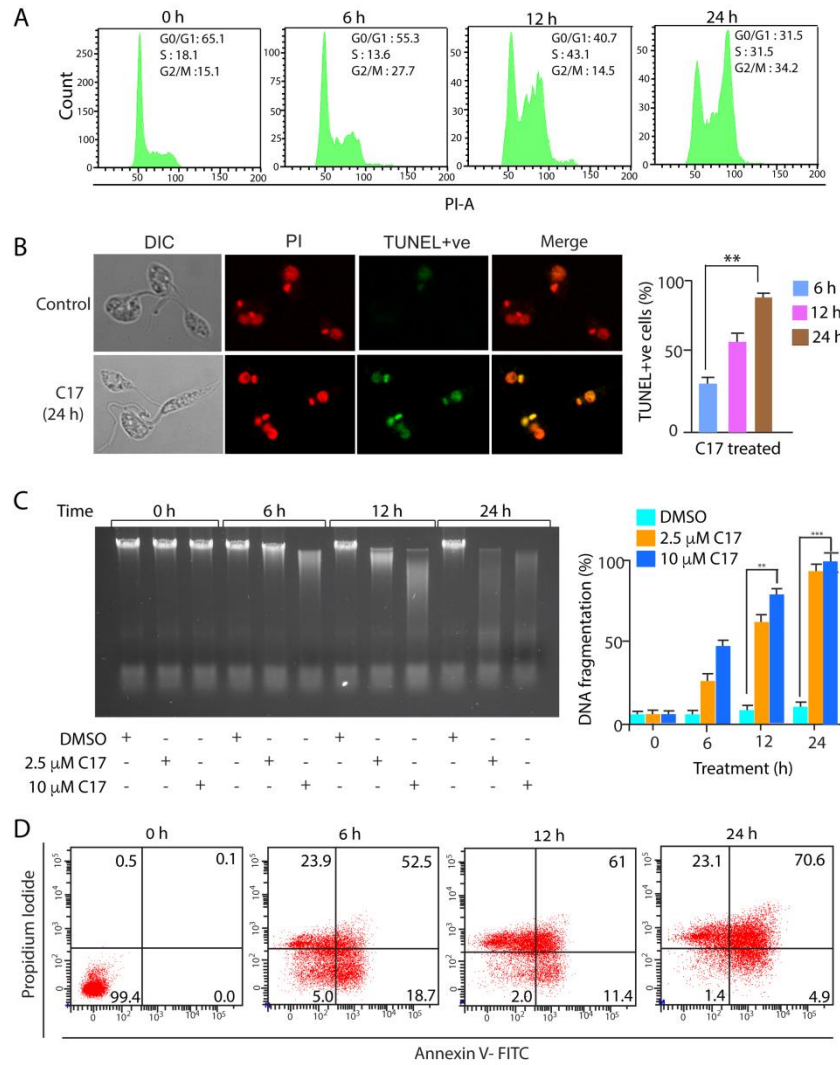


Figure 6.3.4: C17 abrogates the cell cycle progression of Ag83 promastigotes and induces DNA breaks leading to apoptosis-like cell death. (A) Histograms of the distribution of DNA content by flow cytometric analyses of the C17-mediated cell cycle arrest in *L. donovani* Ag83 promastigotes. The cell cycle arrest was monitored post-treatment with 0.2% DMSO as control, and with C17 (5 μ M) for 6, 12, and 24 hours. The parasites were then fixed and stained with propidium iodide (PI) and RNase A and a total of 10,000 nuclei were counted from each sample. The percentages of cells within different cell-cycle stages as shown were determined as described in Materials and Methods. The representative histograms show that treatment with 0.2% DMSO (panel I), or with 5 μ M C17 for 6 h (panel II), 12 h (panel III), and 24 h (panel IV) respectively. The experiments were repeated thrice and histograms from one data set have been shown. (B) Ag83 promastigotes were either left untreated or treated with 5 μ M C17 for 6, 12, and 24 hours following which the TUNEL assay was performed. The DNA breaks were analyzed by confocal microscopy and the representative images show the breaks accumulated 12 hours post-DMSO/C17 treatment. The percentage of TUNEL +ve cells over the indicated periods have been quantified and represented as bar diagrams which are representative of three independent experiments as mean \pm SD. Variations among different sets of experiments were <10%. * p <0.05, ** p <0.01 (Student's t-test). ** Indicates a significant increase in TUNEL +ve Ag83 promastigotes between 6 and 24 hours of C17 treatment. (C) Ag83 promastigotes were left untreated or treated with two different concentrations of C17 (2.5 μ M and 10 μ M) for the indicated time points (6, 12, and 24 hours) and genomic DNA was isolated from each. Apoptotic DNA was resolved on a 2% agarose gel. Representative images of three independent experiments have been shown with * P <0.01, and ** P <0.001. Quantification of the time and dose-dependent percentage of DNA fragmentation has been provided in the form of bar graphs. (D) Flow cytometric analysis of Ag83

promastigote death through the externalization of phosphatidyl serine was evaluated. The parasites were stained with FITC-annexin V and propidium iodide after treatment with 0.2% DMSO (panel I), 5 μ M C17 for 6 hours (panel II), 12 hours (panel III), and 24 hours (panel IV), respectively. The experiments were repeated thrice and representative plots from one data set have been shown.

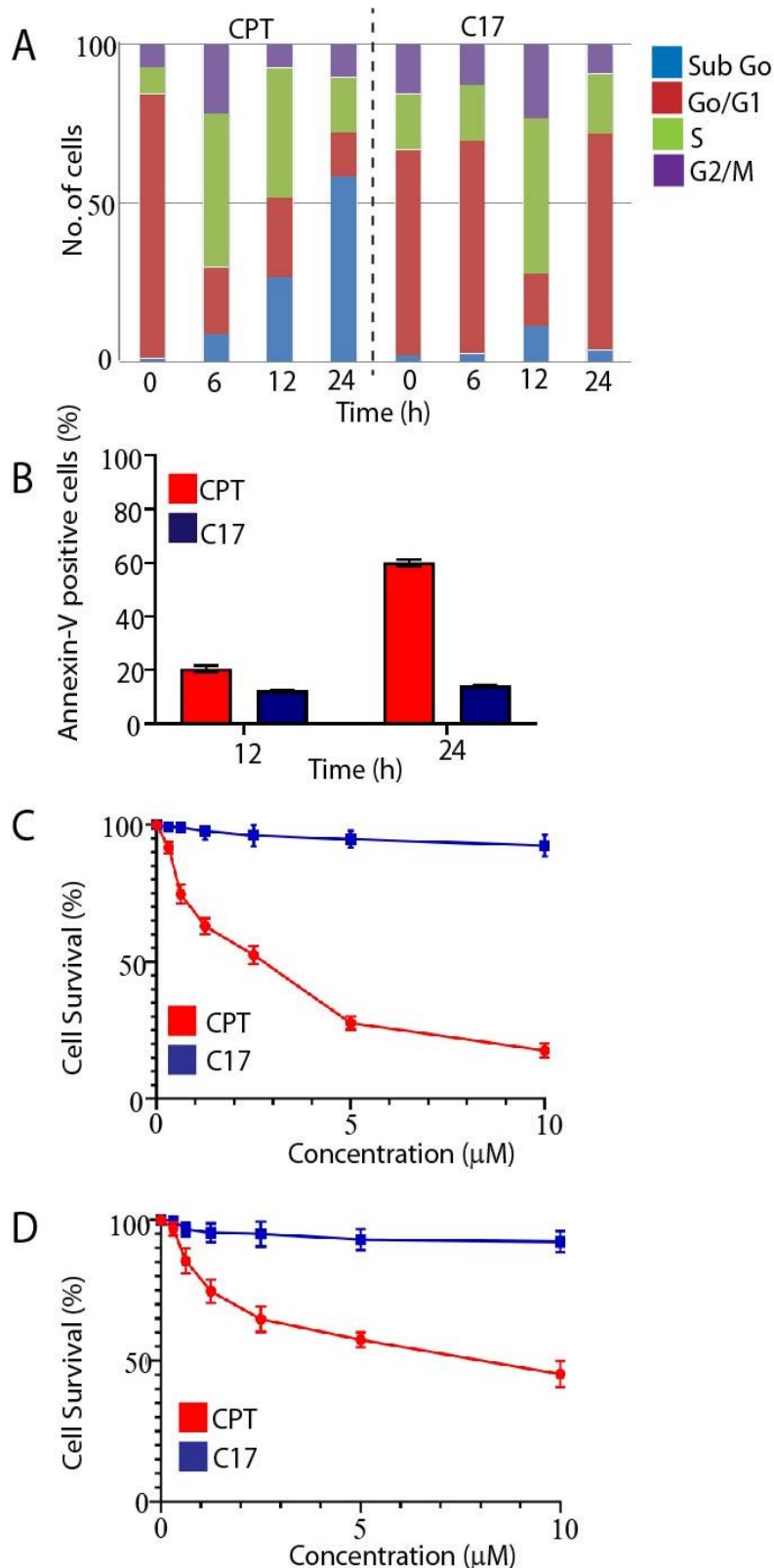


Figure 6.3.5: C17 is not cytotoxic for human cell lines unlike CPT (A) Bar graphs showing distribution of sub cellular populations in different phases of cell cycle by flow-cytometric analyses of the CPT or C17-mediated cell cycle arrest in MCF7 cell lines. The cell cycle arrest was monitored post treatment with 0.2% DMSO as control, and with CPT or C17 (5 μ M each) for 6, 12 and 24 hours. The parasites were then fixed and stained with propidium iodide (PI) and total, 10,000 nuclei were counted from each sample. The percentages of cells within different cell-cycle stages as shown were determined as described in materials and methods. The experiments have been repeated three times and data from one experimental set has been shown. **(B)** Flow cytometric analysis of apoptotic death in MCF7 cell lines through the externalization of phosphatidyl serine post treatment with CPT or C17 (5 μ M each) for 12 and 24 hours. The cells were fixed followed by staining with FITC-annexinV and propidium iodide. The percentage of FITC-annexin V positive cells were estimated and represented in bar graphs. The experiments have been repeated three times and data from one experimental set has been shown. The graphical representation of percentage survival (%) of **(C)** MCF7 human adenocarcinoma cells and **(D)** HEK293 human embryonic kidney cells plotted

as a function of indicated concentrations of CPT or C17. The percentage inhibition of viability for each concentration of CPT and C17 were calculated with respect to the control, and EC₅₀ (μM) values were estimated. Each point corresponds to the mean ± SD of at least three experiments in duplicates. Error bars represent SD (n = 3).

6.3.4 C17 accumulates persistent and less reversible DNA breaks inside the *Leishmania* parasites compared to CPT

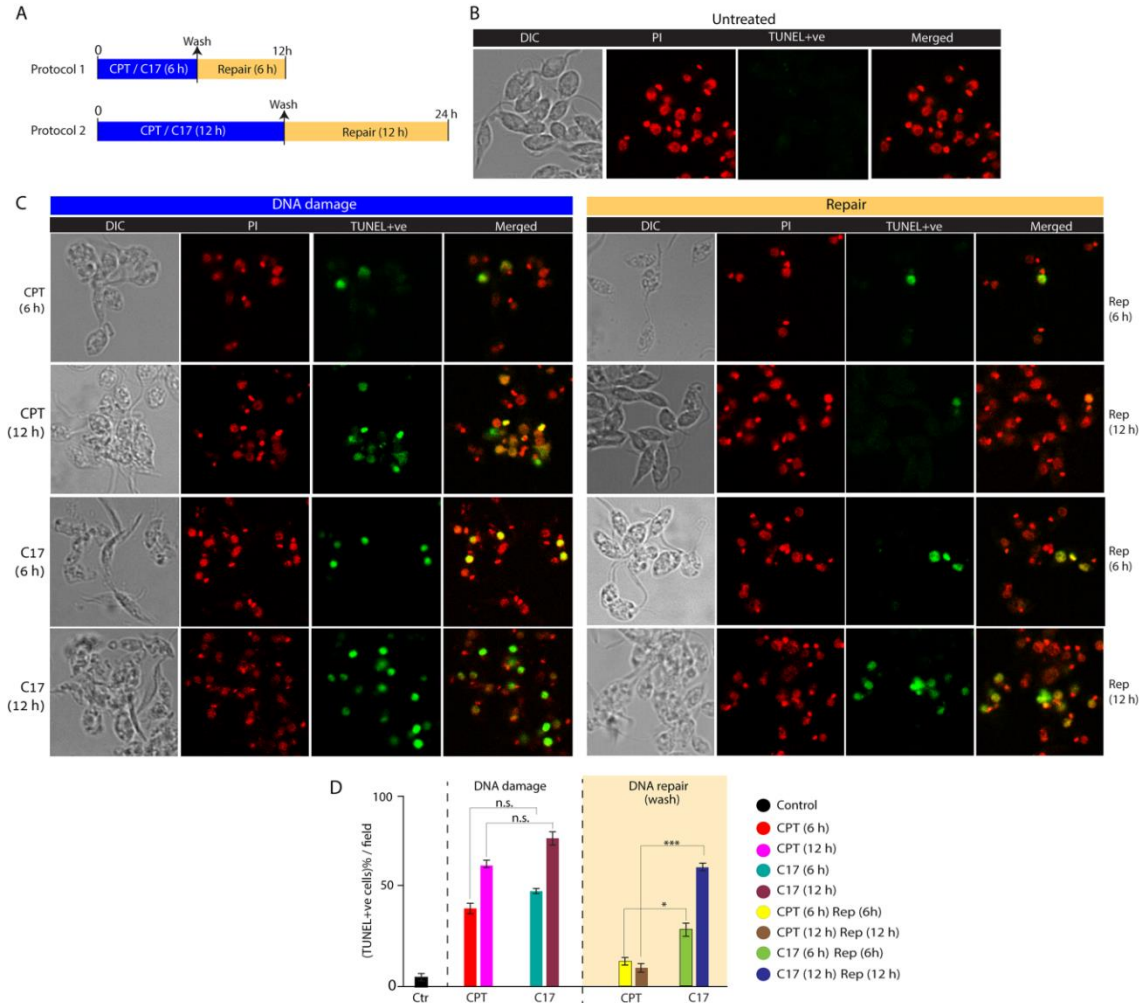


Figure 6.3.6: C17 generates persistent LdTop1cc-induced DNA breaks as detected by the TUNEL assays. (A) Overview of the protocol of C17/CPT treatment and reversal in *L. donovani* promastigotes to study the comparative repair kinetics between CPT and C17. (B) Representative confocal microscopic images of the 0.2% DMSO treated control Ag83 promastigotes showing the Propidium iodide (red) stained nuclear and kinetoplast DNA with negligible TUNEL positive (green) cells. (C) Time-dependent escalation of TUNEL +ve parasites treated with C17 or CPT for 6 and 12 h (DNA damage) and the persistence of such TUNEL +ve cells after the removal of the respective drugs for indicated time points (Repair). (D) Quantification of the percentage of TUNEL positive cells after C17/CPT treatment and after the removal of indicated inhibitors (C17 or CPT) as obtained from immunofluorescence confocal microscopy calculated for 80-100 parasites (mean ± SEM). Experiments were performed three times and representative images from one set of experiments are shown. Variations among different sets of experiments were <10%. *p<0.05, **p<0.01 (Student's t-test). *** Indicates a significant difference between CPT and C17 treatments following repair (p<0.001).

Because C17 poisons LdTop1cc in the Ag83 promastigotes (Figure 6.3.3H) and generates DNA strand breaks (Figures 3B and 3C), we investigated the accumulation and disappearance of Top1cc-induced DNA breaks in Ag83 promastigotes treated either with C17 or CPT by measuring the number of TUNEL +ve cells using the confocal microscopy (Figure 6.3.6A). Under similar conditions, we detected a time-dependent increase in TUNEL +ve parasites post-treatment with C17 that was comparable with CPT (see Figure 6.3.6C DNA damage), suggesting that both C17 and CPT generate similar levels of DNA breaks at the indicated periods in Ag83 promastigotes (Figure 6.3.6D). CPT-induced DNA breaks have a short half-life which are reversed immediately upon the removal of the drug from the medium (Kundu et al, 2019; Pommier, 2006). This is consistent with the reversal of TUNEL +ve cells within a small duration of washing out CPT (Figure 6.3.6C; Repair). On the contrary, C17 engenders more persistent and less reversible DNA breaks after subsequent wash and reculturing of the parasites in the C17-free medium (Figure 6.3.6C; Repair). Figure 6.3.6C and D shows a faster disappearance in the number of TUNEL +ve Ag83 parasites after washing out CPT from media at indicated periods (see the quantification in Figure 6.3.6D). In contrast, Ag83 promastigotes showed (~ 3–4 fold) more persistent TUNEL +ve cells (Figure 6.3.6D) even after washing out C17 at the indicated time. Together, our data suggest that C17 generates more persistent and less reversible LdTop1cc-induced DNA breaks which accounts for the increased C17-induced cytotoxicity in the parasites compared to CPT.

6.3.5 C17 poisons LdTop1cc and sensitizes the antimony-resistant *Leishmania donovani* clinical isolate

Next, to propound C17 as a new drug candidate against drug-resistant leishmaniasis, we tested its efficacy towards the LdTop1 from the antimony-resistant field isolate of *L. donovani*, BHU575 (less susceptible to SSG, amphotericin B, [21 and miltefosine), obtained

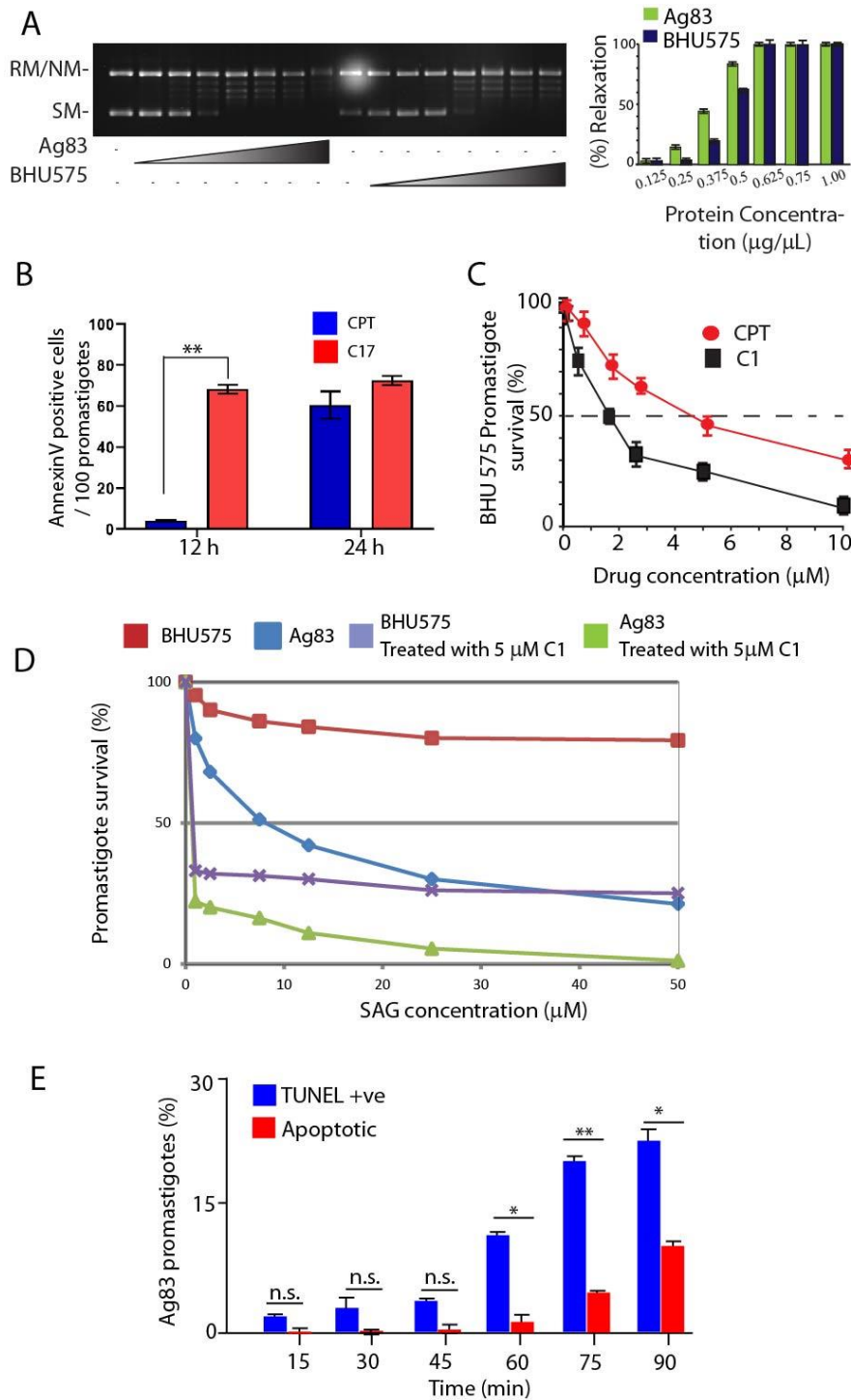


Figure 6.3.7: C17 sensitizes antimony resistant *Leishmania* strain BHU575 by targeting LdTop1
(A) Activity profiles of BHU575 and Ag83 Top1 enzymes were measured by the plasmid DNA relaxation assay using equal concentrations of whole cell lysates from the two strains as the endogenous source of Top1. Relaxation of supercoiled pBS (SK+) DNA by Top1 activity from the BHU575 or Ag83 cellular extract. Lanes 1 and 9, pBS (SK+) DNA (0.3 μg); lane 2-8, same as lane 1, but pBS (SK+) DNA (0.3 μg) was incubated with indicated concentrations of Ag83 cell lysates; lanes 9-16 pBS (SK+) DNA (0.3 μg) was incubated with indicated concentrations of BHU-575 cell lysates. Positions of supercoiled monomer (SM) and nicked and relaxed monomer (RM) are indicated. Bar graph showing quantifications of the percentage relaxation with respect to the protein concentrations has been provided. **(B)** Flow cytometric analysis of apoptotic death in BHU-575 promastigotes through the externalization of phosphatidyl serine post treatment with CPT or C17 (5 μM each) for 12

and 24 hours. The cells were fixed followed by staining with FITC-annexin V and propidium iodide. The percentage of FITC-annexin V positive cells were estimated and represented in bar graphs. The experiments have been repeated three times and data from one experimental set has been shown. (C) The graphical representation of percentage survival (%) of BHU-575 promastigotes plotted as a function of indicated concentrations of CPT or C17. The percentage inhibition of viability for each concentration of CPT and C17 were calculated with respect to the control, and EC_{50} (μM) values were estimated. Each point corresponds to the mean \pm SD of at least three experiments in duplicates. Error bars represent SD ($n = 3$). (D) The graphical representation of percentage survival (%) of Ag83 and BHU575 promastigotes plotted as a function of indicated concentrations of SAG and/or C17 as indicated. The percentage inhibition of viability for each concentration of SAG and C17 were calculated with respect to the control, and EC_{50} (μM) values were estimated. In mentioned cases the promastigotes were treated with C17 (5 μM) and increasing SAG concentrations. Each point corresponds to the mean \pm SD of at least three experiments in duplicates. Error bars represent SD ($n = 3$). (E) The graphical representation of percentage of either TUNEL positive (blue) or apoptotic (red) Ag83 promastigotes as detected by microscopic analysis post C17 treatment at the indicated time points. Experiments were performed three times and expressed as the mean \pm SD. Variations among different sets of experiments were $<10\%$. * $p < 0.05$, ** $p < 0.01$ (Student's t-test). ** Indicates a significant difference between detection of DNA breaks and induction of apoptosis following C17 treatment ($p < 0.01$). n.s. non-significant.

from severely VL affected belt of India (Ghosh et al, 2021; Mukherjee et al, 2013). First, we confirmed the similar levels of endogenous LdTop1 activity from the two strains of *L. donovani* AG83 (wild type) and BHU575 (antimony-resistant) in the plasmid DNA relaxation assays (Figure 6.3.7A). Figure 6.3.8A shows that indeed C17 inhibited the relaxation activity of LdTop1 from *Leishmania* BHU575 whole cell extracts in a dose-dependent manner (Figure 6.3.8A, lanes 4–8), with an IC_{50} of 8.75 μM (Figure 6.3.8B) which was comparable with wild type parasites (Table 6.2).

Next, to investigate the C17-mediated poisoning of endogenous LdTop1cc from the BHU575 *Leishmania* strain, we performed plasmid DNA cleavage assays with the whole-cell extracts from BHU575 parasites as the source of endogenous Top1. Figure 6.3.8C confirmed that C17 stabilizes LdTop1cc formation in BHU575 parasites like CPT. Notably, we detected a ~5-fold increased efficacy of C17-induced LdTop1cc formation compared to CPT in BHU575 promastigotes (see the quantification in Figure 6.3.8D). Accordingly, we detected C17-induced DNA breaks in the BHU575 parasites detected by the TUNEL assay. Like wild-type parasites (Figure 6.3.6C), C17 efficiently generates LdTop1cc-induced DNA breaks in BHU575 promastigotes (Figure 6.3.8F). We detected 60 % TUNEL +ve BHU575 cells after 12 hours of treatment with C17 (5 μM) which increased to 85-90% after treatment for 24 h (Figure 6.3.8F). C17 treatment also inhibits the replication cycle leading to a wide-scale G2/M arrest (Figure 6.3.8E) and promotes apoptosis-like cell death in BHU575 parasites as detected by using FITC-Annexin V- based flow cytometry analysis (Figure 6.3.7B).

TABLE: 6.3 (EC₅₀ for Promastigotes)

	Ag83	BHU575
CPT (μM)	3.794 ± 0.029	6.582 ± 0.092
C17 (μM)	2.311 ± 0.56	4.796 ± 0.269

We further substantiated that C17-induced DNA breaks in the BHU575 parasites accumulate cell death. The BHU575 promastigotes survival was monitored over a time of 24 hours in presence of C17 which shows that the antimony-resistant parasites are hypersensitive to the LdTop1 poisons (EC₅₀ value of C17 in Table 6.3 and Figure 6.3.7C). We also showed the ability of C17 to re-sensitize the antimony-resistant parasites upon co-treatment with SAG (Figure 6.3.7D). Taken together these findings suggest that C17 could be a potential new drug candidate against drug-resistant leishmaniasis.

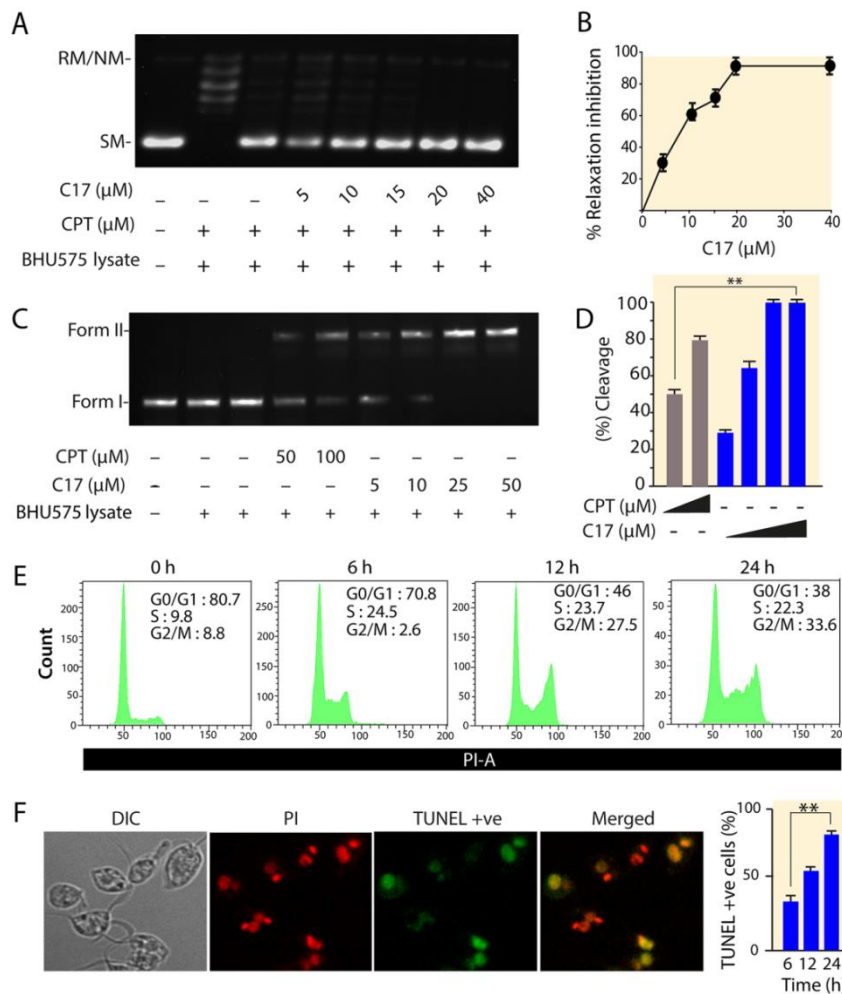


Figure 6.3.8: C17 poisons the LdTop1 from antimony-resistant BHU575 parasites and inhibits

the proliferation of the promastigotes. (A) Relaxation assay of supercoiled pBS (SK+) DNA by Top1 activity from the BHU575 cellular lysate (each reaction volume contains 0.1 μ g protein). Lane 1, pBS (SK+) DNA (0.3 μ g); lane 2, same as lane 1, but pBS (SK+) DNA (0.3 μ g) was incubated with BHU-575 cell lysates; lanes 3–8, same as lane 2, but BHU575 whole cell lysates were incubated simultaneously with 50 μ M CPT or with increasing concentrations of C17 (as indicated) together with plasmid DNA at 37 °C for 30 minutes. (B) Quantitative representation of BHU575 Top1 DNA relaxation inhibition (%) at variable concentrations of C17. All the experiments were performed in triplicate and expressed as the mean \pm SD. (C) Representative gel image showing plasmid DNA cleavage mediated by BHU575 cellular lysate as the source of Top1 enzyme in the presence of CPT or C17. Lane 1, 0.2 μ g of pBS (SK+) DNA; lane 2, with 0.6 μ g lysate; lane 3, same as lane 2, but with SDS–proteinase K treatment; lanes 4 and 5, same as lane 3, but in the presence of 50 and 100 μ M CPT, respectively, as control; lanes 6–9, same as lane 3, but in the presence of 5, 10, 25 and 50 μ M C17 respectively. Positions of the supercoiled substrate (form I) and nicked monomers (form II) are indicated. (D) Quantitative measurement of cleavage complex (Top1cc) formation (%) by CPT and compound C17 by BHU-575 Top1. All the experiments were performed three times and expressed as the mean \pm SD. * p <0.05, ** p <0.01 (Student's t-test). ** Indicates a significant difference between CPT and C17 treatments. (E) Histograms of the distribution of DNA content by flow cytometric analyses of the C17-mediated cell cycle arrest in *L. donovani* BHU-575 promastigotes. The cell cycle arrest was monitored post-treatment with 0.2% DMSO as control, and with C17 (5 μ M) for 6, 12 and 24 hours. The parasites were then fixed and stained with propidium iodide (PI) and RNase A and a total of 10,000 nuclei were counted from each sample. The percentages of cells within different cell-cycle stages are shown. The representative histograms show that treatment with 0.2% DMSO (panel I), C17 (5 μ M) for 6 h (panel II), 12 h (panel III), and 24 h (panel IV) respectively. The experiments were repeated thrice and the representative histograms from one data set are shown. (F) BHU575 promastigotes were either left untreated or treated with 5 μ M PIQ derivative for 6, 12, and 24 hours following which the TUNEL assay was performed. The DNA breaks were analyzed by confocal microscopy and the representative images show the breaks accumulated in the promastigotes 12 hours post C17 treatment. (G) The percentage of TUNEL positive cells over the indicated periods post 5 μ M C17 treatment have been quantified and represented as bar diagrams which are representative of three independent experiments. Variations among different sets of experiments were <10%. * p <0.05, ** p <0.01 (Student's t-test). ** Indicates a significant difference between 6 and 24 hours treatment time points (p <0.01).

6.3.6 C17 inhibits the growth of intracellular amastigotes in murine macrophages infected with the *Leishmania* antimony-resistant parasites

Subsequently, to investigate the potency of C17 as an anti-leishmanial drug, primary murine peritoneal macrophages were infected with early passage *L. donovani* wild-type (Ag83) and antimony-resistant (BHU575) strains *in vitro* and incubated with different concentrations of C17 for 48--96 h (Figure 6.3.9A). Counting of the macrophage internalized amastigotes after C17 treatment showed markedly down-regulated macrophage infection of both Ag83 and BHU575 strains (Figures 6.3.9B and 6.3.9D and Figure 6.3.10A-B) in a time dependent manner. The antimony-resistant BHU575 parasite burden was lowered by almost 90% after 96 h of treatment with C17 at 10 μ M (Figure 6.3.9C and 6.3.9E and Figure 6.3.10A-B).

TABLE: 6.4 (EC₅₀ for Amastigotes at 48 hours)

	Ag83	BHU575	Macrophages
CPT (μM)	7.84 ± 0.029	12.82 ± 0.042	18.32 ± 0.206
C17 (μM)	2.50 ± 0.56	7.06 ± 0.269	50.18 ± 0.009

The EC₅₀ values of infected intracellular amastigotes and the extracellular promastigote clearance were estimated using nonlinear curve fitting (Table 6.4). C17 shows markedly high EC₅₀ (~50 μM) towards the peritoneal macrophages with a relatively high selectivity index (SI) of 9.25, further strengthening C17 as a potential anti-leishmanial drug candidate (Table 6.4).

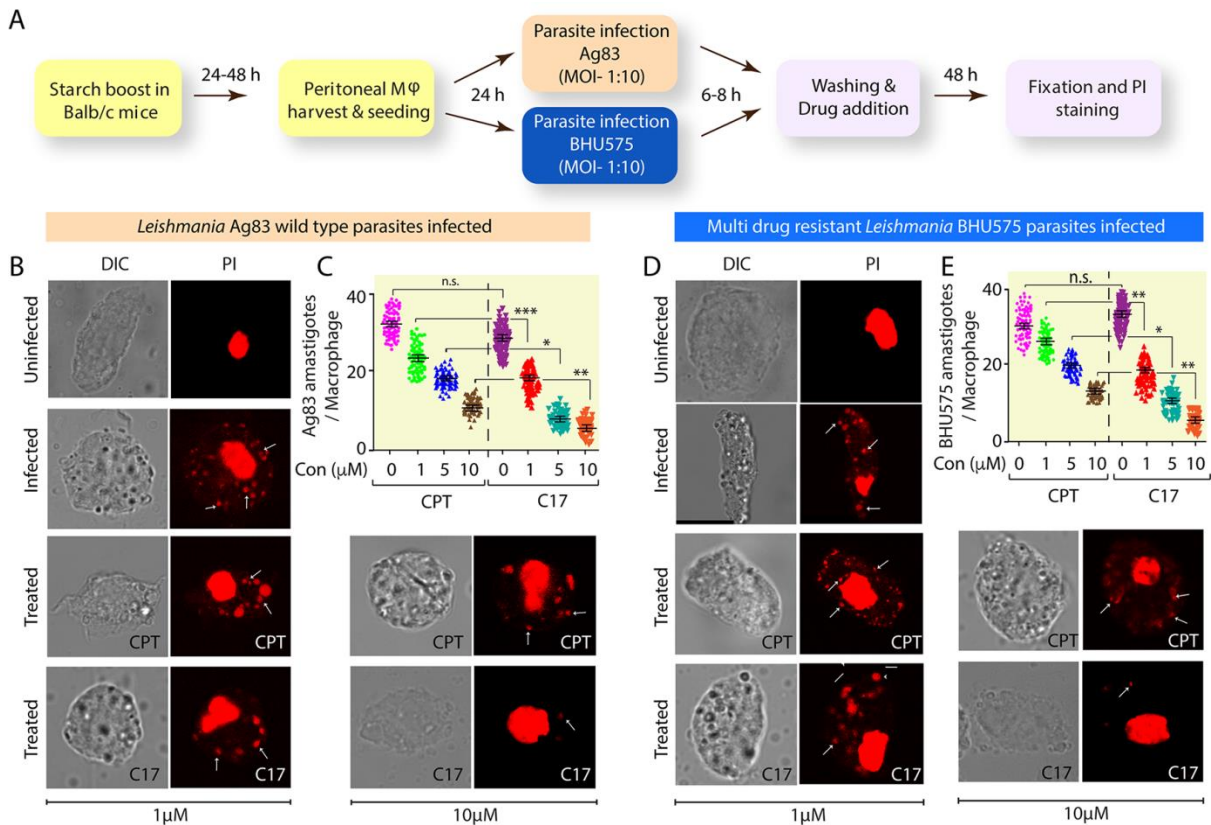


Figure 6.3.9: C17 efficiently reduces both *L. donovani* wildtype (Ag83) and antimony- resistant (BHU575) parasites from infected murine macrophages. (A) Schematic representation showing the procedure followed for the estimation of parasite clearance from Ag83 and BHU575 infected murine macrophages following treatment with CPT/C17. (B and D) Representative images showing propidium iodide stained Ag83 and BHU575 intracellular parasites as indicated in cultured murine macrophages treated with 1 and 10 μM of C17 compared to uninfected control, infection control and CPT treated control. Arrows indicate internalized parasites. All experiments have been repeated three times and images from one experimental set are shown. (C and E) Quantification of dose-dependent clearance of Ag83 and BHU575 amastigotes respectively by 1, 5, and 10 μM PIQ derivative from infected macrophages to CPT. The number of internalized amastigotes within each infected

macrophage was counted under the confocal fluorescence microscope. The quantifications are the means of three independent experiments and are plotted as mean \pm SD. * $p < 0.05$, ** $p < 0.01$, *** $p < 0.001$ (Student's t-test) indicate statistical significance between infection control or CPT treatment and the respective C17 treatment.

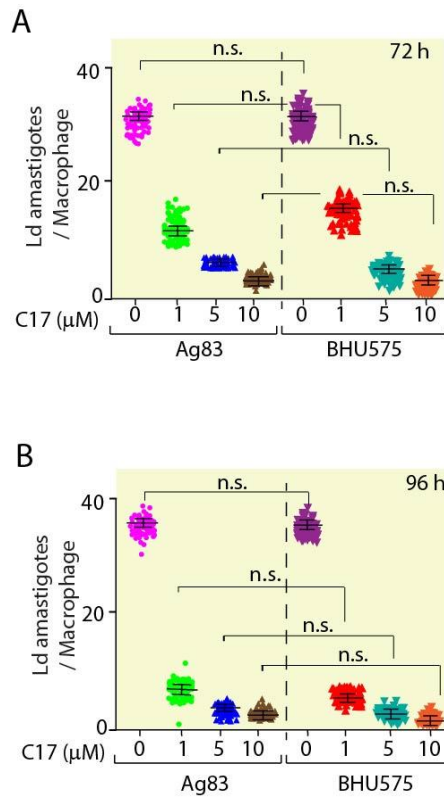


Figure 6.3.10: Panel A and B: Quantification of clearance of Ag83 and BHU575 amastigotes infected macrophages at 72-96 hours post drug treatments with 1, 5, and 10 μ M C17 derivative. The number of internalized amastigotes within each infected macrophage was counted under the confocal fluorescence microscope. The quantifications are the means of three independent experiments and are plotted as mean \pm SD. n.s. stands for non-significant.

6.3.7 C17 markedly reduces the antimony-resistant (BHU575) and Ag83 parasites in a mouse model of experimental Visceral Leishmaniasis (VL) and boosts host protective Th1 cytokine response

Finally, we evaluated the *in vivo* anti-leishmanial efficacy of C17 using BALB/c mice model of *L. donovani* infected with wildtype (Ag83) or antimony-resistant (BHU575) strains *via* the intracardiac route (Chowdhury et al, 2012). During the study, all mice remained alive and healthy and no remarkable change in body weight was observed. C17 was administered intraperitoneally following the treatment regimen outlined in Figure 6.3.12A, which led to a marked reduction in BHU575 and Ag83 parasite burden in both spleen and liver which was estimated using the stamp smear method (Figure 6.3.12B and 7C) and Limiting Dilution Assay (LDA) (Figure 6.3.11A-B). The reduction in the Ag83 and BHU575 parasite burdens

in the infected Balb/c mice was further confirmed by the qPCR based kinetoplastid DNA (kDNA)-dependent determination of parasite counts in peripheral blood, spleen, and liver of the untreated and C17 treated mice. (Das et al, 2020; Das et al, 2021b). (Figure 6.3.11E), suggesting C17 is a potential antileishmanial agent.

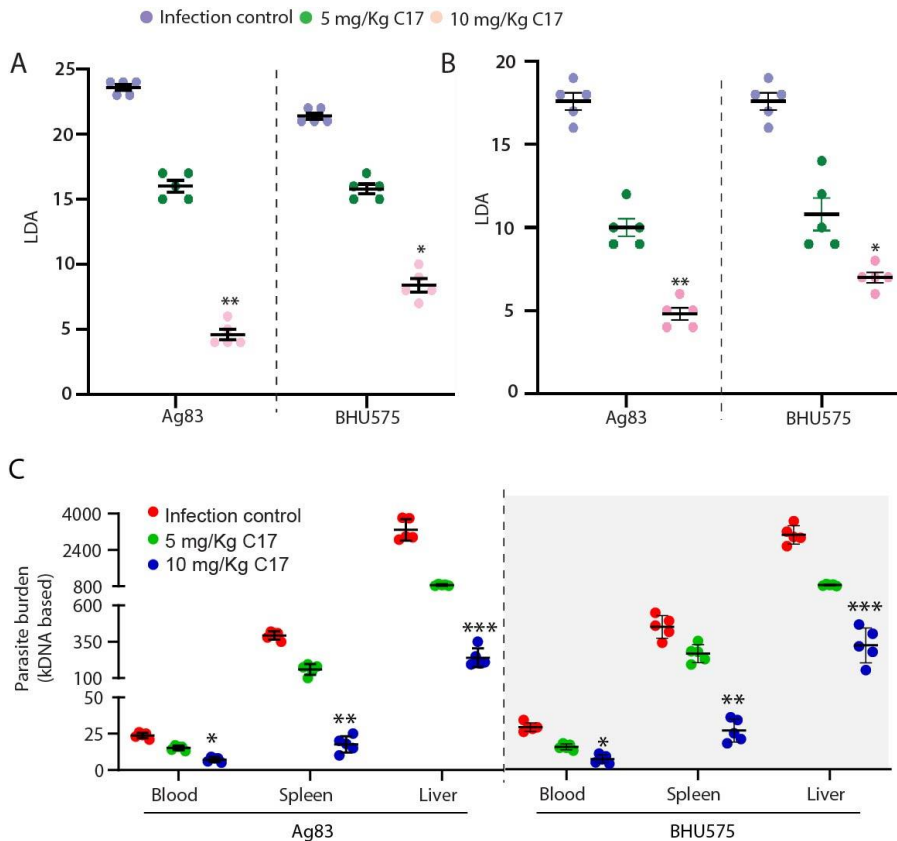


Figure 6.3.11: C17 clears both antimony resistant (BHU-575) and drug sensitive (Ag83) parasites from infected female BALB/c mice. Panel A and B: *In vivo* anti-leishmanial property of C17 was studied in BALB/c mice infected with Ag83 or BHU575 promastigotes *via* intracardiac route. C17 was given at a dosage of 5 and 10 mg/kg/day intraperitoneally for 3 weeks (2 times per week), starting on day 21 after infection. Animals were sacrificed 10 days post treatment to determine the hepatic (C) and splenic parasite (D) load for all treatment groups. Untreated and infected mice were used as controls. The parasite burden in the organs were determined by limiting dilution assay method and expressed as Limiting Dilution Assay (LDA; log₁₀ parasite numbers/ml for each Group)). Data represent mean SEM (n=5 mice per group). (C) Estimation of kDNA based parasite burden from blood, spleen and liver using qPCR as described in materials and methods. Ct values of kDNA from Ag83 or BHU575 infected, C17 treated or untreated Balb/c mice whole blood, spleen, and liver were obtained and plotted in the standard curve of kDNA to calculate the parasite burden of each organ, and results were plotted in this scatter graph. Each experimental set is representative of five samples, and error bars are mean±S.D. Statistical significance was analyzed using one-way analysis of variance followed by Dunnett's multiple- comparison test. *, p < 0.05, **, p < 0.01; ***, p < 0.001 indicates significant difference between C17 treated and untreated samples.

The progression of VL is widely associated with a deregulated cell-mediated immune response emulated by marked T-cell anergy (Chowdhury et al, 2012) specific to *Leishmania* antigens (Chowdhury et al, 2012). The establishment of VL infection is associated with host

immune response where T helper type 1 (Th1) and T helper type 2 (Th2) paradigms play an important role (Olivier et al, 2005). The Th1 response confers a protective role to the host while the Th2 promotes parasite survival and disease progression (Chowdhury et al, 2012). To test the type of immunological response evoked with C17 treatment in Ag83 infected BALB/c, we examined the splenic cytokine expression levels by RT-PCR. We detected ~4-fold and 5.5-fold increased interferon (IFN- γ) levels after intraperitoneal C17 treatment of infected mice with 5 mg/kg and 10 mg/kg dosages, respectively, suggesting a Th1 dominance in C17-treated mice (Figure 6.3.12D).

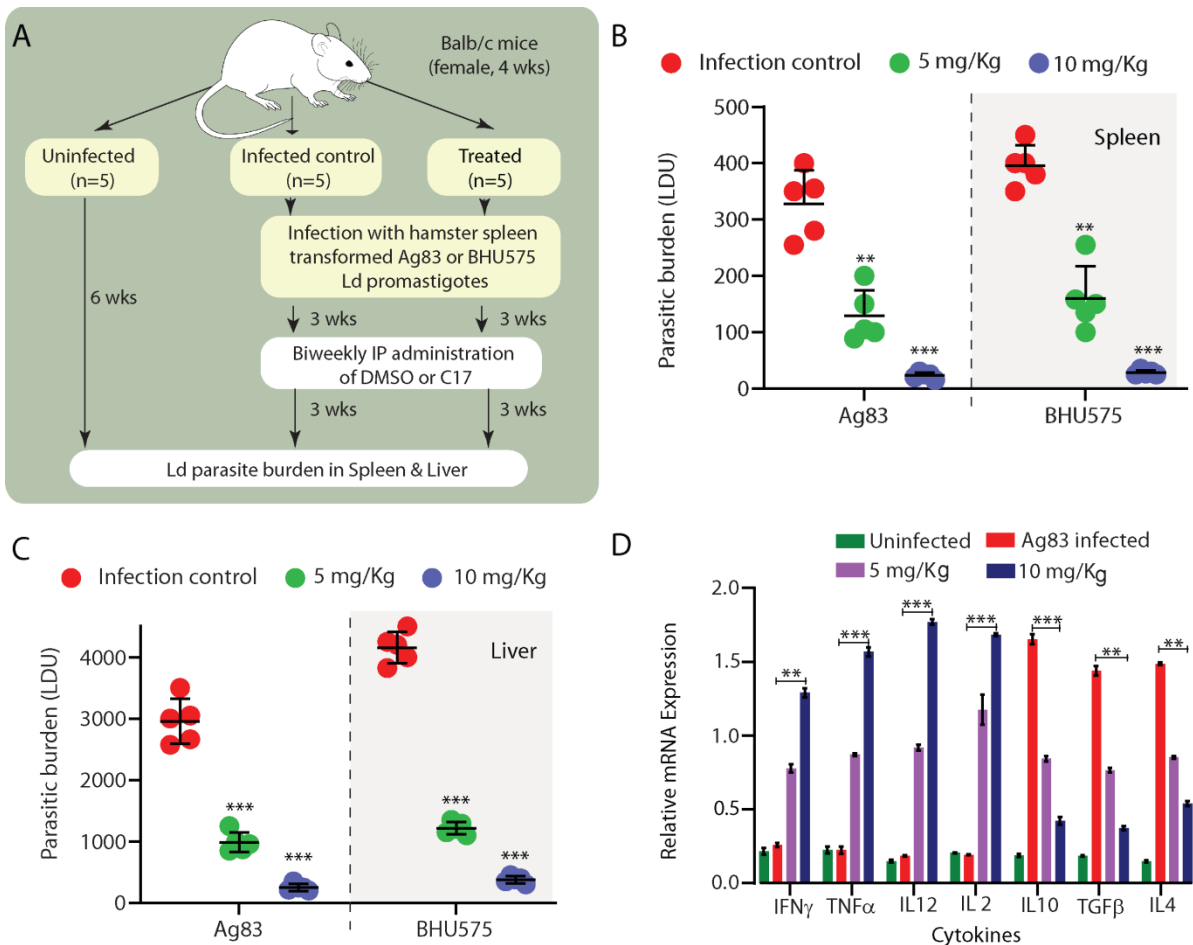


Figure 6.3.12: C17 markedly reduced the parasite burden in BALB/c mice by fine-tuning the Th1 and Th2 cytokine responses. (A) Schematic representation showing the protocol for the generation of the experimental murine model of Visceral Leishmaniasis (VL) using the Ag83/BHU575 promastigotes. *In vivo* anti-leishmanial property of C17 was studied in BALB/c mice infected with Ag83 or BHU575 promastigotes via the intracardiac route. C17 was given at a dosage of 5 and 10 mg/kg/day intraperitoneally for 3 weeks (2 times per week), starting on day 21 post-infection. Animals were sacrificed 10 days post drug treatment to determine the hepatic (B) and splenic (C) parasite load for all treatment groups. Untreated and infected mice were used as controls. The parasite burden in the organs was determined by the stamp-smear method and expressed as Leishman-Donovan Unit (LDU). Data represent mean SEM (n=5 mice per group). *p<0.05, **p<0.01, and ***p<0.005 (Student's t-test), indicate a significant difference in the change of parasite burden with C17 treatment as compared with infection control. (D) Semiquantitative RT-PCR

cytokine profiles of *L. donovani* infected and C17 treated infected Balb/c mice. Equivalent amounts of RNA from splenic tissues of four groups of Balb/c (n = 5) were used as the input for RT-PCR analysis, where the GAPDH gene was used as the housekeeping control gene. A differential pattern of Th1 cytokine expression was observed following C17 administration in infected BALB/c mice. Splenocytes isolated from Ag83-infected mice after indicated treatments were used for RNA extraction followed by RT-PCR. Downregulation of the Th2-cytokine expression profile following treatment with C17 was obtained. *p<0.05, **p<0.01, and ***p<0.005 (Student's t-test), indicate a significant change in the levels of the indicated cytokines with C17 treatment as compared with the infection control.

Notably, the level of IFN- γ was coupled with a concomitant up-regulation of TNF- α (~5 fold) and IL-12 (~10 fold) expression post-treatment, respectively (Figure 6.3.12D). The immunosuppressive cytokines promote the survival of intracellular parasites inside the host macrophages and their down-regulation propels convalescence of VL *in vivo* (Olivier et al, 2005). Accordingly, C17-treated parasite-infected mice exhibited a marked decline in the expression of the immunosuppressive cytokine (~2 to 4-fold reduction for IL-10) with increasing concentration of C17 (Figure 6.3.12D). C17 treatment markedly reduced TGF- β expression (2-4.7-fold after treatment) compared to the Ag83 infected mice and a concomitant increase in the level of IL-4 (1.7-fold and 5-fold) production in all the experimental groups of mice (Figure 6.3.12D). Taken together, these data advocate that C17 can plausibly serve as an anti-leishmanial candidate through the switching of immune balance to the host protective Th1 response *in vivo*.

6.4 Discussion

A series of twenty one pyrido[2',1':2,3]imidazo[4,5-*c*]quinoline derivatives (**C1-C21**) were prepared and evaluated for their anti-leishmanial activity. Our work proposes the novel PIQ derivative C17 as a potential chemotherapeutic candidate against both the *Leishmania* promastigotes (sandfly gut form) and the amastigotes (human infected form). *Leishmania* heterodimeric bi-subunit Top1 enzyme is essential for parasite survival (Das et al, 2008; Das et al, 2006a; Das et al, 2006b; Das et al, 2006c) and was rationalized to serve as a validated druggable pathway (Chowdhury et al, 2012; Chowdhury et al, 2017; Chowdhury & Majumder, 2019; Das et al, 2006c). We provided evidence that C17 is a potent inhibitor of LdTop1 imparting a significant level of cytotoxicity to the promastigotes and amastigotes of both the wild type (Ag83) and the antimony-resistant field isolate (BHU575) without inducing any lethality in host cells (human and murine). We showed that C17 stabilizes LdTop1-DNA covalent complex, and generates C17-induced DNA break formation in parasite culture which triggers apoptosis-like cell death in both the Ag83 and BHU575

parasites. C17 generates persistent and less reversible DNA breaks when compared with CPT after removal of the respective drugs from the culture medium causing enhanced parasite killing. We also showed that C17 exhibits anti-leishmanial activity as it markedly reduces both Ag83 and BHU575 strains of *L. donovani* using *in vivo* VL-infected mice model. The control of the progression of leishmaniasis is correlated with the switching of the cytokine balance from Th1 to Th2 response (Chowdhury et al, 2012). An effective leishmanicidal response evoked against *L. donovani* stems from an IL-12-mediated Th1 response leading to induction of IFN- γ production (Chowdhury et al, 2012). We found that C17 therapy mounts a polarized Th1 response with an up-regulated IFN- γ secretion, with a marked increase in the pro-inflammatory cytokine TNF- α which is thought to stimulate IL-12 driven IFN- γ secretion implicating a strong IL-12-driven IFN- γ , and TNF- α which might account for conferring the high levels of protection post-treatment. This up-regulated expression of IFN- γ coupled amplified IL-12 production bears a synergistic effect on the activation of iNOS (Chowdhury et al, 2012) and reduces the Th2-associated cytokines IL-4, IL-10, and TGF- β responses which could be observed in the C17 treated mice. Collectively, we provide compelling evidence that the novel PIQ derivatives as a promising anti-leishmanial drug candidate to overcome the emerging cases of multi-drug resistance and therapeutic failures. However, further validation is required in clinical trials to confirm the lab results and be used and practiced in the clinics.



References

- Ackerman P, Glover CV, Osheroff N (1985) Phosphorylation of DNA topoisomerase II by casein kinase II: modulation of eukaryotic topoisomerase II activity in vitro. *Proceedings of the National Academy of Sciences of the United States of America* **82**: 3164-3168
- Adachi N, Miyaike M, Ikeda H, Kikuchi A (1992) Characterization of cDNA encoding the mouse DNA topoisomerase II that can complement the budding yeast top2 mutation. *Nucleic Acids Res* **20**: 5297-5303
- Altamura F, Rajesh R, Catta-Preta CMC, Moretti NS, Cestari I The current drug discovery landscape for trypanosomiasis and leishmaniasis: Challenges and strategies to identify drug targets. *Drug development research* **n/a**
- DS, Kamhawi S (2001) Molecular Aspects of Parasite-Vector and Vector-Host Interactions in Leishmaniasis. *Annual Review of Microbiology* **55**: 453-483
- Arguello F, Alexander MA, Greene JF, Jr., Stinson SF, Jordan JL, Smith EM, Kalavar NT, Alvord WG, Klabansky RL, Sausville EA (1998) Preclinical evaluation of 9-chloro-2-methylellopticinium acetate alone and in combination with conventional anticancer drugs for the treatment of human brain tumor xenografts. *Journal of cancer research and clinical oncology* **124**: 19-26
- Arlt MF, Glover TW (2010) Inhibition of topoisomerase I prevents chromosome breakage at common fragile sites. *DNA repair* **9**: 678-689
- Ashour ME, Atteya R, El-Khamisy SF (2015) Topoisomerase-mediated chromosomal break repair: an emerging player in many games. *Nature reviews Cancer* **15**: 137-151
- Bakhoun SF, Cantley LC (2018) The Multifaceted Role of Chromosomal Instability in Cancer and Its Microenvironment. *Cell* **174**: 1347-1360
- Bakhoun SF, Kabeche L, Compton DA, Powell SN, Bastians H (2017) Mitotic DNA Damage Response: At the Crossroads of Structural and Numerical Cancer Chromosome Instabilities. *Trends in cancer* **3**: 225-234
- Balaña-Fouce R, Alvarez-Velilla R, Fernández-Prada C, García-Estrada C, Reguera RM (2014) Trypanosomatids topoisomerase re-visited. New structural findings and role in drug discovery. *Int J Parasitol Drugs Drug Resist* **4**: 326-337
- Balaña-Fouce R, García-Estrada C, Pérez-Pertejo Y, Reguera RM (2008) Gene disruption of the DNA topoisomerase IB small subunit induces a non-viable phenotype in the hemoflagellate *Leishmania major*. *BMC microbiology* **8**: 113

- Baranello L, Wojtowicz D, Cui K, Devaiah BN, Chung HJ, Chan-Salis KY, Guha R, Wilson K, Zhang X, Zhang H, Piotrowski J, Thomas CJ, Singer DS, Pugh BF, Pommier Y, Przytycka TM, Kouzine F, Lewis BA, Zhao K, Levens D (2016) RNA Polymerase II Regulates Topoisomerase I Activity to Favor Efficient Transcription. *Cell* **165**: 357-371
- Barnes DE, Lindahl T (2004) Repair and genetic consequences of endogenous DNA base damage in mammalian cells. *Annual review of genetics* **38**: 445-476
- Barthelmes HU, Habermeyer M, Christensen MO, Mielke C, Interthal H, Pouliot JJ, Boege F, Marko D (2004) TDP1 overexpression in human cells counteracts DNA damage mediated by topoisomerases I and II. *The Journal of biological chemistry* **279**: 55618-55625
- Bauer WR (1978) STRUCTURE AND REACTIONS OF CLOSED DUPLEX DNA. *Annual Review of Biophysics and Bioengineering* **7**: 287-313
- Beck DE, Agama K, Marchand C, Chergui A, Pommier Y, Cushman M (2014) Synthesis and biological evaluation of new carbohydrate-substituted indenoisoquinoline topoisomerase I inhibitors and improved syntheses of the experimental anticancer agents indotecan (LMP400) and indimitecan (LMP776). *J Med Chem* **57**: 1495-1512
- Belotserkovskaya R, Jackson SP (2014) Keeping 53BP1 out of focus in mitosis. *Cell Research* **24**: 781-782
- Beltrao P, Bork P, Krogan NJ, van Noort V (2013) Evolution and functional cross-talk of protein post-translational modifications. *Molecular systems biology* **9**: 714
- Bergerat A, Gadelle D, Forterre P (1994) Purification of a DNA topoisomerase II from the hyperthermophilic archaeon *Sulfolobus shibatae*. A thermostable enzyme with both bacterial and eucaryal features. *The Journal of biological chemistry* **269**: 27663-27669
- Bertolin AP, Hoffmann JS (2020) Under-Replicated DNA: The Byproduct of Large Genomes? **12**
- Bhattacharjee S, Rehman I, Basu S, Nandy S, Richardson JM, Das BB (2022) Interplay between symmetric arginine dimethylation and ubiquitylation regulates TDP1 proteostasis for the repair of topoisomerase I-DNA adducts. *Cell Reports* **39**: 110940
- Bhattacharjee S, Richardson JM, Das BB (2023) Fluorescence-resonance-energy-transfer-based assay to estimate modulation of TDP1 activity through arginine methylation. *STAR protocols* **4**: 102218

- Bhowmick R, Minocherhomji S, Hickson ID (2016) RAD52 Facilitates Mitotic DNA Synthesis Following Replication Stress. *Mol Cell* **64**: 1117-1126
- Bi K, Chen Y, Zhao S, Kuang Y, John Wu C-H (2018) Current Visceral Leishmaniasis Research: A Research Review to Inspire Future Study. *BioMed Research International* **2018**: 9872095
- Blackford AN, Stucki M (2020) How Cells Respond to DNA Breaks in Mitosis. *Trends Biochem Sci* **45**: 321-331
- Bodley AL, Shapiro TA (1995) Molecular and cytotoxic effects of camptothecin, a topoisomerase I inhibitor, on trypanosomes and Leishmania. *Proceedings of the National Academy of Sciences* **92**: 3726-3730
- Borst P, Hoeijmakers JHJ (1979) Kinetoplast DNA. *Plasmid* **2**: 20-40
- Brata Das B, Sen N, Ganguly A, Majumder HK (2004) Reconstitution and functional characterization of the unusual bi-subunit type I DNA topoisomerase from Leishmania donovani. *FEBS letters* **565**: 81-88
- Brown NR, Korolchuk S, Martin MP, Stanley WA, Moukhametzianov R, Noble MEM, Endicott JA (2015) CDK1 structures reveal conserved and unique features of the essential cell cycle CDK. *Nature Communications* **6**: 6769
- Caldecott KW (2003) XRCC1 and DNA strand break repair. *DNA repair* **2**: 955-969
- Caldecott KW (2008) Single-strand break repair and genetic disease. *Nature reviews Genetics* **9**: 619-631
- Capranico G, Guano F, Moro S, Zagotto G, Sissi C, Gatto B, Zunino F, Menta E, Palumbo M (1998) Mapping drug interactions at the covalent topoisomerase II-DNA complex by bisantrene/amsacrine congeners. *The Journal of biological chemistry* **273**: 12732-12739
- Capranico G, Marinello J, Chillemi G (2017) Type I DNA Topoisomerases. *Journal of Medicinal Chemistry* **60**: 2169-2192
- Capranico G, Tinelli S, Austin CA, Fisher ML, Zunino F (1992) Different patterns of gene expression of topoisomerase II isoforms in differentiated tissues during murine development. *Biochimica et biophysica acta* **1132**: 43-48

Cavalcanti DP, de Souza W (2018) The Kinetoplast of Trypanosomatids: From Early Studies of Electron Microscopy to Recent Advances in Atomic Force Microscopy. *Scanning* **2018**: 9603051

Chakravarty J, Sundar S (2010) Drug resistance in leishmaniasis. *Journal of global infectious diseases* **2**: 167-176

Champoux JJ (2001) DNA topoisomerases: structure, function, and mechanism. *Annual review of biochemistry* **70**: 369-413

Champoux JJ, Dulbecco R (1972) An activity from mammalian cells that untwists superhelical DNA--a possible swivel for DNA replication (polyoma-ethidium bromide-mouse-embryo cells-dye binding assay). *Proceedings of the National Academy of Sciences of the United States of America* **69**: 143-146

Champoux JJ, McConaughy BL (1976) Purification and characterization of the DNA untwisting enzyme from rat liver. *Biochemistry* **15**: 4638-4642

Chappuis F, Sundar S, Hailu A, Ghalib H, Rijal S, Peeling RW, Alvar J, Boelaert M (2007) Visceral leishmaniasis: what are the needs for diagnosis, treatment and control? *Nature Reviews Microbiology* **5**: 873-882

Chow KC, Macdonald TL, Ross WE (1988) DNA binding by epipodophyllotoxins and N-acyl anthracyclines: implications for mechanism of topoisomerase II inhibition. *Molecular Pharmacology* **34**: 467-473

Chowdhuri SP, Das BB (2021) Top1-PARP1 association and beyond: from DNA topology to break repair. *NAR Cancer* **3**

Chowdhuri SP, Dhiman S, Das SK, Meena N, Das S, Kumar A (2023) Novel Pyrido[2',1':2,3]imidazo[4,5-c]quinoline Derivative Selectively Poisons Leishmania donovani Bisubunit Topoisomerase 1 to Inhibit the Antimony-Resistant Leishmania Infection in Vivo. **66**: 3411-3430

Chowdhury S, Mukherjee T, Mukhopadhyay R, Mukherjee B, Sengupta S, Chattopadhyay S, Jaisankar P, Roy S, Majumder HK (2012) The lignan niranthin poisons Leishmania donovani topoisomerase IB and favours a Th1 immune response in mice. *EMBO Molecular Medicine* **4**: 1126-1143

Chowdhury SR, Kumar A, Godinho JLP, De Macedo Silva ST, Zuma AA, Saha S, Kumari N, Rodrigues JCF, Sundar S, Dujardin J-C, Roy S, De Souza W, Mukhopadhyay S, Majumder HK

(2017) Voacamine alters Leishmania ultrastructure and kills parasite by poisoning unusual bi-subunit topoisomerase IB. *Biochemical Pharmacology* **138**: 19-30

Chowdhury SR, Majumder HK (2019) DNA Topoisomerases in Unicellular Pathogens: Structure, Function, and Druggability. *Trends in Biochemical Sciences* **44**: 415-432

Clay DE, Fox DT (2021) DNA Damage Responses during the Cell Cycle: Insights from Model Organisms and Beyond. **12**

Clements PM, Breslin C, Deeks ED, Byrd PJ, Ju L, Bieganowski P, Brenner C, Moreira MC, Taylor AM, Caldecott KW (2004) The ataxia-oculomotor apraxia 1 gene product has a role distinct from ATM and interacts with the DNA strand break repair proteins XRCC1 and XRCC4. *DNA repair* **3**: 1493-1502

Cooper S, Wadsworth ES, Schnauffer A (2022) Organization of minicircle cassettes and guide RNA genes in *Trypanosoma brucei*. **28**: 972-992

Cortés-Gutiérrez EI, Hernández-Garza F, García-Pérez JO, Dávila-Rodríguez MI, Aguado-Barrera ME, Cerda-Flores RM (2012) Evaluation of DNA single and double strand breaks in women with cervical neoplasia based on alkaline and neutral comet assay techniques. *Journal of biomedicine & biotechnology* **2012**: 385245

Cozzarelli NR, Krasnow MA, Gerrard SP, White JH (1984) A topological treatment of recombination and topoisomerases. *Cold Spring Harbor symposia on quantitative biology* **49**: 383-400

Cristini A, Ricci G, Britton S, Salimbeni S, Huang SN, Marinello J, Calsou P, Pommier Y, Favre G, Capranico G, Gromak N, Sordet O (2019) Dual Processing of R-Loops and Topoisomerase I Induces Transcription-Dependent DNA Double-Strand Breaks. *Cell Rep* **28**: 3167-3181.e3166

Das BB, Antony S, Gupta S, Dexheimer TS, Redon CE, Garfield S, Shiloh Y, Pommier Y (2009) Optimal function of the DNA repair enzyme TDP1 requires its phosphorylation by ATM and/or DNA-PK. *The EMBO journal* **28**: 3667-3680

Das BB, Dexheimer TS, Maddali K, Pommier Y (2010) Role of tyrosyl-DNA phosphodiesterase (TDP1) in mitochondria. *Proceedings of the National Academy of Sciences of the United States of America* **107**: 19790-19795

Das BB, Ganguly A, Majumder HK (2008) DNA Topoisomerases of Leishmania: The Potential Targets for Anti-Leishmanial Therapy. In *Drug Targets in Kinetoplastid Parasites*, Majumder HK (ed), pp 103-115. New York, NY: Springer New York

- Das BB, Ghosh A, Bhattacharjee S, Bhattacharyya A (2021a) Trapped topoisomerase-DNA covalent complexes in the mitochondria and their role in human diseases. *Mitochondrion* **60**: 234-244
- Das BB, Huang S-yN, Murai J, Rehman I, Amé J-C, Sengupta S, Das SK, Majumdar P, Zhang H, Biard D, Majumder HK, Schreiber V, Pommier Y (2014) PARP1–TDP1 coupling for the repair of topoisomerase I-induced DNA damage. *Nucleic Acids Research* **42**: 4435-4449
- Das BB, Sen N, Dasgupta SB, Ganguly A, Das R, Majumder HK (2006a) Topoisomerase research of kinetoplastic parasite *Leishmania*, with special reference to development of therapeutics. *Indian Journal of Medical Research* **123**: 221
- Das BB, Sen N, Dasgupta SB, Ganguly A, Majumder HK (2005) N-terminal region of the large subunit of *Leishmania donovani* bisubunit topoisomerase I is involved in DNA relaxation and interaction with the smaller subunit. *The Journal of biological chemistry* **280**: 16335-16344
- Das BB, Sen N, Roy A, Dasgupta SB, Ganguly A, Mohanta BC, Dinda B, Majumder HK (2006b) Differential induction of *Leishmania donovani* bi-subunit topoisomerase I–DNA cleavage complex by selected flavones and camptothecin: activity of flavones against camptothecin-resistant topoisomerase I. *Nucleic acids research* **34**: 1121-1132
- Das BB, Sengupta T, Ganguly A, Majumder HK (2006c) Topoisomerases of kinetoplastid parasites: why so fascinating? *Molecular microbiology* **62**: 917-927
- Das S, Banerjee A, Kamran M, Ejazi SA, Asad M, Ali N, Chakrabarti S (2020) A chemical inhibitor of heat shock protein 78 (HSP78) from *Leishmania donovani* represents a potential antileishmanial drug candidate. *Journal of Biological Chemistry* **295**: 9934-9947
- Das S, Mukherjee S, Ali N (2021b) Super enhancer-mediated transcription of miR146a-5p drives M2 polarization during *Leishmania donovani* infection. **17**: e1009343
- Das SK, Ghosh A, Paul Chowdhuri S, Halder N, Rehman I, Sengupta S, Sahoo KC, Rath H, Das BB (2018) Neutral Porphyrin Derivative Exerts Anticancer Activity by Targeting Cellular Topoisomerase I (Top1) and Promotes Apoptotic Cell Death without Stabilizing Top1-DNA Cleavage Complexes. *Journal of Medicinal Chemistry* **61**: 804-817
- Das SK, Rehman I, Ghosh A, Sengupta S, Majumdar P, Jana B, Das BB (2016) Poly(ADP-ribose) polymers regulate DNA topoisomerase I (Top1) nuclear dynamics and camptothecin sensitivity in living cells. *Nucleic Acids Res* **44**: 8363-8375

- Davies DR, Interthal H, Champoux JJ, Hol WG (2002a) The crystal structure of human tyrosyl-DNA phosphodiesterase, Tdp1. *Structure (London, England : 1993)* **10**: 237-248
- Davies DR, Interthal H, Champoux JJ, Hol WGJ (2002b) Insights into Substrate Binding and Catalytic Mechanism of Human Tyrosyl-DNA Phosphodiesterase (Tdp1) from Vanadate and Tungstate-inhibited Structures. *Journal of Molecular Biology* **324**: 917-932
- de Mello H, Echevarria A, Bernardino AM, Canto-Cavalheiro M, Leon LL (2004) Antileishmanial Pyrazolopyridine Derivatives: Synthesis and Structure–Activity Relationship Analysis. *Journal of Medicinal Chemistry* **47**: 5427-5432
- Dean RA, Fam HK, An J, Choi K, Shimizu Y, Jones SJM, Boerkoel CF, Interthal H, Pfeifer TA (2014) Identification of a Putative Tdp1 Inhibitor (CD00509) by in Vitro and Cell-Based Assays. *SLAS Discovery* **19**: 1372-1382
- Deb ethune L, Kohlhagen G, Grandas A, Pommier Y (2002) Processing of nucleopeptides mimicking the topoisomerase I–DNA covalent complex by tyrosyl-DNA phosphodiesterase. *Nucleic Acids Research* **30**: 1198-1204
- Denchi EL, Li J (2014) Let it go: how to deal with a breakup in mitosis. *Nature structural & molecular biology* **21**: 433-435
- Dereuddre S, Frey S, Delaporte C, Jacquemin-Sablon A (1995) Cloning and characterization of full-length cDNAs coding for the DNA topoisomerase II beta from Chinese hamster lung cells sensitive and resistant 9-OH-ellipticine. *Biochimica et biophysica acta* **1264**: 178-182
- Deribe YL, Pawson T, Dikic I (2010) Post-translational modifications in signal integration. *Nature structural & molecular biology* **17**: 666-672
- Desjeux P (2001) The increase in risk factors for leishmaniasis worldwide. *Transactions of the royal society of tropical medicine and hygiene* **95**: 239-243
- Diril MK, Ratnacaram CK, Padmakumar VC, Du T, Wasser M, Coppola V, Tessarollo L, Kaldis P (2012) Cyclin-dependent kinase 1 (Cdk1) is essential for cell division and suppression of DNA re-replication but not for liver regeneration. *Proceedings of the National Academy of Sciences of the United States of America* **109**: 3826-3831
- Drake FH, Zimmerman JP, McCabe FL, Bartus HF, Per SR, Sullivan DM, Ross WE, Mattern MR, Johnson RK, Crooke ST, et al. (1987) Purification of topoisomerase II from amsacrine-resistant P388

leukemia cells. Evidence for two forms of the enzyme. *The Journal of biological chemistry* **262**: 16739-16747

Duffy S, Fam HK, Wang YK, Styles EB, Kim JH, Ang JS, Singh T, Larionov V, Shah SP, Andrews B, Boerkoel CF, Hieter P (2016) Overexpression screens identify conserved dosage chromosome instability genes in yeast and human cancer. *Proceedings of the National Academy of Sciences of the United States of America* **113**: 9967-9976

Durban E, Mills JS, Roll D, Busch H (1983) Phosphorylation of purified Novikoff hepatoma topoisomerase I. *Biochem Biophys Res Commun* **111**: 897-905

Durban E, Roll D, Beckner G, Busch H (1981) Purification and characterization of a nuclear DNA-binding phosphoprotein in fetal and tumor tissues. *Cancer research* **41**: 537-545

El-Khamisy SF, Saifi GM, Weinfeld M, Johansson F, Helleday T, Lupski JR, Caldecott KW (2005) Defective DNA single-strand break repair in spinocerebellar ataxia with axonal neuropathy-1. *Nature* **434**: 108-113

Enserink JM, Kolodner RD (2010) An overview of Cdk1-controlled targets and processes. *Cell division* **5**: 11

Escribano-Díaz C, Orthwein A, Fradet-Turcotte A, Xing M, Young JT, Tkáč J, Cook MA, Rosebrock AP, Munro M, Canny MD (2013) A cell cycle-dependent regulatory circuit composed of 53BP1-RIF1 and BRCA1-CtIP controls DNA repair pathway choice. *Molecular cell* **49**: 872-883

Fam HK, Walton C, Mitra SA, Chowdhury M, Osborne N, Choi K, Sun G, Wong PC, O'Sullivan MJ, Turashvili G, Aparicio S, Triche TJ, Bond M, Pallen CJ, Boerkoel CF (2013) TDP1 and PARP1 deficiency are cytotoxic to rhabdomyosarcoma cells. *Molecular cancer research : MCR* **11**: 1179-1192

Fernandez-Vidal A, Vignard J, Mirey G (2017) Around and beyond 53BP1 Nuclear Bodies. **18**

Flett FJ, Ruksenaite E, Armstrong LA, Bharati S, Carloni R, Morris ER, Mackay CL, Interthal H, Richardson JM (2018) Structural basis for DNA 3'-end processing by human tyrosyl-DNA phosphodiesterase 1. *Nature Communications* **9**: 24

Flotho A, Melchior F (2013) Sumoylation: a regulatory protein modification in health and disease. *Annual review of biochemistry* **82**: 357-385

- Forterre P, Mirambeau G, Jaxel C, Nadal M, Duguet M (1985) High positive supercoiling in vitro catalyzed by an ATP and polyethylene glycol-stimulated topoisomerase from *Sulfolobus acidocaldarius*. *The EMBO journal* **4**: 2123-2128
- Froelich-Ammon SJ, Osheroff N (1995) Topoisomerase Poisons: Harnessing the Dark Side of Enzyme Mechanism (*). *The Journal of biological chemistry* **270**: 21429 - 21432
- Galande S, Muniyappa K (1996) Purification and functional characterization of type II DNA topoisomerase from rat testis and comparison with topoisomerase II from liver. *Biochimica et biophysica acta* **1308**: 58-66
- Gellert M (1981) DNA Topoisomerases. *Annual review of biochemistry* **50**: 879-910
- Gellert M, Mizuuchi K, O'Dea MH, Nash HA (1976) DNA gyrase: an enzyme that introduces superhelical turns into DNA. *Proceedings of the National Academy of Sciences of the United States of America* **73**: 3872-3876
- Ghelli Luserna di Rorà A, Cerchione C, Martinelli G, Simonetti G (2020) A WEE1 family business: regulation of mitosis, cancer progression, and therapeutic target. *Journal of Hematology & Oncology* **13**: 126
- Ghosh S, Biswas S, Mukherjee S, Pal A, Saxena A, Sundar S, Dujardin JC, Das S, Roy S, Mukhopadhyay R, Mukherjee B (2021) A Novel Bioimpedance-Based Detection of Miltefosine Susceptibility Among Clinical *Leishmania donovani* Isolates of the Indian Subcontinent Exhibiting Resistance to Multiple Drugs. *Frontiers in cellular and infection microbiology* **11**: 768830
- Gomez Godinez V, Kabbara S, Sherman A, Wu T, Cohen S (2020) DNA damage induced during mitosis undergoes DNA repair synthesis. **15**: e0227849
- Goodwin A, Wang SW, Toda T, Norbury C, Hickson ID (1999) Topoisomerase III is essential for accurate nuclear division in *Schizosaccharomyces pombe*. *Nucleic Acids Res* **27**: 4050-4058
- Goto T, Wang JC (1982) Yeast DNA topoisomerase II. An ATP-dependent type II topoisomerase that catalyzes the catenation, decatenation, unknotting, and relaxation of double-stranded DNA rings. *Journal of Biological Chemistry* **257**: 5866-5872
- Goto T, Wang JC (1984) Yeast DNA topoisomerase II is encoded by a single-copy, essential gene. *Cell* **36**: 1073-1080
- Groelly FJ, Dagg RA, Petropoulos M, Rossetti GG, Prasad B, Panagopoulos A, Paulsen T, Karamichali A, Jones SE, Ochs F, Dionellis VS, Puig Lombardi E, Miossec MJ, Lockstone H, Legube

- G, Blackford AN, Altmeyer M, Halazonetis TD, Tarsounas M (2022) Mitotic DNA synthesis is caused by transcription-replication conflicts in BRCA2-deficient cells. *Mol Cell* **82**: 3382-3397.e3387
- Hajduk S, Ochsenreiter T (2010) RNA editing in kinetoplastids. *RNA Biology* **7**: 229-236
- Haldar AK, Sen P, Roy S (2011) Use of antimony in the treatment of leishmaniasis: current status and future directions. *Molecular biology international* **2011**: 571242
- Harrigan JA, Belotserkovskaya R, Coates J, Dimitrova DS, Polo SE, Bradshaw CR, Fraser P, Jackson SP (2011) Replication stress induces 53BP1-containing OPT domains in G1 cells. *The Journal of cell biology* **193**: 97-108
- Hassa PO, Hottiger MO (2008) The diverse biological roles of mammalian PARPS, a small but powerful family of poly-ADP-ribose polymerases. *Frontiers in bioscience : a journal and virtual library* **13**: 3046-3082
- Heck MM, Earnshaw WC (1986) Topoisomerase II: A specific marker for cell proliferation. *The Journal of cell biology* **103**: 2569-2581
- Hirano R, Interthal H, Huang C, Nakamura T, Deguchi K, Choi K, Bhattacharjee MB, Arimura K, Umehara F, Izumo S, Northrop JL, Salih MA, Inoue K, Armstrong DL, Champoux JJ, Takashima H, Boerkoel CF (2007) Spinocerebellar ataxia with axonal neuropathy: consequence of a Tdp1 recessive neomorphic mutation? *The EMBO journal* **26**: 4732-4743
- Holden JA, Dresler SL, Low RL (1990) Identification of DNA topoisomerase-II activity in terminally differentiated mammalian organs and in non-growing cultured cells. *Enzyme* **43**: 197-206
- Holt LJ, Tuch BB, Villén J, Johnson AD, Gygi SP, Morgan DO (2009) Global analysis of Cdk1 substrate phosphorylation sites provides insights into evolution. *Science (New York, NY)* **325**: 1682-1686
- Hsiang YH, Liu LF (1988) Identification of mammalian DNA topoisomerase I as an intracellular target of the anticancer drug camptothecin. *Cancer research* **48**: 1722-1726
- Hsieh T (1983) Knotting of the circular duplex DNA by type II DNA topoisomerase from *Drosophila melanogaster*. *The Journal of biological chemistry* **258**: 8413-8420
- Hsieh T, Brutlag D (1980) ATP-dependent DNA topoisomerase from *D. melanogaster* reversibly catenates duplex DNA rings. *Cell* **21**: 115-125

- Huang SN, Pommier Y, Marchand C (2011) Tyrosyl-DNA Phosphodiesterase 1 (Tdp1) inhibitors. *Expert opinion on therapeutic patents* **21**: 1285-1292
- Huang SY, Murai J, Dalla Rosa I, Dexheimer TS, Naumova A, Gmeiner WH, Pommier Y (2013) TDP1 repairs nuclear and mitochondrial DNA damage induced by chain-terminating anticancer and antiviral nucleoside analogs. *Nucleic Acids Res* **41**: 7793-7803
- Hudson JJ, Chiang SC, Wells OS, Rookyard C, El-Khamisy SF (2012) SUMO modification of the neuroprotective protein TDP1 facilitates chromosomal single-strand break repair. *Nat Commun* **3**: 733
- Interthal H, Chen HJ, Kehl-Fie TE, Zotzmann J, Leppard JB, Champoux JJ (2005) SCAN1 mutant Tdp1 accumulates the enzyme–DNA intermediate and causes camptothecin hypersensitivity. *The EMBO journal* **24**: 2224-2233
- Interthal H, Pouliot JJ, Champoux JJ (2001) The tyrosyl-DNA phosphodiesterase Tdp1 is a member of the phospholipase D superfamily. *Proceedings of the National Academy of Sciences of the United States of America* **98**: 12009-12014
- Juenke JM, Holden JA (1993) The distribution of DNA topoisomerase II isoforms in differentiated adult mouse tissues. *Biochimica et biophysica acta* **1216**: 191-196
- Katyal S, el-Khamisy SF, Russell HR, Li Y, Ju L, Caldecott KW, McKinnon PJ (2007) TDP1 facilitates chromosomal single-strand break repair in neurons and is neuroprotective in vivo. *The EMBO journal* **26**: 4720-4731
- Kaye P, Scott P (2011) Leishmaniasis: complexity at the host–pathogen interface. *Nature Reviews Microbiology* **9**: 604-615
- Keller W (1975) Determination of the number of superhelical turns in simian virus 40 DNA by gel electrophoresis. *Proceedings of the National Academy of Sciences of the United States of America* **72**: 4876-4880
- Kim RA, Wang JC (1989) Function of DNA topoisomerases as replication swivels in *Saccharomyces cerevisiae*. *Journal of Molecular Biology* **208**: 257-267
- King IF, Yandava CN, Mabb AM, Hsiao JS, Huang HS, Pearson BL, Calabrese JM, Starmer J, Parker JS, Magnuson T, Chamberlain SJ, Philpot BD, Zylka MJ (2013) Topoisomerases facilitate transcription of long genes linked to autism. *Nature* **501**: 58-62
- Kirkegaard K, Wang JC (1978) *Escherichia coli* DNA topoisomerase I catalyzed linking of single-stranded rings of complementary base sequences. *Nucleic Acids Res* **5**: 3811-3820

- Kishbaugh TL (2016) Pyridines and Imidazopyridines with Medicinal Significance. *Current topics in medicinal chemistry* **16**: 3274-3302
- Kramara J, Osia B, Malkova A (2018) Break-Induced Replication: The Where, The Why, and The How. *Trends in genetics : TIG* **34**: 518-531
- Krupina K, Goginashvili A, Cleveland DW (2021) Causes and consequences of micronuclei. *Current opinion in cell biology* **70**: 91-99
- Kundu B, Das SK, Paul Chowdhuri S, Pal S, Sarkar D, Ghosh A, Mukherjee A, Bhattacharya D, Das BB, Talukdar A (2019) Discovery and Mechanistic Study of Tailor-Made Quinoline Derivatives as Topoisomerase 1 Poison with Potent Anticancer Activity. *Journal of Medicinal Chemistry* **62**: 3428-3446
- Kundu B, Sarkar D, Chowdhuri SP, Pal S, Das SK, Das BB, Talukdar A (2020) Development of a metabolically stable topoisomerase I poison as anticancer agent. *European journal of medicinal chemistry* **202**: 112551
- Kwan KY, Moens PB, Wang JC (2003) Infertility and aneuploidy in mice lacking a type IA DNA topoisomerase III beta. *Proceedings of the National Academy of Sciences of the United States of America* **100**: 2526-2531
- Langelier M-F, Servent KM, Rogers EE, Pascal JM (2008) A Third Zinc-binding Domain of Human Poly(ADP-ribose) Polymerase-1 Coordinates DNA-dependent Enzyme Activation*. *Journal of Biological Chemistry* **283**: 4105-4114
- Lau HW, Ma HT, Yeung TK, Tam MY, Zheng D, Chu SK, Poon RYC (2021) Quantitative differences between cyclin-dependent kinases underlie the unique functions of CDK1 in human cells. *Cell Rep* **37**: 109808
- Levine MS, Holland AJ (2018) The impact of mitotic errors on cell proliferation and tumorigenesis. *Genes & development* **32**: 620-638
- Li M, He F (2020) CDK1 serves as a potential prognostic biomarker and target for lung cancer. **48**: 300060519897508
- Li S, Wu X (2020) Common fragile sites: protection and repair. *Cell & Bioscience* **10**: 29
- Li W, Wang JC (1998) Mammalian DNA topoisomerase IIIalpha is essential in early embryogenesis. *Proceedings of the National Academy of Sciences of the United States of America* **95**: 1010-1013

Liao C, Beveridge R, Hudson JJR, Parker JD, Chiang SC, Ray S, Ashour ME, Sudbery I, Dickman MJ, El-Khamisy SF (2018) UCHL3 Regulates Topoisomerase-Induced Chromosomal Break Repair by Controlling TDP1 Proteostasis. *Cell Rep* **23**: 3352-3365

Lindahl T (1993) Instability and decay of the primary structure of DNA. *Nature* **362**: 709-715

Lisby M, Olesen JR, Skouboe C, Krogh BO, Straub T, Boege F, Velmurugan S, Martensen PM, Andersen AH, Jayaram M, Westergaard O, Knudsen BR (2001) Residues within the N-terminal domain of human topoisomerase I play a direct role in relaxation. *The Journal of biological chemistry* **276**: 20220-20227

Liu C, Pouliot JJ, Nash HA (2002) Repair of topoisomerase I covalent complexes in the absence of the tyrosyl-DNA phosphodiesterase Tdp1. *Proceedings of the National Academy of Sciences of the United States of America* **99**: 14970-14975

Liu C, Zhou S, Begum S, Sidransky D, Westra WH, Brock M, Califano JA (2007) Increased expression and activity of repair genes TDP1 and XPF in non-small cell lung cancer. *Lung cancer (Amsterdam, Netherlands)* **55**: 303-311

Liu LF (1989) DNA topoisomerase poisons as antitumor drugs. *Annual review of biochemistry* **58**: 351-375

Liu LF, Depew RE, Wang JC (1976) Knotted single-stranded DNA rings: a novel topological isomer of circular single-stranded DNA formed by treatment with Escherichia coli omega protein. *J Mol Biol* **106**: 439-452

Liu LF, Liu CC, Alberts BM (1980) Type II DNA topoisomerases: enzymes that can unknot a topologically knotted DNA molecule via a reversible double-strand break. *Cell* **19**: 697-707

Liu LF, Wang JC (1979) Interaction between DNA and Escherichia coli DNA topoisomerase I. Formation of complexes between the protein and superhelical and nonsuperhelical duplex DNAs. *The Journal of biological chemistry* **254**: 11082-11088

Mailand N, Bekker-Jensen S, Bartek J, Lukas J (2006) Destruction of Claspin by SCFbetaTrCP restrains Chk1 activation and facilitates recovery from genotoxic stress. *Mol Cell* **23**: 307-318

Majumdar P, Bathula C, Basu SM, Das SK, Agarwal R, Hati S, Singh A, Sen S, Das BB (2015) Design, synthesis and evaluation of thiohydantoin derivatives as potent topoisomerase I (Top1) inhibitors with anticancer activity. *European journal of medicinal chemistry* **102**: 540-551

- Mankouri HW, Huttner D, Hickson ID (2013) How unfinished business from S-phase affects mitosis and beyond. *The EMBO journal* **32**: 2661-2671
- Mann S, Frasca K, Scherrer S, Henao-Martínez AF, Newman S, Ramanan P, Suarez JA (2021) A Review of Leishmaniasis: Current Knowledge and Future Directions. *Curr Trop Med Rep* **8**: 121-132
- Mao Y, Sun M, Desai SD, Liu LF (2000) SUMO-1 conjugation to topoisomerase I: A possible repair response to topoisomerase-mediated DNA damage. *Proceedings of the National Academy of Sciences of the United States of America* **97**: 4046-4051
- Matos DA, Zhang JM, Ouyang J, Nguyen HD, Genoia MM, Zou L (2020) ATR Protects the Genome against R Loops through a MUS81-Triggered Feedback Loop. *Mol Cell* **77**: 514-527.e514
- Maxwell A, Gellert M (1986) Mechanistic aspects of DNA topoisomerases. *Advances in protein chemistry* **38**: 69-107
- Menzel R, Gellert M (1987) Modulation of transcription by DNA supercoiling: a deletion analysis of the Escherichia coli gyrA and gyrB promoters. *Proceedings of the National Academy of Sciences of the United States of America* **84**: 4185-4189
- Mills JS, Busch H, Durban E (1982) Purification of a protein kinase from human Namalwa cells that phosphorylates topoisomerase I. *Biochemical and Biophysical Research Communications* **109**: 1222-1227
- Minocherhomji S, Ying S, Bjerregaard VA, Bursomanno S, Aleliunaite A, Wu W, Mankouri HW, Shen H, Liu Y, Hickson ID (2015) Replication stress activates DNA repair synthesis in mitosis. *Nature* **528**: 286-290
- Mishra A, Vinayagam J, Saha S, Chowdhury S, Chowdhury SR, Jaisankar P, Majumder HK (2014) Isobenzofuranone derivatives exhibit antileishmanial effect by inhibiting type II DNA topoisomerase and inducing host response. *Pharmacology research & perspectives* **2**: e00070
- Mohapatra S (2014) Drug resistance in leishmaniasis: Newer developments. *Trop Parasitol* **4**: 4-9
- Mukherjee B, Mukhopadhyay R, Bannerjee B, Chowdhury S, Mukherjee S, Naskar K, Allam US, Chakravorty D, Sundar S, Dujardin J-C, Roy S (2013) Antimony-resistant but not antimony-sensitive *Leishmania donovani* up-regulates host IL-10 to overexpress multidrug-resistant protein 1. *Proceedings of the National Academy of Sciences* **110**: E575-E582

- Murai J, Huang SY, Das BB, Dexheimer TS, Takeda S, Pommier Y (2012) Tyrosyl-DNA phosphodiesterase 1 (TDP1) repairs DNA damage induced by topoisomerases I and II and base alkylation in vertebrate cells. *The Journal of biological chemistry* **287**: 12848-12857
- Nitiss JL (1998) Investigating the biological functions of DNA topoisomerases in eukaryotic cells. *Biochimica et biophysica acta* **1400**: 63-81
- Olivier M, Gregory DJ, Forget G (2005) Subversion mechanisms by which Leishmania parasites can escape the host immune response: a signaling point of view. *Clinical microbiology reviews* **18**: 293-305
- Orthwein A, Fradet-Turcotte A, Noordermeer SM, Canny MD, Brun CM, Strecker J, Escribano-Diaz C, Durocher D (2014) Mitosis inhibits DNA double-strand break repair to guard against telomere fusions. *Science (New York, NY)* **344**: 189-193
- Osheroff N (1989) Effect of antineoplastic agents on the DNA cleavage/religation reaction of eukaryotic topoisomerase II: inhibition of DNA religation by etoposide. *Biochemistry* **28**: 6157-6160
- Osheroff N, Shelton ER, Brutlag DL (1983) DNA topoisomerase II from *Drosophila melanogaster*. Relaxation of supercoiled DNA. *Journal of Biological Chemistry* **258**: 9536-9543
- Osman F, Dixon J, Doe CL, Whitby MC (2003) Generating Crossovers by Resolution of Nicked Holliday Junctions: A Role for Mus81-Eme1 in Meiosis. *Molecular Cell* **12**: 761-774
- Park SH, Yoon JH, Kwon YD, Park SD (1993) Nucleotide Sequence Analysis of the cDNA for Rat DNA Topoisomerase II. *Biochemical and Biophysical Research Communications* **193**: 787-793
- Pearson RD, Wheeler DA, Harrison LH, Kay HD (1983) The Immunobiology of Leishmaniasis. *Reviews of Infectious Diseases* **5**: 907-927
- Petsalaki E, Zachos G (2020) DNA damage response proteins regulating mitotic cell division: double agents preserving genome stability. *The FEBS Journal* **287**: 1700-1721
- Pfister TD, Reinhold WC, Agama K, Gupta S, Khin SA, Kinders RJ, Parchment RE, Tomaszewski JE, Doroshow JH, Pommier Y (2009) Topoisomerase I levels in the NCI-60 cancer cell line panel determined by validated ELISA and microarray analysis and correlation with indenoisoquinoline sensitivity. *Molecular cancer therapeutics* **8**: 1878-1884
- Pladevall-Morera D, Munk S, Ingham A, Garribba L, Albers E, Liu Y, Olsen JV, Lopez-Contreras AJ (2019) Proteomic characterization of chromosomal common fragile site (CFS)-associated proteins uncovers ATRX as a regulator of CFS stability. *Nucleic Acids Res* **47**: 8004-8018

- Pommier Y (2006) Topoisomerase I inhibitors: camptothecins and beyond. *Nature Reviews Cancer* **6**: 789-802
- Pommier Y (2013) Drugging topoisomerases: lessons and challenges. *ACS chemical biology* **8**: 82-95
- Pommier Y, Cushman M (2009) The indenoisoquinoline noncamptothecin topoisomerase I inhibitors: update and perspectives. *Molecular cancer therapeutics* **8**: 1008-1014
- Pommier Y, Huang SY, Gao R, Das BB, Murai J, Marchand C (2014) Tyrosyl-DNA-phosphodiesterases (TDP1 and TDP2). *DNA repair* **19**: 114-129
- Pommier Y, Kerrigan D, Hartman KD, Glazer RI (1990) Phosphorylation of mammalian DNA topoisomerase I and activation by protein kinase C. *The Journal of biological chemistry* **265**: 9418-9422
- Pommier Y, Sun Y, Huang SN, Nitiss JL (2016) Roles of eukaryotic topoisomerases in transcription, replication and genomic stability. *Nature reviews Molecular cell biology* **17**: 703-721
- Rao VA, Fan AM, Meng L, Doe CF, North PS, Hickson ID, Pommier Y (2005) Phosphorylation of BLM, dissociation from topoisomerase IIIalpha, and colocalization with gamma-H2AX after topoisomerase I-induced replication damage. *Molecular and cellular biology* **25**: 8925-8937
- Ray Chaudhuri A, Hashimoto Y, Herrador R, Neelsen KJ, Fachinetti D, Bermejo R, Cocito A, Costanzo V, Lopes M (2012) Topoisomerase I poisoning results in PARP-mediated replication fork reversal. *Nature structural & molecular biology* **19**: 417-423
- Regairaz M, Zhang YW, Fu H, Agama KK, Tata N, Agrawal S, Aladjem MI, Pommier Y (2011) Mus81-mediated DNA cleavage resolves replication forks stalled by topoisomerase I-DNA complexes. *The Journal of cell biology* **195**: 739-749
- Rehman I, Basu SM, Das SK, Bhattacharjee S, Ghosh A, Pommier Y, Das BB (2018) PRMT5-mediated arginine methylation of TDP1 for the repair of topoisomerase I covalent complexes. *Nucleic Acids Research* **46**: 5601-5617
- Rialdi A, Campisi L, Zhao N, Lagda AC, Pietzsch C, Ho JSY, Martinez-Gil L, Fenouil R, Chen X, Edwards M, Metreveli G, Jordan S, Peralta Z, Munoz-Fontela C, Bouvier N, Merad M, Jin J, Weirauch M, Heinz S, Benner C, van Bakel H, Basler C, García-Sastre A, Bukreyev A, Marazzi I (2016) Topoisomerase 1 inhibition suppresses inflammatory genes and protects from death by inflammation. *Science (New York, NY)* **352**: aad7993

- Rodgers K, McVey M (2016) Error-Prone Repair of DNA Double-Strand Breaks. *Journal of cellular physiology* **231**: 15-24
- Roy A, Das BB, Ganguly A, Bose Dasgupta S, Khalkho NV, Pal C, Dey S, Giri VS, Jaisankar P, Dey S, Majumder HK (2008) An insight into the mechanism of inhibition of unusual bi-subunit topoisomerase I from *Leishmania donovani* by 3,3'-di-indolylmethane, a novel DNA topoisomerase I poison with a strong binding affinity to the enzyme. *The Biochemical journal* **409**: 611-622
- Sander M, Nolan JM, Hsieh T (1984) A protein kinase activity tightly associated with *Drosophila* type II DNA topoisomerase. *Proceedings of the National Academy of Sciences of the United States of America* **81**: 6938-6942
- Satyanarayana A, Berthet C, Lopez-Molina J, Coppola V, Tessarollo L, Kaldis P (2008) Genetic substitution of Cdk1 by Cdk2 leads to embryonic lethality and loss of meiotic function of Cdk2. *Development (Cambridge, England)* **135**: 3389-3400
- Sekiguchi J, Cheng C, Shuman S (2000) Resolution of a Holliday junction by vaccinia topoisomerase requires a spacer DNA segment 3' of the CCCTT/ cleavage sites. *Nucleic Acids Res* **28**: 2658-2663
- Sekiguchi J, Seeman NC, Shuman S (1996) Resolution of Holliday junctions by eukaryotic DNA topoisomerase I. *Proceedings of the National Academy of Sciences of the United States of America* **93**: 785-789
- Sen N, Das BB, Ganguly A, Banerjee B, Sen T, Majumder HK (2006) *Leishmania donovani*: intracellular ATP level regulates apoptosis-like death in luteolin induced dyskinetoplastid cells. *Experimental parasitology* **114**: 204-214
- Sen N, Das BB, Ganguly A, Mukherjee T, Bandyopadhyay S, Majumder HK (2004a) Camptothecin-induced imbalance in intracellular cation homeostasis regulates programmed cell death in unicellular hemoflagellate *Leishmania donovani*. *The Journal of biological chemistry* **279**: 52366-52375
- Sen N, Das BB, Ganguly A, Mukherjee T, Tripathi G, Bandyopadhyay S, Rakshit S, Sen T, Majumder H (2004b) Camptothecin induced mitochondrial dysfunction leading to programmed cell death in unicellular hemoflagellate *Leishmania donovani*. *Cell Death & Differentiation* **11**: 924-936
- Shadab M, Jha B, Asad M, Deepthi M, Kamran M, Ali N (2017) Apoptosis-like cell death in *Leishmania donovani* treated with KalsomeTM10, a new liposomal amphotericin B. *PLoS One* **12**
- Shaiu WL, Hsieh TS (1998) Targeting to transcriptionally active loci by the hydrophilic N-terminal domain of *Drosophila* DNA topoisomerase I. *Molecular and cellular biology* **18**: 4358-4367

- Shapiro TA, Englund PT (1995) The structure and replication of kinetoplast DNA. *Annu Rev Microbiol* **49**: 117-143
- Shoaib M, Nair N, Sørensen CS (2020) Chromatin Landscaping At Mitotic Exit Orchestrates Genome Function. *Frontiers in Genetics* **11**
- Shorokhova M, Nikolsky N, Grinchuk T (2021) Chromothripsis-Explosion in Genetic Science. *Cells* **10**
- Simpson L, Thiemann OH, Savill NJ, Alfonzo JD, Maslov DA (2000) Evolution of RNA editing in trypanosome mitochondria. *Proceedings of the National Academy of Sciences of the United States of America* **97**: 6986-6993
- Song Y, Shao Z, Dexheimer TS, Scher ES, Pommier Y, Cushman M (2010) Structure-based design, synthesis, and biological studies of new anticancer norindenoisoquinoline topoisomerase I inhibitors. *Journal of medicinal chemistry* **53**: 1979-1989
- Spell RM, Holm C (1994) Nature and distribution of chromosomal intertwinings in *Saccharomyces cerevisiae*. *Molecular and cellular biology* **14**: 1465-1476
- Stewart L, Ireton GC, Champoux JJ (1996) The domain organization of human topoisomerase I. *The Journal of biological chemistry* **271**: 7602-7608
- Stewart L, Redinbo MR, Qiu X, Hol WG, Champoux JJ (1998) A model for the mechanism of human topoisomerase I. *Science (New York, NY)* **279**: 1534-1541
- Stivison EA, Young KJ, Symington LS (2020) Interstitial telomere sequences disrupt break-induced replication and drive formation of ectopic telomeres. *Nucleic Acids Res* **48**: 12697-12710
- Sundar S, Chakravarty J (2010) Liposomal amphotericin B and leishmaniasis: dose and response. *Journal of global infectious diseases* **2**: 159-166
- Takashima H, Boerkoel CF, John J, Saifi GM, Salih MA, Armstrong D, Mao Y, Quiocho FA, Roa BB, Nakagawa M, Stockton DW, Lupski JR (2002) Mutation of TDP1, encoding a topoisomerase I-dependent DNA damage repair enzyme, in spinocerebellar ataxia with axonal neuropathy. *Nature genetics* **32**: 267-272
- Tan KB, Dorman TE, Falls KM, Chung TD, Mirabelli CK, Crooke ST, Mao J (1992) Topoisomerase II alpha and topoisomerase II beta genes: characterization and mapping to human chromosomes 17 and 3, respectively. *Cancer research* **52**: 231-234

- Tang D (1978) Purification of a DNA nicking-closing enzyme from mouse L cells. *Nucleic Acids Research* **5**: 2861-2876
- Torres-Guerrero E, Quintanilla-Cedillo MR, Ruiz-Esmenjaud J, Arenas R (2017) Leishmaniasis: a review. *F1000Res* **6**: 750-750
- Tsai-Pflugfelder M, Liu LF, Liu AA, Tewey KM, Whang-Peng J, Knutsen T, Huebner K, Croce CM, Wang JC (1988) Cloning and sequencing of cDNA encoding human DNA topoisomerase II and localization of the gene to chromosome region 17q21-22. *Proceedings of the National Academy of Sciences of the United States of America* **85**: 7177-7181
- Tse-Dinh YC, Beran RK (1988) Multiple promoters for transcription of the Escherichia coli DNA topoisomerase I gene and their regulation by DNA supercoiling. *J Mol Biol* **202**: 735-742
- Tsutsui K, Tsutsui K, Okada S, Watanabe M, Shohmori T, Seki S, Inoue Y (1993) Molecular cloning of partial cDNAs for rat DNA topoisomerase II isoforms and their differential expression in brain development. *The Journal of biological chemistry* **268**: 19076-19083
- Tuduri S, Crabbé L, Conti C, Tourrière H, Holtgreve-Grez H, Jauch A, Pantesco V, De Vos J, Thomas A, Theillet C, Pommier Y, Tazi J, Coquelle A, Pasero P (2009) Topoisomerase I suppresses genomic instability by preventing interference between replication and transcription. *Nature cell biology* **11**: 1315-1324
- Uhlorn BL, Gamez ER, Li S, Campos SK (2020) Attenuation of cGAS/STING activity during mitosis. **3**
- Vance JR, Wilson TE (2002) Yeast Tdp1 and Rad1-Rad10 function as redundant pathways for repairing Top1 replicative damage. *Proceedings of the National Academy of Sciences of the United States of America* **99**: 13669-13674
- Vinograd J, Lebowitz J, Radloff R, Watson R, Laipis P (1965) The twisted circular form of polyoma viral DNA. *Proceedings of the National Academy of Sciences* **53**: 1104-1111
- Vosberg HP (1985) DNA topoisomerases: enzymes that control DNA conformation. *Current topics in microbiology and immunology* **114**: 19-102
- Vosberg HP, Grossman LI, Vinograd J (1975) Isolation and partial characterisation of the relaxation protein from nuclei of cultured mouse and human cells. *European journal of biochemistry* **55**: 79-93
- Wallis JW, Chrebet G, Brodsky G, Rolfe M, Rothstein R (1989) A hyper-recombination mutation in *S. cerevisiae* identifies a novel eukaryotic topoisomerase. *Cell* **58**: 409-419

- Wang JC (1971) Interaction between DNA and an Escherichia coli protein ω . *Journal of Molecular Biology* **55**: 523-516
- Wang JC (1996) DNA topoisomerases. *Annual review of biochemistry* **65**: 635-692
- Wang JC (2002) Cellular roles of DNA topoisomerases: a molecular perspective. *Nature reviews Molecular cell biology* **3**: 430-440
- Wassermann K, Markovits J, Jaxel C, Capranico G, Kohn KW, Pommier Y (1990) Effects of morpholinyl doxorubicins, doxorubicin, and actinomycin D on mammalian DNA topoisomerases I and II. *Molecular Pharmacology* **38**: 38-45
- Wiegard A, Kuzin V, Cameron DP, Grosser J, Ceribelli M, Mehmood R, Ballarino R, Valant F, Grochowski R, Karabogdan I, Crosetto N, Lindqvist A, Bizard AH, Kouzine F, Natsume T, Baranello L (2021) Topoisomerase 1 activity during mitotic transcription favors the transition from mitosis to G1. *Mol Cell* **81**: 5007-5024.e5009
- Wu X, Wang B (2021) Abraxas suppresses DNA end resection and limits break-induced replication by controlling SLX4/MUS81 chromatin loading in response to TOP1 inhibitor-induced DNA damage. *Nature Communications* **12**: 4373
- Yang SW, Burgin AB, Jr., Huizenga BN, Robertson CA, Yao KC, Nash HA (1996) A eukaryotic enzyme that can disjoin dead-end covalent complexes between DNA and type I topoisomerases. *Proceedings of the National Academy of Sciences of the United States of America* **93**: 11534-11539
- Yu D, Khan E, Khaleque MA, Lee J, Laco G, Kohlhagen G, Kharbanda S, Cheng YC, Pommier Y, Bharti A (2004) Phosphorylation of DNA topoisomerase I by the c-Abl tyrosine kinase confers camptothecin sensitivity. *The Journal of biological chemistry* **279**: 51851-51861
- Yu J, Shannon WD, Watson MA, McLeod HL (2005) Gene expression profiling of the irinotecan pathway in colorectal cancer. *Clinical cancer research : an official journal of the American Association for Cancer Research* **11**: 2053-2062
- Zhang CX, Chen AD, Gettel NJ, Hsieh TS (2000) Essential functions of DNA topoisomerase I in *Drosophila melanogaster*. *Developmental biology* **222**: 27-40
- Zhang H, Barceló JM, Lee B, Kohlhagen G, Zimonjic DB, Popescu NC, Pommier Y (2001) Human mitochondrial topoisomerase I. *Proceedings of the National Academy of Sciences of the United States of America* **98**: 10608-10613

Zhang H, Xiong Y, Su D, Wang C, Srivastava M, Tang M, Feng X, Huang M, Chen Z, Chen J (2022) TDP1-independent pathways in the process and repair of TOP1-induced DNA damage. *Nature Communications* **13**: 4240

Zhao L-X, Moon Y-S, Basnet A, Kim E-k, Jahng Y, Park JG, Jeong TC, Cho W-J, Choi S-U, Lee CO, Lee S-Y, Lee C-S, Lee E-S (2004) Synthesis, topoisomerase I inhibition and structure–activity relationship study of 2,4,6-trisubstituted pyridine derivatives. *Bioorganic & Medicinal Chemistry Letters* **14**: 1333-1337

Zhou BB, Elledge SJ (2000) The DNA damage response: putting checkpoints in perspective. *Nature* **408**: 433-439



Publications
&
Proceedings

1. **Chowdhuri, S.P.** and Das, BB, 2023. Phosphorylation of TDP1 at Serine 61 by CDK1 promotes genomic stability by preventing its trapping on mitotic chromosome. (Manuscript under preparation)
2. **Chowdhuri, S.P.**, Dhiman, S., Das, S.K., Meena, N., Das, S., Kumar, A. and Das, B.B., 2023. Novel pyrido [2', 1': 2, 3] imidazo [4, 5-c] quinoline derivative selectively poisons leishmania donovani bisubunit topoisomerase 1 to inhibit the antimony-resistant leishmania infection in vivo. *Journal of Medicinal Chemistry*, 66(5), pp.3411-3430.
3. Chowdhury, S.R., Das, S.K., Banerjee, B., **Paul Chowdhuri, S.**, Majumder, H.K. and Das, B.B., 2022. TDP1 knockout Leishmania donovani accumulate topoisomerase 1-linked DNA damage and are hypersensitive to clinically used antileishmanial drugs. *The FASEB Journal*, 36(4), p.e22265.
4. **Chowdhuri, S.P.** and Das, B.B., 2021. Top1-PARP1 association and beyond: from DNA topology to break repair. *Nar Cancer*, 3(1), p.zcab003.
5. Kundu, B*., Sarkar, D*., **Chowdhuri, S.P*.**, Pal, S., Das, S.K., Das, B.B. and Talukdar, A., 2020. Development of a metabolically stable topoisomerase I poison as anticancer agent. *European Journal of Medicinal Chemistry*, 202, p.112551. (***equal contribution**)
6. Kundu, B*., Das, S.K*., **Paul Chowdhuri*., S.**, Pal, S., Sarkar, D., Ghosh, A., Mukherjee, A., Bhattacharya, D., Das, B.B. and Talukdar, A., 2019. Discovery and mechanistic study of tailor-made quinoline derivatives as topoisomerase 1 poison with potent anticancer activity. *Journal of Medicinal Chemistry*, 62(7), pp.3428-3446. (***equal contribution**)
7. Ghosh, A., Bhattacharjee, S., **Chowdhuri, S.P.**, Mallick, A., Rehman, I., Basu, S. and Das, B.B., 2019. SCAN1-TDP1 trapping on mitochondrial DNA promotes mitochondrial dysfunction and mitophagy. *Science Advances*, 5(11), p.eaax9778.
8. Das, S.K., Ghosh, A., **Paul Chowdhuri, S.**, Halder, N., Rehman, I., Sengupta, S., Sahoo, K.C., Rath, H. and Das, B.B., 2018. Neutral porphyrin derivative exerts anticancer activity by targeting cellular topoisomerase I (Top1) and promotes apoptotic cell death without stabilizing Top1-DNA cleavage complexes. *Journal of Medicinal Chemistry*, 61(3), pp.804-817.
9. De, A., Bala, S., Saha, S., Das, K.S., Akhtar, S., Adhikary, A., Ghosh, A., Huang, G.Z., **Chowdhuri, S.P.**, Das, B.B. and Tong, M.L., 2021. Lanthanide clusters of phenanthroline containing a pyridine-pyrazole based ligand: magnetism and cell imaging. *Dalton Transactions*, 50(10), pp.3593-3609.
10. Bhowal, S., Ghosh, A., **Chowdhuri, S.P.**, Mondal, R. and Das, B.B., 2018. A novel metallogel based approach to synthesize (Mn, Cu) doped ZnS quantum dots and labeling of MCF-7 cancer cells. *Dalton Transactions*, 47(18), pp.6557-6569.

Poster & Oral presentation:

1. Presented a poster entitled “Neutral Porphyrin Derivative Exerts Anticancer Activity by Targeting Cellular Topoisomerase I (Top1) and Promotes Apoptotic Cell Death without Stabilizing Top1-DNA Cleavage Complexes” at the international symposium on “An Interdisciplinary Approach To Biological Sciences” (IABS-2018) held at Indian Association for the Cultivation of Science (IACS), Kolkata, India, on February 1-3, 2018.
2. Presented a poster entitled “Discovery and Mechanistic Study of Tailor-Made Quinoline Derivatives as Topoisomerase 1 Poison with Potent Anticancer Activity” at the symposium organized by the Society of Biological Chemist Society (SBC-Kolkata Chapter) held at Indian Institute for Chemical Biology (IICB), Kolkata, India, in 2019.
3. Selected to Present a poster entitled “Discovery and Mechanistic Study of Tailor-Made Quinoline Derivatives as Topoisomerase 1 Poison with Potent Anticancer Activity” at the American Chemical Society (Spring) Meet that was scheduled to be held at Philadelphia, USA in 2020 but got cancelled due to COVID19. Received the DST-International Travel Support to attend the Conference.
4. Delivered an oral presentation entitled “Novel Pyrido[2',1':2,3]imidazo[4,5-c]quinoline Derivative Selectively Poisons *Leishmania donovani* Bisubunit Topoisomerase 1 to Inhibit the Antimony-Resistant *Leishmania* Infection *in Vivo*” at School of Biological Chemists (Kolkata Chapter) held at Sister Nivedita University, Kolkata in 2022.
5. Presented a poster entitled “TDP1 knockout *Leishmania donovani* accumulate Topoisomerase 1-linked DNA damage and are hypersensitive to clinically used antileishmanial drugs” at Gordon Research Conference on Genomic Instability, DNA repair and Human Diseases held at Ventura, California, USA held in July 2022. Received the IACS international travel award for attending the conference.
6. Delivered an oral presentation and presented a poster entitled “Novel Pyrido [2',1':2,3] imidazo [4,5-c] quinoline Derivative Selectively Poisons *Leishmania donovani* Bisubunit Topoisomerase 1 to Inhibit the Antimony-Resistant *Leishmania* Infection *in Vivo*” at Gordon Research Conference on “DNA Topoisomerases in Biology and Medicine” held at Bryant University, Smithfield, Rhode Island, USA from 7th to 12th August 2022. Received the DST-International Travel Support and the GRC travel awards for attending the conferences.
7. Presented a poster entitled “CDK1 mediated phosphorylation of TDP1 at S61 promotes repair of trapped Top1ccs during mitosis” at the international symposium on “An Interdisciplinary Approach To Biological Sciences” (IABS-2023) held at Indian Association for the Cultivation of Science (IACS), Kolkata, India, on February 1-3, 2023. **(Best poster award)**.

Novel Pyrido[2',1':2,3]imidazo[4,5-c]quinoline Derivative Selectively Poisons *Leishmania donovani* Bisubunit Topoisomerase 1 to Inhibit the Antimony-Resistant *Leishmania* Infection *in Vivo*

Srijita Paul Chowdhuri, Shiv Dhiman, Subhendu K. Das, Neha Meena, Sonali Das, Anil Kumar,* and Benu Brata Das*

Cite This: *J. Med. Chem.* 2023, 66, 3411–3430

Read Online

ACCESS |



Metrics & More

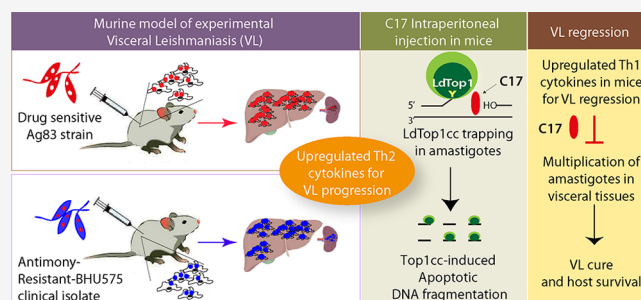


Article Recommendations



Supporting Information

ABSTRACT: The unique bisubunit structure of *Leishmania donovani* topoisomerase 1B (LdTop1) is a potential drug target in the parasites unlike the monomeric Top1 from its human host counterpart. Here, we report the design, synthesis, and validation of a chimeric pyrido[2',1':2,3]imidazo[4,5-c]quinoline derivative (C17) as a novel antileishmanial agent that poisons topoisomerase 1-DNA covalent complexes (LdTop1cc) inside the parasites and inhibits Top1 religation activity both in the drug sensitive and antimony-resistant *L. donovani* clinical isolates. Importantly, the human Top1 is not sensitive to C17. Further, C17 overcomes the chemical instability of camptothecin (CPT) by generating persistent LdTop1cc-induced DNA breaks inside the parasites even after 12 h of drug removal. Intraperitoneal administration of C17 results in marked reduction of the *Leishmania* amastigotes from the infected spleen and liver of BALB/c mice. C17 confers a host protective immune-response up-regulating the Th1 cytokines facilitating parasite clearance which can be exploited for treating drug-resistant leishmaniasis.



INTRODUCTION

Leishmania donovani is an obligate intracellular protozoan parasite that contributes to an annual estimate of 50,000 to 90,000 new cases of kala-azar or Visceral leishmaniasis (VL), worldwide in 98 countries with 350 million people at risk of infection.^{1,2} *Leishmania* propels an immune-suppressive infection in the host by colonizing within macrophages, followed by trans-differentiation from the extracellular insect gut form promastigotes to the intracellular amastigote stage.^{3,4} The broad spectrum of clinical manifestations¹ includes localized cutaneous leishmaniasis characterized by ulcerative skin lesions, damaging mucosal inflammation, and disseminated systemic visceral infection.⁵ Pentavalent antimonials or sodium stibogluconate are no longer recommended owing to their toxicity and high levels of resistance in the Indian subcontinent.^{6–10} Alternatively, other drugs like the orally active polyene antibiotic miltefosine (hexadecyl phosphocholine) shows clinical limitations that include potential fetotoxicity, nausea, vomiting, and other adverse side effects, while the currently used liposomal formulation of an antifungal agent amphotericin B is restricted by severe nephrotoxicity which raise serious concerns for their future applications.¹⁰ The lack of effective drugs, vaccines against any form of human leishmaniasis, and emerging cases of drug-resistant strains call for immediate identification of new molecular targets for antileishmanial therapy.^{5,6,9,11}

DNA topoisomerases are essential enzymes that regulate DNA topology by catalyzing the nicking and resealing of DNA strands to facilitate relaxation of supercoiling generated during the DNA metabolic processes.^{12,13} Unlike the other type IB eukaryotic topoisomerases, *Leishmania* topoisomerase 1B (LdTop1) is a heterodimeric enzyme (Figure 1A) with the core DNA binding domain 'VAILCNH' located on the large subunit (LdTOP1L, 635 amino acids) and catalytic domain harboring the consensus catalytic 'SKXXY' motif on the small subunit (LdTOP1S, 262 amino acids).^{14–17} The two subunits are encoded by two different genes, which associate with each other through protein–protein interactions to form an active heterodimeric Top1 (LdTop1) within the parasite.¹⁸ Therefore, LdTop1 bisubunit could be exploited as a novel drug target for the treatment of leishmaniasis, which is starkly distinct from the monosubunit human counterpart.^{15,17} Camptothecin (CPT), the human Top1B poison, has already been reported to inhibit LdTop1B *in vitro* and induce

Received: November 25, 2022

Published: February 24, 2023



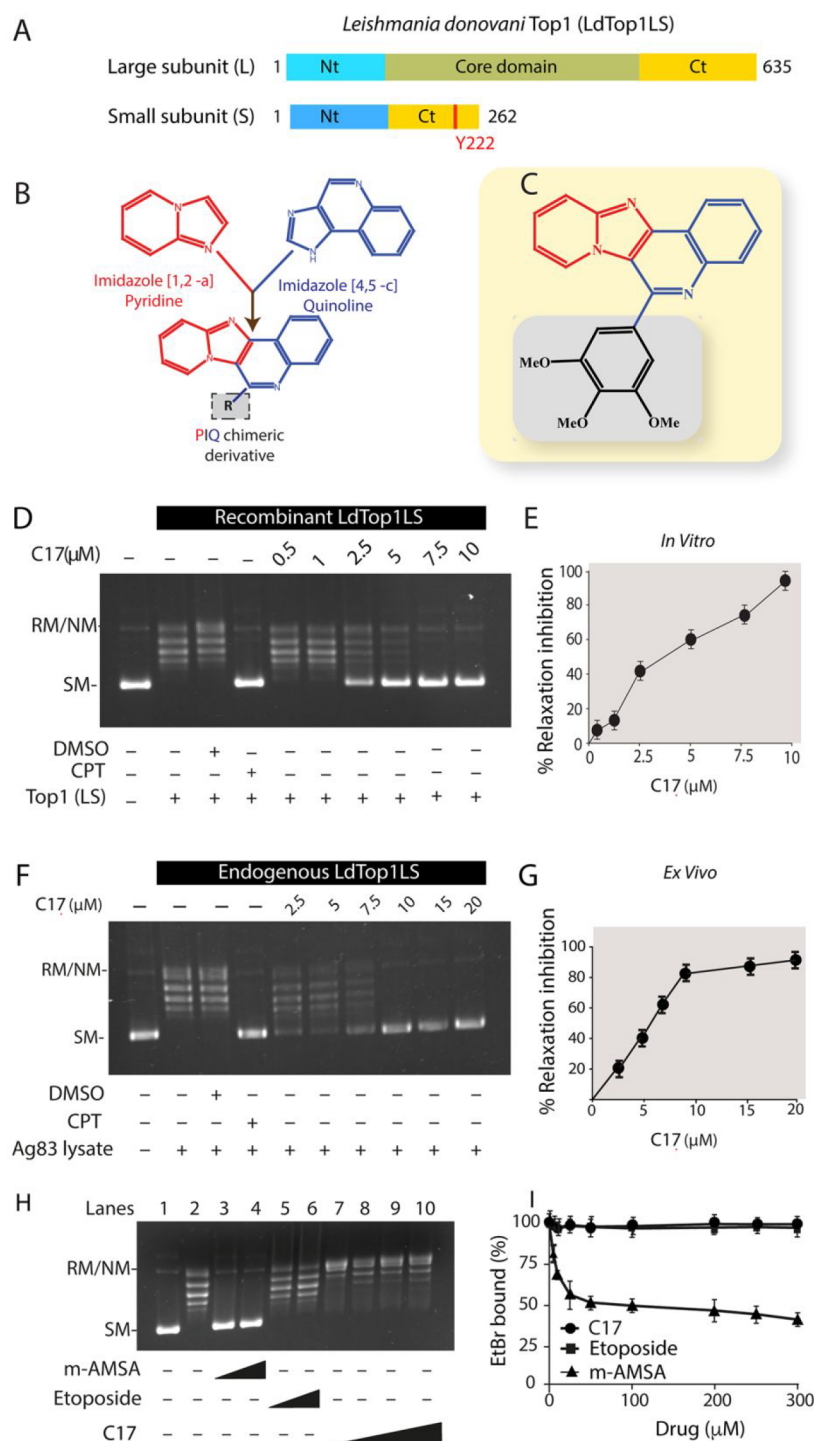
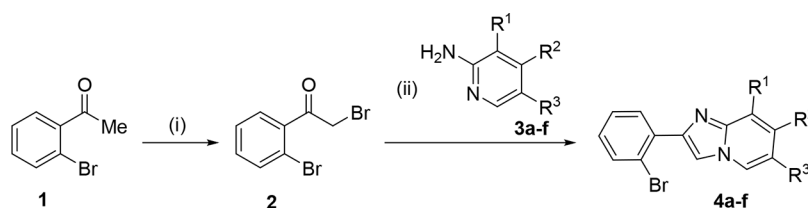


Figure 1. Inhibition of *Leishmania donovani* Top1-induced plasmid DNA relaxation activity by C17. (A) Schematic representation of the large and small subunits of the *Leishmania donovani* heterodimeric bisubunit Top1 (LdTop1LS) enzyme. The catalytic residue (Y222) in the small subunit is indicated. (B) Design for the synthesis of the chimeric PIQ derivatives from the parental imidazo[1,2-*a*]pyridine and imidazo[4,5-*c*]quinoline molecules with different substitutions in the “R” group. (C) Structure of the “R” group for the most active compound C17. (D) Relaxation assays of supercoiled plasmid DNA using recombinant LdTop1LS at 3:1 molar ratio. Lane 1, pBS (SK+) DNA (90 fmol); lane 2, same as lane 1 but incubated with 30 fmol of recombinant LdTop1LS; lane 3, same as lane 2, additionally Top1 was incubated with 2% DMSO as the solvent control; lane 4, same as lane 2 but incubated simultaneously with 50 μM CPT; lanes 5–10, same as lane 2 but incubated with increasing concentrations of C17 as indicated, at 37 °C for 30 min. Positions of supercoiled monomer (SM) and nicked and relaxed monomer (RM) are indicated. (E) Quantitative representation of inhibition (%) of recombinant LdTop1 at variable concentrations of C17 in plasmid DNA relaxation assays. The experiments were performed in triplicate and expressed as the mean ± SD. (F) Relaxation of supercoiled pBS (SK+) DNA by endogenous Top1 from the *Leishmania* Ag83 cellular extract (each reaction volume contains 0.1 μg protein). Lane 1, pBS (SK+) DNA (0.3 μg); lane 2, same as lane 1, but DNA was incubated with Ag83 cell lysates; lane 3, same as lane 2 but incubated with 2% DMSO; lanes 4–10, same as lane 2, but Ag83 whole cell lysates were incubated simultaneously with 50 μM CPT or with increasing concentrations of C17 (as indicated) together with plasmid DNA at 37 °C for 30 min. (G) Quantitative representation of endogenous Top1 DNA relaxation inhibition (%) at variable concentrations of C17. The

Figure 1. continued

experiments were performed in triplicate and expressed as the mean \pm SD. (H) C17–DNA interaction as investigated by agarose gel electrophoresis in Top1 relaxation assays. Lane 1, 50 fmol of pBS (SK+) DNA. Lane 2, relaxed pBS (SK+) DNA generated by incubation with a molar excess of Top1. Lanes 3–4, same as lane 2 but incubated with 25 and 50 μ M m-amsacrine (AMSA); Lanes 5–6, same as lane 2 but incubated with 100 and 200 μ M etoposide; Lanes 7–10, same as lane 2 but incubated with 20, 50, 100, and 200 μ M C17 as indicated. (I) Fluorescence-based ethidium bromide (EtBr) displacement assay. All samples contained 1 μ M EtBr and 5 nM calf thymus (CT) DNA in the presence or absence of the indicated drugs. Graphical representation of the percentage of bound EtBr with increasing concentration (0–300 μ M) of C17, m-AMSA, and etoposide. EtBr fluorescence was monitored with an excitation wavelength of 510 nm and an emission wavelength of 590 nm.

Scheme 1. Synthesis of 2-(2'-Bromophenyl)imidazo[1,2-a]pyridines^a



^aReagents and conditions: (i). 1 (1.0 eq.), NBS (1.0 eq.), *p*-TsOH (0.10 eq.), acetonitrile, 80 °C, 4 h; (ii). 2 (1.0 eq.), 3 (1.0 eq.), NaHCO₃ (1.5 eq.), ethanol, 80 °C, 12 h.

cytotoxicity in *Leishmania donovani* promastigotes and amastigotes leading to apoptosis.¹⁹ CPT promotes the formation of protein–DNA adducts both with the nuclear as well as kinetoplast DNA of *Leishmania* and *Trypanosoma* parasites.^{16,19,20} However, there are several limitations associated with CPT including the chemical instability of the CPT alpha-hydroxy-lactone ring and loss of efficacy due to the drug efflux-mediated resistance generation,^{21–24} as well as its dose-limiting cytotoxicity.²¹

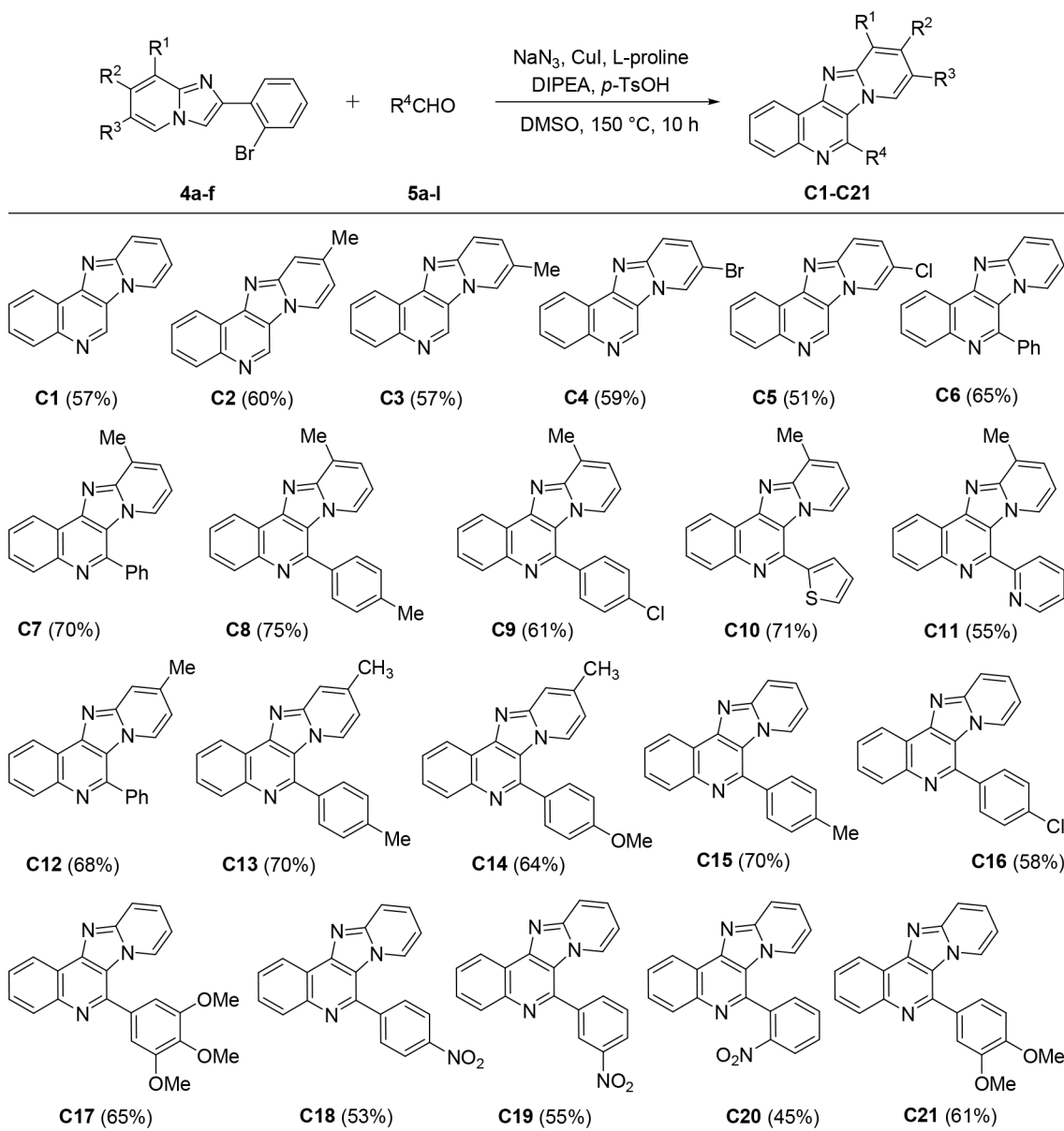
Noncamptothecin compounds like pyridine derivatives have a broad range of pharmaceutical properties that strengthen their medicinal application as antileishmanial, antiviral, antimalarial, and anticancer agents.^{25,26} Pyridine derivatives have also been reported to target the Top1 enzyme.²⁷ The quinoline core structure is shared by CPT and its clinically approved derivatives like topotecan and irinotecan which have anticancer activities.^{23,24,28–30} Moreover, imidazole groups represent broad non-CPT based Top1 inhibitors like indotecan, indimitecan, and other indenoisoquinolines^{31–33} derivatives which are in clinical trials as anticancer agents.^{23,24,28} Therefore, we rationalized that a pyrido[2',1':2,3]imidazo[4,5-*c*]quinoline (PIQ) derivative harboring the pyridine, imidazole, and quinoline scaffolds could potentially target the unique heterodimeric bisubunit Top1 enzyme of the *Leishmania donovani*.

In the present study, we report the characterization and validation of a novel class of chimeric compounds based on the pyrido[2',1':2,3]imidazo[4,5-*c*]quinoline (PIQ) core identified through the structural features of known ligands (Figure 1B) and tested their potential role in the inhibition of *Leishmania* Top1 activity. The structure–activity relationships (SAR) of the twenty compounds resulting from the parental structure of the PIQ core suggested that compound C17 is the most potent LdTop1 inhibitor both in the *in vitro* and *ex vivo* DNA relaxations assays (Table 2). C17 inhibits the growth of both the antimony-resistant field isolate of *Leishmania* (BHUS75) which is also known to be less susceptible toward the clinically used antileishmanials like sodium stibogluconate (SSG), miltefosine, paromomycin, and amphotericin B,³⁴ as well as the wild-type drug-responsive strain (Ag83) by targeting

LdTop1. C17 did not inhibit the activity of human monomeric Top1 which further exalts its promise as a selective antileishmanial drug candidate. C17 poisons LdTop1–DNA covalent complex's (LdTop1cc) formation in the parasites leading to the accumulation of apoptotic DNA breaks that was evidenced by *in vitro* biochemical assays coupled with microscopic examination and *in vivo* studies. Furthermore, administration of C17 by intraperitoneal route results in marked reduction of the *Leishmania* amastigotes burden from the wildtype and antimony-resistant BHUS75 parasite-infected spleen and liver of BALB/c mice implicating a new drug candidate against drug-resistant leishmaniasis.

CHEMISTRY

Initially, 2-(2'-bromophenyl)imidazo[1,2-*a*]pyridines (4) were synthesized starting from 2'-bromoacetophenone (1) according to published procedure^{35,36} (Scheme 1). Next, a series of experiments were performed to optimize the reaction conditions for the synthesis of pyrido[2',1':2,3]imidazo[4,5-*c*]quinolines by taking 2-(2'-bromophenyl)imidazo[1,2-*a*]pyridine (4a), 4-methylbenzaldehyde (5c), and sodium azide as model substrates. The best yield of the desired product, 6-(*p*-tolyl)pyrido[[2',1':2,3]imidazo[4,5-*c*]quinoline (C8) was obtained by using CuI (20 mol%), L-proline (30 mol%), *p*-TsOH (0.5 eq.), and *N,N*-diisopropylethylamine (DIPEA) (1.0 eq.) in DMSO at 150 °C after 10 h (Table S2, entry 11, see Supporting Information). With the optimized conditions in hand, we synthesized a series of pyrido[[2',1':2,3]imidazo[4,5-*c*]quinolines (C1–C21) in moderate to good (45–75%) yields from the reaction of 4a–f with aldehydes 5a–I and sodium azide (Table 1). Aldehydes with electron-withdrawing groups produced desired products in lower yields as compared with the aldehydes having electron donating groups. Interestingly, heteroaryl aldehydes, such as thiophene-2-carbaldehyde and 2-picolinaldehyde, were well tolerated under the optimized conditions and gave corresponding products C10 and C11 in 71% and 55% yields, respectively. All compounds are >95% pure by HPLC analysis.

Table 1. Synthesis of Pyrido[[2',1':2,3]imidazo[4,5-c]quinoline Derivatives (C1–C21)^a

^aReagents and conditions: **4** (0.366 mmol), **5** (0.439 mmol) NaN_3 (0.549 mmol), CuI (20 mol%), L-proline (30 mol%), *p*-TsOH (0.183 mmol), DIPEA (0.366 mmol), DMSO, 150 °C, air atmosphere, 10 h. Numbers in parentheses are isolated yields.

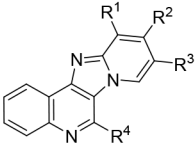
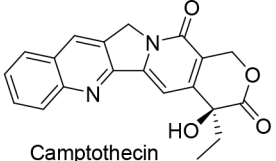
RESULTS AND DISCUSSION

To test the inhibitory effect of the synthetic library of pyrido[[2',1':2,3]imidazo[4,5-c]quinoline compounds on LdTop1 activity, we performed the *in vitro* and *ex vivo* plasmid DNA relaxation assays in standard assay conditions using either recombinant LdTop1 or the Ag83 lysates as the source of endogenous LdTop1. Table 2 shows inhibitory patterns of the LdTop1 mediated relaxation of supercoiled plasmid DNA with the different derivatives of the PIQ compounds (C1–C21) with relative efficiencies of LdTop1 inhibition as a measure of their effective drug concentrations (IC_{50} value), indicating the highest activity for the selected PIQ derivative compound C17.

C17 Poisons the *Leishmania* Top1–DNA Cleavage Complexes without Intercalating with DNA. To evaluate the inhibitory activity of C17 toward the bisubunit LdTop1,

we performed the plasmid DNA relaxation assays using both the recombinant LdTop1 enzyme (Figure 1D) and endogenous LdTop1 from the whole-cell extracts of *Leishmania donovani* Ag83 strain (Figure 1F). When LdTop1 and C17 were added simultaneously to the plasmid DNA in the relaxation assays, C17 inhibited the plasmid DNA relaxation activity of LdTop1 in a dose-dependent manner (Figure 1D, lanes 5–10), with 85–90% inhibition of Top1 achieved at 5 μM concentration of C17 (Figure 1D, lane 8, see the quantification in 1E). Accordingly, the *ex vivo* plasmid DNA relaxation assay using Ag83 cellular lysate as a source of endogenous LdTop1 (Figure 1F) was inhibited to ~85% at 10 μM concentration of C17 (Figure 1F, lane 8 and see the quantification in 1G). Additionally, to investigate whether C17 interacts with the free enzyme, we preincubated C17 with recombinant or endogenous LdTop1 for 5 min. at 37 °C before the addition of substrate plasmid DNA. We observed no

Table 2. Half Maximal Inhibitory Concentrations (IC₅₀) of Screened PIQ Derivatives (C1–C21) on the *Leishmania donovani* Top1 Mediated Plasmid DNA Relaxation Inhibition

Compound					Top1 inhibition IC ₅₀ (μM)		Activity index ^a
					<i>In vitro</i>	<i>Ex vivo</i>	
							
	R¹	R²	R³	R⁴			
C1	H	H	H	H	>10	NT ^b	+
C2	H	CH ₃	H	H	>10	NT ^b	+
C3	H	H	CH ₃	H	>10	NT ^b	+
C4	H	H	Br	H	>10	NT ^b	+
C5	H	H	Cl	H	>10	NT ^b	+
C6	H	H	H	C ₆ H ₅	>10	NT ^b	+
C7	CH ₃	H	H	C ₆ H ₅	6.75 ± 0.211	12.75 ± 0.117	++
C8	CH ₃	H	H	4-MeC ₆ H ₄	7.25 ± 0.018	15.06 ± 0.811	++
C9	CH ₃	H	H	4-ClC ₆ H ₄	5.5 ± 0.022	12.5 ± 0.314	++
C10	CH ₃	H	H	2-thienyl	7.25 ± 0.078	14.9 ± 0.036	++
C11	CH ₃	H	H	2-pyridyl	>10	NT ^b	+
C12	H	CH ₃	H	C ₆ H ₅	>10	NT ^b	+
C13	H	CH ₃	H	4-MeC ₆ H ₄	>10	NT ^b	+
C14	H	CH ₃	H	4-MeOC ₆ H ₄	>10	NT ^b	+
C15	H	H	H	4-MeC ₆ H ₄	>10	NT ^b	+
C16	H	H	H	4-ClC ₆ H ₄	8.52 ± 0.014	NT ^b	++
C17	H	H	H	3,4,5-(MeO) ₃ C ₆ H ₂	3.75 ± 0.122	6.5 ± 0.34	+++
C18	H	H	H	4-NO ₂ C ₆ H ₄	>10	NT ^b	+
C19	H	H	H	3-NO ₂ C ₆ H ₄	>10	NT ^b	+
C20	H	H	H	2-NO ₂ C ₆ H ₄	>10	NT ^b	+
C21	H	H	H	3,4-(MeO) ₂ C ₆ H ₃	5.25 ± 0.261	11.95 ± 0.611	++
 Camptothecin					9.2 ± 0.148	21.91 ± 0.125	++

^aCompound-induced *in vitro* inhibition of Top1 with scores given according to the following system based on the activity of camptothecin: + = IC₅₀ > 10 μM; ++ = IC₅₀ in between 5 μM and 10 μM; +++ = IC₅₀ in between 2 μM and 5 μM; ^bNT = not tested.

significant increment in the inhibition pattern of LdTop1 in the preincubation as compared to simultaneous incubation of C17 with LdTop1 in the plasmid DNA relaxation inhibition assays (Figure S1A–D), suggesting C17 might not interact with the free enzyme.^{37,38} Notably, C17 was ~2.5 fold more potent in inhibiting LdTop1-mediated DNA relaxation activities when compared with CPT (Figure S1E; Table 2). Further, C17 failed to inhibit the plasmid DNA relaxation activities (Figure S1F–G, lanes 4–8) and stabilize the cleavage complexes (Figure S1H–I) with recombinant human Top1 even at 10-fold molar excess of C17. Consequently, the relative extent of C17-mediated LdTop1 inhibition was increased by ~2.5 fold (IC₅₀ value 3.75 μM) in comparison with CPT (IC₅₀ value 9.2 μM) (see Table 2), implying C17 is a specific

inhibitor for LdTop1 as it failed to inhibit human Top1 both in the plasmid DNA cleavage and relaxation assays (Figure S1).

Next, to test the DNA intercalating property of C17 as a mechanism of LdTop1 inhibition, we used both gel-based Top1 unwinding assays and fluorescence-based Ethidium Bromide (EtBr) displacement assays. Topoisomerase unwinding assay exploits the ability of the intercalating compounds to unwind the DNA duplex and thereby change the DNA twist inducing net negative supercoiling. It was found that in the presence of a strong DNA intercalator such as m-AMSA, net negative supercoiling of the relaxed substrate DNA was induced at 50 and 200 μM concentration (Figure 1H, lanes 3 and 4), while nonintercalative compounds such as Etoposide failed to show any such effect at 50 and 200 μM concentrations

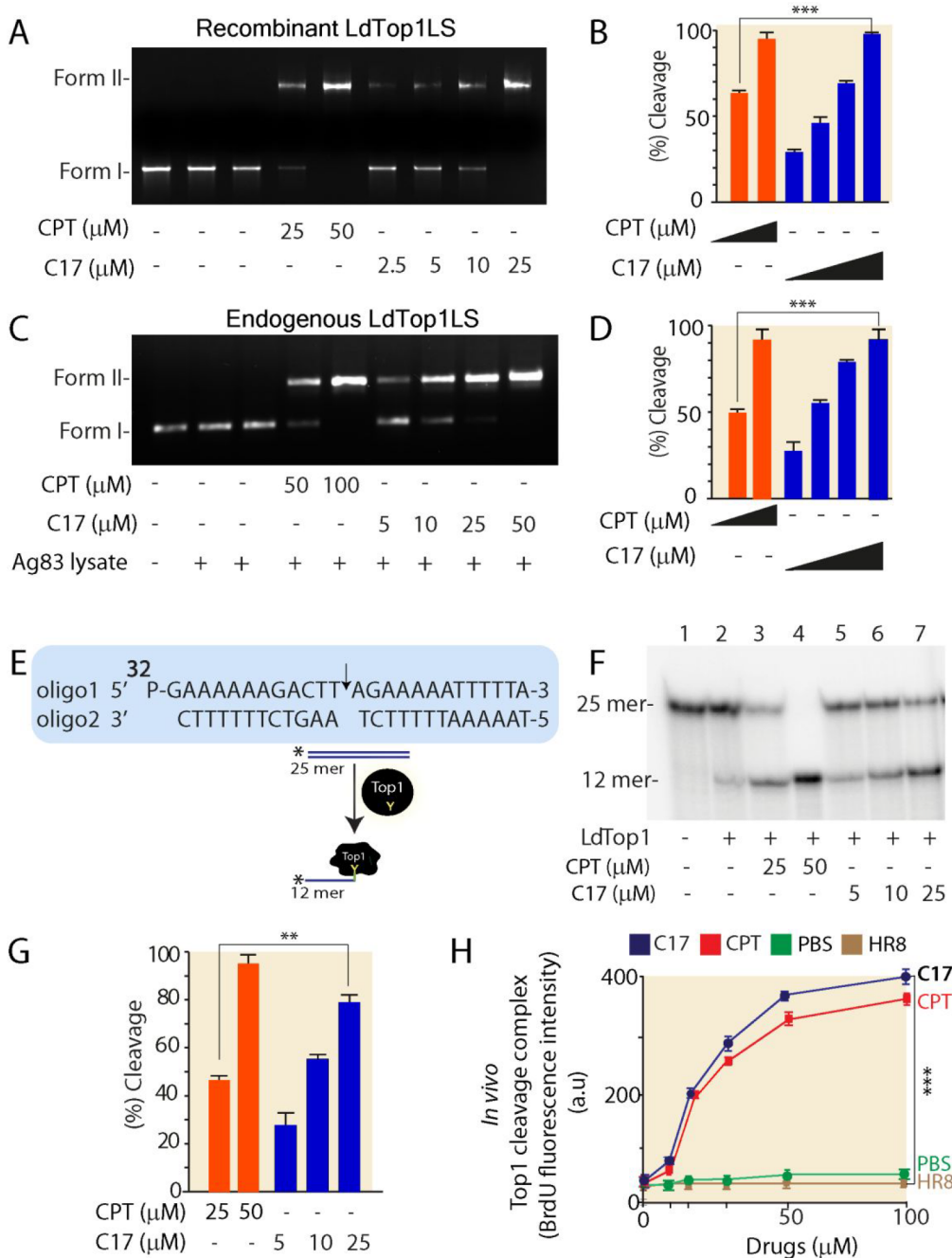


Figure 2. C17-mediated trapping of Top1–DNA cleavage complexes. (A) Representative gel showing plasmid DNA cleavage mediated by recombinant LdTop1LS in the presence of CPT or C17. Lane 1, 50 fmol of pBS (SK+) DNA; lane 2, with 150 fmol LdTop1LS; lane 3, same as lane 2, but with SDS–proteinase K treatment; lanes 4 and 5, same as lane 3, but in the presence of 25 and 50 μM CPT, respectively, as control; lanes 6–9, same as lane 3, but in the presence of 2.5, 5, 10, and 25 μM C17, respectively. Positions of the supercoiled substrate (form I) and nicked monomers (form II) are indicated. (B) Quantitative measurement of LdTop1cc (%) formation induced by CPT and C17 by recombinant LdTop1LS. (C) Representative gel showing plasmid DNA cleavage mediated by endogenous LdTop1 from Ag83 lysate in the presence of CPT or C17. Lane 1, 0.2 μg of pBS (SK+) DNA; lane 2, with 0.6 μg lysate; lane 3, same as lane 2, but with SDS–proteinase K treatment; lanes 4 and 5, same as lane 3, but in the presence of 50 and 100 μM CPT, respectively, as control; lanes 6–9, same as lane 3, but in the presence of 5, 10, 25, and 50 μM C17, respectively. Positions of the supercoiled substrate (form I) and nicked monomers (form II) are indicated. (D) Quantitative measurement of LdTop1cc (%) induced by CPT and C17 using endogenous LdTop1 from Ag83 lysate. All the experiments were performed three times and expressed as the mean \pm SD * p < 0.05, ** p < 0.01 (Student's t test). *** Indicates a significant difference between CPT and C17 treatments (p < 0.001). (E) Schematic representation of the formation of LdTop1cc with 5'-³²P-end-labeled oligonucleotide substrates in the presence of Top1 poison. (F) Representative gel showing Top1-mediated 25-mer duplex oligonucleotide cleavage in the presence of CPT and C17. Lane 1, 15 nM 5'-³²P-end-labeled 25-mer duplex oligo as indicated above. Lane 2, same as lane 1 but incubated with recombinant LS (0.2 μM). Lanes 3–4, same as lane 2 but incubated with an indicated concentration of CPT. Lanes 5–7, same as lane 2 but incubated with an indicated concentration of C17. Positions of uncleaved oligonucleotide (25-mer) and the cleavage product (12-mer oligonucleotide complexed with residual Top1) are indicated. (G) Quantitative measurement of cleavage complex (Top1cc) formation (%) by CPT and C17 by oligo cleavage assay. All the experiments were performed three times and expressed as the mean \pm SD * p < 0.05, ** p < 0.01 (Student's t test). ** Indicates a significant

Figure 2. continued

difference between CPT and C17 treatments ($p < 0.01$). (H) Exponentially growing *L. donovani* promastigotes (5×10^6 cells/mL) were labeled with BrdU at 22 °C for 24 h and then treated with different concentrations of CPT, C17, and a catalytic inhibitor of Top1 as indicated. SDS-K+ precipitable complexes were measured as described in [Materials and Methods](#). All the experiments were performed three times and representative data from one set of experiments are expressed as mean \pm SD. Variations among different sets of experiments were $< 10\%$. * $p < 0.05$, ** $p < 0.01$ (Student's *t* test). *** Indicates a significant difference between catalytic inhibitor control and C17 treatments ($p < 0.001$).

([Figure 1H](#), lanes 5 and 6). C17 also rendered no effect on the substrate DNA topology leading to its complete relaxation at the indicated concentrations ([Figure 1H](#), lanes 7–10), ruling out the possibility of C17 acting as a DNA intercalator. To further substantiate this observation, we carried out the EtBr displacement assays. The DNA intercalator mAMSA ($50 \mu\text{M}$) dislodges the already bound fluorophore (EtBr) from the plasmid DNA while ([Figure 1I](#)), C17 was unable to induce any EtBr displacement even at a high concentration ($200 \mu\text{M}$) confirming that C17 is not a DNA intercalator.

To further investigate the ability of C17-mediated stabilization of LdTop1 cleavage complex, we performed *in vitro* DNA cleavage reactions under equilibrium conditions by reacting LdTop1 with plasmid DNA in the presence of C17 or CPT. Covalently closed circular DNA (Form I) are converted to nicked circular DNA (Form II) by Top1 which are trapped in the presence of Top1 poisons and are referred to as “cleavage complex; Top1cc”. C17 acts as a poison to stabilize Top1cc in plasmid DNA cleavage assays both with recombinant LdTop1 ([Figure 2A](#)), and with endogenous Top1 from Ag83 lysate ([Figure 2C](#)) like CPT.

Next, we confirmed the C17-induced stabilization of Top1cc in single turnover equilibrium cleavage assays by using recombinant LdTop1 and 25-mer duplex oligonucleotides harboring Top1 cleavage sites ([Figures 2E and F](#)). The quantification of LdTop1-mediated cleavage assays ([Figure 2B, 2D, and 2G](#)) indicates that the extent of Top1–DNA cleavage complex formation (% cleavage) with C17 was increased by ~ 2 – 3 fold when compared with CPT at indicated concentrations, which is in keeping with C17-mediated increased inhibition of LdTop1 in the plasmid DNA relaxation assays ([Table 2](#)).

We further tested the ability of C17 to induce Top1-linked DNA complexes in the *L. donovani* promastigotes by using modified KCl-SDS precipitation assays.³⁷ BrdU-labeled promastigotes were treated with various concentrations of C17, as well as CPT and a catalytic inhibitor of Top1 (compound 8 or HR8) as controls.²² Treatment of promastigotes with different concentrations of C17 markedly increased the SDS-KCl precipitable complex compared with the untreated control cells as detected by anti-BrdU staining ([Figure 2H](#)), which was similar to that obtained by treatment with different concentrations of CPT for 24 h. These results show that the formation of SDS-KCl precipitable complexes is due to the formation of protein-linked DNA complexes following treatment with C17. Together, we conclude that C17 selectively stabilizes the LdTop1 cleavable complex and acts as poison inside the *Leishmania* parasites. Cumulatively, our data suggest that C17 selectively poisons LdTop1 cleavage complexes abrogating the religation activity.

C17 Treatment Inhibits Cell Cycle Progression, Accumulates DNA Breaks, and Triggers Apoptosis-Like Death in Ag83 Promastigotes. Trapped LdTop1cc generates toxic DNA lesions which result in DNA double-strand breaks (DSBs) upon collision with ongoing replication

forks and/or transcription machinery leading to cell cycle arrest and killing of the parasites.³⁹ To test such a possibility, we examined the cell cycle profile of the parasites after treatment with C17 using the flow-cytometric analysis ([Figure 3A](#)). In the absence of C17 treatment *Leishmania* promastigotes exhibited regular cell cycle distribution in G1, S, and G2/M phases (G1: 65.1%, S: 18.1%, and G2/M: 15.1%), while, after treatment with $5 \mu\text{M}$ C17 led to a time-dependent arrest at the S/G2-M phase and concomitantly inhibited entry into the next cell cycle phase as evident from a declining G1 phase promastigote population at 6 h (55.3%), 12 h (40.7%), and 24 h (31.5%) post C17 treatment compared to untreated control parasites. Also, continuous exposure to C17 led to S/G2-M phase arrest with 41.3% at 6 h, 57.6% at 12 h, and 65.7% after 24 h after treatment, suggesting C17-induced disruption of the parasite replication cycle.

Next, we performed TUNEL staining that detects C17-induced DNAs breaks inside the parasites by labeling their DNA-free ends with dUTP. This assay utilizes a reaction catalyzed by exogenous terminal deoxynucleotidyl transferase for labeling DNA breaks with fluorophore tagged-dUTP in a template-independent addition to the 3'-hydroxyl (OH) termini of double- and single-stranded DNA.^{37,40} C17 significantly increased TUNEL positive (+ve) cells in a time-dependent manner compared to the untreated control parasites ([Figure 3B](#); see the quantification). The representative confocal microscopic images show TUNEL +ve cells induced by $5 \mu\text{M}$ of C17 treatment for 24 h compared to the untreated control ([Figure 3B](#)). The TUNEL+ staining not only colocalize with the nucleus but also with the kinetoplast, suggesting C17 might trap LdTop1cc's both in the nucleus as well as the kinetoplast as reflected in the accumulation of DNA breaks in both the compartments. This is consistent with the role of LdTop1 both in the nucleus and mitochondria in the *Leishmania* parasites.^{37,40} We confirmed that DNA breaks in the *Leishmania* promastigotes was detected as early as 15 min post treatment with C17 using TUNEL assays (blue). Under similar condition we failed to detect, significant increase in apoptotic *Leishmania* promastigotes (Annexin V-FITC + staining cells) ([Figure S3E](#)), suggesting C17-inuced LdTop1cc generates DNA breaks in the parasites ([Figure 2](#)). In the later time point of C17 treatment, we detected significant increase in the apoptotic cells 1.5 h post treatment ([Figures 3B–D and S3E](#)). Further, we also confirmed the extent of DNA fragmentation in the *Leishmania* Ag83 promastigotes after treatment with C17 using DNA laddering assays.^{37,40} Consistent with TUNEL staining ([Figure 3B](#)), C17-induced apoptotic DNA breaks in the promastigotes were also confirmed by a marked increase in genomic DNA fragmentation when promastigotes were treated with C17 post 6h treatment ([Figure 3C](#)).

Further, we confirmed that C17-induced DNA fragmentation triggers apoptotic-like cell death in *Leishmania* promastigotes using fluorescein isothiocyanate (FITC)-annexin V and propidium iodide (PI) staining.^{37,40} Externalization of

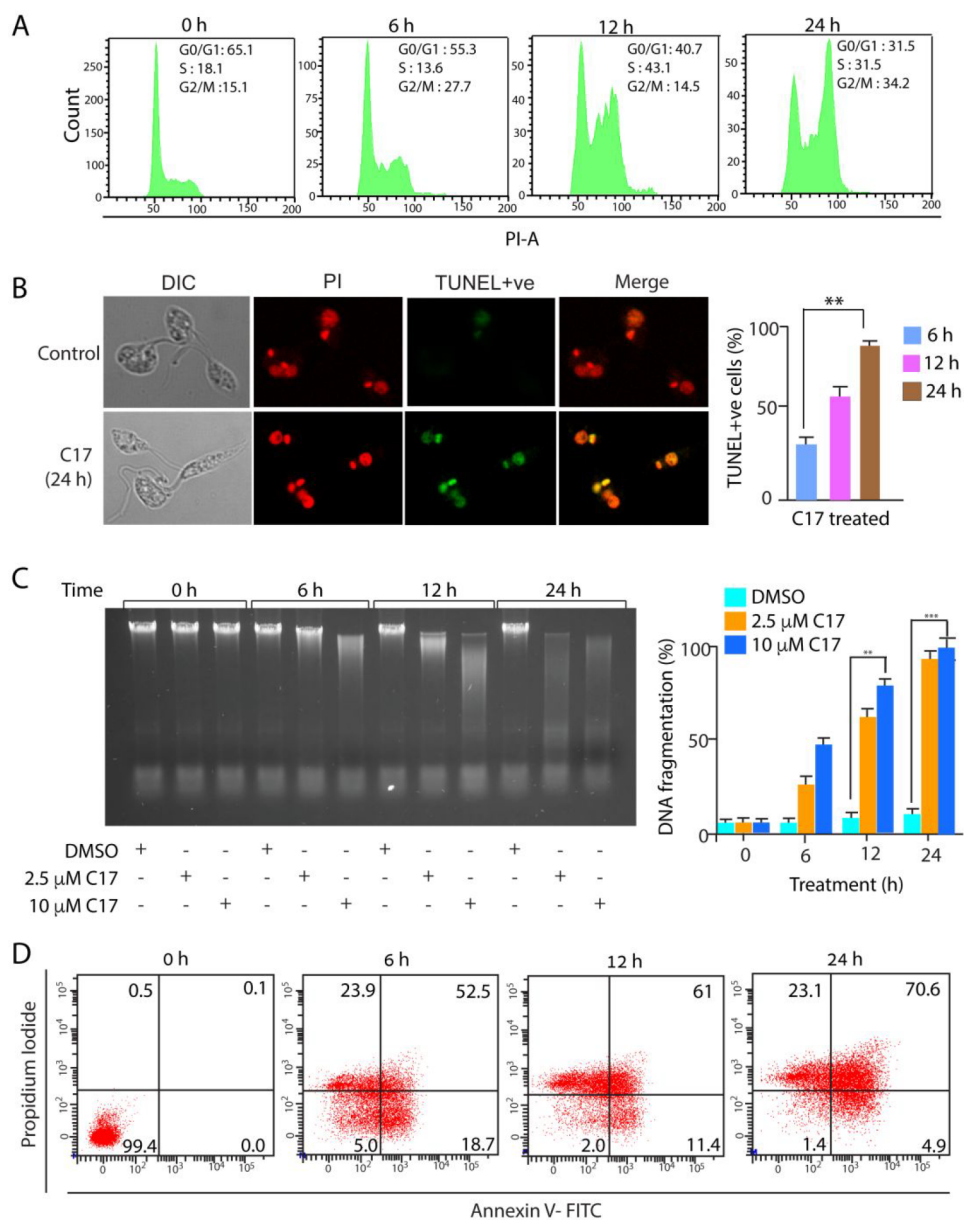


Figure 3. C17 abrogates the cell cycle progression of Ag83 promastigotes and induces DNA breaks leading to apoptosis-like cell death. (A) Histograms of the distribution of DNA content by flow cytometric analyses of the C17-mediated cell cycle arrest in *L. donovani* Ag83 promastigotes. The cell cycle arrest was monitored post-treatment with 0.2% DMSO as control, and with C17 (5 μ M) for 6, 12, and 24 h. The parasites were then fixed and stained with propidium iodide (PI) and RNase A and a total of 10,000 nuclei were counted from each sample. The percentages of cells within different cell-cycle stages as shown were determined as described in [Materials and Methods](#). The representative histograms show that treatment with 0.2% DMSO (panel I), or with 5 μ M C17 for 6 h (panel II), 12 h (panel III), and 24 h (panel IV) respectively. The experiments were repeated thrice and histograms from one data set have been shown. (B) Ag83 promastigotes were either left untreated or treated with 5 μ M C17 for 6, 12, and 24 h following which the TUNEL assay was performed. The DNA breaks were analyzed by confocal microscopy and the representative images show the breaks accumulated 12 h post-DMSO/C17 treatment. The percentage of TUNEL +ve cells over the indicated periods have been quantified and represented as bar diagrams which are representative of three independent experiments as mean \pm SD. Variations among different sets of experiments were < 10%. * p < 0.05, ** p < 0.01 (Student's *t* test). ** Indicates a significant increase in TUNEL +ve Ag83 promastigotes between 6 and 24 h of C17 treatment. (C) Ag83 promastigotes were left untreated or treated with two different concentrations of C17 (2.5 μ M and 10 μ M) for the indicated time points (6, 12, and 24 h) and genomic DNA was isolated from each. Apoptotic DNA was resolved on a 2% agarose gel. Representative images of three independent experiments have been shown with * P < 0.01 and *** P < 0.001. Quantification of the time and dose-dependent percentage of DNA fragmentation has been provided in the form of bar graphs. (D) Flow cytometric analysis of Ag83 promastigote death through the externalization of phosphatidyl serine was evaluated. The parasites were stained with FITC-annexin V and propidium iodide after treatment with 0.2% DMSO (panel I), 5 μ M C17 for 6 h (panel II), 12 h (panel III), and 24 h (panel IV), respectively. The experiments were repeated thrice and representative plots from one data set have been shown.

phosphatidyl serine (stained by annexin V) and the presence of impermeant cell membrane (negative PI staining) are hallmarks of apoptosis or programmed cell death

(PCD).^{19,41,42} Figure 3D confirmed that C17 treatment leads to an increment of the late apoptotic population in a time-dependent manner compared to the untreated control.

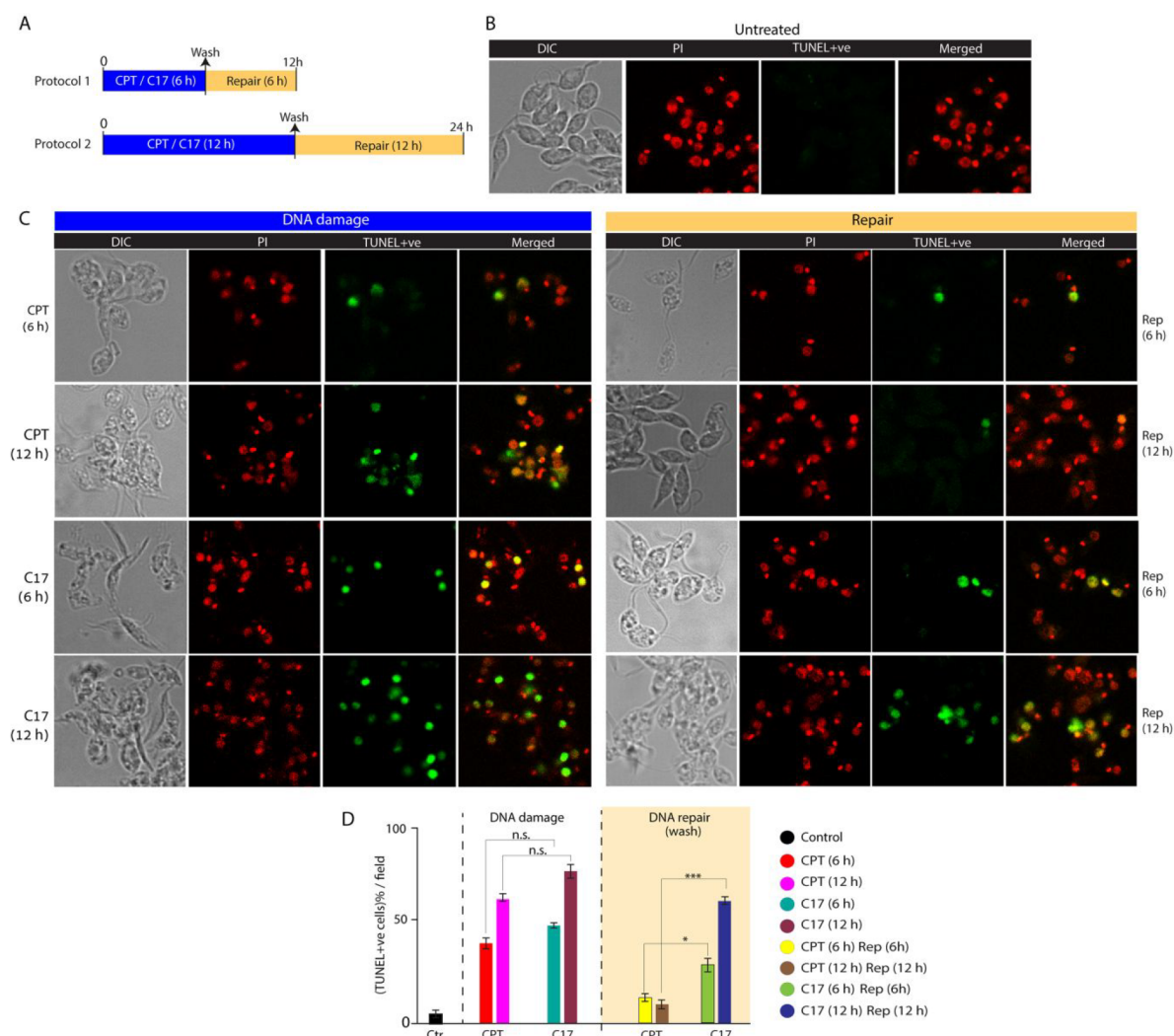


Figure 4. C17 generates persistent LdTop1cc-induced DNA breaks as detected by the TUNEL assays. (A) Overview of the protocol of C17/CPT treatment and reversal in *L. donovani* promastigotes to study the comparative repair kinetics between CPT and C17. (B) Representative confocal microscopic images of the 0.2% DMSO treated control Ag83 promastigotes showing the Propidium iodide (red) stained nuclear and kinetoplast DNA with negligible TUNEL positive (green) cells. (C) Time-dependent escalation of TUNEL +ve parasites treated with C17 or CPT for 6 and 12 h (DNA damage) and the persistence of such TUNEL +ve cells after the removal of the respective drugs for indicated time points (Repair). (D) Quantification of the percentage of TUNEL positive cells after C17/CPT treatment and after the removal of indicated inhibitors (C17 or CPT) as obtained from immunofluorescence confocal microscopy calculated for 80–100 parasites (mean \pm SEM). Experiments were performed three times and representative images from one set of experiments are shown. Variations among different sets of experiments were $< 10\%$. $*p < 0.05$, $**p < 0.01$ (Student's *t* test). $***$ Indicates a significant difference between CPT and C17 treatments following repair ($p < 0.001$).

Next, we tested whether C17 treatment promotes cell cycle arrest and cell death in human cells. CPT treatment impairs the cell cycle progression of human MCF7 cells with a decrease in G1-sub population leading to apoptosis-like cell death (Figure S2A and S2B; CPT). Unlike CPT, C17 neither affects the progression of the human MCF7 cell cycle (Figure S2A; C17) nor causes any apoptotic-like cell death in human MCF7 cells (Figure S2B). Accordingly, in the cell viability assays, the IC_{50} of the C17 treated cancerous MCF7 cell lines (Figure S2C) and the noncancerous HEK293 cell lines (Figure S2D) were significantly high (~ 90 fold) as compared to CPT. These data are in agreement that C17 is not an inhibitor of human Top1 (Figure S1F–I), implying the specificity of C17-induced DNA breaks, inhibition of cell cycle progression, and apoptosis-like cell death in the parasites is due to trapping of LdTop1cc in the promastigotes.

C17 Accumulates Persistent and Less Reversible DNA Breaks Inside the *Leishmania* Parasites Compared to CPT. Because C17 poisons LdTop1cc in the Ag83 promastigotes (Figure 2H) and generates DNA strand breaks (Figures 3B and 3C), we investigated the accumulation and disappearance of Top1cc-induced DNA breaks in Ag83 promastigotes treated either with C17 or CPT by measuring the number of TUNEL +ve cells using the confocal microscopy (Figure 4A). Under similar conditions, we detected a time-dependent increase in TUNEL +ve parasites post-treatment with C17 that was comparable with CPT (see Figure 4C DNA damage), suggesting that both C17 and CPT generate similar levels of DNA breaks at the indicated periods in Ag83 promastigotes (Figure 4D). CPT-induced DNA breaks have a short half-life which are reversed immediately upon the removal of the drug from the medium.^{23,28} This is consistent with the reversal of TUNEL +ve cells within a small

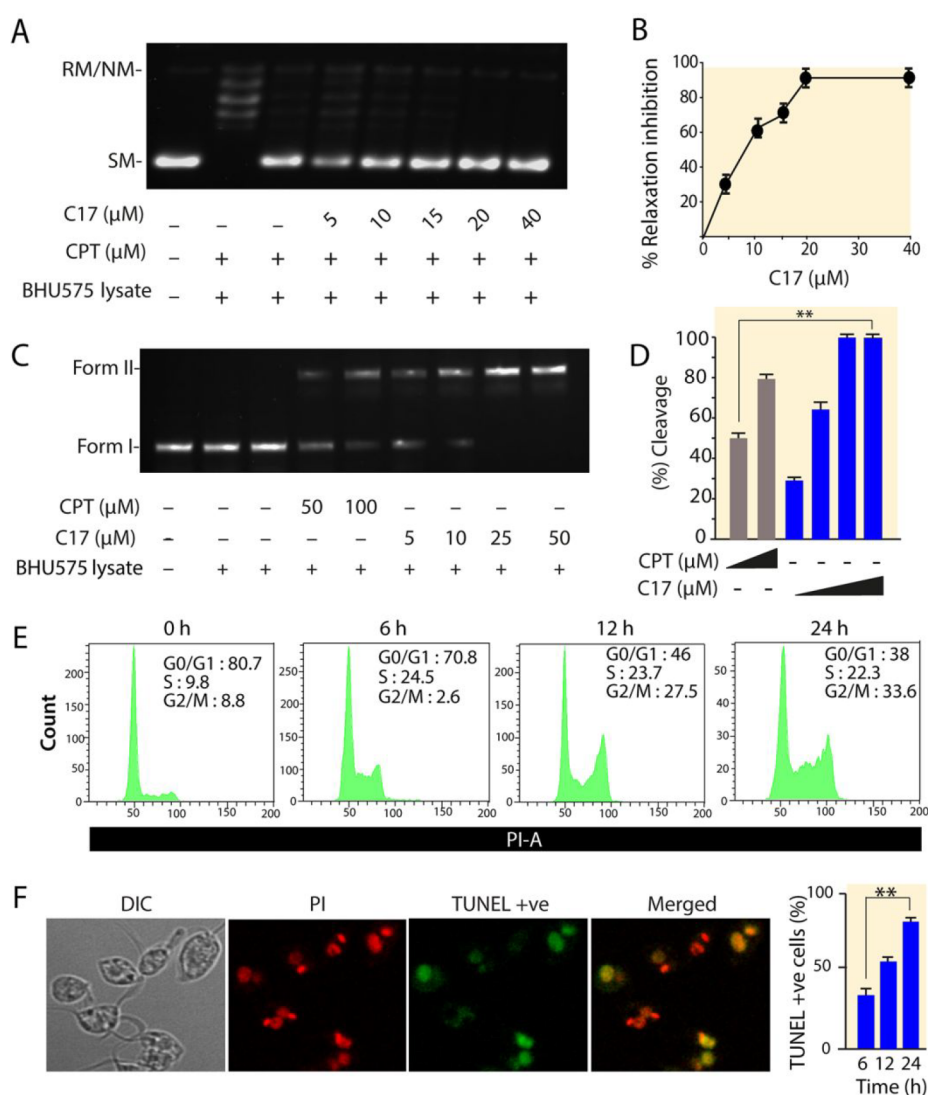


Figure 5. C17 poisons the LdTop1 from antimony-resistant BHU575 parasites and inhibits the proliferation of the promastigotes. (A) Relaxation assay of supercoiled pBS (SK+) DNA by Top1 activity from the BHU575 cellular lysate (each reaction volume contains 0.1 μg protein). Lane 1, pBS (SK+) DNA (0.3 μg); lane 2, same as lane 1, but pBS (SK+) DNA (0.3 μg) was incubated with BHU-575 cell lysates; lanes 3–8, same as lane 2, but BHU575 whole cell lysates were incubated simultaneously with 50 μM CPT or with increasing concentrations of C17 (as indicated) together with plasmid DNA at 37 °C for 30 min. (B) Quantitative representation of BHU575 Top1 DNA relaxation inhibition (%) at variable concentrations of C17. All the experiments were performed in triplicate and expressed as the mean ± SD. (C) Representative gel image showing plasmid DNA cleavage mediated by BHU575 cellular lysate as the source of Top1 enzyme in the presence of CPT or C17. Lane 1, 0.2 μg of pBS (SK+) DNA; lane 2, with 0.6 μg lysate; lane 3, same as lane 2, but with SDS–proteinase K treatment; lanes 4 and 5, same as lane 3, but in the presence of 50 and 100 μM CPT, respectively, as control; lanes 6–9, same as lane 3, but in the presence of 5, 10, 25, and 50 μM C17 respectively. Positions of the supercoiled substrate (form I) and nicked monomers (form II) are indicated. (D) Quantitative measurement of cleavage complex (Top1cc) formation (%) by CPT and compound C17 by BHU-575 Top1. All the experiments were performed three times and expressed as the mean ± SD **p* < 0.05, ***p* < 0.01 (Student's *t* test). ** Indicates a significant difference between CPT and C17 treatments. (E) Histograms of the distribution of DNA content by flow cytometric analyses of the C17-mediated cell cycle arrest in *L. donovani* BHU-575 promastigotes. The cell cycle arrest was monitored post-treatment with 0.2% DMSO as control, and with C17 (5 μM) for 6, 12, and 24 h. The parasites were then fixed and stained with propidium iodide (PI) and RNase A and a total of 10,000 nuclei were counted from each sample. The percentages of cells within different cell-cycle stages are shown. The representative histograms show that treatment with 0.2% DMSO (panel I), C17 (5 μM) for 6 h (panel II), 12 h (panel III), and 24 h (panel IV), respectively. The experiments were repeated thrice and the representative histograms from one data set are shown. (F) BHU575 promastigotes were either left untreated or treated with 5 μM PIQ derivative for 6, 12, and 24 h following which the TUNEL assay was performed. The DNA breaks were analyzed by confocal microscopy and the representative images show the breaks accumulated in the promastigotes 12 h post C17 treatment. (G) The percentage of TUNEL positive cells over the indicated periods post 5 μM C17 treatment have been quantified and represented as bar diagrams which are representative of three independent experiments. Variations among different sets of experiments were <10%. **p* < 0.05, ***p* < 0.01 (Student's *t* test). ** Indicates a significant difference between 6 and 24 h treatment time points (*p* < 0.01).

duration of washing out CPT (Figure 4C; Repair). On the contrary, C17 engenders more persistent and less reversible DNA breaks after subsequent wash and reculturing of the

parasites in the C17-free medium (Figure 4C; Repair). Figure 4C and D shows a faster disappearance in the number of TUNEL +ve Ag83 parasites after washing out CPT from

media at indicated periods (see the quantification in Figure 4D). In contrast, Ag83 promastigotes showed (~3–4 fold) more persistent TUNEL +ve cells (Figure 4D) even after washing out C17 at the indicated time. Together, our data suggest that C17 generates more persistent and less reversible LdTop1cc-induced DNA breaks which accounts for the increased C17-induced cytotoxicity in the parasites compared to CPT.

C17 Poisons LdTop1cc and Sensitizes the Antimony-Resistant *Leishmania donovani* Clinical Isolate. Next, to propound C17 as a new drug candidate against drug-resistant leishmaniasis, we tested its efficacy toward the LdTop1 from the antimony-resistant field isolate of *L. donovani*, BHU575 (less susceptible to SSG, amphotericin B, and miltefosine), obtained from severely VL affected belt of India.^{34,43} First, we confirmed the similar levels of endogenous LdTop1 activity from the two strains of *L. donovani* AG83 (wild type) and BHU575 (antimony-resistant) in the plasmid DNA relaxation assays (Figure S3A). Figure 5A shows that indeed C17 inhibited the relaxation activity of LdTop1 from *Leishmania* BHU575 whole cell extracts in a dose-dependent manner (Figure 5A, lanes 4–8), with an IC₅₀ of 8.75 μM (Figure 5B) which was comparable with wild type parasites (Table 2).

Next, to investigate the C17-mediated poisoning of endogenous LdTop1cc from the BHU575 *Leishmania* strain, we performed plasmid DNA cleavage assays with the whole-cell extracts from BHU575 parasites as the source of endogenous Top1. Figure 5C confirmed that C17 stabilizes LdTop1cc formation in BHU575 parasites like CPT. Notably, we detected a ~5-fold increased efficacy of C17-induced LdTop1cc formation compared to CPT in BHU575 promastigotes (see the quantification in Figure 5D). Accordingly, we detected C17-induced DNA breaks in the BHU575 parasites detected by the TUNEL assay. Like wild-type parasites (Figure 4C), C17 efficiently generates LdTop1cc-induced DNA breaks in BHU575 promastigotes (Figure 5F). We detected 60% TUNEL +ve BHU575 cells after 12 h of treatment with C17 (5 μM) which increased to 85–90% after treatment for 24 h (Figure 5G). C17 treatment also inhibits the replication cycle leading to a wide-scale G2/M arrest (Figure 5E) and promotes apoptosis-like cell death in BHU575 parasites as detected by using FITC-Annexin V-based flow cytometry analysis (Figure S3B).

We further substantiated that C17-induced DNA breaks in the BHU575 parasites accumulate cell death. The BHU575 promastigotes survival was monitored over a time of 24 h in presence of C17 which shows that the antimony-resistant parasites are hypersensitive to the LdTop1 poisons (EC₅₀ value of C17 in Table 3 and Figure S3C). We also showed the ability

Table 3. EC₅₀ for Promastigotes

	Ag83	BHU575
CPT (μM)	3.794 ± 0.029	6.582 ± 0.092
C17 (μM)	2.311 ± 0.56	4.796 ± 0.269

of C17 to resensitize the antimony-resistant parasites upon cotreatment with SAG (Figure S3D). Ag83 and BHU575 are variable strains of *Leishmania* that show differential drug sensitivity to antimonials suggesting they have an internal rewiring of the signaling pathways and genes to the outcome of the drug sensitivities as reflected in the Top 1 inhibition assays. Taken together these findings suggest that C17 could be a

potential new drug candidate against drug-resistant leishmaniasis.

C17 Inhibits the Growth of Intracellular Amastigotes in Murine Macrophages Infected with the *Leishmania* Antimony-Resistant Parasites. Subsequently, to investigate the potency of C17 as an antileishmanial drug, primary murine peritoneal macrophages were infected with early passage *L. donovani* wild-type (Ag83) and antimony-resistant (BHU575) strains *in vitro* and incubated with different concentrations of C17 for 48–96 h (Figure 6A). Counting of the macrophage internalized amastigotes after C17 treatment showed markedly down-regulated macrophage infection of both Ag83 and BHU575 strains (Figures 6B and 6D and S4A–B) in a time dependent manner. The antimony-resistant BHU575 parasite burden was lowered by almost 90% after 96 h of treatment with C17 at 10 μM (Figures 6C and 6E and S4A–B).

The EC₅₀ values of infected intracellular amastigotes and the extracellular promastigote clearance were estimated using nonlinear curve fitting (Table 4). C17 shows markedly high EC₅₀ (~50 μM) toward the peritoneal macrophages with a relatively high selectivity index (SI) of 9.25, further strengthening C17 as a potential antileishmanial drug candidate (Table 4).

C17 Markedly Reduces the Antimony-Resistant (BHU575) and Ag83 Parasites in a Mouse Model of Experimental Visceral Leishmaniasis (VL) and Boosts Host Protective Th1 Cytokine Response. Finally, we evaluated the *in vivo* antileishmanial efficacy of C17 using BALB/c mice model of *L. donovani* infected with wildtype (Ag83) or antimony-resistant (BHU575) strains *via* the intracardiac route.³⁷ During the study, all mice remained alive and healthy and no remarkable change in body weight was observed. C17 was administered intraperitoneally following the treatment regimen outlined in Figure 7A, which led to a marked reduction in BHU575 and Ag83 parasite burden in both spleen and liver which was estimated using the stamp smear method (Figure 7B and 7C) and Limiting Dilution Assay (LDA) (Figure S5A–B). The reduction in the Ag83 and BHU575 parasite burdens in the infected Balb/c mice was further confirmed by the qPCR based kinetoplastid DNA (kDNA)-dependent determination of parasite counts in peripheral blood, spleen, and liver of the untreated and C17 treated mice^{44,45} (Figure S5E), suggesting C17 is a potential antileishmanial agent.

The progression of VL is widely associated with a deregulated cell-mediated immune response emulated by marked T-cell anergy³⁷ specific to *Leishmania* antigens.³⁷ The establishment of VL infection is associated with host immune response where T helper type 1 (Th1) and T helper type 2 (Th2) paradigms play an important role.⁴⁶ The Th1 response confers a protective role to the host, while the Th2 promotes parasite survival and disease progression.³⁷ To test the type of immunological response evoked with C17 treatment in Ag83 infected BALB/c, we examined the splenic cytokine expression levels by RT-PCR. We detected ~4 fold and 5.5 fold increased interferon (IFN-γ) levels after intraperitoneal C17 treatment of infected mice with 5 mg/kg and 10 mg/kg dosages, respectively, suggesting a Th1 dominance in C17-treated mice (Figure 7D).

Notably, the level of IFN-γ was coupled with a concomitant up-regulation of TNF-α (~5 fold) and IL-12 (~10 fold) expression post-treatment, respectively (Figure 7D). The immunosuppressive cytokines promote the survival of intra-

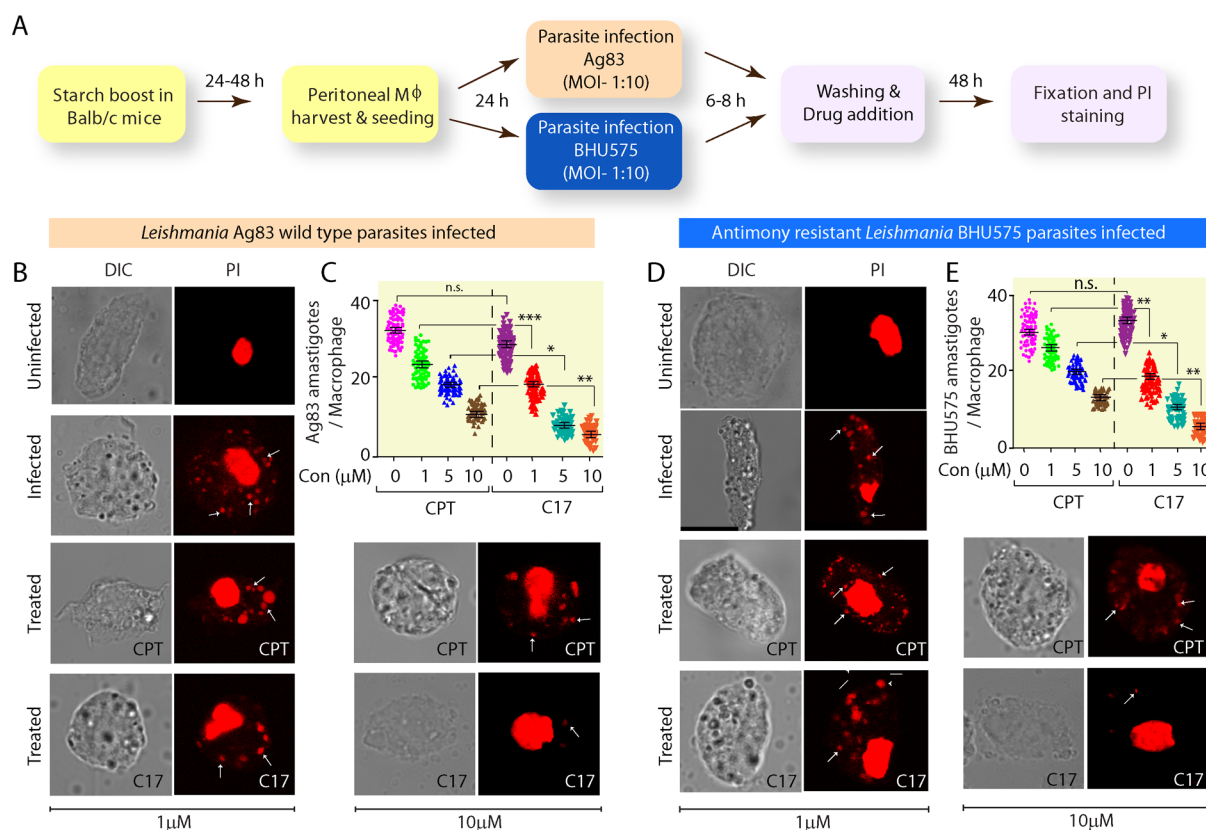


Table 4. EC₅₀ for Amastigotes at 48 h

	Ag83	BHUS75	macrophages
CPT (μM)	7.84 \pm 0.029	12.82 \pm 0.042	18.32 \pm 0.206
C17 (μM)	2.50 \pm 0.56	7.06 \pm 0.269	50.18 \pm 0.009

cellular parasites inside the host macrophages and their downregulation propels convalescence of VL *in vivo*.⁴⁶ Accordingly, C17-treated parasite-infected mice exhibited a marked decline in the expression of the immunosuppressive cytokine (\sim 2–4 fold reduction for IL-10) with increasing concentration of C17 (Figure 7D). C17 treatment markedly reduced TGF- β expression (2–4.7 fold after treatment) compared to the Ag83 infected mice and a concomitant increase in the level of IL-4 (1.7-fold and 5-fold) production in all the experimental groups of mice (Figure 7D). The mRNA transcript levels of cytokine genes were measured by RT-PCR only. Taken together, these data advocate that C17 can plausibly serve as an antileishmanial candidate through the switching of immune balance to the host protective Th1 response *in vivo*.

CONCLUSION

A series of twenty one pyrido[[2',1':2,3]imidazo[4,5-*c*]-quinoline derivatives (C1–C21) were prepared and evaluated for their antileishmanial activity. Our work proposes the novel PIQ derivative C17 as a potential chemotherapeutic candidate against both the *Leishmania* promastigotes (sandfly gut form) and the amastigotes (human infected form). *Leishmania* heterodimeric bisubunit Top1 enzyme is essential for parasite survival^{15–17,39} and was rationalized to serve as a validated druggable pathway.^{17,37,38,47} We provided evidence that C17 is a potent inhibitor of LdTop1 imparting a significant level of cytotoxicity to the promastigotes and amastigotes of both the wild type (Ag83) and the antimony-resistant field isolate (BHUS75) without inducing any lethality in host cells (human and murine). We showed that C17 stabilizes LdTop1–DNA covalent complex, and generates C17-induced DNA break formation in parasite culture which triggers apoptosis-like cell death in both the Ag83 and BHUS75 parasites. C17 generates persistent and less reversible DNA breaks when compared with CPT after removal of the respective drugs from the culture medium causing enhanced parasitic killing. We also showed that C17 exhibits antileishmanial activity as it markedly reduces both Ag83 and BHUS75 strains of *L. donovani* using *in vivo* VL-infected mice model. The control of the progression

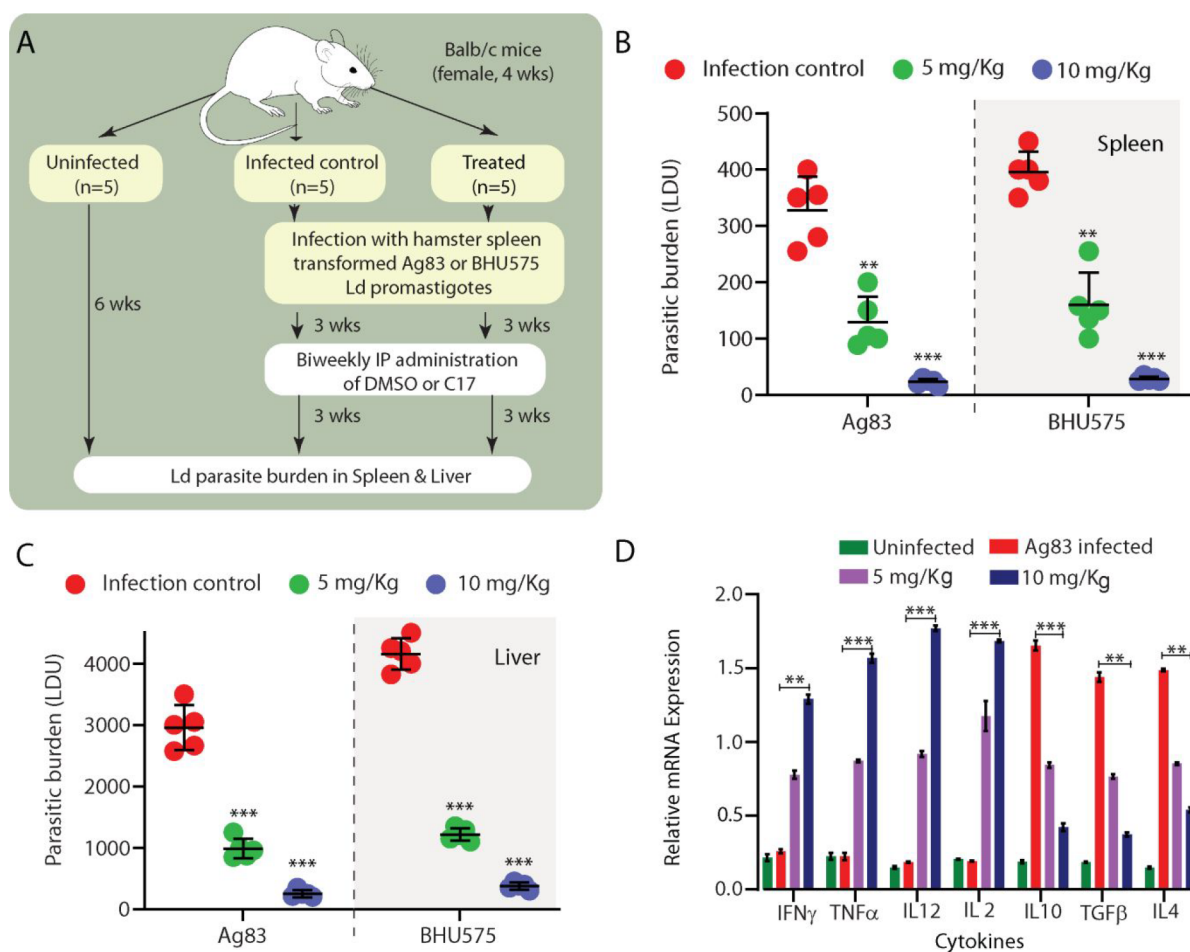


Figure 7. C17 markedly reduced the parasite burden in BALB/c mice by fine-tuning the Th1 and Th2 cytokine responses. (A) Schematic representation showing the protocol for the generation of the experimental murine model of Visceral Leishmaniasis (VL) using the Ag83/BHU575 promastigotes. *In vivo* antileishmanial property of C17 was studied in BALB/c mice infected with Ag83 or BHU575 promastigotes via the intracardiac route. C17 was given at a dosage of 5 and 10 mg/kg/day intraperitoneally for 3 weeks (2 times per week), starting on day 21 postinfection. Animals were sacrificed 10 days post drug treatment to determine the hepatic (B) and splenic (C) parasite load for all treatment groups. Untreated and infected mice were used as controls. The parasite burden in the organs was determined by the stamp-smear method and expressed as Leishman–Donovan Unit (LDU). Data represent mean SEM ($n = 5$ mice per group). * $p < 0.05$, ** $p < 0.01$, and *** $p < 0.005$ (Student's t test), indicate a significant difference in the change of parasite burden with C17 treatment as compared with infection control. (D) Semiquantitative RT-PCR cytokine profiles of *L. donovani* infected and C17 treated infected Balb/c mice. Equivalent amounts of RNA from splenic tissues of four groups of Balb/c ($n = 5$) were used as the input for RT-PCR analysis, where the GAPDH gene was used as the housekeeping control gene. A differential pattern of Th1 cytokine expression was observed following C17 administration in infected BALB/c mice. Splenocytes isolated from Ag83-infected mice after indicated treatments were used for RNA extraction followed by RT-PCR. Downregulation of the Th2-cytokine expression profile following treatment with C17 was obtained. * $p < 0.05$, ** $p < 0.01$, and *** $p < 0.005$ (Student's t test), indicate a significant change in the levels of the indicated cytokines with C17 treatment as compared with the infection control.

of leishmaniasis is correlated with the switching of the cytokine balance from Th1 to Th2 response.³⁷ An effective leishmanicidal response evoked against *L. donovani* stems from an IL-12-mediated Th1 response leading to induction of IFN- γ production.³⁷ We found that C17 therapy mounts a polarized Th1 response with an up-regulated IFN- γ secretion, with a marked increase in the pro-inflammatory cytokine TNF- α which is thought to stimulate IL-12 driven IFN- γ secretion implicating a strong IL-12-driven IFN- γ , and TNF- α which might account for conferring the high levels of protection post-treatment. This up-regulated expression of IFN- γ coupled amplified IL-12 production bears a synergistic effect on the activation of iNOS³⁷ and reduces the Th2-associated cytokines IL-4, IL-10, and TGF- β responses which could be observed in the C17 treated mice. Considering the decrease in parasite burden as a function of increased C17 treatment, it is

conceivable that C17 treatment allowed the expansion of antileishmanial T-cell repertoire with a Th1 tropism which is contributing to the host protective cytokine production and a significant reduction in the systemic parasite load. Collectively, we provide compelling evidence that the novel PIQ derivatives as a promising antileishmanial drug candidate to overcome the emerging cases of multidrug resistance and therapeutic failures. Further studies are warranted to explore whether C17 may drug develop resistance to antileishmanial therapy by generating point mutations in LdTop1.⁴⁸ Moreover, additional steps are required for testing this drug resistance potential prior to clinical trials and further validation will confirm the lab results to be used and practiced in the clinics.

MATERIALS AND METHODS

Chemistry. General Information. Melting points were determined in open capillary tubes on an automated melting point apparatus and are uncorrected. Reactions were monitored by using thin layer chromatography (TLC) on 0.2 mm silica gel F₂₅₄ plates. The chemical structures of final products were determined by their NMR and mass analysis. NMR spectra were recorded on Bruker Ascend 400. Chemical shifts are reported in parts per million (ppm) using tetramethylsilane (TMS) as an internal standard or deuterated solvent peak (CDCl₃ and DMSO-*d*₆). The HRMS data were recorded on Agilent 6545 mass spectrometer with an electrospray ionization and TOF mass analyzer. The HPLC data were recorded on Shimadzu HPLC. All compounds are >95% pure by HPLC analysis. All other chemicals and solvents were obtained from commercial suppliers and used without further purification.

General Procedure for Synthesis of Pyrido[2',1':2,3]imidazo[4,5-*c*]quinolines. A mixture of 2-(2'-bromophenyl)imidazo[1,2-*a*]pyridine (0.366 mmol), aldehyde (0.439 or 1.09 mmol for paraformaldehyde), sodium azide (0.549 mmol), CuI (20 mol%), *L*-proline (30 mol%), DIPEA (1 eq.), and *p*-T₂OH (0.5 eq.) were stirred in DMSO (2.0 mL) at room temperature and then slowly heated at 150 °C for 10 h. After cooling to ambient temperature, the reaction mass was quenched with ice-cold aqueous solution of NH₄Cl (30 mL), filtered through celite bed, and washed with ethyl acetate (20 mL). Filtrate was extracted with ethyl acetate (2 × 20 mL). Organic layers were combined and again washed with ice-cold water (2 × 30 mL). The organic layer was dried over anhydrous Na₂SO₄ and concentrated under reduced pressure. The desired product (C1–C20) was isolated by column chromatography on silica gel (100–200 mesh) using ethyl acetate/hexane (20%, *v/v*) as eluent.

Pyrido[2',1':2,3]imidazo[4,5-*c*]quinoline (C1). The general procedure was used with 2-(2'-bromophenyl)imidazo[1,2-*a*]pyridine (4a) (0.366 mmol) and paraformaldehyde (5a) (1.04 mmol) as starting material. Purified the crude compound by column chromatography on silica gel (100–200 mesh) using ethyl acetate/hexane (80%, *v/v*) as eluent and obtained C1 as off white solid; 46 mg (57%); mp 253–255 °C; ¹H NMR (400 MHz, DMSO-*d*₆ + CDCl₃) δ 9.77 (s, 1H), 9.31 (d, *J* = 6.7 Hz, 1H), 8.60 (d, *J* = 7.7 Hz, 1H), 8.16 (d, *J* = 8.2 Hz, 1H), 7.86 (d, *J* = 9.1 Hz, 1H), 7.74 (t, *J* = 7.1 Hz, 1H), 7.71–7.62 (m, 2H), 7.17 (t, *J* = 6.7 Hz, 1H); ¹³C NMR (100 MHz, DMSO-*d*₆ + CDCl₃) δ 149.1, 145.9, 145.7, 137.9, 131.2, 129.8, 128.4, 127.6, 126.6, 122.7, 122.1, 117.5, 112.9; HRMS calculated for C₁₄H₁₀N₃ [M + H]⁺ 220.0869, found 220.0868; HPLC purity 98.45%.

10-Methylpyrido[2',1':2,3]imidazo[4,5-*c*]quinoline (C2). The general procedure was used with 2-(2'-bromophenyl)-7-methylimidazo[1,2-*a*]pyridine (4b) (0.349 mmol) and paraformaldehyde (5a) (1.04 mmol) as starting material. Purified the crude compound by column chromatography on silica gel (100–200 mesh) using ethyl acetate/hexane (80%, *v/v*) as eluent and obtained C2 as off white solid; 49 mg (60%); mp 243–245 °C; ¹H NMR (400 MHz, CDCl₃) δ 9.41 (s, 1H), 8.70 (d, *J* = 7.6 Hz, 1H), 8.53 (d, *J* = 6.9 Hz, 1H), 8.25 (d, *J* = 8.2 Hz, 1H), 7.79–7.74 (m, 1H), 7.71 (t, *J* = 7.3 Hz, 1H), 7.61 (s, 1H), 6.85 (dd, *J* = 6.8, 0.8 Hz, 1H), 2.51 (s, 3H); ¹³C NMR (100 MHz, CDCl₃) δ 149.7, 146.7, 145.7, 142.1, 135.4, 129.7, 128.4, 126.6, 124.3, 122.7, 116.4, 115.3, 22.0; HRMS calculated for C₁₅H₁₂N₃ [M + H]⁺ 234.1026, found 234.1028; HPLC purity 99.83%.

9-Methylpyrido[2',1':2,3]imidazo[4,5-*c*]quinoline (C3). The general procedure was used with 2-(2'-bromophenyl)-6-methylimidazo[1,2-*a*]pyridine (4c) (0.349 mmol) and paraformaldehyde (5a) (1.04 mmol) as starting material. Purified the crude compound by column chromatography on silica gel (100–200 mesh) using ethyl acetate/hexane (80%, *v/v*) as eluent and obtained C3 as off white solid; 46 mg (57%); mp 228–230 °C; ¹H NMR (400 MHz, CDCl₃) δ 9.28 (s, 1H), 8.62 (d, *J* = 7.7 Hz, 1H), 8.26 (s, 1H), 8.19 (d, *J* = 8.2 Hz, 1H), 7.72 (t, *J* = 7.0 Hz, 1H), 7.67–7.64 (m, 2H), 7.29–7.25 (m, 1H), 2.30 (s, 3H); ¹³C NMR (100 MHz, CDCl₃) δ 148.0, 146.1, 145.5, 135.6, 133.4, 129.6, 128.3, 126.6, 122.7, 122.6, 122.5, 122.0, 121.7, 117.1, 18.1; HRMS calculated for C₁₅H₁₂N₃ [M + H]⁺ 234.1026, found 234.1028; HPLC purity 99.28%.

9-Bromopyrido[2',1':2,3]imidazo[4,5-*c*]quinoline (C4). The general procedure was used with 2-(2'-bromophenyl)-6-bromoimidazo[1,2-*a*]pyridine (4d) (0.349 mmol) and paraformaldehyde (5a) (1.04 mmol) as starting material. Purified the crude compound by column chromatography on silica gel (100–200 mesh) using ethyl acetate/hexane (80%, *v/v*) as eluent and obtained C4 as off white solid; 42 mg (51%); Light brown oil; 39 mg (46%); ¹H NMR (400 MHz, CDCl₃) δ 9.47 (s, 1H), 8.78–8.76 (m, 1H), 8.71 (dd, *J* = 8.0, 1.7 Hz, 1H), 8.28 (d, *J* = 7.5 Hz, 1H), 7.88 (dd, *J* = 9.7, 0.9 Hz, 1H), 7.83–7.79 (m, 1H), 7.75 (td, *J* = 7.6, 7.0, 1.4 Hz, 1H), 7.57 (dd, *J* = 9.7, 2.1 Hz, 1H); ¹³C NMR (100 MHz, CDCl₃) δ 149.26, 146.61, 145.88, 135.84, 130.50, 129.86, 128.78, 127.01, 125.40, 122.85, 122.20, 118.32, 112.82; HRMS for C₁₄H₉BrN₃ [M + H]⁺ calcd 297.9974 found 297.9982.

9-Chloropyrido[2',1':2,3]imidazo[4,5-*c*]quinoline (C5). The general procedure was used with 2-(2'-bromophenyl)-6-chloroimidazo[1,2-*a*]pyridine (4e) (0.349 mmol) and paraformaldehyde (5a) (1.04 mmol) as starting material. Purified the crude compound by column chromatography on silica gel (100–200 mesh) using ethyl acetate/hexane (80%, *v/v*) as eluent and obtained C5 as off white solid; 42 mg (51%); mp 260–262 °C; ¹H NMR (400 MHz, CDCl₃) δ 9.49 (s, 1H), 8.79 (d, *J* = 1.1 Hz, 1H), 8.74 (dd, *J* = 8.0, 1.2 Hz, 1H), 8.30 (d, *J* = 7.9 Hz, 1H), 7.90 (dd, *J* = 9.7, 0.6 Hz, 1H), 7.86–7.81 (m, 1H), 7.80–7.75 (m, 1H), 7.59 (dd, *J* = 9.7, 2.0 Hz, 1H); ¹³C NMR (100 MHz, CDCl₃) δ 147.3, 146.8, 145.8, 135.7, 131.6, 129.9, 129.0, 127.2, 123.3, 122.7, 122.0, 120.9, 118.6; HRMS calculated for C₁₄H₉ClN₃ [M + H]⁺ 254.0480, found 254.0479; HPLC purity 96.92%.

6-Phenylpyrido[2',1':2,3]imidazo[4,5-*c*]quinoline (C6). The general procedure was used with 2-(2'-bromophenyl)imidazo[1,2-*a*]pyridine (4a) (0.366 mmol) and benzaldehyde (5b) (0.439 mmol) as starting material. Purified the crude compound by column chromatography on silica gel (100–200 mesh) using ethyl acetate/hexane (20%, *v/v*) as eluent and obtained C6 as off white solid; 70 mg (65%); mp 207–209 °C (Lit.⁴⁹ 207–208 °C); ¹H NMR (400 MHz, CDCl₃) δ 8.82 (dd, *J* = 8.0, 1.1 Hz, 1H), 8.33 (dd, *J* = 8.3, 0.4 Hz, 1H), 8.07 (dt, *J* = 7.0, 1.1 Hz, 1H), 7.95 (dt, *J* = 9.2, 1.1 Hz, 1H), 7.86–7.80 (m, 1H), 7.78–7.73 (m, 3H), 7.70–7.63 (m, 3H), 7.58–7.52 (m, 1H), 6.81 (td, *J* = 6.9, 1.2 Hz, 1H); ¹³C NMR (100 MHz, CDCl₃) δ 149.7, 148.2, 147.5, 145.0, 138.3, 130.0, 129.64, 129.62, 129.3, 128.9, 128.7, 127.2, 126.6, 122.6, 121.5, 120.5, 118.1, 112.0; HRMS calculated for C₂₀H₁₄N₃ [M + H]⁺ 296.1182, found 296.1185; HPLC purity 99.16%.

11-Methyl-6-phenylpyrido[2',1':2,3]imidazo[4,5-*c*]quinoline (C7). The general procedure was used with 2-(2'-bromophenyl)-8-methylimidazo[1,2-*a*]pyridine (4f) (0.349 mmol) and benzaldehyde (5b) (0.418 mmol) as starting material. Purified the crude compound by column chromatography on silica gel (100–200 mesh) using ethyl acetate/hexane (20%, *v/v*) as eluent and obtained C7 as off white solid; 75 mg (70%); mp 234–236 °C (Lit.⁴⁹ 234–235 °C); ¹H NMR (400 MHz, CDCl₃) δ 8.88 (dd, *J* = 8.0, 1.2 Hz, 1H), 8.33 (d, *J* = 8.2 Hz, 1H), 7.92 (d, *J* = 6.9 Hz, 1H), 7.83–7.79 (m, 1H), 7.78–7.69 (m, 3H), 7.70–7.58 (m, 3H), 7.34 (dt, *J* = 6.9, 1.3 Hz, 1H), 6.71 (t, *J* = 6.9 Hz, 1H), 2.85 (s, 3H); ¹³C NMR (100 MHz, CDCl₃) δ 150.3, 148.3, 147.2, 144.7, 138.1, 129.6, 129.3, 129.3, 128.82, 128.79, 128.5, 128.1, 126.4, 124.9, 122.9, 121.6, 120.9, 112.0, 17.7; HRMS calculated for C₂₁H₁₆N₃ [M + H]⁺ 310.1339, found 310.1340; HPLC purity 99.31%.

11-Methyl-6-(*p*-tolyl)pyrido[2',1':2,3]imidazo[4,5-*c*]quinoline (C8). The general procedure was used with 2-(2'-bromophenyl)-8-methylimidazo[1,2-*a*]pyridine (4f) (0.349 mmol) and 4-methylbenzaldehyde (5c) (0.418 mmol) as starting material. Purified the crude compound by column chromatography on silica gel (100–200 mesh) using ethyl acetate/hexane (20%, *v/v*) as eluent and obtained C8 as off white solid; 84 mg (75%); mp 229–230 °C; ¹H NMR (400 MHz, CDCl₃) δ 8.86 (dd, *J* = 8.0, 1.2 Hz, 1H), 8.31 (d, *J* = 8.2 Hz, 1H), 7.99 (d, *J* = 6.9 Hz, 1H), 7.83–7.77 (m, 1H), 7.76–7.69 (m, 1H), 7.63 (d, *J* = 8.0 Hz, 2H), 7.45 (d, *J* = 7.8 Hz, 2H), 7.36–7.30 (m, 1H), 6.71 (t, *J* = 6.9 Hz, 1H), 2.85 (s, 3H), 2.54 (s, 3H); ¹³C NMR (100 MHz, CDCl₃) δ 150.2, 148.5, 147.1, 144.9, 139.5, 135.4, 129.9, 129.4, 128.7, 128.3, 128.0, 126.2, 125.0, 122.8, 121.6, 121.0, 111.8,

21.5, 17.7; HRMS calculated for $C_{22}H_{18}N_3 [M + H]^+$ 324.1495, found 324.1505; HPLC purity 99.18%.

6-(4-Chlorophenyl)-11-methylpyrido[2',1':2,3]-imidazo[4,5-c]-quinoline (C9). The general procedure was used with 2-(2'-bromophenyl)-8-methylimidazo[1,2-a]pyridine (**4f**) (0.349 mmol) and 4-chlorobenzaldehyde (**5d**) (0.418 mmol) as starting material. Purified the crude compound by column chromatography on silica gel (100–200 mesh) using ethyl acetate/hexane (20%, v/v) as eluent and obtained **C9** as off white solid; 73 mg (61%); mp 269–270 °C; 1H NMR (400 MHz, $CDCl_3$) δ 8.85 (dd, $J = 8.0, 1.1$ Hz, 1H), 8.28 (d, $J = 7.8$ Hz, 1H), 7.94 (d, $J = 6.9$ Hz, 1H), 7.84–7.77 (m, 1H), 7.76–7.69 (m, 3H), 7.68–7.61 (m, 2H), 7.38–7.30 (m, 1H), 6.74 (t, $J = 6.9$ Hz, 1H), 2.84 (s, 3H); ^{13}C NMR (100 MHz, $CDCl_3$) δ 150.3, 147.2, 146.9, 144.8, 136.8, 135.7, 130.3, 129.5, 129.4, 128.8, 128.5, 128.2, 126.5, 124.7, 122.8, 121.7, 120.7, 112.1, 17.7; HRMS calculated for $C_{21}H_{15}ClN_3 [M + H]^+$ 344.0949, found 344.0951; HPLC purity 99.80%.

11-Methyl-6-(thiophen-2-yl)pyrido[2',1':2,3]-imidazo[4,5-c]-quinoline (C10). The general procedure was used with 2-(2'-bromophenyl)-8-methylimidazo[1,2-a]pyridine (**4f**) (0.349 mmol) and thiophene-2-carbaldehyde (**5e**) (0.418 mmol) as starting material. Purified the crude compound by column chromatography on silica gel (100–200 mesh) using ethyl acetate/hexane (25%, v/v) as eluent and obtained **C10** as off white solid; 78 mg (71%); mp 215–217 °C; 1H NMR (400 MHz, $CDCl_3$) δ 8.86 (dd, $J = 8.0, 1.2$ Hz, 1H), 8.30 (d, $J = 8.1$ Hz, 1H), 8.25 (d, $J = 7.0$ Hz, 1H), 7.82–7.78 (m, 1H), 7.76–7.72 (m, 1H), 7.66 (dd, $J = 5.2, 1.2$ Hz, 1H), 7.51–7.47 (m, 1H), 7.36 (dt, $J = 6.9, 1.2$ Hz, 1H), 7.33–7.31 (m, 1H), 6.79 (t, $J = 6.9$ Hz, 1H), 2.85 (s, 3H); ^{13}C NMR (100 MHz, $CDCl_3$) δ 150.3, 147.2, 144.8, 141.6, 139.6, 129.5, 128.8, 128.5, 128.3, 128.2, 128.1, 127.6, 126.7, 125.0, 122.8, 121.8, 121.3, 112.0, 17.7; HRMS calculated for $C_{19}H_{14}N_3S [M + H]^+$ 316.0903, found 316.0905; HPLC purity 98.46%.

11-Methyl-6-(pyridin-2-yl)pyrido[2',1':2,3]imidazo[4,5-c]-quinoline (C11). The general procedure was used with 2-(2'-bromophenyl)-8-methylimidazo[1,2-a]pyridine (**4f**) (0.349 mmol) and picolinaldehyde (**5f**) (0.418 mmol) as starting material. Purified the crude compound by column chromatography on silica gel (100–200 mesh) using ethyl acetate/hexane (25%, v/v) as eluent and obtained **C11** as light brown solid; 60 mg (55%); mp 231–233 °C; 1H NMR (400 MHz, $CDCl_3$) δ 8.90 (dd, $J = 8.0, 1.2$ Hz, 1H), 8.88–8.85 (m, 1H), 8.82 (d, $J = 7.0$ Hz, 1H), 8.31 (d, $J = 8.0$ Hz, 2H), 8.06 (td, $J = 7.7, 1.8$ Hz, 1H), 7.84–7.79 (m, 1H), 7.78–7.73 (m, 1H), 7.57–7.53 (m, 1H), 7.38 (dt, $J = 6.8, 1.3$ Hz, 1H), 6.82 (t, $J = 6.9$ Hz, 1H), 2.86 (s, 3H); ^{13}C NMR (100 MHz, $CDCl_3$) δ 157.3, 150.5, 148.6, 148.0, 146.7, 144.6, 137.8, 129.5, 128.7, 128.6, 127.6, 127.4, 126.8, 125.4, 124.4, 123.0, 122.1, 121.3, 111.5, 17.7; HRMS calculated for $C_{20}H_{15}N_4 [M + H]^+$ 311.1291, found 311.1295; HPLC purity 99.32%.

10-Methyl-6-phenylpyrido[2',1':2,3]imidazo[4,5-c]quinoline (C12). The general procedure was used with 2-(2'-bromophenyl)-7-methylimidazo[1,2-a]pyridine (**4b**) (0.349 mmol) and benzaldehyde (**5b**) (0.418 mmol) as starting material. Purified the crude compound by column chromatography on silica gel (100–200 mesh) using ethyl acetate/hexane (20%, v/v) as eluent and obtained **C12** as off white solid; 73 mg (68%); mp 223–225 °C; 1H NMR (400 MHz, $CDCl_3$) δ 8.79 (dd, $J = 8.0, 1.0$ Hz, 1H), 8.31 (d, $J = 8.2$ Hz, 1H), 7.92 (d, $J = 7.1$ Hz, 1H), 7.83–7.78 (m, 1H), 7.77–7.71 (m, 3H), 7.68 (s, 1H), 7.67–7.62 (m, 3H), 6.62 (dd, $J = 7.1, 1.5$ Hz, 1H), 2.50 (s, 3H); ^{13}C NMR (100 MHz, $CDCl_3$) δ 150.3, 147.9, 147.8, 145.1, 141.6, 138.4, 129.6, 129.5, 129.3, 128.7, 126.4, 126.2, 122.6, 121.5, 120.4, 116.3, 114.7, 21.8; HRMS calculated for $C_{21}H_{16}N_3 [M + H]^+$ 310.1339, found 310.1341; HPLC purity 97.72%.

10-Methyl-6-(p-tolyl)pyrido[2',1':2,3]imidazo[4,5-c]quinoline (C13). The general procedure was used with 2-(2'-bromophenyl)-7-methylimidazo[1,2-a]pyridine (**4b**) (0.349 mmol) and 4-methylbenzaldehyde (**5c**) (0.418 mmol) as starting material. Purified the crude compound by column chromatography on silica gel (100–200 mesh) using ethyl acetate/hexane (20%, v/v) as eluent and obtained **C13** as off white solid; 78 mg (70%); mp 240–241 °C; 1H NMR (400 MHz,

$CDCl_3$) δ 8.77 (d, $J = 7.6$ Hz, 1H), 8.29 (d, $J = 8.3$ Hz, 1H), 7.98 (d, $J = 7.1$ Hz, 1H), 7.78 (t, $J = 7.0$ Hz, 1H), 7.71 (t, $J = 7.3$ Hz, 1H), 7.66 (s, 1H), 7.63 (d, $J = 7.9$ Hz, 2H), 7.44 (d, $J = 7.7$ Hz, 2H), 6.61 (d, $J = 6.1$ Hz, 1H), 2.53 (s, 3H), 2.47 (s, 3H); ^{13}C NMR (100 MHz, $CDCl_3$) δ 150.2, 148.1, 147.5, 145.0, 141.6, 139.5, 135.4, 129.9, 129.5, 128.7, 128.6, 126.3, 126.2, 122.6, 121.4, 120.4, 116.2, 114.6, 21.8, 21.5; HRMS calculated for $C_{22}H_{18}N_3 [M + H]^+$ 324.1495, found 324.1498; HPLC purity 95.23%.

6-(4-Methoxyphenyl)-10-methylpyrido[2',1':2,3]-imidazo[4,5-c]-quinoline (C14). The general procedure was used with 2-(2'-bromophenyl)-7-methylimidazo[1,2-a]pyridine (**4b**) (0.349 mmol) and 4-methoxybenzaldehyde (**5g**) (0.418 mmol) as starting material. Purified the crude compound by column chromatography on silica gel (100–200 mesh) using ethyl acetate/hexane (20%, v/v) as eluent and obtained **C14** as off white solid; 76 mg (64%); mp 248–250 °C; 1H NMR (400 MHz, $CDCl_3$) δ 8.76 (d, $J = 7.9$ Hz, 1H), 8.28 (d, $J = 8.3$ Hz, 1H), 8.03 (d, $J = 7.1$ Hz, 1H), 7.81–7.75 (m, 1H), 7.74–7.63 (m, 4H), 7.16 (d, $J = 8.6$ Hz, 2H), 6.62 (dd, $J = 7.1, 1.3$ Hz, 1H), 3.96 (s, 3H), 2.48 (s, 3H); ^{13}C NMR (100 MHz, $CDCl_3$) δ 160.6, 150.2, 147.8, 147.6, 145.1, 141.5, 130.7, 130.2, 129.4, 128.7, 126.3, 126.2, 122.6, 121.4, 120.5, 116.2, 114.64, 114.61, 55.5, 21.8; HRMS calculated for $C_{22}H_{18}N_3O [M + H]^+$ 340.1444, found 340.1447; HPLC purity 97.61%.

6-(p-Tolyl)pyrido[2',1':2,3]imidazo[4,5-c]quinoline (C15). The general procedure was used with 2-(2'-bromophenyl)imidazo[1,2-a]pyridine (**4a**) (0.366 mmol) and 4-methylbenzaldehyde (**5c**) (0.439 mmol) as starting material. Purified the crude compound by column chromatography on silica gel (100–200 mesh) using ethyl acetate/hexane (20%, v/v) as eluent and obtained **C15** as off white solid; 79 mg (70%); mp 237–239 °C (Lit.⁵⁰ 239–240 °C); 1H NMR (400 MHz, $CDCl_3$) δ 8.81 (dd, $J = 8.0, 1.1$ Hz, 1H), 8.32 (d, $J = 8.3$ Hz, 1H), 8.14 (d, $J = 7.0$ Hz, 1H), 7.93 (d, $J = 9.1$ Hz, 1H), 7.85–7.78 (m, 1H), 7.78–7.71 (m, 1H), 7.64 (d, $J = 8.0$ Hz, 2H), 7.57–7.51 (m, 1H), 7.46 (d, $J = 7.8$ Hz, 2H), 6.81 (t, $J = 6.9$ Hz, 1H), 2.54 (s, 3H); ^{13}C NMR (100 MHz, $CDCl_3$) δ 149.7, 148.4, 147.4, 145.1, 139.6, 135.5, 130.0, 129.9, 129.6, 128.8, 128.6, 127.3, 126.5, 122.6, 121.5, 120.5, 118.0, 111.9, 21.5; HRMS calculated for $C_{21}H_{16}N_3 [M + H]^+$ 310.1339, found 310.1322; HPLC purity 97.67%.

6-(4-Chlorophenyl)pyrido[2',1':2,3]imidazo[4,5-c]quinoline (C16). The general procedure was used with 2-(2'-bromophenyl)imidazo[1,2-a]pyridine (**4a**) (0.366 mmol) and 4-chlorobenzaldehyde (**5d**) (0.439 mmol) as starting material. Purified the crude compound by column chromatography on silica gel (100–200 mesh) using ethyl acetate/hexane (20%, v/v) as eluent and obtained **C16** as off white solid; 70 mg (58%); mp 255–257 °C; 1H NMR (400 MHz, $CDCl_3$) δ 8.81 (dd, $J = 8.0, 1.1$ Hz, 1H), 8.30 (d, $J = 8.0$ Hz, 1H), 8.12 (d, $J = 7.0$ Hz, 1H), 7.96 (d, $J = 9.1$ Hz, 1H), 7.86–7.80 (m, 1H), 7.79–7.74 (m, 1H), 7.74–7.63 (m, 4H), 7.60–7.55 (m, 1H), 6.87 (td, $J = 6.9, 1.0$ Hz, 1H); ^{13}C NMR (100 MHz, $CDCl_3$) δ 149.7, 147.6, 146.9, 145.0, 136.8, 135.8, 130.3, 130.1, 129.6, 129.1, 127.0, 126.8, 122.7, 121.5, 120.3, 118.2, 112.2; HRMS calculated for $C_{20}H_{13}ClN_3 [M + H]^+$ 330.0793, found 330.0794; HPLC purity 99.80%.

6-(3,4,5-Trimethoxyphenyl)pyrido[2',1':2,3]-imidazo[4,5-c]-quinoline (C17). The general procedure was used with 2-(2'-bromophenyl)imidazo[1,2-a]pyridine (**4a**) (0.366 mmol) and 3,4,5-trimethoxybenzaldehyde (**5h**) (0.439 mmol) as starting material. Purified the crude compound by column chromatography on silica gel (100–200 mesh) using ethyl acetate/hexane (30%, v/v) as eluent and obtained **C17** as off white solid; 92 mg (65%); mp 244–245 °C; 1H NMR (400 MHz, $CDCl_3$) δ 8.82 (dd, $J = 8.0, 1.2$ Hz, 1H), 8.33 (d, $J = 8.3$ Hz, 1H), 8.15 (d, $J = 7.0$ Hz, 1H), 7.96 (d, $J = 9.1$ Hz, 1H), 7.84–7.82 (m, 1H), 7.79–7.75 (m, 1H), 7.61–7.56 (m, 1H), 6.94 (s, 2H), 6.88 (td, $J = 6.9, 1.1$ Hz, 1H). ^{13}C NMR (100 MHz, $CDCl_3$) δ 154.1, 149.7, 147.9, 147.4, 144.9, 138.9, 133.6, 130.1, 129.5, 129.0, 127.4, 126.7, 122.7, 121.5, 120.3, 118.0, 112.2, 105.5, 61.1, 56.3; HRMS calculated for $C_{23}H_{20}N_3O_3 [M + H]^+$ 386.1499, found 386.1504; HPLC purity 98.52%.

6-(4-Nitrophenyl)pyrido[2',1':2,3]imidazo[4,5-c]quinoline (C18). The general procedure was used with 2-(2'-bromophenyl)imidazo[1,2-a]pyridine (**4a**) (0.366 mmol) and 4-nitrobenzaldehyde (**5i**)

(0.439 mmol) as starting material. Purified the crude compound by column chromatography on silica gel (100–200 mesh) using ethyl acetate/hexane (25%, v/v) as eluent and obtained **C18** as yellow solid; 66 mg (53%); mp 271–273 °C (Lit.⁴⁹ 285–286 °C); ¹H NMR (400 MHz, CDCl₃) δ 8.83 (dd, *J* = 8.0, 1.2 Hz, 1H), 8.55 (dt, *J* = 8.7, 1.9 Hz, 2H), 8.31 (dd, *J* = 8.2, 0.7 Hz, 1H), 8.05 (dt, *J* = 7.0, 1.0 Hz, 1H), 8.02–7.96 (m, 3H), 7.88–7.84 (m, 1H), 7.82–7.8 (m, 1H), 7.62–7.58 (m, 1H), 6.89 (td, *J* = 6.9, 1.2 Hz, 1H); ¹³C NMR (100 MHz, CDCl₃) δ 149.9, 148.6, 147.8, 145.4, 144.9, 144.6, 130.3, 130.2, 129.7, 129.4, 127.3, 126.7, 124.5, 122.8, 121.6, 120.0, 118.5, 112.6; HRMS calculated for C₂₀H₁₃N₄O₂ [M + H]⁺ 341.1033, found 341.1032; HPLC purity 99.88%.

6-(3-Nitrophenyl)pyrido[2',1':2,3]imidazo[4,5-c]quinoline (C19). The general procedure was used with 2-(2'-bromophenyl)imidazo[1,2-a]pyridine (**4a**) (0.366 mmol) and 3-nitrobenzaldehyde (**5j**) (0.439 mmol) as starting material. Purified the crude compound by column chromatography on silica gel (100–200 mesh) using ethyl acetate/hexane (25%, v/v) as eluent and obtained **C19** as yellow solid; 68 mg (55%); mp 219–221 °C; ¹H NMR (400 MHz, CDCl₃) δ 8.84 (dd, *J* = 8.0, 1.2 Hz, 1H), 8.71 (t, *J* = 1.8 Hz, 1H), 8.54–8.51 (m, 1H), 8.31 (dd, *J* = 8.4, 0.8 Hz, 1H), 8.16–8.13 (m, 1H), 8.06 (d, *J* = 7.0 Hz, 1H), 8.00 (d, *J* = 9.2 Hz, 1H), 7.91–7.84 (m, 2H), 7.82–7.80 (m, 1H), 7.63–7.58 (m, 1H), 6.89 (td, *J* = 6.9, 1.1 Hz, 1H); ¹³C NMR (100 MHz, CDCl₃) δ 149.9, 148.7, 147.9, 145.1, 144.9, 140.1, 134.9, 130.4, 130.3, 129.6, 129.4, 127.3, 126.6, 124.4, 124.2, 122.8, 121.6, 120.1, 118.5, 112.6; HRMS calculated for C₂₀H₁₃N₄O₂ [M + H]⁺ 341.1033, found 341.1033; HPLC purity 99.56%.

6-(2-Nitrophenyl)pyrido[2',1':2,3]imidazo[4,5-c]quinoline (C20). The general procedure was used with 2-(2'-bromophenyl)imidazo[1,2-a]pyridine (**4a**) (0.366 mmol), and 2-nitrobenzaldehyde (**5k**) (0.439 mmol) as starting material. Purified the crude compound by column chromatography on silica gel (100–200 mesh) using ethyl acetate/hexane (25%, v/v) as eluent and obtained **C20** as yellow solid; 56 mg (45%); mp 219–221 °C; ¹H NMR (400 MHz, CDCl₃) δ 8.84 (dd, *J* = 7.8, 1.4 Hz, 1H), 8.38 (dd, *J* = 8.2, 1.1 Hz, 1H), 8.23–8.22 (m, 1H), 7.98 (dt, *J* = 9.2, 1.2 Hz, 1H), 7.92 (td, *J* = 7.5, 1.3 Hz, 1H), 7.86–7.84 (m, 1H), 7.82 (dt, *J* = 9.1, 1.8 Hz, 1H), 7.72–7.76 (m, 1H), 7.71 (dd, *J* = 7.5, 1.4 Hz, 1H), 7.68 (dt, *J* = 7.0, 1.0 Hz, 1H), 7.58–7.53 (m, 1H), 6.81 (td, *J* = 6.9, 1.1 Hz, 1H); ¹³C NMR (100 MHz, CDCl₃) δ 149.6, 148.1, 147.0, 144.8, 144.2, 134.4, 133.5, 131.7, 130.7, 130.1, 129.5, 129.1, 127.1, 125.9, 125.3, 122.8, 121.8, 120.8, 118.3, 112.7; HRMS calculated for C₂₀H₁₃N₄O₂ [M + H]⁺ 341.1033, found 341.1026; HPLC purity 98.90%.

6-(3,4-Dimethoxyphenyl)pyrido[2',1':2,3]imidazo[4,5-c]quinoline (C21). The general procedure was used with 2-(2'-bromophenyl)imidazo[1,2-a]pyridine (**4a**) (0.366 mmol) and 3,4-dimethoxybenzaldehyde (**5l**) (0.439 mmol) as starting material. Purified the crude compound by column chromatography on silica gel (100–200 mesh) using ethyl acetate/hexane (50%, v/v) as eluent and obtained **C21** as off white solid; 79 mg (61%); mp 235–237 °C; ¹H NMR (400 MHz, CDCl₃) δ 8.77 (dd, *J* = 8.0, 1.6 Hz, 1H), 8.29 (d, *J* = 8.2 Hz, 1H), 8.16–8.12 (m, 1H), 7.93–7.89 (m, 1H), 7.81–7.76 (m, 1H), 7.73–7.68 (m, 1H), 7.55–7.49 (m, 1H), 7.28–7.26 (m, 2H), 7.13–7.09 (m, 1H), 6.80 (td, *J* = 6.9, 1.2 Hz, 1H), 4.02 (s, 3H), 3.95 (s, 3H); ¹³C NMR (100 MHz, CDCl₃) δ 150.2, 149.7, 149.7, 148.0, 144.9, 130.7, 130.0, 129.4, 128.9, 127.3, 126.5, 122.6, 121.4, 121.3, 120.5, 119.9, 118.0, 112.0, 111.7, 111.6, 77.4, 56.1; HRMS calculated for C₂₂H₁₈N₃O₂ [M + H]⁺ 356.1394, found 386.1504; HPLC purity 98.45%.

Animal Ethics Statement. The study was approved by and carried out under the guidelines of the Ethical Committee of the Indian Association for the Cultivation of Science, Kolkata. All subjects who participated in this study provided informed consent in writing according to the Indian Association for the Cultivation of Science guidelines and approval. The animal experiments were approved by the Animal Ethical Committee of the institute, according to the National Regulatory Guidelines issued by the Committee for the Purpose of Control and Supervision on Experimental Animals (CPCSEA), under the Division of Animal Welfare, Ministry of Environment and Forest, Government of India.

Chemicals. 3-(4,5-Dimethyl-2-thiazolyl)-2,5-diphenyl-2H-tetrazolium-bromide (MTT), dimethyl sulfoxide (DMSO), isopropyl-β-D-thiogalactoside (IPTG), camptothecin (CPT), amphotericin B, penicillin, and streptomycin were purchased from Sigma-Aldrich (St. Louis, MO, USA). CPT and **C17** were dissolved in 100% DMSO (Sigma) at a concentration of 10 mM and stored at –20 °C.

Parasite Maintenance and Culture. The *Leishmania donovani* cells were cultured in M199 containing 10% (v/v) heat-inactivated fetal bovine serum (FBS) supplemented with 100 IU/mL of penicillin and 100 mg/mL of streptomycin at 22 °C. Promastigotes were obtained from amastigotes of the spleens of infected hamsters and were cultured in 10% (v/v) heat-inactivated FBS for 3–5 days at 22 °C. The antimony-resistant field isolates MHOM/IN/2009/BHU575/0 (BHU-575) strains of *Leishmania donovani* cells were cultured as discussed previously and utilized for the experiments.^{37,38}

Cell Extracts. Cellular extracts from Ag83 or BHU575 cells were prepared as described previously.^{37,38} Briefly, cells were lysed in buffer (10 mM Tris-HCl, pH 7.5, 0.1 mM EGTA, 1 mM EDTA, 1 mM PMSE, 5 mM DTT, and 1 mM Benzamide hydrochloride), homogenized and was centrifuged at 10,000 rpm for 10 min at 4 °C. The lysate was utilized as the source of the endogenous LdTop1 enzyme for plasmid DNA relaxation assays.

Purification of Recombinant *Leishmania* Bisubunit Top1 (LdTop1). The large (LdTOP1L, 73 kDa) and the small (LdTOP1S, 29 kDa) subunits of LdTop1 were cloned in pET16b separately.^{14,37,38} *Escherichia coli* BL21(DE3)/pLysS cells harboring pET16b-LdTOP1L and pET16b-LdTOP1S were separately induced at an optical density of 0.6 at 600 nm with 0.5 mM IPTG (isopropyl-β-D-thiogalactoside) at 22 °C for 12 h. Cells were separately lysed by lysozyme and then sonicated. The proteins were purified through Ni-NTA column (Qiagen, Hilden, Germany) followed by a phosphocellulose column (P11 cellulose; Whatman, Maidstone, Kent, United Kingdom). Both the subunits were mixed at a molar ratio of 1:1 at a total protein concentration of 0.5 mg/mL in reconstitution buffer and dialyzed overnight at 4 °C as described.^{14,37,38}

Recombinant Human Top1 Purification. The recombinant human Top1 was purified from Sf-9 insect cells which were infected with the recombinant baculovirus (a kind gift from Prof. James J. Champoux) as described previously.^{22–24,51}

Plasmid DNA Relaxation Assay. DNA topoisomerases were assayed by decreased mobility of the relaxed isomers of supercoiled pBluescript SK(+) [pBS SK(+)] DNA at 37 °C for 30 min in 1% agarose gel.^{22–24,51} LdTop1 was diluted in the relaxation buffer (25 mM Tris-HCl [pH 7.5], 5% glycerol, 0.5 mM DTT, 10 mM MgCl₂, 50 mM KCl, 25 mM EDTA, and 150 μg/mL bovine serum albumin [BSA]) and supercoiled plasmid pBS SK(+) DNA (85 to 95% were negatively supercoiled, with the remaining being nicked circles). For recombinant human Top1, the relaxation assay was carried out as described elsewhere.^{22–24,51}

Ex vivo relaxation assays were carried out with whole-cell extracts obtained from indicated cells as described.^{22,23} Briefly, the equivalent amount of whole-cell extracts from indicated cells was incubated with supercoiled pBS SK(+) DNA (200 ng) in the relaxation buffer (25 mM Tris-HCl [pH 7.5], 10 mM MgCl₂, 5% glycerol, 50 mM KCl, 0.5 mM DTT, 25 mM EDTA, and 150 mg/mL bovine serum albumin [BSA]) at 37 °C for 30 min and products from relaxation assay were analyzed by agarose gel electrophoresis as discussed before.

Plasmid DNA Cleavage Assay. For cleavage assay, 50 fmol of pBS SK(+) supercoiled DNA and 100 fmol of reconstituted

Lsco or recombinant human Top1 were incubated in a standard reaction mixture (50 μL) containing 50 mM Tris-HCl (pH 7.5), 100 mM KCl, 10 mM MgCl₂, 0.5 mM DTT, 0.5 mM EDTA, and 30 μg/mL BSA^{37,38} at 37 °C for 30 min. The reactions were terminated by adding 1% SDS and 150 μg/mL proteinase K, and the mixtures were further incubated for 1 h at 37°C. DNA samples were electrophoresed in 1% agarose gel containing 0.5 μg/mL EtBr to resolve more slowly migrating nicked product (form II) from the supercoiled molecules (form I).

Oligonucleotide Cleavage Assay. Equilibrium cleavage assays with a 25-mer duplex of an oligonucleotide containing a Top1 binding

motif were labeled and annealed as described previously.²³ Samples were analyzed by 12% sequencing gel electrophoresis, dried, exposed on PhosphorImager screens, and imaged with Typhoon FLA 7000 (GE Healthcare, UK).

Analysis of Compound 17–DNA Intercalation. The ability of the drug to intercalate into plasmid DNA was determined by the Top1 unwinding assay.^{22,23} Assays were performed with 50 fmol of pBluscript (SK+) DNA in the presence or absence of C17, m-AMSA, and etoposide. Relaxed DNA was prepared by treatment of the supercoiled plasmid DNA with an excess of LdTop1, followed by proteinase K digestion at 37 °C, phenol/chloroform extraction, and ethanol precipitation. After incubation at 37 °C for 15 min, reactions were terminated and electrophoresed onto 1% agarose gel as described above.^{22,23} The DNA band was stained with 0.5 μg/mL of EtBr and visualized by UV light as described above.

Second, an ethidium displacement fluorescence assay^{22,23} was employed to determine whether compound 17 binds in the minor groove of DNA. Fluorescence emission spectra ($\lambda_{\text{max}} = 590$ nm, excitation wavelength 510 nm) were obtained at 25 °C. The assays contained 1 μM EtBr, 0–300 mM compound 28, and 5 nM CT DNA in 2 mL of fluorescence buffer.

Cell Cycle Analysis. DNA synthesis or replication was measured by flow cytometry analysis (FACS). *L. donovani* promastigote (2.5×10^6 cells) were treated with camptothecin or C17 (5 μM) for the indicated time, harvested, and washed several times with PBS (1×). Fixation and staining of cells were performed and were analyzed via flow cytometry as discussed previously.³⁷ Detection of cells in individual G1, S, and G2/M phases of the cell cycle was carried out using a Becton Dickson flow cytometer and further data were processed by BD FACS Scan Software (San Diego, CA).

DNA Laddering Experiment. Fragmentation of DNA into oligonucleosomal bands, as a function of apoptotic cell death, was studied by DNA laddering assay as described before.⁴⁰ Briefly, the treated and untreated cells were suspended in 500 μL of extraction buffer followed by incubation on ice for 30 min and centrifuged at 15000g for 5 min. Isolated DNA aliquots were electrophoresed on 1.5% agarose gel containing ethidium bromide (0.5 μg/mL), using Tris-acetate-EDTA (pH 8.0) running buffer, and then observed and photographed under UV illumination in a BioRad gel documentation system (Bio-Rad Laboratories, Inc., Hercules, CA, USA).

SDS-KCl Precipitation Assay. For C17-induced protein–DNA complex determination, *L. donovani* promastigotes were labeled with 1X BrdU for 24 h and exposed to different concentrations of CPT, C17, and Top1 catalytic inhibitor (HR8) for 30 min. Cells were pelleted and permeabilized by incubation at 60 °C for 10 min in the presence of 2.5% (wt/vol) SDS, 0.8 mg/mL salmon sperm DNA, and 10 mM EDTA. After the addition of 65 mM KCl, the reaction mixture was incubated on ice for 60 min. The pellet was resuspended in 100 mM KCl (10 min at 65 degrees) followed by the repetition of the washing step. The resulting pellet was resuspended in anti-BrdU (Alexa-488 conjugated) antibody for 2 h, followed by a 1× PBS wash and spectrophotometric reading at 488 nm.

Measurement of Cell Viability. The viability of the *Leishmania donovani* promastigotes was measured by MTT assay.^{37,38,52,53} All EC₅₀ values were calculated by using the nonlinear variable slope model for finding EC₅₀ in Prism (ver. 5.0; GraphPad Software, USA).

Terminal Deoxyribonucleotide Transferase (TdT)-Mediated dUTP Nick-End Labeling (TUNEL) Assay. TUNEL assay was performed according to the manufacturer's instructions (ApoDirect Kit, BD Biosciences, Cat. 556381). Briefly, CPT/C17 treated and untreated promastigotes were harvested by centrifugation and fixed by adding 5 mL of fresh, prechilled 1% paraformaldehyde/PBS. The cell suspension was centrifuged for 5 min at 300g, and the pellets resuspended in 0.5 mL of PBS were then permeabilized by adding 5 mL of 70% ice-cold ethanol and incubated at –20 °C for at least 24 h before staining. The cells were then resuspended in 80 μL of equilibration buffer and incubated at room temperature for 5 min. The cells were washed with PBS and resuspended in 50 μL of TdT incubation buffer and incubated at 37 °C in a water bath for 60 min, followed by the addition of 20 mM EDTA to terminate the reaction,

and mixed by gentle vortexing. The cells were pelleted down by centrifugation and resuspended in 1 mL of 0.1% Triton X-100/BSA/PBS. The cells were then resuspended gently in 0.5 mL of PI/RNase/PBS to stain with PI following incubation at room temperature in the dark for 15 ± 30 min and spread on polylysine-coated glass slides. They were analyzed by confocal microscopy.

Double Staining with Annexin V and PI. The externalization of phosphatidyl-serine of indicated promastigotes with or without treatment of C17 or CPT was measured by attachment of FITC-annexin V and PI by an annexin V-FITC staining kit (Invitrogen Incorporation, Ltd.). Flow cytometry was also performed for treated and untreated parasites. The gating was fixed in such a way that the mean intensity of FITC-annexin V and the mean intensity of PI were depicted by FL-1 and FL-2 channels, respectively. The data presented are the mean of three independent experiments.³⁷

In vitro Macrophage Infection. Macrophages were isolated from Balb/c mice 36–48 h postinjection (intraperitoneal) with 2% (w/v) hydrolyzed starch by peritoneal lavage with ice-cold phosphate-buffered saline. *In vitro* infection with promastigotes was carried out as described previously.³⁷ C17 was added to infected macrophages and left for another 48–96 h period. Cells were then fixed in methanol and stained with Propidium Iodide (PI). Percentages of infected cells and the total number of intracellular parasites were determined by manual counting in at least 200 cells using a fluorescent microscope.

In vivo Studies. For experimental visceral infections, female BALB/c mice (4 weeks old and 20–25 g each) were divided into the following groups: (i) uninfected control group (ii) infection control group infected with Ag83 and BHU575 separately and (ii) two treatment groups for each infection group viz. Five and 10 mg C17/kg body weight, respectively. Each group consisted of 5 animals. The animals were injected via the intracardiac route with 2×10^7 hamster spleen-transformed *L. donovani* promastigotes (suspended in 200 μL of 0.02 M PBS per mouse).³⁷ Three weeks postinfection, C17 was administered to infected animals via intraperitoneal routes separately twice a week for 3 weeks. Visceral infection was determined by Giemsa-stained impression smears of spleen and liver from 6-week infected mice and reported as Leishman–Donovan Units (LDU), calculated as the number of parasites per 1000 nucleated cells × organ weight in mg,^{44,45} as well as by the Limiting Dilution Assay.^{44,45} For LDA calculation, a 1 mg/mL (w/v) organ suspension (spleen or liver) prepared in Schneider drosophila media was serially diluted and cultured at 22 °C for 2 weeks. Parasite burden was expressed as a 10 fold logarithm scale of the highest dilution containing viable parasites, and the mean values of five mice per group were represented. All the animals were euthanized by carbon dioxide exposure.

RT-PCR for mRNA Expression of Cytokines. Total RNA was isolated from 1 mg organ (in presence of liquid nitrogen) of different control and treatment groups of Balb/c mice used for the study, using TriZOL method (15596018, Invitrogen), which includes deoxyribonuclease (AMPD1; Sigma-Aldrich) treatment for each sample. The RNA pellet obtained was dissolved in diethyl pyrocarbonate (DEPC) treated water and the concentration was measured using a UV-visible spectrophotometer. An aliquot of 2 μg of RNA was reverse-transcribed using a reverse transcription kit (4368814, Applied Biosystems). For RT-PCR, 2 μL of cDNA, 0.5 μL of 25 nM primer pairs of the respective gene as well as internal control, 5 μL of SYBR green master mix (A25742, Applied Biosystems), and nuclease free water were added in 10 μL of reaction mixture, and PCR was performed in ABI 7500 thermocycler (Applied Biosystems) software and fold change was calculated using the following formula:

$$\begin{aligned} \text{fold change} &= 2^{-\Delta\Delta C_t}; \\ \Delta\Delta C_t &= (\Delta C_{t_{\text{experiment}}} - \Delta C_{t_{\text{control}}}); \\ (\Delta C_t &= \Delta C_{t_{\text{gene}}} - \Delta C_{t_{\text{Actin}}}) \end{aligned}$$

All the experiments were performed in triplicate, and mouse β-actin was used as a reference gene. Details of primers are provided in Table S1. A negative control containing all reaction components except the reverse transcriptase enzyme was included and subjected to RT-PCR

to confirm the absence of DNA contamination in RNA. The primers used for the experiment have been enlisted Table S1.

DNA Isolation from Blood and Parasites. Blood samples were collected in heparinized tubes. DNA extraction was performed using QIAamp DNA Blood mini kits (Qiagen, Germany) from whole blood or organs according to the manufacturer's instructions. DNA was isolated from 400 μL of sample and eluted in 25 μL elution buffer. A stock solution of *L. donovani* DNA was also obtained by extraction (QIAamp DNA mini kit, Qiagen, Germany) from 2.5×10^6 promastigotes. After eluting in 25 μL of elution buffer, assuming the extraction was nearly 100% efficient, the DNA concentration corresponded to 10^5 parasites/ μL . All the DNAs were stored at -20°C until use.

qPCR Assay for the Estimation of Parasite Burden in Mice.

SYBR Green-based real-time PCR was applied for quantification of the *Leishmania* parasites in mice blood. For accurate sensitivity, *L. donovani*-specific kinetoplast DNA was chosen as the target region. The PCR was performed in a final volume of 20 μL containing 10 μL of SYBR Green master mixture, 3 μL of MilliQ water, 5 μL of DNA template, and 1 μL (50 pmol/ μL) of forward and reverse primers, 5'-CTTTTCTGGTCCCTCCGGGTAGG-3' and 5'-CCACCCGGCCC-TATTTACACCAA-3', respectively. To construct the standard curve 10-fold serially diluted *L. donovani* DNA stocks corresponding to 10^5 , 10^4 , 10^3 , 10^2 , 10, and 1 parasite/ μL were included in the assay. The thermal cycling conditions included an initial incubation at 50°C for 2 min, followed by a 10 min denaturation at 95°C and 40 cycles at 95°C for 15 s and 60°C for 1 min each. Each sample was tested in triplicate. Negative controls with no template were included in each plate to deal with contamination issues. For all the real-time PCR reactions we used specific primers for the constitutively expressed GAPDH gene as a quality control to verify the integrity of the DNA samples. Threshold cycle values (Ct) were calculated by determining the point at which the fluorescence exceeded the threshold limit plotted against known concentrations of parasite DNA, and the parasite load of Balb/c mice was then determined using the standard curve.

Statistical Calculations. Results are reported as mean SEM and statistical significance was determined with the unpaired *t* test with Welch's or Mann–Whitney correction test by GraphPad Software, LLC.

■ ASSOCIATED CONTENT

SI Supporting Information

The Supporting Information is available free of charge at <https://pubs.acs.org/doi/10.1021/acs.jmedchem.2c01932>.

A table of molecular formula strings for each derivative (C1–C21) with their *in vitro* and *ex vivo* IC₅₀ (CSV)

Supporting Figures S1–S5 and their corresponding Figure legends; Table S1, List of primers for qPCR used in the study; Table S2, Optimization of the reaction conditions for the synthesis of pyrido[2',1':2,3]imidazo[4,5-c]quinolones; ¹H NMR, ¹³C NMR, HRMS, and HPLC spectra of pyrido[2',1':2,3]imidazo[4,5-c]quinolines (C1–C21) (PDF)

■ AUTHOR INFORMATION

Corresponding Authors

Benu Brata Das – Laboratory of Molecular Biology, School of Biological Sciences, Indian Association for the Cultivation of Science, Jadavpur, Kolkata 700032, India; orcid.org/0000-0003-2519-7105; Email: pcbhd@iacs.res.in

Anil Kumar – Department of Chemistry, Birla Institute of Technology and Science, Pilani 333 031 Rajasthan, India; orcid.org/0000-0003-4699-3178; Email: anilkumar@pilani.bits-pilani.ac.in

Authors

Srijita Paul Chowdhuri – Laboratory of Molecular Biology, School of Biological Sciences, Indian Association for the Cultivation of Science, Jadavpur, Kolkata 700032, India

Shiv Dhiman – Department of Chemistry, Birla Institute of Technology and Science, Pilani 333 031 Rajasthan, India; Present Address: University of Manitoba, Winnipeg, MB R3T 2N2, Canada

Subhendu K. Das – Laboratory of Molecular Biology, School of Biological Sciences, Indian Association for the Cultivation of Science, Jadavpur, Kolkata 700032, India; Present Address: National Cancer Institute, NIH, MD 20892–4255, USA.

Neha Meena – Department of Chemistry, Birla Institute of Technology and Science, Pilani 333 031 Rajasthan, India

Sonali Das – Infectious Diseases & Immunology Division, CSIR-Indian Institute of Chemical Biology, Kolkata 700 032, India; Present Address: National Heart, Lung, and Blood Institute, NIH, MD 20892–4255, USA.

Complete contact information is available at:

<https://pubs.acs.org/10.1021/acs.jmedchem.2c01932>

Author Contributions

S.P.C. performed the biochemical assays, cellular, and *in vivo* experiments. S.D. and N.M. performed the synthesis of the PIQ derivatives. Recombinant human Top1 was purified by S.K.D. S.D. helped animal studies, and S.P.C. analyzed the data. B.B.D. supervised the project. S.P.C. wrote the draft manuscript which was edited by B.B.D. and A.K. All authors put their comments to improve the quality of the manuscript.

Notes

The authors declare no competing financial interest.

■ ACKNOWLEDGMENTS

The authors wish to thank Dr. Syamal Roy and Dr. Nahid Ali, Council of Scientific and Industrial Research–Indian Institute of Chemical Biology (CSIR-IICB), Kolkata 700032 for the kind gift of the drug-resistant parasite (MHOM/IN/2005/BHU575) and help during the study. Dr. Syamal Roy helped the discussion during addressing reviewers' comments. The B.B.D. team is supported by S Ramachandran National Bioscience Award for Career Development (NBACD)—2019 grant (102/IFD/SAN/3574/2019-20) and IACS intramural funds. S.K.D. and S.P.C. are recipients of the IACS senior research fellowship, India.

■ ABBREVIATIONS

BrdU, bromodeoxyuridine; CPT, camptothecin; DSB, double strand break; EtBr, ethidium bromide; FITC, fluorescein isothiocyanate; IFN- γ , interferon- γ ; IL, interleukin; iNOS, inducible nitric oxide synthase; kDNA, kinetoplast DNA; Ld, *Leishmania donovani*; LDA, limiting dilution assay; LDU, Leishman–Donovan unit; PCR, polymerase chain reaction; PI, propidium iodide; PIQ, pyrido-imidazo-quinoline; qPCR, quantitative polymerase chain reaction; RT PCR, real-time polymerase chain reaction; SSG, sodium stibo-gluconate; TGF- β , transforming growth factor- β ; Th, T-helper; TNF- α , tumor necrosis factor- α ; Top1, topoisomerase 1; Top1cc, topoisomerase 1-DNA covalent complexes; TUNEL, terminal deoxynucleotidyl transferase dUTP nick end labeling; VL, visceral leishmaniasis

REFERENCES

- (1) Torres-Guerrero, E.; Quintanilla-Cedillo, M. R.; Ruiz-Esmenjaud, J.; Arenas, R. Leishmaniasis: a review. *F1000Research* **2017**, *6*, 750–750.
- (2) Desjeux, P. The increase in risk factors for leishmaniasis worldwide. *Transactions of the royal society of tropical medicine and hygiene* **2001**, *95*, 239–243.
- (3) Kaye, P.; Scott, P. Leishmaniasis: complexity at the host–pathogen interface. *Nature Reviews Microbiology* **2011**, *9*, 604–615.
- (4) Sacks, D.; Kamhawi, S. Molecular Aspects of Parasite-Vector and Vector-Host Interactions in Leishmaniasis. *Annu. Rev. Microbiol.* **2001**, *55*, 453–483.
- (5) Mann, S.; et al. A Review of Leishmaniasis: Current Knowledge and Future Directions. *Current tropical medicine reports* **2021**, *8*, 121–132.
- (6) Altamura, F.; Rajesh, R.; Catta-Preta, C. M. C.; Moretti, N. S.; Cestari, I. The current drug discovery landscape for trypanosomiasis and leishmaniasis: Challenges and strategies to identify drug targets. *Drug Development Research* **2022**, *83*, 225.
- (7) Chappuis, F.; et al. Visceral leishmaniasis: what are the needs for diagnosis, treatment and control? *Nature Reviews Microbiology* **2007**, *5*, 873–882.
- (8) Bi, K.; Chen, Y.; Zhao, S.; Kuang, Y.; John Wu, C.-H. Current Visceral Leishmaniasis Research: A Research Review to Inspire Future Study. *BioMed Research International* **2018**, 9872095.
- (9) Mohapatra, S. Drug resistance in leishmaniasis: Newer developments. *Tropical parasitology* **2014**, *4*, 4–9.
- (10) Sundar, S.; Chakravarty, J. Liposomal amphotericin B and leishmaniasis: dose and response. *Journal of global infectious diseases* **2010**, *2*, 159–166.
- (11) Chakravarty, J.; Sundar, S. Drug resistance in leishmaniasis. *J Glob Infect Dis* **2010**, *2*, 167–176.
- (12) Champoux, J. J. DNA topoisomerases: structure, function, and mechanism. *Annu. Rev. Biochem.* **2001**, *70*, 369–413.
- (13) Capranico, G.; Marinello, J.; Chillemi, G. Type I DNA Topoisomerases. *J. Med. Chem.* **2017**, *60*, 2169–2192.
- (14) Brata Das, B.; Sen, N.; Ganguly, A.; Majumder, H. K. Reconstitution and functional characterization of the unusual bi-subunit type I DNA topoisomerase from *Leishmania donovani*. *FEBS letters* **2004**, *565*, 81–88.
- (15) Das, B. B.; et al. Topoisomerase research of kinetoplastic parasite *Leishmania*, with special reference to development of therapeutics. *Indian Journal of Medical Research* **2006**, *123* (3), 221.
- (16) Das, B. B.; et al. Differential induction of *Leishmania donovani* bi-subunit topoisomerase I–DNA cleavage complex by selected flavones and camptothecin: activity of flavones against camptothecin-resistant topoisomerase I. *Nucleic acids research* **2006**, *34*, 1121–1132.
- (17) Das, B. B.; Sengupta, T.; Ganguly, A.; Majumder, H. K. Topoisomerases of kinetoplastid parasites: why so fascinating? *Molecular microbiology* **2006**, *62*, 917–927.
- (18) Das, B. B.; Sen, N.; Dasgupta, S. B.; Ganguly, A.; Majumder, H. K. N-terminal region of the large subunit of *Leishmania donovani* bisubunit topoisomerase I is involved in DNA relaxation and interaction with the smaller subunit. *J. Biol. Chem.* **2005**, *280*, 16335–16344.
- (19) Sen, N.; et al. Camptothecin induced mitochondrial dysfunction leading to programmed cell death in unicellular hemoflagellate *Leishmania donovani*. *Cell Death & Differentiation* **2004**, *11*, 924–936.
- (20) Balaña-Fouce, R.; Alvarez-Velilla, R.; Fernández-Prada, C.; García-Estrada, C.; Reguera, R. M. Trypanosomatids topoisomerase re-visited. New structural findings and role in drug discovery. *International journal for parasitology. Drugs and drug resistance* **2014**, *4*, 326–337.
- (21) Pommier, Y. Drugging topoisomerases: lessons and challenges. *ACS Chem Biol* **2013**, *8*, 82–95.
- (22) Das, S. K.; et al. Neutral Porphyrin Derivative Exerts Anticancer Activity by Targeting Cellular Topoisomerase I (Top1) and Promotes Apoptotic Cell Death without Stabilizing Top1–DNA Cleavage Complexes. *J. Med. Chem.* **2018**, *61*, 804–817.
- (23) Kundu, B.; et al. Discovery and Mechanistic Study of Tailor-Made Quinoline Derivatives as Topoisomerase I Poison with Potent Anticancer Activity. *J. Med. Chem.* **2019**, *62*, 3428–3446.
- (24) Kundu, B.; et al. Development of a metabolically stable topoisomerase I poison as anticancer agent. *Eur. J. Med. Chem.* **2020**, *202*, 112551.
- (25) de Mello, H.; Echevarria, A.; Bernardino, A. M.; Canto-Cavalheiro, M.; Leon, L. L. Antileishmanial Pyrazolopyridine Derivatives: Synthesis and Structure-Activity Relationship Analysis. *J. Med. Chem.* **2004**, *47*, 5427–5432.
- (26) Kishbaugh, T. L. S. Pyridines and Imidazopyridines with Medicinal Significance. *Curr Top Med Chem* **2016**, *16*, 3274–3302.
- (27) Zhao, L.-X.; et al. Synthesis, topoisomerase I inhibition and structure–activity relationship study of 2,4,6-trisubstituted pyridine derivatives. *Bioorg. Med. Chem. Lett.* **2004**, *14*, 1333–1337.
- (28) Pommier, Y. Topoisomerase I inhibitors: camptothecins and beyond. *Nature Reviews Cancer* **2006**, *6*, 789–802.
- (29) Das, B. B.; Ghosh, A.; Bhattacharjee, S.; Bhattacharyya, A. Trapped topoisomerase-DNA covalent complexes in the mitochondria and their role in human diseases. *Mitochondrion* **2021**, *60*, 234–244.
- (30) Chowdhuri, S. P.; Das, B. B. Top1-PARP1 association and beyond: from DNA topology to break repair. *NAR Cancer* **2021**, DOI: 10.1093/narcan/zcab003.
- (31) Beck, D. E.; et al. Synthesis and biological evaluation of new carbohydrate-substituted indenoisoquinoline topoisomerase I inhibitors and improved syntheses of the experimental anticancer agents indotecan (LMP400) and indimitecan (LMP776). *J. Med. Chem.* **2014**, *57*, 1495–1512.
- (32) Pommier, Y.; Cushman, M. The indenoisoquinoline non-camptothecin topoisomerase I inhibitors: update and perspectives. *Mol Cancer Ther* **2009**, *8*, 1008–1014.
- (33) Song, Y.; et al. Structure-based design, synthesis, and biological studies of new anticancer norindenoisoquinoline topoisomerase I inhibitors. *Journal of medicinal chemistry* **2010**, *53*, 1979–1989.
- (34) Ghosh, S.; et al. A Novel Bioimpedance-Based Detection of Miltefosine Susceptibility Among Clinical *Leishmania donovani* Isolates of the Indian Subcontinent Exhibiting Resistance to Multiple Drugs. *Front Cell Infect Microbiol* **2021**, *11*, 768830.
- (35) Pericherla, K.; Khedar, P.; Khungar, B.; Kumar, A. One-pot sequential C–N coupling and cross dehydrogenative couplings: synthesis of novel azole fused imidazo[1,2-a]pyridines. *Chemical Communications* **2013**, *49*, 2924–2926.
- (36) Zhu, Y.; et al. Target-oriented synthesis: miscellaneous synthetic routes to access 1,4-enediones through the coupling of 1,3-dicarbonyl compounds with multiform substrates. *Tetrahedron* **2013**, *69*, 6392–6398.
- (37) Chowdhury, S.; et al. The lignan niranthin poisons *Leishmania donovani* topoisomerase IB and favours a Th1 immune response in mice. *EMBO Molecular Medicine* **2012**, *4*, 1126–1143.
- (38) Chowdhury, S. R.; et al. Voacamine alters *Leishmania* ultrastructure and kills parasite by poisoning unusual bi-subunit topoisomerase IB. *Biochem. Pharmacol.* **2017**, *138*, 19–30.
- (39) Das, B. B.; Ganguly, A.; Majumder, H. K. In *Drug Targets in Kinetoplastid Parasites*; Springer, 2008; pp 103–115.
- (40) Shadab, M. Apoptosis-like cell death in *Leishmania donovani* treated with KalsomeTM10, a new liposomal amphotericin B. *PLoS One* **2017**, *12*, e0171306.
- (41) Sen, N.; et al. *Leishmania donovani*: intracellular ATP level regulates apoptosis-like death in luteolin induced dyskinetoplastid cells. *Exp Parasitol* **2006**, *114*, 204–214.
- (42) Sen, N.; et al. Camptothecin-induced imbalance in intracellular cation homeostasis regulates programmed cell death in unicellular hemoflagellate *Leishmania donovani*. *J. Biol. Chem.* **2004**, *279*, 52366–52375.
- (43) Mukherjee, B.; et al. Antimony-resistant but not antimony-sensitive *Leishmania donovani* up-regulates host IL-10 to overexpress

multidrug-resistant protein 1. *Proceedings of the National Academy of Sciences* **2013**, *110*, No. E575-E582.

(44) Das, S.; et al. A chemical inhibitor of heat shock protein 78 (HSP78) from *Leishmania donovani* represents a potential anti-leishmanial drug candidate. *J. Biol. Chem.* **2020**, *295*, 9934–9947.

(45) Das, S.; Mukherjee, S.; Ali, N. Super enhancer-mediated transcription of miR146a-5p drives M2 polarization during *Leishmania donovani* infection **2021**, *17*, No. e1009343.

(46) Olivier, M.; Gregory, D. J.; Forget, G. Subversion mechanisms by which *Leishmania* parasites can escape the host immune response: a signaling point of view. *Clin Microbiol Rev* **2005**, *18*, 293–305.

(47) Chowdhury, S. R.; Majumder, H. K. DNA Topoisomerases in Unicellular Pathogens: Structure, Function, and Druggability. *Trends Biochem. Sci.* **2019**, *44*, 415–432.

(48) Rosa-Teijeiro, C.; et al. Three different mutations in the DNA topoisomerase 1B in *Leishmania infantum* contribute to resistance to antitumor drug topotecan **2021**, *14*, 438.

(49) Fan, X.-S.; Zhang, J.; Li, B.; Zhang, X.-Y. One-pot Sequential Reactions Featuring a Copper-catalyzed Amination Leading to Pyrido[2',1':2,3]imidazo[4,5-c]quinolines and Dihydropyrido[2',1':2,3]imidazo[4,5-c]quinolines. *Chem. Asian J.* **2015**, *10*, 1281–1285.

(50) Sharma, S.; Saha, B.; Sawant, D.; Kundu, B. Synthesis of Novel N-Rich Polycyclic Skeletons Based on Azoles and Pyridines. *Journal of Combinatorial Chemistry* **2007**, *9*, 783–792.

(51) Majumdar, P.; et al. Design, synthesis and evaluation of thiohydantoin derivatives as potent topoisomerase I (Top1) inhibitors with anticancer activity. *Eur. J. Med. Chem.* **2015**, *102*, 540–551.

(52) Bhattacharjee, S.; et al. Interplay between symmetric arginine dimethylation and ubiquitylation regulates TDP1 proteostasis for the repair of topoisomerase I-DNA adducts. *Cell Reports* **2022**, *39*, 110940.

(53) Bhattacharjee, S.; Rehman, I.; Nandy, S.; Das, B. B. Post-translational regulation of Tyrosyl-DNA phosphodiesterase (TDP1 and TDP2) for the repair of the trapped topoisomerase-DNA covalent complex. *DNA Repair* **2022**, *111*, 103277.

Recommended by ACS

Structure–Activity Relationship of Novel Pyrimidine Derivatives with Potent Inhibitory Activities against *Mycobacterium tuberculosis*

Chungen Li, Youfu Luo, *et al.*

FEBRUARY 03, 2023
JOURNAL OF MEDICINAL CHEMISTRY

READ 

Pyrimido[5,4-d]pyrimidine-Based Compounds as a Novel Class of Antitrypanosomal and Antileishmanial Agents

André Lopes, M. Alice Carvalho, *et al.*

AUGUST 09, 2022
ACS MEDICINAL CHEMISTRY LETTERS

READ 

Identification of Novel 2,4,5-Trisubstituted Pyrimidines as Potent Dual Inhibitors of Plasmodial *PfGSK3/PfPK6* with Activity against Blood Stage Parasites In Vitro

Kareem A. Galal, David H. Drewry, *et al.*

SEPTEMBER 27, 2022
JOURNAL OF MEDICINAL CHEMISTRY

READ 

Design, Synthesis, and Biological Evaluation of Pyrrole-2-carboxamide Derivatives as Mycobacterial Membrane Protein Large 3 Inhibitors for Treating Drug-Resistant T...

Hongyi Zhao, Dongfeng Zhang, *et al.*


AUGUST 01, 2022
JOURNAL OF MEDICINAL CHEMISTRY

READ 

Get More Suggestions >

RESEARCH ARTICLE

TDP1 knockout *Leishmania donovani* accumulate topoisomerase 1-linked DNA damage and are hypersensitive to clinically used antileishmanial drugs

Somenath Roy Chowdhury¹ | Subhendu K. Das² | Bijoylaxmi Banerjee¹ |
 Srijita Paul Chowdhuri² | Hemanta K. Majumder¹ | Benu Brata Das² 

¹Infectious Diseases & Immunology Division, CSIR-Indian Institute of Chemical Biology, Kolkata, India

²Laboratory of Molecular Biology, School of Biological Sciences, Indian Association for the Cultivation of Science, Kolkata, India

Correspondence

Benu Brata Das, Laboratory of Molecular Biology, School of Biological Sciences, Indian Association for the Cultivation of Science, 2A & B, Raja S. C. Mullick Road, Jadavpur-700032, Kolkata, India. Email: pcbbd@iacs.res.in

Present address

Somenath Roy Chowdhury, Institut für Physikalische Chemie, Westfälische Wilhelms-Universität Münster, Münster, 48149, Germany

Subhendu K. Das, Laboratory of Pathology, National Cancer Institute, National Institutes of Health, Bethesda, Maryland 20892-4255, USA

Funding information

BBD team is supported by DBT-S Ramachandran National Bioscience Award for Career Development (NBACD)-2019 grant (102/IFD/SAN/3574/2019-20); DST-SERB core research grant (EMR/2017/001652),

Abstract

Leishmania donovani, a unicellular protozoan parasite, causes a wide range of human diseases including fatal visceral leishmaniasis. Tyrosyl DNA-phosphodiesterase 1 (TDP1) hydrolyzes the phosphodiester bond between DNA 3'-end and a tyrosyl moiety of trapped topoisomerase I-DNA covalent complexes (Top1cc). We have previously shown *Leishmania* harbors a TDP1 gene (LdTDP1), however, the biological role of TDP1 remains largely unknown. In the present study, we have generated TDP1 knockout *L. donovani* (LdTDP1^{-/-}) promastigotes and have shown that LdTDP1^{-/-} parasites are deficient in 3'-phosphodiesterase activities and were hypersensitive to Top1-poison like camptothecin (CPT), DNA alkylation agent like methyl methanesulfonate, and oxidative DNA lesions generated by hydrogen peroxide but were not sensitive to etoposide. We also detected elevated levels of CPT-induced reactive oxygen species triggering cell cycle arrest and cell death in LdTDP1^{-/-} promastigotes. LdTDP1^{-/-} promastigotes accumulate a significant change in the membrane morphology with the accumulation of membrane pores, which is associated with oxidative stress and lipid peroxidation. To our surprise, we detected that LdTDP1^{-/-} parasites were hypersensitive to antileishmanial drugs like amphotericin B and miltefosine, which could be rescued by complementation of wild-type TDP1 gene in the LdTDP1^{-/-} parasites. Notably, multidrug-resistant *L. donovani* clinical isolates showed a marked reduction in TDP1 expression and were sensitive to Top1 poisons. Taken together, our study provides a new role of LdTDP1 in protecting *L. donovani* parasites from oxidative stress-induced DNA damage and resistance to amphotericin B and miltefosine.

Abbreviations: CPT, camptothecin; Ld, *Leishmania donovani*; LdTop1, *Leishmania donovani* topoisomerase 1; LdTDP1, *Leishmania donovani* tyrosyl-DNA phosphodiesterase 1; MDR, multi-drug resistance; MMS, methyl methanesulfonate; PCR, polymerase chain reaction; PDA, protein-linked DNA adduct; PI, propidium iodide; ROS, reactive oxygen species; SAG, sodium antimony(stibo) gluconate.

Somenath Roy Chowdhury, Subhendu K. Das, and Bijoylaxmi Banerjee contributed equally to this work.

and Wellcome Trust/DBT India alliance intermediate fellowship grant (Award# IA/I/13/1/500888). SRC was supported by the CSIR-Research Associateship (31/002(1128)/2019-EMR-I). SKD and SPC are the recipients of the IACS senior Research Fellowship, India

KEYWORDS

camptothecin, DNA repair, *Leishmania donovani*, oxidative stress, phosphodiesterase, TDP1, topoisomerase 1

1 | INTRODUCTION

Topoisomerases maintain dynamic homeostasis between different topological states of DNA both in the prokaryotes and eukaryotes through a molecular coalition of three reactions: (i) transient single or double-strand cleavage of DNA, (ii) passage of another intact strand through the gap thus created, and (iii) religation of the gap.^{1–3} Topoisomerase targeting inhibitors are in clinical use as anti-cancer drugs, anti-bacterial and anti-parasitic agents.^{3–6} *Leishmania donovani* topoisomerase 1B (LdTop1) has emerged as a potential drug target due to its unique bi-subunit structure that is distinct from the human host counterpart. Accordingly, several *Leishmania* Top1-targeted compounds, including camptothecin (CPT) and its clinical derivatives are in the development as antileishmanial agents.^{3,4,7–11} Top1 poisons like CPT stabilize the Top1-DNA covalent complex (Top1cc) and result in the formation of protein-linked DNA adducts (PDAs) associated with DNA damage. Unrepaired Top1cc generates DNA double-strand breaks during its collision with replication and transcription machinery which triggers cell cycle arrest and cell death.^{2,3,6,12,13} Accordingly, in the *Leishmania* parasites, Top1 poisons like CPT accumulate LdTop1 covalent complexes (LdTop1cc) and activate DNA damage and cell death.^{3,7,13,14} Therefore, repair of the trapped Top1cc is an important part of the DNA metabolism and DNA damage response in the parasite.

Tyrosyl-DNA phosphodiesterase (TDP1) can repair the Top1cc by hydrolyzing the phosphodiester bond formed between tyrosine of Top1 and the 3'-phosphate of DNA both in the nucleus and mitochondria.^{15–23} Accordingly, TDP1 knockout mice, flies, yeast, and human cultured cell lines are hypersensitive to Top1 poisons. Consequently, TDP1 over-expressed in a specific group of cancers results in resistance toward Top1 poisons.^{15,17,18,20,24–28} The role of TDP1 in the excision of trapped Top1cc is phylogenetically conserved across different species, which led to the discovery of the parasitic TDP1 counterpart in the *Leishmania*. Sequence analysis and point mutational studies confirmed *L. donovani* TDP1 gene has conserved amino acid residues that are considered to be the signature active site motifs for TDP1 proteins and established it to be a member of the PLD superfamily. LdTDP1 shows 18% sequence identity with the human TDP1 with the homology is mainly restricted around the active site region.²⁹ Consequently, LdTDP1 knockdown sensitizes the *Leishmania* parasites

to CPT, while *Leishmania* promastigotes selected for CPT-resistance shows increased expression of LdTDP1, which is consistent with its role in LdTop1cc repair.²⁹

Beyond TDP1's role in cleaving 3'-phosphotyrosyl bond associated with Top1cc, TDP1 has been found to process wide varieties of 3'-DNA blocking lesions that include oxidative damage: 3'-phosphoglycolate ends, 3'-deoxyribose phosphate ends, 3'-abasic sites, and an artificial 3'-biotin adduct from the DNA.^{17,18,21,27} TDP1 can also process DNA damage induced by chain-terminating anticancer agents, and antiviral nucleosides.^{18,22,30} Accordingly, over-expression of LdTDP1 in *L. donovani* protects the parasites against oxidative DNA damage-mediated cell death.²⁹

Despite extensive studies on higher eukaryotes,^{17–20,24} pathways associated with Top1cc repair in trypanosomatid protozoa including *Leishmania* are substantially under-explored. Though a functional TDP1 from *Leishmania donovani* (LdTDP1) was previously reported, nevertheless its biological function in *Leishmania* is unknown. Here, we report for the first-time generation of *Leishmania donovani* TDP1 knockout parasites (LdTDP1^{-/-}) and evaluate its critical role in the *Leishmania* genome maintenance. LdTDP1^{-/-} parasites are deficient in 3'-phosphodiesterase activities and show hypersensitivity to a broad range of DNA damaging agents including Top1 poisons but were insensitive toward Top2 poison, etoposide. Intriguingly, LdTDP1^{-/-} parasites were hypersensitive to clinically used antileishmanial drugs like amphotericin B and miltefosine. Subsequently, multidrug-resistant clinical isolates of *Leishmania* show a marked reduction in TDP1 protein expression. Notably, both LdTDP1^{-/-} or multidrug-resistant *Leishmania* promastigotes were proficient in Top1 expression as well as activity. Finally, we show that multidrug-resistant *Leishmania* promastigotes could be sensitized to Top1 poisons implicating LdTop1 is a plausible therapeutic target for drug-resistant leishmaniasis.

2 | MATERIALS AND METHODS

2.1 | Generation of TDP1 knockout *Leishmania donovani* (LdTDP1^{-/-})

To generate TDP1 knockout *Leishmania donovani* (LdTDP1^{-/-}), the *Leishmania* transfection vectors

pXG-Neo and pXG-Hyg³¹ were modified by site-directed mutagenesis at positions 1981 and 1952, respectively, to generate unique HindIII site using the following primers:

Primer-SDM1: 5'-CACACACAAAAGCTGCCTTGCACACAACG-3' and Primer-SDM2: 5'-CGTTGTGTGCAAGGCAGCTTTGTGTGTG-3'. The underlined portions denote the site of mutation. Next, a 0.976 kb flanking sequence upstream to LdTDP1 (5'F) and 1.051 kb flanking sequence downstream (3'F) to LdTDP1 were separately PCR amplified from *L. donovani* genomic DNA using the following primers: Primer 3: 5'-CCCAAGCTTCAACCGCATGTCGTCGCTGCGC-3', Primer 4: 5'-ACGCGTCGACGAGTGCACGGCGAGGGATGTGGTG-3', Primer 5: 5'-TCCCCGGGAGCGCGAGGGA GACAGGCACGCGC-3', and Primer 6: 5'-GGGATCCTTCGGTGGTGTACGCCTCTTG-3'. The purified 5'F fragments were then cloned at the HindIII/SalI site of the modified pXG-Neo and pXG-Hygro vectors and 3'F fragments were subsequently cloned at SmaI/BamHI sites of the vectors bearing the 5'F. Both the vectors bearing 5'F and 3'F were then digested with HindIII and BamHI to generate the gene deletion constructs LdTDP1::NEO and LdTDP1::HYG. Both the linear fragments bearing neomycin and hygromycin resistance cassettes were purified. Next, LdTDP1^{-/-} cells were generated by replacing the entire ORF of TDP1 by inserting these two purified deletion constructs LdTDP1::NEO and LdTDP1::HYG by two successive rounds of transfection.^{31,32} Recombinants were selected in presence of 500 µg/ml of hygromycin B and 300 µg/ml of G418 (Neomycin). After 4–5 passages, cells resistant to the drug selection were spread on blood-agar plates (1%) in the presence of antibiotics at the same concentrations. The LdTDP1^{-/-} clones were further confirmed by PCR and western blotting.

2.2 | Complementation of LdTDP1 in knockout *Leishmania donovani* (LdTDP1^{-/-})

To restore LdTDP1 in the TDP1 knockout parasites, LdTDP1 ORF was PCR amplified from a LdTDP1 containing plasmid as a template using the primers pairs FP 5'-TCCCCGGGATGATAGAGCTGATGGTGTGC-3' and RP 5'-CGGGATCCCGCCTCACGCGTGCCTTACG-3'. The amplified ORF was then cloned in SmaI and BamHI site of pXG-Phleo vector to generate LdTDP1::PHLEO construct.²⁹ The construct was transfected into the TDP1 knockout promastigotes and selected with 500 µg/ml of hygromycin B, 300 µg/ml of G418 (Neomycin), and 200 µg/ml of phleomycin. After 4–5 passages, cells resistant to the drug selection were spread on

blood-agar plates (1%) in the presence of antibiotics at the same concentrations. Stable complementation of LdTDP1 in the TDP1 knockout parasites was confirmed by western blotting with LdTDP1 specific antibody.

2.3 | Generation of LdTDP1 antibody

Leishmania donovani TDP1 (LdTDP1) antibody was raised in rabbit against the following LdTDP1 conserved immunogenic peptide **vqksmg(ps)qeddsgn** using the standard protocol.⁷ The LdTDP1 antibodies were affinity purified and were confirmed by ELISA and western blotting.

2.4 | Parasite maintenance and culture

The *Leishmania donovani* cells (AG83) with the genotype TDP1^{+/+}, TDP1^{-/-}, or TDP1^{-/-} cells complemented with LdTDP1 were cultured in M199 containing 20% (v/v) heat-inactivated fetal bovine serum (FBS) supplemented with 100 IU/ml of penicillin and 100 mg/ml of streptomycin at 22°C. Promastigotes were obtained from amastigotes from the spleens of infected hamsters and were further cultured in 10% (v/v) heat-inactivated FBS for 3–5 days at 22°C. The multidrug-resistant field isolates MHOM/IN/2009/BHU575/0 (BHU-575), sodium antimony gluconate (SAG)-sensitive MHOM/IN/1983/AG83 (AG83), or (SAG)-resistant MHOM/IN/2005/BHU138 (BHU-138) strains of *Leishmania donovani* cells were cultured as discussed previously and utilized for the experiments.^{11,33,34}

2.5 | Cell extracts and immunoblotting

Leishmania donovani cells (2×10^7) were grown at 22°C in the presence and absence of indicated drug treatment. Nuclear extracts were prepared as described previously.^{35,36} Briefly, cells were lysed in buffer (10 mM Tris-HCl, pH 7.5, 0.1 mM EGTA, 1 mM EDTA, 1 mM PMSF, 5 mM DTT, and 1 mM Benzamidine hydrochloride), homogenized and was centrifuged at 10 000 g for 10 min at 4°C. The pellet was utilized as the source of the nuclear fraction. Pellet was lysed with 1% SDS and boiled at 95°C for 5 min were subjected to electrophoresis on 10% Tris-glycine gels and the proteins were transferred into nitrocellulose membranes. Immunoblotting of immobilized proteins was carried out using a rabbit antibody raised against LdTDP1 (90 kDa), LdTOP1S (29 kDa) of *L. donovani*,⁷ and immunoreactivity was detected by ECL chemiluminescence reaction (Amersham) under ChemiDoc™ MP System (Bio-Rad, USA).

2.6 | Oligonucleotides and preparation of DNA substrates

The oligonucleotide N14Y (5'-GATCTAAAAGACTTY-3') contains a 3'-phosphotyrosine (Y) was produced by Midland Certified Reagents Company (Midland, TX, USA). The 5'-end labeling of N14Y oligonucleotide was carried out by T4 polynucleotide kinase and [γ - 32 P] ATP. Inactivation of the kinase was performed by heating for 5 min at 95°C and unlabeled radioactive nucleotides were removed by mini-Quick Spin Oligo column (Roche Diagnostics).^{15,25,29}

2.7 | Assessment of 3'-phosphodiesterase activities

TDP1 activity assays were performed as described previously.^{15,25,29} Briefly, cellular lysates obtained from LdTDP1^{+/+}, LdTDP1^{-/-} cells, or LdTDP1^{-/-} cells complemented with LdTDP1 were utilized for gel-based TDP1 assay. The 5'-end radiolabeled N14Y substrate (1 nM) was incubated with the indicated cell lysates for 30 min at 25°C in assay buffer (1×PBS, 80 mM KCl, and 0.01% Tween-20) and stopped by the addition of two volumes of gel loading buffer (96% (v/v) formamide, 1% (w/v) xylene cyanol, 10 mM EDTA and 1% (w/v) bromophenol blue). Next, samples were subsequently boiled for 5 min at 95°C and subjected to sequencing gel electrophoresis (20%). Then, gels were dried and exposed on PhosphorImager screens (GE Healthcare, UK). Imaging and quantification were performed using Typhoon FLA 7000 and ImageQuant software (GE Healthcare, UK), respectively. 3'-phosphodiesterase activities were analyzed by measuring the conversion percentage of 14Y to 14P by densitometry analysis.

2.8 | Plasmid DNA relaxation assay

Ex-vivo plasmid DNA relaxation assays were carried out with whole-cell extracts obtained from indicated cells as described.^{35,36} Briefly, the equivalent amount of whole-cell extracts (also confirmed by western blot of specific protein) from indicated cells were incubated with supercoiled DNA (200 ng) in Top1 buffer (25 mM Tris-HCl [pH 7.5], 10 mM MgCl₂, 5% glycerol, 50 mM KCl, 0.5 mM DTT, 25 mM EDTA, and 150 mg/ml bovine serum albumin [BSA]) at 37°C for 15 min and products from relaxation assay were analyzed by agarose gel electrophoresis.^{3,7,36}

2.9 | Measurement of cell viability

L. donovani (AG83) promastigotes or primary macrophages (3.0×10⁶ cells/ml) from indicated cells were incubated with

different concentrations of camptothecin and the viability of cells or promastigotes were measured using 3-(4,5-dimethylthiazol-2-yl)-2,5-diphenyl-tetrazolium bromide dye (Sigma), a non-toxic water-soluble cell-permeable tetrazolium (yellow) which is converted to the insoluble formazan (purple) by the nicotinamide adenine dinucleotide phosphate (NADPH)-dependent cellular oxidoreductase enzymes of viable cells. So, the transformation of tetrazolium to formazan by metabolically active cells produced a quantitative measurement of cytotoxicity and viability.^{10,11}

2.10 | Double staining with annexin V and PI

The outer membrane externalization of phosphatidylserine of indicated cells or promastigotes with or without treatment of camptothecin was measured by attachment of FITC-annexin V and PI by an annexin V staining kit (Invitrogen Incorporation Ltd). Flow cytometry was also performed for treated and untreated parasites. The gating was fixed in such a way that the mean intensity of FITC-annexin V and the mean intensity of PI were depicted by FL-1 and FL-2 channels, respectively. The data presented are the mean of three independent experiments.¹³

2.11 | Cell cycle analysis

DNA synthesis or replication was measured by flow cytometry analysis (FACS). *L. donovani* promastigote cells from LdTDP1^{+/+}, LdTDP1^{-/-}, or LdTDP1^{-/-} complemented with LdTDP1 cells (2.5 × 10⁶ cells) were treated with camptothecin (5 μM) for the indicated time, harvested, washed several times with PBS (1X). Fixation and staining of cells were performed and were analyzed via flow cytometry as discussed previously.^{10,11,13} Detection of cells in individual sub G₀, G1, S, and G2/M phases of the cell cycle was carried out using a Becton Dickson flow cytometer and further data were processed by BD FACS Scan Software (San Diego, CA).

2.12 | Estimation of reactive oxygen species (ROS)

Intracellular ROS levels were measured in indicated parasites in the presence and absence of indicated drug doses. Parasites treated with 0.5% DMSO served as controls. After treatment, promastigotes (~2 × 10⁷ cells/ml) were washed, resuspended in 1X PBS buffer (500 μl), and incubated with a cell-permeable dye, H₂DCFDA for 30 min at room temperature and were depicted as the mean fluorescence intensity (per 10⁶ cells) was calculated from fluorometric results.^{10,22}

2.13 | Scanning electron microscopy

Promastigotes of various indicated *Leishmania Donovanii* were fixed in glutaraldehyde (2.5%) in 0.1 M cacodylate buffer (pH 7.2) and postfixed in a solution (1% OsO₄, 0.1 M cacodylate buffer, pH 7.2, and 1.25% potassium ferrocyanide) as discussed previously.¹¹ For scanning electron microscopy, promastigotes were dehydrated, mounted as discussed before, and observed under an FEI Quanta 250 scanning electron microscope.

2.14 | Reverse transcriptase PCR analysis

Reverse transcriptase PCR was employed to study LdTDP1 mRNA expression. Total RNA was isolated using the Total RNA isolation kit (Roche Biochemicals). Two micrograms of total RNA were used to synthesize the first-strand cDNA with the Superscript reverse transcriptase (Invitrogen) and oligo (dT) primers (Invitrogen) according to the manufacturer's protocol. cDNAs were PCR amplified with gene-specific primers as follows: LdTDP1; 5'-CGACTCCCATTCTGCTATTTACC-3' (forward), 5-ACGGCCTGCTCACCTTAT-3' (reverse). The amplification reaction was carried out with the following profile: initial denaturation at 95°C for 5 min; 25 cycles with denaturation at 95°C for 1 min, annealing at 55°C for 50 s and extension at 68°C for 30 s and a final extension of 7 min.²⁹

2.15 | Quantitative PCR analysis

To identify the expression of LdTDP1 mRNA level, quantitative PCR analysis was done using the following primer combination: Forward: 5'-GAGATCCTTCGTCTCCATACAC-3', Reverse 5'-GAAATCCGTTTCGAAGATTCGAG-3'. GAPDH was employed as a loading control to normalize the fold expression [GAPDH; 5'-AGAAGACGGTCCATAGTCACTCCC-3' (forward), 5'-GCCACA CCGTTGAAGTCTGAAGG-3' (reverse)].²⁹

3 | RESULTS

3.1 | TDP1 knockout abrogates 3'-phosphodiesterase activities in *Leishmania* parasites

The emerging role of TDP1 in the excision activity of a broad spectrum of 3'-blocking DNA lesions including TOP1cc prompted us to test its role in the protozoan parasites *Leishmania donovani*.²⁹ To investigate TDP1

function in the parasites, we have generated TDP1 knockout *Leishmania* promastigotes (LdTDP1^{-/-}) by targeted gene deletion (Figure 1A-C). We first generated a heterozygous TDP1 mutant parasite (LdTDP1^{+/-}) by replacing one allele of the TDP1 gene using a targeted construct carrying a neomycin resistance gene (NEO) (Figure 1A). To disrupt the second allele of TDP1 in the LdTDP1^{+/-} parasites, we used a second targeted construct carrying a hygromycin resistance gene (HYG) (Figure 1A). We confirmed LdTDP1 gene disruption by performing PCR amplification of drug-resistance cassettes within the *Leishmania* genome (Figure 1B). We further confirmed the TDP1 homozygous knockout (LdTDP1^{-/-}) and heterozygous mutant (LdTDP1^{+/-}) by PCR amplification using gene-specific primers. Figure 1C shows the amplification of LdTDP1 gene (2.49 kb) was partly reduced in the TDP1 heterozygous mutant (LdTDP1^{+/-}) (Figure 1C; lane 3), while it was completely abrogated in LdTDP1^{-/-} promastigotes (Figure 1C; lane 4). We further stably complemented the *Leishmania* TDP1 gene (LdTDP1) in the LdTDP1^{-/-} promastigotes (LdTDP1^{-/-wtTDP1}) that were confirmed by PCR amplification using gene-specific primers (Figure 1C; lane 5) and western blotting with LdTDP1 specific antibody (Figure 1D), to explore the role of TDP1 specific function in the parasites.

Next to examine the 3'-phosphodiesterase enzymatic activity in LdTDP1^{-/-} parasites; we performed gel-based TDP1 activity assays.^{15,21,29} TDP1 catalyzes the hydrolysis of a 3'-tyrosyl-DNA nucleo-peptide substrate (14-Y) to a product with a 3'-phosphate (14-P) with increased electrophoretic mobility (Figure 2A). We employed an ex vivo approach with the parasite lysate to test TDP1 catalytic activity. The assays were performed with cellular extracts from TDP1 knockout (LdTDP1^{-/-}) or LdTDP1^{-/-wtTDP1} and TDP1 wild-type (LdTDP1^{+/+}) promastigotes. Figure 2B shows that cellular extracts from LdTDP1^{-/-} promastigotes were deficient in the conversion of the 14-Y substrate to the 14-P product compared to cellular extracts from wild-type TDP1 promastigotes, confirming nuclear-encoded LdTDP1 gene is the source of 3'-phosphodiesterase activity in the parasites. We further confirmed that stable complementation of the LdTDP1 gene leads to the complete restoration of the 3'-phosphodiesterase activity in the TDP1 knockout *Leishmania* promastigotes. Sodium orthovanadate (Na₃VO₄), a known inhibitor of TDP1,¹⁷ inhibited the conversion of the 14-Y to the 14-P both in the LdTDP1^{+/+} or LdTDP1^{-/-wtTDP1} parasite extracts (Figure 2C), indicating that parasite TDP1 was sensitive to Na₃VO₄.

We further investigated the expression and plasmid DNA relaxation activity of *Leishmania* topoisomerase 1B (LdTop1) in the LdTDP1^{-/-} promastigotes.

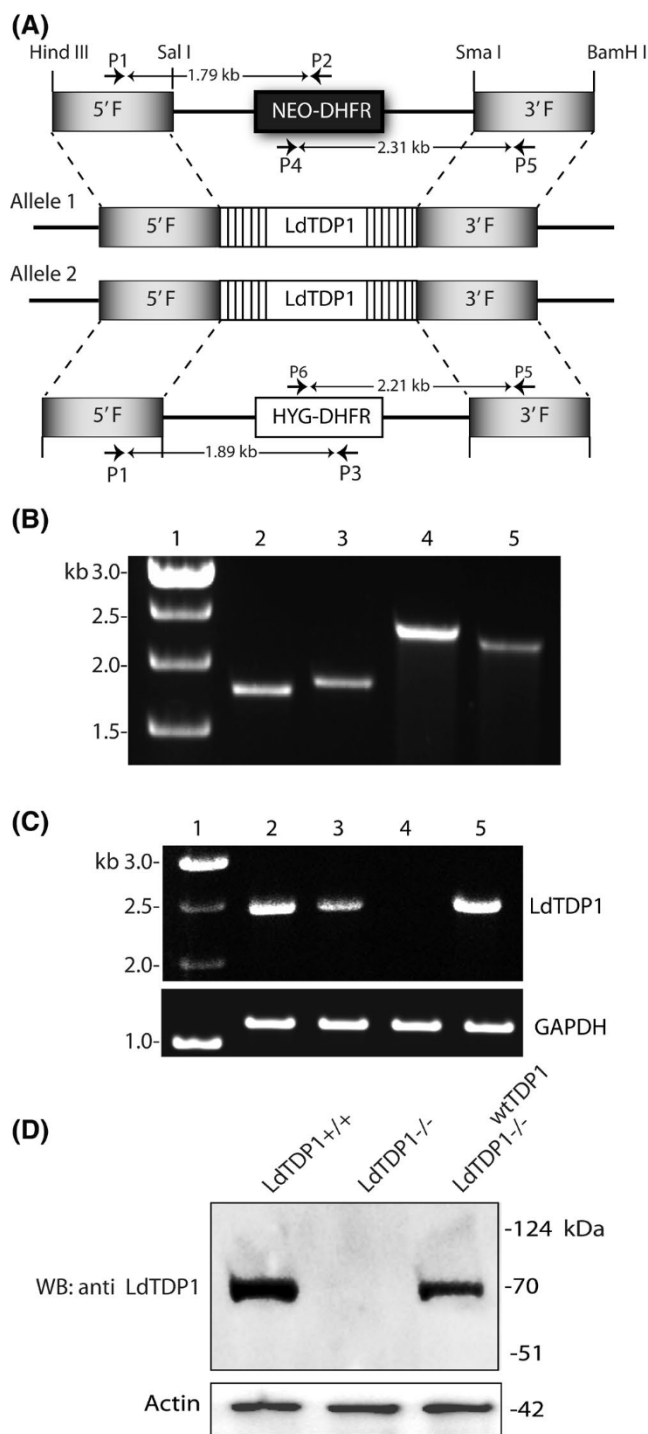


FIGURE 1 Generation of TDP1 knockout *Leishmania donovani* promastigotes by targeted gene replacement. (A) Schematic representation of the *LdTDP1* locus and the plasmid constructs used to generate TDP1 knockout in *Leishmania donovani* by homologous recombination (*LdTDP1*^{-/-}). Positions of the primers (P1, P2, P3, P4, P5, P6) were used to check the integration of the two inactivation cassettes (neomycin phosphotransferase [NEO-DHFR] and hygromycin phosphotransferase [HYG-DHFR]) in the *L. donovani* genome are indicated. (B) Representative agarose gel electrophoresis of PCR amplified products using the genomic DNA of *LdTDP1*^{-/-} parasites as a template. Lane 1: DNA marker; Lane 2-5: Amplicons with primer combinations P1-P2, P1-P3, P4-P5, P6-P5, respectively. P1, P4, P6 are forward primers, and P2, P3, P5 are reverse primers confirming the integration of the two inactivation cassettes as indicated in panel A. (C) Representative agarose gel electrophoresis of PCR amplified products of *LdTdp1* gene using gene-specific primers. Lane 1: DNA marker; Lane 2-5: Amplicons using genomic DNAs of wild type (*LdTDP1*^{+/+}), TDP1 heterozygous (*LdTDP1*^{+/-}), TDP1 knockout (*LdTDP1*^{-/-}), and TDP1 knockout *Leishmania* cells stably complemented with wild type TDP1 (*LdTDP1*^{-/-wtTDP1}), respectively. GAPDH was used as the loading control (lower panel C). (D) Representative western blot showing the protein expression of TDP1 from cellular lysates of *Leishmania donovani* promastigotes of variable genotypes (*LdTDP1*^{+/+}, *LdTDP1*^{-/-}, and *LdTDP1*^{-/-wtTDP1}) are indicated. Actin served as the loading control

3.2 | *LdTDP1* protect the parasites against Top1cc-induced cell death

TDP1 is one of the key repair enzymes for Top1cc.^{17,18,21,24,26,28} We hence examined the impact of *LdTDP1* knockout in the parasite survival and cell cycle progression in the presence and absence of camptothecin (CPT). Figure 3A shows that the knockout of TDP1 *Leishmania* promastigotes (*LdTDP1*^{-/-}) was hypersensitive to Top1 poison; CPT compared to wild-type cells. Intriguingly, *LdTDP1*^{-/-} promastigotes complemented with *LdTDP1* (*LdTDP1*^{-/-wtTDP1}) could rescue the CPT hypersensitivity of the *LdTDP1*^{-/-} parasites. The EC₅₀ values for parasites with variable genotypes against CPT are shown in Table 1. We further confirmed the marked elevation of CPT-mediated programmed cell death in the TDP1 null mutants. At 5 μM CPT, ~80% of the total population of *LdTDP1*^{-/-} promastigotes became annexin-V positive compared to ~20% of wild-type cells (Figure 3B). Cell cycle analysis further confirmed CPT induced elevated levels of cell death in *LdTDP1*^{-/-} as revealed by a significant increase in Sub G₀ cell population after CPT treatment (Figure 3C). CPT-induced Sub G₀ apoptotic cellular population could be protected by complementation of *LdTDP1* in the *LdTDP1*^{-/-} parasites (Figure 3C), consistent with the survival assays

TDP1 knockout promastigotes (*LdTDP1*^{-/-}) showed unaltered expression of *Leishmania* Top1 catalytic subunit (Figure 2D), which is consistent with the similar *LdTop1* mediated plasmid DNA relaxation activity of *LdTDP1*^{+/+}, *LdTDP1*^{-/-}, or *LdTDP1*^{-/-wtTDP1} parasite extracts (Figure 2E). Therefore, we concluded that TDP1 knockout abrogated 3'-phosphodiesterase activities in the *Leishmania* parasites without interfering with *LdTop1* catalytic activity.

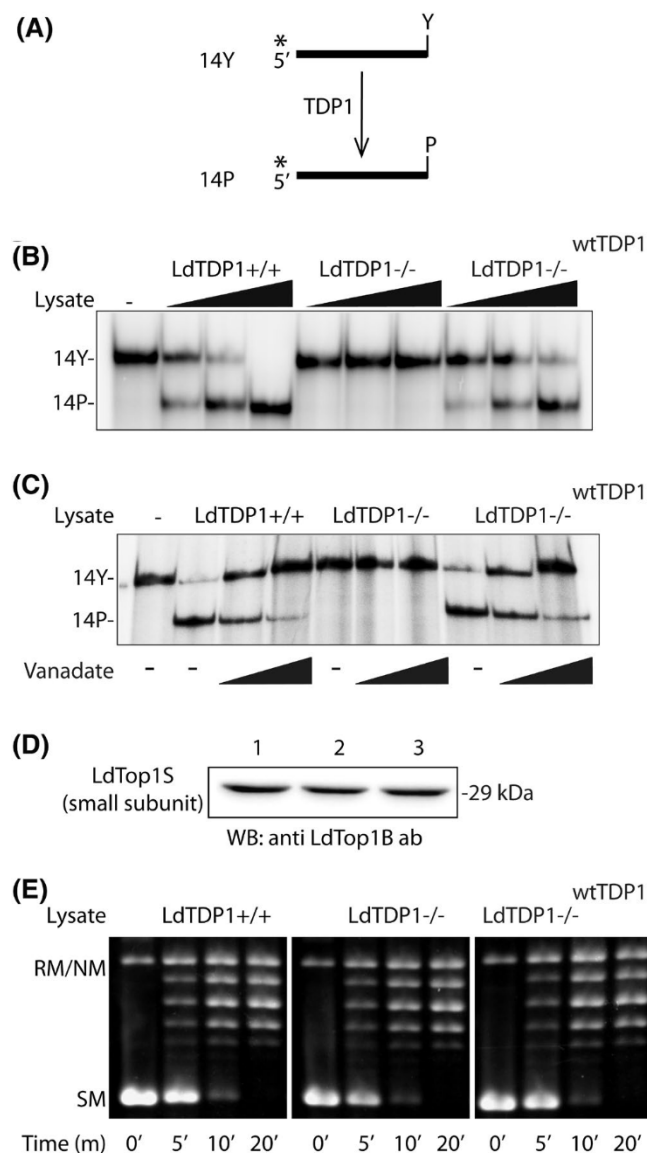


FIGURE 2 *Leishmania donovani* TDP1 knockout (LdTDP1^{-/-}) promastigotes are defective in 3'-phosphodiesterase activities.

(A) Schematic representation of the 3'-phosphodiesterase activity of TDP1 in biochemical assays. 5'-³²P labeled 14-nt 3'-phosphotyrosyl substrate (14Y) is converted to 3'-phosphate (14P) by the action of TDP1. (B) Representative gel images showing the 3'-phosphotyrosyl cleavage activities by *L. donovani* lysate of variable genotypes (LdTDP1^{+/+}, LdTDP1^{-/-}, and LdTDP1^{-/-wtTDP1}) as indicated. The substrate (14Y) was incubated with increasing concentrations of *Leishmania* whole cell lysates (0.5; 1.5; 4.5 μg protein as a source of TDP1) at 25°C for 30 min as indicated. The reactions were quenched and analyzed in denaturing PAGE. The 3'-phosphate oligonucleotide product (14P) runs more quickly than the corresponding tyrosyl oligonucleotide substrate (14Y) in PAGE. (C) Same as panel B, but in presence of increasing concentrations of sodium orthovanadate (2.5 and 10 mM), an inhibitor of 3'-phosphodiesterase activity of TDP1. (D) LdTdp1 expression was determined by western blotting using anti-LdTop1S (LdTop1 small subunit) antibody with variable cell lysates as indicated. Lanes 1–3 contain cell *Leishmania* lysates from variable genotypes LdTdp1^{+/+}, LdTdp1^{-/-} and LdTDP1^{-/-wtTDP1}, respectively. (Representative western blot using anti-LdTop1S antibody) (E) Time-dependent relaxation of supercoiled pBS (SK+) DNA (0.3 μg) with *Leishmania* whole cell lysates (0.1 μg) of variable genotypes as indicated. *Leishmania* whole-cell lysates were used for the source of LdTop1. The reactions were carried out at 37°C for 30 min. Positions of relaxed/nicked monomer (RM/NM) and supercoiled monomer (SM) have been denoted. All results depicted were performed three times and representative data are from one set of these experiments

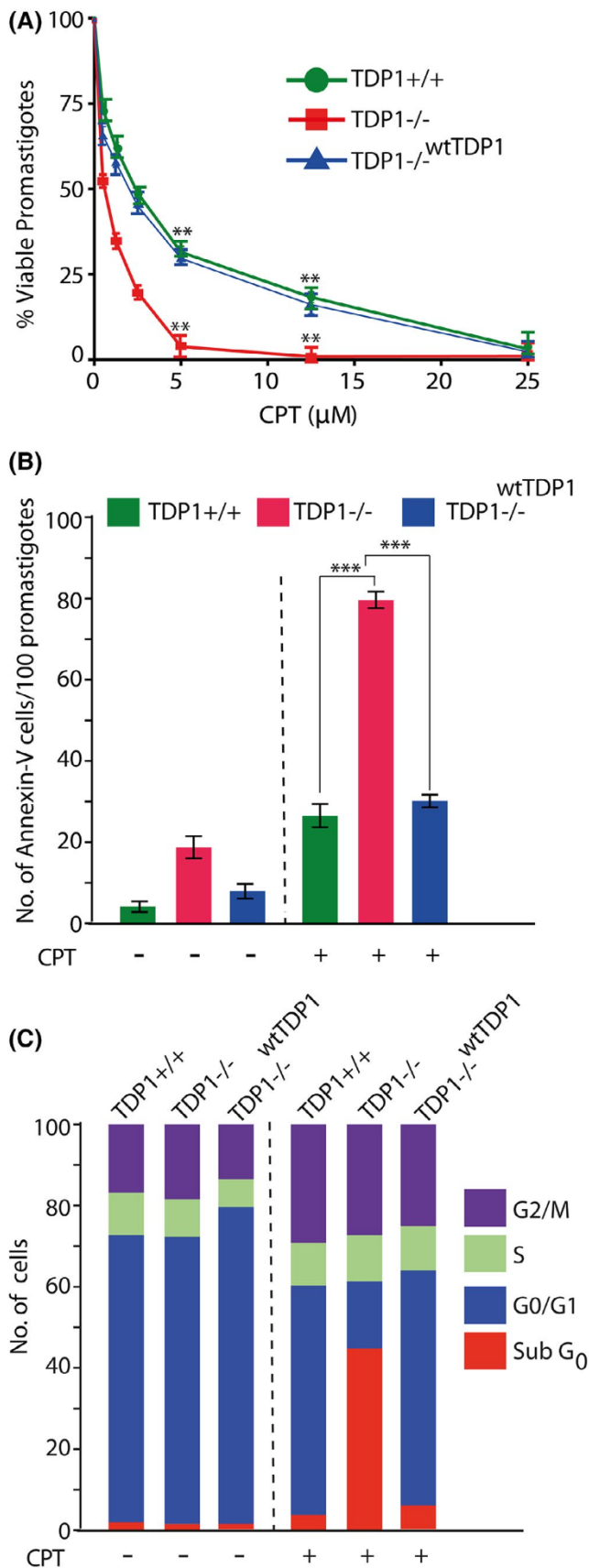
(Figure 3A). Together, we conclude that LdTDP1 protected the parasites against Top1cc-induced DNA damage and cytotoxicity.

3.3 | TDP1 protects membrane morphology and induction of oxidative stress in *L. donovani*

To test the mechanistic link between TDP1 and parasite morphology, we investigated the morphology of the parasite using scanning electron microscopy in TDP1 variant cells (Figure 4A). Figure 4A shows that deletion of LdTDP1 induces significant alterations in the membrane morphology of the *Leishmania* parasites compared to the wild-type control parasites which is independent of exogenous DNA damage. LdTDP1^{-/-} promastigotes accumulate (~3-fold) increase in membrane pores (Figure 4B), which

was further elevated (~4-fold) after CPT treatment. The membrane porosity could be rescued by complementation of LdTDP1 in the LdTDP1^{-/-} parasites (LdTDP1^{-/-wtTDP1}) both in the presence and absence of CPT (Figure 4A,B), suggesting a protective role of TDP1 in limiting membrane damage.

One interpretation of this result is that TDP1 deficiency may accumulate increased Reactive Oxygen species (ROS) in the parasites that could result in lipid peroxidation and membrane porosity.^{13,37} To test this possibility, we used 2',7'-dichlorodihydrofluorescein diacetate (H2DCFDA) which is converted to the highly fluorescent 2',7'-dichlorofluorescein (DCF) in the presence of reactive oxygen species (ROS) that include singlet oxygen, superoxide, hydroxyl radical, and various peroxide and hydroperoxides in the cells. Figure 4C shows that LdTDP1^{-/-} cells accumulate a threefold increase in the basal level of reactive oxygen species (ROS) compared to wild-type parasites. CPT markedly enhanced an additional (~3-fold) increase in the formation of ROS in LdTDP1^{-/-} parasites, which is consistent with the CPT-induced increased cytotoxicity in LdTDP1 knockout parasites (Figure 3A). We also confirmed that H₂O₂ treatment causes a marked increase in ROS production in the LdTDP1^{-/-} parasites (Figure 4C), while LdTDP1 complemented TDP1^{-/-} promastigotes



(LdTDP1^{-/-}wtTDP1) abrogated both CPT- or H₂O₂- induced ROS production in the parasites. The N-acetyl-cysteine (NAC), a specific inhibitor of ROS formation abrogated

FIGURE 3 *Leishmania donovani* TDP1 knockout (LdTDP1^{-/-}) cells are hypersensitive to CPT. (A) The survival curve of *Leishmania* promastigotes with indicated genotypes (LdTDP1^{+/+}, LdTDP1^{-/-}, and LdTDP1^{-/-}wtTDP1) treated with variable concentrations of camptothecin for 16 h as indicated. The percent inhibition of promastigotes viability for each concentration of the CPT was calculated with respect to the control. Each point corresponds to the mean \pm SD of at least three experiments in duplicates. Error bars represent SD ($n = 3$). (B) Annexin V labeling of the indicated promastigotes with variable genotype (LdTDP1^{+/+}, LdTDP1^{-/-}, and LdTDP1^{-/-}wtTDP1) treated with 5 μ M CPT for 12 h and analyzed by flow cytometry. (C) Cell cycle analysis of *L. donovani* promastigotes with variable genotype (LdTDP1^{+/+}, LdTDP1^{-/-}, and LdTDP1^{-/-}wtTDP1) treated without or with 5 μ M of camptothecin for 16 h and analyzed by flow cytometry. The cell cycle arrest was monitored post-treatment with 5 μ M CPT for 16 h. The parasites were then fixed and stained with propidium iodide (PI) and total, 10,000 events were counted from each sample. The percentages of cells within different cells stages are indicated. * $p < .05$, ** $p < .01$ (Student's t -test). ***Indicates significant difference between DMSO control and indicated concentrations of the drugs ($p < .001$) over the studied time-points. n.s. $p > .05$

the formation of fluorescent 2',7'-dichlorofluorescein from H2DCFDA in the *Leishmania* cellular lysates independent of TDP1 expression.

3.4 | LdTDP1^{-/-} promastigotes are susceptible to oxidative DNA damage and antileishmanial drugs

As LdTDP1^{-/-} promastigotes showed increased susceptibility toward CPT (Figure 3A) and accumulate oxidative stress (Figure 4C), we examined the sensitivity of LdTDP1^{-/-} parasites to various types of DNA damaging and antileishmanial drugs (Figure 5). LdTDP1^{-/-} promastigotes showed significant sensitivity H₂O₂ (Figure 5A) and marginal sensitivity toward methyl methanesulfonate (MMS) (Figure 5B) which are known to generate oxidative stress and 3'-DNA blocking lesions.^{17,27,38} Unlike TDP1^{-/-} chicken DT40 cells,³⁸ LdTDP1^{-/-} parasites were insensitive to etoposide (Figure 5C), a specific inhibitor of topoisomerase 2.² Next, we tested the cytotoxicity of clinically used antileishmanial drugs like amphotericin B and miltefosine on LdTDP1^{-/-} promastigotes, which are also known to generate oxidative DNA damage.³⁹⁻⁴¹ Interestingly, LdTDP1^{-/-} parasites showed strong sensitivity toward miltefosine (Figure 5D) and also showed significant sensitivity toward amphotericin B (Figure 5E). The EC₅₀ values for parasites with variable genotypes against indicated drugs are shown in Table 1. We further confirmed that TDP1^{-/-} mouse embryonic fibroblast cells (TDP1^{-/-} MEFs) were also sensitive to amphotericin B

TABLE 1 Half maximal effective concentrations (EC₅₀) of selected drugs against different strains of *Leishmania donovani*

Drugs	LdTDP1 ^{+/+}	LdTDP1 ^{-/-}	LdTDP1 ^{-/-} + wtTDP1	BHU-138	BHU-575
CPT (μM)	3.822 ± 0.079**	1.404 ± 0.111**	3.946 ± 0.092	4.015 ± 0.015	5.221 ± 0.065
MMS (μM)	106.79 ± 0.356*	40.18 ± 0.171*	84.88 ± 0.269	N.T.	N.T.
H ₂ O ₂ (mM)	0.433 ± 0.092*	0.293 ± 0.107*	0.423 ± 0.161	N.T.	N.T.
Amphotericin B (μM)	0.546 ± 0.079**	0.255 ± 0.102**	0.554 ± 0.087	N.T.	N.T.
Miltefosine (μM)	13.179 ± 0.105**	4.806 ± 0.109**	11.649 ± 0.112	N.T.	N.T.
SAG (μM)	4.877 ± 0.117 (n.s.)	4.957 ± 0.123 (n.s.)	4.884 ± 0.136	>>100	>>100

Note: **p* < .05, ***p* < .01, n.s. *p* > .05 (Student's *t*-test) indicates significant difference between the EC₅₀ of selected drugs against different strains of *Leishmania*. Abbreviation: N.T., not tested.

and miltefosine (Figure S1), suggesting the protective role of TDP1 against amphotericin B and miltefosine-induced DNA lesions. The specificity of LdTDP1^{-/-} cells for amphotericin B and miltefosine-induced DNA damage is also justified by the observation that they showed no additional hypersensitivity toward sodium stibogluconate (SAG) when compared to the WT parasites. SAG kills *Leishmania* in a different mechanism other than trapping Top1cc.³⁹ The complementation of LdTDP1^{-/-} cells with the LdTDP1 gene restored the resistance of the parasites toward the DNA damaging agents (Figure 5). These results suggest that *Leishmania* TDP1 has extensive involvement in the repair of DNA lesions induced by DNA-damaging agents and oxidative stress.

3.5 | Drug-resistant field isolates of *L. donovani* promastigotes were sensitive to Top1 poison

As LdTDP1^{-/-} parasites were sensitive to amphotericin B and miltefosine, to determine the functional relationship between TDP1 and drug-resistant *L. donovani*, we tested TDP1 expression in two drug unresponsive field strains (viz BHU-138 and BHU-575) of *L. donovani*, isolated from severely visceral leishmaniasis affected regions of India.¹¹ Figure 6A,B shows that LdTDP1 expression is downregulated in BHU-138 and BHU-575 *Leishmania* promastigotes as confirmed by western blotting (Figure 6A,B) and real-time analysis of TDP1 mRNA levels (Figure 6C). Notably, both the drug-resistant *Leishmania* strains (viz BHU-138 and BHU-575) have an unaltered expression of LdTop1S (Figure 6D), which is consistent with the similar Top1-mediated plasmid DNA relaxation activity in the BHU-138 and BHU-575 parasite extracts (Figure 6E,F). As LdTDP1^{-/-} parasites were markedly sensitive to CPT (Figure 3A), we, therefore, tested the CPT-mediated cytotoxicity in the drug-resistant cells. Both BHU-138 and BHU-575 promastigotes significantly lost their viability in a dose-dependent CPT treatment (Figure 6G). The EC₅₀ values for the drug-resistant parasites against CPT

are shown in Table 1. As expected, BHU-138 and BHU-575 strains were unresponsive toward SAG at 40 μM concentration (Figure 6G, inset),^{33,34} indicating elevated Top1-mediated DNA damage due to downregulated LdTDP1 is a potential mechanism in killing drug-resistant *Leishmania* parasites. Taken together, these results suggest that *Leishmania* TDP1 is the key repair enzyme at Top1cc- and oxidative stress-induced DNA lesions.

4 | DISCUSSION

To our knowledge, the present study provides unique evidence for the role of TDP1 from kinetoplastid protozoan parasite *Leishmania donovani* in protecting their genome from DNA damage induced by clinically used antileishmanial drugs like Amphotericin B and Miltefosine. By generating TDP1 knockout *Leishmania donovani* (LdTDP1^{-/-}) promastigotes (Figure 1), we provide the first *in vivo* evidence that LdTDP1^{-/-} parasites are deficient in 3'-phosphodiesterase activities that make the parasites hypersensitive to a broad range of 3'- blocking DNA lesions including trapped Top1cc induced by CPT, DNA alkylation agent like methyl methanesulfonate, and oxidative DNA lesions generated by hydrogen peroxide and Amphotericin B and Miltefosine, which could rescue by complementation of wild-type TDP1 gene in the LdTDP1^{-/-} parasites. It also shows that LdTDP1^{-/-} parasites were not sensitive to Top2 poisons. Intriguingly, LdTDP1 plays a critical role in protection against oxidative stress that favors the parasite membrane morphology. We further show that multidrug-resistant *L. donovani* clinical isolates^{33,34} have decreased expression of TDP1, which makes them significantly sensitive to Top1 poisons and could be an alternative strategy for the treatment of the frequently detected multidrug-resistant leishmaniasis.

Leishmania donovani is a protozoan parasite that belongs to the early branches of eukaryotes responsible for a wide spectrum of human diseases. Unfortunately, in practice, there are no effective vaccines available against these parasites. Pentavalent antimonials remain the mainstay of

treatment against leishmaniasis.⁴² But resistance to this class of drug is very high in some parts of the world that is quickly making it obsolete.^{33,34} So, the search for a new and effective target is the need of the day. DNA topoisomerase I (Top1) is the primary target of many antitumor drugs. Many antiparasitic compounds have been found to act *via* topoisomerases having a more profound effect on the parasite protein than the host.^{3,4} The bi-subunit topoisomerase 1B of the kinetoplastid parasites offers a unique target for antileishmanial drug development.^{3,4,8} The large subunit (LdTop1L) of *Leishmania* Top1B is closely homologous to the core domain of human topoisomerase I. While the small subunit (LdTop1S) of *Leishmania*, contains the phylogenetically conserved 'SKXXY' motif placed at the C-terminal domain of all type I DNA topoisomerases, which conserves a tyrosine residue playing the catalytic role in DNA cleavage/religation reaction.^{7,9} Thus, the ability of LdTDP1 to resolve 3'-phosphotyrosine linkages is consistent with the role of the enzyme in protecting cells against cytotoxic Top1-DNA lesions. Accordingly, LdTDP1^{-/-} parasites accumulate elevated levels of CPT-induced Top1cc, triggering cell death mechanisms which potentially implicate LdTDP1 as a co-target with LdTop1 for targeting leishmaniasis.

We detected that TDP1 knockout *Leishmania* parasites are hypersensitive to oxidative DNA damage (Figure 5). Top1cc can also be trapped by endogenous DNA lesions, including abasic sites, mismatches, oxidative DNA damage, oxidized bases, and DNA nicks,^{2,17,20} which is consistent with the role of TDP1 in repairing such lesions in *Leishmania* parasites treated with H₂O₂ that generates oxidative DNA lesions (Figure 5). Apart from resection of the trapped Top1cc, the critical role of human, mouse, and chicken TDP1 is implicated in clearing various 3'-damaged DNA termini generated from ROS-mediated DNA damage, ionizing radiation, radiomimetic drug-like bleomycin, etc. The diverse physiological TDP1 substrates include 3'-abasic site, 3'-phosphoglycolate, 3'-deoxyribose phosphate, 3'-histidine, and synthetic substrates like 3'-biotin adducts, independent of DNA sequence.^{17,18} Accordingly, *Leishmania* TDP1 knockout parasites are hypersensitive to DNA damage induced by DNA alkylation agents like MMS, and DNA lesions generated by H₂O₂ and

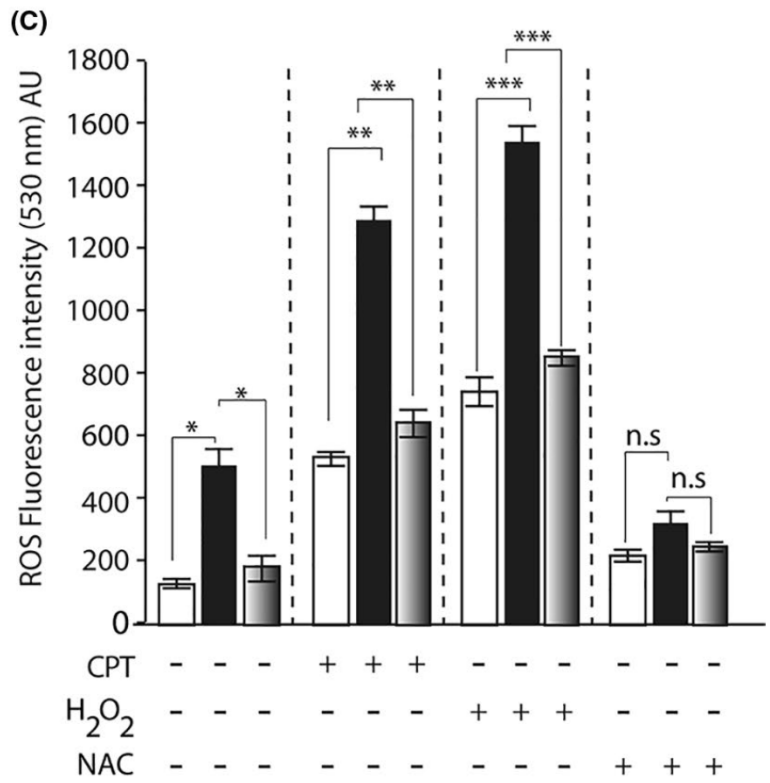
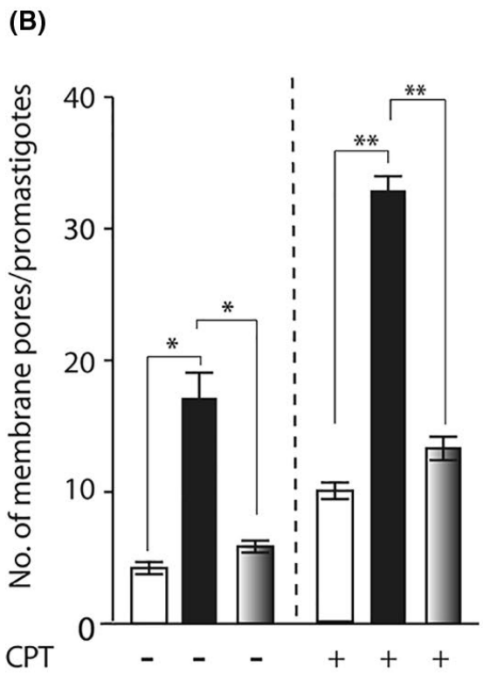
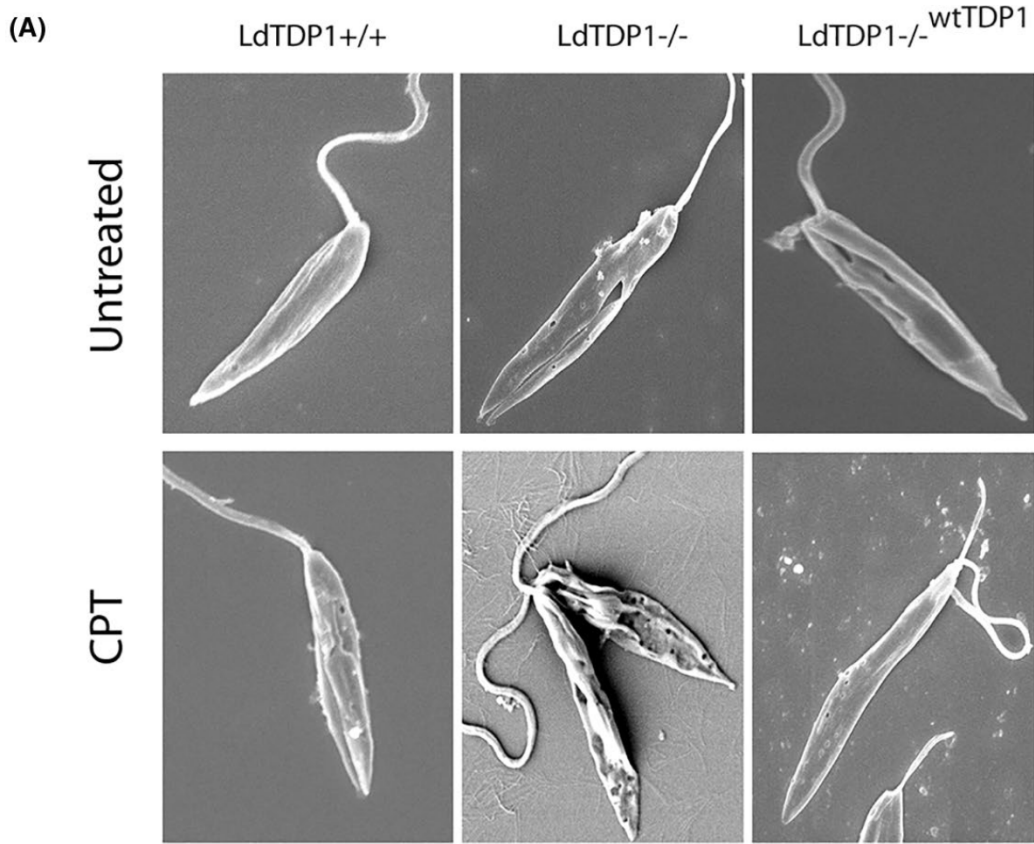
Amphotericin B and Miltefosine, which could be rescued by complementation of wild-type LdTDP1 gene in the LdTDP1^{-/-} parasites (Figure 5). Therefore, our results implicate the critical broad role of LdTDP1 in repairing DNA lesions which is not limited to Top1cc lesions (Figure S2).

TDP1 is conserved in all eukaryotes including *Leishmania* and is the fundamental enzyme dedicated to hydrolyze the trapped Top1cc both in the nucleus and mitochondria.^{15,16,20,22,29,38} Consequently, cells deficient for TDP1 accumulate mitochondrial DNA (mtDNA) damage and are hypersensitive to mitochondria-targeted Top1 poison or H₂O₂.^{15,16,20,22,29,38} MtDNA encodes a critical subset of proteins for the production of cellular ATP; however, mitochondria are solely dependent on nuclear-encoded TDP1 for the repair of trapped mitochondrial Top1cc.^{15,16,20,22} Therefore, LdTDP1 knockout parasites plausibly accumulate mtDNA damage that is linked with the defective function of the electron transport chain that results in ROS formation in the *Leishmania* parasites (Figure 4C).^{13,37,43} Thus, the elevated level of ROS results in lipid peroxidation and membrane porosity (Figure 4A,B) in the *Leishmania* parasites (Figure S2).

Knockout of the TDP1 gene renders the chicken DT40 cells, human cancer cell lines particularly sensitive to selective topoisomerase II poison etoposide.^{17,38,44} This is consistent with the role of TDP1 in the repair of yeast topoisomerase II (Top2) cleavage complexes.⁴⁴ Moreover, TDP1 overexpression in human cells counteracts DNA damage mediated not only by Top1 but also by Top2.⁴⁵ However, we detected no significant difference in the TDP1 knockout parasite viability when compared with TDP1 wild-type parasites after treatment with etoposide (Figure 5C). Thus, our study favors the plausibility for the presence of a dedicated TDP2 ortholog in the kinetoplastid protozoa parasites which is implicated in selective removal of trapped Topoisomerase II-DNA covalent complexes (Top2cc).^{17,46}

LdTDP1 has a role in oxidative stress management generated primarily by DNA targeting agents. Different oxidative stress-inducing antileishmanial drugs like sodium antimony gluconate, amphotericin B, and miltefosine, are employed to treat the patients. Targets of these drugs in *Leishmania* are yet unknown. Intriguingly, amphotericin B is known to generate oxidative DNA damage through its

FIGURE 4 TDP1 protects membrane morphology and induction of oxidative stress in *L. donovani* parasites. (A) Representative images of scanning electron microscope (SEM) using LdTDP1^{+/+}, LdTDP1^{-/-} and LdTDP1^{-/-} wtTDP1 promastigotes following treatment with 5 μM CPT for 3 h. Note: LdTDP1^{-/-} show altered membrane morphology with the accumulation of membrane pores both in the presence or absence of CPT (middle panel) (B) Bar graphs reflecting the quantification for the number of pores/parasites calculated from 25 promastigote cells (± standard deviation) from LdTDP1^{+/+}, LdTDP1^{-/-}, and LdTDP1^{-/-} wtTDP1 promastigotes in presence and absence of CPT treatment (5 μM CPT for 3 h) as indicated. (C) Quantitative representation of reactive oxygen species (ROS) in the TDP1 variants using a cell-permeable dye, H₂DCFDA in presence of CPT (5 μM CPT for 3 h), H₂O₂ (1 mM for 3 h), and with NAC (20 mM for 3 h) as indicated. Data represent mean value ± SD (n = 3). *p < .05, **p < .01 (Student's *t*-test). ***Indicates significant difference between DMSO control and indicated concentrations of the drugs (p < .001). n.s. p > .05



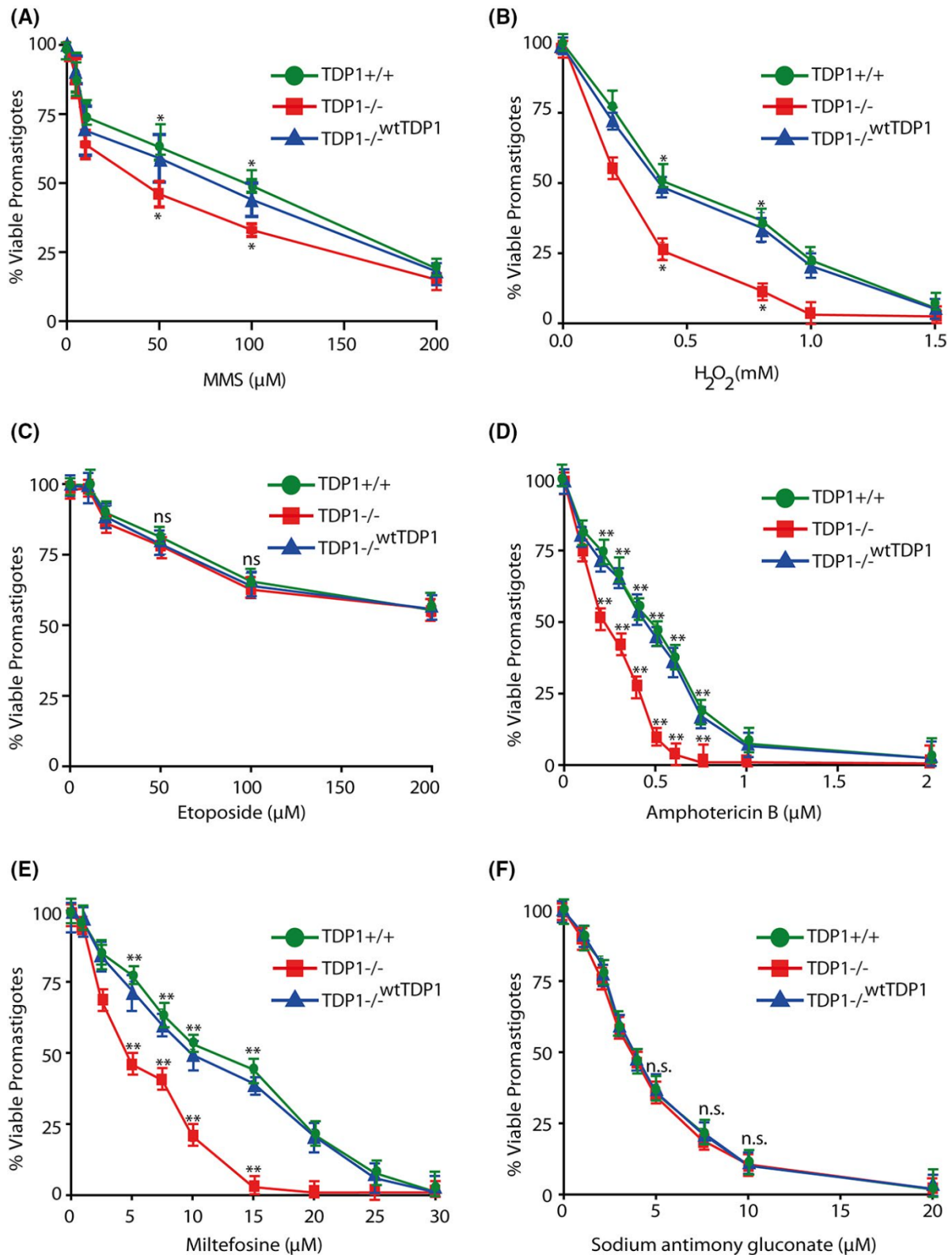


FIGURE 5 *Ld*TDP1^{-/-} promastigotes are hypersensitive to oxidative stress and antileishmanial drugs. Survival curves of *L. donovani* promastigotes with variable genotype (*Ld*TDP1^{+/+}, *Ld*TDP1^{-/-}, and *Ld*TDP1^{-/-wtTDP1}) treated with different DNA-targeting agents viz. (A) Methyl methanesulphonate (MMS), (B) Hydrogen peroxide (H_2O_2), (C) Etoposide and antileishmanial drugs viz. (D) Amphotericin B (E) Miltefosine (F) Sodium antimony gluconate at indicated concentrations. The percent inhibition of promastigotes viability for each indicated concentration of the agents was calculated with respect to the control. Each point corresponds to the mean \pm SD of at least three experiments in duplicates. Error bars represent SD ($n = 3$). * $p < .05$, ** $p < .01$ (Student's *t*-test). ***Indicates significant difference between DMSO control and indicated concentrations of the drugs ($p < .001$) over the studied time-point. n.s. $p > .05$

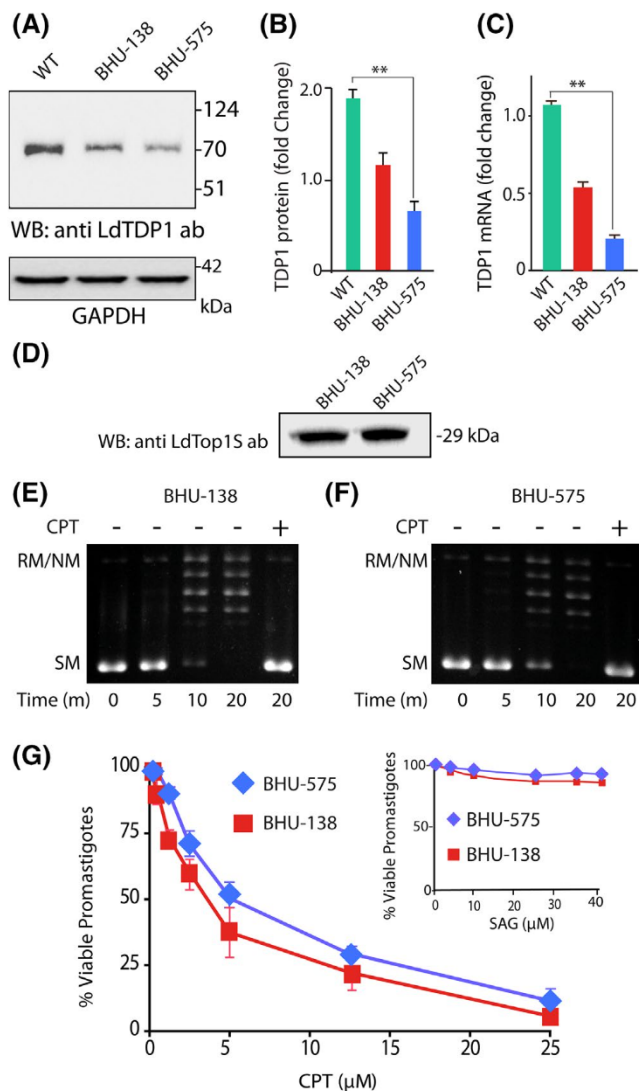


FIGURE 6 Drug-resistant *L. donovani* parasites down-regulate TDP1 expression. Expression of LdTDP1 in two drug unresponsive field isolates of *L. donovani* viz. MHOM/IN/2005/BHU138 and MHOM/IN/2005/BHU575. (A) Representative image showing the LdTDP1 protein levels in the indicated *Leishmania* variants (WT-AG83, BHU138, BHU575) as determined by western blotting (representative experiment), GAPDH served as loading control (B) Densitometry analysis of LdTDP1 expression normalized to GAPDH in the indicated parasites. Data represent the mean \pm standard error of independent experiments. (C) LdTDP1 mRNA levels were determined by using real-time PCR normalized to GAPDH transcript. Data represent the mean \pm standard error of independent experiments ($n = 3$). (D) LdTop1 expression was determined by western blotting using anti-LdTop1S (LdTop1 small subunit) antibody with cell lysates of BHU-138 and BHU-575 parasite strains as indicated. Note LdTop1 expression remains unchanged in the drug unresponsive field isolates of *L. donovani*. (E and F) Representative ex vivo plasmid DNA relaxation experiments showing time-dependent relaxation of 0.3 μ g supercoiled pBS (SK+) DNA by endogenous LdTop1 from the whole-cell lysates (each reaction volume contains 0.1 μ g whole cell lysates) of drug unresponsive *L. donovani* (BHU-138 and BHU-575) parasite strains, respectively. Inhibition of endogenous LdTop1 DNA relaxation activity was confirmed by treatment with camptothecin (CPT; 10 μ M) as indicated. The reactions were carried out at 37°C for indicated times. Positions of relaxed/nicked monomer (RM/NM) and supercoiled monomer (SM) have been denoted. (G) Survival curves of drug unresponsive *L. donovani* (BHU-138 and BHU-575) parasite strains treated with CPT for 16 h. Inset shows the relative drug resistance of the *L. donovani* (BHU-138 and BHU-575) parasite strains treated with antileishmanial drug Sodium stibogluconate (SAG). The percent inhibition of promastigotes viability for each concentration of the drugs was calculated with respect to the control. Each point corresponds to the mean \pm SD of at least three experiments in duplicates. Error bars represent SD ($n = 3$)

interaction with DNA, accordingly, LdTDP1^{-/-} cells are hypersensitive to amphotericin B.⁴⁷ Intriguingly, despite the reduced levels of TDP1 in the two-drug unresponsive field isolates of *Leishmania* (BHU-575 and BHU-138) (Figure 6 A-C), the CPT sensitivities were less when compared to the wild-type parasites (EC₅₀ in Table 1), which may be due to the differential uptake or retention of CPT in the drug-resistant *Leishmania* strains. The ATP-binding cassette (ABC) protein PGPA and the multidrug resistance protein (MDR)-1 pump are known to be frequently up-regulated in drug-resistant *Leishmania* parasites⁴⁸ which might account for the differential sensitivities of the wild-type and MDR (BHU-575 and BHU-138) parasites against CPT. However, the absence of TDP1 could not significantly alter the sensitivity of the parasites toward SAG. Collectively, these indicate that probably the parasitic TDP1 has a broader role than just mending 3'-DNA lesions (Figure 5). Accordingly, we detected a marked reduction of TDP1 expression in both of the drug-resistant strains of *L. donovani* namely BHU-138 (resistant to SAG) and BHU-575 (resistant to SAG, amphotericin B, and miltefosine)

(Figure 6). This is in keeping with the recent study that shows drug-resistant parasites (BHU-138 and BHU-575) were sensitive to Top1 poison voacamine that stabilizes LdTop1cc.^{4,11} However, the difference in the extent of CPT hypersensitivity between TDP1 knockout (Figure 3A) and the two drug unresponsive field strains (viz BHU-138 and BHU-575) (Figure 6G) may be due to the presence of residual level of LdTDP1 both in the BHU-138 and BHU-575 as detected in the protein (Figure 6A,B) and mRNA level (Figures 1A and 6A-C). Alternatively, Top1cc's can be repaired in cells through DNA cleavage by 3'-flap endonucleases such as XPF-ERCC1, Mre11/Rad50; CtIP, and APE2.^{2,12,20} Despite extensive studies in the higher eukaryotes, pathways associated with alternative Top1cc repair in trypanosomatid protozoa including *Leishmania* are substantially under-explored. In *Leishmania*, an ortholog of mammalian Mre11 (LdMre11) has been reported.⁴⁹ However, LdMre11 has not yet been characterized for the

repair of trapped Top1cc in the parasites. Further studies are warranted to explore the role of alternative endonuclease pathways in the repair of trapped Top1cc in the parasites. Yet, it is still not clear how TDP1 downregulation assisted the parasite to gain multidrug resistance, as the role of SAG in DNA damage is still not established. Future investigations are warranted to establish the role of TDP1 in attaining resistance against classical drugs against leishmaniasis. Cumulatively, our report establishes a new role of TDP1 in oxidative stress management as well as drug resistance in the protozoan parasites.

ACKNOWLEDGMENTS

The authors wish to thank Prof. Stephen Beverley, Washington University School of Medicine, for providing the *Leishmania* transfection vectors. We also thank Dr. Syamal Roy, Council of Scientific and Industrial Research–Indian Institute of Chemical Biology, Kolkata 700032 for the kind gift of the drug-resistant parasites (MHOM/IN/2005/BHU138 and MHOM/IN/2005/BHU575).

DISCLOSURES

No conflict of interest was declared.

AUTHOR CONTRIBUTIONS

Somenath Roy Chowdhury, Subhendu K. Das, Bijoylaxmi Banerjee, and Srijita Paul Chowdhuri performed the biochemical experiments and cell survival assays. Bijoylaxmi Banerjee generated *Leishmania* TDP1 Knockout cells. Somenath Roy Chowdhury, Subhendu K. Das, Bijoylaxmi Banerjee, Srijita Paul Chowdhuri, Hemanta K. Majumder, and Benu Brata Das analyzed the data. Somenath Roy Chowdhury, Subhendu K. Das, and Srijita Paul Chowdhuri wrote the draft manuscript. Benu Brata Das supervised the project, edited the manuscript. All authors put their comments to improve the quality of the manuscript.

DATA AVAILABILITY STATEMENT

The data that support the findings of this study are available on request from the corresponding author.

ORCID

Benu Brata Das  <https://orcid.org/0000-0003-2519-7105>

REFERENCES

1. Champoux JJ. DNA topoisomerases: structure, function, and mechanism. *Annu Rev Biochem.* 2001;70:369-413.
2. Pommier Y, Sun Y, Huang SN, Nitiss JL. Roles of eukaryotic topoisomerases in transcription, replication and genomic stability. *Nat Rev Mol Cell Biol.* 2016;17:703-721.
3. Das BB, Sen N, Roy A, et al. Differential induction of *Leishmania donovani* bi-subunit topoisomerase I-DNA cleavage complex by selected flavones and camptothecin: activity of flavones against camptothecin-resistant topoisomerase I. *Nucleic Acids Res.* 2006;34:1121-1132.
4. Chowdhury SR, Majumder HK. DNA Topoisomerases in unicellular pathogens: structure, function, and druggability. *Trends Biochem Sci.* 2019;44:415-432.
5. Pommier Y. Topoisomerase I inhibitors: camptothecins and beyond. *Nat Rev Cancer.* 2006;6:789-802.
6. Capranico G, Marinello J, Chillemi G. Type I DNA topoisomerases. *J Med Chem.* 2017;60:2169-2192.
7. Das BB, Sen N, Ganguly A, Majumder HK. Reconstitution and functional characterization of the unusual bi-subunit type I DNA topoisomerase from *Leishmania donovani*. *FEBS Lett.* 2004;565:81-88.
8. D'Annessa I, Castelli S, Desideri A. Topoisomerase 1B as a target against leishmaniasis. *Mini Rev Med Chem.* 2015;15:203-210.
9. Villa H, Otero Marcos AR, Reguera RM, et al. A novel active DNA topoisomerase I in *Leishmania donovani*. *J Biol Chem.* 2003;278:3521-3526.
10. Chowdhury S, Mukherjee T, Mukhopadhyay R, et al. The ligand niranthin poisons *Leishmania donovani* topoisomerase IB and favours a Th1 immune response in mice. *EMBO Mol Med.* 2012;4:1126-1143.
11. Chowdhury SR, Kumar A, Godinho JLP, et al. Voacamine alters *Leishmania* ultrastructure and kills parasite by poisoning unusual bi-subunit topoisomerase IB. *Biochem Pharmacol.* 2017;138:19-30.
12. Chowdhuri SP, Das BB. Top1-PARP1 association and beyond: from DNA topology to break repair. *NAR Cancer.* 2021;3:zcab003.
13. Sen N, Das BB, Ganguly A, Mukherjee T, Bandyopadhyay S, Majumder HK. Camptothecin-induced imbalance in intracellular cation homeostasis regulates programmed cell death in unicellular hemoflagellate *Leishmania donovani*. *J Biol Chem.* 2004;279:52366-52375.
14. Sen N, Banerjee B, Gupta SS, Das BB, Ganguly A, Majumder HK. *Leishmania donovani*: dyskinetoplastid cells survive and proliferate in the presence of pyruvate and uridine but do not undergo apoptosis after treatment with camptothecin. *Exp Parasitol.* 2007;115:215-219.
15. Das BB, Dexheimer TS, Maddali K, Pommier Y. Role of tyrosyl-DNA phosphodiesterase (TDP1) in mitochondria. *Proc Natl Acad Sci.* 2010;107:19790-19795.
16. Chiang S-C, Meagher M, Kassouf N, et al. Mitochondrial protein-linked DNA breaks perturb mitochondrial gene transcription and trigger free radical-induced DNA damage. *Sci Adv.* 2017;3:e1602506.
17. Pommier Y, Huang SY, Gao R, Das BB, Murai J, Marchand C. Tyrosyl-DNA-phosphodiesterases (TDP1 and TDP2). *DNA Repair.* 2014;19:114-129.
18. Kawale AS, Povirk LF. Tyrosyl-DNA phosphodiesterases: rescuing the genome from the risks of relaxation. *Nucleic Acids Res.* 2018;46:520-537.
19. Ashour ME, Atteya R, El-Khamisy SF. Topoisomerase-mediated chromosomal break repair: an emerging player in many games. *Nat Rev Cancer.* 2015;15:137-151.
20. Das BB, Ghosh A, Bhattacharjee S, Bhattacharyya A. Trapped topoisomerase-DNA covalent complexes in the mitochondria and their role in human diseases. *Mitochondrion.* 2021;60:234-244.

21. Das BB, Antony S, Gupta S, et al. Optimal function of the DNA repair enzyme TDP1 requires its phosphorylation by ATM and/or DNA-PK. *EMBO J*. 2009;28:3667-3680.
22. Ghosh A, Bhattacharjee S, Chowdhuri SP, et al. SCAN1-TDP1 trapping on mitochondrial DNA promotes mitochondrial dysfunction and mitophagy. *Sci Adv*. 2019;5:eaax9778.
23. Bhattacharjee S, Rehman I, Nandy S, Das BB. Post-translational regulation of Tyrosyl-DNA phosphodiesterase (TDP1 and TDP2) for the repair of the trapped topoisomerase-DNA covalent complex. *DNA Repair*. 2022;111:103277.
24. Zagnoli-Vieira G, Caldecott KW. Untangling trapped topoisomerases with tyrosyl-DNA phosphodiesterases. *DNA Repair*. 2020;94:102900.
25. Rehman I, Basu SM, Das SK, et al. PRMT5-mediated arginine methylation of TDP1 for the repair of topoisomerase I covalent complexes. *Nucleic Acids Res*. 2018;46:5601-5617.
26. Das BB, Huang S-Y, Murai J, et al. PARP1-TDP1 coupling for the repair of topoisomerase I-induced DNA damage. *Nucleic Acids Res*. 2014;42:4435-4449.
27. Interthal H, Chen HJ, Champoux JJ. Human Tdp1 cleaves a broad spectrum of substrates, including phosphoamide linkages. *J Biol Chem*. 2005;280:36518-36528.
28. Katyal S, El-Khamisy SF, Russell HR, et al. TDP1 facilitates chromosomal single-strand break repair in neurons and is neuroprotective in vivo. *EMBO J*. 2007;26:4720-4731.
29. Banerjee B, Roy A, Sen N, Majumder HK. A tyrosyl DNA phosphodiesterase 1 from kinetoplastid parasite *Leishmania donovani* (LdTdp1) capable of removing topo I-DNA covalent complexes. *Mol Microbiol*. 2010;78:119-137.
30. Huang S-YN, Murai J, Dalla Rosa I, et al. TDP1 repairs nuclear and mitochondrial DNA damage induced by chain-terminating anticancer and antiviral nucleoside analogs. *Nucleic Acids Res*. 2013;41:7793-7803.
31. Cruz A, Coburn CM, Beverley SM. Double targeted gene replacement for creating null mutants. *Proc Natl Acad Sci U S A*. 1991;88:7170-7174.
32. Pal DS, Mondal DK, Datta R. Identification of metal dithiocarbamates as a novel class of antileishmanial agents. *Antimicrob Agents Chemother*. 2015;59:2144-2152.
33. Mukhopadhyay R, Mukherjee S, Mukherjee B, et al. Characterisation of antimony-resistant *Leishmania donovani* isolates: biochemical and biophysical studies and interaction with host cells. *Int J Parasitol*. 2011;41:1311-1321.
34. Mukherjee B, Mukhopadhyay R, Bannerjee B, et al. Antimony-resistant but not antimony-sensitive *Leishmania donovani* up-regulates host IL-10 to overexpress multidrug-resistant protein 1. *Proc Natl Acad Sci U S A*. 2013;110:E575-E582.
35. Das SK, Ghosh A, Paul Chowdhuri S, et al. Neutral porphyrin derivative exerts anticancer activity by targeting cellular topoisomerase I (Top1) and promotes apoptotic cell death without stabilizing Top1-DNA cleavage complexes. *J Med Chem*. 2018;61:804-817.
36. Das SK, Rehman I, Ghosh A, et al. Poly (ADP-ribose) polymers regulate DNA topoisomerase I (Top1) nuclear dynamics and camptothecin sensitivity in living cells. *Nucleic Acids Res*. 2016;44:8363-8375.
37. Sen N, Das BB, Ganguly A, et al. Camptothecin induced mitochondrial dysfunction leading to programmed cell death in unicellular hemoflagellate *Leishmania donovani*. *Cell Death Differ*. 2004;11:924-936.
38. Murai J, Shar-yin NH, Das BB, Dexheimer TS, Takeda S, Pommier Y. Tyrosyl-DNA phosphodiesterase 1 (TDP1) repairs DNA damage induced by topoisomerases I and II and base alkylation in vertebrate cells. *J Biol Chem*. 2012;287:12848-12857.
39. Mookerjee Basu J, Mookerjee A, Sen P, et al. Sodium antimony gluconate induces generation of reactive oxygen species and nitric oxide via phosphoinositide 3-kinase and mitogen-activated protein kinase activation in *Leishmania donovani*-infected macrophages. *Antimicrob Agents Chemother*. 2006;50:1788-1797.
40. Paris C, Loiseau PM, Bories C, Bréard J. Miltefosine induces apoptosis-like death in *Leishmania donovani* promastigotes. *Antimicrob Agents Chemother*. 2004;48:852-859.
41. Vermeersch M, da Luz RI, Toté K, Timmermans J-P, Cos P, Maes L. In vitro susceptibilities of *Leishmania donovani* promastigote and amastigote stages to antileishmanial reference drugs: practical relevance of stage-specific differences. *Antimicrob Agents Chemother*. 2009;53:3855-3859.
42. Sundar S, Chakravarty J. An update on pharmacotherapy for leishmaniasis. *Expert Opin Pharmacother*. 2015;16:237-252.
43. Boonnoy P, Jareerattanachai V, Karttunen M, Wong-Ekkabut J. Bilayer deformation, pores, and micellation induced by oxidized lipids. *J Phys Chem Lett*. 2015;6:4884-4888.
44. Nitiss KC, Malik M, He X, White SW, Nitiss JL. Tyrosyl-DNA phosphodiesterase (Tdp1) participates in the repair of Top2-mediated DNA damage. *Proc Natl Acad Sci U S A*. 2006;103:8953-8958.
45. Barthelme HU, Habermeyer M, Christensen MO, et al. TDP1 overexpression in human cells counteracts DNA damage mediated by topoisomerases I and II. *J Biol Chem*. 2004;279:55618-55625.
46. Ledesma FC, El Khamisy SF, Zuma MC, Osborn K, Caldecott KW. A human 5'-tyrosyl DNA phosphodiesterase that repairs topoisomerase-mediated DNA damage. *Nature*. 2009;461:674-678.
47. Mandal SM, Chakraborty A, Hossain M, et al. Amphotericin B and anidulafungin directly interact with DNA and induce oxidative damage in the mammalian genome. *Mol BioSyst*. 2015;11:2551-2559.
48. Croft SL, Sundar S, Fairlamb AH. Drug resistance in leishmaniasis. *Clin Microbiol Rev*. 2006;19:111-126.
49. Laffitte MC, Leprohon P, Hainse M, Légaré D, Masson JY, Ouellette M. Chromosomal translocations in the parasite leishmania by a MRE11/RAD50-independent microhomology-mediated end joining mechanism. *PLoS Genet*. 2016;12:e1006117.

SUPPORTING INFORMATION

Additional supporting information may be found in the online version of the article at the publisher's website.

How to cite this article: Chowdhury SR, Das SK, Banerjee B, Paul Chowdhuri S, Majumder HK, Das BB. TDP1 knockout *Leishmania donovani* accumulate topoisomerase 1-linked DNA damage and are hypersensitive to clinically used antileishmanial drugs. *FASEB J*. 2022;36:e22265. doi:[10.1096/fj.202101668RR](https://doi.org/10.1096/fj.202101668RR)

Top1-PARP1 association and beyond: from DNA topology to break repair

Srijita Paul Chowdhuri and Benu Brata Das¹*

Laboratory of Molecular Biology, School of Biological Sciences, Indian Association for the Cultivation of Science, 2A & B, Raja S. C. Mullick Road, Jadavpur, Kolkata 700032, India

Received October 08, 2020; Revised December 15, 2020; Editorial Decision January 08, 2021; Accepted January 12, 2021

ABSTRACT

Selective trapping of human topoisomerase 1 (Top1) on the DNA (Top1 cleavage complexes; Top1cc) by specific Top1-poisons triggers DNA breaks and cell death. Poly(ADP-ribose) polymerase 1 (PARP1) is an early nick sensor for trapped Top1cc. New mechanistic insights have been developed in recent years to rationalize the importance of PARP1 beyond the repair of Top1-induced DNA breaks. This review summarizes the progress in the molecular mechanisms of trapped Top1cc-induced DNA damage, PARP1 activation at DNA damage sites, PAR-dependent regulation of Top1 nuclear dynamics, and PARP1-associated molecular network for Top1cc repair. Finally, we have discussed the rationale behind the synergy between the combination of Top1 poison and PARP inhibitors in cancer chemotherapies, which is independent of the ‘PARP trapping’ phenomenon.

INTRODUCTION

DNA repair systems provide a critical defence mechanism against exogenous DNA-damaging agents and endogenous sources that assault the stability and integrity of our genomes linked to various diseases (1–3). One of the most common forms of DNA damage that arise in cells are single-strand breaks (SSBs). The SSBs can occur from the abortive activity of DNA topoisomerase 1 (Top1), due to the covalent trapping of Top1 with the 3'-end of the DNA leading to the generation of Top1-linked DNA covalent cleavage complexes (Top1cc) (2–5). The antitumor activity of camptothecin (CPT) and other non-CPT Top1 poisons that trigger cell death through selective trapping of the Top1cc of the highly proliferating cells exploit the severity of these breaks (6). Structural alterations in the DNA, including nicks, gaps, trapped protein–DNA complexes, replication lesions and double-strand breaks (DSBs) are sensed by sensor proteins that control cell cycle checkpoints and DNA damage response (DDR) pathways (1,2,5).

Poly(ADP-ribose)polymerase-1 (PARP1 or ARTD1) is a DNA nick sensor and has been proposed to play a critical role in the early detection of diverse types of DNA lesions including trapped Top1cc's (7–10). PARP1 catalyzes the addition of ADP-ribose polymers (PAR polymers) onto itself and other chromatin proteins that modulate their biological activities during DNA repair. Remarkable advancement has been made in the past few years in the clinical application of PARP inhibitors in cancer chemotherapy particularly in tumors deficient for homologous recombination repair pathways (8,9,11,12). Some of these inhibitors impart a dominant-negative effect by trapping PARPs at DNA breaks (9,13). Concerning combination therapy, PARP inhibitors synergize with DNA base alkylating agents, cisplatin and Top1 poisons in cancers (9). This review outlines the mechanism of PARP activation, molecular networks of PARP1 for the repair of Top1-induced DNA breaks, and the rationale for the combination of PARP and Top1 poisons in cancer.

TRAPPING OF TOPOISOMERASE 1 CLEAVAGE COMPLEXES (TOP1CC) ACCUMULATES DETRIMENTAL DNA DAMAGE

Topoisomerase 1 (Top1)

Human DNA Top1 (Top1) is essential as it relaxes positive DNA supercoiling in advance of replication forks and transcription complexes as well as negative supercoiling behind such complexes both in the nucleus and in the mitochondria to enable faithful transmission of our genetic information (5,14). Top1-mediated DNA supercoil relaxation involves three main steps: (i) DNA strand cleavage by a trans-esterification reaction involving a nucleophilic attack by the hydroxyl group of the active site tyrosine (Y⁷²³) on DNA phosphodiester bond resulting in the formation of a covalent DNA 3'-phosphotyrosyl linkage (Top1cc); (ii) DNA relaxation by controlled free rotation; and (iii) religation of the DNA strand which involves a similar trans-esterification reaction by the free DNA 5'-hydroxyl that releases the enzyme from the DNA (14). Under normal physiological conditions, the Top1 enzyme–DNA covalent complexes (Top1cc) are fleeting catalytic intermediates and nor-

*To whom correspondence should be addressed. Tel: +91 33 2473 4971 (Ext. 2108); Fax: +91 33 2473 2805; Email: pcbbd@iacs.res.in

mally not detectable (5). However, aborted topoisomerase catalytic activity results in the trapping of Top1 on 3'-DNA termini, which generates protein-linked DNA breaks (PDBs) (Figure 1A).

The occurrence of trapped Top1cc on DNA is markedly enhanced by the Top1 poisons, such as camptothecin (CPT) and its clinical derivatives like irinotecan and topotecan as well as several other non-CPT Top1 poisons (6,15), which bind to the interface of the ternary complex of enzyme-drug and the nicked DNA, thereby stabilizing the Top1cc and slowing the religation reaction of the nicking closing cycle (Figure 1). Top1-linked DNA single-strand break can be subsequently transformed into a DNA double-stranded break (DSB) plausibly through collision with the replication and transcription machineries (5). Trapped Top1cc's are potent transcription-blocking DNA lesions, which may include a transient stabilization of R-loops, leading to transcription-dependent DSBs and genome instability (16,17).

Top1 has intrinsic RNA nicking activity which converts ribonucleotides embedded in cellular DNA into nicks with 2'-3'-cyclophosphate and 5'-hydroxyl ends and is responsible for the repair of misincorporated ribonucleotides during DNA replication as an alternative to RNase II activity (5). However, this activity of Top1 appears to be mutagenic and detrimental as it generates short base deletions or nicks that can then trap Top1cc (5). Therefore, repairing trapped Top1cc is an important part of DNA metabolism, which is primarily catalyzed by DNA repair proteins including Poly(ADP-ribose)Polymerase 1 and Tyrosyl-DNA Phosphodiesterase 1 (TDP1).

Poly(ADP-ribose)polymerase-1 (PARP1)

PARP1 is a nuclear enzyme with multiple activities including the transfer of the negatively charged ADP-ribose units from nicotinamide adenine dinucleotide (NAD⁺) onto itself (a phenomenon termed as auto-PARylation) and to several histone and non-histone targets (chromatin-associated protein). PARP1 is the founding member of a superfamily of 17 enzyme isoforms that have been identified in eukaryotes and prokaryotes but not in yeast (8,18). Though PARP isoforms have different primary structures but they share homology in the domain responsible for poly(ADP-ribose) synthesis, termed PARylation (11,18). The PAR polymers are synthesized by PARP1, PARP2, PARP5A and PARP5B. The other members of the family catalyze only single ADP-ribose units and are therefore classified as mono(ADP-ribosyl)ases (MARs) (11). It is important to note that cellular PARylation is highly dynamic and fully reversible. Poly(ADP-ribose) glycohydrolase (PARG) and ADP-ribosylhydrolase 3 (ARH3) are responsible for the removal of PAR chains in almost all eukaryotic cells. The uncontrolled accumulation of PAR polymers is cytotoxic (8).

PARP1 is composed of six domains with distinct DNA binding, catalytic and regulatory functions as shown in Figure 2A. The N-terminal region includes the DNA-binding zinc finger domains (Zn1, Zn2 and Zn3) and the central auto-modification domain harboring the BRCT (BRCA1 C-terminal) fold. The WGR (Tryptophan-Glycine-Arginine) domain is positioned next to the C-

terminal catalytic domain (CAT) containing two subdomains: the helical (HD) and the ADP-ribosyltransferase (ART) (19). PARP1 stands as an exemplary to the class of multi-domain containing DDR proteins joined by a flexible 'beads-on-a-string' assembly by unstructured linkers that are rendered more ordered domain architecture upon binding to damaged DNA, an allosteric regulation that initiates catalytic activation and subsequent poly(ADP-ribose)-dependent DNA repair (Figure 2A) (18,19).

PARylation is one of the predominant post-translational modification (PTM) that regulates diverse biological processes such as DNA repair, oxidative stress, chromatin remodeling, regulation of transcription and apoptosis (8,11).

PARP1 is the key player for the repair of single-strand breaks (SSBR). Because SSBs are produced as an intermediate of Base-Excision Repair (BER); therefore, PARP1 is an integral part of BER and promotes DNA repair through its interaction and PARylation of several proteins involved in SSBR and BER. PARP1 has also been implicated in DNA double-strand break (DSBs) repair by regulating the upstream classical Non Homologous End Joining (cNHEJ) components (KU70, KU80, ARTEMIS and DNA-PKCs). However, the importance of PARP1 to these pathways is not completely clear (8,20). PARP1 inhibition triggers the activation of ataxia-telangiectasia-mutated kinase (ATM) (21) and is also implicated in the alternative or back up pathway for the NHEJ, which involves key factors of SSBR such as XRCC1, DNA ligase 3, and FEN1, as well as DSB repair proteins (8,11).

Further studies have suggested the role of PARP activity in protecting cells from DNA replication-associated DNA lesions. PARP1 protects stalled replication forks and promotes the restart of DNA synthesis (22). PARP activity is enriched on the DNA lagging strand of the replication fork, which is associated with PARP1 activation at unligated Okazaki fragment intermediates of DNA replication (23).

Beyond DDR pathways, PARP1 has diverse biological functions that include protein translocation, and degradation, cell division, gene silencing, RNA biology, and triggering cell death mechanism (8,18). PARylation also orchestrates a variety of processes in the nucleolar niche, which aids in the maintenance of the nucleolar structure, ribosome biogenesis, rRNA synthesis, and the epigenetic upkeep of the rDNA (8,18).

PARP1 REGULATES SUBNUCLEAR DYNAMICS OF TOP1

Nucleoli are the subnuclear compartments without a prominent membrane, harboring repeated clusters of 200–400 ribosomal DNA (rDNA) genes. Intriguingly, the nucleolus has turned out to be the regulatory hub for multiple nuclear functions and has been attributed to stress response and DNA damage signalling. Accordingly, the dysregulation of nucleolar functions has been linked to carcinogenesis and neurological diseases (24). Due to the absence of a structural barrier between the nucleolus and the surrounding nucleoplasm, proteins can freely traffic from the nucleolus to the nucleoplasm and vice versa. However, the mech-

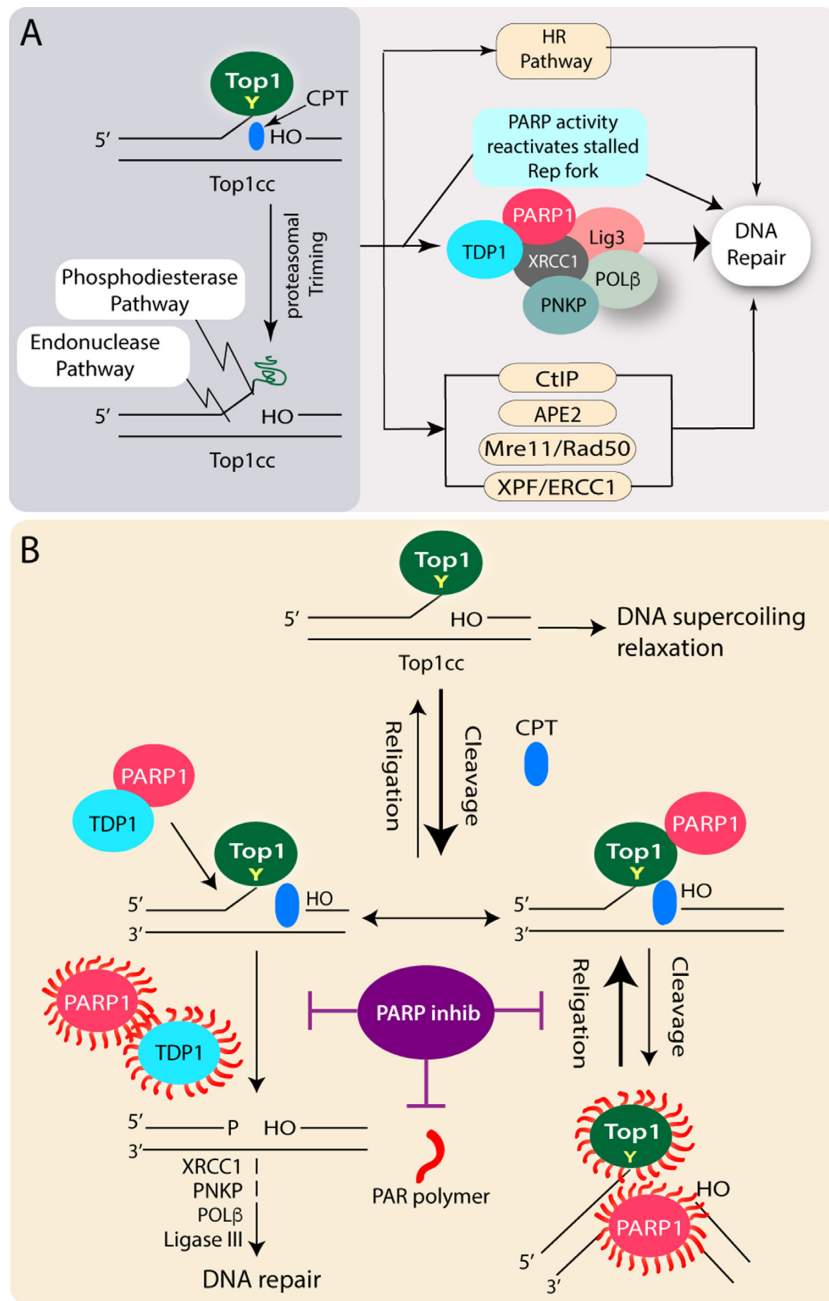


Figure 1. Induction of DNA damage with trapped Top1-DNA cleavage complexes (TOP1cc) and repair pathways. **(A)** Top1 cleaves one strand of duplex DNA *via* the nucleophilic attack of its active site tyrosine on the DNA phosphodiester backbone to yield a 3'-phosphotyrosyl bond. The short-lived covalent Top1-DNA cleavage complex (Top1cc) is readily trapped by Top1 poisons *i.e.* Camptothecin (CPT; blue) which binds in the interface of Top1-DNA complexes, stabilizes Top1cc, and inhibits the Top1-religation reaction. Scheme illustrating the repair pathways involved downstream to the proteasomal degradation of trapped Top1cc's, which can be repaired in cells by broadly three pathways: (i) phosphodiesterase pathway: Excision of Top1 by TDP1 which is coupled with PARP1. PARP1 also reactivates stalled replication fork encountered by transient Top1cc; (ii) Endonuclease pathway: DNA cleavage by 3'-flap endonucleases such as XPF-ERCC1, Mre11/Rad50, CtIP and APE2; (iii) The Top1cc associated DSBs generated by replication run-off, results in a Top1-linked double-stranded end (DSE) which are repaired by homologous recombination repair. **(B)** PARP inhibitors the double-edged sword: Killing Top1 activity and inhibiting TDP1-mediated Top1cc repair. The short-lived covalent Top1-DNA cleavage complex (Top1cc) is readily reversed and facilitates DNA supercoil relaxation. The bold arrow indicates the shift in the cleavage/religation equilibrium in the presence of CPT (blue). PARylation of Top1 helps in the religation of the CPT-induced Top1 cleavage complex (Top1cc). While PARP coupling with TDP1 stimulates the excision of Top1cc by the phosphodiesterase activity of TDP1 and facilitates DNA repair. PARP inhibitors (purple) in combination with CPT abrogate Top1 and TDP1-PARylation, impair the repair of CPT-induced Top1cc, and promoting DSBs and cell death.

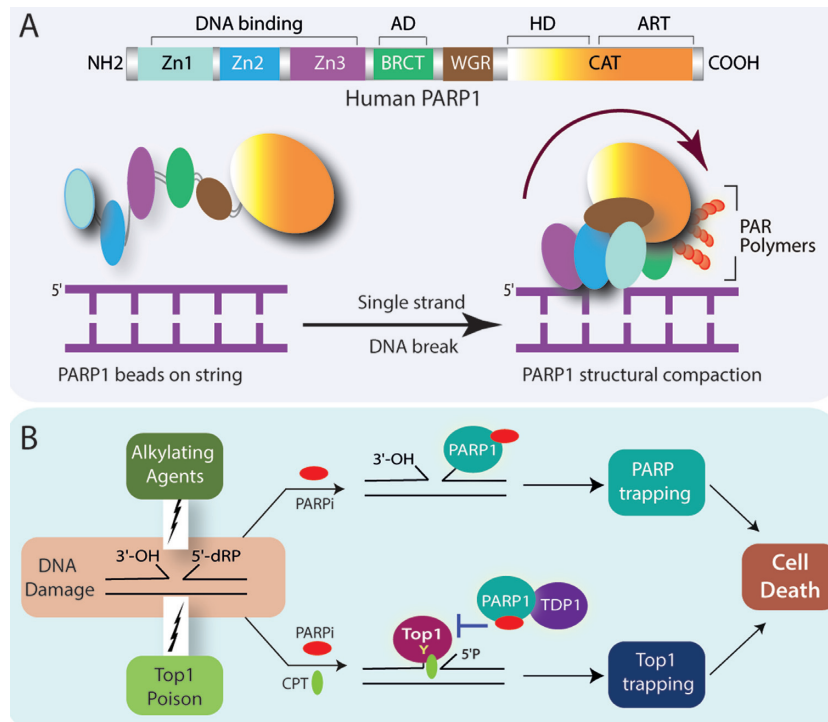


Figure 2. PARP1 and PARP trapping with PARP inhibitors. (A) PARP1 structural rearrangements facilitate the PARP1 activation at DNA damage sites. Cartoon showing the domain architecture of human PARP1 (top panel) indicating the three DNA binding zinc finger domains (Zn1, Zn2 and Zn3), BRCT (auto modification domain; AD), the WGR domain, and the Catalytic domain (CAT) composed of the helical (HD) and ART (ADP-ribosyl transferase) subdomains. PARP1 inter-domain rearrangements post DNA damage recognition (bottom panel). In absence of DNA damage PARP1 forms loose 'beads on a string' conformation (left) which rapidly changes into a collapsed conformation upon recruitment to DNA damage sites (right). The arrow indicates the folding of the 'beads-on-a-string' form of PARP1 to the compact conformation. (B) Top1 poisons synergize with PARP inhibitors by the catalytic inhibition of PARP1 independent of PARP trapping. The mechanistic rationale for the combination of PARP inhibitors (PARPi) with DNA damaging alkylating agents and by Top1 poisons is illustrated. The alkylating agents generate a single-nucleotide gap with 3'-OH and 5'-deoxyribose phosphate (5'-dRP) groups at the ends of the breaks which remain unrepaired by PARP inhibition. Additionally, PARP gets trapped on the DNA resulting in cell death due to the competitive binding of the PARPi to the NAD⁺ pocket abrogating the auto-PARylation followed by the concomitant dissociation of PARP from DNA. Camptothecins (Top1 poisons; Top1i) traps Top1cc's at the 3'-end of the DNA with 5'-sugar hydroxyl intermediates which are not preferred substrates for PARP trapping. PARP1 and TDP1 coupling involve the catalytic activity of PARP that outlines the synergy of Top1 and PARP inhibitors is through prolong Top1 trapping and cell death independent of PARP trapping.

anisms by which proteins are retained in the nucleolus are still not fully understood.

Top1 is predominantly localized in the nucleolus (7,25,26). Since the nucleolus serves as the storehouse for ribosomal RNA synthesis it inevitably demands the presence of nuclear Top1 activity for the relaxation of rDNA supercoiling generated during the RNA's replication and transcription (25).

Like Top1, PARP1 is also highly mobile in the nucleus; PARP1 is localized in the nucleoli and required for ribosomal biogenesis. Both PARP1 and PARP2 interact with nucleophosmin/B23 and accumulate in transcriptionally active nucleoli. Genetic inactivation of PARP1 activity disrupts rRNA processing and maturation (27). Top1 is an acceptor of PAR polymers which is catalyzed by PARP1 and colocalizes with PARP1 in the nucleolus and nucleoplasm throughout the cell cycle (7).

PARP1 favors a faster Top1 religation activity in the presence of CPT either through its direct interaction with Top1 or by the formation of PARylated Top1 (7,25,26). This was further supported by live-cell microscopy coupled with FRAP kinetic modeling study that shows PARP inhibitor prolongs the trapping of *in vivo* Top1cc in combination with

CPT that allows accumulation of cellular DNA double-strand breaks (7,28). However, the underlying molecular mechanism by which Top1-PARylation regulates the nuclear mobility of Top1 was mostly obscure until recently, using live-cell microscopy demonstrated that disruption of PARP1 activity by PARP inhibitors delocalized Top1 from the nucleolus to the nucleoplasm which is independent of the interactions between the two proteins (7). These studies also suggest that the PARylation of Top1 serves to engage Top1 to the active sites of rDNA and rRNA synthesis.

Like PARP1, the shuttling of the repair factors including XRCC1 (X-ray repair cross-complementing protein 1), and WRN (Werner syndrome helicase), between the nucleolus and nucleoplasm is dependent on PARP1 enzymatic activity and response to DNA damage with CPT or H₂O₂ (29). Accordingly, the abrogation of PARP1 activity abolishes the nucleolar-nucleoplasmic shuttling of XRCC1, WRN and PARP1 (30).

REPAIR OF TOP1CC-INDUCED DNA BREAKS

There has been a notable advancement regarding the elucidation of the repair pathways involved in the removal

of trapped Top1 cleavage complexes (Top1cc). Irreversibly trapped Top1cc is trimmed through proteolysis (Figure 1A) before it is channeled to the DNA repair pathways. The Top1cc's can be repaired in cells by broadly three pathways: (i) Excision of Top1 by tyrosyl-DNA phosphodiesterase 1 (TDP1) which is coupled with PARP1, (ii) Endonuclease pathway: DNA cleavage by 3'-flap endonucleases such as XPF-ERCC1, Mre11/Rad50; CtIP and APE2, (iii) The Top1cc associated DSBs generated by replication run-off, results in a Top1-linked double-stranded end (DSE) which are repaired by homologous recombination repair (aided by BRCA1 and BRCA2 proteins), supporting the rationale behind the hypersensitivity of BRCA-deficient cancer cells to Top1 poisons (4,5,10,31) (Figure 1A).

Tyrosyl-DNA phosphodiesterase 1 (TDP1)

The key enzyme for the excision of Top1cc is TDP1, which was discovered by Nash and colleagues (32). TDP1 is conserved in all eukaryotes and present both in the nucleus and mitochondria. TDP1 hydrolyzes the phosphodiester bond between the Top1 tyrosyl moiety and the DNA 3'-end. TDP1's ability to resolve 3'-phosphotyrosyl linkages is consistent with its role in protecting cells against Top1-induced DNA lesions (4,10,33–35) (Figure 1A).

The ability of TDP1 to resolve 3'-phosphotyrosyl linkages is not limited to the removal of Top1-DNA adducts both in the nucleus and mitochondria but is also required for the removal of a variety of blocking lesions at the 3'-DNA ends during DNA repair which includes 3'-abasic sites and 3'-phosphoglycolate (10,35,36). TDP1 also possesses a limited DNA and RNA 3'-exonuclease activity in which a single nucleoside is removed from the 3'-hydroxyl end of the substrate (36). TDP1 is involved in the excision repair of 3'-chain-terminating anticancer and antiviral nucleosides and have weak excision activity against 5'-tyrosyl ends (10).

Human TDP1 is a neuroprotective enzyme and a homozygous mutation of TDP1 (H⁴⁹³R) is responsible for the neurodegenerative syndrome, spinocerebellar ataxia with axonal neuropathy (SCAN1) (37,38). Cells from SCAN1 patients or TDP1 knockout mice are hypersensitive to camptothecin (CPT) that selectively trap nuclear Top1-DNA covalent complexes (Top1cc) (2,3,35,39). TDP1 is critical for mitochondrial DNA (mtDNA) repair (34), accordingly SCAN1-mutant TDP1 is trapped in the specific loci of mtDNA, which increases mitochondrial DNA damage, and mitochondrial fission that leads to neuronal damage associated with SCAN1 etiology (40). Loss of TDP1 also resulted in gradual age-related cerebellar atrophy in one of the mouse model (2,35,39). Therefore, the SCAN1 pathology is a combination of both TDP1 deficiency and TDP1 trapping.

Post-translational modifications have been implicated in the recruitment, modulation of enzymatic activity, and stability of DNA damage response of TDP1. ATM (ataxia-telangiectasia mutated) and DNA-dependent protein kinase (DNA-PK) are activated in response to Top1cc-associated DSBs (1–3) that phosphorylate TDP1 at serine 81 in response to CPT or with ionizing radiation (41). CPT-induced phosphorylation at TDP1-S⁸¹ promotes its bind-

ing with XRCC1 and ligase III α , which potentially stabilizes TDP1 from degradation and enhances recruitment of pS⁸¹-TDP1 foci together with γ H2AX and XRCC1 foci at Top1cc damage sites (41). These sites most likely correspond to the small fraction of the Top1cc's that are converted into irreversible Top1-DNA lesions by replication and transcription (2,10,41).

Because DNA damage increases the half-life of TDP1 through phosphorylation and PARylation (28,41); therefore, the ubiquitin–proteasome system plays an important role in regulating TDP1 turnover which led to the identification of UCHL3 as the deubiquitylase enzyme controlling TDP1 proteostasis (42). TDP1-SUMOylation at lysine 111 (K111) promotes DNA repair and has been implicated in the recruitment of TDP1 at transcription-dependent Top1cc damage sites (43).

Intriguingly, protein arginine methyltransferases (PRMT5) catalyzed arginine methylation of TDP1 at residues R³⁶¹ and R⁵⁸⁶ through binding with TDP1. Unlike other PTMs, arginine methylation stimulates TDP1's 3'-phosphodiesterase activity (44). TDP1 methylation also stimulates its repair function and promotes cell survival in response to CPT and ionizing radiation.

Coupling TDP1 and PARP1 for the repair of Top1cc-induced DNA breaks

Top1cc-induced DNA damage response is a complex signaling network that initiates with proteolysis of Top1, thereby allowing subsequent access of DNA repair enzymes including TDP1 to the Top1 active site tyrosyl-DNA linkage. Because TDP1 generates 3'-phosphate ends, its cellular activity needs to be coupled with polynucleotide kinase phosphatase (PNKP) to generate 3'-hydroxyl ends that can be extended by DNA polymerase β and DNA ligase III α seals the nicks in DNA backbone (10) (Figure 1).

The involvement of PARP1 for the repair of Top1cc stems from various reports which include the hypersensitivity of PARP1 knockout cells to camptothecin (CPT); PARP inhibitors enhance the activity of CPT and its clinical derivatives both in cell cultures and in xenograft systems, and PARP accumulates in the nucleus of CPT-treated cells (5,7,10).

PARP inhibitors markedly increase DNA breaks in response to Top1cc but without a concomitant increase in Top1–DNA complexes. It is evidenced that PARP inactivation is associated with TDP1 deficiency, accordingly, PARP1 knockout cells have less TDP1 activity and the PARP inhibitor ABT-888 (veliparib) fails to sensitize Top1 poisons in TDP1-deficient cells which is implicated for the repair of Top1cc (10,28,45). Furthermore, PARP inactivation is also implicated in preventing the release of trapped Top1 from stalled replication complexes by suppressing the restart of replication forks reversed by Top1cc (8,20,23).

PARP1 appears to act as a molecular determinant for the choice between TDP1 and the endonuclease pathway for the repair of trapped Top1cc (Figure 1A). These conclusions are based on the genetic studies that suggest PARP1 and TDP1 are epistatic and show a tight coupling of TDP1 and PARP1 through direct protein–protein interaction. Furthermore, TDP1 is PARylated by PARP1 that essentially stabilizes TDP1 and enhances its recruitment to DNA dam-

age sites without interfering with TDP1 catalytic activity. Though PARP1 facilitates XRCC1 recruitment at DNA damage sites (3), PARP1–TDP1 complexes, in turn, also recruit XRCC1 at the trapped Top1cc-DNA breaks as TDP1 deficient cells fail to generate CPT-induced XRCC1 foci (10,28).

RATIONALE FOR THE COMBINATION OF PARP INHIBITORS WITH TOPOISOMERASE 1 POISONS

PARP inhibitors (PARPi) are a class of anticancer drugs that compete with nicotinamide adenine dinucleotide (NAD⁺) for the catalytically active site of PARP molecules, thereby ablating the PAR synthesizing activity of the enzyme (11). The clinical success of PARP inhibitors can be primarily reasoned to be due to the phenomenon of *synthetic lethality* wherein cells with an intrinsic perturbation or defect in one DNA repair pathway can be selectively killed or targeted by disrupting the backup pathway for the repair (11,12).

PARP inhibitors not only catalytically inactivate PARPs but also interfere with the subsequent process of release of the enzyme from the site of DNA damage; this phenomenon is called the ‘PARP trapping’ (9,13). These trapped PARPs are DNA lesions that not only block the further recruitment of other repair proteins at the DNA damage sites but also stall the DNA replication fork, and activate S-phase checkpoints leading to cell cycle arrest (11). The PARP inhibitors differ markedly in their trapping potency which corresponds to their cytotoxic potency and overall clinical doses (9,11,13).

These clinical responses for PARP inhibitors seem to be transient, as cases of revertants and PARP inhibitor resistance are on the high. Therefore, the personalized regimen of chemotherapies has started exploiting the inhibition of PARP in combination with a wide variety of DNA damaging drugs including alkylating agents (temozolomide) and Top1 poisons (camptothecin and its clinical derivatives topotecan and irinotecan). It is, however, critical to explore whether different PARP inhibitors can be considered to be equipotent in combination chemotherapies because of the PARP trapping phenomenon (11,13). Synergistic effects of PARP inhibitors combined with Top1 poisons (camptothecins and indenoisoquinolines) are well evidenced (9). The wide-scale prevalence of preclinical models exemplifying PARP inhibitors that show clinical activity in ovarian cancer, breast and prostate cancer as single agents, sensitize tumor cells to Top1 poisons *in vitro* and *in vivo* propelled combining PARP inhibitors with Top1 poison in the clinics. A combination of olaparib with topotecan or irinotecan with veliparib was effective at a much lower dose than the individual single-agents (9,46,47). It came out from one such early case of a phase I trial with Veliparib combination with topotecan or irinotecan showed significant reductions in peripheral blood mononuclear cells (PBMC) (47).

Further studies confirmed that despite the apparent similarity in the mode of action for the Top1 poisons and alkylating agents (i.e. generation of DNA SSBs which are sensed by PARP1); however, the molecular mechanisms underlying the synergy are markedly different based on the nature of

the DNA breaks. The synergistic effects of PARP inhibitors in combination with Top1 poisons is due to catalytic inhibition of PARP activity that is further supported by biochemical and cellular studies. Top1 poisons like CPT or its derivatives block the 3'-end of the DNA through Top1cc formation with a free 5'-sugar hydroxyl intermediate (9,13); however, the preferred DNA substrates for PARP1 binding are with a 5'-deoxyribose phosphate (dRP) compared to 5'-phosphate end (48,49), therefore, the specificity for the synergistic combination of PARP catalytic inhibitors with Top1 poisons is due to prolonged Top1 trapping (Figure 1B) and is independent of PARP trapping mechanism. The catalytic inhibitors of PARP abrogate PARP1–TDP1 coupling that inactivates TDP1 (28), and inhibits PAR-dependent Top1 nuclear mobility which is further trapped by Top1 poisons (7) (Figure 2B). Conversely, PARP inhibition also promotes DSB formation through replication fork collisions with CPT-induced Top1 cleavage complexes (5,8). Eventually, the failure of the synergistic cytotoxicity for a combination of Top2 inhibitors (etoposide) that trap Top2cc at DNA 5'-end with PARP inhibitors (NU1025) (11,50) does not induce PARP trapping (9), strongly suggest that PARP and Top2 inhibitors are not rational for combination therapy.

In contrast, PARP trapping and PARylation inhibition both account for the synergy with alkylating agents like methyl methanesulfonate (MMS) or Temozolomide that generates abasic sites, which are cleaved by apurinic/aprimidinic endonuclease 1 (APE1), resulting in a single-nucleotide gap with 3'-OH and 5'-dRP at the DNA breaks that promote trapping of PARP–DNA complexes at the damage sites (Figure 2B) (9,13,48,49).

Summarily, it can be construed that when veliparib is combined with the Top1 poison (Topotecan/Irinotecan) hematologic toxicity is dose-limiting, but both agents can be administered at lower doses than the individual agent (46,47). Future studies warrant that in a more personalized tumor-specific environment the combination of PARP and Top1 poisons may benefit patients with tumors expressing high levels of PARP1 and Top1.

CONCLUSION

PARP1 has a multifaceted role in regulating a myriad of cellular functions and a host of DNA repair pathways. PARP inhibitors as pharmacological targets in the treatment of cancers resistant to the current chemotherapeutic regimens revolutionized precision cancer therapy. However, the frequently acquired resistance to PARP inhibitors in monotherapies has spurred the need to combine PARP inhibitors with other agents. Our review summarizes that PARP1 serves as a key protein in the repair of the Top1cc's while PARP inhibitors hold much promise as combinatorial agents when combined with Top1 poisons. The synergy that exists between Top1 poisons and PARP inhibitors seems to be driven by the catalytic inhibition of PARP1 and is not significantly incremented by the trapping potential of the PARP inhibitors (Figure 2B). Therefore, discrimination between PARP inhibitors on their ability to catalytically block the PARP1 function is necessary for future evaluation of the potential efficacy for the combination of PARP inhibitors

with Top1 poison. Thus, it can be claimed that the combinatorial therapy might in a way assuage the monotherapeutic doses of the individual drugs used in tumor regression.

ACKNOWLEDGMENTS

We wish to thank Dr Yves Pommier of the National Cancer Institute, National Institutes of Health, USA, Dr Subhendu K. Das, Dr Ishita Rehman, Mr Arijit Ghosh and Ms Banhi Chowdhury of the Laboratory of Molecular Biology, IACS, India for the help during the study. We also thank Prof. C. Austin of the Institute for Cell and Molecular Biosciences, Newcastle University, UK, for critically reading the manuscript. BBD is the DBT/Wellcome Trust India alliance, intermediate fellow

Author contributions: B.B.D and S.P.C wrote and edited the manuscript.

FUNDING

B.B.D team was supported by DST-SERB core research grant [EMR/2017/001652], DBT/Wellcome Trust India Alliance intermediate fellowship grant [IA/I/13/1/500888] and IACS intramural research grant. SPC is the recipient of UGC-NET Senior Research Fellowship.

Conflict of interest statement. None declared.

REFERENCES

- Shiloh, Y. and Ziv, Y. (2013) The ATM protein kinase: regulating the cellular response to genotoxic stress, and more. *Nat. Rev. Mol. Cell Biol.*, **14**, 197–210.
- McKinnon, P.J. and Caldecott, K.W. (2007) DNA strand break repair and human genetic disease. *Annu. Rev. Genomics Hum. Genet.*, **8**, 37–55.
- Caldecott, K.W. (2008) Single-strand break repair and genetic disease. *Nat. Rev. Genet.*, **9**, 619–631.
- Ashour, M.E., Atteya, R. and El-Khamisy, S.F. (2015) Topoisomerase-mediated chromosomal break repair: an emerging player in many games. *Nat. Rev. Cancer*, **15**, 137–151.
- Pommier, Y., Sun, Y., Huang, S.N. and Nitiss, J.L. (2016) Roles of eukaryotic topoisomerases in transcription, replication and genomic stability. *Nat. Rev. Mol. Cell Biol.*, **17**, 703–721.
- Pommier, Y. (2013) Drugging topoisomerases: lessons and challenges. *ACS Chem. Biol.*, **8**, 82–95.
- Das, S.K., Rehman, I., Ghosh, A., Sengupta, S., Majumdar, P., Jana, B. and Das, B.B. (2016) Poly(ADP-ribose) polymers regulate DNA topoisomerase I (Top1) nuclear dynamics and camptothecin sensitivity in living cells. *Nucleic Acids Res.*, **44**, 8363–8375.
- Ray Chaudhuri, A. and Nussenzweig, A. (2017) The multifaceted roles of PARP1 in DNA repair and chromatin remodelling. *Nat. Rev. Mol. Cell Biol.*, **18**, 610–621.
- Murai, J. and Pommier, Y. (2019) PARP trapping beyond homologous recombination and platinum sensitivity in cancers. *Ann. Rev. Cancer Biol.*, **3**, 131–150.
- Pommier, Y., Huang, S.Y., Gao, R., Das, B.B., Murai, J. and Marchand, C. (2014) Tyrosyl-DNA-phosphodiesterases (TDP1 and TDP2). *DNA Repair (Amst.)*, **19**, 114–129.
- Curtin, N.J. and Szabo, C. (2020) Poly(ADP-ribose) polymerase inhibition: past, present and future. *Nat. Rev. Drug Discovery*, **19**, 711–736.
- Lord, C.J. and Ashworth, A. (2017) PARP inhibitors: Synthetic lethality in the clinic. *Science*, **355**, 1152–1158.
- Murai, J., Huang, S.-y.N., Das, B.B., Renaud, A., Zhang, Y., Doroshov, J.H., Ji, J., Takeda, S. and Pommier, Y. (2012) Trapping of PARP1 and PARP2 by clinical PARP inhibitors. *Cancer Res.*, **72**, 5588–5599.
- Champoux, J.J. (2001) DNA Topoisomerases: Structure, function, and mechanism. *Annu. Rev. Biochem.*, **70**, 369–413.
- Capranico, G., Marinello, J. and Chillemi, G. (2017) Type I DNA topoisomerases. *J. Med. Chem.*, **60**, 2169–2192.
- Marinello, J., Chillemi, G., Bueno, S., Manzo, S.G. and Capranico, G. (2013) Antisense transcripts enhanced by camptothecin at divergent CpG-island promoters associated with bursts of topoisomerase I-DNA cleavage complex and R-loop formation. *Nucleic Acids Res.*, **41**, 10110–10123.
- Cristini, A., Ricci, G., Britton, S., Salimbeni, S., Huang, S.N., Marinello, J., Calsou, P., Pommier, Y., Favre, G., Capranico, G. *et al.* (2019) Dual processing of R-Loops and topoisomerase I induces transcription-dependent DNA double-strand breaks. *Cell Rep.*, **28**, 3167–3181.
- Hottiger, M.O. (2015) Nuclear ADP-Ribosylation and its role in chromatin plasticity, cell differentiation, and epigenetics. *Annu. Rev. Biochem.*, **84**, 227–263.
- Langelier, M.F., Planck, J.L., Roy, S. and Pascal, J.M. (2012) Structural basis for DNA damage-dependent poly(ADP-ribosylation) by human PARP-1. *Science (New York, N.Y.)*, **336**, 728–732.
- Hochegger, H., Dejsuphong, D., Fukushima, T., Morrison, C., Sonoda, E., Schreiber, V., Zhao, G.Y., Saberi, A., Masutani, M., Adachi, N. *et al.* (2006) Parp-1 protects homologous recombination from interference by Ku and Ligase IV in vertebrate cells. *EMBO J.*, **25**, 1305–1314.
- Bryant, H.E. and Helleday, T. (2006) Inhibition of poly (ADP-ribose) polymerase activates ATM which is required for subsequent homologous recombination repair. *Nucleic Acids Res.*, **34**, 1685–1691.
- Ray Chaudhuri, A., Ahuja, A.K., Herrador, R. and Lopes, M. (2015) Poly(ADP-ribose) glycohydrolase prevents the accumulation of unusual replication structures during unperturbed S phase. *Mol. Cell Biol.*, **35**, 856–865.
- Hanzlikova, H. and Caldecott, K.W. (2019) Perspectives on PARPs in S Phase. *Trends Genet.*, **35**, 412–422.
- Weeks, S.E., Metge, B.J. and Samant, R.S. (2019) The nucleolus: a central response hub for the stressors that drive cancer progression. *Cell. Mol. Life Sci.*, **76**, 4511–4524.
- Mao, Y., Mehl, I.R. and Muller, M.T. (2002) Subnuclear distribution of topoisomerase I is linked to ongoing transcription and p53 status. *Proc. Natl. Acad. Sci.*, **99**, 1235–1240.
- Christensen, M.O., Barthelmes, H.U., Feineis, S., Knudsen, B.R., Andersen, A.H., Boege, F. and Mielke, C. (2002) Changes in mobility account for camptothecin-induced subnuclear relocation of topoisomerase I. *J. Biol. Chem.*, **277**, 15661–15665.
- Engbrecht, M. and Mangerich, A. (2020) The Nucleolus and PARP1 in cancer biology. *Cancers*, **12**, 1813.
- Das, B.B., Huang, S.-y.N., Murai, J., Rehman, I., Amé, J.-C., Sengupta, S., Das, S.K., Majumdar, P., Zhang, H., Biard, D. *et al.* (2014) PARP1–TDP1 coupling for the repair of topoisomerase I-induced DNA damage. *Nucleic Acids Res.*, **42**, 4435–4449.
- Hanzlikova, H., Gittens, W., Krejčíková, K., Zeng, Z. and Caldecott, K.W. (2017) Overlapping roles for PARP1 and PARP2 in the recruitment of endogenous XRCC1 and PNKP into oxidized chromatin. *Nucleic Acids Res.*, **45**, 2546–2557.
- Veith, S., Schink, A., Engbrecht, M., Mack, M., Rank, L., Rossatti, P., Hakobyan, M., Goly, D., Hefele, T., Frensch, M. *et al.* (2019) PARP1 regulates DNA damage-induced nucleolar-nucleoplasmic shuttling of WRN and XRCC1 in a toxicant and protein-specific manner. *Sci. Rep.*, **9**, 10075.
- Álvarez-Quilón, A., Wojtaszek, J.L., Mathieu, M.C., Patel, T., Appel, C.D., Hustedt, N., Rossi, S.E., Wallace, B.D., Setiapatra, D., Adam, S. *et al.* (2020) Endogenous DNA 3' blocks are vulnerabilities for BRCA1 and BRCA2 deficiency and are reversed by the APE2 nuclease. *Mol. Cell*, **78**, 1152–1165.
- Yang, S.W., Burgin, A.B., Huizenga, B.N., Robertson, C.A., Yao, K.C. and Nash, H.A. (1996) A eukaryotic enzyme that can disjoin dead-end covalent complexes between DNA and type I topoisomerases. *Proc. Natl. Acad. Sci.*, **93**, 11534–11539.
- Interthal, H., Pouliot, J.J. and Champoux, J.J. (2001) The tyrosyl-DNA phosphodiesterase Tdp1 is a member of the phospholipase D superfamily. *Proc. Natl. Acad. Sci.*, **98**, 12009–12014.
- Das, B.B., Dexheimer, T.S., Maddali, K. and Pommier, Y. (2010) Role of tyrosyl-DNA phosphodiesterase (TDP1) in mitochondria. *Proc. Natl. Acad. Sci.*, **107**, 19790–19795.

35. Kawale,A.S. and Povirk,L.F. (2018) Tyrosyl-DNA phosphodiesterases: rescuing the genome from the risks of relaxation. *Nucleic Acids Res.*, **46**, 520–537.
36. Interthal,H., Chen,H.J. and Champoux,J.J. (2005) Human Tdp1 cleaves a broad spectrum of substrates, including phosphoamide linkages. *J. Biol. Chem.*, **280**, 36518–36528.
37. Takashima,H., Boerkoel,C.F., John,J., Saifi,G.M., Salih,M.A., Armstrong,D., Mao,Y., Quijcho,F.A., Roa,B.B., Nakagawa,M. *et al.* (2002) Mutation of TDP1, encoding a topoisomerase I-dependent DNA damage repair enzyme, in spinocerebellar ataxia with axonal neuropathy. *Nat. Genet.*, **32**, 267–272.
38. Caldecott,K.W. (2003) DNA single-strand break repair and spinocerebellar ataxia. *Cell*, **112**, 7–10.
39. Katyal,S., el-Khamisy,S.F., Russell,H.R., Li,Y., Ju,L., Caldecott,K.W. and McKinnon,P.J. (2007) TDP1 facilitates chromosomal single-strand break repair in neurons and is neuroprotective in vivo. *EMBO J.*, **26**, 4720–4731.
40. Ghosh,A., Bhattacharjee,S., Chowdhuri,S.P., Mallick,A., Rehman,I., Basu,S. and Das,B.B. (2019) SCAN1-TDP1 trapping on mitochondrial DNA promotes mitochondrial dysfunction and mitophagy. *Sci. Adv.*, **5**, eaax9778.
41. Das,B.B., Antony,S., Gupta,S., Dexheimer,T.S., Redon,C.E., Garfield,S., Shiloh,Y. and Pommier,Y. (2009) Optimal function of the DNA repair enzyme TDP1 requires its phosphorylation by ATM and/or DNA-PK. *EMBO J.*, **28**, 3667–3680.
42. Liao,C., Beveridge,R., Hudson,J.J.R., Parker,J.D., Chiang,S.-C., Ray,S., Ashour,M.E., Sudbery,I., Dickman,M.J. and El-Khamisy,S.F. (2018) UCHL3 regulates topoisomerase-induced chromosomal break repair by controlling TDP1 proteostasis. *Cell Rep.*, **23**, 3352–3365.
43. Hudson,J.J.R., Chiang,S.-C., Wells,O.S., Rookyard,C. and El-Khamisy,S.F. (2012) SUMO modification of the neuroprotective protein TDP1 facilitates chromosomal single-strand break repair. *Nat. Commun.*, **3**, 733.
44. Rehman,I., Basu,S.M., Das,S.K., Bhattacharjee,S., Ghosh,A., Pommier,Y. and Das,B.B. (2018) PRMT5-mediated arginine methylation of TDP1 for the repair of topoisomerase I covalent complexes. *Nucleic Acids Res.*, **46**, 5601–5617.
45. Patel,A.G., Sarkaria,J.N. and Kaufmann,S.H. (2011) Nonhomologous end joining drives poly(ADP-ribose) polymerase (PARP) inhibitor lethality in homologous recombination-deficient cells. *Proc. Natl. Acad. Sci.*, **108**, 3406–3411.
46. LoRusso,P.M., Li,J., Burger,A., Heilbrun,L.K., Sausville,E.A., Boerner,S.A., Smith,D., Pilat,M.J., Zhang,J., Tolaney,S.M. *et al.* (2016) Phase I safety, pharmacokinetic, and pharmacodynamic study of the Poly(ADP-ribose) polymerase (PARP) inhibitor veliparib (ABT-888) in combination with irinotecan in patients with advanced solid tumors. *Clin. Cancer Res.*, **22**, 3227–3237.
47. Wahner Hendrickson,A.E., Menefee,M.E., Hartmann,L.C., Long,H.J., Northfelt,D.W., Reid,J.M., Boakye-Agyeman,F., Kayode,O., Flatten,K.S., Harrell,M.I. *et al.* (2018) A phase I clinical trial of the Poly(ADP-ribose) polymerase inhibitor veliparib and weekly topotecan in patients with solid tumors. *Clin. Cancer Res.*, **24**, 744–752.
48. Cistulli,C., Lavrik,O.I., Prasad,R., Hou,E. and Wilson,S.H. (2004) AP endonuclease and poly(ADP-ribose) polymerase-1 interact with the same base excision repair intermediate. *DNA Repair (Amst.)*, **3**, 581–591.
49. Horton,J.K. and Wilson,S.H. (2013) Strategic combination of DNA-damaging agent and PARP inhibitor results in enhanced cytotoxicity. *Front. Oncol.*, **3**, 257–257.
50. Bowman,K.J., Newell,D.R., Calvert,A.H. and Curtin,N.J. (2001) Differential effects of the poly (ADP-ribose) polymerase (PARP) inhibitor NU1025 on topoisomerase I and II inhibitor cytotoxicity in L1210 cells in vitro. *Br. J. Cancer*, **84**, 106–112.



Research paper

Development of a metabolically stable topoisomerase I poison as anticancer agent

Biswajit Kundu ^{a, 1}, Dipayan Sarkar ^{a, c, 1}, Srijita Paul Chowdhuri ^{b, 1}, Sourav Pal ^{a, c}, Subhendu K. Das ^b, Benu Brata Das ^{b, **}, Arindam Talukdar ^{a, c, *}

^a Department of Organic and Medicinal Chemistry, CSIR-Indian Institute of Chemical Biology, 4 Raja S. C. Mullick Road, Kolkata, 700032, WB, India

^b Laboratory of Molecular Biology, School of Biological Sciences, Indian Association for the Cultivation of Science, 2A & 2B, Raja S. C. Mullick Road, Kolkata, 700032, WB, India

^c Academy of Scientific and Innovative Research, Ghaziabad, 201002, India

ARTICLE INFO

Article history:

Received 21 January 2020

Received in revised form

14 May 2020

Accepted 4 June 2020

Available online 2 July 2020

Keywords:

Topoisomerase 1

Camptothecin

Poison

Metabolic stability

In vitro pharmacokinetics

Molecular dynamics

ABSTRACT

We have recently reported a new chemotype of a potent topoisomerase I poison with compound **1** as a potential anticancer chemotherapeutic agent. During further optimization, it has been observed that compound **1** suffers from high intrinsic clearance in human liver microsomes. To overcome the metabolic instability of compound **1**, we report design and synthesis of metabolically stable Top1 poison **3**. Newly identified Top1 poison **3** exhibits $t_{1/2}$ of 69.1 min in human liver microsomes in comparison to compound **1** with $t_{1/2}$ of 9.9 min. Molecular dynamic study of the newly optimized Top1 poison **3** was performed to get the insight into the stability of the binding pose in the active site. Compound **3** was able to trap DNA-Top1 cleavage complex and found to be less cytotoxic in non-cancerous cell line as compared to compound **1**.

© 2020 Elsevier Masson SAS. All rights reserved.

1. Introduction

Topoisomerases are ubiquitous enzymes that participate in the overwinding or underwinding of DNA and resolve the topological problems arising during DNA replication and transcription [1–3]. Human topoisomerase I (HTop1) relieves the torsional strain due to DNA supercoiling by nicking one of the strands of double helical DNA followed by relaxation through controlled rotation around the unbroken strand and finally religation of DNA and release of the enzyme. Topoisomerase 1 (Top1) is expressed much higher than the normal cells in various tumor cells, hence, modulating the Top1 levels in tumor cells to block DNA replication and cell division has been validated drug target for anticancer therapy. Camptothecin (CPT) was the first compound found in systematic screening of

natural products to exhibit inhibitory activity against Top1. CPT and its clinically approved derivatives, topotecan and irinotecan are Top1 inhibitors that stabilize Top1–DNA cleavage complex resulting in a ternary complex of Top1–DNA–ligand (Top1cc) [4]. Prevention of DNA religation results in DNA damage and subsequent apoptosis of cancer cell. However, CPT and its derivatives suffer from severe limitations such as dose-limiting toxicity, poor pharmacokinetic properties resulting from lactone hydrolysis affecting the bioavailability. Therefore, there was a need to find metabolically stable CPT analogs as well as non-CPT analogs which can overcome the drawbacks of camptothecin [5]. Camptothecin derivatives such as homocamptothecin [6], α -hydroxyketocamptothecin [7] and fluorocamptothecin [8] and indenoisoquinoline [9–11] class of compounds showed promising Top1 inhibitory activity with improved metabolic stability.

Metabolic instability of lactone has markedly decreased the efficacy of biologically active natural products. Replacement of lactone moiety with α -fluoroether, a novel bioisostere of lactone provides significant increase in metabolic stability. The utility of the α -fluoroether/lactone substitution was authenticated by the discovery of (20S, 21S)-21-fluorocamptothecin derivatives as stable

* Corresponding author. Department of Organic and Medicinal Chemistry, CSIR-Indian Institute of Chemical Biology, 4 Raja S. C. Mullick Road, Kolkata, 700032, WB, India.

** Corresponding author.

E-mail addresses: pcbdb@iacs.res.in (B.B. Das), atalukdar@iicb.res.in (A. Talukdar).

¹ Authors contributed equally.

Top1 inhibitors. One such example is compound **2** (Fig. 1), a highly potent CPT derivative which was found to exhibit excellent in vitro and in vivo antitumor activities [8].

In our previous study we have reported a new class of Top1 poison having quinoline moiety as the core [12]. We have depicted that our most potent compound **1** (IC_{50} 29 nM) possesses high plasma stability and suitable log D value required for oral absorption. We established better efficacy of compound **1** based on γ H2AX assay which showed that compound **1** generates less reversible DNA double strand breaks (DSBs) compared to CPT. With an objective to progress with compound **1** further, we have checked the metabolic stability of the same in human liver microsomes. The result shows that compound **1** has high intrinsic clearance (CL_{int}) in human liver microsomes. Cytochrome P450 (CYP) enzymes which are present in human liver microsomes are major contributors to phase I drug metabolism [13–17]. The present work comprises of strategic development and synthesis of metabolically stable Top1 poison (compound **3**), evaluation of metabolic stability of compound **1** and **3** in human liver microsomes, determination of in vitro pharmacokinetics, ability of compound **3** to be Top1 poison by forming stable Top1–DNA–compound **3** ternary complex and molecular dynamic simulations of compound **3** in the active site (Fig. 2).

2. Chemistry

Compound **4** and 1-(3-aminopropyl)pyrrole and 1-(3-aminopropyl)pyrrolidine was dissolved 1,4-dioxane and in the presence of a base [N,N-diisopropylethylamine (DIPEA)] was heated at 60 °C for 12 h to afford compound **5** and **6** respectively. Sequentially, compound **5** and **6** were first converted to carbohydrazide derivatives **7** and **8** and thereafter on heating with triethyl orthoformate provided compound **9** and **10** respectively. Suzuki coupling reaction of compound **9** and **10** with 4-[4,4,5,5-tetramethyl-1,3,2-dioxaborolan-2-yl]anisole provided compound **11** and **12** respectively (Scheme 1).

Similarly, compound **4** was stirred with 1-(3-aminopropyl)imidazole in the presence of a base [N,N-diisopropylethylamine

(DIPEA)] in 1,4-dioxane solvent at room temperature for 12 h to afford compound **13** in excellent yield. Compound **13** was converted to carbohydrazide derivative **14** which on heating with triethyl orthoformate afforded compound **15**. Finally, compound **15** was subjected to Suzuki reaction with various boronic acids to provide compound **1**, **3**, **16**, **17**, **18**, **19** and **20** (Scheme 2).

3. Results and discussion

During the lead optimization it was observed that compound **1** has a high intrinsic clearance ($CL_{int} = 69.70$ and $t_{1/2} = 9.94$ min) (Fig. 1) in human liver microsomes. In order to address the issue, the present study was designed to identify a metabolically stable analog through appropriate structural modification to decrease the intrinsic clearance with retention of human Top1 inhibitory activity. Metabolic stability of the potent Top1 poisons was evaluated using human liver microsomes and determined as intrinsic clearance (CL_{int}). The previous structure-activity relationship (SAR) revealed the importance of appropriate substituents at C-4 and C-6 position of quinoline ring [12]. In particular, suitable substituents at C-6 position containing 4'-substituted phenyl group and flexible amino chain at the C-4 position showed drastic effect on human Top1 inhibitory activity. We have observed that at the C-4 position, the alkyl amino chain containing imidazole and morpholine group at the terminal position can enhance the Top1 inhibition. To determine the effect of heterocycle ring attached to alkyl chain, further we have synthesized compound **11** and **12** which did not show promising Top1 inhibition at 10 μ M. In compound **11**, imidazole ring was replaced with pyrrole group lacking terminal N atom which was predicted to interact with Asn352 through hydrogen bond in our hypothetical model [12].

In compound **12** we have substituted the imidazole ring with a saturated pyrrolidine ring but was found to have no significant Top1 inhibitory activity at 10 μ M. The results depict the significance of the terminal nitrogen atom of the imidazole ring at C-4 position. Thus, we believe that any structural modification at C-4 position to obtain metabolically stable analogs with retention of Top1 inhibitory

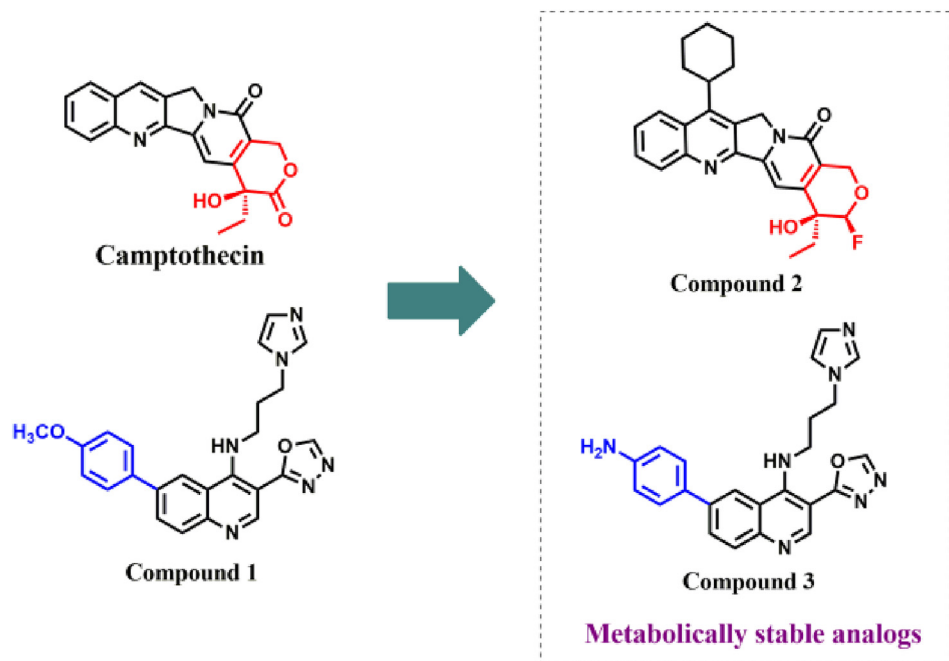


Fig. 1. Enhancing metabolic stability with proper replacement.

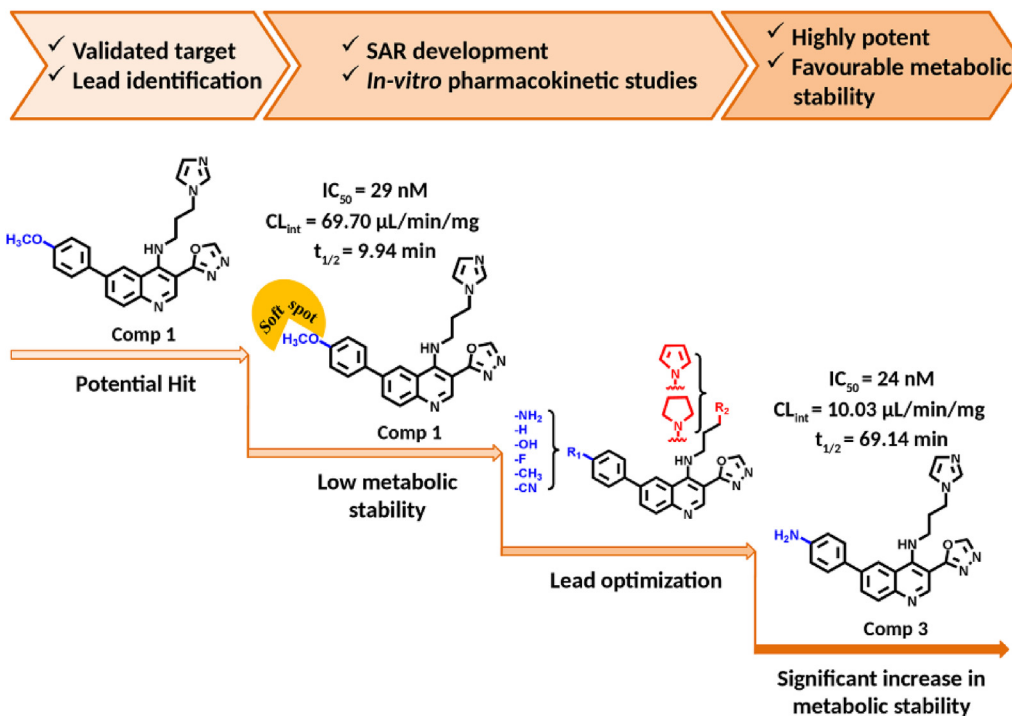
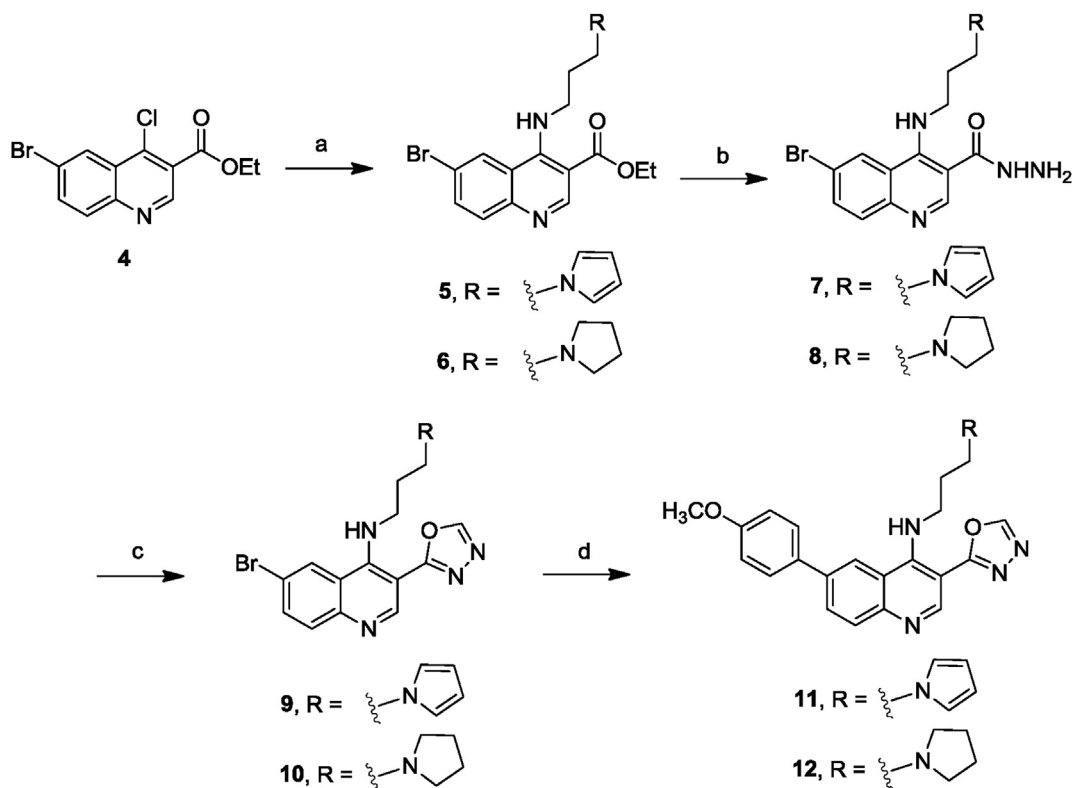


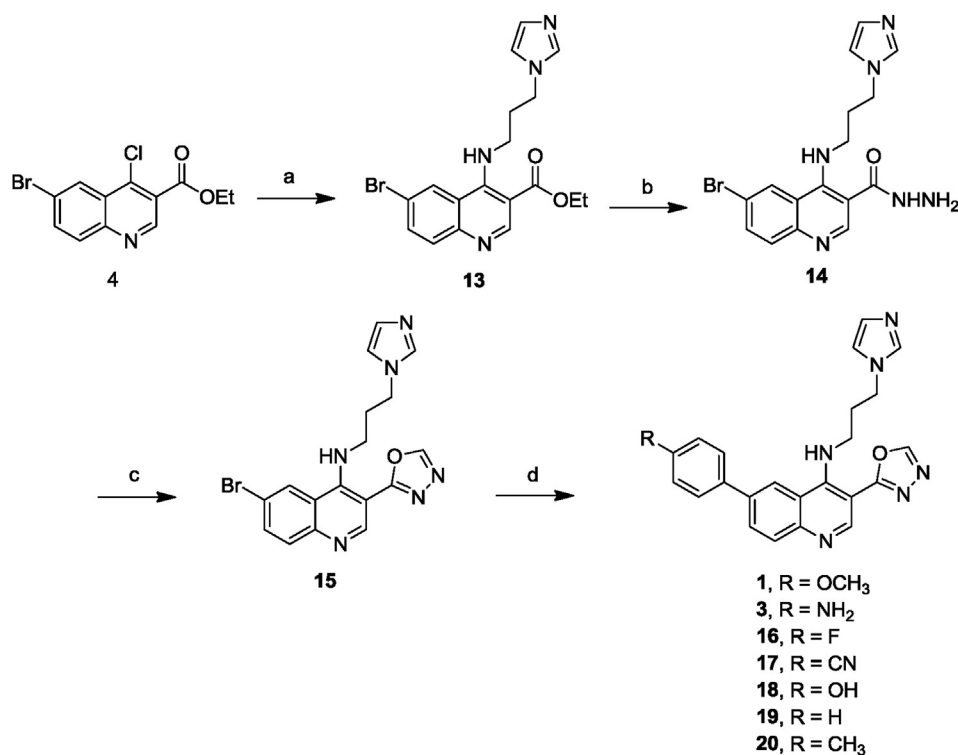
Fig. 2. Cascade development of metabolically stable analog.



Scheme 1. Reagents and conditions: (a) 1-(3-aminopropyl)pyrrole (for **5**) and 1-(3-aminopropyl)pyrrolidine (for **6**), DIPEA, 1,4-dioxane, 60 °C, 12 h; (b) Hydrazine monohydrate, EtOH, rt, 12 h; (c) Triethyl orthoformate, 110 °C, 12 h; (d) 4-[4,4,5,5-tetramethyl-1,3,2-dioxaborolan-2-yl]anisole, Pd(PPh₃)₂Cl₂, 2M Na₂CO₃, 1,4-dioxane, DMF, 100 °C, 12 h.

activity would be futile. As a logical step, we have focused our attention towards C-6 position of the quinoline ring and intended to strategically modify the aromatic ring. The methoxy group bonded to

benzene ring is known to undergo dealkylation reaction by liver CYP enzymes [18,19]. Thus, we envisioned that the 4'-OCH₃ of compound **1** is the metabolically sensitive position and the -OCH₃ group



Scheme 2. Reagents and conditions: (a) 1-(3-aminopropyl)imidazole, DIPEA, 1,4-dioxane, rt, 12 h; (b) Hydrazine monohydrate, EtOH, rt, 8 h; (c) Triethyl orthoformate, 100 °C, 12 h; (d) Various boronic acids, Pd(PPh₃)₄, 2M Na₂CO₃, 1,4-dioxane, DMF, 100 °C, 12 h.

can be converted to –OH group by human liver microsomes. Keeping this in mind we intended to replace the –OCH₃ group with bioisosteric groups.

During the development of more metabolically stable camptothecin analogs, it was observed that replacement of lactone with α -fluoro ether led to metabolically stable Top1 poison (Fig. 1) [8]. Unfortunately, in our study compound **16** with fluoro substitution resulted in marked decrease in the activity. Replacement with –CN group (compound **17**) at 4' position was unable to show any promising inhibitory activity. Interestingly, 4'–OH compound (**18**) did not exhibit any significant Top1 inhibition at 10 μ M. Expectedly, compound **19** without 4' substituent did not manifest significant Top1 inhibition at 10 μ M. Substituting –OCH₃ group with polar –NH₂ group in compound **3** resulted in similar Top1 inhibitory activity both with recombinant Top1 and MCF7 cell lysate (Table 1) [20,21]. Replacing the –OCH₃ group with –CH₃ in compound **20** provided IC₅₀ of 1.06 μ M against recombinant human Top1 (Table 1). However, in our metabolic study compound **20** also showed high intrinsic clearance similar to compound **1**. The high intrinsic clearance of compound **20** can be attributed to presence of α C–H bond next to an electron withdrawing phenyl ring where oxidation can take place resulting in –CH₂OH metabolite [22,23]. To explore the mechanism of Top1 inhibition, we have performed ex vivo plasmid DNA cleavage assay with compound **3**. Fig. 3A shows that compound **3** is capable of stabilizing Top1cc with a similar efficiency with compound **1** [12], implicating its Top1 poisoning potential. Further, the quantification of cleavage assay (Fig. 3B) suggests that at the indicated concentration formation of the Top1–DNA cleavage complex (% cleavage) with compound **3** is comparable to that by compound **1** (Fig. 3B). Compound **3** was also evaluated for its cytotoxicity in the cancerous human breast adenocarcinoma cell lines (MCF7) and the non-cancerous human embryonic kidney cell line (HEK293) (Fig. 4, Table 2). It is evident

from the Table 2 that compound **3** has a preferential cell killing activity in the cancerous cells (IC₅₀: 2.5 μ M) compared to the noncancerous cells HEK293 (IC₅₀: >10 μ M). Thereafter, compound **3** was strategically progressed through in vitro pharmacokinetics. The aqueous solubility, plasma stability and log D values were similar to that of our previously reported compound **1** (Table 3). To our satisfaction, the metabolic stability assay showed that compound **3** has low intrinsic clearance (CL_{int} = 10.03) compared to that of compound **1** (CL_{int} = 69.70, Table 4). As expected, half-life of compound **3** has drastically increased (t_{1/2} = 69.14 min) in comparison to compound **1** (t_{1/2} = 9.94 min, Table 4).

3.1. Cytotoxicity data

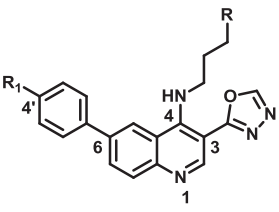
3.2. Molecular docking study

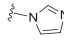
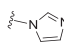
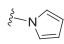
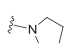
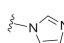
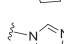
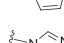
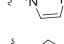
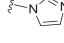
Crystal structure of HTop1–DNA–CPT (PDB ID: 1T81) was utilized for molecular docking study in order to understand Top1 inhibitory results of compound **3** [24]. The energy minimized structure of compound **3** was docked into the binding pocket with coordinates x = 21.386168, y = –2.148207, z = 28.116527 using LibDock in Discovery Studio 4.1 client. The docking analysis revealed that compound **3** can readily intercalates at the DNA cleavage site between the +1 and –1 base pairs. Subsequently, the entire complex was minimized by executing 2000 steps maintaining the root-mean-square gradient of 0.01 kcal mol^{–1} (Fig. 5) [12,25].

3.3. Molecular dynamic study of compound 3 in the active site

In our docking experiment we observed that compound **3** attains similar hydrogen bonding as well as π – π hydrophobic interactions similar to that of compound **1** (Fig. 5). In the hypothetical model, compound **3** was found to interact with Arg364, Asn722, and Asn352 through hydrogen bond formation along with π – π

Table 1
Human Top1 Inhibitory Activities in Plasmid DNA Relaxation Assays with Recombinant Top1 (In vitro) or MCF7 Cell Lysates (Ex vivo) [12].



Comp	R	R ₁	Top1 inhibition IC ₅₀ (μM)		Activity index ^a
			In vitro	Ex vivo	
CPT			0.025	2.5	+++
Topotecan			0.021	1.8	+++
1		-OCH ₃	0.029 ± 0.004	2.74 ± 0.314	+++
3		-NH ₂	0.024 ± 0.002	2.50 ± 0.12	+++
11		-OCH ₃	>10	NT	+
12		-OCH ₃	>10	NT	+
16		-F	>10	NT	+
17		-CN	>10	NT	+
18		-OH	>10	NT	+
19		-H	>10	NT ^b	+
20		-CH ₃	1.06 ± 0.417	3.75 ± 0.102	++

^a Compound-induced in vitro inhibition of Top1 with scores given as follows: + = IC₅₀ > 10 μM; ++ = IC₅₀ in between 100 nM and 10 μM; +++ = IC₅₀ < 100 nM.

^b NT = Not tested.

hydrophobic interactions with DNA base pairs. In order to determine the quality of the binding of compound **3** at the Top1-DNA cleavage complex (Top1cc) to form ternary complex of Top1-DNA-**3**, compound **3** has been subjected to all atoms molecular dynamics simulation by GROMACS 5.1.5 in Intel(R) Xeon(R) CPU E5-2650 v4. RMSD (Fig. S1A), RMSF (Fig. S1B) and radius of gyration (R_g) (Fig. S1C) have been analyzed for the Top1 cleavage complex after the 10 ns all atoms MD simulation run. Expectedly, the deviations of the RMSD values of the Top1 cleavage complex were not significantly different compared to that of the actual Top1 native protein backbone deviations during the entire period of 10 ns MD simulations (Fig. S1A). Finally radius of gyration (R_g) for compound **3** was evaluated along with the protein-DNA complex. Fewer swirls have been observed on R_g graph when compound **3** interacts with Top1-DNA duplex model with respect to native duplex system. The result revealed that the binding pose of **3** retains similar conformation as that of the initial one throughout the 10 ns dynamic trajectories. Also, the binding pockets of the **3** after the dynamic runs remain same as before (Fig. 6). The docked conformation of compound **3** exhibits very little change after the 10 ns simulations with heavy atoms RMSD values of 1.083 Å. In the following picture (Fig. 6), the docked conformation (green color) is superimposed with the after simulation conformation (violet color).

4. Conclusion

The present study puts forth strategic modification at the

metabolically sensitive spot with different groups leading to compound **3** with -NH₂ substitution, which showed marked increase in the metabolic stability with retention of Top1 inhibitory activity with IC₅₀ value of 24 nM against recombinant human Top1. Compound **3** showed low intrinsic clearance in human liver microsomes with CL_{int} = 10.03 and t_{1/2} = 69.14 min. Top1 poison **3** depicted moderate aqueous solubility, high plasma stability and good lipophilicity for oral absorption. We further provided mechanistic evidence that compound **3** is a potent Top1 poison in ex vivo plasmid DNA cleavage assay. To our satisfaction, compound **3** was found to be less cytotoxic in non-cancerous cell line. Summarily, the data demonstrate compound **3** as a promising lead with improved metabolic stability compared to our reported Top1 poison (compound **1**) as well as CPT and could pave the way for the development of effective anticancer drugs.

5. Experimental section

All chemicals, reagents, and solvents were purchased from commercial sources and were used without further purification unless otherwise noted. General reagents and solvents for the synthesis of compounds were analytical grade (AR) and used as supplied. Air-sensitive reactions were carried out under dry nitrogen or argon atmosphere. Solvents were distilled before use and also dried using standard methods. Thin-layer chromatography was performed on silica gel plates (Merck Silica Gel 60, F254), and the spots were visualized under UV light (254 and 365 nm). ¹H NMR was recorded at 300 MHz (Bruker DPX), 400 MHz (Jeol), and 600 MHz (Bruker Avance) frequency, and ¹³C NMR spectra were recorded at 75 MHz (Bruker DPX), 100 MHz (Jeol), and 150 MHz (Bruker Avance) frequency in CDCl₃ or CD₃OD solvent using tetramethylsilane (TMS) as the internal standard. Compound purities were estimated by reversed phase C-18 HPLC, with UV detection at 254 nm. The major peak area of each tested compound was ≥95% of the combined total peak area. The synthesis, spectral analysis and purity check of compound **1**, **4**, and **13–20** have already been reported in our previous study [12].

5.1. Synthesis of N-(3-(1H-imidazol-1-yl)propyl)-6-(4-aminophenyl)-3-(1,3,4-oxadiazol-2-yl)quinolin-4-amine (3)

Compound **15** (0.08 g, 0.20 mmol) was taken along with 4-(4,4,5,5-tetramethyl-1,3,2-dioxaborolan-2-yl)aniline (0.088 g, 0.4 mmol) in 1,4-dioxane (4 mL) and DMF (1 mL). 2(M) Na₂CO₃ solution (0.5 mL) was added to the reaction mixture, and argon was purged for 15 min. Pd(PPh₃)₄ (0.018 g, 0.016 mmol) was added to the mixture, and argon purging was performed for 15 min. The mixture was heated for 12 h at 100 °C. Solvent was removed under vacuum, the residue was dissolved in CHCl₃, and the organic layer was washed with water and brine, dried, and concentrated. The residue was purified by silica gel column chromatography, eluting with 5% methanol in CHCl₃ to produce compound **3** (0.03 g, 36%) as a brown solid. mp 202 °C. ¹H NMR (600 MHz, CD₃OD): δ 8.97 (s, 1H), 8.67 (s, 1H), 8.11 (s, 1H), 7.81 (d, J = 8.4 Hz, 1H), 7.72 (d, J = 8.4 Hz, 1H), 7.61 (s, 1H), 7.34 (d, J = 8.4 Hz, 2H), 7.10 (s, 1H), 6.93 (s, 1H), 6.80 (d, J = 7.8 Hz, 2H), 4.17 (t, J = 7.2 Hz, 2H), 3.75 (t, J = 6.6 Hz, 2H), 2.25–2.21 (m, 2H). ¹³C NMR (150 MHz, CD₃OD): δ 163.6, 152.3, 152.0, 148.0, 147.7, 146.9, 138.0, 137.0, 129.7, 128.7, 128.4, 127.9, 127.5, 121.2, 119.2, 119.0, 115.4, 98.3, 45.6, 43.9, 31.7. MS (ESI) m/z [M+H]⁺ 412.33. HRMS (ESI) m/z [M+H]⁺ calculated for C₂₃H₂₁N₇O 412.1886; found 412.1884. HPLC purity 97.37%.

5.2. Synthesis of ethyl 4-((3-(1H-pyrrol-1-yl)propyl)amino)-6-bromoquinoline-3-carboxylate (5)

Compound **4** (1 g, 3.18 mmol) was dissolved in 1,4-dioxane

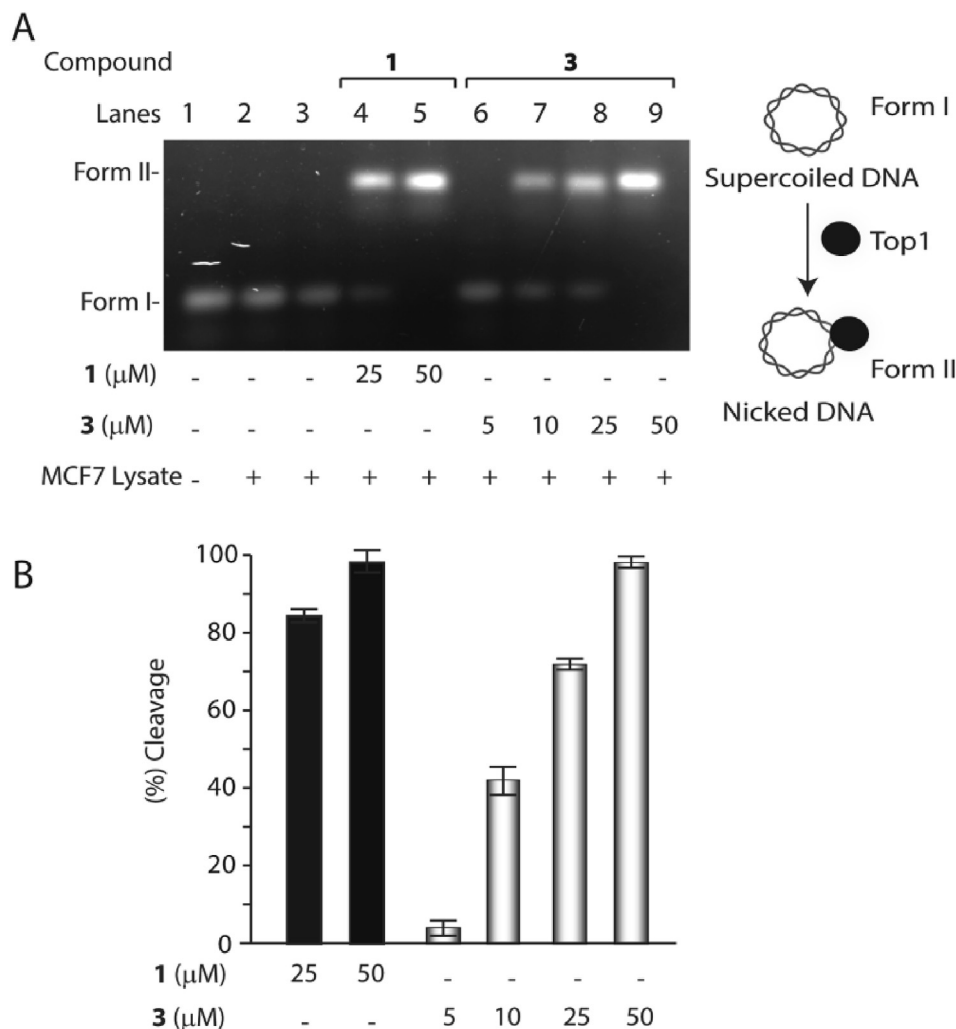


Fig. 3. Compound **3**-mediated ex vivo trapping of Top1-DNA cleavage complexes: (A) Representative gel image showing plasmid DNA cleavage by Top1 from the MCF7 lysate in the presence of compound **1** or **3**. Lane 1, 0.2 μg of pBS (SK+) supercoiled DNA. Lanes 2–9, same as lane 1 but incubated with equal amounts of MCF7 lysate (0.3 μg) at the indicated concentrations of compound **1** or **3** or only DMSO (lane 3) at 37 $^{\circ}\text{C}$ for 30 min. Positions of the supercoiled substrate (form I) and nicked monomers (form II) are indicated. (B) Quantitative measurement (% cleavage) of cleavage complex (Top1cc) formation by compound **1** and **3** by supercoiled plasmid DNA.

(5 mL) under N_2 atmosphere. To the reaction mixture dry DIPEA (1.3 mL, 7.98 mmol) and 3-(1H-pyrrol-1-yl)propan-1-amine (0.793 g, 6.39 mmol) were added respectively. The reaction mixture was allowed to stir for 12 h at 60 $^{\circ}\text{C}$. The reaction mixture was cooled to room temperature and extracted with ethyl acetate. The crude mass obtained was purified by column chromatography by 50% ethyl acetate in pet ether to give compound **5** (0.25 g, 20%) as a white solid. mp 106 $^{\circ}\text{C}$. ^1H NMR (400 MHz, CDCl_3): δ 9.39 (br. s, -NH), 9.08 (s, 1H), 8.24 (d, $J = 2$ Hz, 1H), 7.83 (d, $J = 9.2$ Hz, 1H), 7.70 (dd, $J = 8.8$ Hz, 2 Hz, 1H), 6.60 (t, $J = 2$ Hz, 2H), 6.11 (t, $J = 2$ Hz, 2H), 4.38 (q, $J = 7.2$ Hz, 2H), 4.06 (t, $J = 6.8$ Hz, 2H), 3.71 (q, $J = 5.2$ Hz, 2H), 2.24–2.18 (m, 2H), 1.41 (t, $J = 7.2$ Hz, 3H). ^{13}C NMR (100 MHz, CDCl_3): δ 168.8, 156.1, 151.5, 149.3, 134.6, 131.1, 128.3, 120.6, 117.8, 108.7, 103.5, 61.2, 46.4, 45.7, 32.8, 14.4. MS (ESI) m/z $[\text{M}+\text{H}]^+$ 402.10.

5.3. Synthesis of ethyl 6-bromo-4-((3-(pyrrolidin-1-yl)propyl)amino)quinoline-3-carboxylate (**6**)

Compound **4** (1 g, 3.19 mmol) was dissolved in 1,4-dioxane (5 mL) under N_2 atmosphere. To the reaction mixture dry DIPEA (1.3 mL, 7.98 mmol) and 3-(pyrrolidin-1-yl)propan-1-amine (0.818 g, 6.39 mmol) were added respectively. The reaction

mixture was allowed to stir for 12 h at 60 $^{\circ}\text{C}$. The reaction mixture was cooled to room temperature and extracted with chloroform. The crude mass obtained was purified by column chromatography by 10% MeOH in CHCl_3 to give compound **6** (0.22 g, 17%) as a white solid. mp 110 $^{\circ}\text{C}$. ^1H NMR (400 MHz, CDCl_3): δ 9.24 (br. s, -NH), 9.02 (s, 1H), 8.31 (d, $J = 2$ Hz, 1H), 7.78 (d, $J = 8.8$ Hz, 1H), 7.70 (dd, $J = 8.8$ Hz, 2 Hz, 1H), 4.37 (q, $J = 7.2$ Hz, 2H), 3.8–3.76 (m, 2H), 2.67 (t, $J = 6.8$ Hz, 2H), 2.57 (t, $J = 7.2$ Hz, 4H), 2.0–1.94 (m, 2H), 1.84–1.81 (m, 4H), 1.40 (t, $J = 7.2$ Hz, 3H). ^{13}C NMR (100 MHz, CDCl_3): δ 168.6, 155.5, 152.1, 149.6, 134.2, 131.5, 127.9, 121.0, 117.5, 103.5, 60.3, 54.4, 54.0, 47.4, 29.9, 23.6, 14.4. MS (ESI) m/z $[\text{M}+\text{H}]^+$ 406.10.

5.4. Synthesis of 4-((3-(1H-pyrrol-1-yl)propyl)amino)-6-bromoquinoline-3-carbohydrazide (**7**)

Compound **5** (0.2 g, 0.498 mmol) was dissolved in ethanol (4 mL). To the solution hydrazine hydrate (4 mL) was added. The reaction mixture was stirred for 12 h at room temperature. Ethanol was removed under vacuum. The residue was then dissolved in CHCl_3 and the organic layer was washed with water and brine, dried and concentrated to give compound **7** (0.15 g, 78%) as a yellow solid. mp 242 $^{\circ}\text{C}$. ^1H NMR (400 MHz, $\text{CDCl}_3 + 1$ drop CD_3OD): δ 8.51

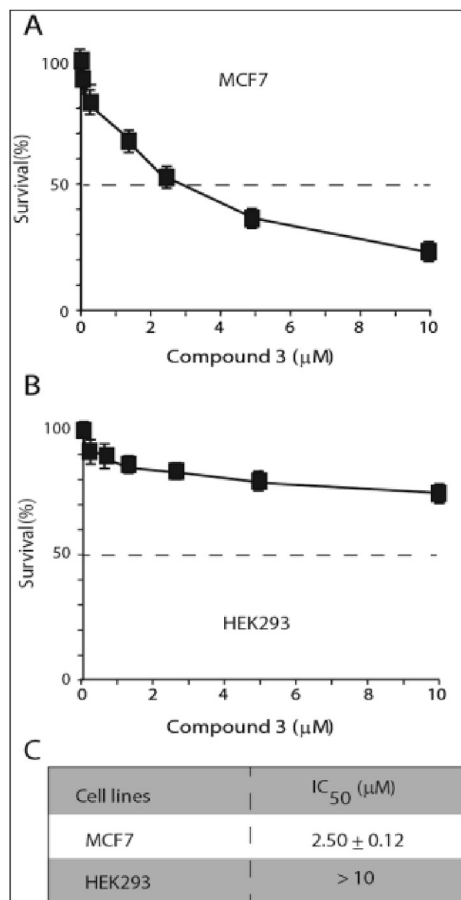


Fig. 4. Compound **3** exhibits cytotoxicity in different cell lines.

Table 2

Cytotoxicity data of compound **3** in MCF7 and HEK293 cell line in comparison to compound **1** and CPT.

Cell line	IC ₅₀ of CPT(μM)	IC ₅₀ of 1 (μM)	IC ₅₀ of 3 (μM)
MCF7	2.5 ± 0.36	2.74 ± 0.31	2.50 ± 0.12
HEK293	8.75 ± 0.63	8.34 ± 0.96	>10

Table 3

Aqueous solubility, plasma stability and Log D data of compound **1**, **3** and **20** at pH 7.4

Comp	Aq. Sol (μg/mL)	Plasma Stability ^a	LogD @ pH 7.40
CPT	2.5	15.70	1.74 ^b
1	30.09 ± 0.66	93.34	2.48 ± 0.04
3	30.19 ± 0.64	91.32	2.56 ± 0.03
20	0.3	90.80	>3.5

^a Mean % remaining at 2 h in human Plasma.

^b Log P value.

Table 4

Metabolic stability of compound **1**, **3** and **20**.

Comp	Half life (min)	% Rem @ 60 min	% Rem @ 60 min W/O Cofactor	CL _{int} protein (μL/min/mg protein)	CL _{int} in vivo (mL/min/kg BW)	CL in vivo (mL/min/kg BW)-Well stirred model	%QH (Well stirred model)	Classification
1	9.94	1.68	112.04	69.70	57.99	15.42	73.42	High clearance
3	69.14	53.67	93.75	10.03	8.35	5.97	28.44	Low clearance
20	7.77	0.00	92.99	89.35	—	63.74	70.83	High clearance

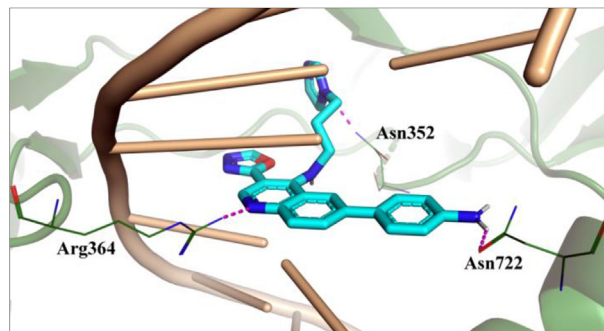


Fig. 5. Binding interactions of compound **3** in the active site of human Top1 protein-DNA duplex. Magenta dotted line indicates the hydrogen bonding interaction with the active residues. (For interpretation of the references to color in this figure legend, the reader is referred to the Web version of this article.)

(d, $J = 7.6$ Hz, 1H), 8.13 (s, 1H), 7.70–7.63 (m, 2H), 6.59 (t, $J = 2$ Hz, 2H), 6.08 (t, $J = 1.6$ Hz, 2H), 4.04 (t, $J = 6.4$ Hz, 2H), 3.59–3.54 (m, 2H), 2.19–2.13 (m, 2H). ¹³C NMR (100 MHz, CDCl₃ + 1 drop CD₃OD): δ 148.0, 134.2, 130.4, 127.5, 120.9, 120.6, 118.1, 108.7, 106.3, 46.6, 45.4, 32.5. MS (ESI) m/z [M+H]⁺ 388.10.

5.5. Synthesis of 6-bromo-4-((3-(pyrrolidin-1-yl)propyl)amino)quinoline-3-carbohydrazide (**8**)

Compound **6** (0.3 g, 0.958 mmol) was dissolved in ethanol (4 mL). To the solution hydrazine hydrate (4 mL) was added. The reaction mixture was stirred for 12 h at room temperature. Ethanol was removed under vacuum. The residue was then dissolved in CHCl₃ and the organic layer was washed with water and brine, dried and concentrated to give compound **8** (0.190 g, 66%) as a yellow solid. mp 254 °C. ¹H NMR (400 MHz, CDCl₃ + 1 drop CD₃OD): δ 8.70 (br. s, –NH), 8.39 (s, 1H), 7.93 (s, 1H), 7.83 (br. s, 1H), 7.74 (d, $J = 9.2$ Hz, 1H), 7.65 (dd, $J = 8.8$ Hz, 2 Hz, 1H), 4.10 (br. s, 2H), 3.49–3.45 (m, 2H), 2.74 (t, $J = 5.6$ Hz, 2H), 2.63 (t, $J = 6.4$ Hz, 4H), 1.99–1.95 (m, 4H), 1.87–1.81 (m, 2H). ¹³C NMR (100 MHz, CDCl₃ + 1 drop CD₃OD): δ 150.1, 147.6, 143.5, 133.4, 131.3, 126.3, 124.6, 121.26, 118.7, 109.5, 107.3, 54.7, 47.6, 26.9, 23.7. MS (ESI) m/z [M+H]⁺ 392.10.

5.6. Synthesis of N-(3-(1H-pyrrol-1-yl)propyl)-6-bromo-3-(1,3,4-oxadiazol-2-yl)quinolin-4-amine (**9**)

Compound **7** (0.19 g, 0.490 mmol) was taken in triethyl orthoformate (4 mL) and the mixture was heated for 12 h at 110 °C. Then the reaction mixture was allowed to come to room temperature. Excess hexane was added to the mixture. A precipitation formed which was filtered and purified by column chromatography, eluting with 1% methanol in CHCl₃ to give compound **9** (0.07 g, 39%) as a light yellow solid. mp 124 °C. ¹H NMR (600 MHz, CDCl₃): δ 9.08 (s, 1H), 8.29 (br. s, –NH), 8.50 (s, 1H), 8.35 (d, $J = 1.2$ Hz, 1H), 7.88 (d,

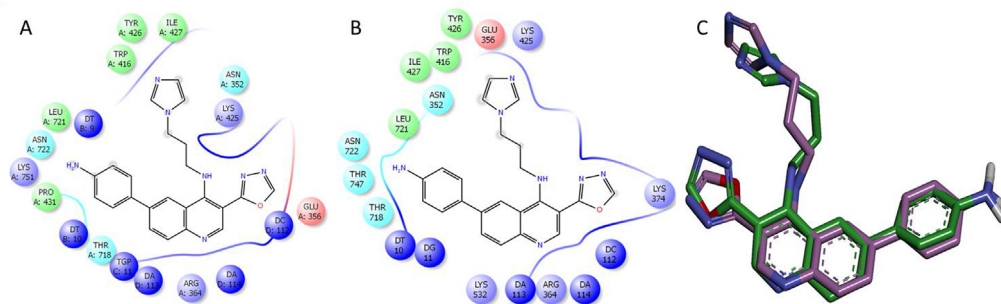


Fig. 6. Molecular dynamics simulation status of compound **3** after 10 ns dynamics runs. (A) and (B) 2D conformational pose of compound **3** at before and after MD simulation in the binding pocket. (C) Molecular overlay of conformation for compound **3** before (violet) and at the end (green) of the simulation run. (For interpretation of the references to color in this figure legend, the reader is referred to the Web version of this article.)

$J = 9$ Hz, 1H), 7.76 (dd, $J = 9$ Hz, 1.8 Hz, 1H), 6.63 (t, $J = 1.8$ Hz, 2H), 6.13 (t, $J = 1.8$ Hz, 2H), 4.14 (t, $J = 6.6$ Hz, 2H), 3.85 (q, $J = 4.8$ Hz, 2H), 2.34–2.30 (m, 2H). ^{13}C NMR (150 MHz, CDCl_3): δ 177.5, 166.2, 154.0, 153.5, 151.1, 150.7, 136.9, 133.6, 130.4, 123.0, 122.6, 120.8, 111.1, 101.5, 48.8, 48.4, 35.1, 23.3. MS (ESI) m/z $[\text{M}+\text{H}]^+$ 398.10.

5.7. Synthesis of 6-bromo-3-(1,3,4-oxadiazol-2-yl)-N-(3-pyrrolidin-1-yl)propylquinolin-4-amine (10)

Compound **8** (0.19 g, 0.485 mmol) was taken in triethyl orthoformate (3 mL) and the mixture was heated for 12 h at 110 °C. Then the reaction mixture was allowed to come to room temperature. Excess hexane was added to the mixture. A precipitation formed which was filtered and purified by column chromatography, eluting with 2% methanol in CHCl_3 to give compound **10** (0.06 g, 31%) as a light yellow solid. mp 128 °C. ^1H NMR (600 MHz, CDCl_3): δ 8.98 (s, 1H), 8.88 (br. s, -NH), 8.48 (s, 1H), 8.42 (d, $J = 1.2$ Hz, 1H), 7.84 (d, $J = 9$ Hz, 1H), 7.73 (dd, $J = 9$ Hz, 1.8 Hz, 1H), 3.88 (q, $J = 5.4$ Hz, 2H), 2.70 (t, $J = 6.6$ Hz, 2H), 2.58 (t, $J = 5.4$ Hz, 4H), 2.07–2.03 (m, 2H), 1.83–1.82 (m, 4H). ^{13}C NMR (150 MHz, CDCl_3): δ 166.3, 153.9, 153.6, 151.5, 136.5, 134.1, 130.1, 122.9, 120.58, 101.0, 56.8, 56.3, 49.8, 32.1, 25.9. MS (ESI) m/z $[\text{M}+\text{H}]^+$ 402.01.

5.8. Synthesis of N-(3-(1H-pyrrol-1-yl)propyl)-6-(4-methoxyphenyl)-3-(1,3,4-oxadiazol-2-yl)quinolin-4-amine (11)

Compound **9** (0.053 g, 0.133 mmol) was dissolved in 1,4-dioxane (2 mL) and DMF (0.5 mL) under Ar atmosphere. Then 4-[4,4,5,5-tetramethyl-1,3,2-dioxaborolan-2-yl]anisole (0.046 g, 0.200 mmol) was added to the mixture. 2(M) Na_2CO_3 solution (0.1 mL) was added to the reaction mixture and Ar was purged for 15 min. Then $\text{Pd}(\text{PPh}_3)_2\text{Cl}_2$ (0.009 g, 0.01 mmol) was added to the reaction mixture and Ar purging was performed for about 10 min. Then the mixture was heated for 12 h at 100 °C. Solvent was removed under vacuum, the residue then dissolved in CHCl_3 and the organic layer was washed with water and brine, dried and concentrated. The residue was purified by column chromatography, eluting with 80% ethyl acetate in pet ether to give compound **11** (0.021 g, 37%) as a brown solid. mp 222 °C. ^1H NMR (300 MHz, CDCl_3): δ 9.06 (s, 1H), 8.82 (br. s, -NH), 8.50 (s, 1H), 8.34 (s, 1H), 8.04 (d, $J = 8.4$ Hz, 1H), 7.92 (d, $J = 8.4$ Hz, 2H), 7.56 (d, $J = 8.1$ Hz, 2H), 7.04 (d, $J = 8.1$ Hz, 1H), 6.63 (s, 2H), 6.12 (s, 2H), 4.14 (t, $J = 6$ Hz, 2H), 3.97–3.93 (m, 2H), 3.89 (s, 3H), 2.37–2.29 (m, 2H). ^{13}C NMR (100 MHz, CDCl_3): δ 164.3, 159.6, 152.7, 151.0, 148.0, 137.3, 132.9, 130.4, 128.4, 123.1, 120.6, 114.6, 108.6, 55.5, 46.6, 46.4, 33.0. MS (ESI) m/z $[\text{M}+\text{H}]^+$ 426.02. HRMS (ESI) m/z $[\text{M}+\text{H}]^+$ calculated for $\text{C}_{25}\text{H}_{24}\text{N}_5\text{O}_2$ 426.1925; found 426.1931. HPLC purity 97.22%

5.9. Synthesis of 6-(4-methoxyphenyl)-3-(1,3,4-oxadiazol-2-yl)-N-(3-(pyrrolidin-1-yl)propyl)quinolin-4-amine (12)

Compound **10** (0.053 g, 0.132 mmol) was dissolved in 1,4-dioxane (2 mL) and DMF (0.5 mL) under Ar atmosphere. Then 4-[4,4,5,5-tetramethyl-1,3,2-dioxaborolan-2-yl]anisole (0.046 g, 0.198 mmol) was added to the mixture. 2(M) Na_2CO_3 solution (0.1 mL) was added to the reaction mixture and Ar was purged for 15 min. Then $\text{Pd}(\text{PPh}_3)_2\text{Cl}_2$ (0.009 g, 0.01 mmol) was added to the reaction mixture and Ar purging was performed for about 10 min. Then the mixture was heated for 12 h at 100 °C. Solvent was removed under vacuum, the residue then dissolved in CHCl_3 and the organic layer was washed with water and brine, dried and concentrated. The residue was purified by column chromatography, eluting with 5% MeOH in CHCl_3 to give compound **12** (0.021 g, 37%) as a brown solid. mp 220 °C. ^1H NMR (400 MHz, CDCl_3): δ 9.00 (s, 1H), 8.72 (br. s, -NH), 8.46 (s, 1H), 8.38 (d, $J = 2$ Hz, 1H), 8.00 (d, $J = 8.4$ Hz, 1H), 7.90 (dd, $J = 8.8$ Hz, 1.6 Hz, 1H), 7.59 (d, $J = 8.8$ Hz, 2H), 7.02 (d, $J = 8.4$ Hz, 2H), 4.05 (q, $J = 5.2$ Hz, 2H), 3.86 (s, 3H), 2.83 (t, $J = 7.6$ Hz, 2H), 2.73 (t, $J = 6.8$ Hz, 4H), 2.21–2.14 (m, 2H), 1.86–1.83 (m, 4H). ^{13}C NMR (CDCl_3 , 100 MHz): δ 164.3, 159.6, 152.7, 151.0, 149.6, 148.2, 137.4, 133.0, 130.5, 128.4, 123.1, 119.5, 114.6, 98.8, 55.5, 54.2, 53.6, 47.4, 23.5. MS (ESI) m/z $[\text{M}+\text{H}]^+$ 430.09. HRMS (ESI) m/z $[\text{M}+\text{H}]^+$ calculated for $\text{C}_{25}\text{H}_{28}\text{N}_5\text{O}_2$ 430.2238; found 430.2248. HPLC purity 95.44%.

5.10. Molecular docking study

HTop1–DNA–CPT crystal structure (PDB code 1T8I) was utilized for molecular docking study in order to understand Top1 inhibitory results of compound **3** [24]. The energy minimized structure of compound **3** was docked into the binding pocket ($x = 21.386168$, $y = -2.148207$, $z = 28.116527$) with LibDock in Discovery Studio 4.1 client. It is observed that Compound **3** intercalates at the DNA cleavage site readily, between the +1 and -1 base pairs. Subsequently, the entire complex was minimized by executing 2000 steps, which maintained the root-mean-square gradient of 0.01 kcal mol $^{-1}$ (Fig. 5) [12].

5.11. Molecular dynamics study

Molecular dynamics is an important theoretical approach from where we can get the molecular insight into the stability of the binding pose of the screened molecules in the active site. After performing the molecular docking, in order to understand the quality of the ligand binding towards the Top1-DNA cleavage complex (Top1cc), the selected most potent and metabolically stable compound **3** has been further processed by all atoms

molecular dynamics simulation by GROMACS 5.1.5 in Intel(R) Xeon(R) CPU E5-2650 v4. RMSD, RMSF and radius of gyration (R_g) have been analyzed for the Top1 cleavage complex after the 10 ns all atoms MD simulation run. A little fluctuation was observed on the backbone residues of the Top1cc by Root Means Square Fluctuations (RMSF) collected by over 10 ns trajectory run which was compared with Top1-DNA duplex model (Fig. 6, S1A, S1B, S1C) [25,26].

5.12. Recombinant human Top1 and plasmid DNA relaxation assay

The recombinant human Top1 was purified from Sf-9 insect cells which were infected with the recombinant baculovirus (a kind gift from Prof. James J. Champoux) as described previously [12,20]. The type 1 DNA topoisomerases are assayed by the decreased mobility of the relaxed isomers of supercoiled pBS (SK+) DNA in 1% agarose gel. The relaxation assay was carried out with either recombinant human Top1 or the whole cell extracts of MCF7 cells as a source of endogenous Top1, diluted in the relaxation buffer with supercoiled plasmid DNA as described previously [12,20].

5.13. MCF7 whole cellular lysate preparation

We have prepared MCF7 cell lysates as described previously [27]. Briefly 1×10^6 cells were lysed in lysis buffer containing 50 mM Tris-HCl (pH 8), 300 mM NaCl, 10 mM MgCl₂, 0.4% NP40, 5 mM dithiothreitol, supplemented with complete protease inhibitors (Roche Diagnostics, Indianapolis, IN) and phosphatase inhibitors (Phosphatase Inhibitor Cocktail 1 from Sigma). After thorough mixing and incubation at 4 °C for 1 h, lysates were cleared by centrifugation at 15,000 rpm for 10 min at 4 °C. Supernatants were collected, aliquoted, and stored at -80 °C. Lysates were quantified using BCA (Bicinchonic Acid) assay. MCF7 lysate (0.3 µg per well) was used as a source for Top1 activity.

5.14. Ex vivo plasmid DNA cleavage assay

We have performed ex vivo cleavage assays as described previously [12,20]. For the cleavage assay was 0.2 µg of supercoiled pBS (SK+) DNA, 0.3 µg of MCF whole cellular lysate were incubated in the presence and absence of compounds **1** or **3** or DMSO at the indicated concentrations at 37 °C for 30 min. The reactions were terminated by adding 1% SDS and 150 µg/mL proteinase K. After an additional 1 h incubation at 37 °C, DNA samples were electrophoresed in 1% agarose gel containing 0.5 µg/mL ethidium bromide. EtBr was added to the gel to resolve the more slowly migrating nicked product (Form II) from the supercoiled molecules (Form I).

5.15. Cell survival assay

Cell survival was assessed by the 3-(4,5-dimethylthiazol-2-yl)-2,5-diphenyltetrazolium bromide assay as discussed previously [27]. The percent inhibition of viability for each concentration of the compounds was calculated with respect to the control, and IC₅₀ values were estimated.

5.16. Metabolic stability assay

10 mM stock solution of test compound was prepared in DMSO and diluted with water: acetonitrile (1:1) to a concentration of 1 mM. Working concentration of 100 µM was prepared by further dilution with water: acetonitrile (1:1). Potassium phosphate buffer (pH 7.4) was prepared by adding 100 mL of Milli Q water to K₂HPO₄ (1.398 g) and KH₂PO₄ (0.27 g) to get final pH 7.4. 2.5 µL test compound, 75 µL liver microsomes at concentration of 3.33 mg/mL and

85 µL of 100 mM potassium phosphate buffer were mixed together and preincubated for 10 min at 37 °C to get preincubation mixture. The cofactor was prepared by mixing 32.5 µL of preincubation mixture and 17.5 µL of 100 mM potassium phosphate buffer and incubated for 60 min at 37 °C. The initial sample was prepared by mixing 16.25 µL of preincubation mixture, 200 µL of acetonitrile containing internal standard and 8.75 µL of cofactor. A mixture of 62 µL of cofactor (2.5 mM) and remaining preincubation mixture was incubated for 60 min at 37 °C to afford the final incubation mixture. Sample preparation was performed by mixing 25 µL incubation mixture in 200 µL of acetonitrile containing internal standard, vortexed for 5 min at 1200 rpm followed by centrifuging 10 min at 4000 rpm. Finally, supernatant was diluted 2 fold with water and injected on LC-MS/MS.

Author contributions

BK, DS, SPC equally contributed for this paper.

Declaration of competing interest

The authors declare that they have no known competing financial interests or personal relationships that could have appeared to influence the work reported in this paper.

Acknowledgments

The AT team would like to thank CSIR-IICB intramural research fund and DBT BT/Indo-Aus/10/22/2016 for funding. B.K. and S.P.C. thank UGC for their fellowship. D.S. would like to thank DST-INSPIRE for fellowship. S.P. would like to thank ICMR for SRF. S.K.D. thanks IACS for SRF. The B.B.D. team is supported by DST-SERB core research grant (EMR/2017/001652) and IACS intramural funding. B.B.D. is a Wellcome Trust/DBT India Alliance Intermedial fellow.

Appendix A. Supplementary data

Supplementary data to this article can be found online at <https://doi.org/10.1016/j.ejmech.2020.112551>.

Abbreviations

HTop1	human topoisomerase 1
CPT	camptothecin
Top1cc	topoisomerase 1–DNA cleavage complexes
IC ₅₀	the half maximal inhibitory concentration
CL _{int}	intrinsic clearance
pBS (SK+)	DNA pBlue script plasmid DNA
DIPEA	N,N-diisopropylethylamine.

References

- [1] G. Capranico, J. Marinello, G. Chillemi, Type I DNA topoisomerases, *J. Med. Chem.* 60 (2017) 2169–2192, <https://doi.org/10.1021/acs.jmedchem.6b00966>.
- [2] Y. Pommier, Drugging topoisomerases: lessons and challenges, *ACS Chem. Biol.* 8 (2013) 82–95, <https://doi.org/10.1021/cb300648v>.
- [3] Y. Pommier, Y. Sun, S.N. Huang, J.L. Nitiss, Roles of eukaryotic topoisomerases in transcription, replication and genomic stability, *Nat. Rev. Mol. Cell Biol.* 17 (2016) 703, <https://doi.org/10.1038/nrm.2016.111>.
- [4] Y. Pommier, Topoisomerase I inhibitors: camptothecins and beyond, *Nat. Rev. Canc.* 6 (2006) 789–802, <https://doi.org/10.1038/nrc1977>.
- [5] Y. Pommier, DNA topoisomerase I inhibitors: chemistry, biology, and interfacial inhibition, *Chem. Rev.* 109 (2009) 2894–2902, <https://doi.org/10.1021/cr900097c>.
- [6] O. Lavergne, L. Lesueur-Ginot, F. Pla Rodas, P.G. Kasprzyk, J. Pommier, D. Demarquay, G. Prévost, G. Ulibarri, A. Rolland, A.-M. Schiano-Liberatore, J. Harnett, D. Pons, J. Camara, D.C.H. Bigg, Homocamptothecins: synthesis and

- antitumor activity of novel E-ring-modified camptothecin analogues, *J. Med. Chem.* 41 (1998) 5410–5419, <https://doi.org/10.1021/jm980400l>.
- [7] P. Hautefaye, B. Cimetière, A. Pierré, S. Léonce, J. Hickman, W. Laine, C. Bailly, G. Lavielle, Synthesis and pharmacological evaluation of novel non-lactone analogues of camptothecin, *Bioorg. Med. Chem. Lett* 13 (2003) 2731–2735, [https://doi.org/10.1016/s0960-894x\(03\)00534-1](https://doi.org/10.1016/s0960-894x(03)00534-1).
- [8] Z. Miao, L. Zhu, G. Dong, C. Zhuang, Y. Wu, S. Wang, Z. Guo, Y. Liu, S. Wu, S. Zhu, K. Fang, J. Yao, J. Li, C. Sheng, W. Zhang, A new strategy to improve the metabolic stability of lactone: discovery of (20S,21S)-21-Fluorocamptothecins as novel, hydrolytically stable topoisomerase I inhibitors, *J. Med. Chem.* 56 (2013) 7902–7910, <https://doi.org/10.1021/jm400906z>.
- [9] D. Strumberg, Y. Pommier, K. Paull, M. Jayaraman, P. Nagafuji, M. Cushman, Synthesis of cytotoxic indenoisoquinoline topoisomerase I poisons, *J. Med. Chem.* 42 (1999) 446–457, <https://doi.org/10.1021/jm9803323>.
- [10] D.E. Beck, M. Abdelmalak, W. Lv, P.V.N. Reddy, G.S. Tender, E. O'Neill, K. Agama, C. Marchand, Y. Pommier, M. Cushman, Discovery of potent indenoisoquinoline topoisomerase I poisons lacking the 3-nitro toxicophore, *J. Med. Chem.* 58 (2015) 3997–4015, <https://doi.org/10.1021/acs.jmedchem.5b00303>.
- [11] M.S.A. Elsayed, Y. Su, P. Wang, T. Sethi, K. Agama, A. Ravji, C.E. Redon, E. Kiselev, K.A. Horzmann, J.L. Freeman, Y. Pommier, M. Cushman, Design and synthesis of chlorinated and fluorinated 7-azaindenoisoquinolines as potent cytotoxic anticancer agents that inhibit topoisomerase I, *J. Med. Chem.* 60 (2017) 5364–5376, <https://doi.org/10.1021/acs.jmedchem.6b01870>.
- [12] B. Kundu, S.K. Das, S. Paul Chowdhuri, S. Pal, D. Sarkar, A. Ghosh, A. Mukherjee, D. Bhattacharya, B.B. Das, A. Talukdar, Discovery and mechanistic study of tailor-made quinoline derivatives as topoisomerase I poison with potent anticancer activity, *J. Med. Chem.* 62 (2019) 3428–3446, <https://doi.org/10.1021/acs.jmedchem.8b01938>.
- [13] T.A. Baillie, Metabolism and toxicity of drugs. Two decades of progress in industrial drug metabolism, *Chem. Res. Toxicol.* 21 (2008) 129–137, <https://doi.org/10.1021/bx7002273>.
- [14] D.J. Edmonds, D.W. Kung, A.S. Kalgutkar, K.J. Filipi, D.C. Ebner, S. Cabral, A.C. Smith, G.E. Aspnes, S.K. Bhattacharya, K.A. Borzilleri, J.A. Brown, M.F. Calabrese, N.L. Caspers, E.C. Cokorinos, E.L. Conn, M.S. Dowling, H. Eng, B. Feng, D.P. Fernando, N.E. Genung, M. Herr, R.G. Kurumbail, S.Y. Lavergne, E.C.-Y. Lee, Q. Li, S. Mathialagan, R.A. Miller, J. Panteleev, J. Polivkova, F. Rajamohan, A.R. Reyes, C.T. Salatto, A. Shavnya, B.A. Thuma, M. Tu, J. Ward, J.M. Withka, J. Xiao, K.O. Cameron, Optimization of metabolic and renal clearance in a series of indole acid direct activators of 5'-adenosine monophosphate-activated protein kinase (AMPK), *J. Med. Chem.* 61 (2018) 2372–2383, <https://doi.org/10.1021/acs.jmedchem.7b01641>.
- [15] U.M. Zanger, M. Schwab, Cytochrome P450 enzymes in drug metabolism: regulation of gene expression, enzyme activities, and impact of genetic variation, *Pharmacol. Therapeut.* 138 (2013) 103–141, <https://doi.org/10.1016/j.pharmthera.2012.12.007>.
- [16] P. M, S. Nagini*, Cytochrome P450 structure, function and clinical significance: a review, *Curr. Drug Targets* 19 (2018) 38–54, <https://doi.org/10.2174/1389450118666170125144557>.
- [17] Z. Bibi, Role of cytochrome P450 in drug interactions, *Nutr. Metabol.* 5 (2008) 27, <https://doi.org/10.1186/1743-7075-5-27>.
- [18] M.B. El-Haj, B.M.S. Ahmed, A.M. Garawi, S.H. Ali, Linking aromatic hydroxy metabolic functionalization of drug molecules to structure and pharmacologic activity, *Molecules* 23 (2018), <https://doi.org/10.3390/molecules23092119>.
- [19] J. Oláh, A.J. Mulholland, J.N. Harvey, Understanding the determinants of selectivity in drug metabolism through modeling of dextromethorphan oxidation by cytochrome P450, *Proc. Natl. Acad. Sci. Unit. States Am.* 108 (2011), <https://doi.org/10.1073/pnas.1010194108>, 6050 LP – 6055.
- [20] S.K. Das, A. Ghosh, S. Paul Chowdhuri, N. Halder, I. Rehman, S. Sengupta, K.C. Sahoo, H. Rath, B.B. Das, Neutral porphyrin derivative exerts anticancer activity by targeting cellular topoisomerase I (Top1) and promotes apoptotic cell death without stabilizing top1-DNA cleavage complexes, *J. Med. Chem.* 61 (2018) 804–817, <https://doi.org/10.1021/acs.jmedchem.7b01297>.
- [21] P. Majumdar, C. Bathula, S.M. Basu, S.K. Das, R. Agarwal, S. Hati, A. Singh, S. Sen, B.B. Das, Design, synthesis and evaluation of thiohydantoin derivatives as potent topoisomerase I (Top1) inhibitors with anticancer activity, *Eur. J. Med. Chem.* 102 (2015) 540–551, <https://doi.org/10.1016/j.ejmech.2015.08.032>.
- [22] J.C. Dinh, R.E. Pearce, L. Van Haandel, A. Gaedigk, J.S. Leeder, Characterization of atomoxetine biotransformation and implications for development of PBPK models for dose individualization in children, *Drug Metabol. Dispos.* 44 (2016), <https://doi.org/10.1124/dmd.116.069518>, 1070 LP – 1079.
- [23] L. Reidy, B. Nolan, A.R. Ramos, H.C. Walls, B.W. Steele, Zolpidem urine excretion profiles and cross-reactivity with ELISA® kits in subjects using zolpidem or Ambien® CR as a prescription sleep aid, *J. Anal. Toxicol.* 35 (2011) 294–301, <https://doi.org/10.1093/anatox/35.5.294>.
- [24] B.L. Staker, M.D. Feese, M. Cushman, Y. Pommier, D. Zembower, L. Stewart, A.B. Burgin, Structures of three classes of anticancer agents bound to the human topoisomerase I–DNA covalent complex, *J. Med. Chem.* 48 (2005) 2336–2345, <https://doi.org/10.1021/jm049146p>.
- [25] S. Pal, V. Kumar, B. Kundu, D. Bhattacharya, N. Preethy, M.P. Reddy, A. Talukdar, Ligand-based pharmacophore modeling, virtual screening and molecular docking studies for discovery of potential topoisomerase I inhibitors, *Comput. Struct. Biotechnol. J.* 17 (2019) 291–310, <https://doi.org/10.1016/j.csbj.2019.02.006>.
- [26] U. Debnath, S. Verma, P. Singh, K. Rawat, S.K. Gupta, R.K. Tripathi, H.H. Siddiqui, S.B. Katti, Y.S. Prabhakar, Synthesis, biological evaluation and molecular modeling studies of new 2,3-diheteroaryl thiazolidin-4-ones as NNRTIs, *Chem. Biol. Drug Des.* 86 (2015) 1285–1291, <https://doi.org/10.1111/cbdd.12591>.
- [27] I. Rehman, S.M. Basu, S.K. Das, S. Bhattacharjee, A. Ghosh, Y. Pommier, B.B. Das, PRMT5-mediated arginine methylation of TDP1 for the repair of topoisomerase I covalent complexes, *Nucleic Acids Res.* 46 (2018) 5601–5617, <https://doi.org/10.1093/nar/gky291>.

MOLECULAR BIOLOGY

SCAN1-TDP1 trapping on mitochondrial DNA promotes mitochondrial dysfunction and mitophagy

Arijit Ghosh¹, Sangheeta Bhattacharjee¹, Srijita Paul Chowdhuri¹, Abhik Mallick², Ishita Rehman¹, Sudipta Basu³, Benu Brata Das^{1*}

A homozygous mutation of human tyrosyl-DNA phosphodiesterase 1 (TDP1) causes the neurodegenerative syndrome, spinocerebellar ataxia with axonal neuropathy (SCAN1). TDP1 hydrolyzes the phosphodiester bond between DNA 3'-end and a tyrosyl moiety within trapped topoisomerase I (Top1)-DNA covalent complexes (Top1cc). TDP1 is critical for mitochondrial DNA (mtDNA) repair; however, the role of mitochondria remains largely unknown for the etiology of SCAN1. We demonstrate that mitochondria in cells expressing SCAN1-TDP1 (TDP1^{H493R}) are selectively trapped on mtDNA in the regulatory non-coding region and promoter sequences. Trapped TDP1^{H493R}-mtDNA complexes were markedly increased in the presence of the Top1 poison (mito-SN38) when targeted selectively into mitochondria in nanoparticles. TDP1^{H493R}-trapping accumulates mtDNA damage and triggers Drp1-mediated mitochondrial fission, which blocks mitobiogenesis. TDP1^{H493R} prompts PTEN-induced kinase 1-dependent mitophagy to eliminate dysfunctional mitochondria. SCAN1-TDP1 in mitochondria creates a pathological state that allows neurons to turn on mitophagy to rescue fit mitochondria as a mechanism of survival.

INTRODUCTION

Spinocerebellar ataxia with axonal neuropathy (SCAN1) is an autosomal recessive neurodegenerative disorder that is linked with a homozygous point mutation (H493R) in human tyrosyl-DNA phosphodiesterase 1 (TDP1) (1). TDP1 is primarily involved in the repair of DNA strand breaks linked with abortive topoisomerase I (Top1) activity (2–8). Cells derived from patients with SCAN1 are hypersensitive to camptothecin that selectively traps Top1-DNA covalent complexes (Top1cc) (5, 9–12). Patients with SCAN1 develop progressive cerebellar ataxia and peripheral neuropathy, which becomes noticeable at late childhood (13 to 15 years), indicating a slow onset of neurodegeneration (1). However, three independently developed TDP1 knockout mouse models revealed no obvious behavioral phenotypes related to patients with SCAN1 (8, 13, 14). Nevertheless, in one of these mouse models, loss of TDP1 resulted in gradual age-related cerebellar atrophy (8). This suggests that the SCAN1 phenotype is a complex phenomenon and has a multifactorial mechanism that has not been elucidated.

TDP1 hydrolyzes the phosphodiester bond between the Top1-tyrosyl moiety and the DNA 3'-end that involves a two-step mechanism: The first nucleophilic attack is initiated by catalytic H263 on the phosphate bond linking the DNA and the tyrosyl-containing peptide. The C-terminal domain of TDP1 harboring H493 residue acts as a general acid and donates a proton to the apical tyrosine-containing peptide-leaving group. This results in the generation of a TDP1-DNA covalent intermediate (step 1). The H493 acts as a general base catalyst and activates a water molecule that subsequently hydrolyzes the phosphoenzyme intermediate (step 2) (3, 4). The SCAN1 point mutation (H493R) retains partial TDP1

activity and results in defective turnover owing to the formation of TDP1^{H493R}-DNA complexes (8, 10, 14); therefore, SCAN1 cells do not provide a true knockout model of TDP1 (14). The nuclear encoded TDP1 is transported to the mitochondria for mitochondrial DNA (mtDNA) repair (15–18), and the ability of TDP1 to resolve 3'-phosphotyrosyl linkages is not limited to the removal of nuclear Top1-DNA adducts (3–5) but is also required for the excision of mitochondrial Top1 (Top1mt)-DNA covalent complexes (Top1mtcc) that are exclusively formed in the mitochondria (18). TDP1 can also hydrolyze a broad spectrum of 3'-DNA blocking lesions that are formed during oxidative DNA damage (4, 9, 15, 19–22), including 3'-phosphoglycolate and 3'-deoxyribose phosphate ends (19, 21). Accordingly, TDP1-deficient cells are defective in repairing mtDNA damage associated with trapped Top1mtcc or 3'-DNA lesions related to oxidative damage and chain-terminating anticancer or antiviral nucleosides (15, 18, 23, 24). Post-translational modifications by phosphorylation, (ADP)-ribosylation, SUMOylation, arginine methylation, and ubiquitylation are common regulators for the recruitment, turnover, and modulation of enzymatic activity and stability of TDP1 (12, 25–29).

Vertebrate mtDNA constitutes approximately 5% of the total cellular DNA content where several thousand copies of mtDNA are distributed across hundreds of mitochondria as covalently closed circular DNA (16.5 kb) encoding critical components of the mitochondrial adenosine 5'-triphosphate (ATP) production machinery (30, 31). Mitochondrial network dynamics uses the process of fission or fusion as a complex physiological adaptation to coordinate the segregation or unification of two physically distinct mitochondria, which is essential for regulating mitochondrial morphology, biogenesis, and stress response mechanisms (32, 33). In the context of mtDNA copy number maintenance, the mitochondrial network undergoes fusion to complement the mtDNA lesion by transfer of nucleoids (34). In contrast, mitochondrial fission predominates under conditions of nonrepaired mtDNA lesions, which results in mitochondrial dysfunction (35, 36). To preserve mitochondrial homeostasis, increased mitochondrial fission ensues the degradation of dysfunctional

¹Laboratory of Molecular Biology, School of Biological Sciences, Indian Association for the Cultivation of Science, 2A & B, Raja S. C. Mullick Road, Jadavpur, Kolkata 700032, India. ²Department of Chemistry, Indian Institute of Science Education and Research (IISER) Pune, Dr. Homi Bhabha Road, Pashan, Pune, Maharashtra 411008, India. ³Discipline of Chemistry, Indian Institute of Technology (IIT) Gandhinagar, Palaj, Gandhinagar, Gujarat 382355, India.

*Corresponding author. Email: pcbbd@iacs.res.in

mitochondria by autophagy (lysosome-dependent degradation), specifically termed as mitophagy (32, 36–39).

Unlike chromosomal DNA, mtDNA is more vulnerable to oxidative DNA damage, as they are profoundly exposed to reactive oxygen species (ROS) generated from the electron transport chain (40–42). Moreover, the mitochondria are completely dependent on the nucleus for mtDNA repair and integrity (42). Marked elevation of mtDNA damage has been attributed to the progression of several neurodegenerative disorders, including Alzheimer's disease, Parkinson's disease, Huntington's disease, myopathies and diabetes, aging, and age-related disorders (30, 43). Thus, efficient repair of mtDNA in postmitotic cells like neurons is critical for normal brain functioning. However, the role of mitochondria in the pathoetiology of the SCAN1 phenotype has not been elucidated.

This study provides the first evidence for connecting mitochondrial dysfunction with etiology of SCAN1. We show that cells expressing SCAN1-TDP1 are trapped on the mtDNA, which is escalated in the presence of mitochondria-targeted Top1 poison (mito-SN38). We show that trapping TDP1^{H493R} on mtDNA increases the mitochondrial fission rate and abrogates mitobiogenesis. Last, we show that increased mitochondrial degradation may allow identification of dysfunctional daughter mitochondria expressing TDP1^{H493R} and their subsequent removal through mitophagy, which may serve as a mechanism to restore fit mitochondria for cell survival.

RESULTS

Mitochondria harboring SCAN1 mutant TDP1 (H493R) are hypersensitive to mitochondria-targeted Top1 poison

To investigate the role of SCAN1 mutant TDP1 in mitochondria, we stably complemented TDP1 knockout (TDP1^{-/-}) mouse embryonic fibroblasts (MEFs) with lentiviral constructs harboring FLAG-tagged human SCAN1 mutant TDP1^{H493R}. The presence of the exogenous FLAG-TDP1 variants in the mitochondria of TDP1^{-/-} MEFs (TDP1^{-/-/WT} or TDP1^{-/-/H493R}) was confirmed by cell fractionation and Western blotting, and the relative purity of the mitochondrial fraction was further assessed by analysis of mitochondrial cytochrome c oxidase (COX IV) protein (Fig. 1A), which is consistent with previous reports showing the import of exogenous TDP1 into the mitochondria (15–18).

The active metabolite of irinotecan (SN38) stabilizes Top1-cleavage complexes (Top1cc). Irinotecan is a widely used anticancer drug (44). We engineered mitochondrial targeting cationic nanoparticles containing irinotecan (mito-SN38) (45) to selectively trap Top1mt on the mtDNA (Top1mtcc). To test the intracellular delivery of mito-SN38 into the mitochondria, we performed live-cell confocal microscopy in cells treated with mito-SN38 (intrinsically green fluorescent) by costaining with the mitochondrion-specific dye MitoTracker red. Colocalization of mito-SN38 with MitoTracker red (Fig. 1B; see merged image) within 30 min of drug exposure confirmed the accumulation of the mito-SN38 nanoparticle exclusively inside the mitochondria. The correlation between the pixel intensities along a line in the two channels (Fig. 1B) substantiated the colocalization. We further validated the activity of mito-SN38 in the mitochondria by directly measuring *in vivo* trapping of Top1mtcc in isolated mitochondria using ICE (immunocomplex of enzyme) assays (Fig. 1, C and D) (46, 47). Under similar conditions, mito-SN38 failed to trap nuclear Top1 (fig. S1A).

Mitochondrial ICE assays detected covalently trapped Top1mt linked to mtDNA (Top1mtcc) without mito-SN38 in TDP1^{-/-} MEFs ($P < 0.01$; Fig. 1C), which was markedly increased (~7-fold) after mito-SN38 treatment. TDP1-proficient MEFs (TDP1^{+/+} or TDP1^{-/-/WT}) show reduced (~3-fold) Top1mtcc compared to TDP1-deficient cells, consistent with the role of TDP1 in excision of trapped Top1mtcc (Fig. 1D) in the mitochondria. Although TDP1^{-/-/H493R} MEFs partially rescued (~1.5-fold) mito-SN38-induced Top1mtcc compared to TDP1^{-/-} ($P < 0.01$; Fig. 1D), SCAN1-TDP1 was significantly defective in unhooking trapped Top1mtcc in the mitochondria compared to TDP1^{-/-/WT} or TDP1^{+/+} cells (Fig. 1D).

We further performed survival assays to test the impact of mito-SN38 (Fig. 1E). We noted a substantial increase in mito-SN38-induced cell death in TDP1^{-/-/H493R} MEFs compared to TDP1^{-/-} MEFs (Fig. 1E); however, this effect was not due to increased accumulation of Top1mtcc (Fig. 1D). Under similar conditions, TDP1^{-/-} MEFs complemented with wild-type human TDP1 (TDP1^{-/-/WT}) or TDP1^{+/+} MEFs rescued the mito-SN38-mediated hypersensitivity (Fig. 1D). Consistent with TDP1^{-/-/H493R} cells, the SCAN1 patient-derived lymphoblastoid cell lines (BAB1662), harboring TDP1 (H493R) mutation, were also hypersensitive to mito-SN38 compared to its wild-type counterpart (BAB1668) (Fig. 1F). Together, these results suggest that defective TDP1 activity is detrimental to the mitochondria challenged with a Top1 poison.

TDP1^{H493R} trapping accumulates mtDNA damage

Because SCAN1 patient-derived lymphoblastoid cells and TDP1^{-/-/H493R} MEFs are hypersensitive to mito-SN38 (Fig. 1, E and F), we tested whether the additional mito-SN38-mediated toxicity was due to trapping of TDP1^{H493R} in the isolated mitochondria using ICE assays. In the absence of mito-SN38, we detected a significant increase (~1.5- to 2-fold) in TDP1^{H493R}-mtDNA complexes ($P < 0.1$; Fig. 2A), which increased (~4- to 5-fold) after mito-SN38 treatment in TDP1^{-/-/H493R} MEFs compared to TDP1^{-/-} MEFs ($P < 0.001$; Fig. 2A). Similarly, we also detected mito-SN38-induced (~4- to 5-fold) increase in trapping of TDP1^{H493R} ($P < 0.001$; Fig. 2A, right) in human SCAN1 cells (BAB1662), confirming that defective SCAN1-TDP1 activity generates TDP1^{H493R}-mtDNA lesions.

To gain further insight into the sites on mtDNA where TDP1^{H493R} becomes trapped, we performed chromatin immunoprecipitation (ChIP) followed by mtDNA-specific quantitative polymerase chain reaction (qPCR) analysis (18, 48). TDP1 is primarily involved in hydrolysis of trapped Top1cc complexes (Fig. 2B); therefore, we tested the enrichment of TDP1^{H493R} in specific mtDNA segments associated with Top1mtcc binding sites (46). Figure 2B shows that specific trapping of TDP1^{H493R} corresponds to the nucleotide residues 15420, 15690, and 16060 as well as the heavy and light strand promoter (HSP/LSP) along the regulatory noncoding region of mtDNA (mtNCR). Under similar conditions, mito-SN38-induced TDP1^{H493R} enrichment within the coding sequences of the mtDNA was not detected (fig. S1B). Therefore, mito-SN38 recruits TDP1 at sites corresponding to Top1mtcc binding sites on mtDNA (46, 48), generating secondary TDP1-mtDNA cross-links in SCAN1 cells ($P < 0.001$; Fig. 2B).

We next tested whether TDP1^{H493R} trapping instigates mtDNA damage using long-range PCR, a well-established method to evaluate mtDNA damage (15). Top1ccs reverse within minutes after washing out the drug (44); we therefore analyzed the subsequent mtDNA repair by incubating the cells in drug-free medium for an additional 12 hours. Figure 2D shows that mitochondria harboring

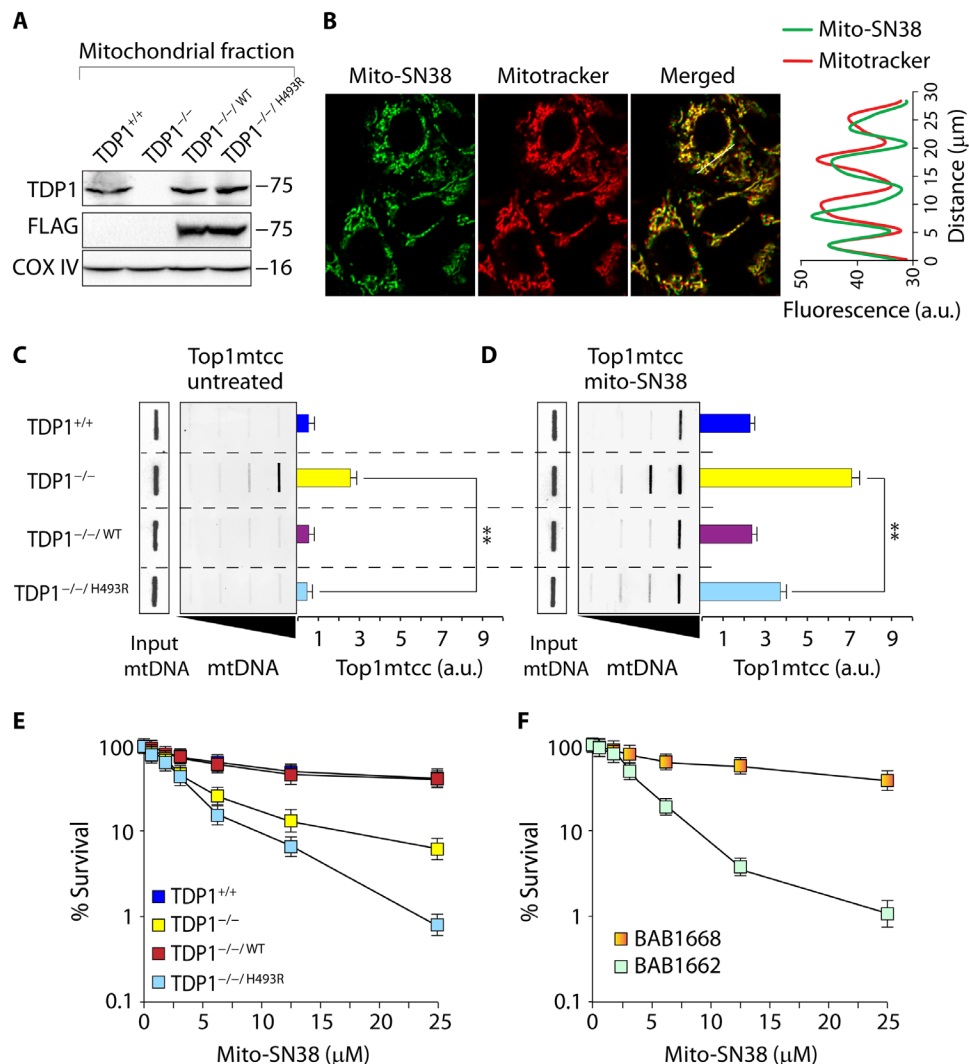


Fig. 1. Mito-SN38 containing nanoparticle poisons Top1mt (Top1mtcc). (A) Western blot analysis of mitochondrial lysates extracted from the indicated MEFs. TDP1^{-/-WT} and TDP1^{-/-H493R}; TDP1^{-/-} complemented with exogenous FLAG-tagged human wild-type or SCAN1 mutant (H493R) TDP1, respectively. Blots were probed with anti-TDP1, anti-FLAG, and anti-COX IV antibodies. COX IV served as a positive mitochondrial marker. (B) Representative confocal images showing accumulation of mitochondria-targeted cationic nanoparticle containing Top1 poison irinotecan (mito-SN38; intrinsic green fluorescence) inside the mitochondria (labeled with MitoTracker red). MEFs were incubated with mito-SN38 (5 μ M for 20 min), and the fluorescence patterns were recorded under live-cell microscopy. Colocalization is shown in the merged image. Quantitation of the pixel intensity of fluorescence along the indicated white line in the merged image (right). The white line was drawn arbitrarily along the region of interest (ROI). a.u., arbitrary units. (C and D) Poisoning of Top1mt (Top1mtcc) in the indicated MEFs expressing TDP1 variants; either untreated (C) or treated with mito-SN38 (5 μ M for 3 hours) (D). Top1mtcc was detected by ICE (immunocomplex of enzyme) bioassay. MtDNA at increasing concentrations (0.5, 1, 2, and 4 μ g) was immunoblotted with an anti-Top1mt-specific antibody. The mtDNA input was probed with anti-dsDNA (double-stranded DNA) antibody. Densitometry analysis of trapped Top1mtcc band intensity was quantified and expressed as fold increase relative to mtDNA input (error bars represent means \pm SEM). Asterisks denote statistically significant differences (** $P < 0.01$, t test). (E and F) Cell survival curves of indicated MEF variants (E) and a SCAN1 patient-derived lymphoblastoid cell line (BAB1662) and its wild-type counterpart (BAB1668) (F). Mito-SN38-induced cytotoxicity (%) was calculated with respect to the untreated control. Each point corresponds to the mean \pm SD of at least three experiments. Error bars represent SDs ($n = 3$).

defective TDP1 (H493R) display rapid depletion of mtDNA (~ 2 -fold) and were significantly deficient in recovery of mtDNA even after 12 hours of repair in drug-free medium (~ 4 -fold) compared to TDP1-deficient (TDP1^{-/-}) or TDP1-proficient MEFs (TDP1^{-/-WT} or TDP1^{+/+}) ($P < 0.001$; Fig. 2, D and E). Similarly, SCAN1 patient-derived lymphoblastoid cells show a marked depletion (~ 3 - to 4-fold) and impaired recovery of mtDNA (~ 6 - to 7-fold) even after 12 hours of culture in drug-free medium ($P < 0.001$; Fig. 2, D and E), suggesting that mito-SN38-induced hypersensitivity in

TDP1^{-/-H493R} cells is primarily attributed to toxic mtDNA lesions linked to TDP1^{H493R}.

Mitochondrial network harboring TDP1^{H493R} undergoes fission upon mito-SN38 treatment

Mitochondrial dynamics is critical in regulating morphology and function (32). Therefore, to investigate the role of TDP1^{H493R} on the dynamics of the mitochondrial network, i.e., the fission and fusion rates, we used a fluorescence recovery after photobleaching (FRAP)

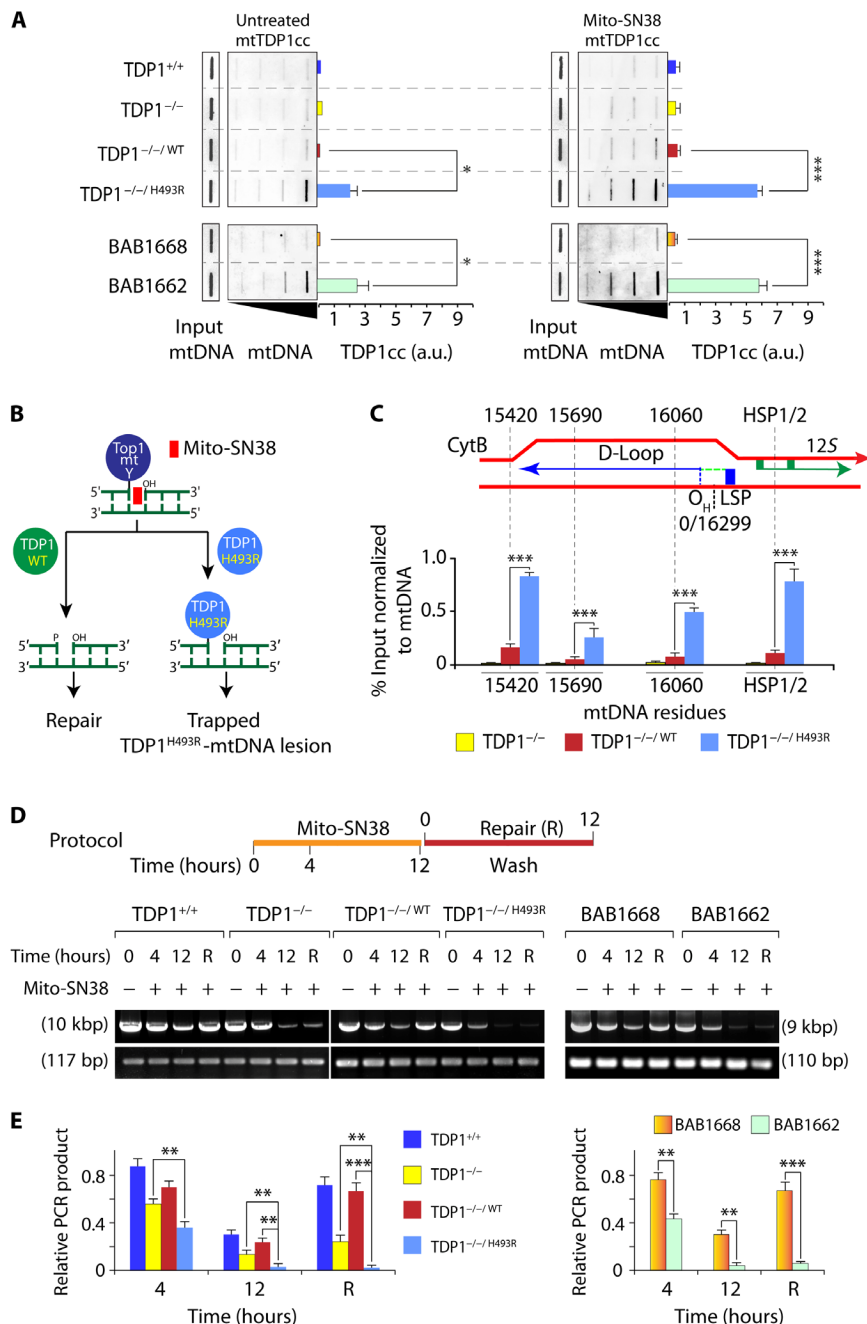


Fig. 2. Induction of irreversible mtDNA damage through selective trapping of TDP1^{H493R}. (A) Detection of trapped TDP1-mtDNA complexes (mtTDP1cc) by ICE bioassays in the indicated cells following no treatment or treated with mito-SN38 (5 μM for 3 hours). MtDNA at increasing concentrations (0.5, 1, 2, and 4 μg) was immunoblotted with an anti-TDP1-specific antibody. The mtDNA input was probed with anti-dsDNA antibody. Densitometry analysis of the trapped mtTDP1cc band intensity was quantified and expressed as fold increase relative to mtDNA input (error bars represent means ± SEM). Asterisks denote statistically significant difference (**P* < 0.1 and ****P* < 0.001, *t* test). (B) Catalytically defective SCAN1-TDP1 was hypothesized to be trapped at the Top1mtcc binding sites; this is shown schematically. (C) Detection of TDP1^{H493R} trapping sites on mtDNA by chromatin immunoprecipitation (ChIP) followed by mtDNA-specific quantitative polymerase chain reaction (qPCR) analysis. FLAG-TDP1-DNA adducts were immunoprecipitated with anti-FLAG antibody in the indicated cells after treatment with mito-SN38 treatment (5 μM for 3 hours), and the putative TDP1-binding site was quantified by qPCR. The mtDNA copy numbers of each cell line were concomitantly measured using primers for the ND2 (mitochondrial) and B2M (nuclear) genes. Enrichment of TDP1-bound mtDNA is expressed as percent input, which is then normalized to the mtDNA copy number of the cell line. Data represent means ± SE of independent experiments. Asterisks denote statistically significant differences (****P* < 0.001, *t* test). (D and E) Cells were treated with mito-SN38 for the indicated times. After mito-SN38 removal (R), cells were cultured in drug-free medium for 12 hours (top). Long-range qPCR was used to evaluate mtDNA damage. (D) Induction of mito-SN38-induced mtDNA damage in indicated cell types. Representative images are shown for mtDNA long- and short-fragment PCR after treatment (mito-SN38, 20 μM) and drug removal (R) for the indicated time. Mouse and human mtDNA-specific primers were used. (E) Quantification of mtDNA damage using the ratio of the long-fragment versus short-fragment PCR products. Data represent means ± SE of independent experiments. Asterisks denote statistically significant difference (***P* < 0.01 and ****P* < 0.001, *t* test). kbp, kilobase pair; bp, base pair.

technique to analyze the rate of redistribution of mitochondrial matrix-localized mito-YFP (yellow fluorescent protein), ectopically expressed in MEFs expressing TDP1 variants (49). In the absence of mito-SN38, mitochondrial FRAP recovery of TDP1-proficient (TDP1^{+/+} and TDP1^{-/-WT}) and TDP1^{-/-} MEFs was fast (65 to 75% in 60 s), indicating that, under steady-state conditions, there is a rapid and large-scale diffusion of mito-YFP due to the existence of a closely associated mitochondrial network (see Fig. 3A and the quantification in Fig. 3B). However, the mitochondrial fluorescence recovery of TDP1^{-/-H493R} MEFs was slower after 30 s of bleaching and only reached a maximum intensity of 55 to 60% in 60 s (Fig. 3B), suggesting a delay in mitochondrial fusion rate. Mito-SN38 pretreatment significantly blocked the mitochondrial FRAP recovery (~10 to 15% in 60 s) in TDP1^{-/-H493R} MEFs (Fig. 3, C and D) compared to TDP1^{-/-} MEFs. Under similar conditions, catalytically active TDP1 (TDP1^{+/+} or TDP1^{-/-WT}) rescued (~20 to 25%) the FRAP recovery (Fig. 3, C and D), suggesting the existence of a dispersed mitochondrial network due to increased mitochondrial fission in SCAN1-TDP1-expressing MEFs.

Further evidence for mitochondrial fragmentation in SCAN1-TDP1-harboring cells was seen by live-cell microscopy with the mitochondria-specific dye MitoTracker red. The average length of a mitochondrion was substantially shorter in TDP1^{-/-H493R} MEFs (~2.7 μ m), as compared with TDP1^{-/-WT} MEFs (~4.3 μ m) and TDP1^{-/-} MEFs (~3.4 μ m; Fig. 3, E and F; untreated). Mito-SN38 treatment markedly induced mitochondrial fragmentation in TDP1^{-/-H493R} MEFs (~1.2 μ m) compared to TDP1^{-/-} (1.7 μ m) or TDP1^{-/-WT} (2.8 μ m) MEFs (Fig. 3, E and F; treated) consistent with increased fission rates (Fig. 3, C and D).

To further validate the mitochondrial fragmentation in TDP1^{-/-H493R} MEFs, we directly measured the expression of the key proteins associated with mitochondrial fission and fusion like Drp1 (dynamitin-associated protein 1; mitochondrial fission protein) and Mfn1 (mitofusin 1; mitochondrial fusion protein) (32) in cells expressing TDP1 variants in the presence or absence of mito-SN38 (Fig. 3G). We detected a ~2-fold reduction in Mfn1 expression in TDP1^{-/-H493R} MEFs compared to TDP1^{-/-WT} MEFs after mito-SN38 treatment (Fig. 3E). In contrast, under similar conditions, the expression of Drp1 was enhanced ~2.5-fold in TDP1^{-/-H493R} MEFs compared to TDP1^{-/-WT} MEFs, confirming mitochondrial fragmentation (Fig. 3H), which is in agreement with an increased fission rate (Fig. 3, C and D). Similarly, we also detected a mito-SN38-induced increase (~2.5-fold) in Drp1 levels in human SCAN1 cells (BAB1662) compared to their wild-type counterpart (BAB1668) (Fig. 3F), confirming that TDP1^{H493R} trapping directs mitochondrial dynamics toward mitochondrial fission.

TDP1^{H493R}-mtDNA lesions impair mitochondrial biogenesis and OXPHOS function

We next tested the impact of TDP1^{H493R} trapping on the integrity of the mitochondrial membrane potential ($\Delta\psi$ m) in cells expressing TDP1 variants by tetramethylrhodamine methyl ester (TMRM) staining and flow cytometry analysis. Figure 4A shows that mito-SN38 treatment caused pronounced depolarization of $\Delta\psi$ m in TDP1^{-/-H493R} MEFs, which were rescued by complementation of wild-type human TDP1 (Fig. 4A). SCAN1 cells treated with mito-SN38 showed a marked reduction (~15-fold) in the mRNA expression of OXPHOS subunits encoded by mtDNA such as ND2, ND5, ND6, CytB, Cox1, Cox2, and ATP8 along the mitochondrial polycistronic heavy- and light-chain transcript (fig. S1C). We also detected a ~3- to 4-fold

depletion of mitochondrial respiratory complex V subunit (nuclear encoded) (fig. S1D) and (~4-fold) reduction in ATP content in SCAN1 cells (fig. S1E). Collectively these data indicate that irreversible mtDNA damage in TDP1^{-/-H493R} (Fig. 2D) impaired the assembly of mitochondrial respiratory chain complexes and maintenance of membrane potential (Fig. 4A).

Furthermore, we quantitatively measured mitochondrial mass by staining cells with MitoTracker green using flow cytometry (50). Figure 4B indicates a subtle reduction in the overall mitochondrial volume in TDP1^{-/-H493R} MEFs without treatment, while mito-SN38 treatment caused steady reduction in mitochondrial volume in TDP1^{-/-H493R} MEFs, which is in keeping with a marked increase of mitochondrial fission rate as obtained from FRAP experiment (Fig. 4B).

Mitobiogenesis is a coordinated process licensing increased production of nuclear and mitochondria-encoded proteins to increase mitochondrial function or to compensate for removal of the damaged mitochondria (32, 51). This prompted us to test the expression of nuclear genes in SCAN1 cells that are solely responsible for maintaining the mitochondrial homeostasis. We detected ~1.5-fold reduction in the mRNA and the protein levels of PGC1 α (peroxisome proliferator-activated receptor gamma coactivator 1- α), NRF1 (nuclear respiratory factor 1), and TFAM (mitochondrial transcription factor A) after mito-SN38 treatment for 6 hours ($P < 0.01$; Fig. 4, C and D). Prolonged treatment (mito-SN38, 12 hours) resulted in a ~5-fold reduction in protein levels for TFAM, NRF1, and PGC1 α in SCAN1 cells (Fig. 4D).

To investigate the mechanistic link between mitochondrial dysfunction and nuclear gene function essential for the mitochondrial biogenesis and OXPHOS, we tested ROS formation and accumulation of DNA damage in the nucleus by γ H2AX staining (52). TDP1^{-/-H493R} MEFs treated with mito-SN38 for 12 hours accumulate (~2.5-fold) increased ROS formation ($P < 0.01$; Fig. 4E and quantitation in Fig. 4F) and ~3-fold increase in nuclear γ H2AX compared to 6-hour treatment ($P < 0.001$; Fig. 4G and quantitation of γ H2AX foci in Fig. 4H). We further confirmed that pretreatment with ROS inhibitor *N*-acetyl-L-cysteine significantly blocked ROS formation ($P < 0.01$; Fig. 4, E and F) and nuclear DNA damage in TDP1^{-/-H493R} MEFs ($P < 0.01$; Fig. 4, G and H) after treatment with mito-SN38 for 12 hours. Collectively, we provide evidence that selective trapping of TDP1^{H493R} in the mitochondria triggers nuclear DNA damage as a bystander effect through ROS formation.

Mito-SN38 activates autophagy in SCAN1 cells

Accumulation of damaged mitochondria in cells expressing TDP1^{H493R} prompted us to test the mechanism of its removal through autophagy (38, 53, 54). We directly measured steady-state levels of autophagosomes by testing the level of endogenous microtubule-associated protein 1A/1B light chain 3B (LC3-II) lipidation using immunoblotting in cells expressing TDP1 variants after treatment with mito-SN38. Figure 5 (A and B) shows a marked increase (~2-fold) in LC3-II conversion after incubation with sublethal dosage of mito-SN38 in TDP1^{-/-H493R} MEFs compared to TDP1^{-/-WT} MEFs, which is consistent with human SCAN1 cells showing marked increase in LC3-II conversion compared to their wild-type counterpart after mito-SN38 treatment (Fig. 5, A and B).

To further confirm autophagy activation in cells harboring SCAN1-TDP1, we performed green fluorescent protein (GFP)-LC3 puncta formation assay by using live-cell confocal microscopy (53, 55). Bafilomycin A1 (Baf A1; an autophagy inhibitor) (56) alone increases

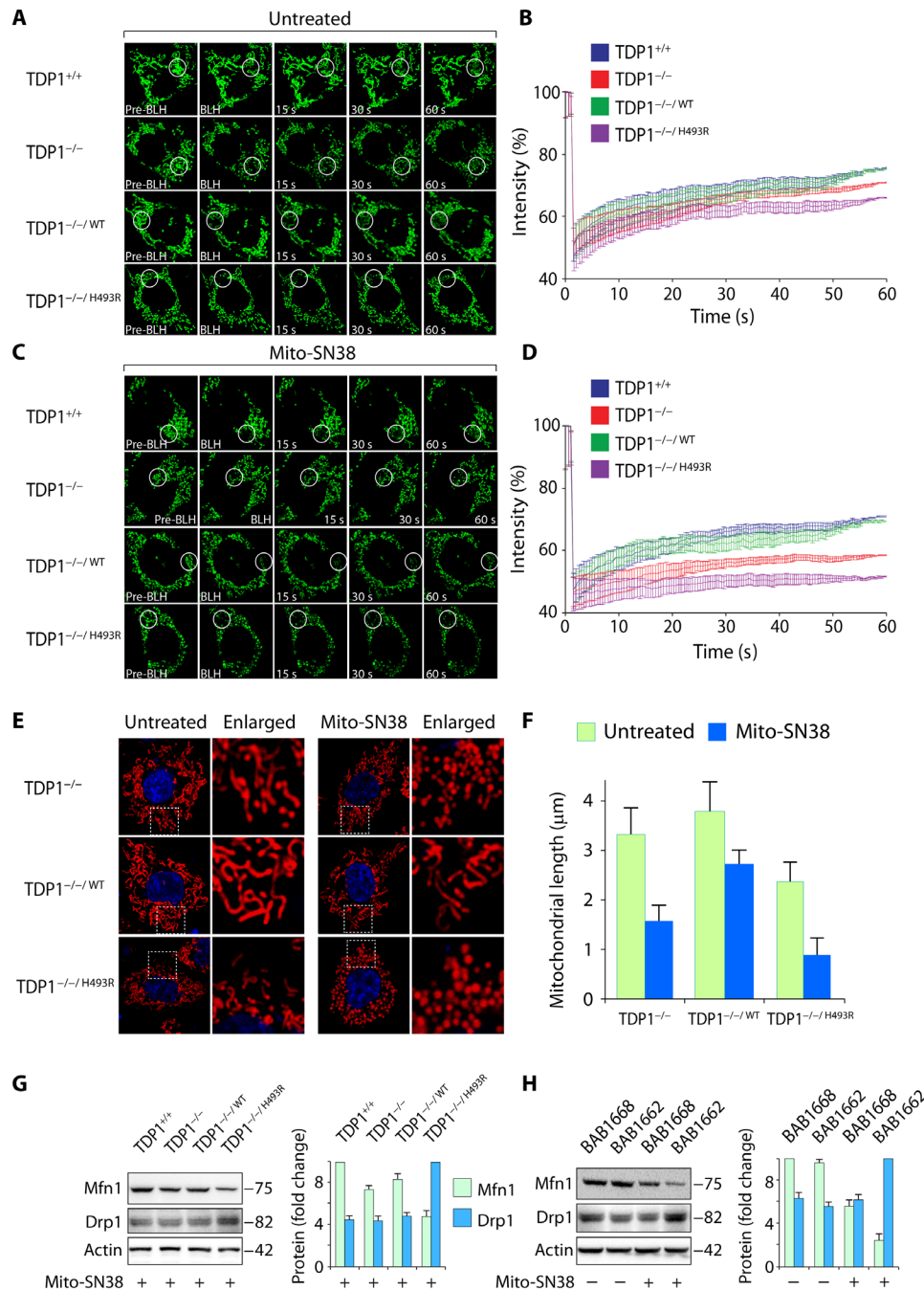


Fig. 3. TDP1^{H493R} trapping promotes mitochondrial fission. Mitochondrial network dynamics were analyzed in the indicated cells using live-cell microscopy and photobleaching (FRAP analysis) of cells ectopically expressing the mitochondrial targeted fluorescence protein construct (mito-YFP). Cells were either untreated (A) or pretreated with mito-SN38 (5 μM for 3 hours) (C). A submitochondrial spot indicated by a circle was bleached (BLH) with a 514-nm laser for 30 ms and imaged at regular intervals of 500 ms thereafter. Successive images taken for 60 s after bleaching illustrate the level of return of fluorescence into the bleached areas. (B and D) Quantitative mitochondrial FRAP data (n = 25). Error bars represent means ± SEM. (E and F) Mitochondrial length was measured in the indicated MEFs by staining with MitoTracker red with or without mito-SN38 (5 μM for 3 hours). Nuclei were stained with Hoechst 33342 (blue). The bar graph (n = 25) represents means ± SEM. (G and H) Western blot analysis of Mfn1 (mitofusin 1) and Drp1 (dynamin-related protein 1) in total lysates obtained from the indicated cells after treatment with mito-SN38 (5 μM for 6 hours). Actin served as the loading control. Migration of protein molecular weight markers is indicated on the right. Bar graphs represent the fold change in densitometry analysis of Mfn1 and Drp1 normalized to actin (error bars represent means ± SEM).

the number of GFP-LC3 puncta in TDP1^{-/-H493R} MEFs that were markedly elevated (~2- to 3-fold) when combined with mito-SN38 (P < 0.001; Fig. 5C; see the quantification in Fig. 5D) in contrast to its wild-type counterpart.

To further investigate the role of TDP1^{H493R} trapping in neuronal cells, we differentiated human neuroblastoma cells (SH-SY5Y) to neurons (fig. S2A) (34) and then ectopically expressed TDP1^{WT} or TDP1^{H493R} (fig. S2A). The SH-SY5Y cells were stably selected with

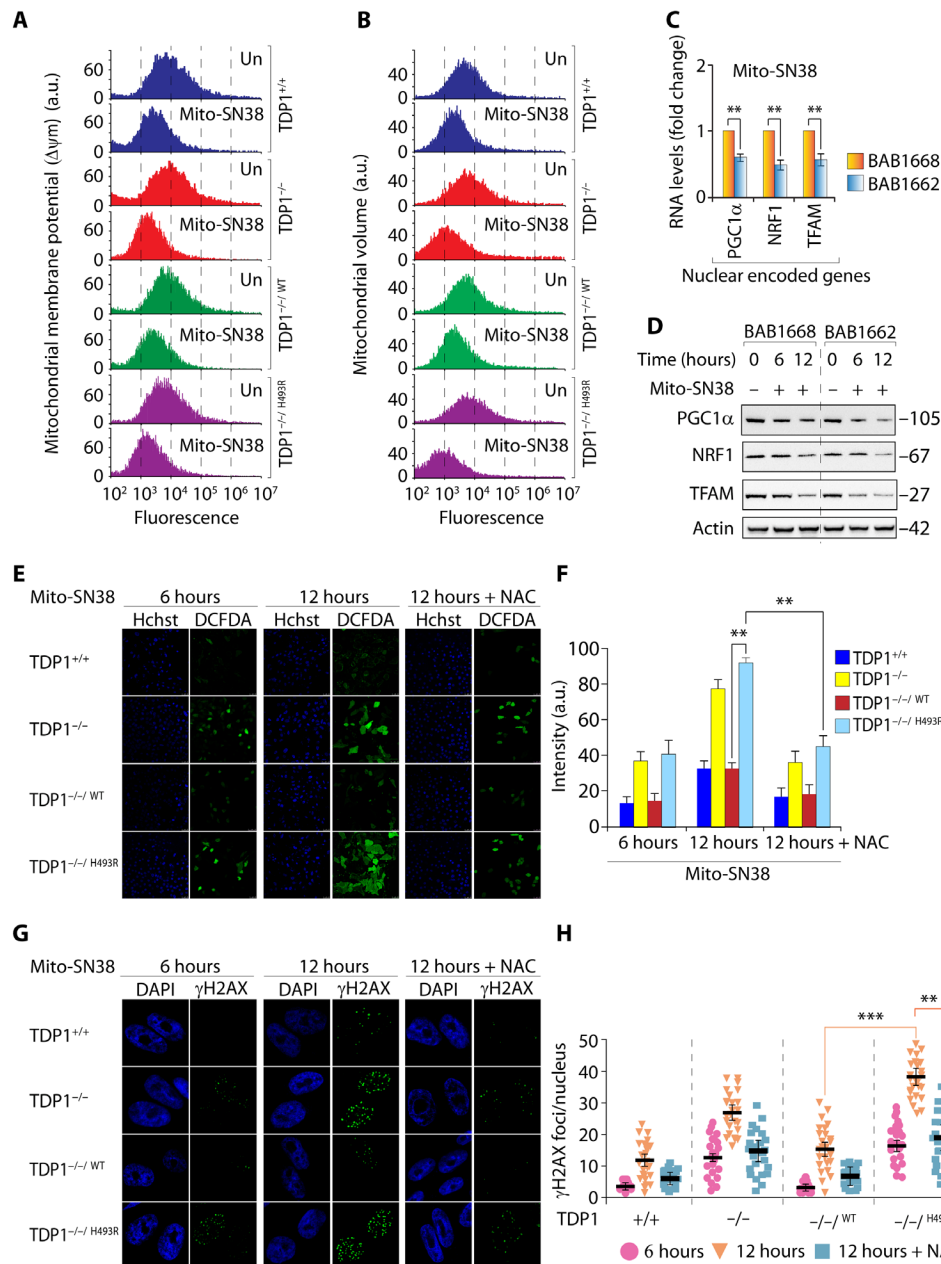


Fig. 4. TDP1^{H493R} trapping promotes mitochondrial dysfunction in SCAN1 cells. (A) Fluorescence-activated cell sorting (FACS) analysis of mitochondrial membrane potential ($\Delta\psi_m$) using TMRM before or after treatment with mito-SN38 (5 μ M for 6 hours) in the indicated cells. TMRM fluorescence was plotted against cell numbers (count). Data represent means \pm SE of independent experiments. (B) FACS analysis of mitochondrial volume in the indicated cells using MitoTracker green before and after treatment with mito-SN38 (5 μ M for 6 hours). Data represent means \pm SE of independent experiments. (C) The gene expression profile of nuclear-encoded genes [nuclear respiratory factor 1 (NRF1), peroxisome proliferator-activated receptor gamma coactivator 1- α (PGC1 α), and mitochondrial transcription factor A (TFAM)] for mitochondrial biogenesis by reverse transcription PCR. Indicated cells were either not treated or treated with mito-SN38 (5 μ M for 6 hours). Data represent means \pm SE of three independent experiments. Asterisks denote statistically significant differences (** P < 0.01, t test). (D) Representative Western blots for nuclear-encoded NRF1, PGC1 α , and TFAM in SCAN1 patient-derived lymphoblastoid cell lines (BAB1662) and their wild-type counterpart (BAB1668) before and after treatment with mito-SN38 (5 μ M) for the indicated time periods. Actin is shown as the loading control. (E and F) ROS formation was measured by fluorescent dye CM-H₂DCFDA in live-cell microscopy after treatment with mito-SN38 (5 μ M) or with pretreatment of *N*-acetyl-L-cysteine (NAC) (10 mM for 2 hours) for the indicated time. The ROS intensity is shown in green, and nuclei were stained with Hoechst 33342 (blue) in the indicated cells. Plots shown on the right represent means \pm SDs of at least three experiments. Asterisks denote statistically significant difference (** P < 0.01, t test). (G and H) Representative γ H2AX visualization by immunofluorescence microscopy in MEFs expressing TDP1 variants after treatment with mito-SN38 (5 μ M) or with pretreatment of NAC (10 mM for 2 hours) for the indicated time. The γ H2AX is shown in green, and nuclei were stained with 4',6-diamidino-2-phenylindole (DAPI) (blue). Scattergrams are shown on the right for at least three experiments; means \pm SDs are indicated. Asterisks denote statistically significant differences (** P < 0.01 and *** P < 0.001, t test).

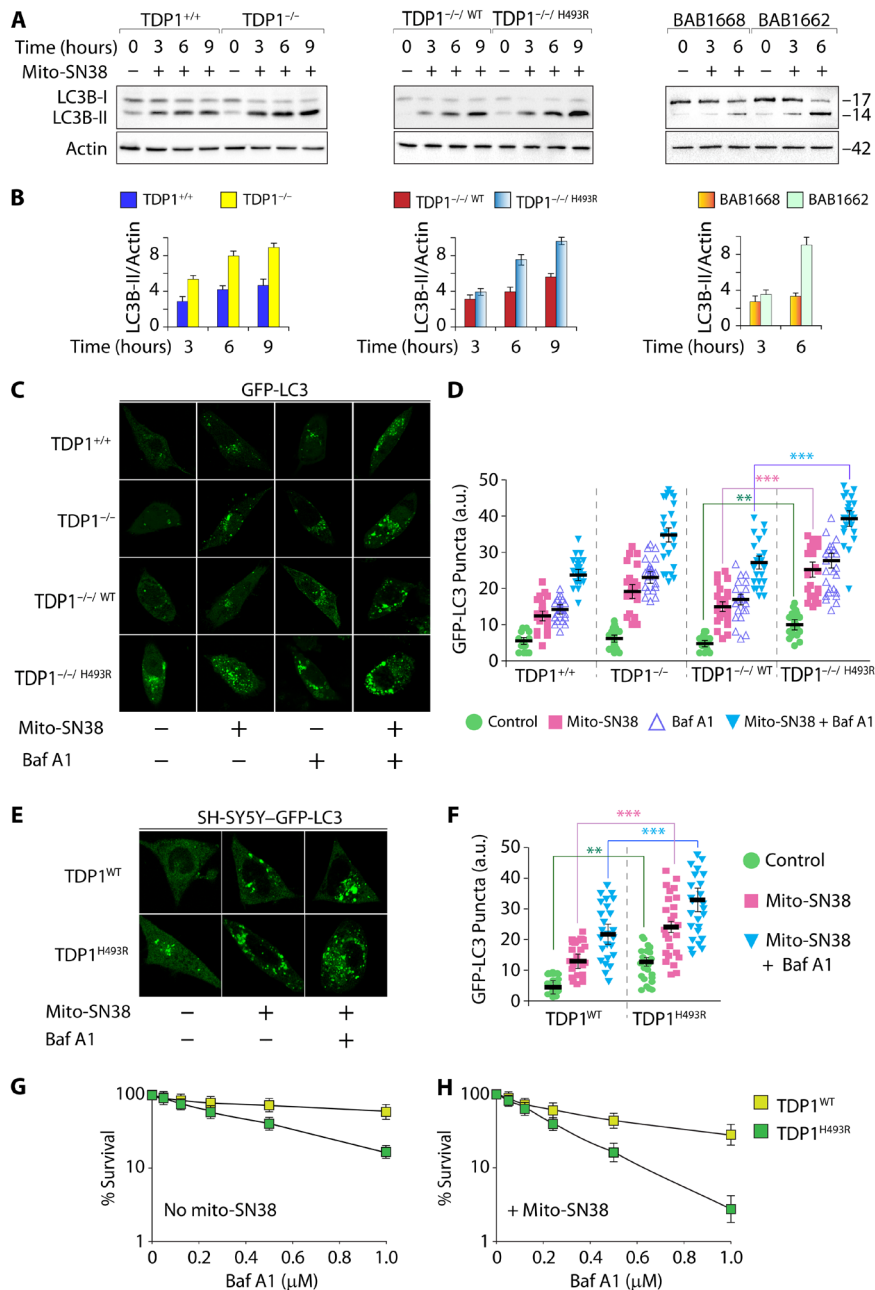


Fig. 5. SCAN1-TDP1 in mitochondria activates autophagy. (A) Immunoblotting for LC3-II lipidation with an anti-LC3B-specific antibody with the indicated cell lysates before or after treatment with a sublethal dose of mito-SN38 (2.5 μ M) for the indicated time periods. The positions of LC3B-I and LC3B-II are indicated. Actin is shown as the loading control. (B) Plots represent fold increase in LC3B-II band intensity in the indicated cells, normalized to actin (error bars represent means \pm SEM). (C) Representative images of GFP-LC3 puncta formation using live-cell confocal microscopy in the indicated cells by ectopically expressing GFP-LC3. The cells were either untreated or treated with mito-SN38 (2.5 μ M for 12 hours) or the autophagy inhibitor Baf A1 (200 nM for 4 hours) alone or in combination with Baf A1 (200 nM for 4 hours) + mito-SN38 (2.5 μ M for 12 hours). The translocation of GFP-LC3 to phagosome triggers steady-state levels of autophagosomes, as indicated by GFP-LC3 puncta formation. (D) Quantification of GFP-LC3 puncta per cell after the indicated treatment obtained from immunofluorescence confocal microscopy was calculated for 20 to 25 cells (mean \pm SEM) from independent experiments. Asterisks denote statistically significant differences (** P < 0.01 and *** P < 0.001, t test). (E) Representative images of differentiated neuronal cells derived from human neuroblastoma cells (SH-SY5Y) stably expressing GFP-LC3 were transfected with lentiviral constructs of TDP1^{WT} or TDP1^{H493R} and were analyzed for GFP-LC3 puncta formation under live-cell confocal microscopy. The cells were either kept untreated or treated with mito-SN38 (2.5 μ M for 12 hours) or the autophagy inhibitor Baf A1 (200 nM for 4 hours) alone or in combination with Baf A1 (200 nM for 4 hours) + mito-SN38 (2.5 μ M for 12 hours). (F) Quantification of GFP-LC3 puncta per cell after the indicated treatments was obtained from live-cell microscopy calculated for 20 to 25 cells (mean \pm SEM) from independent experiments. Asterisks denote statistically significant differences (** P < 0.01 and *** P < 0.001, t test). (G and H) Cell survival of differentiated neuronal cells from SH-SY5Y cells expressing TDP1^{WT} or TDP1^{H493R}. Baf A1-induced cytotoxicity (%) was calculated with respect to the untreated control (G). Combination of mito-SN38 (2.5 μ M for 12 hours) + Baf A1 (for the next 24 hours)-induced cytotoxicity (%) was calculated with respect to the untreated control (H). Each point corresponds to the mean \pm SD of at least three experiments. Error bars represent SD (n = 3).

GFP-LC3, so we tested GFP-LC3 puncta formation in differentiated SH-SY5Y expressing TDP1 variants under live-cell microscopy. We detected notable increase in the basal levels of GFP-LC3 puncta formation in the differentiated SH-SY5Y cells only by expressing TDP1^{H493R}, which was significantly increased after treatment with the autophagy inhibitor Baf A1 ($P < 0.001$; Fig. 5E; see the quantification in Fig. 5F) compared to wild-type TDP1 expression. GFP-LC3 puncta were markedly elevated by ~3-fold in the presence of mito-SN38 + Baf A1 in differentiated SH-SY5Y cells expressing TDP1^{H493R} compared to wild-type TDP1 ($P < 0.001$; Fig. 5E; see the quantification in Fig. 5F).

To test the functional role of autophagy in the survival of the differentiated neuronal cells expressing TDP1^{H493R}, we performed survival assays with the autophagy inhibitor Baf A1 alone or in combination with a sublethal dose of mito-SN38 in the neuronal cells expressing TDP1 variants. We noted that inhibition of autophagy by Baf A1 alone significantly induced cell death in TDP1^{H493R}-expressing neuronal cells (Fig. 5G), which was markedly increased in combination with a sublethal dose of mito-SN38 (Fig. 5G; see mito-SN38 + Baf A1) compared to cells expressing the TDP1 wild-type counterpart, suggesting that autophagy rescues mito-SN38-induced mitochondrial toxicity in SCAN1 cells. Collectively, our data provide evidence that TDP1^{H493R} trapping promotes the steady-state level of autophagosome formation, and upon inhibition of autophagy, this shifts toward apoptosis.

Trapping of TDP1^{H493R} activates PTEN-induced kinase 1-dependent mitophagy

Elimination of damaged mitochondria occurs through a specialized form of autophagy referred to as mitophagy (32, 33, 53). Thus, for the quantitative assessment of mitophagy in cells expressing TDP1 variants, we used a specific traffic light mitophagy reporter (mito-mRFP-EGFP) construct consisting of a pH-stable red fluorescent protein (RFP) fused to an acidic pH-labile GFP with a mitochondria-targeting signal (36). Localization of autophagic mitochondria inside the lysosome leads to formation of red-only fluorescence against yellow fluorescence for nonautophagic mitochondrial counterparts in cells expressing the mito-mRFP-EGFP construct (Fig. 6A). Without mito-SN38 treatment, we detected significant increases in red-only fluorescence in 30 to 35% of mitochondria in TDP1^{-/-H493R} MEFs compared to TDP1-proficient cells expressing the traffic light construct ($P < 0.01$; Fig. 6B), which is in keeping with the significant increase in the number of GFP-LC3 puncta without drug treatment in TDP1^{-/-H493R} MEFs (Fig. 5, C and D) or differentiated neuronal cells expressing TDP1^{H493R} (Fig. 5, E and F) and related to drug-independent trapping of TDP1^{H493R} (Fig. 2A). Mito-SN38 treatment markedly increased mitophagy in TDP1^{H493R} MEFs as revealed by more than 80% red-only fluorescence in the mitochondria ($P < 0.001$; Fig. 6C) compared to TDP1^{+/+} or TDP1^{-/-WT} MEFs. Furthermore, we confirmed that the red-only fluorescent mitochondria in TDP1^{H493R} MEFs correspond to mitochondria engulfed by lysosomes, as shown by colocalization with the lysosomal-specific LysoTracker dye (fig. S2C).

The sequential events that promote mitophagy is initiated by mitochondrial depolarization and accumulation of PINK1 (PTEN-induced kinase 1) in the outer mitochondrial membrane of the dysfunctional mitochondria (32, 37). Therefore, we ectopically expressed GFP-PINK1 in cells harboring TDP1 variants and investigated PINK1 accumulation in the mitochondria by costaining the cells with the mitochondrion-specific dye MitoTracker red under live-cell confocal microscopy. Figure 6D shows that 70 to 80% of TDP1^{-/-H493R} MEFs

accumulate significantly higher expression of GFP-PINK1 in the mitochondria ($P < 0.01$; see merged image Fig. 6D) within 3 hours of mito-SN38 treatment compared to (20 to 25%) TDP1^{+/+} or TDP1^{-/-WT} MEFs. Therefore, mitochondrial depolarization in TDP1 defective MEFs (Fig. 4A) activates PINK1-dependent mitophagy. These observations highlight the role of SCAN1-TDP1 trapping in mitochondrial fragmentation, a phenomenon in mitophagy associated with mitochondrial clearance.

DISCUSSION

To our knowledge, the present study provides the first evidence that mitochondria in cells harboring SCAN1-TDP1 (TDP1^{H493R}) are selectively trapped on the mtDNA at Top1mt cleavage sites, are shorter in length, and have increased fission rates. We demonstrate that TDP1^{H493R} trapping prevents mitochondrial transcription, energy production, and mitobiogenesis. SCAN1-TDP1 trapping triggers autophagy that allows identification of dysfunctional mitochondria through PINK1 accumulation and their subsequent removal through mitophagy. Our current work offers further evidence that inhibition of autophagy in the neuronal cells expressing TDP1^{H493R} is detrimental, suggesting that mitophagy is critical for SCAN1.

MtDNA is essential for cell viability, as it encodes subunits of OXPHOS as well as mitochondrial mRNA and tRNA (30). The mitochondrial genome accumulates topological stress from bidirectional transcription and replication, resolved by recruiting the Top1mt to the regulatory noncoding region of mtDNA (mtNCR) to relax mtDNA supercoiling generated during these processes (46, 48, 57). Accordingly, Top1mt knockout mice accumulate increased negative supercoiling in the mtDNA that impairs mtDNA replication (58, 59), promoting mitochondrial dysfunction (52). A number of things enhance the trapping of Top1mtcc in mitochondria including anticancer drugs like marine alkaloids lamellarin D (47), mitochondria-targeted irinotecan (mito-SN38; Fig. 1), and camptothecin treatment of purified mitochondria (46). Top1cc can also be trapped by endogenous DNA breaks, oxidized bases, nicks, and DNA modifications generated by ROS (6, 60).

MtDNA repair is particularly critical for the mitochondrial genome, as the mtNCR region is mostly prone to genome instability (61), because it is the most exposed region, which harbors the primary replication initiation site and the critical promoter elements both for the heavy and light strands (30). Thus, the ability of TDP1 to resolve 3'-phosphotyrosyl linkages is consistent with the role of the enzyme in protecting cells against cytotoxic Top1-DNA lesions generated both in the nucleus and in mitochondria (Fig. 1) (4, 12, 18, 27). We detected significant trapping of TDP1^{H493R} in mitochondria without drug treatment (Fig. 2A), plausibly corresponding to the defective catalytic turnover of SCAN1-TDP1 at endogenous mtDNA lesions (10, 20, 21) or drug-independent Top1mtcc break sites, which were markedly enhanced after mito-SN38 treatment (Fig. 2A). TDP1^{H493R} is selectively trapped at mitochondrial nucleotide residues 15420, 15690, and 16060 along the mtNCR (Fig. 2C) at Top1mtcc binding sites (46, 48). SCAN1-TDP1 displays a rapid depletion of mtDNA (~2-fold) and was deficient in recovery of mtDNA even after 12 hours of repair in drug-free medium (Fig. 2, D and E). Subsequently, TDP1^{H493R} trapping induces transcriptional collapse of OXPHOS genes and is defective in organelle assembly of oxidative phosphorylation complexes in SCAN1 cells, which results in reduction in the steady-state level of ATP. This is in agreement with the recent

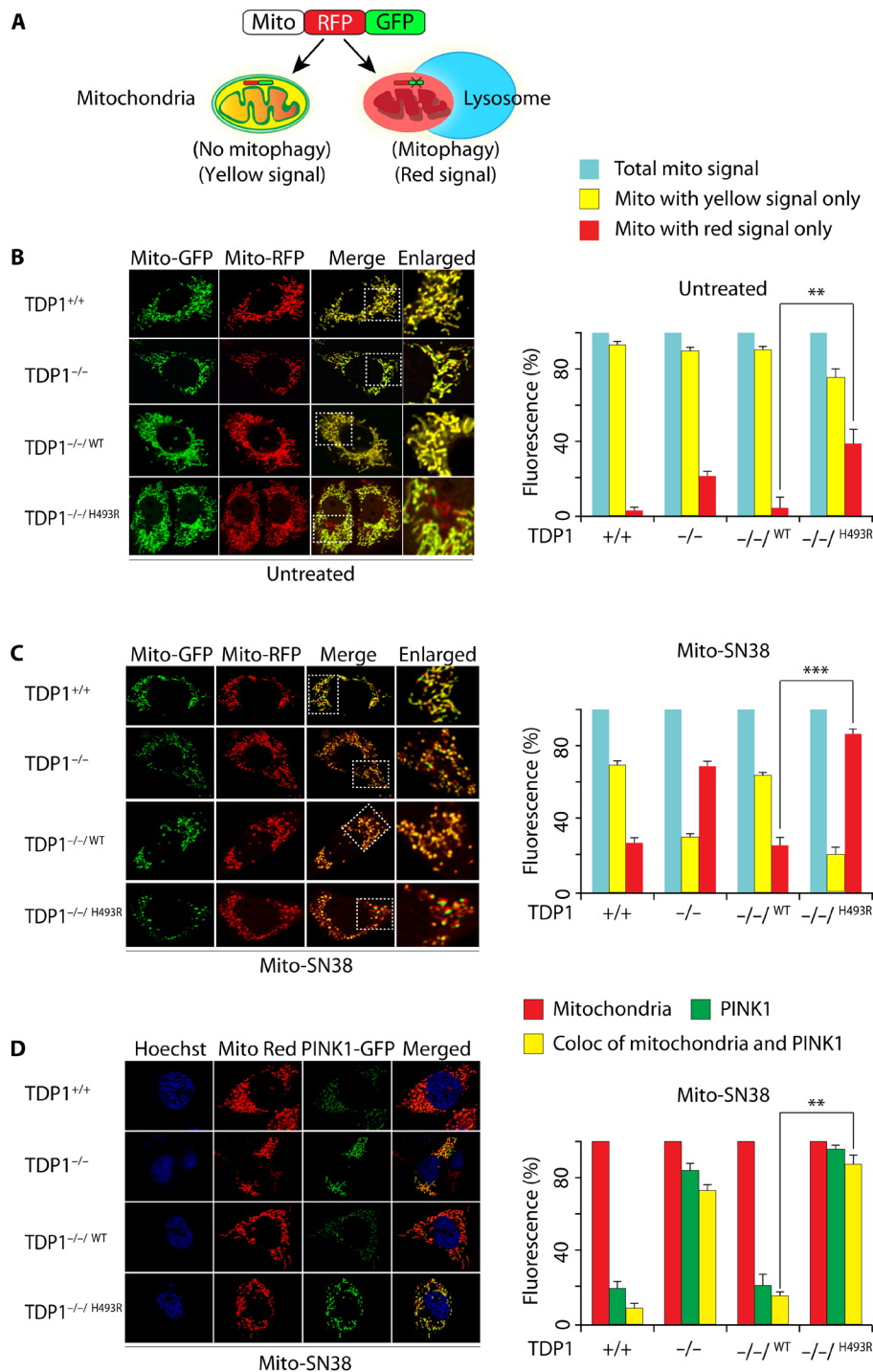


Fig. 6. TDP1^{H493R} trapping in mitochondria activates mitophagy. (A) Schematic representation for mitophagy monitoring using the dual fluorescence reporter construct p-mito-mRFP-EGFP (pAT016). Lysosomal delivery of the tandem fusion protein mito-mRFP-EGFP along with entire mitochondria results in pH-dependent quenching of green fluorescence resulting in red-only fluorescence for visual analysis of mitophagic flux. (B and C) Representative confocal live images of indicated MEFs ectopically expressing mito-mRFP-EGFP targeting mitochondria. Cells were kept untreated (B) or treated with mito-SN38 (2.5 μ M for 12 hours) (C) and were analyzed under live-cell microscopy. The yellow fluorescence signals denote no mitophagy (merged image); red-only fluorescence signals denote mitophagy or mitochondria inside lysosomes. The enlarged panel shows higher-magnification image. Quantification of the indicated fluorescence obtained from live-cell confocal microscopy was calculated for 20 to 25 cells (calculated value \pm SEM) in at least three independent experiments. Asterisks denote statistically significant differences (** P < 0.01 and *** P < 0.001, t test). (D) Representative confocal images of live cells for the indicated MEFs showing accumulation of ectopic PTEN-induced kinase 1 (PINK1)-GFP after mito-SN38 (2.5 μ M for 3 hours) treatment. Mitochondria are labeled with MitoTracker red; the colocalization of PINK1-GFP (green) in the mitochondrial network (red) is indicated in the merged image. Quantification of the indicated fluorescence obtained from live-cell confocal microscopy was calculated for 20 to 25 cells (calculated value \pm SEM) obtained from independent experiments. Asterisks denote statistically significant differences (** P < 0.01, t test).

report showing that TDP1 promotes the integrity of electron transport chain (18). Further evidence for dysregulated oxidative phosphorylation across the mitochondrial inner membrane is revealed by depolarization of the membrane potential in TDP1^{H493R} harboring MEFs after mito-SN38 treatment (Fig. 4D).

The dynamic equilibrium between mitochondrial fusion and fission preserves the mitochondrial network (32–34, 39). Here, our live-cell imaging shows that cells harboring SCAN1-TDP1 have reduced mitochondrial networks because of an increase in mitochondrial fission rate (Fig. 3C), which results in shortening of mitochondrial length (Fig. 3, E and F) together with the quantitative loss of mitochondrial volume (Fig. 4E). This is further supported by increased levels of mitochondrial fission-associated protein Drp1 in SCAN1 cells (Fig. 3F) and is in agreement with the observation that expression of catalytically active TDP1 rescues the mitochondrial fission-fusion dynamics, mitochondrial length (Fig. 2), and respiratory capacity (Fig. 3) in TDP1^{-/-} MEFs.

Fusion and fission dynamically regulate mitochondrial morphology and mitobiogenesis (32, 51), which occurs by division of preexisting organelles in coordination with nuclear encoded proteins and cellular proliferation. In SCAN1 cells, we observed a significant reduction in the transcription (Fig. 4F) and protein level (Fig. 4G) of nuclear encoded mitobiogenesis genes including PGC1 α , NRF1, and TFAM after prolonged treatment with mito-SN38, which is associated with nuclear DNA damage mediated through ROS (Fig. 4, H and I). We provide evidence that trapping of TDP1^{H493R} in the mitochondria produces potentially toxic DNA lesions that not only dampens mitochondrial activity but also triggers nuclear DNA damage as a bystander effect through ROS formation (Fig. 4). Maneuvering of fission or fusion improves mitochondrial physiology. Disruption of mitochondrial dynamics is common in severe disorders, including Alzheimer's disease, Parkinson's disease, and Huntington's disease, which show neurodegeneration (32, 33, 38, 39, 42, 43, 54).

Because SCAN1 cells accumulate a fragmented mitochondrial network and disrupted respiratory complexes that fail to manage the cellular energy requirements, they have low levels of ATP. To match the metabolic demand, SCAN1-TDP1-harboring cells increase autophagosomes (Fig. 5) to retain a lower number of fit mitochondria and channel the damaged ones to mitophagy by PINK1 accumulation on the outer mitochondrial membrane of the damaged mitochondria (Fig. 6).

In conclusion, the present study establishes the significance of autophagy to overcome TDP1^{H493R}-induced mitochondrial toxicity in neuronal cells (Fig. 5, E to G). Through evolution, cells that are critically dependent on mitochondria for energy production like neurons have acquired useful mechanisms to sequester and eliminate dysfunctional mitochondria for cell survival. It is worth mentioning that caloric restriction and mammalian target of rapamycin inhibition show life span-extending interventions via increased autophagy and mitophagy (62). This supports the argument that mitophagy in the SCAN1 phenotype may play a crucial role in neuroprotection and plausibly is associated with the late onset of neurological disorders as in patients with SCAN1.

MATERIALS AND METHODS

Drugs, reagents, and antibodies

Puromycin (P8833), Baf A1 (J61835), polybrene (H9268), irinotecan (I1406), all-*trans*-retinoic acid (R2625), and *N*-acetyl-L-cysteine (A9165) were all purchased from Sigma-Aldrich (USA). Anti-Top1mt-

specific antibody (47, 52) (Top1mt, polyclonal mouse) was a gift from Y. Pommier [Center for Cancer Research, National Cancer Institute, National Institutes of Health (NIH), USA]. Rabbit polyclonal antibodies [TDP1 (Ab4166), PGC1 α (Ab54481), NRF1 (Ab34682), and mtTFAM (Ab47517)] and mouse monoclonal antibodies [COX IV (Ab14744), DRP1 (Ab56788), Mfn1 (Ab57602), and double-stranded DNA (dsDNA) (Ab27156)] were purchased from Abcam (Cambridge, USA). Mouse monoclonal antibodies [FLAG (M2) (F3165)] and rabbit polyclonal antibodies [FLAG (F7425) and LC3B (L7543)] were purchased from Sigma-Aldrich (St. Louis, MO, USA). Mouse monoclonal γ H2AX (05-636) antibody was purchased from Millipore, USA. Rabbit monoclonal GFP (G10362) and anti OXPHOS complex kit (457999) antibodies were purchased from Invitrogen. Mouse monoclonal actin (SC-8432) and secondary antibodies [horseradish peroxidase-conjugated anti-rabbit immunoglobulin G (IgG) or anti-mouse IgG] were purchased from Santa Cruz Biotechnology (Santa Cruz, USA). MitoTracker red (M22426), MitoTracker green (M7514), TMRM (T668), CM-H₂DCFDA (C6827), and LysoTracker red DND-99 (L7528) were obtained from Molecular Probes.

Synthesis of mitochondria-targeted nanoparticle containing irinotecan (mito-SN38)

Production of a mitochondria-targeting cationic nanoparticle containing Top1 poison irinotecan (mito-SN38) was described previously (45). Briefly, 6.0 mg of L- α -phosphatidylcholine, 1.0 mg of α -tocopherylsuccinate-triphenylphosphine conjugate, 1.0 mg of irinotecan, and 0.6 mg of 1,2-distearoyl-*sn*-glycero-3-phosphoethanolamine-*N*-[amino (polyethylene glycol) 2000] were dissolved in 5.0 ml of dichloromethane-methanol mixture. Solvent was evaporated thoroughly to form a thin uniform lipid film. The lipid film was hydrated with 1 ml of water for 1 hour at 60°C. The nanoparticles formed were passed through Sephadex G-25 followed by extrusion through a 200-nm filter. The nanoparticles (mito-SN38) were stored at 4°C for further use.

Cell culture, plasmids, and generation of stable cell lines

Cells were cultured at 37°C with 5% CO₂ in Dulbecco's minimum essential medium (DMEM) or RPMI containing 10% fetal bovine serum (FBS) (Life Technologies) (12, 15, 27, 28, 63). TDP1^{+/+} and TDP1^{-/-} primary MEF cells were a gift from C. F. Boerkoel (University of British Columbia, Vancouver, British Columbia, Canada). Lymphoblastoid cell lines homozygous for the TDP1-H493R mutation (BAB1662; SCAN1) and normal individual (BAB1668) were a gift from J. R. Lupski (Departments of Pediatrics and Molecular and Human Genetics, Baylor College of Medicine, Houston, USA). The human embryonic kidney 293T [American Type Culture Collection (ATCC)] and human SH-SY5Y cells (ATCC) were a gift from D. Biswas (Council of Scientific and Industrial Research-Indian Institute of Chemical Biology, Kolkata, India). The cloning of pCMV-Tag2B-FLAG-TDP1 construct was described previously (12, 27, 28). Plasmid MDK124-FLAG-TDP1 was generated by digesting a FLAG-TDP1 fragment from pCMV-Tag2B-FLAG-TDP1 construct using Nhe I and Eco RI restriction sites and cloned into the pMDK124 lentiviral vector. The following point mutation (pMDK124-FLAG-TDP1^{H493R}) was generated using the "QuikChange" protocol (Stratagene, La Jolla, CA, USA). All constructs were confirmed by DNA sequencing. The plasmids were then used for lentivirus generation using a standard protocol and were transduced into TDP1^{-/-} MEFs using lentivirus particles containing FLAG-TDP1^{WT} or FLAG-TDP1^{H493R} in the presence of polybrene (5 μ g/ml) (Sigma-Aldrich) and were subjected

to puromycin selection (4 µg/ml) for 2 weeks. Individual colonies obtained by this method were further amplified and screened for expression of target proteins using Western blotting against epitope tag-specific antibodies.

The pYFP-Mito construct (15, 49) (protein targeted to the mitochondrial matrix) was a gift from R. J. Youle (National Institutes of Neurological Disorders and Stroke, NIH), the traffic light mitophagy reporter construct pAT016 (p-mito-mRFP-EGFP) was a gift from A. Till (University of Bonn, Germany), the pEGFP-LC3 construct was a gift from A. Saha (Presidency University, India), and the pPINK1 C-GFP construct was a gift from P. Mukherjee (Presidency University, India). All plasmid DNA constructs were transfected with Lipofectamine 2000 (Invitrogen) or FuGENE (Roche) according to the manufacturer's protocol.

Human SH-SY5Y cells were grown in DMEM containing 10% FBS and 1% penicillin and streptomycin and were stably selected for pEGFP-LC3 construct with puromycin (10 µg/ml). Differentiation of SH-SY5Y was performed (34) using 10 µM all-*trans*-retinoic acid (Sigma-Aldrich) dissolved in dimethyl sulfoxide for 7 to 10 days with changing retinoic acid-containing media on alternate days. Microscopic images of differentiated SH-SY5Y cells were taken using a Leica TCS SP8 microscope. The lentiviral particles containing FLAG-TDP1^{WT} or FLAG-TDP1^{H493R} were transduced into differentiated SH-SY5Y cells in the presence of polybrene (5 µg/ml) (Sigma-Aldrich) and incubated for 48 hours for ectopic expression of proteins. Expression of the target proteins was checked by Western blotting using epitope tag-specific antibodies. Cells were treated with different concentrations of mito-SN38 and Baf A1, as indicated.

Live-cell confocal microscopy and immunocytochemistry

Live-cell imaging was carried out as described previously (12, 27, 63, 64). Briefly, indicated cells were grown on confocal dishes (Genetix Biotech Asia Pvt. Ltd.). All the plasmid DNA were transfected as above and examined by live-cell confocal microscopy, as indicated. Nuclei were stained with Hoechst 33342 (Sigma-Aldrich). Fluorophores were excited using either separately or in combination with ultraviolet (Diode 405), 488-nm (argon), 561-nm (DPSS 561), or 633-nm (HeNe 633) laser lines using a confocal laser scanning microscope (Leica TCS SP8) with 63×/1.4 numerical aperture oil objective equipped with a heated environmental chamber set to 37°C with an optimal CO₂ facility. The percentage of cells displaying the indicated fluorescence was determined using Adobe Photoshop 7.0 from at least 20 to 25 cells expressing individual constructs.

Immunofluorescence staining and confocal microscopy were performed as described previously (12, 27, 28, 63, 64). Briefly, cells were fixed with 4% paraformaldehyde for 20 min at room temperature. Primary antibodies against γH2AX were detected with anti-mouse IgG secondary antibodies labeled with Alexa Fluor 488 (Invitrogen). Cells were mounted in anti-fade solution with 4',6-diamidino-2-phenylindole (Invitrogen) and examined using a laser scanning confocal microscope (Leica TCS SP8). Images were collected and processed using the Leica LAS X software and sized in Adobe Photoshop 7.0. The γH2AX intensity per nucleus was determined using Adobe Photoshop 7.0 by measuring the fluorescence intensities normalized to the number of cell count.

Measurements of mitochondrial connectivity using FRAP assays

Photobleaching experiments were carried out as described previously (12, 27, 49, 63) to measure mitochondrial connectivity using a confocal

laser scanning microscope (Leica TCS SP8). FRAP analyses were carried out with MEFs stably expressing TDP1 variants and ectopically expressing mitochondrial matrix targeted (pYFP-Mito) with or without mito-SN38. Bleaching of YFP-mito was applied at randomly chosen mitochondrial regions using a 514-nm laser for 30 ms and photographed at intervals of 500 ms thereafter. Successive images taken for 60 s after bleaching illustrated the level of recovery of fluorescence into the bleached areas. Relative fluorescence intensities of the bleached region were corrected for background. To show the FRAP curves, the fluorescence signal measured in a region of interest (ROI) was individually normalized to the pre-bleach signal in the ROI according to the following equation: $ROI = (I_t - I_{bg}) / (I_0 - I_{bg}) \times 100$, where I_0 is the intensity in the ROI during pre-bleach, I_t is the intensity in the ROI at time point t , and I_{bg} is the background signal determined in a region outside of the mitochondria.

Cell extracts and immunoblotting

Preparation of whole cell extracts and immunoblotting were carried out as described previously (12, 27, 63). Briefly, cells were harvested and lysed in a lysis buffer [10 mM tris-HCl (pH 8), 150 mM NaCl, 0.1% SDS, 1% NP-40, and 0.5% Na-deoxycholate supplemented with complete protease inhibitors] (Roche Diagnostics, Indianapolis, IN) and phosphatase inhibitors (Phosphatase Inhibitor Cocktail 1 from Sigma-Aldrich). After thorough mixing and incubation at 4°C for 2 hours, lysates were then centrifuged at 12,000g at 4°C for 20 min. Supernatants were collected and stored in aliquots at -80°C. Immunoblots were carried out following standard procedures, and immunoreactivity was detected using enhanced chemiluminescence reaction (170-5061, Bio-Rad) under ChemiDoc MP System (Bio-Rad).

Preparation of mitochondria

Mitochondria were prepared as described previously (15). Briefly, cell pellets were suspended in 10 mM NaCl, 1.5 mM CaCl₂, and 10 mM tris-HCl (pH 7.5) at 25°C for 5 min. Following osmotic shock, cells were homogenized using a glass Dounce homogenizer and mixed with stabilizing buffer [2 M sucrose, 35 mM EDTA, and 50 mM tris-HCl (pH 7.5) at 25°C]. Cell lysates were centrifuged at 750g for 5 min to remove nuclei and cell debris. Mitochondria were spun down from the supernatant at 10,000g for 20 min, washed three times with MT buffer [250 mM sucrose, 10 mM KCl, 1.5 mM MgCl₂, 1 mM EDTA, 1 mM EGTA, 5 mM dithiothreitol (DTT), and 20 mM HEPES-KOH (pH 7.4) at 25°C], and resuspended in MT buffer. For all experiments, freshly prepared mitochondria were used.

ICE bioassay

Detection of Top1mt, TDP1, and nuclear Top1-cleavage complexes by ICE bioassay was performed as described previously (47). Briefly, cells (5×10^6) expressing TDP1 variants were either untreated or treated with the indicated concentration of drugs. Mitochondria were isolated as described above and lysed by adding lysis buffer [6 M guanidinium thiocyanate, 10 mM tris-HCl (pH 6.5), 20 mM EDTA, 4% Triton X-100, 1% sarosyl, and 1% DTT]. Mitochondrial lysates were mixed with 0.4 ml of 100% ethanol, incubated at -20°C for 5 min, and cleared by centrifugation (12,000g for 10 min). Supernatants were discarded, and pellets were washed two times with 100% ethanol and then dissolved in 0.2 ml of 8 mM NaOH (freshly made) and sonicated for 10 to 20 s at 20% power. For immunodetection, mtDNA at varying concentrations were spotted onto a nitrocellulose membrane (Millipore, USA) using a slot-blot vacuum system (Bio-Rad, USA).

For detection of nuclear Top1cc, whole cells were lysed by adding lysis buffer, cleared by centrifugation, and the pellet was dissolved in 8 mM NaOH and slot-blotted as indicated above. Immunoblotting was carried out with anti-Top1mt (47, 52) or anti-TDP1 (15) and anti-nuclear Top1-specific antibodies. Anti-dsDNA was used for loading control. Immunoblots were visualized using enhanced chemiluminescence reactions on a ChemiDoc MP System.

Cell survival assays

Cell survival was carried out as described previously (28, 45, 65). Briefly, TDP1^{+/+} MEFs, TDP1^{-/-} MEFs, and TDP1^{-/-} MEF cells stably expressing FLAG-TDP1 variants (TDP^{-/-/WT}, TDP^{-/-/H493R}, or TDP^{+/+/H493R}) or human lymphoblastoid cells (BAB1662 or BAB168) or differentiated SH-SY5Y cells ectopically expressing FLAG-TDP1^{WT} or FLAG-TDP1^{H493R} (1×10^3) cells were seeded in 96-well plates (BD Biosciences, USA). After 24 hours, cells were treated with the indicated drugs and kept for a further 48 hours. Cell survival was then assessed by 3-(4,5-dimethylthiazol-2-yl)-2,5-diphenyltetrazolium bromide (MTT; Sigma-Aldrich, M5655). Plates were analyzed on a Molecular Devices Spectra MaxM2 Microplate Reader at 570 nm. The percent inhibition of viability for each concentration of drugs was calculated with respect to the control. Data represent means \pm SD for three independent experiments.

Quantification of mtDNA damage

To compare the levels of mtDNA damage and repair in cells expressing TDP1 variants, cells were treated with mito-SN38 (20 μ M) for the indicated times or further cultured in drug-free medium to measure repair using mtDNA long-range PCR as described previously (15, 66). We used human and mouse mtDNA sequence-specific primers to amplify a 9- or 10-kbp (kilo-base pair) fragment of mtDNA, respectively. A small 110-bp (for human) or 117-bp (for mouse-specific) mtDNA fragment was also amplified for normalization. PCR reactions were limited to 18 cycles to ensure that the amplification process was still in the exponential phase. The damage index was determined by the ratio LR/SR of long-range PCR product (LR) by the short-range PCR product (SR). The sequences of the primers are listed in table S1.

ChIP and reverse transcription qPCR

ChIP was performed as described previously (18, 48). Briefly, MEF cells expressing TDP1 variants (1×10^7) were treated with mito-SN38 (5 μ M) for 6 hours followed by fixation with formaldehyde (1.1% final concentration) for 10 min at room temperature, and reactions were stopped by adding 125 mM glycine for 5 min. Cells were then washed with phosphate-buffered saline (PBS), scraped, and lysed in 0.5 ml of ChIP lysis buffer [50 mM Hepes-KOH (pH 7.5), 140 mM NaCl, 1 mM EDTA (pH 8), 1% Triton X-100, 0.1% sodium deoxycholate, 0.1% SDS, and 1 \times protease inhibitor] on ice for 30 min. Lysates were sonicated 10 times for 30 s at 30% power to yield fragments of 200 to 300 bp and cleared by centrifugation at 14,000g for 10 min at 4°C. The supernatant (50 μ l) was stored at -20°C as input and labeled as “no-IP.” The remainder was diluted fourfold in dilution buffer [50 mM tris-HCl (pH 8), 150 mM NaCl, 2 mM EDTA (pH 8), 1% NP-40, 0.5% sodium deoxycholate, 0.1% SDS, and 1 \times protease inhibitors] and incubated with 10 μ l of FLAG antibody on a rotating platform overnight at 4°C. The following day, 150 μ l of A/G PLUS-Agarose beads (Santa Cruz Biotechnology) was added and further incubated on a rotating platform for 2 hours at 4°C. The beads were then washed twice with low-salt wash buffer [0.1% SDS, 1% Triton X-100, 2 mM

EDTA, 20 mM tris-HCl (pH 8), and 150 mM NaCl], twice with high-salt wash buffer [0.1% SDS, 1% Triton X-100, 2 mM EDTA, 20 mM tris-HCl (pH 8), and 500 mM NaCl], followed by one wash with lithium chloride buffer [0.25 M LiCl, 1% NP-40, 1% sodium deoxycholate, 1 mM EDTA, and 10 mM tris-HCl (pH 8)], and twice with TE buffer. The immunoprecipitated complex was then eluted from the beads in 150 μ l of elution buffer (1% SDS and 100 mM NaHCO₃). The eluent and the no-IP control samples were then treated with RNase A and proteinase K. The DNA was purified using phenol-chloroform extraction and ethanol precipitation. The pellets were resuspended in 30 μ l of distilled water.

For qPCR, the no-IP or input and ChIP samples were diluted 1:10; then, 5 μ l was mixed with 2.5 μ l of 5 μ M forward and reverse primers (table S 1) with 10 μ l of 2 \times SYBR Green PCR mix (Applied Biosystems). The PCR mix was aliquoted into reaction volumes (20 μ l) in triplicate and amplified using an ABI 7500 thermocycler (Applied Biosystems). The PCR reactions were carried out with thermocycling conditions of 95°C for 10 min and then 40 cycles at 90°C for 15 s, 50°C for 15 s, and 72°C for 30 s, with signal acquisition at the end of each cycle. Quantification of chromatin enrichment was calculated by percent input normalized to the mtDNA copy number in the input samples. The sequences of the primers are listed in table S1.

Quantification of mitochondrial gene transcription by real-time PCR

The total RNA was extracted from indicated cells (1×10^6) using TRIzol reagent (15596018, Invitrogen) according to the manufacturer's protocols, which includes deoxyribonuclease (AMPD1; Sigma-Aldrich) treatment for each sample (52). An aliquot of 1 μ g of RNA was reverse-transcribed using a reverse transcription kit (4368814, Applied Biosystems). Real-time PCR was performed with SYBR Green PCR master mix (A25742, Applied Biosystems) on the ABI 7500 thermocycler (Applied Biosystems). Reaction mixtures contained 5 μ l of 2 \times SYBR-Green PCR master mix and 2 μ l of reverse transcriptase-generated cDNA diluted 10-fold in a final volume of 10 μ l containing primers at 25 nM. The thermocycling conditions were 95°C for 5 min, followed by 40 cycles at 95°C for 50 s, 50°C (variable) for 50 s, and 72°C for 60 s. Relative gene expression was expressed as a ratio of the expression level of the gene of interest to that of β -actin RNA, with values in wild-type cells defined as 100%. The sequences of the primers are listed in table S1.

Analysis of mitochondrial length

Mitochondrion length was measured as described previously (49). Briefly, MEFs expressing TDP1 variants were incubated with or without mito-SN38, as indicated. Then, cells were stained with MitoTracker red and were subjected to live-cell confocal microscopy (Leica TCS SP8). Individual mitochondrial length analysis was performed using the line measurement property of Leica LAS X software. An average length of ~20 to 25 mitochondria per cell was measured.

Mitochondrial membrane potential

Determination of $\Delta\psi_m$ was performed using TMRM (200 nM for 30 min at 37°C) (50, 52), which is a positively charged, colorless dye that enters mitochondria in a membrane potential-dependent manner and emits bright red-orange fluorescence that was analyzed by flow cytometry (BD, FACSAria III).

Determination of mitochondrial mass

Mitochondrial mass was measured by MitoTracker Green FM (Molecular Probes) staining (50, 52). Cells were trypsinized and resuspended in PBS with 200 nM MitoTracker Green FM (30 min at 37°C) in the dark and were analyzed by flow cytometry (BD, FACSAria III).

ATP determination

ATP level in indicated cells was determined using an ATP determination kit (A22066; Molecular Probes) following the manufacturer's protocol (52).

Intracellular ROS detection by confocal microscopy

For intracellular ROS detection by live-cell confocal (Leica TCS SP8) microscopy, MEFs expressing TDP1 variants were seeded in confocal dishes and treated with or without mito-SN38 for the indicated time periods and then washed twice with PBS (pH 7.4) and 10 μ M CM-H₂DCFDA in PBS was applied to live cells and kept at 37°C for 5 min (28, 45, 65). The CM-H₂DCFDA diffuses into cells where the free nonfluorescent 2',7'-dichlorodihydrofluorescein in the cytoplasm is oxidized to the green fluorescent moiety, dichlorofluorescein, by intracellular ROS upon excitation with 488-nm argon laser. Nuclei were stained with Hoechst 33342.

SUPPLEMENTARY MATERIALS

Supplementary material for this article is available at <http://advances.sciencemag.org/cgi/content/full/5/11/eaax9778/DC1>

Fig. S1. Mito-SN38 does not trap nuclear-Top1cc but impairs mitochondrial metabolism through SCAN1-TDP1 trapping in the mitochondria.

Fig. S2. Differentiation of SH-SY5Y cells showing expression of FLAG-TDP1 and lysosomal localization of SCAN1 mitochondria showing mitophagy.

Table S1. List of primers used.

[View/request a protocol for this paper from Bio-protocol.](#)

REFERENCES AND NOTES

- H. Takashima, C. F. Boerkoel, J. John, G. M. Saifi, M. A. M. Salih, D. Armstrong, Y. Mao, F. A. Quiocho, B. B. Roa, M. N. Nakagawa, Mutation of *TDP1*, encoding a topoisomerase I-dependent DNA damage repair enzyme, in spinocerebellar ataxia with axonal neuropathy. *Nat. Genet.* **32**, 267–272 (2002).
- S.-W. Yang, A. B. Burgin Jr., B. N. Huizenga, C. A. Robertson, K. C. Yao, H. A. Nash, A eukaryotic enzyme that can disjoin dead-end covalent complexes between DNA and type I topoisomerases. *Proc. Natl. Acad. Sci. U.S.A.* **93**, 11534–11539 (1996).
- A. S. Kawale, L. F. Povirk, Tyrosyl-DNA phosphodiesterases: Rescuing the genome from the risks of relaxation. *Nucleic Acids Res.* **46**, 520–537 (2017).
- Y. Pommier, S.-y. N. Huang, R. Gao, B. B. Das, J. Murai, C. Marchand, Tyrosyl-DNA-phosphodiesterases (tdp1 and tdp2). *DNA Repair* **19**, 114–129 (2014).
- S. F. El-Khamisy, To live or to die: A matter of processing damaged DNA termini in neurons. *EMBO Mol. Med.* **3**, 78–88 (2011).
- Y. Pommier, Y. Sun, S.-y. N. Huang, J. L. Nitiss, Roles of eukaryotic topoisomerases in transcription, replication and genomic stability. *Nat. Rev. Mol. Cell Biol.* **17**, 703–721 (2016).
- S. Katyal, Y. Lee, K. C. Nitiss, S. M. Downing, Y. Li, M. Shimada, J. Zhao, H. R. Russell, J. H. Petrini, J. L. Nitiss, Aberrant topoisomerase-1 DNA lesions are pathogenic in neurodegenerative genome instability syndromes. *Nat. Neurosci.* **17**, 813–821 (2014).
- S. Katyal, S. F. El-Khamisy, H. R. Russell, Y. Li, L. Ju, K. W. Caldecott, P. J. McKinnon, TDP1 facilitates chromosomal single-strand break repair in neurons and is neuroprotective in vivo. *EMBO J.* **26**, 4720–4731 (2007).
- S. F. El-Khamisy, G. M. Saifi, M. Weinfeld, F. Johansson, T. Helleday, J. R. Lupski, K. W. Caldecott, Defective DNA single-strand break repair in spinocerebellar ataxia with axonal neuropathy-1. *Nature* **434**, 108–113 (2005).
- H. Interthal, H. J. Chen, T. E. Kehl-Fie, J. Zotzmann, J. B. Leppard, J. J. Champoux, SCAN1 mutant Tdp1 accumulates the enzyme-DNA intermediate and causes camptothecin hypersensitivity. *EMBO J.* **24**, 2224–2233 (2005).
- K. W. Caldecott, Single-strand break repair and genetic disease. *Nat. Rev. Genet.* **9**, 619–631 (2008).
- B. B. Das, S. Antony, S. Gupta, T. S. Dexheimer, C. E. Redon, S. Garfield, Y. Shiloh, Y. Pommier, Optimal function of the DNA repair enzyme TDP1 requires its phosphorylation by ATM and/or DNA-PK. *EMBO J.* **28**, 3667–3680 (2009).
- R. Hirano, H. Interthal, C. Huang, T. Nakamura, K. Deguchi, K. Choi, M. B. Bhattacharjee, K. Arimura, F. Umehara, S. Izumo, Spinocerebellar ataxia with axonal neuropathy: Consequence of a Tdp1 recessive neomorphic mutation? *EMBO J.* **26**, 4732–4743 (2007).
- A. J. Hawkins, M. A. Subler, K. Akopiants, J. L. Wiley, S. M. Taylor, A. C. Rice, J. J. Windle, K. Valerie, L. F. Povirk, In vitro complementation of Tdp1 deficiency indicates a stabilized enzyme-DNA adduct from tyrosyl but not glycolate lesions as a consequence of the SCAN1 mutation. *DNA Repair* **8**, 654–663 (2009).
- B. B. Das, T. S. Dexheimer, K. Maddali, Y. Pommier, Role of tyrosyl-DNA phosphodiesterase (TDP1) in mitochondria. *Proc. Natl. Acad. Sci. U.S.A.* **107**, 19790–19795 (2010).
- J. Murai, S.-y. N. Huang, B. B. Das, T. S. Dexheimer, S. Takeda, Y. Pommier, Tyrosyl-DNA phosphodiesterase 1 (TDP1) repairs DNA damage induced by topoisomerases I and II and base alkylation in vertebrate cells. *J. Biol. Chem.* **287**, 12848–12857 (2012).
- H. K. Fam, K. Choi, L. Fougner, C. J. Lim, C. F. Boerkoel, Reactive oxygen species stress increases accumulation of tyrosyl-DNA phosphodiesterase 1 within mitochondria. *Sci. Rep.* **8**, 4304 (2018).
- S.-C. Chiang, M. Meagher, N. Kassouf, M. Hafezparast, P. J. McKinnon, R. Haywood, S. F. El-Khamisy, Mitochondrial protein-linked DNA breaks perturb mitochondrial gene transcription and trigger free radical-induced DNA damage. *Sci. Adv.* **3**, e1602506 (2017).
- K. V. Inamdar, J. J. Pouliot, T. Zhou, S. P. Lees-Miller, A. Rasouli-Nia, L. F. Povirk, Conversion of phosphoglycolate to phosphate termini on 3' overhangs of DNA double strand breaks by the human tyrosyl-DNA phosphodiesterase hTdp1. *J. Biol. Chem.* **277**, 27162–27168 (2002).
- H. Interthal, H. J. Chen, J. J. Champoux, Human Tdp1 cleaves a broad spectrum of substrates including phosphoamide linkages. *J. Biol. Chem.* **280**, 36518–36528 (2005).
- T. Zhou, J. W. Lee, H. Tatavarthi, J. R. Lupski, K. Valerie, L. F. Povirk, Deficiency in 3'-phosphoglycolate processing in human cells with a hereditary mutation in tyrosyl-DNA phosphodiesterase (TDP1). *Nucleic Acids Res.* **33**, 289–297 (2005).
- S. B. Hassine, B. Arcangioli, Tdp1 protects against oxidative DNA damage in non-dividing fission yeast. *EMBO J.* **28**, 632–640 (2009).
- W. Zhang, X. Hu, Q. Shen, D. Xing, Mitochondria-specific drug release and reactive oxygen species burst induced by polyprodrug nanoreactors can enhance chemotherapy. *Nat. Commun.* **10**, 1704 (2019).
- S.-y. N. Huang, J. Murai, I. Dalla Rosa, T. S. Dexheimer, A. Naumova, W. H. Gmeiner, Y. Pommier, TDP1 repairs nuclear and mitochondrial DNA damage induced by chain-terminating anticancer and antiviral nucleoside analogs. *Nucleic Acids Res.* **41**, 7793–7803 (2013).
- S.-C. Chiang, J. Carroll, S. F. El-Khamisy, TDP1 serine 81 promotes interaction with DNA ligase III α and facilitates cell survival following DNA damage. *Cell Cycle* **9**, 588–595 (2014).
- J. J. R. Hudson, S.-C. Chiang, O. S. Wells, C. Rookyard, S. F. El-Khamisy, SUMO modification of the neuroprotective protein TDP1 facilitates chromosomal single-strand break repair. *Nat. Commun.* **3**, 733 (2012).
- B. B. Das, S.-y. N. Huang, J. Murai, I. Rehman, J.-C. Amé, S. Sengupta, S. K. Das, P. Majumdar, H. Zhang, D. Biard, PARP1-TDP1 coupling for the repair of topoisomerase I-induced DNA damage. *Nucleic Acids Res.* **42**, 4435–4449 (2014).
- I. Rehman, S. M. Basu, S. K. Das, S. Bhattacharjee, A. Ghosh, Y. Pommier, B. B. Das, PRMT5-mediated arginine methylation of TDP1 for the repair of topoisomerase I covalent complexes. *Nucleic Acids Res.* **46**, 5601–5617 (2018).
- C. Liao, R. Beveridge, J. J. Hudson, J. D. Parker, S.-C. Chiang, S. Ray, M. E. Ashour, I. Sudbery, M. J. Dickman, S. F. El-Khamisy, UCHL3 regulates topoisomerase-induced chromosomal break repair by controlling TDP1 proteostasis. *Cell Rep.* **23**, 3352–3365 (2018).
- D. C. Wallace, A mitochondrial paradigm of metabolic and degenerative diseases, aging, and cancer: A dawn for evolutionary medicine. *Annu. Rev. Genet.* **39**, 359–407 (2005).
- I. J. Holt, Mitochondrial DNA replication and repair: All a flap. *Trends Biochem. Sci.* **34**, 358–365 (2009).
- D. C. Chan, Mitochondria: Dynamic organelles in disease, aging, and development. *Cell* **125**, 1241–1252 (2006).
- R. J. Youle, A. M. Van Der Bliek, Mitochondrial fission, fusion, and stress. *Science* **337**, 1062–1065 (2012).
- H. Chen, M. Vermulst, Y. E. Wang, A. Chomyn, T. A. Prolla, J. M. McCaffery, D. C. Chan, Mitochondrial fusion is required for mtDNA stability in skeletal muscle and tolerance of mtDNA mutations. *Cell* **141**, 280–289 (2010).
- T. Lieber, S. P. Jeedigunta, J. M. Palozzi, R. Lehmann, T. R. Hurd, Mitochondrial fragmentation drives selective removal of deleterious mtDNA in the germline. *Nature* **570**, 380–384 (2019).
- S.-J. Kim, M. Khan, J. Quan, A. Till, S. Subramani, A. Siddiqui, Hepatitis B virus disrupts mitochondrial dynamics: Induces fission and mitophagy to attenuate apoptosis. *PLOS Pathog.* **9**, e1003722 (2013).

37. R. J. Youle, D. P. Narendra, Mechanisms of mitophagy. *Nat. Rev. Mol. Cell Biol.* **12**, 9–14 (2011).
38. D. C. Rubinsztein, C. F. Bento, V. Deretic, Therapeutic targeting of autophagy in neurodegenerative and infectious diseases. *J. Exp. Med.* **212**, 979–990 (2015).
39. E. S. Chocron, E. Munkácsy, A. M. Pickering, Cause or casualty: The role of mitochondrial DNA in aging and age-associated disease. *Biochim. Biophys. Acta Mol. Basis Dis.* **1865**, 285–297 (2019).
40. F. M. Yakes, B. Van Houten, Mitochondrial DNA damage is more extensive and persists longer than nuclear DNA damage in human cells following oxidative stress. *Proc. Natl. Acad. Sci. U.S.A.* **94**, 514–519 (1997).
41. C. Richter, J.-W. Park, B. N. Ames, Normal oxidative damage to mitochondrial and nuclear DNA is extensive. *Proc. Natl. Acad. Sci. U.S.A.* **85**, 6465–6467 (1988).
42. M. Scheibye-Knudsen, E. F. Fang, D. L. Croteau, D. M. Wilson III, V. A. Bohr, Protecting the mitochondrial powerhouse. *Trends Cell Biol.* **25**, 158–170 (2015).
43. N. C. de Souza-Pinto, D. M. Wilson, T. V. Stevensner, V. A. Bohr, Mitochondrial DNA, base excision repair and neurodegeneration. *DNA Repair* **7**, 1098–1109 (2008).
44. Y. Pommier, Drugging topoisomerases: Lessons and challenges. *ACS Chem. Biol.* **8**, 82–95 (2013).
45. A. Mallick, M. M. Kuman, A. Ghosh, B. B. Das, S. Basu, Cerberus nanoparticles: Cotargeting of mitochondrial DNA and mitochondrial topoisomerase I in breast cancer cells. *ACS Appl. Nano Mater.* **1**, 2195–2205 (2018).
46. H. Zhang, Y. Pommier, Mitochondrial topoisomerase I sites in the regulatory D-loop region of mitochondrial DNA. *Biochemistry* **47**, 11196–11203 (2008).
47. S. Khiati, Y. Seol, K. Agama, I. Dalla Rosa, S. Agrawal, H. Zhang, K. Neuman, Y. Pommier, Poisoning of mitochondrial topoisomerase I by lamellarin D. *Mol. Pharmacol.* **86**, 193–199 (2014).
48. I. Dalla Rosa, S.-y. N. Huang, K. Agama, S. Khiati, H. Zhang, Y. Pommier, Mapping topoisomerase sites in mitochondrial DNA with a poisonous mitochondrial topoisomerase I (Top1mt). *J. Biol. Chem.* **289**, 18595–18602 (2014).
49. M. Karbowski, K. L. Norris, M. M. Cleland, S.-Y. Jeong, R. J. Youle, Role of Bax and Bak in mitochondrial morphogenesis. *Nature* **443**, 658–662 (2006).
50. S. Dingley, K. A. Chapman, M. J. Falk, in *Mitochondrial Disorders* (Springer, 2012), pp. 231–239.
51. C. Ploumi, I. Daskalaki, N. Tavernarakis, Mitochondrial biogenesis and clearance: A balancing act. *FEBS J.* **284**, 183–195 (2016).
52. C. Douarre, C. Sourbier, I. Dalla Rosa, B. B. Das, C. E. Redon, H. Zhang, L. Neckers, Y. Pommier, Mitochondrial topoisomerase I is critical for mitochondrial integrity and cellular energy metabolism. *PLOS ONE* **7**, e41094 (2012).
53. L. Galluzzi, E. H. Baehrecke, A. Ballabio, P. Boya, J. M. Bravo-San Pedro, F. Cecconi, A. M. Choi, C. T. Chu, P. Codogno, M. I. Colombo, A. M. Cuervo, J. Debnath, V. Deretic, I. Dikic, E. L. Eskelinen, G. M. Fimia, S. Fulda, D. A. Gewirtz, D. R. Green, M. Hansen, J. W. Harper, M. Jäättelä, T. Johansen, G. Juhasz, A. C. Kimmelman, C. Kraft, N. T. Ktistakis, S. Kumar, B. Levine, C. Lopez-Otin, F. Madeo, S. Martens, J. Martinez, A. Melendez, N. Mizushima, C. Münz, L. O. Murphy, J. M. Penninger, M. Piacentini, F. Reggiori, D. C. Rubinsztein, K. M. Ryan, L. Santambrogio, L. Scorrano, A. K. Simon, H. U. Simon, A. Simonsen, N. Tavernarakis, S. A. Tooze, T. Yoshimori, J. Yuan, Z. Yue, Q. Zhong, G. Kroemer, Molecular definitions of autophagy and related processes. *EMBO J.* **36**, 1811–1836 (2017).
54. P. Boya, F. Reggiori, P. Codogno, Emerging regulation and functions of autophagy. *Nat. Cell Biol.* **15**, 713–720 (2013).
55. N. Mizushima, T. Yoshimori, B. Levine, Methods in mammalian autophagy research. *Cell* **140**, 313–326 (2010).
56. D. C. Rubinsztein, A. M. Cuervo, B. Ravikumar, S. Sarkar, V. I. Korolchuk, S. Kaushik, D. J. Klionsky, In search of an “autophagometer”. *Autophagy* **5**, 585–589 (2009).
57. H. Zhang, J. M. Barceló, B. Lee, G. Kohlhaagen, D. B. Zimonjic, N. C. Popescu, Y. Pommier, Human mitochondrial topoisomerase I. *Proc. Natl. Acad. Sci. U.S.A.* **98**, 10608–10613 (2001).
58. I. Dalla Rosa, H. Zhang, S. Khiati, X. Wu, Y. Pommier, Transcription profiling suggests that mitochondrial topoisomerase IB acts as a topological barrier and regulator of mitochondrial DNA transcription. *J. Biol. Chem.* **292**, 20162–20172 (2017).
59. H. Zhang, Y.-W. Zhang, T. Yasukawa, I. Dalla Rosa, S. Khiati, Y. Pommier, Increased negative supercoiling of mtDNA in *TOP1mt* knockout mice and presence of topoisomerases II α and II β in vertebrate mitochondria. *Nucleic Acids Res.* **42**, 7259–7267 (2014).
60. Y. Pommier, J. M. Barcelo, V. A. Rao, O. Sordet, A. G. Jobson, L. Thibaut, Z. H. Miao, J. A. Seiler, H. Zhang, C. Marchand, K. Agama, J. L. Nitiss, C. Redon, Repair of topoisomerase I-mediated DNA damage. *Prog. Nucleic Acid Res. Mol. Biol.* **81**, 179–229 (2006).
61. O. Rothfuss, T. Gasser, N. Patenge, Analysis of differential DNA damage in the mitochondrial genome employing a semi-long run real-time PCR approach. *Nucleic Acids Res.* **38**, e24 (2009).
62. S. C. Johnson, P. S. Rabinovitch, M. Kaeblerlein, mTOR is a key modulator of ageing and age-related disease. *Nature* **493**, 338–345 (2013).
63. S. K. Das, I. Rehman, A. Ghosh, S. Sengupta, P. Majumdar, B. Jana, B. B. Das, Poly (ADP-ribose) polymers regulate DNA topoisomerase I (Top1) nuclear dynamics and camptothecin sensitivity in living cells. *Nucleic Acids Res.* **44**, 8363–8375 (2016).
64. B. Kundu, S. K. Das, S. Paul Chowdhuri, S. Pal, D. Sarkar, A. Ghosh, A. Mukherjee, D. Bhattacharya, B. B. Das, A. Talukdar, Discovery and mechanistic study of tailor-made quinoline derivatives as topoisomerase 1 poison with potent anticancer activity. *J. Med. Chem.* **62**, 3428–3446 (2019).
65. S. K. Das, A. Ghosh, S. Paul Chowdhuri, N. Halder, I. Rehman, S. Sengupta, K. C. Sahoo, H. Rath, B. B. Das, Neutral porphyrin derivative exerts anticancer activity by targeting cellular topoisomerase I (Top1) and promotes apoptotic cell death without stabilizing Top1-DNA cleavage complexes. *J. Med. Chem.* **61**, 804–817 (2018).
66. S. Khiati, I. Dalla Rosa, C. Sourbier, X. Ma, V. A. Rao, L. M. Neckers, H. Zhang, Y. Pommier, Mitochondrial topoisomerase I (Top1mt) is a novel limiting factor of doxorubicin cardiotoxicity. *Clin. Cancer Res.* **20**, 4873–4881 (2014).

Acknowledgments: We thank Y. Pommier of the NCI, NIH, USA, for the reagents and help during the study. We are also thankful to C. Austin of the Institute for Cell and Molecular Biosciences, Newcastle University, UK, for critically reading the manuscript. **Funding:** B.B.D.'s team was supported by a Wellcome Trust/DBT India alliance intermediate fellowship grant (award no. IA/I/13/1/500888), a DST-SERB core research grant (EMR/2017/001652), and the Indian Association for the Cultivation of Science intramural fund. A.G. and S.B. are the recipients of CSIR-NET Senior and Junior Research Fellowship, respectively, in India. A.M. and S.B. thank CSIR-UGC doctoral fellowship and DST-Nanomission [SB/NM/NB-1083/2017 (G)], respectively, for financial support. B.B.D. is a Wellcome Trust/DBT India alliance intermediate fellow. **Author contributions:** A.G., S.B., S.P.C., A.M., I.R., and S.B. performed the experiments. A.G. and B.B.D. designed and analyzed the data and wrote the manuscript. B.B.D. provided supervision. **Competing interests:** The authors declare that they have no competing interests. **Data and materials availability:** All data needed to evaluate the conclusions in the paper are present in the paper and/or the Supplementary Materials. Additional data related to this paper may be requested from the authors.

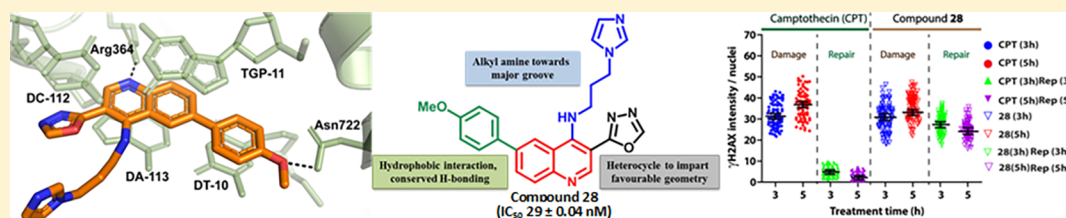
Submitted 9 May 2019
Accepted 17 September 2019
Published 6 November 2019
10.1126/sciadv.aax9778

Citation: A. Ghosh, S. Bhattacharjee, S. P. Chowdhuri, A. Mallick, I. Rehman, S. Basu, B. B. Das, SCAN1-TDP1 trapping on mitochondrial DNA promotes mitochondrial dysfunction and mitophagy. *Sci. Adv.* **5**, eaax9778 (2019).

Discovery and Mechanistic Study of Tailor-Made Quinoline Derivatives as Topoisomerase 1 Poison with Potent Anticancer Activity

Biswajit Kundu,^{†,||} Subhendu K. Das,^{‡,||} Srijita Paul Chowdhuri,^{‡,||} Sourav Pal,^{†,§} Dipayan Sarkar,^{†,§} Arijit Ghosh,[‡] Ayan Mukherjee,^{†,§} Debomita Bhattacharya,[†] Benu Brata Das,^{*,‡,§} and Arindam Talukdar^{*,†,||}[†]Department of Organic and Medicinal Chemistry, CSIR-Indian Institute of Chemical Biology, 4 Raja S. C. Mullick Road, Kolkata 700032, West Bengal, India[‡]Laboratory of Molecular Biology, School of Biological Sciences; Indian Association for the Cultivation of Science, 2A & 2B, Raja S. C. Mullick Road, Kolkata, 700032 West Bengal, India[§]Academy of Scientific and Innovative Research, Kolkata 700032, West Bengal, India

Supporting Information



ABSTRACT: To overcome chemical limitations of camptothecin (CPT), we report design, synthesis, and validation of a quinoline-based novel class of topoisomerase 1 (Top1) inhibitors and establish that compound 28 (*N*-(3-(1*H*-imidazol-1-yl)propyl)-6-(4-methoxyphenyl)-3-(1,3,4-oxadiazol-2-yl)quinolin-4-amine) exhibits the highest potency in inhibiting human Top1 activity with an IC_{50} value of 29 ± 0.04 nM. Compound 28 traps Top1–DNA cleavage complexes (Top1ccs) both in the in vitro cleavage assays and in live cells. Point mutation of Top1-N722S fails to trap compound 28-induced Top1cc because of its inability to form a hydrogen bond with compound 28. Unlike CPT, compound 28 shows excellent plasma serum stability and is not a substrate of P-glycoprotein 1 (permeability glycoprotein) advancing its potential anticancer activity. Finally, we provide evidence that compound 28 overcomes the chemical instability of CPT in human breast adenocarcinoma cells through generation of persistent and less reversible Top1cc-induced DNA double-strand breaks as detected by γ H2AX foci immunostaining after 5 h of drug removal.

INTRODUCTION

Topoisomerases are ubiquitous enzymes, which are indispensable for relaxing the topological constraints arising during the DNA metabolic processes of replication, transcription, and chromatin remodeling.^{1–4} Human topoisomerase 1 (HTop1) creates a single-stranded nick onto the DNA by a nucleophilic attack on the DNA phosphodiester bond to form a “cleavage complex” in which the enzyme is covalently linked to the 3' end of the broken DNA strand (Top1–DNA cleavage complexes, Top1ccs). This is then followed by a “controlled rotation” of the broken scissile strand around the intact strand, resulting in the relaxation of the DNA superhelical tension. Eventually, the 5' end of the scissile strand mediates a nucleophilic attack on the phosphotyrosyl–DNA phosphodiester to religate the DNA and release the enzyme, which ends the catalytic cycle of the enzyme.^{5,6} Trapped Top1ccs generate detrimental lesions, which lead to the formation of DNA double-strand breaks (DSBs) upon collision with ongoing replication forks and/or transcription machinery and are

accountable for the killing of proliferating malignant cancer cells.^{2,7–9}

There are two types of topoisomerase inhibitors, which include catalytic inhibitors and poisons.^{2,5,10,11} Catalytic inhibitors directly bind with the free topoisomerase and inhibit its catalytic activity.^{12,13} While poisons reveal their anticancer activity by selectively trapping the Top1–DNA covalent cleavage complexes^{9,14,15} inside cells, which include camptothecin (CPT)¹⁶ and its clinical derivatives as well as several non-CPT Top1 poisons including indenoisoquinolines,^{17,18} indolocarbazoles,¹⁹ and thiohydantoin²⁰ derivatives. Clinical derivatives of CPT such as topotecan and irinotecan are used for advanced colorectal carcinomas and ovarian cancers. However, CPT and its derivatives suffer from dose-limiting toxicity, resulting in severe diarrhea and neutropenia, rapidly inactivated in plasma because of hydrolysis of lactone E-ring

Received: December 11, 2018

Published: March 21, 2019

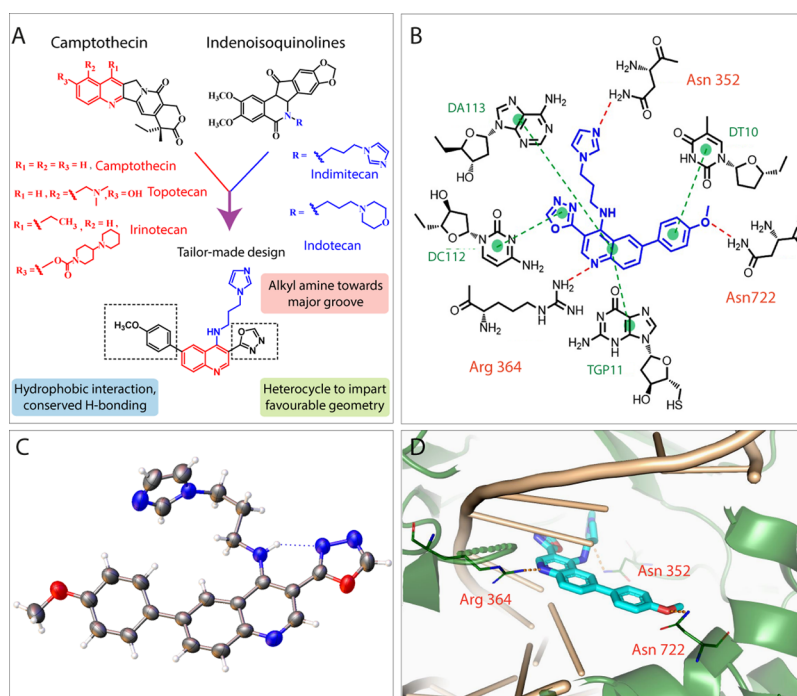


Figure 1. (A) Design of tailor-made analogue conceived from the structural features of known ligand and analysis of the active site; (B) 2D binding interactions of compound 28 with the important amino acid residues and base pairs. Red dotted lines indicate hydrogen bond and green dotted lines indicate π - π stacking interaction; (C) X-ray crystal structure of compound 28; (D) hypothetical binding model of the ternary complex of human Top1-DNA-28. The structure was generated from the crystal structure of Top1-DNA-CPT (PDB ID: 1T8I).

and binding of the ensuing hydroxyl acid to plasma proteins, and finally accumulate resistance in the topoisomerase 1 (Top1) gene.^{6,15} CPT was also found to be a substrate of permeability glycoprotein (Pgp).²¹ Moreover, irinotecan is a prodrug, which requires a carboxylesterase enzyme to convert into an active metabolite.²² Recent advances in developing a non-CPT Top1-targeted drug lead to the discovery of indenoisoquinolines (indotecan and indimitecan), which are in clinical trials for treatment in adults with solid tumors and lymphomas.^{15,22,23}

Here, we report the design, synthesis, mechanism study, and validation of a novel class of Top1 poisons based on the quinoline core, identified through the structural features of known ligands (CPT, topotecan, irinotecan, and indenoisoquinolines) that bind through the network of interactions in the active site of human Top1 enzyme as revealed by cocrystal structures^{18,24–29} (Figure 1A) for potent anticancer activity. Compound 28-mediated induction of Top1cc formation in live cells was substantiated by fluorescence recovery after photobleaching (FRAP) assays. We also show that Top1-N722^{30,31} is critical for the compound's in vivo trapping of Top1cc in cancer cells treated with compound 28. We provide compelling in vitro absorption, distribution, metabolism, and excretion (ADME), biochemical, and cellular evidence that advocate compound 28 as a potential anticancer agent.

CHEMISTRY

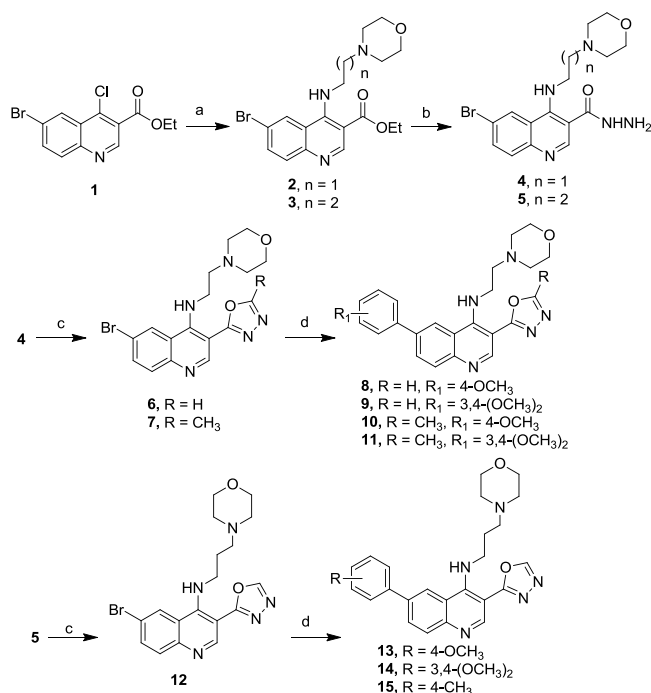
Compound 1 was treated with suitable aminoalkyl amines in the presence of a base [*N,N*-diisopropylethylamine (DIPEA)] in 1,4-dioxane solvent to afford compounds 2 and 3 in excellent yield. Compound 2 or 3 was dissolved in ethanol and treated with the solution of hydrazine monohydrate to obtain compounds 4 and 5. Compound 6 was prepared by heating compound 4 with triethyl orthoformate at 110 °C for 12 h.

Similarly, compound 4 was refluxed with triethyl orthoacetate in ethanol for 8 h to obtain 7. Compound 4 was subjected to Suzuki coupling reaction with suitable boronic acids to get compounds 8–11. A similar Suzuki reaction of 5 with the respective boronic acid provided compounds 13–15 (Scheme 1). By following the similar reaction sequence (Scheme 2), imidazole analogues were produced. Finally, the Suzuki coupling reaction was performed to produce a series of compounds (22–34).

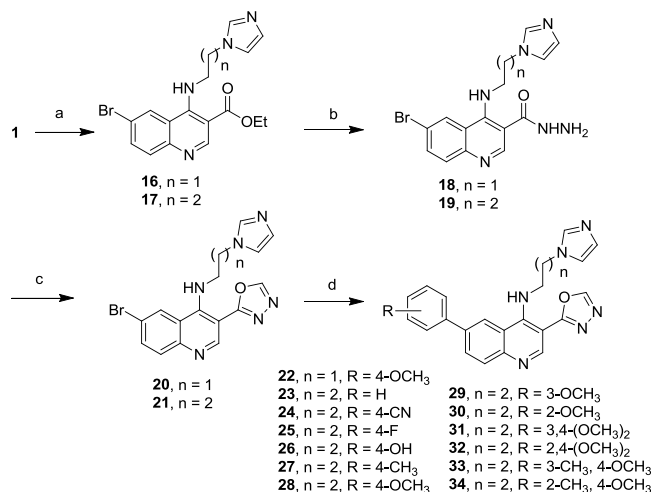
In Scheme 3, compound 19 was converted to oxadiazol-2-amine derivative 35 and oxadiazol-5-methyl derivative 37 by treating with cyanogen bromide in methanol and triethyl orthoacetate in ethanol, respectively, under refluxing condition. Suzuki reaction of 35 and 37 with 2-(4-methoxyphenyl)-boronic ester provided compounds 36 and 38, respectively. Similar Suzuki reaction of 17 with the respective boronic acid provided compounds 39 and 40. By following the similar reaction sequence in Scheme 1, compound 1 was converted to methylamine derivative 41, followed by hydrazine derivative 42. Subsequent oxadiazole formation with triethyl orthoformate leads to compound 43, which on Suzuki coupling with 2-(4-methoxyphenyl)boronic ester provided compound 44. All compounds subjected to assay were checked for >95% purity by high-performance liquid chromatography (HPLC).

RESULTS AND DISCUSSION

Design of the Top1 Inhibitor. The basis of design has been depicted in Figure 1A or 1B. As CPT and its clinically approved derivatives topotecan and irinotecan suffer from several limitations, we embarked on the discovery of “non-CPT” Top1 poisons^{21,32} with improved efficacy. We initiated our design from the quinoline core, which is also shared by CPT and its clinically approved derivatives topotecan and irinotecan (Figure 1A). The substitution pattern on the

Scheme 1^a

^aReagents and conditions: (a) 2-morpholinoethanamine (for 2) or 3-morpholinopropan-1-amine (for 3), DIPEA, 1,4-dioxane, rt, 12 h; (b) hydrazine monohydrate, EtOH, rt, 8–12 h; (c) triethyl orthoformate, 110 °C, 12 h (for 6 and 12) or triethyl orthoacetate, EtOH, reflux, 8 h (for 7); (d) 2-(4-methoxyphenyl)-4,4,5,5-tetramethyl-1,3,2-dioxaborolane (for 8, 10, and 13), (3,4-dimethoxyphenyl)boronic acid (for 9, 11, and 14), *p*-tolylboronic acid (for 15), Pd(PPh₃)₄, 2 M Na₂CO₃, 1,4-dioxane, 100 °C, 8–12 h.

Scheme 2^a

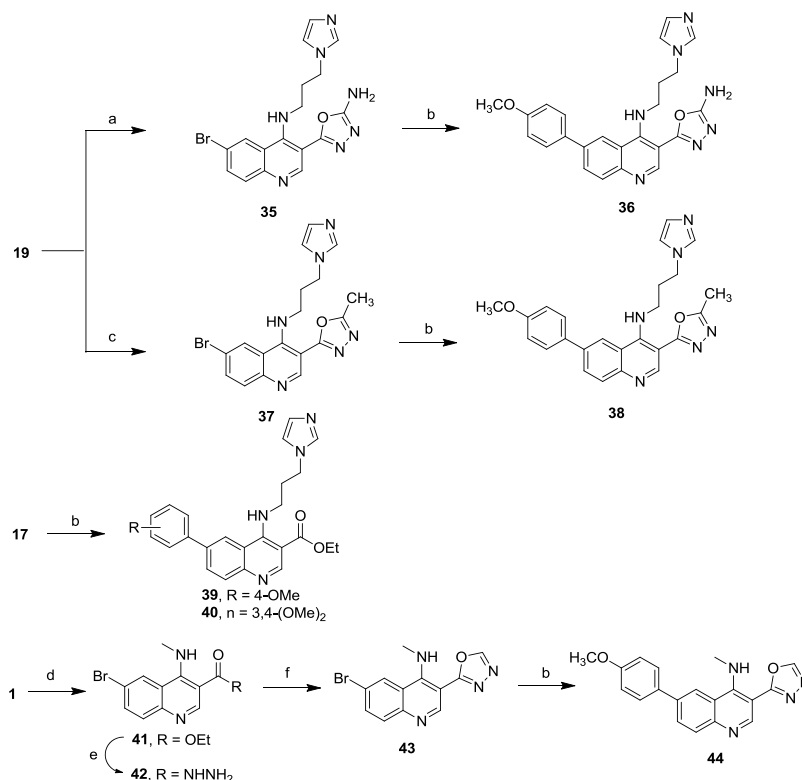
^aReagents and conditions: (a) 2-(1*H*-imidazole-1-yl)ethanamine (for 16) or 1-(3-aminopropyl)imidazole (for compound 17), DIPEA, 1,4-dioxane, rt (for 16) or 100 °C (for 17), 12 h; (b) hydrazine monohydrate, EtOH, rt, 8–12 h; (c) triethyl orthoformate, 100 °C, 12 h; (d) various boronic acids, Pd(PPh₃)₄, 2 M Na₂CO₃, 1,4-dioxane, 100 °C, 7–24 h.

quinoline core was strategically positioned at C-3, C-4, and C-6 to avail the conserved hydrogen bond interactions and hydrophobic interactions such as π - π stacking and to attain the requisite geometry to be able to stabilize the Top1–DNA

cleavage complex (Figure 1B).⁵ In the indenoisoquinoline series, the importance of a suitable alkyl amino chain containing a heteroatom has been previously validated as it is capable of serving as a hydrogen-bond acceptor into the major groove of the ternary complex.^{33–35} Also, the dimethylamine group in topotecan is predicted to project into the major groove to attain similar interactions. We presumed that similar alkyl amino chain at the C-4 position of the quinoline core will project in the major groove toward interacting residue Asn352. The alkyl chain-attached heterocycle installed at C-4 can serve a similar purpose and attain similar interactions as observed in indenoisoquinoline and CPT derivatives.³⁶ The crystal structures of the ternary complex of CPT and indenoisoquinoline revealed the importance of polycyclic rings with flat planar geometry that can accommodate in the interface of the Top1–DNA cleavage complexes and block the religation reaction. We envisioned that the strategically placed C-6-substituted aromatic ring along with a heterocycle at the C-3 position would impart requisite geometry and suitable curvature essential to attain the conserved hydrogen bond interactions as well as hydrophobic interactions such as π - π stacking for stabilizing the Top1–DNA cleavage complex (Figure 1B). As a next logical step, we explored the nature of substitution on the aromatic ring at C-6 and on heterocycles at C-3 that can modulate Top1 inhibition to identify potent Top1 poison.

Related to Top1 inhibition, half-maximal inhibitory concentration (IC₅₀) values for the designed analogues were investigated in plasmid DNA relaxation inhibition assays by using either recombinant Top1 or MCF7 cellular lysates as a source of Top1 (Table 1). We used both biochemical and cellular studies to validate the mechanism of Top1 inhibition. Further insight into the ability of the potent Top1 inhibitor (compound 28) to trap mutant Top1 at residue Asn722 was justified by FRAP assays in live cells. The accumulation and disappearance of DNA damage by the identified compounds were measured by immunological staining with phosphorylated histone H2AX (γ H2AX) under confocal microscopy. Subsequently, *in vitro* ADME studies were conducted to determine the metabolic stability and efflux property of these analogues.

Morpholine Analogues. We synthesized the first batch of compounds by keeping the alkyl-substituted morpholine group at the C-4 position, 4-methoxy and 3,4-dimethoxy phenyl groups at the C-6 position, and the oxadiazole group at C-3 (Scheme 1). The choice of substitution pattern at C-4 and C-6 positions was inspired from the structural features present in CPT derivatives and indenoisoquinoline derivatives (indotecan and indimitecan) (Figure 1A) established as Top1 poison, which are currently under clinical trials.^{15,23,34,37} Previous reports have suggested that installation of such moiety resulted in improved Top1 inhibitory activity.^{33,34} Compound 8 with two carbon morpholine groups at C-4 and the 4-methoxy group at C-6 and compound 9 with two carbon morpholine groups at C-4 and the 3,4-dimethoxy phenyl group at C-6 did not show significant Top1 inhibitory activity in the plasmid DNA relaxation assays at 10 μ M concentration (Table 1). Although 4-methoxy derivative 8 and 3,4-dimethoxy phenyl derivative 9 did not show significant inhibition at 10 μ M, at higher concentration (100 μ M) compound 8 showed 50% inhibition as compared to 9 with 20% inhibition. Installation of a methyl group at the C-5" position of the oxadiazole ring in 8 and 9 resulted in compounds 10 and 11 (Scheme 1), respectively, which also failed to show 50% Top1 inhibition

Scheme 3^a

^aReagents and conditions: (a) cyanogen bromide, MeOH, reflux, 4 h; (b) 2-(4-methoxyphenyl)-4,4,5,5-tetramethyl-1,3,2-dioxaborolane (for 36, 38, 39, and 44) or (3,4-dimethoxyphenyl)boronic acid (for 40), Pd(PPh₃)₄, 2 M Na₂CO₃, 1,4-dioxane, 100 °C, 6–12 h. (c) Triethyl orthoacetate, EtOH, reflux, 6 h; (d) methylamine, DIPEA, THF, 60 °C, 16 h; (e) hydrazine monohydrate, EtOH, rt, 12 h; (f) triethyl orthoformate, 140 °C, 14 h.

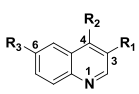
(Table 1) at 10 μ M concentration. Thereafter, we increased the chain length connected to the morpholine group at C-4 from two carbons to three carbons. Indeed, increasing the chain length in compound 13 with the 4-methoxyphenyl group at C-6 showed marked increase in Top1 inhibitory activity with an IC₅₀ value of 1.79 μ M against recombinant human Top1.^{20,38–40} However, 14 with the 3,4-dimethoxy phenyl group failed to inhibit at least 50% Top1 relaxation activity (Table 1) at 10 μ M concentration. An initial comparison between 8, 9, 13, and 14 suggests that combination of three carbon-chain lengths at C-4 with the monosubstitution of the 4-methoxyphenyl group at C-6 reinforces Top1 inhibitory activity. The importance of the 4-methoxyphenyl group at C-6 was further substantiated by replacement of the –OCH₃ group present at the C-6-substituted phenyl ring by a methyl group (–CH₃) in compound 15, leading to loss of activity. Taken together, the initial studies indicate that morpholine-substituted propylamine at C-4 and the 4-methoxyphenyl group at the C-6 position are two important features that can trigger Top1 inhibition in the quinoline core.

Imidazole Analogues. As both morpholine and imidazole groups are present in indotecan, indimitecan, and indenoisoquinolines derivatives, we replaced the C-4 substituents containing a morpholine moiety with imidazole in our newly synthesized analogues and investigated the Top1 inhibition. A series of compounds were prepared bearing an imidazole group with varying chain length at C-4, substituted phenyl group at C-6, and oxadiazole ring at C-3 (Scheme 2). On the basis of our previous observation which showed the importance of

morpholine-substituted propylamine at C-4, it seemed prudent to keep the chain length of the flexible aminoalkyl group to three carbon linkers. A series of compounds were prepared by substituting the C-4' position of the phenyl group at C-6 with cyano (24), fluoro (25), hydroxyl (26), methyl (27), and methoxy (28) group (Scheme 2). Compounds with cyano (24), fluoro (25), and hydroxyl (26) modifications failed to show significant Top1 inhibitory activity in plasmid DNA relaxation assays at 10 μ M (Table 1). Remarkably, compound 28 bearing a 4-methoxy group at C-4' showed the highest ability to inhibit recombinant Top1 activity with an IC₅₀ of 29 nM in the plasmid DNA relaxation assay (Table 1).¹² Notably, compound 27 with 4-methyl substitution at the C-4' position of the phenyl group also showed Top1 inhibitory activity with an IC₅₀ value of 1.06 μ M in Top1 inhibition. Installing the unsubstituted phenyl group at C-6 in 23 resulted in a sharp decrease in Top1 inhibitory activity (40% inhibition at 10 μ M). A direct comparison of the activities of morpholine (13 and 15) and imidazole series (23 and 27) shows that the imidazole-substituted propylamine at C-4 along with the 4-methoxyphenyl group at the C-6 position confers increased Top1 inhibitory activity.

For a better understanding, hypothetical binding model of 28–Top1–DNA ternary complex was constructed with the human Top1 crystal structure (PDB code 1T8I). The oxygen atom of the methoxy group forms a hydrogen bonding interaction with Asn722 in the C-terminal domain of Top1. Asn722 is an important amino acid responsible for binding of the ligands with Top1 cleavage complexes.⁴¹ The nitrogen

Table 1. Analysis of Human Top1 Inhibition in Plasmid DNA Relaxation Assays with Recombinant Top1 (In vitro) or MCF7 Cell Lysates (Ex vivo)



Comp	R ₁	R ₂	R ₃	Top1 inhibition IC ₅₀ (μM)		Activity index ^a
				In vitro	Ex vivo	
CPT				0.025	2.5	++++
Topotecan				0.021	1.8	++++
8				>10	NT ^b	+
9				>10	NT	+
10				>10	NT	+
11				>10	NT	+
13				1.79 ± 0.62	2.51 ± 0.39	+++
14				>10	NT	+
15				>10	NT	+
22				>10	NT	+
23				>10	NT	+
24				>10	NT	+
25				>10	NT	+
26				>10	NT	+
27				1.06±0.417	3.75±0.102	+++
28				0.029±0.004	2.74±0.314	++++
29				1.054±0.792	4.11±0.339	+++
30				>10	NT	+
31				>10	NT	+
32				>10	NT	+
33				2.36±0.884	3±0.98	++
34				>10	NT	+
36				>10	NT	+
38				>10	NT	+
39				>10	NT	+
40				>10	NT	+
44				>10	NT	+

^aCompound-induced in vitro inhibition of Top1 with scores given according to the following system based on the activity of CPT: + = IC₅₀ > 10 μM; ++ = IC₅₀ in between 2 and 10 μM; +++ = IC₅₀ in between 100 nM and 2 μM; ++++ = IC₅₀ < 100 nM. ^bNT = Not tested.

atom in the quinoline ring also forms a hydrogen bond with Arg364, and the three carbon alkyl chain length is ideal for the imidazole ring to attain hydrogen bond interaction with Asn352. The aminopropylamino chain at C-4 and the 4-methoxyphenyl group substitution at the C-6 position of the quinoline ring come in contact with Top1cc and DNA, which may be attributed to Top1 inhibition (Figure 1B,D). In keeping with the docking analysis (Figure 1B,D), the X-ray

crystal structure of compound 28 (Figure 1C) reveals that it has favorable geometry to fit into the 3' end of the broken DNA strand covalently linked with Top1 and the free 5'-OH end to inhibit Top1 religation activity.⁴²

To further demonstrate the importance of substitution at C-4' in compound 28, we synthesized positional analogues of 28 having -OCH₃ group at the C-2' (30) and C-3' (29) positions of the phenyl ring (Scheme 2), which were tested for

Top1 inhibitory activity. Interestingly, changing the position of the $-\text{OCH}_3$ group from C-4' to C-3' results in a slight decrease in Top1 inhibition as compound **29** shows an IC_{50} value of $1.05 \mu\text{M}$ (Table 1). These findings were noteworthy as **29** showed that suitable substitution at the C-3' position can also confer Top1 inhibition. However, compound **30** failed to show any significant Top1 inhibition at $10 \mu\text{M}$. These results underline the importance of suitable substitution at C-4' and C-3' of the phenyl group at the C-6 position of the quinoline core required for Top1 inhibition. The result prompted us to revisit the disubstitution pattern on the phenyl group at the C-6 position. In the next series of disubstituted compounds (**31**, **32**, **33**, and **34**), the position of the $-\text{OCH}_3$ group was fixed at C-4' and another $-\text{OCH}_3$ or $-\text{CH}_3$ was introduced at C-2' and C-3' positions (Scheme 2). Compounds **31** and **32** with dimethoxy substitution on the phenyl group at C-6 failed to show significant Top1 inhibition at $10 \mu\text{M}$ (Table 1). A similar result was obtained for morpholine analogue **14**. Interestingly, replacing one of the $-\text{OCH}_3$ groups at the 3' position with $-\text{CH}_3$ in **33** provided best Top1 inhibition (IC_{50} value $2.36 \mu\text{M}$) among disubstituted phenyl groups at C-6 (Table 1).

In the next development, by keeping the optimized features at C-4 and C-6 positions constant, a limited survey of the C-5'' position of the oxadiazole ring was performed by incorporating small hydrophilic and hydrophobic groups to determine the nature of substituents that can be accommodated for modulation of Top1 inhibition. Compound **36** with a hydrophilic $-\text{NH}_2$ group resulted in a drastic fall in the inhibitory activity. Installation of a small hydrophobic $-\text{CH}_3$ group at C-5'' resulted in a similar drop in Top1 activity (compound **38**). On a similar note, substituting aminopropylamino chain at C-4 with methylamine in compound **44** fails to show any Top1 inhibitory activity at $10 \mu\text{M}$. The result validated the importance of aminopropylamino side chain at the C-4 position of the quinoline core for providing significant impact on Top1 inhibition.

Our efforts to develop an acceptable hypothetical binding model that rationalize the structure–activity relationships of all the molecules resulting from minor changes in the structure proved difficult. However, molecular modeling indicates that depending on the nature of substituents at C-3, C-4, and C-6 positions of the quinoline ring, it might be capable of forming hydrogen bond interactions with important residues such as Arg364, Asn722, and Asn352 as well as stacking interactions with DA113, DC112, TGP11, and DT10 in the ternary complex. In representative compound **22** with the flexible two-carbon linker, the molecular modeling indicated that the heteroatom present in the heterocycles was unable to form a hydrogen bond with Asn352 in the major groove (Figure S2). The result signifies the importance of the length of the flexible chain containing heterocycles. Analysis of the various poses of disubstituted compounds **31** and **33** within the ternary complex revealed that the 3,4-dimethoxy phenyl group is not orientated in the same plane as observed in compound **28**. As a result, compound **31** was unable to form a hydrogen bond with Arg364 and Asn722 along with the loss in π – π stacking interactions. Interestingly, compound **33** was found to attain the stacking interactions with DA113, DC112, TGP11, and DT10 along with hydrogen bond with Arg364, which signifies the importance of specific substitutions at the C-6 position of the quinoline ring.

The structure–activity relationship signifies the importance of a perfect balance of substitution patterns at C-3, C-4, and C-

6 positions in our design. All these results together indicate the robustness of our design and rationalize the highest activity of compound **28** against Top1 in plasmid relaxation activity (Table 1). Compound **28** was selected for further lead assessment and mechanistic insight.

In Vitro ADME Study. Compounds **13** and **28** with similar structural features except for the nature of the weak basic group present at the C-4 position were evaluated in a panel of in vitro ADME assays (Tables 2 and 3). Both these

Table 2. Solubility, Plasma Stability, and log *D* Results of Potent Compounds at pH 7.4

compd	aq sol ($\mu\text{g}/\text{mL}$)	plasma stability ^a	log <i>D</i> @ pH 7.40
CPT	2.5	15.70	1.74 ^b
13	28.08 ± 0.11	83.38	3.26 ± 0.01
28	30.09 ± 0.66	93.34	2.48 ± 0.04

^aMean % remaining at 2 h in human plasma. ^blog *P* value.

Table 3. Caco-2 Permeability of Compounds **13** and **28**

compd	P_{app} (10^{-6} cm/s)		efflux ratio
	apical to basal	basal to apical	
13	10.89	10.98	1.02
28	7.42	11.55	1.60

compounds were found to have moderate aqueous solubility as compared to CPT. It is noteworthy to mention that both **13** and **28** demonstrated admirable human plasma stability even after 2 h, whereas CPT due to its unstable lactone was not stable. The most active compound **28** was found to be highly stable in human plasma with 93% present after 2 h. The in vitro log *D* values of **13** and **28** are 3.26 and 2.48, respectively, which are considered to be ideal for oral absorption.^{43–45} As CPT is known to be a substrate of Pgp, we examined the Caco-2 permeability for these compounds as well as the efflux ratio to evaluate whether **13** and **28** are Pgp substrates.^{46,47} To our great satisfaction, the efflux ratios of **13** and **28** are found to be <2, which signify that these compounds are not Pgp substrates. We conclude that unlike CPT, our “tailor-made” compounds **13** and **28** are highly plasma stable with an ideal log *D* value for oral absorption and are not Pgp substrates. On the basis of ADME study^{48,49} (Tables 2 and 3) and human Top1 plasmid DNA relaxation inhibition assays (Table 1), we further extend our study with compound **28** to get mechanistic insight into Top1 inhibition and evaluate its role in the anticancer activity.

Compound 28 Poisons Human Top1–DNA Cleavage Complexes. To examine the specificity of compound **28** (Figure 2A) for Top1, we used both recombinant Top1 enzyme (Figure 2B) and endogenous Top1 from the whole cell extracts of human breast adenocarcinoma (MCF7) cells^{12,20} (Figure 2C,D). When recombinant Top1 and compound **28** were added simultaneously in the plasmid DNA relaxation assays (Figure 2B, lanes 5–9), 85–90% inhibition of Top1 could be achieved at $0.1 \mu\text{M}$ concentration of compound **28** (Figure 2B, lane 7). Next, the cellular extracts were utilized as a source of Top1 (Figure 2B) for the plasmid DNA relaxation assays (ex vivo) (Figure 2C). The utility of using whole cell extract lies in the fact that the Top1 enzyme in the extract is conserved in its native structure among a plethora of other cellular proteins. The ex vivo relaxation inhibition assays with compound **28** efficiently inhibited Top1 activity when the cellular extracts were incubated with compound **28**

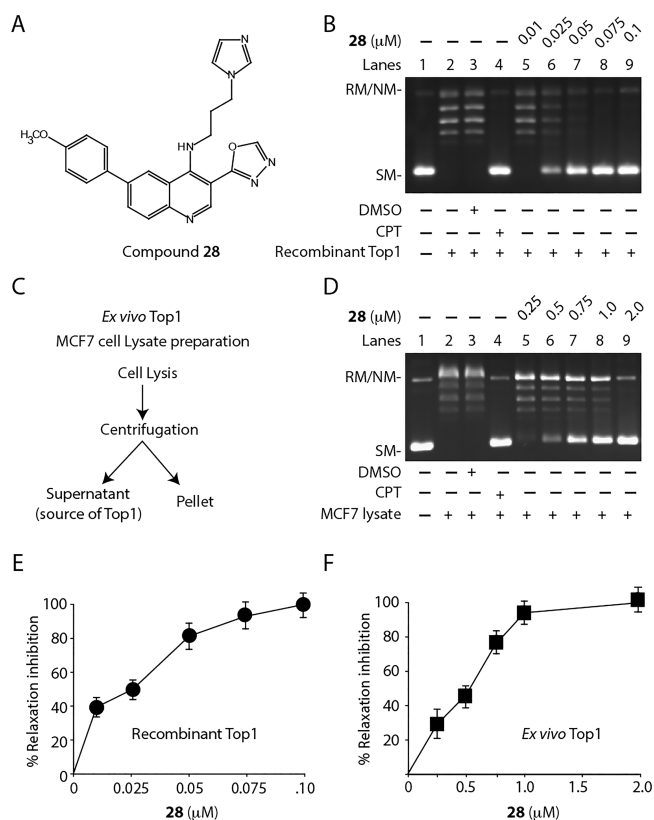


Figure 2. Inhibition of Top1-induced plasmid DNA relaxation activity by compound 28. (A) Most active compound 28. (B) Relaxation assay of supercoiled plasmid DNA using recombinant HTop1 at 3:1 molar ratio. Lane 1, pBS (SK+) DNA (90 fmol); lane 2, pBS (SK+) DNA (90 fmol) incubated with 30 fmol of recombinant Top1; lane 3, same as lane 2, additionally Top1 was incubated with 2% DMSO; lane 4, same as lane 2 but incubated simultaneously with 2 μM CPT; lanes 5–9, same as lane 2 but incubated with variable concentrations of compound 28 (as per indication) at 37 °C for 30 min. (C) Schematic representation for MCF7 whole cell lysate preparation used as the source of endogenous human Top1 for ex vivo Top1 relaxation assays. (D) Relaxation of supercoiled pBS (SK+) DNA by Top1 activity from the MCF7 cellular extract (each reaction volume contains 0.1 μg protein). Lane 1, pBS (SK+) DNA (0.3 μg); lane 2, same as lane 1, but pBS (SK+) DNA (0.3 μg) was incubated with MCF7 cell lysates; lane 3, same as lane 2 but incubated with 2% DMSO; lanes 4–9, same as lane 2, but MCF7 whole cell lysates were incubated simultaneously with 5 μM CPT or with varying concentrations of 28 (as indicated) together with plasmid DNA at 37 °C for 30 min. Positions of supercoiled monomer and nicked and relaxed monomer are indicated. (E,F) Quantitative representation of Top1 DNA relaxation inhibition (%) at variable concentrations of 28 as shown in (B,D). Recombinant Top1 (E) or endogenous Top1 from cellular extracts (F). All the experiments were performed in triplicate and expressed as the mean ± SD.

(Figure 2D, lanes 5–9) and the quantification in Figure 2E,F. Taken together, all these results indicate that compound 28 selectively inhibits human Top1, both as a recombinant enzyme (Figure 2B) and as an endogenous protein (Figure 2D), without being impaired by the pool of proteins contained in the whole cell extracts.

As both CPT and indenoisoquinolines stabilize Top1–DNA cleavable complexes (Top1cc) to inhibit Top1 activity,^{5,9,14,15,38,39,50} the mechanism of Top1 inhibition with compound 28 was investigated in the plasmid DNA cleavage assays. Closed circular DNA (form I) get converted to nicked

circular DNA (form II) by Top1 in the presence of specific inhibitors and are referred to as “cleavage complex” (Figure 3A, right panel). Figure 3A shows that compound 28 also stabilizes Top1cc formation like CPT, suggesting that compound 28 acts as a Top1 poison. We further confirmed that compound 28 is capable of stabilizing Top1cc in single turnover equilibrium cleavage assays (Figure 3B, lanes 3–8) by allowing recombinant Top1 to react with 25-mer duplex oligonucleotides modified to harbor preferred Top1 cleavage sites in the presence of indicated concentrations of compound 28 or CPT consistent with plasmid DNA cleavage assays (Figure 3A). In addition, quantification of cleavage assays (Figure 3C,D) suggests that the extent or rate of Top1–DNA cleavage complex formation (% cleavage) with compound 28 at indicated concentration is similar to CPT (Figure 3C,D). Cumulatively, our data are indicative that compound 28 is able to stabilize Top1 cleavage complexes and inhibit the religation activity with similar efficacy as that of CPT.

To investigate the ability of compound 28 to intercalate into DNA, we carried out both Top1 unwinding assays and EtBr displacement assays.^{12,40} Topoisomerase unwinding assay is based on the ability of the intercalating compounds to unwind the DNA duplex and thereby change the DNA twist. Figure 3E clearly shows that in the presence of a strong intercalative drug such as *m*-AMSA, a net negative supercoiling of the relaxed substrate DNA was induced at 50 and 200 μM concentration (Figure 3E, lanes 3 and 4). However, under similar conditions, nonintercalative compounds such as etoposide failed to show such effect at 50 and 200 μM concentrations (Figure 3E, lanes 5 and 6). Compound 28 had no effect on the topological state of the relaxed plasmid DNA at the indicated concentrations (Figure 3E, lanes 7–10), suggesting that compound 28 is not a DNA intercalator (Figure 3). Next, we further confirm that compound 28 is not a DNA intercalator by performing EtBr displacement assays. Figure 3F shows that the intercalative drug *m*-AMSA has the capability to dislodge the bound fluorophore (EtBr) at 50 μM concentration. However, nonintercalative drug such as etoposide was unable to do so. Under similar condition, compound 28 induces no displacement of fluorophore even at high concentration (200 μM) compared with the very low IC₅₀ (29 nM) of Top1 inhibition. Taken altogether, our data suggest that compound 28 is not a DNA intercalator.

Compound 28 Traps Top1 Cleavage Complexes in Live Cancer Cells. To obtain direct evidence for compound 28-mediated trapping of Top1cc (Figure 4A) in live cells, we ectopically expressed a green fluorescent-tagged human Top1 (EGFP-Top1) in MCF7 cells and tested the nuclear mobility of Top1 under live cell confocal microscopy combined with FRAP technology as described previously.^{12,51} In the absence of compound 28, FRAP recovery of EGFP-Top1 was fast (~85–90%), suggesting a large mobile population and a smaller (~10–15%) immobile population of EGFP-Top1 (Figure 4B, and the quantification in 4C; untreated). These data indicate that Top1 is mostly mobile and binds transiently with the DNA (reversible Top1cc) and are freely exchanged in the nuclear compartments.

In the presence of compound 28, the fluorescence recovery of EGFP-Top1 was markedly impeded (~55–65%) with increasing concentration of compound 28 (Figure 4B, and the quantification in 4C; (+) compound 28; 1 and 5 μM). These data suggest that compound 28 traps Top1cc on DNA in live cells like CPT,^{10,18} leading to a subsequent increase in bound/

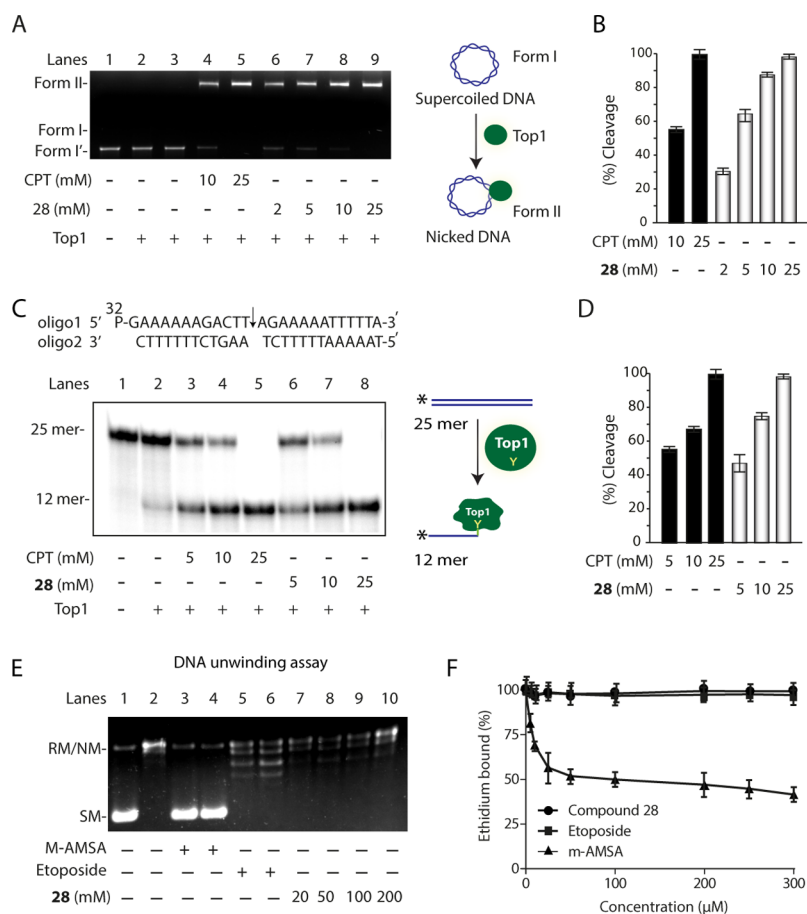


Figure 3. Compound 28-mediated trapping of Top1–DNA cleavage complexes. (A) Representative gel image depicting plasmid DNA cleavage mediated by Top1 in the presence of CPT or compound 28. Lane 1, 60 fmol of pBS (SK+) supercoiled DNA. Lanes 2–9, same as lane 1 but incubated with equal amounts of recombinant human Top1 (100 fmol) at the indicated concentrations of CPT or compound 28 or only DMSO at 37 °C for 30 min. Positions of the supercoiled substrate (form I) and nicked monomers (form II) are indicated. Schematic representation of Top1-mediated nicked DNA formation. (C) Representative gel showing Top1-mediated 25 mer duplex oligonucleotide cleavage in the presence of CPT and compound 28. Lane 1, 15 nM 5'-³²P-end labeled 25-mer duplex oligo as indicated above. Lane 2, same as lane 1 but incubated with recombinant Top1 (0.2 μ M). Lanes 3–5, same as lane 2 but incubated with an indicated concentration of CPT. Lanes 6–8, same as lane 2 but incubated with an indicated concentration of compound 28. Positions of uncleaved oligonucleotide (25-mer) and the cleavage product (12-mer oligonucleotide complexed with residual Top1) are indicated. Schematic representation of the formation of 12-mer oligonucleotide attached with Top1 in the presence of Top1 poison. Quantitative measurement of cleavage complex (Top1cc) formation (%) by CPT and compound 28 either by supercoiled DNA (B) or through oligo cleavage assay (D). All the experiments were performed three times and expressed as the mean \pm SD. (E) Compound 28 is not a DNA intercalator. Compound 28–DNA interaction as investigated by agarose gel electrophoresis in Top1 unwinding assays. Lane 1, 50 fmol of pBS (SK+) DNA. Lane 2, relaxed pBS (SK+) DNA generated by an excess of Top1. Lanes 3–6, same as lane 2 but incubated with 50 μ M *m*-amsacrine (AMSA) and 200 μ M etoposide. Lanes 7–10, same as lane 2 but incubated with 20, 50, 100, and 200 μ M of compound 28 as indicated. (F) Fluorescence-based ethidium bromide displacement assay. All samples contained 1 μ M EtBr and 5 nM calf thymus (CT) DNA. Graphical representation of EtBr bound (%) of increasing concentration (0–300 μ M) of compound 28, *m*-AMSA, and etoposide. EtBr fluorescence was monitored with an excitation wavelength of 510 nm and an emission wavelength of 590 nm.

immobile fraction of EGFP-Top1 (Figure 4B,C), which is consistent with 28-mediated stabilization of Top1cc in the *in vitro* cleavage assays (Figure 3). The molecular modeling indicates that compound 28 possibly forms a hydrogen bonding interaction with Asn722 located in the catalytic domain of HTop1, which may contribute to the stabilization of Top1 cleavage complexes with the nicked DNA (Figure 4A). To investigate this possibility, we tested the ability of compound 28 to trap mutant Top1 at residue Asn722 (EGFP-Top1^{N722S}) in live cells by using FRAP kinetic analysis [see Figure 4D,E, panel (+) 28]. Figure 4E suggests that the FRAP recovery of EGFP-Top1^{N722S} was unaffected in the presence of increasing dosage of 28 (Figure 4D,E) and was similar to no drug treatment condition (Figure 4E), suggesting that 28 failed to trap Top1cc when Asn722 is mutated to Ser.

Taken together, these data indicate that Asn722 is critical for compound 28-mediated trapping of human Top1cc.

Compound 28 Accumulates Persistent DNA DSBs Compared to CPT. As compound 28 stabilizes Top1cc *in vitro* (Figure 3) and in live cells (Figure 4), we investigated the accumulation and disappearance of DSBs in MCF7 cells treated with compound 28 by measuring γ H2AX foci formation under confocal microscopy (Figure 5), as γ H2AX is a well-defined marker for Top1-mediated DSBs.^{52–57}

Under similar condition, we detected a time-dependent increase in γ H2AX foci formation in cells treated with compound 28 for 3 and 5 h comparable with CPT-induced γ H2AX foci at similar time periods, suggesting that both compound 28 and CPT generate similar levels of DSBs at indicated time periods in MCF7 cells (Figure 5B,C).

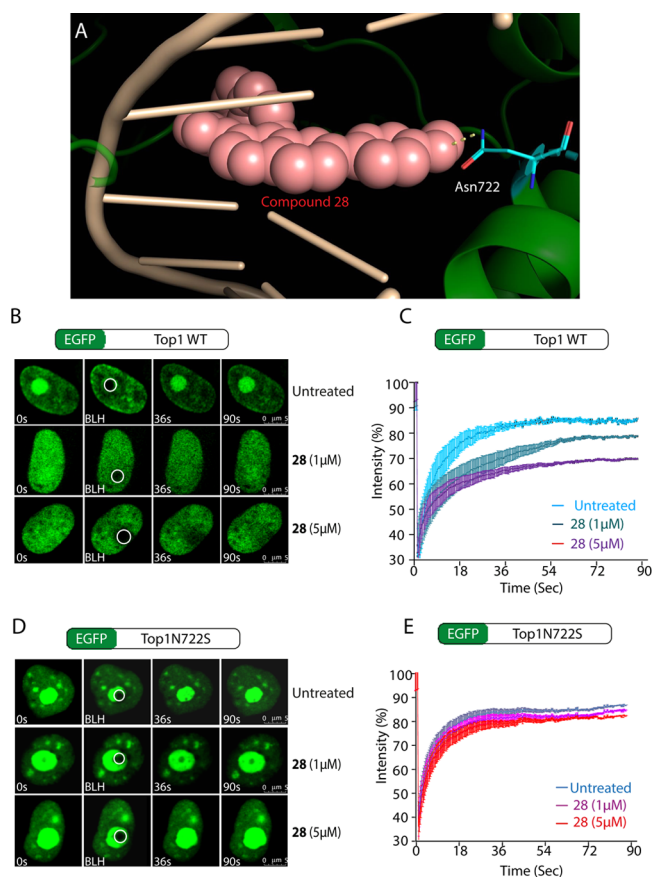


Figure 4. Compound 28-mediated stabilization of the Top1–DNA cleavage complex in live cells. (A) Space-filling model showing conservative H-bonding interaction between Asn722 and 28. (B) Compound 28 accumulates immobile/bound Top1 in the nucleus. Representative images depicting the FRAP of enhanced green fluorescent-tagged HTop1 [enhanced green fluorescent protein (EGFP)-Top1WT] transiently expressed in MCF7 cells. Cells were treated with an indicated concentration of 28 for 10 min and were analyzed by live cell spinning disk confocal microscopy and photobleaching. A subnuclear spot (ROI) indicated by a circle was bleached (BLH) for 30 ms and photographed at regular intervals of 3 ms thereafter. Successive images taken for ~90 s after bleaching illustrate fluorescence return into the bleached areas. (D) Top1N722 residue is critical for 28-induced nuclear dynamics. Representative images showing the FRAP of EGFP-Top1^{N722S} transiently expressed in MCF7 cells. Cells were treated with 28 (indicated concentration) for 10 min and were analyzed by live cell spinning disk confocal microscopy, and FRAP experiments were carried out in a similar way as with the EGFP-Top1WT. Right panels (C,E) quantification of FRAP data showing mean curves of Top1 variants in the presence and absence of 28. Error bars represent mean \pm SE ($n = 15$).

CPT-induced γ H2AX have a short half-life as they are reversible immediately after a wash,^{52,54} which is consistent with the reversal of Top1cc intermediates within minutes after washing out CPT.⁵⁸ Next, to test the ability of compound 28 to induce more persistent and less reversible DNA breaks, we investigated the disappearance of γ H2AX in cells treated with compound 28 and compared it with CPT after subsequent wash and culture in the drug-free medium for indicated time periods (Figure 5A). In Figure 5B, the right panel shows faster disappearance of γ H2AX foci after washing out CPT from media at indicated time periods (see the quantification in Figure 5C). In contrast, cells showed (3–4 fold) more

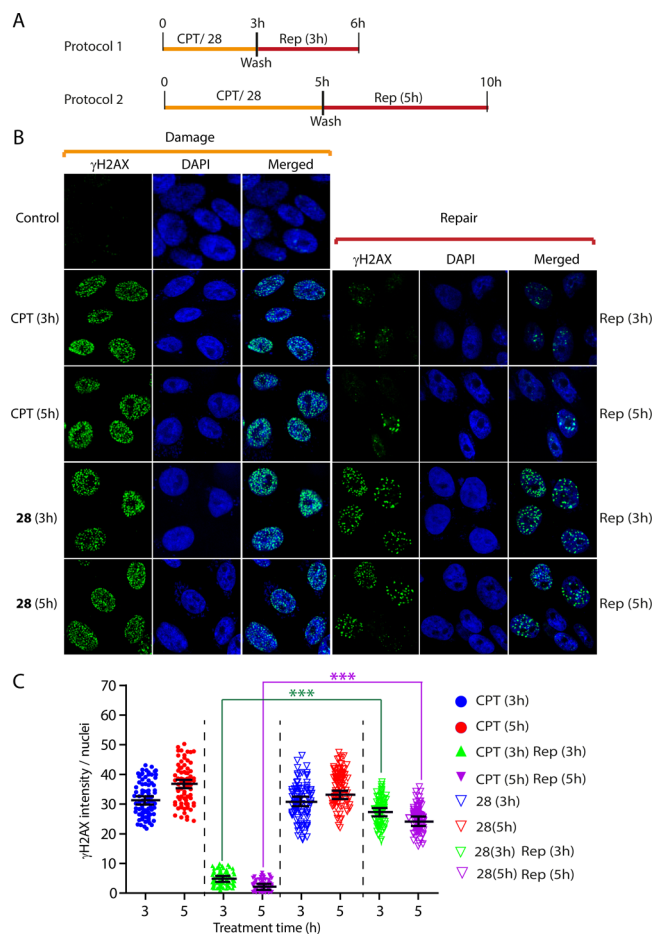


Figure 5. Compound 28 generates persistent and less reversible DNA DSBs as detected by γ H2AX staining. (A) Overview for the protocol of drug treatment and reversal in MCF7 cells. (B) Time-dependent accumulation of γ H2AX foci formation in MCF7 cells treated with compound 28 or CPT for 3 and 5 h and reversal of γ H2AX foci after drug removal for indicated times. (C) Quantification of γ H2AX intensity per nucleus after treatment and after the removal of indicated inhibitors (compound 28 or CPT) obtained from immunofluorescence confocal microscopy was calculated for 35–40 cells (mean \pm SEM) and plotted as a function of time (h).

persistent γ H2AX foci (Figure 5B, right panel and the quantification in Figure 5C) even after washing out compound 28 at the indicated time. Figure 5C further indicates that γ H2AX foci were persistent for 5 h after drug removal in compound 28-treated cells. Taken together, our data suggest that compound 28 generates more persistent and less reversible Top1cc-induced DSBs compared to CPT.

Compound 28 Exhibits Potent Anticancer Activity. Compound 28 was evaluated for its cytotoxicity in the cancer cell lines from different tissue origin.⁵² Cytotoxicity assays were performed in human breast adenocarcinoma cell lines (MCF7), human cervical cancer cell lines (HeLa), human colon carcinoma cell lines (HCT116), human ovarian adenocarcinoma cell lines (NIH:OVCAR-3), as well as noncancerous human embryonic kidney (HEK293) cells with variable concentrations of compound 28. Table S2 (Supporting Information) indicates that compound 28 revealed cytotoxicity in cancerous cells including MCF7 (IC₅₀: 2.74 μ M), HeLa (IC₅₀: 2.61 μ M), HCT116 (IC₅₀: 2.34 μ M), and

NIH:OVCAR-3 (IC_{50} : 2.35 μ M) cells compared to the noncancerous cells such as HEK293 (IC_{50} : 8.34 μ M).

TDP1 hydrolyzes the phosphodiester bond at a DNA 3'-end linked to a tyrosyl moiety of stalled Top1-DNA covalent complexes; therefore, TDP1 $^{-/-}$ cells are hypersensitive toward Top1 poisons.^{51–54,59,60} With further evidence for the poisoning of Top1cc with compound **28** and hypersensitivity in DNA repair-deficient cells, we have performed cytotoxicity assays with TDP1 $^{-/-}$ (IC_{50} : 1.02 μ M) and TDP1 $^{+/+}$ MEFs (IC_{50} : 2.91 μ M) cells in the presence of compound **28**. Table S2 indicates that TDP1 $^{-/-}$ MEFs cells were hypersensitive to compound **28**, further providing evidence that compound **28** induces cytotoxicity by stabilizing Top1cc in cells. Taken together, all data confirm that compound **28** is a potent Top1 poison and is a potential candidate as an anticancer chemotherapeutic agent.

CONCLUSIONS

As CPT and its clinically approved drugs suffer from several limitations, there is a great interest in the development of “non-CPT” Top1 poisons as anticancer agents. In the present study, we successfully report a novel class of Top1 poisons based on the quinoline core through an understanding of the structural features of ligands essential for binding in the active site. The design signifies the importance of a perfect balance of substitution patterns at C-3, C-4, and C-6 positions of the quinoline core. Most potent compound **28** stabilizes Top1cc in vitro and in live cells to inhibit the religation activity without intercalating to the DNA with similar efficacy as that of CPT. The mechanistic insight through the FRAP assay of compound **28**-mediated trapping of human Top1cc revealed the significance of Asn722, an important amino acid residue at the active site. Unlike CPT, compound **28** generates less reversible DNA DSBs because of the accumulation of irreversible Top1cc-induced DSBs. In vitro ADME study revealed that unlike CPT and its derivatives, compound **28** is highly plasma stable with ideal log *D* value for oral absorption and is not a Pgp substrate. In summary, we provide compelling evidence that advocate compound **28** as a potential anticancer agent.

EXPERIMENTAL SECTION

Chemistry. General Methods. All starting materials, reagents, and solvents were purchased from commercial suppliers and used without further purification. Air-sensitive reactions were carried out under dry nitrogen or argon atmosphere. Solvents were distilled before use and also dried using standard methods. Thin-layer chromatography was performed on silica gel plates (Merck Silica Gel 60, F_{254}), and the spots were visualized under UV light (254 and 365 nm) or by charring the plate dipped in ninhydrin or $KMnO_4$ or vanillin solution. For purification of the compounds along with manual column flash chromatography was also performed with RediSep Rf silica gel columns on the Teledyne ISCO CombiFlash Rf system using 230–400 mesh silica gel. 1H NMR was recorded at 300 MHz (Bruker DPX), 400 MHz (Jeol), and 600 MHz (Bruker Avance) frequency, and ^{13}C NMR spectra were recorded at 75 MHz (Bruker DPX), 100 MHz (Jeol), and 150 MHz (Bruker Avance) frequency in $CDCl_3$ or CD_3OD or $DMSO-d_6$ solvent using tetramethylsilane (TMS) as the internal standard. Chemical shifts were measured in parts per million (ppm) referenced to 0.0 ppm for TMS and 7.260 ppm for $CHCl_3$. The following abbreviations were used to explain multiplicities: s = singlet, d = doublet, t = triplet, q = quartet, m = multiplet, br = broad. Coupling constant, *J*, was reported in hertz unit. High-resolution mass spectra, HRMS (*m/z*), were recorded using electron ionization (Jeol-JMS 700 mass spectrometer) and electrospray ionization (ESI; Q-ToF

Micro mass spectrometer and LTQ Orbitrap XL mass spectrometer) techniques. The purity of the selected compounds was analyzed by Hitachi HPLC using column Ximate C18 (4.6 \times 150 mm 5.0 μ m). The HPLC purity of all the compounds subjected to biological assay is >95%.

Ethyl 6-Bromo-4-chloroquinoline-3-carboxylate (1). Ethyl 6-bromo-4-hydroxyquinoline-3-carboxylate (2 g, 6.75 mmol) was taken in $POCl_3$ (15 mL) in ice-cold condition. The reaction mixture was allowed to come to room temperature and heated for 2 h at 100 $^{\circ}C$. The reaction mixture was poured into crushed ice and neutralized with a saturated sodium bicarbonate solution. The organic part was extracted with ethyl acetate, washed with water and brine, concentrated, and dried. The solid was purified by silica gel flash column chromatography, eluting with 15% ethyl acetate in hexane to give compound **1** as a white crystalline solid (1.8 g, 85% yield). 1H NMR (300 MHz, $CDCl_3$): δ 9.2 (s, 1H), 8.58 (d, *J* = 2.4 Hz, 1H), 8.02 (d, *J* = 9.3 Hz, 1H), 7.92 (dd, *J* = 9.0, 1.8 Hz, 1H), 4.51 (q, *J* = 7.5 Hz, 2H), 1.47 (t, *J* = 7.5 Hz, 3H). MS (ESI) *m/z*: $[M + Na]^+$ 338.16.

General Procedure A. Ethyl 6-Bromo-4-(2-morpholinoethylamino)quinoline-3-carboxylate (2). Compound **1** (1 g, 3.18 mmol) was dissolved in 1,4-dioxane (5 mL) under N_2 atmosphere. To the reaction mixture, dry DIPEA (1.11 mL, 6.36 mmol) and 4-(2-aminoethyl)morpholine (0.63 mL, 4.77 mmol) were added. The reaction mixture was allowed to stir for 12 h at room temperature. It was then poured into 50 mL of water. The solid obtained was filtered and purified by column chromatography to give compound **2** as a white solid (1.1 g, 85% yield). 1H NMR (300 MHz, $CDCl_3$): δ 9.51 (br s, -NH), 9.1 (s, 1H), 8.4 (d, *J* = 1.5 Hz, 1H), 7.83 (d, *J* = 9.0 Hz, 1H), 7.73 (dd, *J* = 8.7, 1.8 Hz, 1H), 4.41 (q, *J* = 7.2 Hz, 2H), 3.92–3.87 (m, 2H), 3.78 (t, *J* = 4.5 Hz, 4H), 2.71 (t, *J* = 6.0 Hz, 2H), 2.57 (t, *J* = 4.2 Hz, 4H), 1.44 (t, *J* = 7.5 Hz, 3H). ^{13}C NMR (150 MHz, $CDCl_3$): δ 168.0, 155.7, 152.0, 149.8, 134.0, 131.6, 128.2, 120.9, 117.2, 103.8, 67.0, 60.7, 58.0, 53.3, 45.4, 14.4. MS (ESI) *m/z*: $[M + H]^+$ 410.35. HRMS (EI) *m/z*: $[M]^+$ calcd for $C_{18}H_{22}BrN_3O_3$, 407.0845; found, 407.0852.

Ethyl 6-Bromo-4-(3-morpholinopropylamino)quinoline-3-carboxylate (3). Compound **1** (1 g, 3.18 mmol) was dissolved in 1,4-dioxane (5 mL) under N_2 atmosphere. To the reaction mixture, dry DIPEA (1.11 mL, 6.36 mmol) and 3-morpholinopropan-1-amine (0.63 mL, 4.77 mmol) were added, and the reaction was performed according to general procedure A. The solid obtained was filtered and dried to give compound **3** as a white solid (1.2 g, 90% yield). 1H NMR (300 MHz, $CDCl_3$): δ 9.23 (br s, -NH), 9.06 (s, 1H), 8.36 (d, *J* = 2.1 Hz, 1H), 7.81 (d, *J* = 9.0 Hz, 1H), 7.72 (dd, *J* = 9.0, 2.1 Hz, 1H), 4.38 (q, *J* = 7.2 Hz, 2H), 3.87–3.81 (m, 2H), 3.69 (t, *J* = 4.5 Hz, 4H), 2.50 (t, *J* = 7.2 Hz, 2H), 2.44 (t, *J* = 4.5 Hz, 4H), 1.99–1.90 (m, 2H), 1.42 (t, *J* = 7.2 Hz, 3H). ^{13}C NMR (100 MHz, $CDCl_3$): δ 168.7, 156.1, 152.0, 149.8, 134.3, 131.6, 128.3, 120.9, 117.5, 103.5, 67.0, 61.0, 56.0, 53.8, 46.9, 27.8, 14.4. ESI-MS *m/z*: $[M + H]^+$ 422.30. HRMS *m/z*: $[M + H]^+$ calcd for $C_{19}H_{25}BrN_3O_3$, 422.1079; found, 422.1072.

General Procedure B. 6-Bromo-4-(2-morpholinoethylamino)quinoline-3-carbohydrazide (4). Compound **2** (1 g, 2.45 mmol) was dissolved in ethanol (10 mL). To the solution, hydrazine hydrate (10 mL) was added. The reaction mixture was stirred for 10 h at room temperature. Ethanol was removed under vacuum. The residue was then dissolved in $CHCl_3$, and the organic layer was washed with water and brine, dried, and concentrated to give compound **4** as a yellow solid (0.6 g, 62% yield). mp > 250 $^{\circ}C$. 1H NMR (300 MHz, $CDCl_3$): δ 8.64 (s, 1H), 8.27 (d, *J* = 1.5 Hz, 1H), 7.84 (d, *J* = 8.7 Hz, 1H), 7.73 (dd, *J* = 8.7, 1.5 Hz, 1H), 3.77 (t, *J* = 4.8 Hz, 4H), 3.70–3.65 (m, 2H), 2.68 (t, *J* = 6.3 Hz, 2H), 2.54 (t, *J* = 4.2 Hz, 4H). ^{13}C NMR (100 MHz, $CDCl_3$): δ 169.2, 152.3, 149.1, 148.3, 133.7, 131.2, 126.6, 121.2, 118.2, 107.8, 67.0, 57.7, 53.2, 44.1, 31.6, 22.7. ESI-MS *m/z*: $[M + H]^+$ 394.41. HRMS *m/z*: $[M + H]^+$ calcd for $C_{16}H_{21}BrN_5O_2$, 394.0878; found, 398.0874.

6-Bromo-4-(3-morpholinopropylamino)quinoline-3-carbohydrazide (5). Compound **3** (1 g, 2.37 mmol) was dissolved in ethanol (10 mL). To the solution, hydrazine hydrate (10 mL) was added. The

reaction was performed according to general procedure B. The residue was dissolved in CHCl_3 , and the organic layer was washed with water and brine, dried, and concentrated to give compound 5 (0.85 g, 88% yield) as a pale yellow solid. mp > 250 °C. ^1H NMR (300 MHz, CD_3OD): δ 8.48 (d, J = 2.1 Hz, 1H), 8.40 (s, 1H), 7.82 (dd, J = 8.7 Hz, 1H), 7.74 (d, J = 9.0 Hz, 1H), 3.76 (t, J = 4.5 Hz, 4H), 3.71 (t, J = 4.8 Hz, 2H), 3.56 (t, J = 6.6 Hz, 2H), 2.52–2.50 (m, 4H), 1.96–1.87 (m, 2H). ^{13}C NMR (100 MHz, CD_3OD): δ 169.1, 149.9, 148.6, 146.7, 134.5, 133.4, 129.8, 121.0, 118.5, 108.2, 66.3, 57.0, 53.6, 53.4, 46.3, 44.9, 25.4. ESI-MS m/z : $[\text{M} + \text{H}]^+$ 408.20. HRMS m/z : $[\text{M} + \text{H}]^+$ calcd for $\text{C}_{17}\text{H}_{23}\text{BrN}_5\text{O}_2$, 408.1035; found, 408.1030.

6-Bromo-N-(2-morpholinoethyl)-3-(1,3,4-oxadiazol-2-yl)quinolin-4-amine (6). Compound 4 (1 g, 2.54 mmol) was taken in triethyl orthoformate (5 mL, 30.06 mmol), and the mixture was heated for 12 h at 110 °C. The reaction mixture was allowed to come to room temperature. Excess hexane was added to the mixture. A precipitation formed was filtered and purified by column chromatography, eluting with 1% methanol in CHCl_3 to give compound 6 as a light yellow solid (0.4 g, 39% yield). mp 180 °C. ^1H NMR (300 MHz, CDCl_3): δ 9.22 (br s, –NH), 9.03 (s, 1H), 8.47 (m, 2H), 7.86 (d, J = 8.7 Hz, 1H), 7.75 (dd, J = 8.7, 1.8 Hz, 1H), 4.00–3.95 (m, 2H), 3.77 (t, J = 4.5 Hz, 4H), 2.74 (t, J = 6.0 Hz, 2H), 2.58 (t, J = 4.5 Hz, 4H). ^{13}C NMR (150 MHz, CDCl_3): δ 163.5, 151.4, 151.0, 149.2, 148.7, 134.0, 131.7, 128.0, 120.5, 117.8, 99.2, 67.0, 57.9, 53.3, 45.8. MS (ESI) m/z : $[\text{M} + \text{H}]^+$ 404.37. HRMS (EI) m/z : $[\text{M}]^+$ calcd for $\text{C}_{17}\text{H}_{18}\text{BrN}_5\text{O}_2$, 403.0644; found, 403.0635.

6-Bromo-3-(5-methyl-1,3,4-oxadiazol-2-yl)-N-(2-morpholinoethyl)quinolin-4-amine (7). Compound 4 (0.15 g, 0.38 mmol) was dissolved in ethanol (3 mL), and to the solution, triethyl orthoacetate (3 mL, 16.37 mmol) was added. The reaction mixture was refluxed for 8 h. The reaction mixture was allowed to come to room temperature, and solvent was evaporated. Excess hexane was added to the mixture. A precipitation formed was filtered and purified by column chromatography, eluting with 3% methanol in CHCl_3 to give compound 7 (0.14 g, 88% yield) as a brown solid. mp 230 °C. ^1H NMR (300 MHz, CDCl_3): δ 9.17 (br s, –NH), 8.99 (s, 1H), 8.48 (d, J = 1.8 Hz, 1H), 7.86 (d, J = 8.7 Hz, 1H), 7.74 (dd, J = 8.7, 2.1 Hz, 1H), 4.00–3.94 (m, 2H), 3.78 (t, J = 4.5 Hz, 4H), 2.75 (t, J = 6.0 Hz, 2H), 2.68 (s, 3H), 2.59 (t, J = 4.5 Hz, 4H). ^{13}C NMR (100 MHz, CDCl_3): δ 163.8, 162.2, 151.3, 148.6, 133.8, 131.7, 128.0, 120.7, 117.8, 99.7, 67.1, 58.1, 53.4, 45.9, 11.1. ESI-MS m/z : $[\text{M} + \text{H}]^+$ 418.37. HRMS m/z : $[\text{M} + \text{H}]^+$ calcd for $\text{C}_{18}\text{H}_{21}\text{BrN}_5\text{O}_2$, 418.0878; found, 408.0880.

General Procedure C. 6-(4-Methoxyphenyl)-N-(2-morpholinoethyl)-3-(1,3,4-oxadiazol-2-yl)quinolin-4-amine (8). Compound 6 (0.15 g, 0.37 mmol) was dissolved in 1,4-dioxane (5 mL) under Ar atmosphere. 2-(4-Methoxyphenyl)-4,4,5,5-tetramethyl-1,3,2-dioxaborolane (0.17 g, 0.74 mmol) was added to the mixture. 2(M) Na_2CO_3 solution (0.5 mL) was added to the reaction mixture, and argon was purged for 15 min. $\text{Pd}(\text{PPh}_3)_4$ (0.035 g, 0.03 mmol) was added to the mixture, and argon purging was performed for 15 min. The mixture was heated for 12 h at 100 °C. 1,4-Dioxane was removed under vacuum, the residue was dissolved in CHCl_3 , and the organic layer was washed with water and brine, dried, and concentrated. The residue was purified by silica gel column chromatography to produce compound 8 as a white solid (0.09 g, 56% yield). mp 156 °C. ^1H NMR (600 MHz, CDCl_3): δ 9.05 (s, 1H), 8.49 (s, 1H), 8.45 (d, J = 1.2 Hz, 1H), 8.06 (d, J = 8.4 Hz, 1H), 7.94 (dd, J = 8.4, 1.2 Hz, 1H), 7.62 (d, J = 9.0 Hz, 2H), 7.05 (d, J = 8.4 Hz, 2H), 4.10–4.07 (m, 2H), 3.89 (s, 3H), 3.77 (t, J = 4.8 Hz, 4H), 2.76 (t, J = 6.0 Hz, 2H), 2.58 (br s, 4H). ^{13}C NMR (75 MHz, CDCl_3): δ 163.7, 159.4, 152.6, 150.9, 149.2, 148.0, 136.9, 132.8, 130.1, 130.0, 128.2, 122.9, 119.5, 114.4, 98.9, 67.0, 58.0, 55.4, 53.2, 46.0. MS (ESI) m/z : $[\text{M} + \text{H}]^+$ 432.42. HRMS (FAB) m/z : $[\text{M} + \text{H}]^+$ calcd for $\text{C}_{24}\text{H}_{26}\text{N}_5\text{O}_3$, 432.2035; found, 432.2053. HPLC purity 99.55%.

6-(3,4-Dimethoxyphenyl)-N-(2-morpholinoethyl)-3-(1,3,4-oxadiazol-2-yl)quinolin-4-amine (9). Compound 6 (0.10 g, 0.25 mmol) was taken along with 3,4-dimethoxyphenylboronic acid (0.091 g, 0.5 mmol) in 1,4-dioxane (5 mL). 2(M) Na_2CO_3 solution (0.3 mL) and

$\text{Pd}(\text{PPh}_3)_4$ (0.023 g, 0.02 mmol) were added to the mixture, and the reaction was performed according to procedure A. The reaction mixture was heated at 90 °C for 12 h. The residue was purified by column chromatography, eluting with 5% methanol in CHCl_3 to give compound 9 as a yellow solid (0.035 g, 31% yield). mp 116 °C. ^1H NMR (300 MHz, CDCl_3): δ 9.21 (br s, –NH), 9.06 (s, 1H), 8.51 (s, 1H), 8.45 (d, J = 1.5 Hz, 1H), 8.07 (d, J = 8.7 Hz, 1H), 7.93 (dd, J = 8.7, 1.8 Hz, 1H), 7.25 (dd, J = 8.7, 1.8 Hz, 1H), 7.19 (d, J = 2.1 Hz, 1H), 7.03 (d, J = 8.4 Hz, 1H), 4.11–4.06 (m, 2H), 4.01 (s, 3H), 3.98 (s, 3H), 3.77 (t, J = 4.5 Hz, 4H), 2.76 (t, J = 6.0 Hz, 2H), 2.58 (t, J = 4.5 Hz, 4H). ^{13}C NMR (150 MHz, CDCl_3): δ 163.7, 152.9, 151.0, 149.4, 149.1, 148.9, 147.8, 137.5, 133.4, 130.5, 129.8, 123.3, 119.7, 119.5, 111.7, 110.6, 99.1, 67.0, 58.1, 56.1, 53.3, 46.1. MS (ESI) m/z : $[\text{M} + \text{H}]^+$ 461.51. HRMS (EI) m/z : $[\text{M}]^+$ calcd for $\text{C}_{25}\text{H}_{27}\text{N}_5\text{O}_4$, 461.2063; found, 461.2051. HPLC purity 99.27%.

6-(4-Methoxyphenyl)-3-(5-methyl-1,3,4-oxadiazol-2-yl)-N-(2-morpholinoethyl)quinolin-4-amine (10). Compound 7 (0.075 g, 0.18 mmol) was taken along with 2-(4-methoxyphenyl)-4,4,5,5-tetramethyl-1,3,2-dioxaborolane (0.17 g, 0.36 mmol) in 1,4-dioxane (5 mL). 2(M) Na_2CO_3 solution (0.23 mL) and $\text{Pd}(\text{PPh}_3)_4$ (0.017 g, 0.014 mmol) were added to the mixture, and the reaction was performed according to procedure A. The residue was purified by silica gel column chromatography, eluting with 2% methanol in CHCl_3 to afford compound 10 as an off-white solid (0.025 g, 31% yield). mp 160 °C. ^1H NMR (300 MHz, CDCl_3): δ 9.14 (br s, –NH), 8.99 (s, 1H), 8.44 (d, J = 1.5 Hz, 1H), 8.05 (d, J = 8.7 Hz, 1H), 7.92 (dd, J = 8.7, 1.5 Hz, 1H), 7.63 (d, J = 8.7 Hz, 2H), 7.05 (d, J = 8.7 Hz, 2H), 4.09–4.04 (m, 2H), 3.90 (s, 3H), 3.76 (t, J = 4.5 Hz, 4H), 2.75 (t, J = 6.0 Hz, 2H), 2.69 (s, 3H), 2.57 (t, J = 4.2 Hz, 4H). ^{13}C NMR (75 MHz, CDCl_3): δ 164.0, 162.0, 159.5, 152.6, 147.8, 137.0, 133.0, 130.1, 128.3, 123.0, 119.7, 116.2, 114.5, 99.5, 67.1, 58.2, 55.4, 53.3, 46.2, 11.0. MS (ESI) m/z : $[\text{M} + \text{H}]^+$ 446.50. HRMS (EI) m/z : $[\text{M}]^+$ calcd for $\text{C}_{25}\text{H}_{27}\text{N}_5\text{O}_4$, 445.2114; found, 445.2112. HPLC purity 96.96%.

6-(3,4-Dimethoxyphenyl)-3-(5-methyl-1,3,4-oxadiazol-2-yl)-N-(2-morpholinoethyl)quinolin-4-amine (11). Compound 7 (0.065 g, 0.16 mmol) was taken along with 3,4-dimethoxyphenylboronic acid (0.073 g, 0.4 mmol) in 1,4-dioxane (5 mL). 2(M) Na_2CO_3 solution (0.3 mL) and $\text{Pd}(\text{PPh}_3)_4$ (0.015 g, 0.013 mmol) were added to the mixture, and the reaction was performed according to general procedure A. Purification was done by silica gel column chromatography, eluting with 3% methanol in CHCl_3 to get compound 11 as a light yellow solid (0.03 g, 41% yield). mp 180 °C. ^1H NMR (300 MHz, CDCl_3): δ 9.11 (br s, –NH), 8.99 (s, 1H), 8.42 (s, 1H), 8.05 (d, J = 8.7 Hz, 1H), 7.90 (dd, J = 8.4, 1.5 Hz, 1H), 7.24 (dd, J = 8.1, 1.5 Hz, 1H), 7.17 (d, J = 1.5 Hz, 1H), 7.01 (d, J = 8.4 Hz, 1H), 4.08–4.03 (m, 2H), 3.99 (s, 3H), 3.96 (s, 3H), 3.75 (t, J = 4.5 Hz, 4H), 2.74 (t, J = 6.0 Hz, 2H), 2.68 (s, 3H), 2.56 (t, J = 4.5 Hz, 4H). ^{13}C NMR (75 MHz, CDCl_3): δ 164.0, 162.0, 152.6, 149.4, 149.0, 148.0, 137.2, 133.6, 130.2, 130.1, 123.3, 119.7, 111.7, 110.6, 99.6, 67.1, 58.3, 56.1, 53.3, 46.2, 11.0. MS (ESI) m/z : $[\text{M} + \text{H}]^+$ 476.58. HRMS (EI) m/z : $[\text{M}]^+$ calcd for $\text{C}_{25}\text{H}_{27}\text{N}_5\text{O}_4$, 475.2220; found, 475.2226. HPLC purity 96.38%.

6-Bromo-N-(3-morpholinopropyl)-3-(1,3,4-oxadiazol-2-yl)quinolin-4-amine (12). Compound 5 (1 g, 2.45 mmol) was taken in triethyl orthoformate (5 mL, 30.06 mmol), and the mixture was heated for 12 h at 110 °C. The crude mixture was purified by column chromatography, eluting with 4% methanol in CHCl_3 to give compound 12 as a yellow solid (0.25 g, 25% yield). mp 144 °C. ^1H NMR (300 MHz, CDCl_3): δ 9.03 (s, 1H), 8.82 (br s, –NH), 8.49 (s, 1H), 8.46 (d, J = 0.9 Hz, 1H), 7.86 (d, J = 8.7 Hz, 1H), 7.76 (dd, J = 9.0, 1.8 Hz, 1H), 3.99–3.93 (m, 2H), 3.70 (t, J = 4.5 Hz, 4H), 2.54 (t, J = 6.9 Hz, 2H), 2.45 (t, J = 3.9 Hz, 4H), 2.08–1.99 (m, 2H). ^{13}C NMR (75 MHz, CDCl_3): δ 163.8, 151.6, 151.0, 149.1, 148.7, 134.1, 131.7, 128.0, 120.4, 118.0, 98.9, 66.9, 55.7, 53.7, 46.9, 27.7. MS (ESI) m/z : $[\text{M} + \text{H}]^+$ 418.31. HRMS m/z : $[\text{M} + \text{H}]^+$ calcd for $\text{C}_{18}\text{H}_{21}\text{BrN}_5\text{O}_2$, 418.0878; found, 418.0862.

6-(4-Methoxyphenyl)-N-(3-morpholinopropyl)-3-(1,3,4-oxadiazol-2-yl)quinolin-4-amine (13). Compound 12 (0.10 g, 0.24 mmol) was taken along with 2-(4-methoxyphenyl)-4,4,5,5-tetramethyl-1,3,2-

dioxaborolane (0.11 g, 0.48 mmol) in 1,4-dioxane (5 mL). 2(M) Na₂CO₃ solution (0.3 mL) and Pd(PPh₃)₄ (0.022 g, 0.019 mmol) were added to the mixture, and the reaction was performed according to procedure A. The residue was purified by silica gel column chromatography to produce compound 13 as a gray solid (0.037 g, 35% yield). mp 134 °C. ¹H NMR (600 MHz, CDCl₃): δ 9.06 (s, 1H), 8.86 (br s, -NH), 8.51 (s, 1H), 8.47 (d, J = 1.2 Hz, 1H), 8.08 (d, J = 9.0 Hz, 1H), 7.96 (dd, J = 9.0, 1.8 Hz, 1H), 7.64 (d, J = 9.0 Hz, 2H), 7.07 (d, J = 8.4 Hz, 2H), 4.13–4.10 (m, 2H), 3.91 (s, 3H), 3.69 (t, J = 4.2 Hz, 4H), 2.57 (t, J = 7.2 Hz, 2H), 2.47 (s, 4H), 2.12–2.07 (m, 2H). ¹³C NMR (150 MHz, CDCl₃): δ 164.1, 159.6, 153.0, 150.9, 149.2, 147.9, 137.2, 133.0, 130.4, 130.2, 128.3, 123.2, 119.5, 114.6, 98.8, 66.8, 55.8, 53.7, 47.3, 27.9. MS (ESI) *m/z*: [M + H]⁺ 446.39. HRMS (ESI) *m/z*: [M + H]⁺ calcd for C₂₅H₂₈N₅O₃, 446.2192; found, 446.2190. HPLC purity 98.23%.

6-(3,4-Dimethoxyphenyl)-N-(3-morpholinopropyl)-3-(1,3,4-oxadiazol-2-yl)quinolin-4-amine (14). Compound 12 (0.10 g, 0.24 mmol) was taken along with 3,4-dimethoxyphenylboronic acid (0.087 g, 0.48 mmol) in a mixture of 1,4-dioxane (4 mL) and dimethylformamide (DMF) (1 mL). 2(M) Na₂CO₃ solution (0.3 mL) and Pd(PPh₃)₄ (0.022 g, 0.02 mmol) were added to the mixture, and the reaction was performed according to procedure A. The residue was purified by silica gel column chromatography to afford compound 14 as a white solid (0.033 g, 30% yield). mp 182 °C. ¹H NMR (300 MHz, CD₃OD): δ 9.08 (s, 1H), 8.93 (s, 1H), 8.58 (s, 1H), 8.08 (dd, J = 9.0, 1.5 Hz, 1H), 7.97 (d, J = 8.7 Hz, 1H), 7.35–7.34 (m, 2H), 7.12 (d, J = 9.3 Hz, 1H), 4.09 (t, J = 6.9 Hz, 2H), 3.97 (s, 3H), 3.92 (s, 3H), 3.64 (t, J = 4.8 Hz, 4H), 2.60 (t, J = 6.9 Hz, 2H), 2.49 (t, J = 3.9 Hz, 4H), 2.11–2.07 (m, 2H). ¹³C NMR (150 MHz, CDCl₃): δ 164.2, 152.9, 150.9, 149.6, 149.4, 149.0, 148.2, 137.3, 133.5, 130.4, 123.4, 119.6, 119.5, 111.7, 110.5, 98.8, 66.9, 56.1, 55.8, 53.7, 47.3, 28.1. MS (ESI) *m/z*: [M + H]⁺ 476.37. HRMS (ESI) *m/z*: [M + H]⁺ calcd for C₂₅H₂₈N₅O₃, 476.2298; found, 476.2291. HPLC purity 99.67%.

N-(3-Morpholinopropyl)-3-(1,3,4-oxadiazol-2-yl)-6-(*p*-tolyl)quinolin-4-amine (15). Compound 12 (0.10 g, 0.24 mmol) was taken along with *p*-tolylboronic acid (0.049 g, 0.36 mmol) in 1,4-dioxane (5 mL). 2(M) Na₂CO₃ solution (0.3 mL) and Pd(PPh₃)₄ (0.023 g, 0.02 mmol) were added to the mixture, and the reaction was performed according to procedure A. The reaction took 8 h to complete. The residue was purified by silica gel column chromatography to produce compound 15 as a white solid (0.039 g, 38% yield). mp 168 °C. ¹H NMR (300 MHz, CDCl₃): δ 9.04 (s, 1H), 8.82 (br s, -NH), 8.48 (s, 2H), 8.05 (d, J = 8.7 Hz, 1H), 7.95 (d, J = 8.4 Hz, 1H), 7.58 (d, J = 7.8 Hz, 2H), 7.32 (d, J = 7.5 Hz, 2H), 4.11–4.05 (m, 2H), 3.64 (t, J = 4.5 Hz, 4H), 2.52 (t, J = 7.2 Hz, 2H), 2.44–2.42 (m, 7H), 2.09–2.01 (m, 2H). ¹³C NMR (75 MHz, CDCl₃): δ 165.1, 152.9, 150.8, 148.1, 143.5, 137.7, 137.4, 130.4, 129.8, 127.1, 123.7, 123.6, 66.9, 55.8, 53.7, 47.3, 28.0, 21.1. MS (ESI) *m/z*: [M + H]⁺ 430.41. HRMS *m/z*: [M + H]⁺ calcd for C₂₅H₂₈N₅O₂, 430.2243; found, 430.2240. HPLC purity 98.89%.

Ethyl 4-(2-(1*H*-imidazol-1-yl)ethylamino)-6-bromoquinoline-3-carboxylate (16). Compound 1 (0.5 g, 1.59 mmol) was dissolved in 1,4-dioxane (2.5 mL) and DMF (1 mL) under N₂ atmosphere. To the reaction mixture, dry DIPEA (0.55 mL, 3.18 mmol) and 2-(1*H*-imidazol-1-yl)ethanamine (0.27 g, 2.39 mmol) were added. The reaction mixture was heated for 12 h at 100 °C. 1,4-Dioxane and DMF were removed under vacuum, the residue was dissolved in CHCl₃/MeOH mixture, and the organic layer was washed with water and brine, dried, and concentrated. The residue was purified by silica gel column chromatography, eluting with 4% methanol in CHCl₃ to produce compound 16 as a yellow solid (0.35 g, 57% yield). mp 218 °C. ¹H NMR (600 MHz, DMSO-*d*₆): δ 8.79 (s, 1H), 8.45 (s, 1H), 8.35 (br s, -NH), 7.85 (dd, J = 9.0, 1.8 Hz, 1H), 7.76 (d, J = 9 Hz, 1H), 7.58 (s, 1H), 7.13 (s, 1H), 6.80 (s, 1H), 4.33–4.30 (m, 4H), 3.89–3.88 (m, 2H), 1.32 (t, J = 7.2 Hz, 3H). ¹³C NMR (150 MHz, CDCl₃): δ 168.4, 155.8, 151.6, 149.7, 134.5, 131.9, 127.5, 120.7, 118.2, 105.1, 61.3, 49.6, 47.5, 14.3. MS (ESI) *m/z*: [M + H]⁺ 389.29. HRMS *m/z*: [M + H]⁺ calcd for C₁₇H₁₈BrN₄O₂, 389.0613; found, 389.0609; [M + Na]⁺ calcd, 411.0433; found, 411.0425.

Ethyl 4-((3-(1*H*-imidazol-1-yl)propyl)amino)-6-bromoquinoline-3-carboxylate (17). Compound 1 (1 g, 3.18 mmol) was dissolved in 1,4-dioxane (5 mL) under N₂ atmosphere. To the reaction mixture, dry DIPEA (1.11 mL, 6.36 mmol) and 3-(1*H*-imidazol-1-yl)propan-1-amine (0.57 mL, 4.77 mmol) were added. The reaction mixture was allowed to stir for 12 h at room temperature. Then it was poured into 50 mL of water. The solid obtained was filtered and dried to give compound 17 as a white solid (1.2 g, 94% yield). ¹H NMR (600 MHz, CDCl₃): δ 9.29 (t, J = 4.8 Hz, -NH), 9.10 (s, 1H), 8.23 (d, J = 2.4 Hz, 1H), 7.82 (d, J = 9.0 Hz, 1H), 7.73 (dd, J = 9.0, 1.8 Hz, 1H), 7.46 (s, 1H), 7.06 (s, 1H), 6.90 (s, 1H), 4.41 (q, J = 7.2 Hz, 2H), 4.15 (t, J = 7.2 Hz, 2H), 3.78–3.75 (m, 2H), 2.28–2.23 (m, 2H), 1.43 (t, J = 7.2 Hz, 3H). ¹³C NMR (150 MHz, CDCl₃): δ 168.9, 156.0, 151.8, 149.8, 137.1, 134.5, 131.7, 130.0, 128.0, 120.7, 118.7, 117.8, 103.8, 61.2, 45.3, 43.8, 32.4, 14.3. MS (ESI) *m/z*: [M + H]⁺ 403.32. HRMS *m/z*: [M + H]⁺ calcd for C₁₈H₂₀BrN₄O₂, 403.0769; found, 403.0787.

General Procedure D. 4-(2-(1*H*-imidazol-1-yl)ethyl)amino)-6-bromoquinoline-3-carbohydrazide (18). Compound 16 (1 g, 2.58 mmol) was dissolved in ethanol (10 mL). To the solution, hydrazine hydrate (10 mL) was added. The reaction mixture was stirred for 10 h at room temperature. Ethanol was removed under vacuum. The residue was dissolved in CHCl₃, and the organic layer was washed with water and brine, dried, and concentrated to give compound 18 (0.82 g, 85% yield) as a yellow solid. mp > 250 °C. ¹H NMR (600 MHz, CD₃OD): δ 8.40 (s, 1H), 8.31 (d, J = 1.8 Hz, 1H), 7.78 (dd, J = 9.0, 1.8 Hz, 1H), 7.71 (d, J = 8.4 Hz, 1H), 7.59 (s, 1H), 7.09 (s, 1H), 6.91 (s, 1H), 4.31 (t, J = 6.0 Hz, 2H), 3.83 (t, J = 6.0 Hz, 2H), 1.81 (s, -CONHNH₂, 2H). ¹³C NMR (150 MHz, CD₃OD): δ 168.6, 149.7, 149.2, 146.6, 137.3, 133.5, 129.8, 127.8, 124.8, 121.0, 119.4, 118.9, 109.0, 46.1, 46.0. MS (ESI) *m/z*: [M + H]⁺ 375.05. HRMS *m/z*: [M + H]⁺ calcd for C₁₅H₁₆BrN₆O, 375.0569; found, 375.0575.

4-(3-(1*H*-imidazol-1-yl)propylamino)-6-bromoquinoline-3-carbohydrazide (19). Compound 17 (1 g, 2.48 mmol) was dissolved in ethanol (10 mL). To the solution, hydrazine hydrate (10 mL) was added, and the reaction was performed according to general procedure D. The residue was dissolved in CHCl₃, and the organic layer was washed with water and brine, dried, and concentrated to give compound 19 as a light green solid (0.75 g, 78% yield). mp > 250 °C. ¹H NMR (300 MHz, CD₃OD): δ 9.68 (br s, -NH), 8.59 (d, J = 1.2 Hz, 1H), 8.31 (s, 1H), 7.78 (dd, J = 8.7, 1.5 Hz, 1H), 7.72 (d, J = 8.7 Hz, 1H), 7.60 (s, 1H), 7.42 (t, J = 5.1 Hz, -CONH), 7.16 (s, 1H), 6.88 (s, 1H), 4.52 (br s, -CONHNH₂), 4.02 (t, J = 6.9 Hz, 2H), 3.32–3.26 (m, 2H), 2.10–2.01 (m, 2H). ¹³C NMR (75 MHz, CD₃OD): δ 167.8, 150.5, 147.7, 147.0, 137.3, 132.6, 131.2, 128.4, 125.0, 121.0, 119.3, 117.7, 109.5, 43.8, 42.2, 30.8. MS (ESI) *m/z*: [M + H]⁺ 389.28. HRMS *m/z*: [M + H]⁺ calcd for C₁₆H₁₈BrN₆O, 389.0725; found, 389.0724.

General Procedure E. N-(2-(1*H*-imidazol-1-yl)ethyl)-6-bromo-3-(1,3,4-oxadiazol-2-yl)quinolin-4-amine (20). Compound 18 (1 g, 2.67 mmol) was taken in triethyl orthoformate (5 mL, 30.06 mmol), and the mixture was heated for 12 h at 100 °C. The residue was purified by column chromatography, eluting with 4% methanol in CHCl₃ to give compound 20 as a yellow solid (0.22 g, 43% yield). mp 197 °C. ¹H NMR (600 MHz, DMSO-*d*₆): δ 9.42 (s, 1H), 8.78 (s, 1H), 8.50 (d, J = 2.4 Hz, 1H), 8.14 (t, J = 5.4 Hz, -NH), 7.89 (dd, J = 9.0, 2.4 Hz, 1H), 7.82 (d, J = 9.0 Hz, 1H), 7.55 (s, 1H), 7.09 (s, 1H), 6.78 (s, 1H), 4.27 (t, J = 6.0 Hz, 2H), 3.86–3.84 (m, 2H). ¹³C NMR (150 MHz, CDCl₃): δ 163.5, 151.4, 151.3, 149.1, 148.4, 137.5, 134.5, 132.1, 130.1, 127.2, 120.4, 119.0, 118.7, 100.7, 49.9, 47.5. MS (ESI) *m/z*: [M + H]⁺ 385.27. HRMS *m/z*: [M + H]⁺ calcd for C₁₆H₁₄BrN₆O, 385.0412; found, 385.0409.

N-(3-(1*H*-imidazol-1-yl)propyl)-6-bromo-3-(1,3,4-oxadiazol-2-yl)quinolin-4-amine (21). Compound 19 (1 g, 2.57 mmol) was taken in triethyl orthoformate (5 mL, 30.06 mmol), and the mixture was heated for 12 h at 110 °C. The reaction was carried out according to general procedure E. The crude mixture was purified by column chromatography, eluting with 3% methanol in CHCl₃ to afford compound 21 as a yellow solid (0.2 g, 19% yield). mp 147 °C. ¹H NMR (600 MHz, DMSO-*d*₆): δ 9.40 (s, 1H), 8.77 (s, 1H), 8.56 (d, J = 1.8 Hz, 1H), 8.18 (br s, -NH), 7.87 (dd, J = 9.0, 1.8 Hz, 1H), 7.81

(d, $J = 9.0$ Hz, 1H), 7.56 (s, 1H), 7.11 (s, 1H), 6.87 (s, 1H), 4.03 (t, $J = 7.2$ Hz, 2H), 3.43–3.40 (m, 2H), 2.13–2.08 (m, 2H). ^{13}C NMR (150 MHz, CDCl_3): δ 163.9, 151.4, 151.2, 149.2, 148.5, 134.5, 131.9, 127.8, 120.3, 118.5, 99.4, 45.7, 32.3, 29.7. MS (ESI) m/z : $[\text{M} + \text{H}]^+$ 399.37. HRMS m/z : $[\text{M} + \text{H}]^+$ calcd for $\text{C}_{17}\text{H}_{16}\text{BrN}_6\text{O}$, 399.0569; found, 399.0565. HPLC purity 97.38%.

General Procedure F. *N*-(2-(1*H*-imidazol-1-yl)ethyl)-6-(4-methoxyphenyl)-3-(1,3,4-oxadiazol-2-yl)quinolin-4-amine (**22**). Compound **20** (0.07 g, 0.18 mmol) was dissolved in a mixture of 1,4-dioxane (4 mL) and DMF (1 mL) under argon atmosphere. 2-(4-Methoxyphenyl)-4,4,5,5-tetramethyl-1,3,2-dioxaborolane (0.043 g, 0.18 mmol) was added to the mixture. 2(M) Na_2CO_3 solution (0.24 mL) was added to the reaction mixture, and argon was purged for 15 min. $\text{Pd}(\text{PPh}_3)_4$ (0.017 g, 0.014 mmol) was added to the mixture, and argon purging was performed for 15 min. The mixture was heated for 12 h at 100 °C. 1,4-Dioxane was removed under vacuum, the residue was dissolved in CHCl_3 , and the organic layer was washed with water and brine, dried, and concentrated. The residue was purified by silica gel column chromatography to afford compound **22** as a white solid (0.02 g, 27% yield). mp 213 °C. ^1H NMR (600 MHz, CDCl_3): δ 9.05 (s, 1H), 8.62 (t, $J = 4.2$ Hz, 1H), 8.52 (s, 1H), 8.21 (d, $J = 1.8$ Hz, 1H), 8.08 (d, $J = 9.0$ Hz, 1H), 7.95 (dd, $J = 9.0, 1.8$ Hz, 1H), 7.58 (d, $J = 8.4$ Hz, 2H), 7.46 (s, 1H), 7.06 (d, $J = 8.4$ Hz, 2H), 6.98 (s, 1H), 6.91 (s, 1H), 4.36–4.33 (m, 4H), 3.90 (s, 3H). ^{13}C NMR (150 MHz, CDCl_3): δ 163.8, 159.7, 152.6, 151.2, 149.4, 147.7, 138.0, 137.5, 132.6, 130.7, 130.1, 128.4, 122.2, 119.6, 118.7, 114.7, 100.7, 55.5, 50.1, 47.6. MS (ESI) m/z : $[\text{M} + \text{H}]^+$ 413.16. HRMS (ESI) m/z : $[\text{M} + \text{H}]^+$ calcd for $\text{C}_{23}\text{H}_{21}\text{N}_6\text{O}_2$, 413.1726; found, 413.1732. HPLC purity 98.37%.

N-(3-(1*H*-imidazol-1-yl)propyl)-3-(1,3,4-oxadiazol-2-yl)-6-phenylquinolin-4-amine (**23**). Compound **21** (0.08 g, 0.20 mmol) was taken along with phenylboronic acid (0.049 g, 0.40 mmol) in 1,4-dioxane (4 mL) and DMF (1 mL). 2(M) Na_2CO_3 solution (0.25 mL) and $\text{Pd}(\text{PPh}_3)_4$ (0.018 g, 0.016 mmol) were added to the mixture, and the reaction was performed according to procedure B. The residue was purified by silica gel column chromatography, eluting with 4% methanol in CHCl_3 to produce compound **23** as a white solid (0.032 g, 40% yield). mp 177 °C. ^1H NMR (300 MHz, CDCl_3): δ 9.11 (s, 1H), 8.82 (br s, –NH), 8.53 (s, 1H), 8.38 (s, 1H), 8.09 (d, $J = 9.0$ Hz, 1H), 7.98 (d, $J = 8.4$ Hz, 1H), 7.63 (d, $J = 7.5$ Hz, 2H), 7.53 (t, $J = 7.5$ Hz, 2H), 7.46–7.41 (m, 2H), 7.04 (s, 1H), 6.91 (s, 1H), 4.22 (t, $J = 6.9$ Hz, 2H), 4.03–3.98 (m, 2H), 2.41–2.32 (m, 2H). ^{13}C NMR (150 MHz, CDCl_3): δ 164.2, 152.7, 151.1, 149.9, 148.2, 140.4, 138.0, 137.1, 130.8, 130.7, 129.9, 129.2, 127.9, 127.3, 123.6, 119.3, 118.8, 99.2, 46.0, 44.0, 32.5. MS (ESI) m/z : $[\text{M} + \text{H}]^+$ 397.43. HRMS (ESI) m/z : $[\text{M} + \text{H}]^+$ calcd for $\text{C}_{23}\text{H}_{21}\text{N}_6\text{O}$, 397.1777; found, 397.1771. HPLC purity 99.53%.

4-(3-(1*H*-imidazol-1-yl)propylamino)-3-(1,3,4-oxadiazol-2-yl)quinolin-6-ylbenzotrile (**24**). Compound **21** (0.08 g, 0.20 mmol) was taken along with 4-(4,4,5,5-tetramethyl-1,3,2-dioxaborolan-2-yl)benzotrile (0.092 g, 0.40 mmol) in 1,4-dioxane (4 mL) and DMF (1 mL). 2(M) Na_2CO_3 solution (0.25 mL) and $\text{Pd}(\text{PPh}_3)_4$ (0.018 g, 0.016 mmol) were added to the mixture, and the reaction was performed according to procedure B. The residue was purified by silica gel column chromatography, eluting with 4% methanol in CHCl_3 to afford compound **24** as a bright yellow solid (0.035 g, 41% yield). mp 238 °C. ^1H NMR (300 MHz, $\text{CDCl}_3 + 1$ drop CD_3OD): δ 8.86 (s, 1H), 8.56 (s, 1H), 8.22 (s, 1H), 7.88 (d, $J = 8.7$ Hz, 1H), 7.78 (dd, $J = 8.7, 1.5$ Hz, 1H), 7.64 (d, $J = 8.4$ Hz, 2H), 7.56 (d, $J = 8.1$ Hz, 2H), 7.31 (s, 1H), 6.77 (d, $J = 4.8$ Hz, 2H), 4.06 (t, $J = 6.9$ Hz, 2H), 3.76 (m, 2H), 2.24–2.15 (m, 2H). ^{13}C NMR (150 MHz, CDCl_3): δ 164.1, 152.6, 151.2, 150.5, 148.8, 144.8, 137.2, 135.8, 133.0, 131.2, 130.2, 130.0, 127.9, 124.3, 119.4, 118.8, 118.7, 111.5, 99.5, 46.0, 43.9, 32.3. MS (ESI) m/z : $[\text{M} + \text{H}]^+$ 422.04. HRMS (ESI) m/z : $[\text{M}]^+$ calcd for $\text{C}_{24}\text{H}_{20}\text{N}_7\text{O}$, 422.1729; found, 422.1747. HPLC purity 96.02%.

N-(3-(1*H*-imidazol-1-yl)propyl)-6-(4-fluorophenyl)-3-(1,3,4-oxadiazol-2-yl)quinolin-4-amine (**25**). Compound **21** (0.08 g, 0.20 mmol) was taken along with 4-fluorophenylboronic acid (0.056 g, 0.40 mmol) in 1,4-dioxane (4 mL) and DMF (1 mL). 2(M) Na_2CO_3

solution (0.25 mL) and $\text{Pd}(\text{PPh}_3)_4$ (0.018 g, 0.016 mmol) were added to the mixture, and the reaction was performed according to procedure B. It took 8 h for the reaction to complete. The residue was purified by silica gel column chromatography, eluting with 4% methanol in CHCl_3 to produce compound **25** as a pale yellow solid (0.025 g, 30% yield). mp 218 °C. ^1H NMR (600 MHz, CDCl_3): δ 9.09 (s, 1H), 8.80 (t, $J = 4.8$ Hz, –NH), 8.53 (s, 1H), 8.29 (d, $J = 1.8$ Hz, 1H), 8.07 (d, $J = 9.0$ Hz, 1H), 7.90 (dd, $J = 9.0, 1.8$ Hz, 1H), 7.58–7.55 (m, 2H), 7.46 (s, 1H), 7.20 (t, $J = 9.0$ Hz, 2H), 7.03 (s, 1H), 6.89 (s, 1H), 4.22 (t, $J = 6.6$ Hz, 2H), 3.98–3.96 (m, 2H), 2.37–2.33 (m, 2H). ^{13}C NMR (150 MHz, CDCl_3): δ 164.2, 152.6, 151.1, 149.8, 148.2, 137.1, 137.0, 130.8, 130.6, 130.0, 128.9, 123.4, 119.4, 118.8, 116.2, 116.1, 99.3, 46.0, 43.9, 32.4. ESI-MS m/z : $[\text{M} + \text{H}]^+$ 415.16. HRMS (ESI) m/z : $[\text{M} + \text{H}]^+$ calcd for $\text{C}_{23}\text{H}_{20}\text{FN}_6\text{O}$, 415.1682; found, 415.1682. HPLC purity 96.60%.

4-(4-(3-(1*H*-imidazol-1-yl)propyl)amino)-3-(1,3,4-oxadiazol-2-yl)quinolin-6-yl)phenol (**26**). Compound **21** (0.10 g, 0.25 mmol) was taken along with 4-(4,4,5,5-tetramethyl-1,3,2-dioxaborolan-2-yl)phenol (0.11 g, 0.5 mmol) in 1,4-dioxane (4 mL) and DMF (1 mL). 2(M) Na_2CO_3 solution (0.3 mL) and $\text{Pd}(\text{PPh}_3)_4$ (0.023 g, 0.02 mmol) were added to the mixture, and the reaction was performed according to procedure B. After 7 h, the residue was purified by silica gel column chromatography, eluting with 10% methanol in CHCl_3 to get compound **26** as a pale yellow solid (0.04 g, 39% yield). mp > 250 °C. ^1H NMR (300 MHz, CD_3OD): δ 9.09 (s, 1H), 8.93 (s, 1H), 8.44 (d, $J = 1.5$ Hz, 1H), 8.02 (dd, $J = 8.7, 1.8$ Hz, 1H), 7.94 (d, $J = 8.7$ Hz, 1H), 7.65 (s, 1H), 7.57 (d, $J = 8.7$ Hz, 2H), 7.15 (s, 1H), 6.97 (s, 1H), 6.97–6.94 (m, 3H), 4.27 (t, $J = 6.9$ Hz, 2H), 3.98 (t, $J = 6.6$ Hz, 2H), 2.42–2.33 (m, 2H). ^{13}C NMR (150 MHz, $\text{CDCl}_3 + 1$ drop CD_3OD): δ 164.0, 157.3, 152.5, 151.3, 148.7, 147.4, 138.1, 136.9, 131.3, 130.7, 129.6, 129.3, 128.2, 122.5, 119.2, 118.9, 116.1, 99.0, 46.0, 44.4, 32.1. ESI-MS m/z : $[\text{M} + \text{H}]^+$ 413.31. HRMS (ESI) m/z : $[\text{M} + \text{H}]^+$ calcd for $\text{C}_{23}\text{H}_{21}\text{N}_6\text{O}_2$, 413.1726; found, 413.1724. HPLC purity 99.09%.

N-(3-(1*H*-imidazol-1-yl)propyl)-3-(1,3,4-oxadiazol-2-yl)-6-*p*-tolylquinolin-4-amine (**27**). Compound **21** (0.07 g, 0.18 mmol) was taken along with *p*-tolylboronic acid (0.037 g, 0.27 mmol) in 1,4-dioxane (4 mL) and DMF (1 mL). 2(M) Na_2CO_3 solution (0.23 mL) and $\text{Pd}(\text{PPh}_3)_4$ (0.017 g, 0.014 mmol) were added to the mixture, and the reaction was performed according to procedure B. After 8 h, the residue was purified by silica gel column chromatography, eluting with 6% methanol in CHCl_3 to afford compound **27** as a yellow solid (0.037 g, 51% yield). mp 228 °C. ^1H NMR (600 MHz, CDCl_3): δ 9.07 (s, 1H), 8.77 (t, $J = 4.2$ Hz, –NH), 8.51 (s, 1H), 8.33 (d, $J = 1.8$ Hz, 1H), 8.05 (d, $J = 9.0$ Hz, 1H), 7.94 (dd, $J = 9.0, 1.8$ Hz, 1H), 7.51 (d, $J = 7.8$ Hz, 2H), 7.46 (s, 1H), 7.32 (d, $J = 7.8$ Hz, 2H), 7.04 (s, 1H), 6.90 (s, 1H), 4.21 (t, $J = 7.2$ Hz, 2H), 3.99–3.96 (m, 2H), 2.43 (s, 3H), 2.36–2.32 (m, 2H). ^{13}C NMR (150 MHz, CDCl_3): δ 164.2, 152.6, 151.0, 149.7, 148.0, 137.9, 137.4, 137.1, 130.7, 130.6, 129.9, 127.1, 123.2, 119.3, 118.8, 99.2, 46.0, 44.0, 32.5, 21.2. MS (ESI) m/z : $[\text{M} + \text{H}]^+$ 411.65. HRMS m/z : $[\text{M} + \text{H}]^+$ calcd for $\text{C}_{24}\text{H}_{23}\text{N}_6\text{O}$, 411.1933; found, 411.1930. HPLC purity 99.67%.

N-(3-(1*H*-imidazol-1-yl)propyl)-6-(4-methoxyphenyl)-3-(1,3,4-oxadiazol-2-yl)quinolin-4-amine (**28**). Compound **21** (0.10 g, 0.25 mmol) was taken along with 2-(4-methoxyphenyl)-4,4,5,5-tetramethyl-1,3,2-dioxaborolane (0.12 g, 0.5 mmol) in 1,4-dioxane (4 mL) and DMF (1 mL). 2(M) Na_2CO_3 solution (0.3 mL) and $\text{Pd}(\text{PPh}_3)_4$ (0.023 g, 0.02 mmol) were added to the reaction mixture, and the reaction was performed according to procedure B. The residue was purified by silica gel column chromatography, eluting with 7% methanol in CHCl_3 to afford compound **28** as a yellow solid (0.035 g, 33% yield). mp 202 °C. ^1H NMR (300 MHz, CD_3OD): δ 9.15 (s, 1H), 8.97 (s, 1H), 8.53 (s, 1H), 8.50 (s, 1H), 8.30 (d, $J = 8.7$ Hz, 1H), 7.98 (d, $J = 8.4$ Hz, 1H), 7.70 (d, $J = 8.7$ Hz, 2H), 7.50 (s, 1H), 7.32 (s, 1H), 7.10 (d, $J = 8.4$ Hz, 2H), 4.43 (t, $J = 7.2$ Hz, 2H), 4.13 (t, $J = 6.3$ Hz, 2H), 3.89 (s, 3H), 2.53–2.45 (m, 2H). ^{13}C NMR (75 MHz, CDCl_3): δ 164.2, 159.6, 152.6, 151.0, 149.4, 147.8, 137.6, 137.1, 132.8, 130.6, 130.5, 129.9, 128.3, 122.8, 119.4, 118.8, 114.6, 99.2, 55.4, 46.0, 44.0, 32.5. MS (ESI) m/z : $[\text{M} + \text{H}]^+$ 427.52. HRMS

(EI) m/z : $[M]^+$ calcd for $C_{24}H_{22}N_6O_2$, 426.1804; found, 426.1810. HPLC purity 98.44%.

N-(3-(1*H*-imidazol-1-yl)propyl)-6-(3-methoxyphenyl)-3-(1,3,4-oxadiazol-2-yl)quinolin-4-amine (**29**). Compound **21** (0.10 g, 0.25 mmol) was taken along with (3-methoxyphenyl)boronic acid (0.06 g, 0.38 mmol) in 1,4-dioxane (4 mL) and DMF (1 mL). 2(M) Na_2CO_3 solution (0.3 mL) and Pd(PPh₃)₄ (0.023 g, 0.02 mmol) were added to the reaction mixture, and the reaction was performed according to procedure **B**. The residue was purified by silica gel column chromatography, eluting with 9% methanol in CHCl₃ to get compound **29** as a pale yellow solid (0.052 g, 49% yield). mp 96 °C. ¹H NMR (400 MHz, CDCl₃): δ 9.07 (s, 1H), 8.78 (t, *J* = 4.0 Hz, -NH), 8.50 (s, 1H), 8.34 (d, *J* = 2.0 Hz, 1H), 8.05 (d, *J* = 8.8 Hz, 1H), 7.93 (dd, *J* = 8.4, 2 Hz, 1H), 7.44 (d, *J* = 4.0 Hz, 1H), 7.41 (d, *J* = 8.0 Hz, 1H), 7.18 (dd, *J* = 7.6, 1.2 Hz, 1H), 7.14 (m, 1H), 7.01 (s, 1H), 6.94 (dd, *J* = 8.4, 1.6 Hz, 1H), 6.89 (s, 1H), 4.19 (t, *J* = 6.8 Hz, 2H), 3.99–3.95 (m, 2H), 3.88 (s, 3H), 2.37–2.30 (m, 2H). ¹³C NMR (150 MHz, CDCl₃): δ 164.2, 160.2, 152.6, 151.1, 149.9, 148.2, 141.8, 137.8, 130.8, 130.6, 130.3, 129.9, 123.7, 119.7, 119.3, 118.9, 113.5, 112.7, 99.2, 55.4, 46.0, 44.0, 32.5. MS (ESI) m/z : $[M + H]^+$ 427.37. HRMS (ESI) m/z : $[M + H]^+$ calcd for $C_{24}H_{23}N_6O_2$, 427.1882; found, 427.1880. HPLC purity 95.44%.

N-(3-(1*H*-imidazol-1-yl)propyl)-6-(2-methoxyphenyl)-3-(1,3,4-oxadiazol-2-yl)quinolin-4-amine (**30**). Compound **21** (0.08 g, 0.2 mmol) was taken along with (2-methoxyphenyl)boronic acid (0.06 g, 0.4 mmol) in 1,4-dioxane (4 mL) and DMF (1 mL). 2(M) Na_2CO_3 solution (0.3 mL) and Pd(PPh₃)₄ (0.018 g, 0.02 mmol) were added to the reaction mixture, and the reaction was performed according to procedure **B**. The residue was purified by silica gel column chromatography, eluting with 8% methanol in CHCl₃ to get compound **30** as a white solid (0.024 g, 23% yield). mp 90 °C. ¹H NMR (400 MHz, CDCl₃): δ 9.07 (s, 1H), 8.82 (br s, -NH), 8.50 (s, 1H), 8.39 (s, 1H), 8.03 (d, *J* = 6.6 Hz, 1H), 7.89 (d, *J* = 6.3 Hz, 1H), 7.44 (s, 1H), 7.39–7.35 (m, 2H), 7.09 (t, *J* = 5.4 Hz, 1H), 7.04–7.00 (m, 2H), 6.88 (s, 1H), 4.18 (t, *J* = 5.1 Hz, 2H), 3.97–3.93 (m, 2H), 3.80 (s, 3H), 2.33–2.30 (m, 2H). ¹³C NMR (125 MHz, CDCl₃): δ 164.3, 156.5, 152.6, 151.0, 149.3, 147.9, 135.2, 133.3, 130.8, 129.6, 129.4, 126.1, 121.3, 118.7, 111.6, 98.8, 55.7, 45.7, 44.0, 32.5. MS (ESI) m/z : $[M + H]^+$ 427.29. HRMS (ESI) m/z : $[M + H]^+$ calcd for $C_{24}H_{23}N_6O_2$, 427.1882; found, 427.1889. HPLC purity 96.15%.

N-(3-(1*H*-imidazol-1-yl)propyl)-6-(3,4-dimethoxyphenyl)-3-(1,3,4-oxadiazol-2-yl)quinolin-4-amine (**31**). Compound **21** (0.10 g, 0.25 mmol) was taken along with 3,4-dimethoxyphenylboronic acid (0.091 g, 0.5 mmol) in 1,4-dioxane (4 mL) and DMF (1 mL). 2(M) Na_2CO_3 solution (0.3 mL) and Pd(PPh₃)₄ (0.023 g, 0.02 mmol) were added to the mixture, and the reaction was performed according to procedure **B**. After 24 h, the residue was purified by silica gel column chromatography, eluting with 7% methanol in CHCl₃ to afford compound **31** as an off-white solid (0.04 g, 35% yield). mp 205 °C. ¹H NMR (300 MHz, CDCl₃): δ 9.09 (s, 1H), 8.72 (br s, -NH), 8.53 (s, 1H), 8.31 (s, 1H), 8.07 (d, *J* = 8.7 Hz, 1H), 7.94 (dd, *J* = 8.7, 1.2 Hz, 1H), 7.46 (s, 1H), 7.18–7.14 (m, 2H), 7.02 (d, *J* = 7.8 Hz, 2H), 6.90 (s, 1H), 4.22 (t, *J* = 6.9 Hz, 2H), 4.02–3.99 (m, 2H), 3.98 (s, 3H), 3.96 (s, 3H), 2.39–2.31 (m, 2H). ¹³C NMR (75 MHz, CDCl₃): δ 164.2, 152.6, 151.0, 149.6, 149.5, 149.2, 148.0, 137.9, 137.1, 133.3, 130.7, 130.6, 129.9, 123.0, 119.7, 119.4, 118.8, 111.8, 110.6, 99.3, 56.1, 45.9, 43.9, 32.5. MS (ESI) m/z : $[M + H]^+$ 457.45. HRMS (ESI) m/z : $[M + H]^+$ calcd for $C_{25}H_{25}N_6O_3$, 457.1988; found, 457.1992. HPLC purity 95.37%.

N-(3-(1*H*-imidazol-1-yl)propyl)-6-(2,4-dimethoxyphenyl)-3-(1,3,4-oxadiazol-2-yl)quinolin-4-amine (**32**). Compound **21** (0.07 g, 0.18 mmol) was taken along with 2,4-dimethoxyphenylboronic acid (0.064 g, 0.36 mmol) in 1,4-dioxane (4 mL) and DMF (1 mL). 2(M) Na_2CO_3 solution (0.23 mL) and Pd(PPh₃)₄ (0.017 g, 0.014 mmol) were added to the mixture, and the reaction was performed according to procedure **B**. The crude product was purified by silica gel column chromatography, eluting with 7% methanol in CHCl₃ to afford compound **32** as a yellow solid (0.035 g, 44% yield). mp 140 °C. ¹H NMR (300 MHz, CDCl₃): δ 9.07 (s, 1H), 8.80 (br s, -NH), 8.52 (s, 1H), 8.37 (d, *J* = 1.2 Hz, 1H), 8.02 (d, *J* = 8.4 Hz, 1H), 7.88 (dd, *J* =

9, 1.8 Hz, 1H), 7.47 (s, 1H), 7.30 (d, *J* = 8.4 Hz, 1H), 7.03 (s, 1H), 6.90 (s, 1H), 6.66–6.61 (m, 2H), 4.21 (t, *J* = 6.9 Hz, 2H), 4.00–3.93 (m, 2H), 3.89 (s, 3H), 3.80 (s, 3H), 2.37–2.28 (m, 2H). ¹³C NMR (75 MHz, CDCl₃): δ 164.2, 160.8, 157.5, 152.5, 150.9, 149.1, 147.8, 134.9, 133.1, 131.2, 129.3, 125.6, 122.3, 118.7, 105.1, 99.2, 98.8, 55.6, 55.5, 45.6, 43.9, 32.4. MS (ESI) m/z : $[M + H]^+$ 457.51. HRMS (ESI) m/z : $[M + H]^+$ calcd for $C_{25}H_{25}N_6O_3$, 457.1988; found, 457.1985. HPLC purity 97.51%.

N-(3-(1*H*-imidazol-1-yl)propyl)-6-(4-methoxy-3-methylphenyl)-3-(1,3,4-oxadiazol-2-yl)quinolin-4-amine (**33**). Compound **21** (0.07 g, 0.18 mmol) was taken along with 4-methoxy-3-methylphenylboronic acid (0.058 g, 0.36 mmol) in 1,4-dioxane (4 mL) and DMF (1 mL). 2(M) Na_2CO_3 solution (0.23 mL) and Pd(PPh₃)₄ (0.017 g, 0.014 mmol) were added to the mixture, and the reaction was performed according to procedure **B**. The residue was purified by silica gel column chromatography, eluting with 7% methanol in CHCl₃ to produce compound **33** as a pale yellow solid (0.031 g, 40% yield). mp 191 °C. ¹H NMR (300 MHz, CDCl₃): δ 9.07 (s, 1H), 8.75 (br s, -NH), 8.52 (s, 1H), 8.29 (s, 1H), 8.04 (d, *J* = 8.7 Hz, 1H), 7.93 (dd, *J* = 8.7, 1.2 Hz, 1H), 7.46 (s, 1H), 7.43–7.41 (m, 2H), 7.03 (s, 1H), 6.96 (d, *J* = 9.3 Hz, 1H), 6.90 (s, 1H), 4.21 (t, *J* = 6.9 Hz, 2H), 4.02–3.96 (m, 2H), 3.90 (s, 3H), 2.39–2.34 (m, 2H), 2.33 (s, 3H). ¹³C NMR (150 MHz, CDCl₃): δ 164.3, 157.8, 152.6, 151.0, 149.5, 147.9, 137.9, 137.1, 132.4, 130.7, 130.5, 130.0, 129.5, 127.4, 125.6, 122.7, 119.4, 118.8, 110.4, 99.2, 55.5, 46.0, 44.0, 32.6, 16.6. MS (ESI) m/z : $[M + H]^+$ 441.41. HRMS (ESI) m/z : $[M + H]^+$ calcd for $C_{25}H_{25}N_6O_2$, 441.2039; found, 441.2038. HPLC purity 96.92%.

N-(3-(1*H*-imidazol-1-yl)propyl)-6-(4-methoxy-2-methylphenyl)-3-(1,3,4-oxadiazol-2-yl)quinolin-4-amine (**34**). Compound **21** (0.08 g, 0.20 mmol) was taken along with 4-methoxy-2-methylphenylboronic acid (0.067 g, 0.40 mmol) in 1,4-dioxane (4 mL) and DMF (1 mL). 2(M) Na_2CO_3 solution (0.30 mL) and Pd(PPh₃)₄ (0.018 g, 0.016 mmol) were added to the mixture, and the reaction was performed according to procedure **B**. After 7 h, the residue was purified by silica gel column chromatography, eluting with 6% methanol in CHCl₃ to produce compound **34** as a yellow gummy liquid (0.040 g, 45% yield). ¹H NMR (600 MHz, CDCl₃): δ 9.07 (s, 1H), 8.76 (br s, -NH), 8.52 (d, *J* = 1.8 Hz, 1H), 8.06 (s, 1H), 8.00 (d, *J* = 7.2 Hz, 1H), 7.66 (d, *J* = 8.4 Hz, 1H), 7.41 (s, 1H), 7.17 (d, *J* = 6.6 Hz, 1H), 6.98 (s, 1H), 6.84–6.83 (m, 3H), 4.16 (t, *J* = 4.8 Hz, 2H), 3.88–3.87 (m, 2H), 3.84 (s, 3H), 2.28 (m, 2H), 2.26 (s, 3H). ¹³C NMR (125 MHz, CDCl₃): δ 164.2, 159.6, 152.4, 151.1, 149.3, 148.0, 138.4, 137.1, 136.8, 133.5, 133.2, 131.0, 129.7, 129.6, 125.6, 118.9, 118.8, 116.0, 111.5, 99.0, 55.3, 45.8, 43.9, 32.4, 20.9. MS (ESI) m/z : $[M + H]^+$ 441.15. HRMS (ESI) m/z : $[M + H]^+$ calcd for $C_{25}H_{25}N_6O_2$, 441.2039; found, 441.2040. HPLC purity 96.32%.

5-(4-(3-(1*H*-imidazol-1-yl)propylamino)-6-bromoquinolin-3-yl)-1,3,4-oxadiazol-2-amine (**35**). Compound **19** (0.5 g, 1.28 mmol) was dissolved in methanol (5 mL), to which cyanogen bromide (0.163 g, 1.54 mmol) was added. The mixture was refluxed for 4 h. Excess solvent was evaporated, and the organic part was extracted with CHCl₃, washed with saturated NaHCO₃ solution, dried, and concentrated to give compound **35** (0.1 g, 19% yield). mp > 250 °C. ¹H NMR (600 MHz, DMSO-*d*₆): δ 8.67 (s, 1H), 8.43 (s, 1H), 8.25 (t, *J* = 3.6 Hz, -NH), 7.81 (dd, *J* = 9.0, 1.8 Hz, 1H), 7.78 (d, *J* = 8.4 Hz, 1H), 7.55 (s, 1H), 7.12 (s, 1H), 6.86 (s, 1H), 4.06 (t, *J* = 7.2 Hz, 2H), 3.59–3.56 (m, 2H), 2.14–2.09 (m, 2H). ¹³C NMR (150 MHz, DMSO-*d*₆): δ 163.4, 157.0, 149.5, 148.9, 148.1, 133.6, 132.5, 132.0, 128.9, 127.2, 124.2, 120.6, 117.9, 100.2, 45.0, 43.8, 32.1. MS (ESI) m/z : $[M + H]^+$ 414.23. HRMS m/z : $[M + H]^+$ calcd for C₁₇H₁₇BrN₇O, 414.0678; found, 414.0671.

5-(4-(3-(1*H*-imidazol-1-yl)propylamino)-6-(4-methoxyphenyl)quinolin-3-yl)-1,3,4-oxadiazol-2-amine (**36**). Compound **35** (0.07 g, 0.17 mmol) was taken along with 2-(4-methoxyphenyl)-4,4,5,5-tetramethyl-1,3,2-dioxaborolane (0.08 g, 0.34 mmol) in 1,4-dioxane (4 mL) and DMF (1 mL). 2(M) Na_2CO_3 solution (0.3 mL) and Pd(PPh₃)₄ (0.016 g, 0.014 mmol) were added to the mixture, and the reaction was performed according to procedure **B**. The residue was purified by silica gel column chromatography, eluting with 6% methanol in CHCl₃ to produce compound **36** as a brown solid (0.017

g, 23% yield). mp 215 °C. ¹H NMR (600 MHz, DMSO-*d*₆): δ 8.72 (s, 1H), 8.49 (s, 1H), 8.09 (d, *J* = 8.4 Hz, 1H), 7.96 (d, *J* = 8.4 Hz, 1H), 7.77 (d, *J* = 8.4 Hz, 2H), 7.57 (s, 1H), 7.43–7.40 (m, 2H), 7.12 (d, *J* = 9.0 Hz, 2H), 4.26 (t, *J* = 7.2 Hz, 2H), 3.85 (s, 3H), 3.82–3.80 (m, 2H), 2.30–2.25 (m, 2H). ¹³C NMR (150 MHz, DMSO-*d*₆): δ 163.5, 159.8, 156.8, 137.2, 136.5, 132.1, 130.3, 128.8, 122.1, 121.5, 119.4, 115.1, 99.8, 55.8, 45.8, 45.1, 31.3. MS (ESI) *m/z*: [M + H]⁺ 442.29. HRMS (ESI) *m/z*: [M + H]⁺ calcd for C₂₄H₂₄N₇O₂, 442.1991; found, 442.1991. HPLC purity 97.91%.

N-(3-(1*H*-imidazol-1-yl)propyl)-6-bromo-3-(5-methyl-1,3,4-oxadiazol-2-yl)quinolin-4-amine (37). Compound 19 (1 g, 2.57 mmol) was dissolved in ethanol (5 mL), and to the solution, triethyl orthoacetate (5 mL, 27.27 mmol) was added. The reaction mixture was refluxed for 6 h. The residue was purified by column chromatography, eluting with 4% methanol in CHCl₃ to give 37 as a yellow gummy compound (0.25 g, 24% yield). mp 105 °C. ¹H NMR (600 MHz, DMSO-*d*₆): δ 8.71 (s, 1H), 8.50 (d, *J* = 1.8 Hz, 1H), 8.16 (t, *J* = 4.8 Hz, –NH), 7.84 (dd, *J* = 9.0, 1.8 Hz, 1H), 7.78 (d, *J* = 8.4 Hz, 1H), 7.53 (s, 1H), 7.10 (s, 1H), 6.85 (s, 1H), 4.04 (t, *J* = 7.2 Hz, 2H), 2.59 (s, 3H), 2.13–2.08 (m, 2H). ¹³C NMR (100 MHz, CDCl₃): δ 164.2, 162.4, 151.2, 149.1, 148.4, 134.2, 131.9, 127.7, 120.4, 118.4, 99.9, 45.7, 44.0, 32.4, 11.1. MS (ESI) *m/z*: [M + H]⁺ 413.24. HRMS (ESI) *m/z*: [M + H]⁺ calcd for C₁₈H₁₈BrN₆O, 413.0725; found, 413.0718.

N-(3-(1*H*-imidazol-1-yl)propyl)-6-(4-methoxyphenyl)-3-(5-methyl-1,3,4-oxadiazol-2-yl)quinolin-4-amine (38). Compound 37 (0.10 g, 0.24 mmol) was taken along with 2-(4-methoxyphenyl)-4,4,5,5-tetramethyl-1,3,2-dioxaborolane (0.11 g, 0.5 mmol) in 1,4-dioxane (4 mL) and DMF (1 mL). 2(M) Na₂CO₃ solution (0.3 mL) and Pd(PPh₃)₄ (0.023 g, 0.02 mmol) were added to the mixture, and the reaction was performed according to procedure B. It took 6 h to complete the reaction. The residue was purified by silica gel column chromatography, eluting with 4% methanol in CHCl₃ to afford compound 38 as a white solid (0.033 g, 31% yield). mp 224 °C. ¹H NMR (600 MHz, CDCl₃): δ 9.02 (s, 1H), 8.73 (t, *J* = 4.8 Hz, –NH), 8.29 (d, *J* = 1.8 Hz, 1H), 8.04 (d, *J* = 9.0 Hz, 1H), 7.91 (dd, *J* = 8.4, 1.8 Hz, 1H), 7.55 (d, *J* = 8.4 Hz, 2H), 7.45 (s, 1H), 7.04 (d, *J* = 8.4 Hz, 2H), 7.03 (s, 1H), 6.90 (s, 1H), 4.20 (t, *J* = 7.2 Hz, 2H), 3.97–3.93 (m, 2H), 3.88 (s, 3H), 2.69 (s, 3H), 2.34–2.30 (m, 2H). ¹³C NMR (150 MHz, CDCl₃): δ 164.4, 162.2, 159.6, 152.3, 149.4, 147.8, 137.5, 137.1, 132.9, 130.5, 130.3, 129.9, 128.3, 122.7, 119.5, 118.8, 114.6, 99.8, 55.5, 45.9, 44.0, 32.5, 11.1. MS (ESI) *m/z*: [M + H]⁺ 441.72. HRMS (ESI) *m/z*: [M + H]⁺ calcd for C₂₅H₂₃N₆O₂, 441.2039; found, 441.2140. HPLC purity 95.01%.

Ethyl 4-((3-(1H-imidazol-1-yl)propyl)amino)-6-(4-methoxyphenyl)quinoline-3-carboxylate (39). Compound 17 (0.1 g, 0.25 mmol) was taken along with 2-(4-methoxyphenyl)-4,4,5,5-tetramethyl-1,3,2-dioxaborolane (0.12 g, 0.51 mmol) in 1,4-dioxane (5 mL). 2(M) Na₂CO₃ solution (0.3 mL) and Pd(PPh₃)₄ (0.023 g, 0.02 mmol) were added to the mixture, and the reaction was performed according to procedure B. The reaction was completed in 6 h. The residue was purified by silica gel column chromatography to afford compound 39 as a white solid (0.035 g, 33% yield). mp 190 °C. ¹H NMR (600 MHz, CD₃OD): δ 8.91 (s, 1H), 8.38 (s, 1H), 8.06 (d, *J* = 8.4 Hz, 1H), 7.87 (d, *J* = 8.4 Hz, 2H), 7.61 (d, *J* = 7.2 Hz, 2H), 7.24 (s, 1H), 7.07–7.06 (m, 3H), 4.42 (q, *J* = 7.2 Hz, 2H), 4.26 (t, *J* = 6.6 Hz, 2H), 3.95 (t, *J* = 6.6 Hz, 2H), 3.86 (s, 3H), 2.35–2.32 (m, 2H), 1.43 (t, *J* = 7.2 Hz, 3H). ¹³C NMR (150 MHz, CD₃OD): δ 167.7, 160.1, 157.2, 147.9, 138.1, 131.6, 128.0, 125.6, 123.1, 118.9, 114.3, 102.7, 61.3, 54.5, 48.2, 45.6, 31.2, 13.1. MS (ESI) *m/z*: [M + H]⁺ 431.08. HRMS (ESI) *m/z*: [M + H]⁺ calcd for C₂₅H₂₇N₄O₃, 431.2083; found, 431.2083. HPLC purity 98.92%.

Ethyl 4-((3-(1H-imidazol-1-yl)propyl)amino)-6-(3,4-dimethoxyphenyl)quinoline-3-carboxylate (40). Compound 17 (0.1 g, 0.25 mmol) was taken along with 3,4-dimethoxyphenylboronic acid (0.091 g, 0.5 mmol) in 1,4-dioxane (5 mL). 2(M) Na₂CO₃ solution (0.3 mL) and Pd(PPh₃)₄ (0.023 g, 0.02 mmol) were added to the mixture, and the reaction was performed according to procedure B. After 6 h, the residue was purified by silica gel column chromatography to get compound 40 as a white solid (0.038 g, 33%

yield). mp 162 °C. ¹H NMR (300 MHz, CD₃OD): δ 8.98 (s, 1H), 8.54 (s, 1H), 8.24–8.22 (m, 2H), 7.95 (d, *J* = 8.7 Hz, 1H), 7.41 (s, 1H), 7.33–7.31 (m, 2H), 7.23 (s, 1H), 7.14 (d, *J* = 9.0 Hz, 1H), 4.48 (q, *J* = 6.9 Hz, 2H), 4.37 (t, *J* = 6.9 Hz, 2H), 4.13 (t, *J* = 6.3 Hz, 2H), 3.95 (s, 3H), 3.92 (s, 3H), 2.51–2.42 (m, 2H), 1.47 (t, *J* = 7.2 Hz, 3H). ¹³C NMR (150 MHz, CD₃OD): δ 167.0, 157.8, 149.9, 149.7, 145.9, 139.2, 132.9, 131.9, 123.7, 123.0, 120.4, 119.8, 118.5, 112.1, 110.8, 102.6, 61.8, 55.4, 55.1, 45.6, 45.1, 30.7, 13.1. MS (ESI) *m/z*: [M + H]⁺ 461.1117. HRMS (ESI) *m/z*: [M + H]⁺ calcd for C₂₆H₂₉N₄O₄, 461.2189; found, 461.2192. HPLC purity 98.80%.

Ethyl 6-Bromo-4-(methylamino)quinoline-3-carboxylate (41). Compound 1 (0.5 g, 1.59 mmol) was dissolved in tetrahydrofuran (THF, 3 mL) under N₂ atmosphere in a sealed tube. To the reaction mixture, dry DIPEA (0.6 mL, 3.18 mmol) and methylamine (0.7 mL, 15.9 mmol) were added. The reaction mixture was heated for 16 h at 60 °C. Organic part was extracted with chloroform. The crude was purified by column chromatography to obtain compound 41 (0.2 g, 41% yield). mp 134 °C. ¹H NMR (300 MHz, CDCl₃): δ 9.48 (br s, –NH), 9.07 (s, 1H), 8.48 (d, *J* = 1.8 Hz, 1H), 7.81 (d, *J* = 9.0 Hz, 1H), 7.72 (dd, *J* = 8.7, 2.1 Hz, 1H), 4.38 (q, *J* = 7.2 Hz, 2H), 3.50 (d, *J* = 5.4 Hz, 3H), 1.42 (t, *J* = 7.2 Hz, 3H). ¹³C NMR (150 MHz, CDCl₃): δ 168.8, 156.4, 151.8, 149.8, 134.3, 131.5, 128.4, 120.5, 117.2, 102.8, 60.9, 35.4, 14.3. ESI-MS *m/z*: 309.02 [M + H]⁺. HRMS (ESI) *m/z*: [M + H]⁺ calcd for C₁₃H₁₄BrN₂O₂, 309.0238; found, 309.0236.

6-Bromo-4-(methylamino)quinoline-3-carbohydrazide (42). Compound 41 (0.5 g, 1.62 mmol) was dissolved in ethanol (8 mL). To the solution, hydrazine hydrate (8 mL) was added. The reaction mixture was stirred for 12 h at room temperature. Ethanol was removed under vacuum. The residue was then dissolved in CHCl₃, and the organic layer was washed with water and brine, dried, and concentrated to give compound 42 as a yellow solid (0.34 g, 73% yield). mp > 250 °C. ¹H NMR (600 MHz, DMSO-*d*₆): δ 9.59 (s, 1H), 8.51 (d, *J* = 1.8 Hz, 1H), 8.26 (s, –CONH–, 1H), 7.74 (dd, *J* = 9.0, 1.8 Hz, 1H), 7.69 (d, *J* = 9.0 Hz, 1H), 2.91 (d, *J* = 4.8 Hz, 3H). ¹³C NMR (100 MHz, CDCl₃ + 1 drop CD₃OD): δ 150.3, 149.9, 133.3, 129.6, 124.8, 118.5, 31.3. ESI-MS *m/z*: 295.24 (M + H)⁺. HRMS (ESI) *m/z*: [M + H]⁺ calcd for C₁₁H₁₂BrN₄O, 295.0194; found, 295.0192.

6-Bromo-N-methyl-3-(1,3,4-oxadiazol-2-yl)quinolin-4-amine (43). Compound 42 (0.5 g, 1.7 mmol) was taken in triethyl orthoacetate (5 mL, 30.06 mmol), and the mixture was heated for 14 h at 140 °C. The residue was purified by column chromatography, eluting with 4% methanol in CHCl₃ to afford compound 43 as a yellow solid (0.15 g, 29% yield). mp 220 °C. ¹H NMR (300 MHz, CDCl₃): δ 9.02 (s, 1H), 8.57 (s, 1H), 8.48 (s, 1H), 7.86 (d, *J* = 9.0 Hz, 1H), 7.76 (dd, *J* = 9.0, 1.5 Hz, 1H), 3.62 (d, *J* = 5.1 Hz, 3H). ¹³C NMR (100 MHz, CDCl₃): δ 152.1, 151.0, 148.6, 134.2, 131.8, 128.2, 120.3, 117.9, 98.6, 35.7. ESI-MS *m/z*: 304.86 [M + H]⁺. HRMS (ESI) *m/z*: [M + H]⁺ calcd for C₁₂H₉BrN₄O, 305.0038; found, 305.0029.

6-(4-Methoxyphenyl)-N-methyl-3-(1,3,4-oxadiazol-2-yl)quinolin-4-amine (44). Compound 43 (0.1 g, 0.33 mmol) was taken along with 2-(4-methoxyphenyl)-4,4,5,5-tetramethyl-1,3,2-dioxaborolane (0.12 g, 0.51 mmol) in 1,4-dioxane (5 mL). 2(M) Na₂CO₃ solution (0.4 mL) and Pd(PPh₃)₄ (0.03 g, 0.03 mmol) were added to the mixture, and the reaction was performed according to procedure B. The residue was purified by silica gel column chromatography to afford compound 40 as a white solid (0.038 g, 35% yield). mp 155 °C. ¹H NMR (600 MHz, CDCl₃): δ 9.03 (s, –NH), 8.57 (s, 1H), 8.48 (s, 1H), 8.05 (d, *J* = 8.4 Hz, 1H), 7.93 (d, *J* = 8.4 Hz, 1H), 7.62 (d, *J* = 7.8 Hz, 2H), 7.05 (d, *J* = 7.8 Hz, 2H), 6.79 (s, 1H), 3.89 (s, 3H), 3.71 (d, *J* = 4.8 Hz, 3H). ¹³C NMR (150 MHz, CDCl₃): δ 164.2, 159.5, 153.2, 150.8, 147.9, 137.0, 133.0, 130.3, 130.2, 128.3, 123.3, 119.3, 116.1, 114.8, 114.6, 98.3, 55.5, 36.0. MS (ESI) *m/z*: [M + H]⁺ 333.55. HRMS *m/z*: [M + H]⁺ calcd for C₁₉H₁₇N₄O₂, 333.1351; found, 333.1338. HPLC purity 95.14%.

Recombinant Human Top1 and Plasmid DNA Relaxation Assay. The recombinant human Top1 was purified from Sf-9 insect cells which were infected with the recombinant baculovirus (a kind gift from Prof. James J. Champoux) as described previously.^{12,20} The

type 1 DNA topoisomerases are assayed by the decreased mobility of the relaxed isomers of supercoiled pBS (SK+) DNA in 1% agarose gel. The relaxation assay was carried out with recombinant human Top1 or the whole cell extracts of MCF7 cells as a source of endogenous Top1, diluted in the relaxation buffer with supercoiled plasmid DNA as described previously.^{12,38,40}

Cleavage Assay. Plasmid DNA cleavage assay was carried out as described previously.^{12,20} Equilibrium cleavage assays with a 25-mer duplex of an oligonucleotide containing a Top1 binding motif were labeled and annealed as described previously.^{38,40} Samples were analyzed by 12% sequencing gel electrophoresis, dried, exposed on PhosphorImager screens, and imaged with Typhoon FLA 7000 (GE Healthcare, UK).

Analysis of Compound 28–DNA Intercalation. The ability of the drug to intercalate into plasmid DNA was determined by Top1 unwinding assay.^{12,40} Assays were performed with 50 fmol of pBluscript (SK+) DNA in the presence or absence of compound 28, *m*-AMSA, and etoposide. Relaxed DNA was prepared by treatment of the supercoiled plasmid DNA with an excess of Top1, followed by proteinase K digestion at 37 °C, phenol/chloroform extraction, and ethanol precipitation. After incubation at 37 °C for 15 min, reactions were terminated and electrophoresed onto 1% agarose gel as described above. The DNA band was stained with 0.5 µg/mL of EtBr and visualized by UV light as described above.

Second, an ethidium displacement fluorescence assay⁴⁰ was employed to determine whether compound 28 binds in the minor groove of DNA. Fluorescence emission spectra ($\lambda_{\text{max}} = 590$ nm, excitation wavelength 510 nm) were obtained at 25 °C. The assays contained 1 µM EtBr, 0–300 mM compound 28, and 5 nM CT DNA in 2 mL of fluorescence buffer.

Cell Culture and Transfection. Human cancerous cell lines such as MCF7, HeLa, HCT116, NIH: OVCAR-3, and HEK293 obtained from the Developmental Therapeutics Program as a kind gift from Dr. Yves Pommier (NIH/NCI/USA) and TDP1+/+ and TDP1–/– primary MEF (mouse embryonic fibroblasts) cells as a kind gift from Dr. Cornelius F. Boerkoel (University of British Columbia, Canada) were cultured as described previously.^{51,53} Plasmid DNAs were transfected with Lipofectamine 2000 (Invitrogen) according to the manufacturer's protocol.

Photobleaching Experiments. Photobleaching experiments were performed as described previously^{12,51} using an Andor Spinning disk inverted confocal laser-scanning microscope equipped with a 60×/1.42 NA oil-immersion objective (Olympus) and with a CO₂-controlled on-stage heated environmental chamber set to 37 °C. FRAP analyses were carried out with living MCF7 cells that ectopically express EGFP-human Top1 constructs (wild-type and N722S),⁵⁰ which were grown on chamber cover glass (Genetix, India) and drug-treated as indicated. For FRAP analysis, a subnuclear spot was bleached for 30 ms by solid-state laser line (488 nm for EGFP) adapted to the fluorescent protein of interest, and FRAP curves were generated individually normalized to the prebleach signal as described previously.^{50,52,53}

Immunocytochemistry and Confocal Microscopy. Immunofluorescence staining and confocal microscopy were performed as described previously.^{51–53} After treatment, MCF7 cells were fixed with 4% paraformaldehyde for 10 min at room temperature. Primary antibody against γ H2AX (Cell Signaling, USA) was detected using anti-mouse IgG secondary antibodies labeled with Alexa 488 (Invitrogen). Cells were mounted in anti-fade solution with 4',6-diamidino-2-phenylindole (Vector Laboratories, Burlingame, CA) and examined using a laser scanning confocal microscope (Leica TCS SP8 confocal laser-scanning microscope) with a ×63 oil objective. The γ H2AX intensity per nucleus was determined with Adobe Photoshop 7.0 by measuring the fluorescence intensities normalized to the number of cell count.⁵¹

Cell Survival Assay. Cell survival was assessed by the 3-(4,5-dimethylthiazol-2-yl)-2,5-diphenyltetrazolium bromide assay as discussed previously.^{12,20} The percent inhibition of viability for each concentration of the compounds was calculated with respect to the control, and IC₅₀ values were estimated.

Molecular Docking Study. The molecular docking experiment was performed for selected compounds with LibDock in Discovery Studio 4.1 client. The ligand centroid coordinates of the ternary complex for docking were defined using the ligand in the Top1–DNA–CPT crystal structure (PDB code 1T81) as the center of the binding pocket ($x = 21.386168$, $y = -2.148207$, $z = 28.116527$). The docking study suggests the probable binding poses of these inhibitors in the binding site in the Top1–DNA cleavage complex. The best poses for every ligand were selected based on the hydrogen bond interaction with Arg364, Asn722, and Asp533 and π – π hydrophobic interactions. The entire complex was subsequently subjected to minimization using a full minimization method executing 2000 steps, which maintained the root-mean-square gradient of 0.01 kcal mol⁻¹. The best binding pose of compound 28 is depicted in Figure 1D.

Aqueous Solubility Assay. Five microliters of 20 mM dimethyl sulfoxide (DMSO) stock from the stock plate was added to the reaction deep well plate containing 495 µL of pH 7.4 pION buffer, which includes DMSO control, and the samples were mixed and incubated for 18 h. The plate was sealed well during the incubation process. The DMSO content in the sample was <1.0%. The concentration in deep well plates was 200 µM. The working stock plate was prepared by adding 4 µL of 20 mM stock (including DMSO control) to 996 µL of acetonitrile. The working stock (75 µL) was added to 75 µL of blank buffer and read on a spectrophotometer as a reference plate at 240 nm. At the end of the incubation period, a filter plate was used to vacuum-filter 100 µL of the sample from the storage plate. This step wets the filters, and the filtrate was discarded. Another 200 µL of the sample from a deep well plate was vacuum-filtered into a new filter collection plate. The filtrate (75 µL) from the filter collection plate was transferred to a UV sample plate. Acetonitrile (75 µL) was added to this UV plate. The solution was mixed, and the spectrum was read using the UV spectrophotometer at 240 nm. Plates were read on spectramax using SoftMax Pro software version 5.3.

Human Plasma Stability Assay. The stock solution of 10 mM in DMSO was prepared and stored at 4 °C. Stock (25 µM) of the test compound was prepared in acetonitrile: water by diluting from the previously prepared 10 mM stock (i.e., 2.5 µL of 10 mM stock solution was added to 997.5 µL of acetonitrile/water (50:50)). The frozen plasma was thawed at room temperature and centrifuged at 1400× RCF 4 °C, for 15 min. Approximately 90% of the clear supernatant fraction was transferred to a separate tube and was then used for the assay.

For 0 min samples, plasma was heat-inactivated at 56 °C for 45 min. Three microliters of 25 µM test compound was added to 72 µL of heat-inactivated plasma. A 25 µL aliquot of the mixture was taken and crashed with 200 µL of acetonitrile containing internal standard and further processed along with other time points. A final working stock of 1 µM was prepared by diluting in plasma for other time point samples (i.e., 8 µL of 25 µM acetonitrile/water stock was added to 192 µL of plasma). Two hundred microliters of plasma containing the test compound was incubated for 2 h at 37 °C in a shaker water bath with gentle shaking. A 25 µL aliquot of the sample at 0, 15, 30, 60, and 120 min was precipitated immediately with 200 µL of acetonitrile containing internal standard and centrifuged at 4000× RCF, 4 °C for 20 min. The supernatant (150 µL) was diluted with 150 µL of water and analyzed on liquid chromatography–mass spectrometry (LC–MS)/MS.

Lipophilicity Assay. NaH₂PO₄·2H₂O (1.56 g) was dissolved in 0.5 L of water in a 1 L beaker. The volume of the solution was made up to 1 L after adjusting the pH to 7.4 using NaOH solution. Equal volumes of sodium phosphate buffer (10 mM, pH 7.4) and *n*-octanol were added to a separation funnel and mixed thoroughly. The two layers were allowed to separate for 2 days and then dispensed in two separate glass bottles. Stock solution (10 mM) was prepared in 100% DMSO and stored at 4 °C. The organic phase (1-octanol) (500 µL) was added to each well of a 2 mL deep well plate, followed by 500 µL of buffer, and 15 µL of the test substance was added. The plate was vortexed for 1 h on a plate shaker at 1200 rpm. The samples were allowed to equilibrate for 20 min after incubation, centrifuged at 4000

rpm for 30 min for complete phase separation, and then analyzed by LC-UV.

Caco-2 Permeability Assay. Five microliters of 100 mM sodium pyruvate, 5 mL of 100× nonessential amino acids, and 5 mL of pen-strep were added to 100 mL of heat-inactivated fetal bovine serum to 385 mL of Dulbecco's modified Eagle's medium (DMEM) aseptically and mixed thoroughly. One vial of Hank's balanced salt (Sigma-H1387) was dissolved in 900 mL of Milli-Q water, and the pH was adjusted to 7.4. The volume was made up to 1000 mL with the same. The solution was filter-sterilized and stored at 4 °C. Stock solution of test compound (10 mM) was prepared in DMSO. Stock (10 mM) was diluted with Hank's balanced salt solution (HBSS) buffer to a final concentration of 10 μ M.

Revival of Caco-2 cells: as per SOP-BIO-IA-TCL-013-00.

Subculturing of Caco-2 cells: as per SOP-BIO-TCL-013-00.

DMEM (250 μ L) was added to the basal compartment of a 96-well multiscreen Caco-2 plate, 12 000 cells/well (0.16×10^6 cells/mL) were seeded in all the apical wells required and one well with only media as blank without cells, and the Caco-2 plate was placed in a CO₂ incubator at 37 °C for proliferation of cells. On the day of assay, the medium was removed and washed twice with HBSS buffer. The medium was incubated with HBSS buffer for 30 min in an incubator, and wells with transepithelial electrical resistance values $>230 \Omega \cdot \text{cm}^2$ were selected for the incubation. The test compound (75 μ L) was added to apical wells, and 250 μ L of HBSS buffer with 2% bovine serum albumin (BSA) was added to basal wells. Basal samples (25 μ L) were collected at 120 min and processed as mentioned below. The test compound (250 μ L) was added to basal wells, and 75 μ L of HBSS buffer with 2% BSA was added to apical wells. Apical samples (25 μ L) were collected at 120 min and processed as stated below. Single point calibration curve in HBSS buffer with 2% BSA was used. Donor samples were diluted 1:1 with HBSS containing 2% BSA, and receiver samples were diluted with 1.1 HBSS buffer. It was precipitated with 200 μ L of acetonitrile containing internal standard, vortexed for 5 min @ 1000 rpm, and then centrifuged at 4000 rpm for 10 min. Finally, 100 μ L of the supernatant was diluted with 200 μ L of water and submitted for LC-MS/MS analysis.

■ ASSOCIATED CONTENT

● Supporting Information

The Supporting Information is available free of charge on the ACS Publications website at DOI: [10.1021/acs.jmedchem.8b01938](https://doi.org/10.1021/acs.jmedchem.8b01938).

X-ray crystal data of compound **28**, cytotoxicity data of compound **28** and CPT in various cell lines, molecular docking analysis of compounds **22**, **27**, **31**, and **33**, ¹H NMR and ¹³C NMR spectra of compounds **1–44**, and HPLC chromatogram of tested compounds (PDF)
Molecular formula strings (CSV)

■ AUTHOR INFORMATION

Corresponding Authors

*E-mail: pcbhd@iacs.res.in (B.B.D.).

*E-mail: atalukdar@iicb.res.in (A.T.).

ORCID

Benu Brata Das: 0000-0003-2519-7105

Arindam Talukdar: 0000-0002-7831-1795

Author Contributions

^{||}B.K., S.K.D., and S.P.C. equally contributed for this paper.

Notes

The authors declare no competing financial interest.

■ ACKNOWLEDGMENTS

The A.T. team would like to thank CSIR-IICB intramural research fund and DBT BT/Indo-Aus/10/22/2016 for

funding. B.K., S.P.C., and A.M. thank UGC for their fellowship. S.K.D. thanks IACS for SRF. S.P. would like to thank ICMR for SRF. D.S. and D.B. would like to thank DST-INSPIRE for fellowship. The B.B.D. team is supported by Wellcome Trust/DBT India Alliance intermediate fellowship grant (award# IA/I/13/1/500888) and IACS intramural funding. A.G. is an India Alliance SRF. B.B.D. is a Wellcome Trust/DBT India Alliance Intermediate fellow.

■ ABBREVIATIONS

HTop1, human topoisomerase 1; CPT, camptothecin; Top1cc, topoisomerase 1–DNA cleavage complexes; IC₅₀, the half-maximal inhibitory concentration; FRAP, fluorescence recovery after photobleaching; Pgp, permeability glycoprotein; ADME, absorption, distribution, metabolism, and excretion; DSBs, DNA double-strand breaks; DIPEA, *N,N*-diisopropylethylamine; pBS (SK+) DNA, pBluescript plasmid DNA; EGFP, enhanced green fluorescent protein

■ REFERENCES

- (1) Champoux, J. J. DNA topoisomerases: structure, function, and mechanism. *Annu. Rev. Biochem.* **2001**, *70*, 369–413.
- (2) Pommier, Y. Topoisomerase I inhibitors: camptothecins and beyond. *Nat. Rev. Cancer* **2006**, *6*, 789–802.
- (3) Wang, J. C. Cellular roles of DNA topoisomerases: a molecular perspective. *Nat. Rev. Mol. Cell Biol.* **2002**, *3*, 430–440.
- (4) Bansal, S.; Bajaj, P.; Pandey, S.; Tandon, V. Topoisomerases: resistance versus sensitivity, how far we can go? *Med. Res. Rev.* **2017**, *37*, 404–438.
- (5) Pommier, Y.; Marchand, C. Interfacial inhibitors: targeting macromolecular complexes. *Nat. Rev. Drug Discovery* **2011**, *11*, 25–36.
- (6) Pommier, Y. Drugging topoisomerases: lessons and challenges. *ACS Chem. Biol.* **2013**, *8*, 82–95.
- (7) Ghilarov, D. A.; Shkundina, I. S. DNA topoisomerases and their functions in a cell. *Mol. Biol.* **2012**, *46*, 47–57.
- (8) Kathiravan, M. K.; Khilare, M. M.; Nikoomanesh, K.; Chothe, A. S.; Jain, K. S. Topoisomerase as Target for Antibacterial and Anticancer Drug Discovery. *J. Enzyme Inhib. Med. Chem.* **2013**, *28*, 419–435.
- (9) Capranico, G.; Marinello, J.; Chillemi, G. Type I DNA topoisomerases. *J. Med. Chem.* **2017**, *60*, 2169–2192.
- (10) Akerman, K. J.; Fagenson, A. M.; Cyril, V.; Taylor, M.; Muller, M. T.; Akerman, M. P.; Munro, O. Q. Gold(III) macrocycles: nucleotide-specific unconventional catalytic inhibitors of human topoisomerase I. *J. Am. Chem. Soc.* **2014**, *136*, 5670–5682.
- (11) Cagir, A.; Jones, S. H.; Gao, R.; Eisenhauer, B. M.; Hecht, S. M.; Luotonen, A. Luotonen A. A Naturally Occurring Human DNA Topoisomerase I Poison. *J. Am. Chem. Soc.* **2003**, *125*, 13628–13629.
- (12) Das, S. K.; Ghosh, A.; Paul Chowdhuri, S.; Halder, N.; Rehman, I.; Sengupta, S.; Sahoo, K. C.; Rath, H.; Das, B. B. Neutral porphyrin derivative exerts anticancer activity by targeting cellular topoisomerase I (top1) and promotes apoptotic cell death without stabilizing top1-DNA cleavage complexes. *J. Med. Chem.* **2018**, *61*, 804–817.
- (13) Beretta, G. L.; Ribaud, G.; Menegazzo, I.; Supino, R.; Capranico, G.; Zunino, F.; Zagotto, G. Synthesis and evaluation of new naphthalene and naphthoquinone derivatives as anticancer agents. *Arch. Pharm.* **2017**, *350*, No. e1600286.
- (14) Pommier, Y. DNA topoisomerase I inhibitors: chemistry, biology, and interfacial inhibition. *Chem. Rev.* **2009**, *109*, 2894–2902.
- (15) Pommier, Y.; Cushman, M. The indenoisoquinoline non-camptothecin topoisomerase I inhibitors: update and perspectives. *Mol. Cancer Ther.* **2009**, *8*, 1008–1014.
- (16) Wall, M. E.; Wani, M. C.; Cook, C. E.; Palmer, K. H.; McPhail, A. T.; Sim, G. A. Plant Antitumor Agents. I. The Isolation and Structure of Camptothecin, a Novel Alkaloidal Leukemia and Tumor

Inhibitor from *Camptotheca acuminata*1,2. *J. Am. Chem. Soc.* **1966**, *88*, 3888–3890.

(17) Strumberg, D.; Pommier, Y.; Paull, K.; Jayaraman, M.; Nagafuji, P.; Cushman, M. Synthesis of cytotoxic indenoisoquinoline topoisomerase I poisons. *J. Med. Chem.* **1999**, *42*, 446–457.

(18) Beck, D. E.; Agama, K.; Marchand, C.; Chergui, A.; Pommier, Y.; Cushman, M. Synthesis and biological evaluation of new carbohydrate-substituted indenoisoquinoline topoisomerase I inhibitors and improved syntheses of the experimental anticancer agents indotecan (LMP400) and indimitecan (LMP776). *J. Med. Chem.* **2014**, *57*, 1495–1512.

(19) Prudhomme, M. Biological targets of antitumor indolocarbazoles bearing a sugar moiety. *Curr. Med. Chem.: Anti-Cancer Agents* **2004**, *4*, 509–521.

(20) Majumdar, P.; Bathula, C.; Basu, S. M.; Das, S. K.; Agarwal, R.; Hati, S.; Singh, A.; Sen, S.; Das, B. B. Design, Synthesis and evaluation of thiohydantoin derivatives as potent topoisomerase I (top1) inhibitors with anticancer activity. *Eur. J. Med. Chem.* **2015**, *102*, 540–551.

(21) Beretta, G. L.; Zuco, V.; Perego, P.; Zaffaroni, N. Targeting DNA topoisomerase I with non-camptothecin poisons. *Curr. Med. Chem.* **2012**, *19*, 1238–1257.

(22) Pommier, Y.; Cushman, M.; Doroshow, J. H. Novel clinical indenoisoquinoline topoisomerase I inhibitors: a twist around the camptothecins. *Oncotarget* **2018**, *9*, 26466–26490.

(23) A phase I study of indenoisoquinolines LMP400 and LMP776 in adults with relapsed solid tumors and lymphomas. <https://clinicaltrials.gov/ct2/show/NCT01051635> (accessed Nov 1, 2018).

(24) Prijovich, Z. M.; Burnouf, P.-A.; Chou, H.-C.; Huang, P.-T.; Chen, K.-C.; Cheng, T.-L.; Leu, Y.-L.; Roffler, S. R. Synthesis and antitumor properties of BQC-Glucuronide, a camptothecin prodrug for selective tumor activation. *Mol. Pharm.* **2016**, *13*, 1242–1250.

(25) Xiao, X.; Antony, S.; Kohlhagen, G.; Pommier, Y.; Cushman, M. Novel autoxidative cleavage reaction of 9-fluorenedes discovered during synthesis of a potential DNA-threading indenoisoquinoline. *J. Org. Chem.* **2004**, *69*, 7495–7501.

(26) Morrell, A.; Antony, S.; Kohlhagen, G.; Pommier, Y.; Cushman, M. A systematic study of nitrated indenoisoquinolines reveals a potent topoisomerase I inhibitor. *J. Med. Chem.* **2006**, *49*, 7740–7753.

(27) Nagarajan, M.; Morrell, A.; Fort, B. C.; Meckley, M. R.; Antony, S.; Kohlhagen, G.; Pommier, Y.; Cushman, M. Synthesis and anticancer activity of simplified indenoisoquinoline topoisomerase I inhibitors lacking substituents on the aromatic rings. *J. Med. Chem.* **2004**, *47*, 5651–5661.

(28) Lv, P.-C.; Elsayed, M. S. A.; Agama, K.; Marchand, C.; Pommier, Y.; Cushman, M. Design, synthesis, and biological evaluation of potential prodrugs related to the experimental anticancer agent indotecan (LMP400). *J. Med. Chem.* **2016**, *59*, 4890–4899.

(29) Beck, D. E.; Reddy, P. V. N.; Lv, W.; Abdelmalak, M.; Tender, G. S.; Lopez, S.; Agama, K.; Marchand, C.; Pommier, Y.; Cushman, M. Investigation of the Structure-Activity Relationships of Aza-A-Ring Indenoisoquinoline Topoisomerase I Poisons. *J. Med. Chem.* **2016**, *59*, 3840–3853.

(30) Rasheed, Z. A.; Rubin, E. H. Mechanisms of resistance to topoisomerase I-targeting drugs. *Oncogene* **2003**, *22*, 7296–7304.

(31) Sirikantaramas, S.; Yamazaki, M.; Saito, K. Mutations in topoisomerase I as a self-resistance mechanism coevolved with the production of the anticancer alkaloid camptothecin in plants. *Proc. Natl. Acad. Sci. U.S.A.* **2008**, *105*, 6782–6786.

(32) Taliani, S.; Pugliesi, I.; Barresi, E.; Salerno, S.; Marchand, C.; Agama, K.; Simorini, F.; La Motta, C.; Marini, A. M.; Di Leva, F. S.; Marinelli, L.; Cosconati, S.; Novellino, E.; Pommier, Y.; Di Santo, R.; Da Settimo, F. Phenylpyrazolo[1,5-a]quinazolin-5(4H)-one: A suitable scaffold for the development of noncamptothecin topoisomerase I (top1) inhibitors. *J. Med. Chem.* **2013**, *56*, 7458–7462.

(33) Nagarajan, M.; Xiao, X.; Antony, S.; Kohlhagen, G.; Pommier, Y.; Cushman, M. Design, synthesis, and biological evaluation of indenoisoquinoline topoisomerase I inhibitors featuring polyamine

side chains on the lactam nitrogen. *J. Med. Chem.* **2003**, *46*, 5712–5724.

(34) Nagarajan, M.; Morrell, A.; Ioanoviciu, A.; Antony, S.; Kohlhagen, G.; Agama, K.; Hollingshead, M.; Pommier, Y.; Cushman, M. Synthesis and evaluation of indenoisoquinoline topoisomerase I inhibitors substituted with nitrogen heterocycles. *J. Med. Chem.* **2006**, *49*, 6283–6289.

(35) Cushman, M.; Jayaraman, M.; Vroman, J. A.; Fukunaga, A. K.; Fox, B. M.; Kohlhagen, G.; Strumberg, D.; Pommier, Y. Synthesis of New Indeno[1,2-c]isoquinolines: Cytotoxic Non-Camptothecin Topoisomerase I Inhibitors. *J. Med. Chem.* **2000**, *43*, 3688–3698.

(36) Fox, B. M.; Xiao, X.; Antony, S.; Kohlhagen, G.; Pommier, Y.; Staker, B. L.; Stewart, L.; Cushman, M. Design, Synthesis, and Biological Evaluation of Cytotoxic 11-Alkenylindenoisoquinoline Topoisomerase I Inhibitors and Indenoisoquinoline–Camptothecin Hybrids. *J. Med. Chem.* **2003**, *46*, 3275–3282.

(37) Cinelli, M. A.; Reddy, P. V. N.; Lv, P.-C.; Liang, J.-H.; Chen, L.; Agama, K.; Pommier, Y.; van Breemen, R. B.; Cushman, M. Identification, synthesis, and biological evaluation of metabolites of the experimental cancer treatment drugs indotecan (LMP400) and indimitecan (LMP776) and investigation of isomerically hydroxylated indenoisoquinoline analogues as topoisomerase I Poisons. *J. Med. Chem.* **2012**, *55*, 10844–10862.

(38) Das, B. B.; Sen, N.; Ganguly, A.; Majumder, H. K. Reconstitution and functional characterization of the unusual bi-subunit type I DNA topoisomerase from *Leishmania donovani*. *FEBS Lett* **2004**, *565*, 81–88.

(39) Das, B. B.; Sen, N.; Dasgupta, S. B.; Ganguly, A.; Majumder, H. K. N-terminal Region of the Large Subunit of *Leishmania donovani* Bi-subunit Topoisomerase I Is Involved in DNA Relaxation and Interaction with the Smaller Subunit. *J. Biol. Chem.* **2005**, *280*, 16335–16344.

(40) Das, B. B.; Sen, N.; Roy, A.; Dasgupta, S. B.; Ganguly, A.; Mohanta, B. C.; Dinda, B.; Majumder, H. K. Differential induction of *Leishmania donovani* bi-subunit topoisomerase I-DNA cleavage complex by selected flavones and camptothecin: activity of flavones against camptothecin-resistant topoisomerase I. *Nucleic Acids Res.* **2006**, *34*, 1121–1132.

(41) Staker, B. L.; Feese, M. D.; Cushman, M.; Pommier, Y.; Zembower, D.; Stewart, L.; Burgin, A. B. Structures of Three Classes of Anticancer Agents Bound to the Human Topoisomerase I–DNA Covalent Complex. *J. Med. Chem.* **2005**, *48*, 2336–2345.

(42) Pommier, Y.; Jenkins, J.; Kohlhagen, G.; Leteurtre, F. DNA recombinase activity of eukaryotic DNA topoisomerase I; effects of camptothecin and other inhibitors. *Mutat. Res., DNA Repair* **1995**, *337*, 135–145.

(43) Leeson, P. D.; Springthorpe, B. The influence of drug-like concepts on decision-making in medicinal chemistry. *Nat. Rev. Drug Discovery* **2007**, *6*, 881–890.

(44) Veber, D. F.; Johnson, S. R.; Cheng, H. Y.; Smith, B. R.; Ward, K. W.; Kopple, K. D. Molecular properties that influence the oral bioavailability of drug candidates. *J. Med. Chem.* **2002**, *45*, 2615–2623.

(45) Navia, M.; Chaturvedi, P. Design principles for orally bioavailable drugs. *Drug Discovery Today* **1996**, *1*, 179–189.

(46) Derakhshandeh, K.; Hochhaus, G.; Dadashzadeh, S. In-vitro Cellular Uptake and Transport Study of 9-Nitrocamptothecin PLGA Nanoparticles Across Caco-2 Cell Monolayer Model. *Iran J. Pharm. Res.* **2011**, *10*, 425–434.

(47) Lalloo, A. K.; Luo, F. R.; Guo, A.; Paranjpe, P. V.; Lee, S.-H.; Vyas, V.; Rubin, E.; Sinko, P. J. Membrane transport of camptothecin: facilitation by human P-glycoprotein (ABCB1) and multidrug resistance protein 2 (ABCC2). *BMC Med.* **2004**, *2*, 16.

(48) Garcia-Carbonero, R.; Supko, J. G. Current perspectives on the clinical experience, pharmacology, and continued development of the camptothecins. *Clin. Cancer Res.* **2002**, *8*, 641–661.

(49) Slatter, J. G.; Schaaf, L. J.; Sams, J. P.; Feenstra, K. L.; Johnson, M. G.; Bombardt, P. A.; Cathcart, K. S.; Verburg, M. T.; Pearson, L. K.; Compton, L. D.; Miller, L. L.; Baker, D. S.; Pesheck, C. V.; Lord,

R. S. Pharmacokinetics, metabolism, and excretion of irinotecan (CPT-11) following i.v. infusion of [^{14}C]CPT-11 in cancer patients. *Drug Metab. Dispos.* **2000**, *28*, 423–433.

(50) Antony, S.; Agama, K. K.; Miao, Z.-H.; Takagi, K.; Wright, M. H.; Robles, A. I.; Varticovski, L.; Nagarajan, M.; Morrell, A.; Cushman, M.; Pommier, Y. Novel indenoisoquinolines NSC 725776 and NSC 724998 produce persistent topoisomerase I cleavage complexes and overcome multidrug resistance. *Cancer Res.* **2007**, *67*, 10397–10405.

(51) Das, S. K.; Rehman, I.; Ghosh, A.; Sengupta, S.; Majumdar, P.; Jana, B.; Das, B. B. Poly(ADP-ribose) polymers regulate DNA topoisomerase I (top1) nuclear dynamics and camptothecin sensitivity in living cells. *Nucleic Acids Res.* **2016**, *44*, 8363–8375.

(52) Rehman, I.; Basu, S. M.; Das, S. K.; Bhattacharjee, S.; Ghosh, A.; Pommier, Y.; Das, B. B. PRMT5-mediated arginine methylation of TDP1 for the repair of topoisomerase I covalent complexes. *Nucleic Acids Res.* **2018**, *46*, 5601–5617.

(53) Das, B. B.; Huang, S.-y. N.; Murai, J.; Rehman, I.; Amé, J.-C.; Sengupta, S.; Das, S. K.; Majumdar, P.; Zhang, H.; Biard, D.; Majumder, H. K.; Schreiber, V.; Pommier, Y. PARP1-TDP1 coupling for the repair of topoisomerase I-induced DNA damage. *Nucleic Acids Res.* **2014**, *42*, 4435–4449.

(54) Das, B. B.; Antony, S.; Gupta, S.; Dexheimer, T. S.; Redon, C. E.; Garfield, S.; Shiloh, Y.; Pommier, Y. Optimal function of the DNA repair enzyme TDP1 requires its phosphorylation by ATM and/or DNA-PK. *EMBO J.* **2009**, *28*, 3667–3680.

(55) Furuta, T.; Takemura, H.; Liao, Z.-Y.; Aune, G. J.; Redon, C.; Sedelnikova, O. A.; Pilch, D. R.; Rogakou, E. P.; Celeste, A.; Chen, H. T.; Nussenzweig, A.; Aladjem, M. I.; Bonner, W. M.; Pommier, Y. Phosphorylation of histone H2AX and activation of Mre11, Rad50, and Nbs1 in response to replication-dependent DNA double-strand breaks induced by mammalian DNA topoisomerase I cleavage complexes. *J. Biol. Chem.* **2003**, *278*, 20303–20312.

(56) Sordet, O.; Redon, C. E.; Guirouilh-Barbat, J.; Smith, S.; Solier, S.; Douarre, C.; Conti, C.; Nakamura, A. J.; Das, B. B.; Nicolas, E.; Kohn, K. W.; Bonner, W. M.; Pommier, Y. Ataxia telangiectasia mutated activation by transcription- and topoisomerase I-induced DNA double-strand breaks. *EMBO Rep.* **2009**, *10*, 887–893.

(57) Pommier, Y.; Sun, Y.; Huang, S.-y. N.; Nitiss, J. L. Roles of eukaryotic topoisomerases in transcription, replication and genomic stability. *Nat. Rev. Mol. Cell Biol.* **2016**, *17*, 703–721.

(58) Covey, J. M.; Jaxel, C.; Kohn, K. W.; Pommier, Y. Protein-linked DNA strand breaks induced in mammalian cells by camptothecin, an inhibitor of topoisomerase I. *Cancer Res.* **1989**, *49*, 5016–5022.

(59) Ashour, M. E.; Atteya, R.; El-Khamisy, S. F. Topoisomerase-mediated chromosomal break repair: an emerging player in many games. *Nat. Rev. Cancer* **2015**, *15*, 137–151.

(60) Das, B. B.; Dexheimer, T. S.; Maddali, K.; Pommier, Y. Role of tyrosyl-DNA phosphodiesterase (TDP1) in mitochondria. *Proc. Natl. Acad. Sci. U.S.A.* **2010**, *107*, 19790–19795.

Neutral Porphyrin Derivative Exerts Anticancer Activity by Targeting Cellular Topoisomerase I (Top1) and Promotes Apoptotic Cell Death without Stabilizing Top1-DNA Cleavage Complexes

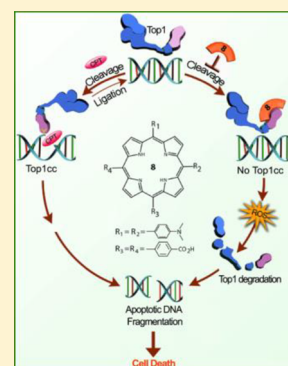
Subhendu K. Das,[†] Arijit Ghosh,[†] Srijita Paul Chowdhuri,[†] Nyancy Halder,[‡] Ishita Rehman,[†] Souvik Sengupta,^{†,§} Krushna Chandra Sahoo,[‡] Harapriya Rath,^{*,‡} and Benu Brata Das^{*,†}

[†]Laboratory of Molecular Biology, Department of Biological Chemistry and [‡]Department of Inorganic Chemistry, Indian Association for the Cultivation of Science, 2A & 2B, Raja S. C. Mullick Road, Jadavpur, Kolkata 700032, India

[§]Division of Biological and Life Sciences, School of Arts and Sciences, Ahmedabad University, Central Campus, Navrangpura, Ahmedabad, Gujarat 380009, India

Supporting Information

ABSTRACT: Camptothecin (CPT) selectively traps topoisomerase 1-DNA cleavable complexes (Top1cc) to promote anticancer activity. Here, we report the design and synthesis of a new class of neutral porphyrin derivative 5,10-bis(4-carboxyphenyl)-15, 20-bis(4-dimethylaminophenyl)-porphyrin (compound 8) as a potent catalytic inhibitor of human Top1. In contrast to CPT, compound 8 reversibly binds with the free enzyme and inhibits the formation of Top1cc and promotes reversal of the preformed Top1cc with CPT. Compound 8 induced inhibition of Top1cc formation in live cells was substantiated by fluorescence recovery after photobleaching (FRAP) assays. We established that MCF7 cells treated with compound 8 trigger proteasome-mediated Top1 degradation, accumulate higher levels of reactive oxygen species (ROS), PARP1 cleavage, oxidative DNA fragmentation, and stimulate apoptotic cell death without stabilizing apoptotic Top1-DNA cleavage complexes. Finally, compound 8 shows anticancer activity by targeting cellular Top1 and preventing the enzyme from directly participating in the apoptotic process.



INTRODUCTION

DNA topoisomerase I (Top1) is often exploited as an imperative anticancer chemotherapeutic target due to its critical role in DNA supercoil relaxation which involves three main steps: (a) DNA strand cleavage by a transesterification reaction initiated by the active site tyrosine attacking DNA phosphodiester backbone and generating a covalent intermediate of DNA 3'-phosphotyrosyl linkage (Top1cc), (b) DNA relaxation by controlled strand rotation, and (c) DNA religation by a similar transesterification and release of the enzyme from the DNA.^{1–5}

Top1 inhibitors are classified into two groups, class I (poisons) and class II (catalytic inhibitors). Top1 poisons include camptothecin (CPT), topotecan, irinotecan, and other CPT derivatives as well as few non-CPT Top1 inhibitors like indenoloquinolines, indolocarbazoles, and thiohydantoin derivatives that reveal their anticancer activity by selectively trapping the Top1-DNA covalent cleavage complexes (Top1cc) and inhibiting further religation of cleaved DNA strands.^{2,3,6–8} Unrepaired Top1cc generates DNA double strand breaks following collision with replication or transcription machinery, which activates cell-cycle arrest and cell death.^{3,9} In contrast, class II catalytic inhibitors hinder other steps of Top1 catalytic cycle by directly binding with enzyme but do not stabilize Top1cc which includes indolizinoquinolinedione.^{10–14} All types

of topoisomerase inhibitors cause DNA breaks and are accountable for the killing of the proliferating cancer cells.^{3–5,9}

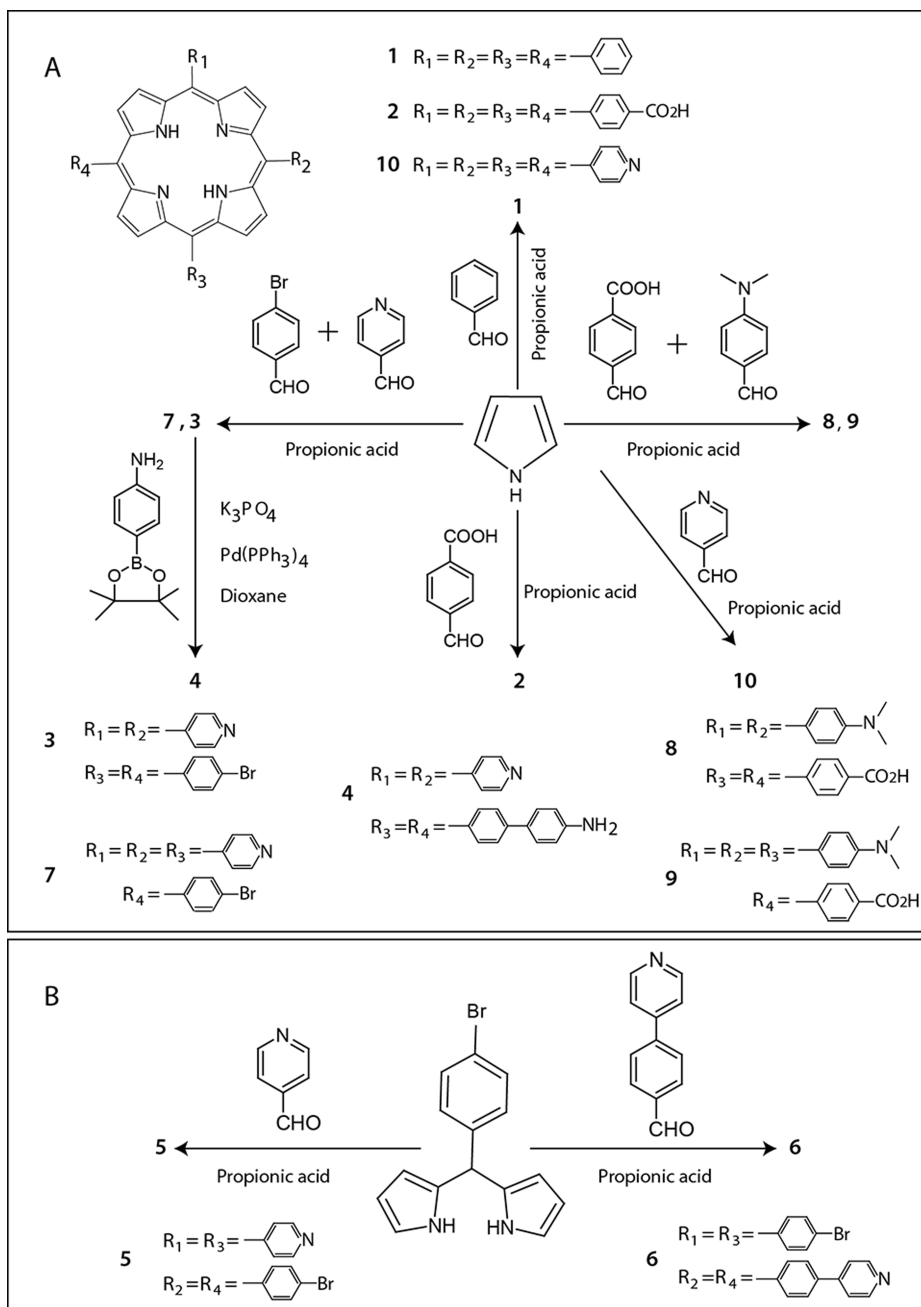
Drug independent trapping of Top1cc's are also evidenced from endogenous DNA lesions, like UV- and IR-radiation-induced DNA damage, abasic sites, oxidized bases, and mismatches.^{3,9} Production of "apoptotic Top1cc" is independent of Top1 poisons but is dependent on variety of agents that are inducers of apoptotic cell death, including staurosporine, a protein kinase C inhibitor,¹⁵ Top2 inhibitor like etoposide, and tubulin inhibitor like vinblastine.¹⁶ All these compounds trigger cellular reactive oxygen species (ROS) that account for oxidative DNA damages that promote stabilization of Top1cc.^{15,17,18}

Despite clinical success of CPT, the major limitations include its unstable chemical structure, poor aqueous solubility, and rapid cellular efflux via membrane pumps, and acquisition of cellular resistance of these drugs impelled the designing and investigation of new noncamptothecin Top1 inhibitors.^{3,4} Porphyrins are a remarkably promising chemotype for development of anticancer agents and photodynamic therapy, which include FDA-approved and clinically used sensitizer Photofrin.^{19,20} Porphyrin derivatives have wide pharmaceutical properties and broad range of biological activities that

Received: September 6, 2017

Published: December 30, 2017

Scheme 1. Synthesis of Library of Neutral Porphyrin Compounds



constitute selective modes of DNA binding, mimicking photosynthetic centers, vitamin B12, and P-450;^{19,21–24} nevertheless, the cellular target of the compounds is still unclear.

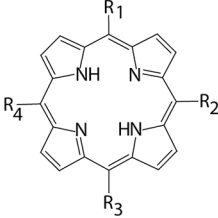
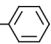
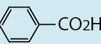
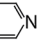
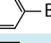
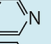
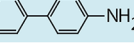
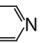
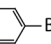
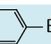
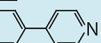
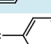
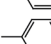
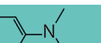
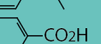
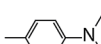
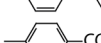
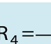
Here, we discuss our study involving design, synthesis, and biological evaluation of a novel series of neutral porphyrin that inhibits human Top1. Selected neutral porphyrin derivative 5,10-bis(4-carboxyphenyl)-15,20-bis(4-dimethylaminophenyl)-porphyrin (compound **8**) exhibited highest potency against human Top1 activity both as purified enzyme and as an endogenous protein in the total cellular extracts of human breast adenocarcinoma (MCF7) cells from our synthetic library. We have further established that the compound **8** binds with the free enzyme and targets cellular Top1 for proteasome-mediated degradation and bolsters ROS-induced apoptotic cell death without stabilizing Top1-DNA cleavage

complexes. Persistent with inhibition of human Top1 activity in vitro, compound **8** was effective in killing cancer cells by targeting cellular Top1.

CHEMISTRY

The macrocycles under biological investigation described in our present manuscript are shown schematically (Scheme 1). We have taken into consideration the parent basic porphyrin, i.e., tetraphenylporphyrin, and variation in the periphery of the macrocycles with other *meso*-substituents. After investigating the biological properties of macrocycles compounds **1**, **2**, **3**, **4**, **5**, **6**, **7**, **9**, and **10**, we designed and synthesized **8** following the literature known synthetic methodology. Synthesis of porphyrins **1**,²⁵ **2**,²⁶ **3**,²⁷ **7**,²⁸ **8**, **9**, and **10**²⁹ were carried out following Adler method;³⁰ macrocycles bearing four identical *meso*-

Table 1. Effective Drug Concentrations (EC_{50}) of Selected Neutral Porphyrin Compounds on the Recombinant Human Top1 (Top1) Plasmid DNA Relaxation Inhibition Assays

Core structure	Compound	Structure	Top1 inhibition EC_{50} (μ M)	
			Simultaneous	Preincubation
	1	$R_1 = R_2 = R_3 = R_4 =$ 	>50	>50
	2	$R_1 = R_2 = R_3 = R_4 =$ 	2.015 ± 0.511	$0.563 \pm .19$
	3	$R_1 = R_2 =$  $R_3 = R_4 =$ 	>50	>50
	4	$R_1 = R_2 =$  $R_3 = R_4 =$ 	82.78 ± 2.34	63.43 ± 1.89
	5	$R_1 = R_3 =$  $R_2 = R_4 =$ 	>50	>50
	6	$R_1 = R_3 =$  $R_2 = R_4 =$ 	>50	>50
	7	$R_1 = R_2 = R_3 =$  $R_4 =$ 	>50	>50
	8	$R_1 = R_2 =$  $R_3 = R_4 =$ 	$1.472 \pm .32$	$0.381 \pm .11$
	9	$R_1 = R_2 = R_3 =$  $R_4 =$ 	1.972 ± 0.411	$1.226 \pm .14$
	10	$R_1 = R_2 = R_3 = R_4 =$ 	>50	>50

substituents such as compound 1, 2, and 10 were obtained by condensation of freshly distilled pyrrole and corresponding arylaldehyde under reflux condition using propionic acid as an acidic solvent. Furthermore, synthesis of compounds 3 and 8 (Scheme 1A) was tuned following the mixed-aldehyde condensation method leading to porphyrins bearing two different types of *meso*-substituents.³¹ The A_3B type porphyrins 7 and 9 are often obtained in mixed-aldehyde condensation methods, and their yield was increased by reaction of 3:1 ratio of aldehydes A and B. It is a well-known fact that haloporphyrins undergo palladium-catalyzed cross-coupling reactions to produce alkyl-, vinyl-, aryl-, pyridyl-, and alkynylporphyrin monomers, dimers, and oligomers.³² Thus, Suzuki coupling was carried out by strategically using a mixture of 3 and 4-aminophenylboronic acid pinacol ester to afford compound 4³³ (Scheme 1A). Subsequently, the *trans*-substituted porphyrins, compounds 5³⁴ and 6 (Scheme 1B), were synthesized based on the MacDonald 2 + 2 condensation of dipyrromethane (synthesized by acid-catalyzed condensation of pyrrole with 4-bromobenzaldehyde) with 4-pyridine-carboxaldehyde and 4-(pyridin-4-yl)benzaldehyde, respectively.³⁵ Detailed spectroscopic characterization data, elemental analysis results, and melting points of all the reported macrocycles in this manuscript have been documented in the

Experimental Section and the Supporting Information (Figures S1–S40).

■ BIOLOGICAL RESULTS AND DISCUSSION

Neutral Porphyrin Derivative 8 Inhibits Human Topoisomerase 1 Catalytic Activity. To test the inhibitory effect of the synthetic library of neutral porphyrin compounds (Scheme 1) on human Top1 activity, we performed the DNA relaxation assays in a standard assay mixture containing the plasmid DNA and recombinant Top1.^{6,13,36,37} Table 1 enlists the compounds with relative efficiencies of Top1 inhibition as a measure of their effective drug concentrations (EC_{50} value), indicating the highest activity for the selected neutral porphyrin derivative compound 8.

To examine the mechanism of Top1 inhibition with compound 8, we used variable incubation conditions in the relaxation assays (Figure 1A). When Top1 and compound 8 were mixed together in the relaxation assays (Figure 1A, lanes 13–16), 35–40% Top1 inhibition was achieved at 1 μ M compound 8 (Figure 1A, lane 16). Next, to test the impact of compound 8 interaction with Top1 in the relaxation assays, we preincubated Top1 with compound 8 at indicated concentrations (Figure 1A, lanes 5–8) separately before the addition of DNA.^{6,13,36,38} Under these conditions, 1 μ M compound 8 was sufficient to induce 85–95% inhibition (Figure 1A, lane 8).

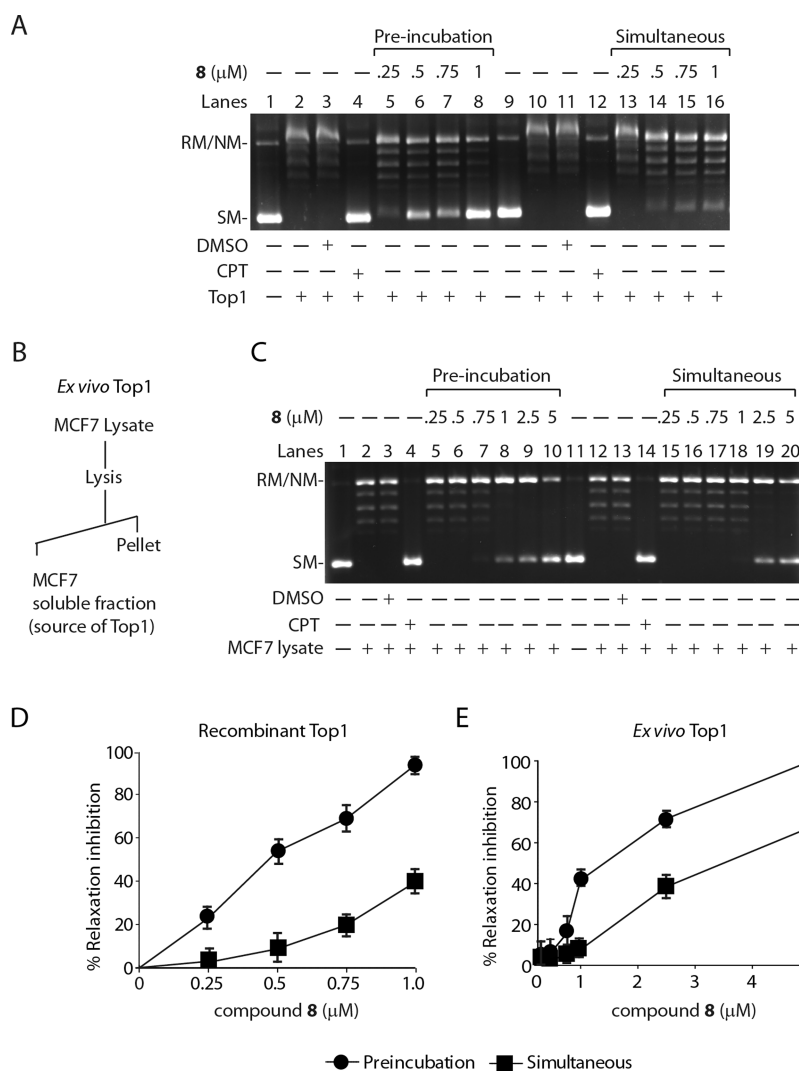


Figure 1. Compound **8** inhibits human Top1 catalytic activity both as recombinant enzyme and as an endogenous protein in the whole cell extracts of human breast adenocarcinoma (MCF7) cells. (A) Relaxation of supercoiled DNA with recombinant human Top1 at a molar ratio of 3:1. Lanes 1 and 9, pBS (SK⁺) DNA (90 fmol); lanes 2 and 10, same as lane 1 but incubated with 30 fmol of Top1; lanes 3 and 11, same as lane 2 but Top1 was incubated with 2% DMSO; lane 4, same as lane 2 but Top1 preincubated with 2 μM CPT for 5 min; lanes 5–8, same as lane 2 but Top1 was preincubated with variable concentrations of compound **8** (as indicated) for 5 min followed by addition of DNA at 37 °C for 15 min; lane 12, same as lane 4 but CPT was incubated simultaneously with DNA and enzyme; lanes 13–16, same as lane 10 but simultaneously incubated with variable concentrations of compound **8** (as indicated) at 37 °C for 15 min. (B) Schematic representation for preparation of MCF7 whole cell lysates which was used as the source of endogenous Top1 for ex vivo Top1 relaxation assays. (C) Relaxation of supercoiled pBS (SK⁺) DNA by Top1 activity from MCF7 cell extract (each reaction volume contains 0.1 μg protein). Lanes 1 and 11, pBS (SK⁺) DNA (0.3 μg); lane 2 and 3, same as lane 1 but DNA was incubated with MCF7 cell lysates; lanes 3 and 13, same as lane 2 but incubated with 2% DMSO; lanes 4–10, same as lane 2 but MCF7 whole lysates were preincubated with 5 μM CPT or the variable concentrations of compound **8** (as indicated) for 5 min followed by addition of DNA at 37 °C for 15 min; lanes 14–20, same as lane 12 but MCF7 cell lysates were incubated simultaneously with 5 μM CPT or variable concentrations of compound **8** (as indicated) at 37 °C for 15 min. Positions of supercoiled monomer (SM) and relaxed and nicked monomer (RL/NM) are indicated. Quantitative representation for percentage relaxation inhibition (%) of recombinant Top1 (D) and endogenous Top1 (E) either preincubated or added simultaneously with Top1 with the variable concentrations of compound **8**. All the experiments were performed three times and expressed as the mean \pm SD.

Panels A and D of Figure 1 show that Top1 inhibition was markedly increased (\sim 4- to 5-fold) when compound **8** was preincubated with the recombinant enzyme compared to the simultaneous incubation (EC_{50} for Top1 inhibition preincubation: $0.381 \pm 0.11 \mu\text{M}$ vs simultaneous $1.472 \pm 0.32 \mu\text{M}$), suggesting that compound **8** may bind to the free enzyme, unlike CPT to inhibit Top1 activity.

To investigate the selectivity of compound **8** toward endogenous Top1 in the whole cell extracts of human breast adenocarcinoma (MCF7) cells (Figure 1B), we used ex vivo

Top1 relaxation inhibition assays.^{6,39} The advantage of employing whole cell extracts as source of Top1 is that the enzyme is maintained in its native structure among a plethora of other proteins. Figure 1C shows that compound **8** markedly inhibited Top1 activity when the cellular extracts were preincubated with compound **8** (Figure 1C, lanes 5–10) compared to simultaneous incubation (Figure 1, panel C, lanes 15–20). Quantification indicates that Top1 inhibition was significantly increased (\sim 2- to 3-fold) when compound **8** was preincubated with whole cell extracts (Figure 1E), consistent

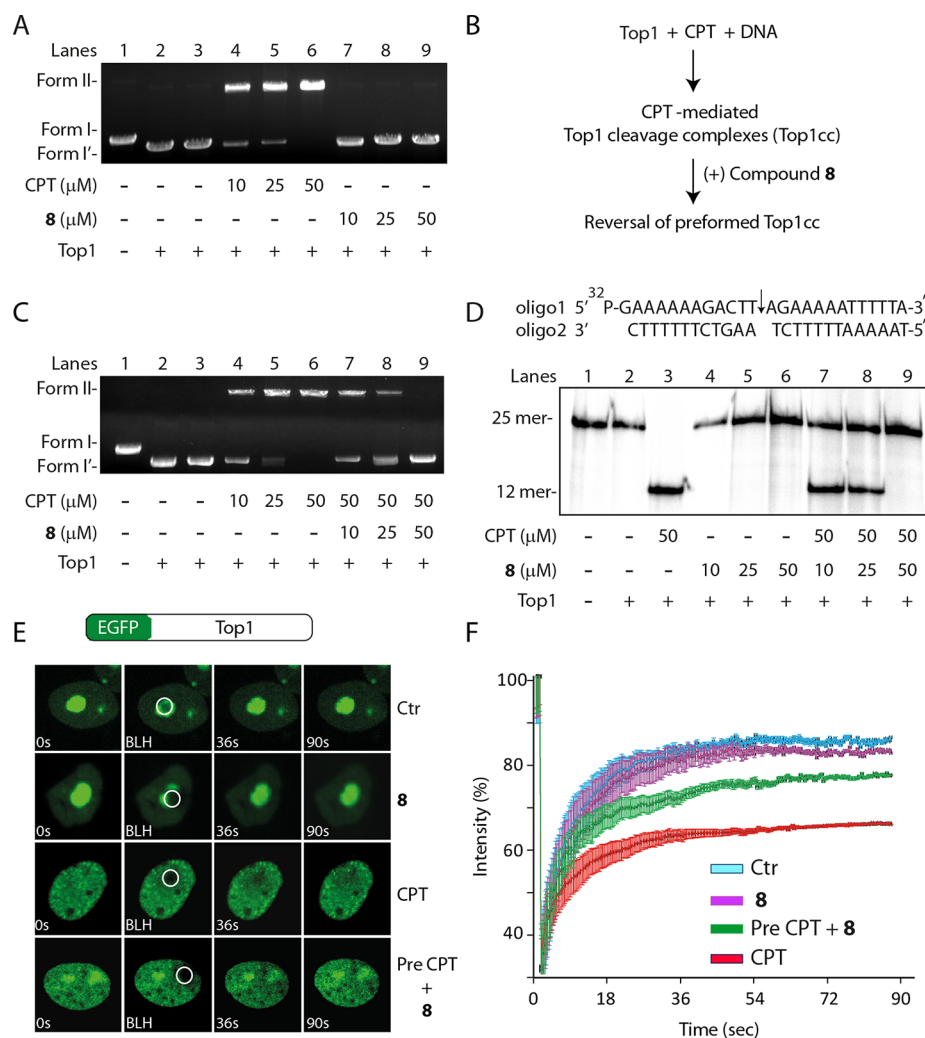


Figure 2. Compound **8** inhibits formation of Top1-DNA cleavage complexes and abrogates CPT-mediated DNA cleavage complex stabilization. (A) Representative gel showing Top1 mediated plasmid DNA cleavage in the presence of CPT or compound **8**. Lane 1, 50 fmol of pBS (SK⁺) supercoiled DNA. Lanes 2–9, same as lane 1 but incubated with equal amounts of recombinant human Top1 (100 fmol) at the indicated concentrations of CPT or compound **8** or only DMSO at 37 °C for 30 min. Positions of supercoiled substrate (form I) and nicked monomers (form II) are indicated. (B) Experimental design to test the impact of compound **8** on CPT-mediated preformed Top1 cleavage complex (Top1cc). (C) Compound **8** abrogates CPT-mediated cleavage. Lane 1, 50 fmol of pBS (SK⁺) supercoiled DNA. Lanes 2–6, same as lane 1 but incubated with equal amounts of Top1 (100 fmol) at the indicated concentrations of CPT or compound **8**. Lanes 7–9, same as lane 1 but incubated with equal amounts of Top1 with CPT before addition of compound **8** as indicated at 37 °C for 30 min. (D) Representative gel showing Top1-mediated 25 mer duplex oligonucleotide cleavage in the presence of CPT and compound **8**. Lane 1, 10 nM 5'-³²P-end labeled 25-mer duplex oligo as indicated above. Lane 2, same as lane 1 but incubated with recombinant Top1 (0.2 μM). Lanes 3–6, same as lane 2 but incubated with indicated concentration of CPT or compound **8**. Lanes 7–9, same as lane 2 but incubated with equal amounts of Top1 with CPT before addition of indicated concentrations of compound **8** at 37 °C for 30 min. Positions of uncleaved oligonucleotide (25-mer) and the cleavage product (12-mer oligonucleotide complexed with residual Top1) are indicated. (E) Compound **8** inhibits formation of Top1-DNA bound complexes (Top1cc) in live cells. Representative images showing the fluorescence recovery after photobleaching (FRAP) of enhanced green fluorescence tagged-human Top1 (EGFP-Top1) transiently expressed in MCF7 cells and their response to CPT (5 μM), compound **8** (20 μM) separately treated for 10 min or pretreatment with CPT (5 μM) for 10 min followed by treatment of compound **8** (20 μM) for 10 min (Pre CPT + **8**). A subnuclear spot (ROI) indicated by a circle was bleached (BLH) for 30 ms and photographed at regular intervals of 3 ms thereafter. Successive images taken for ~90 s after bleaching illustrate fluorescence return into the bleached areas. (F) Quantification of FRAP data ($n = 15$) showing mean curves of Top1 in the presence of CPT or compound **8**. Error bars represent the standard error of the mean.

with the inhibition of recombinant Top1 in preincubation relaxation assays (Figure 1D).

Here we provide evidence that compound **8** selectively inhibits Top1, both as a purified enzyme (Figure 1A) and as an endogenous protein in the total cellular lysate (Figure 1C) without being afflicted by other proteins. Therefore, it is conceivable that compound **8** selectively interacts with human Top1 to promote the inhibition of DNA relaxation activity.

Compound **8 Inhibits Top1-DNA Cleavage Complexes.** Because camptothecin (CPT) stabilizes Top1-DNA cleavable complexes (Top1cc) to inhibit Top1 activity,^{3,5,37} we investigated compound **8** induced Top1cc formation with the plasmid DNA cleavage assays.^{6,8,36,37} Top1 mediated conversion of closed circular DNA (form I) to nicked circular DNA (form II) in the presence of specific inhibitors is referred to as “cleavable complex”. Figure 2A shows that compound **8** failed to stabilize Top1cc in contrast to CPT, suggesting that

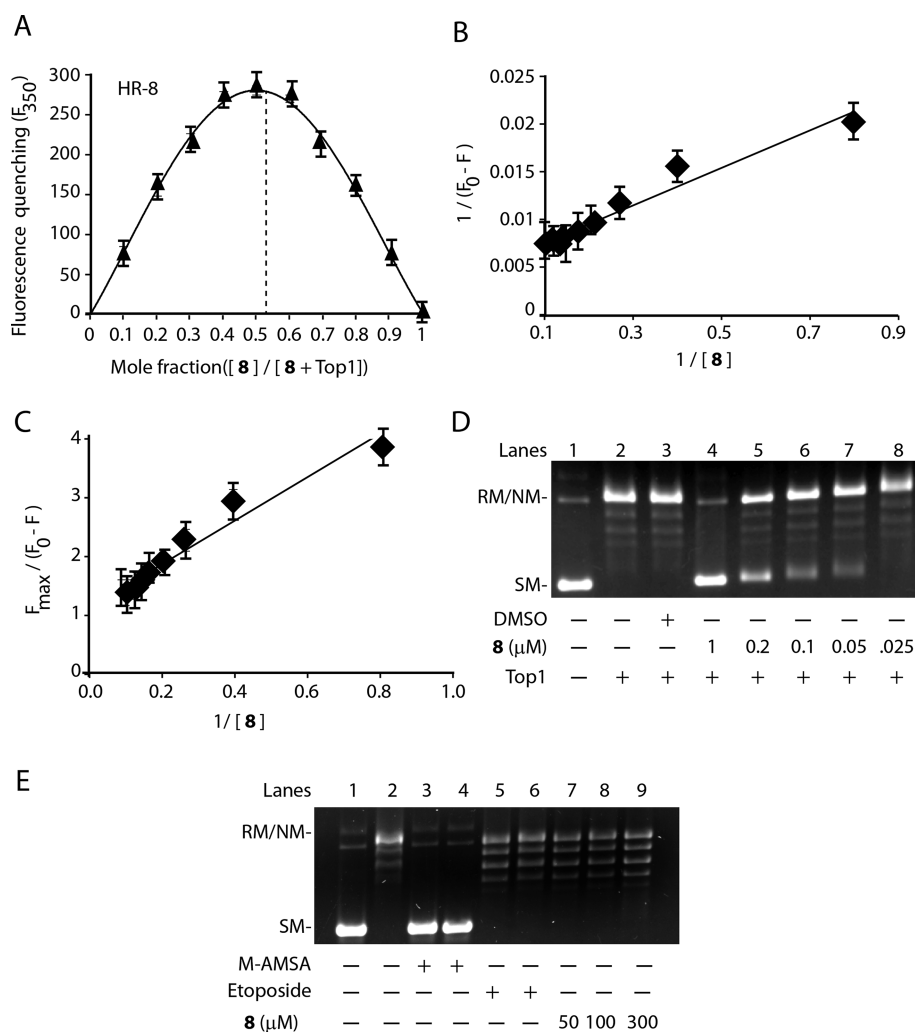


Figure 3. Compound **8** reversibly binds with Top1 at equimolar concentration. (A) Job's plot of compound **8** binding to Top1. Data are represented as the mean \pm SD from three independent experiments. (B) Double reciprocal plot of inhibitor binding to Top1. Data are represented as the mean \pm SD from three independent experiments. (C) Linear plot of binding of compound **8** to Top1. Data are represented as the mean \pm SD from three independent experiments. (D) Compound **8** binds with Top1 in reversible manner. Lane 1, 50 fmol of pBS (SK⁺) DNA. Lane 2, recombinant Top1 (100 fmol) was preincubated with the reaction mixture at 37 °C for 5 min before addition of pBS (SK⁺) DNA. Lane 3, same as lane 2 but in the presence of 2% v/v DMSO. Lane 4, same as lane 2 but in the presence of 1 μ M compound **8**, preincubated with Top1 for 5 min at 37 °C in relaxation buffer followed by addition of 50 fmol of pBS (SK⁺) DNA and was further incubated for 15 min at 37 °C. Lane 5–8, same as lane 4 but diluted to 5-, 10-, 20-, and 40-fold so that the final inhibitor concentrations became 0.2, 0.1, 0.05, and 0.025 μ M compound **8**. These were followed by addition of DNA and were further incubated for 15 min at 37 °C. The experiments were performed three times, and representative result is from one set of experiments. (E) Compound **8**–DNA interaction as studied by agarose gel electrophoresis. Lane 1, 50 fmol of pBS (SK⁺) DNA. Lane 2, relaxed pBS (SK⁺) DNA generated by excess of Top1. Lanes 3–6, same as lane 2 but incubated with 50 and 300 μ M m-AMSA and etoposide, respectively. Lanes 7–9, same as lane 2 but incubated with 50, 100, 300 μ M of compound **8** as indicated.

compound **8** inhibits Top1cc formation. To further investigate the impact of compound **8** on preformed Top1cc, we preincubated Top1 with plasmid DNA and CPT (Figure 2B) before the addition of compound **8** in the cleavage assays. Figure 2C shows that compound **8** completely abrogated CPT-induced Top1cc in a dose dependent manner (Figure 2, panel C, lanes 7–9).

In contrast to CPT (Figure 2D, lane 3), we further established that compound **8** failed to stabilize Top1cc in single turnover equilibrium cleavage assays (Figure 2D, lanes 4–6) by reacting recombinant Top1 with 25-mer duplex oligonucleotides harboring preferred Top1 cleavage sites.^{1,13,36,38} In addition, compound **8** reversed the CPT-induced Top1cc with 12-mer cleaved oligonucleotides (Figure 2D, lane 7–9) consistent with plasmid DNA cleavage assays

(Figure 2C). Taken together, our data indicate that compound **8** inhibits Top1 without trapping Top1cc.

To obtain direct evidence for compound **8** mediated inhibition of Top1cc formation in live human carcinoma cells, we used MCF7 cells and transiently expressed EGFP-Top1. Live cells expressing ectopic Top1 were analyzed under laser confocal microscopy equipped with fluorescence recovery after photobleaching (FRAP) technology.^{40–42} The FRAP recovery curves of EGFP-Top1 in the untreated samples represent a large (~80–85%) mobile population (see Figure 2E and Figure 2F; Ctr) compared to a small (~20%) immobile population, suggesting that Top1 is dynamic, freely exchanged and binds transiently with the DNA (reversible Top1cc).⁴²

However, CPT covalently trapped Top1 on the DNA in the live cells (Figure 2E; CPT), which significantly impedes FRAP

recovery by increasing ~40–50% of Top1 immobile population (Figure 2E and Figure 2F; (+) CPT; 5 μM). Under similar conditions fluorescence recovery of EGFP-Top1 was unaffected in the presence of compound 8 (Figure 2E and the quantification in Figure 2F; (+) compound 8; 20 μM), indicating compound 8 failed to trap Top1cc in live cells. Furthermore, compound 8 can restore ~12–15% of Top1 mobility in cells pretreated with CPT (Figure 2E,F), suggesting compound 8 promotes reversal of CPT-induced Top1cc in live cells consistent with the in vitro cleavage assays (Figure 2A–D). Taken together our data provide evidence that compound 8 inhibits cellular Top1cc formation.

Compound 8 Reversibly Binds with Top1 at Equimolar Concentration. Next we investigated the binding nature of compound 8 with the purified Top1 by measuring the intrinsic tryptophan fluorescence quenching of Top1. Figure 3A shows 1:1 binding stoichiometry of compound 8 with Top1 as measured from Job plot,^{12,14,43} suggesting that there is one binding site for the drug in the enzyme. Figure 3B and Figure 3C shows the quenching profile of Top1 in the presence of variable doses of compound 8, with a dissociation constant ($K_D = 0.381 \mu\text{M}$) calculated from Figure 3B and Figure 3C.

To further investigate the nature of binding of compound 8 with Top1 (reversible vs irreversible),^{12,14} we performed dilution assay with recombinant Top1. Top1 was preincubated with 1 μM compound 8 at which 90–99% inhibition of enzyme has been achieved (Figure 3D, lane 4). The subsequent dilution of the reaction mixtures in the relaxation assays showed an increase in the % relief of inhibition for compound 8. Complete relief of Top1 inhibition was achieved at 40-fold dilution (Figure 3D, lane 5–8). This suggests that compound 8 interacts in a reversible manner with Top1, consistent with its weak dissociation constant.

To investigate the intercalation capacity of the compound 8 into the plasmid DNA, we performed topoisomerase I unwinding assays,^{36,44} which depend on the capacity of intercalating compounds to unwind the duplex DNA and thereby induce a conformational change in the DNA.^{36,44} Figure 3E demonstrates that m-AMSA, a strong DNA intercalative agent, incites a net negative supercoiling of the relaxed plasmid DNA at concentration independent manner (Figure 3E, lanes 3 and 4). Under similar conditions nonintercalative compounds like etoposide failed to show such effect (Figure 3E, lanes 5 and 6). Figure 3E, lanes 7, 8, 9, shows that compound 8 failed to induce negative supercoiling of the relaxed plasmid DNA at 50, 100, 300 μM concentrations, suggesting neutral porphyrin derivative 8 is not a DNA intercalator. Therefore, compound 8 interacts in reversible manner with Top1 to inhibit the plasmid relaxation activity (Figure 1).

Compound 8 Triggers Proteasome-Mediated Degradation of Cellular Top1 without Stabilizing Apoptotic Top1-DNA Covalent Complexes. Because compound 8 binds with free Top1 (Figure 3) and inhibits Top1cc formation in live cells (Figure 2E), we examined the impact of compound 8 on endogenous Top1. Cellular lysates were prepared from MCF7 cells treated with compound 8 for indicated times and were analyzed by Western blotting. Figure 4A, lanes 2–4, shows time dependent depletion of Top1 signal in compound 8 treated cells, suggesting Top1 degradation. Because proteasome has been implicated for Top1 degradation,^{7,9,45} we used proteasome specific inhibitor (MG132) to investigate Top1 proteolysis in compound 8 treated cells. Figure 4B confirmed

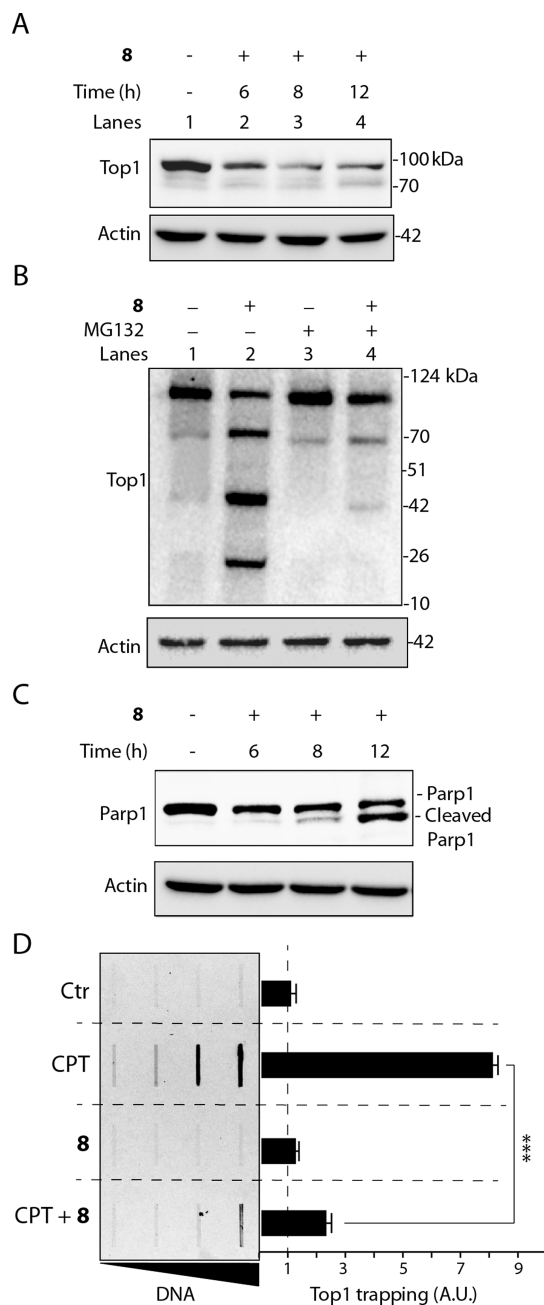


Figure 4. Compound 8 induces proteasome-mediated degradation of cellular Top1 and apoptotic PARP1 cleavage without stabilizing apoptotic Top1-DNA covalent complexes. (A) Western blot analysis of Top1 in whole cell extracts of MCF7 cells treated with compound 8 (10 μM) for indicated time. (B) Western blot analysis of Top1 in whole cell extracts from MCF7 cells without treatment (lane 1) or treated with compound 8 (10 μM) (lane 2) or MG132 (100 nM; proteasome inhibitor) (lane 3) or preincubated with MG132 for 4 h followed by addition of compound 8 for 12 h. Numbers are molecular masses in kDa. (C) Western blot analysis of PARP1 in whole cell extracts from MCF7 cells treated with compound 8 (10 μM) for indicated times. Positions of PARP1 full length and cleaved PARP1 are indicated. (D) Detection of Top1cc by ICE bioassays in MCF7 cells treated with CPT (10 μM) or compound 8 (20 μM) for 12 h or pretreated with CPT for 6 h before the addition of compound 8 was further incubated for 6 h. Genomic DNA at increasing concentrations (0.5, 1, 2, 4 μg) was probed with an anti-Top1 antibody. The bar represents quantification of Top1cc ($n = 3$; calculated value \pm SEM) under different drug treatment. Asterisks denote significant difference (***) $P < 0.001$; t test).

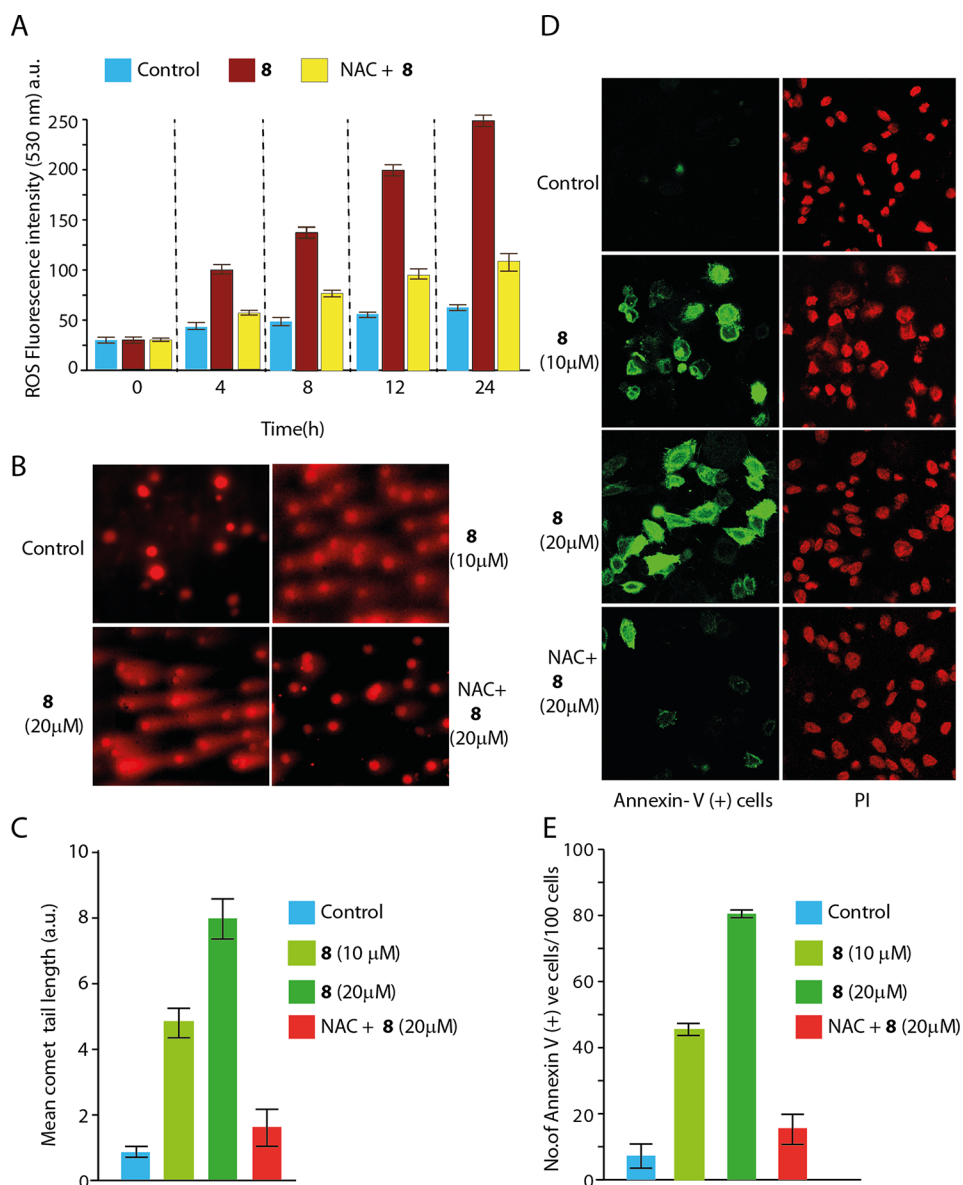


Figure 5. Compound **8** activates reactive oxygen species (ROS) induced oxidative DNA breaks and promotes apoptotic cell death. (A) Generation of ROS was measured using the fluorescent dye CM-H2DCFDA in MCF7 cells after treatment with 0.2% DMSO alone (blue bar) or with 10 μM compound **8** (red bar), and pretreatment with *N*-acetylcysteine (NAC; 10 mM) for 30 min prior to treatment with compound **8** (yellow bar) for indicated times. Data are expressed as mean ± SD of three independent experiments. (B) Representative images of alkaline comet assays with MCF7 cells treated with compound **8** for 12 h or pretreatment with NAC (10 mM) for 30 min prior to treatment with compound **8** as indicated. (C) Quantification of drug induced mean comet tails were calculated for 20–25 cells (average ± SEM). (D) Representative confocal microscopy images showing apoptosis marker phosphatidylserine as detected with annexin V-FITC antibody (green) after compound **8** treatment for 12 h or pretreatment with NAC (10 mM) for 30 min prior to compound **8** as indicated. Cells were counterstained with propidium iodide (PI; red) to visualize nuclei. (E) Quantification of drug induced annexin V (+) cells were calculated from ~100 cells (average ± SEM) as indicated.

that **8**-induced degradation of Top1 (Figure 4B, lane 2) was abrogated in the presence of proteasome inhibitor MG132 (Figure 4B, lane 4), suggesting compound **8** activates proteasome pathway.

Next, to investigate the plausibility between Top1 proteolysis and activation of apoptosis, we tested PARP cleavage, a “hallmark” event of apoptosis in compound **8** treated cells.^{16–18,46,47} Figure 4C shows that compound **8** treatment for 12 h indeed promotes PARP cleavage, suggesting compound **8** activates apoptosis through degradation of Top1.

Because compound **8** stimulates apoptosis (Figure 4C and Figure 5B), we examined accumulation of apoptotic Top1-DNA complexes in compound **8** treated cells (Figure 4D) by

ICE bioassays.^{15,16} Top1cc related to apoptosis is due to secondary DNA modifications and is independent from direct Top1-drug interaction.^{15–17} Under a condition that triggers PARP1 cleavage in MCF7 cells treated with compound **8**, immunoblotting revealed the absence of Top1 in the DNA-containing fractions (Figure 4D; compound **8**), in contrast to camptothecin (Figure 4D; CPT), indicating that compound **8** inhibits Top1cc during apoptosis. Compound **8** abrogates CPT-induced cellular Top1-DNA complexes (Figure 4D; CPT + **8**), in keeping with in vitro cleavage assays (Figure 2B). Therefore, proteasome mediated degradation of Top1 triggers compound **8** induced apoptosis without stabilizing apoptotic Top1-DNA covalent complexes.

Compound 8 Accumulates Reactive Oxygen Species Induced DNA Breaks and Promotes Apoptotic Cell Death.

Next, to investigate the mechanistic link between compound 8 induced cellular Top1 inhibition (Figure 1), degradation (Figure 4A and Figure 4B), and activation of apoptosis (Figure 4C), we tested reactive oxygen species (ROS) formation and accumulation of oxidative DNA fragmentation^{15,17,46} in compound 8 treated MCF7 cells. To examine ROS accumulation, we used nonfluorescent substrate (2',7'-dichlorodihydrofluorescein diacetate; H2DCFDA) which is transformed into fluorescent product (2',7'-dichlorofluorescein; DCF) in the presence of ROS inside the cells.¹³ Figure 5A shows time dependent accumulation of ROS in compound 8 treated cells. We observed a marked elevation (~3- to 5-fold) in ROS accumulation (Figure 5A) under similar conditions that activate PARP1 cleavage (Figure 4C). Nonetheless, MCF7 cells pretreated with *N*-acetylcysteine (NAC), a specific inhibitor of ROS, reduced compound 8 induced ROS generation by ~3-fold (Figure 5A).

One interpretation of this result is that compound 8 induced ROS may accumulate oxidative DNA strand breaks that activate apoptosis^{3,13} as revealed by PARP1 cleavage (Figure 4C). Therefore, we directly measured compound 8 induced DNA strand breaks at single cellular level by using alkaline comet assays (Figure 5B,C) and simultaneously measured the apoptotic cell death by immunofluorescence staining of the apoptotic marker phosphatidylserine with annexin V-FITC antibody (Figure 5D,E). Compound 8 treated MCF7 cells accumulate ~8-fold increase in DNA strand breaks (Figure 5B and Figure 5C) compared to untreated cells, resulting in ~7-fold elevation in compound 8 induced annexin V(+) apoptotic cells (Figure 5D and Figure 5E). We further confirmed that ROS inhibitor NAC resulted in ~4-fold decrease in compound 8 induced DNA breaks (Figure 5C) as well as ~4- to 5-fold reduction in annexin V(+) apoptotic cells (Figure 5E). Therefore, we conclude that compound 8 triggers reactive oxygen species induced DNA degradation and apoptotic cell death without stabilizing Top1-DNA cleavage complexes.

Compound 8 Displays Potent Anticancer Activity.

Compound 8 was investigated for its cytotoxicity in the cancer cell lines from different tissue origin,^{6,41} as well as in the noncancerous human embryonic kidney cell lines (HEK293) and mouse embryonic fibroblasts (MEFs). Figure 6 indicates that compound 8 revealed potent cytotoxicity in cancerous cells including human breast adenocarcinoma cell lines (MCF7, IC_{50} = 2.17 μ M), human cervical cancer cell lines (HeLa, IC_{50} = 4.13 μ M), human ovarian adenocarcinoma cell lines (NIH:OVCA-3, IC_{50} = 5.19 μ M), and human colon carcinoma cell lines (HCT116, IC_{50} = 4.39 μ M) cells, compared to the noncancerous cells like HEK293 or MEFs that show markedly reduced or no toxicity (IC_{50} > 10 μ M). The MCF7 breast cancer cell lines were most susceptible to compound 8.

TDP1 hydrolyzes 3' phosphotyrosyl linkages that are primarily due to Top1cc; therefore TDP1^{-/-} cells are hypersensitive to Top1 poisons.^{40,41,45,48} Figure 6F shows that both TDP^{-/-} and TDP1^{+/+} MEFs cells were equally sensitive to compound 8, further providing evidence that compound 8 exerts cytotoxicity without stabilizing Top1cc (Figure 4D).

To further confirm that Top1 is the cellular target for compound 8 mediated cytotoxicity, we have performed cytotoxicity assays in siRNA mediated Top1 knockdown cells (Figure 6G, inset). Figure 6G indicate that compound 8 treated

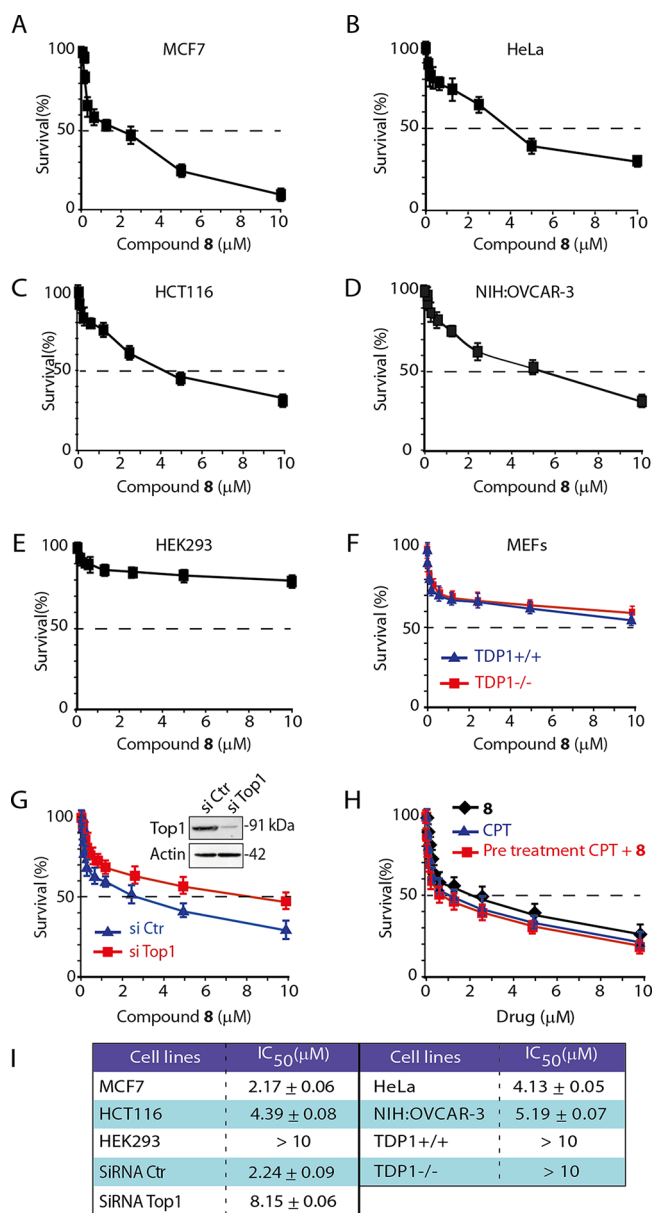


Figure 6. Compound 8 shows potent anticancer activity mediated through topoisomerase 1. The graphical representation of percentage survival (%) of (A) MCF7, (B) HeLa, (C) HCT116, (D) NIH:OVCA-3, (E) HEK293, (F) MEFs (TDP^{+/+} and TDP^{-/-}) cells was plotted as a function of indicated compound 8 concentrations. (G) Top1 knockdown cells are less sensitive to compound 8. Following transfection with Top1 or control (Ctr) siRNA for 72 h, MCF7 cells were analyzed by Western blotting to confirm Top1 knockdown. Actin served as loading control (inset). Percentage survival (%) of MCF7 cells transfected with Top1 or Ctr siRNA was plotted as a function of indicated compound 8 concentrations. (H) Graphical representation of percentage survival (%) of MCF7 cells treated with compound 8 or CPT separately or cells were pretreated with CPT (5 μ M) for 12 h prior to addition of compound 8 as indicated. The percent inhibition of viability for each concentration of compound 8 was calculated with respect to the control, and IC_{50} (μ M) values were estimated. Each point corresponds to the mean \pm SD of at least three experiments in duplicates. Error bars represent SD (n = 3).

Top1 knockdown cells displayed reduced cytotoxicity compared to the Top1 proficient cells, establishing that Top1 is the cellular target for compound 8.

Because compound **8** exerts cytotoxicity without stabilizing Top1cc (Figure 4D), next we tested the impact of compound **8** on CPT-induced preformed Top1cc. Figure 6H shows that pretreatment of CPT and further addition of compound **8** were not additive in cytotoxicity but showed overlapping cytotoxicity in MCF7 cells treated with compound **8** or CPT independently. Therefore, we conclude compound **8** plausibly suppresses the CPT induced cytotoxicity (Figure 6H) because compound **8** reverses CPT-induced Top1cc formation in cells as well as in cleavage assays (Figure 2). Taken together these data suggest that compound **8** is a potential Top1 inhibitor and may be an appropriate lead to develop as a potential anticancer agent.

CONCLUSION

In summary, we have identified neutral porphyrin based compound **8** as a new potent anticancer agent that inhibits cellular Top1 without trapping Top1-DNA cleavage complexes, a mechanism that is unique in comparison to known Top1 poisons like camptothecin (CPT). We provide evidence that in contrast to CPT, the selected porphyrin derivative **8** binds reversibly to the free enzyme (Figure 3) and effectively inhibits the formation of Top1-DNA cleavage complex (Top1cc) both in vitro and in live cell as determined in FRAP assays (Figure 2). Compound **8** abrogates CPT-mediated preformed Top1cc both as recombinant enzyme (Figure 2A-D) and as an endogenous Top1 in the human breast adenocarcinoma (MCF7) cells (Figure 4D), suggesting a plausibility to overcome the limitations of CPT resistance.

ROS-induced DNA damage facilitates trapping of Top1cc in cells and is an obligatory event in the progression of apoptosis.^{15–17} In contrast, compound **8** activates reactive oxygen species (ROS), proteolysis of cellular Top1, which may accumulate DNA torsional strain resulting oxidative DNA damage as revealed by alkaline comet assays and apoptotic cell death (Figure 5) without stabilization of apoptotic Top1-DNA complexes (Figure 4D). Therefore, compound **8** counteracts the cellular Top1 by abrogating its precise engagement in the apoptotic process.

We further show that in contrast to noncancerous cells, compound **8** is effective against cancerous cell lines from different tissue origin including MCF-7, HeLa, NIH:OVCAR-3, and HCT116 cells (Figure 6) by targeting cellular Top1 (Figure 6G). A future challenge includes development of more potent neutral porphyrin based Top1 catalytic inhibitor, which may be exploited for anticancer therapy.

EXPERIMENTAL SECTION

Chemistry. General Methods. Electronic absorption spectra were measured with a PerkinElmer Lambda 950 UV–visible–NIR spectrophotometer. ¹H NMR spectra were recorded on a Bruker AVIII 500 MHz spectrometer, and chemical shifts were reported as the δ scale in ppm relative to CHCl₃ (δ = 7.26 ppm) and DMSO (δ = 2.50 ppm) as internal reference for ¹H. MALDI-TOF MS data were recorded using Bruker Daltonics flex analyzer. All solvents and chemicals were of reagent grade quality, obtained commercially and used without further purification except as noted. For spectral measurements, anhydrous dichloromethane was obtained by refluxing and distillation over CaH₂. Gravity column chromatography was performed using Merck silica gel 230–400 mesh. All reported yields refer to pure isolated compounds. Chemicals and solvents were of reagent grade and used as obtained from commercial sources without further purification. The purities of all of the biologically tested compounds were the peak area of the major product, being $\geq 95\%$ as

estimated by NMR spectroscopy and C, H, N analysis along with melting point.

Synthesis. 5,10,15,20-Tetraphenylporphyrin (1). By use of a general method, 1 mL (10 mmol) of benzaldehyde and 50 mL of propionic acid were mixed and the reaction mixture was magnetically stirred. Freshly distilled pyrrole (0.7 mL; 10 mmol) was then added to the mixture, and the temperature was then brought to reflux and allowed to stir for 2 h at reflux. After allowing the reaction mixture to cool to room temperature, the reaction flask was placed in the freezer overnight to aid precipitation of the porphyrin. The reaction mixture was then vacuum filtered using a sintered funnel, and a dark purple solid was collected, washed with 5 \times 50 mL of DCM, washed with methanol, dried overnight, and purified by silica gel chromatography to give 4.9 g, of 5,10,15,20-tetraphenylporphyrin (79% yields). Mp > 300 °C. ¹H NMR (500 MHz, CDCl₃, 298 K, δ [ppm]) 8.88 (s, 8H, py), 8.25 (m, 8H, Ph-CH), 7.79 (m, 12H, Ph-CH), –2.76 (s, 2H, –NH). UV–vis (CH₂Cl₂, λ [nm], 298 K): 417 nm, 515 nm, 548 nm, 590 nm, 645 nm. MALDI-TOF MS (m/z): 615.635 (calcd for C₄₄H₃₀N₄ exact mass, 614.206). Anal. Calcd for C₄₄H₃₀N₄: C, 85.97; H, 4.92; N, 9.11. Found: C, 86; H, 5.00; N, 9.08.

5,10,15,20-Tetrakis(4-carboxyphenyl)porphyrin (2). By use of a general method, 1.5 g (10 mmol) of 4-formylbenzoic acid and 50 mL of propionic acid were added, and the reaction mixture was stirred at ambient temperature. To increase the solubility of 4-formylbenzoic acid, the reaction mixture was heated to 80 °C at which point the aldehyde fully dissolved. Freshly distilled pyrrole (0.7 mL; 10 mmol) was then added to the mixture, and reaction mixture was allowed to stir for 2 h under reflux. The reaction mixture was cooled to room temperature and placed in the freezer overnight to aid precipitation of the porphyrin. The reaction mixture was then vacuum filtered using a sintered funnel and a dark purple solid was collected, washed with 5 \times 50 mL of DCM, washed with methanol, and dried overnight to give 1.1 g, of 5,10,15,20-tetrakis(4-carboxyphenyl)porphyrin (55% yields). Mp > 300 °C. ¹H NMR (500 MHz, DMSO-*d*₆, 298 K, δ [ppm]) 13.14 (4H, br, –COOH), 8.86 (8H, s, Py β -H), 8.38 (16H, dd, phenyl H), –2.93 (2H, s, NH). UV–vis (CH₃OH, λ [nm], 298 K): 413 nm, 513 nm, 545 nm, 589 nm, 646 nm. MALDI-TOF MS (m/z): 790.604 (calcd for C₄₈H₃₀N₄O₈ exact mass, 790.206). Anal. Calcd for C₄₈H₃₀N₄O₈: C, 72.90; H, 3.82; N, 7.09. Found: C, 73.00; H, 3.86; N, 7.07.

5,10-Bis(4-bromophenyl)-15,20-di(4-pyridyl)porphyrin (3). By use of a general method, 4-pyridinecarboxaldehyde (0.535g, 5 mmol), 4-bromobenzaldehyde (0.925g, 5 mmol), and 50 mL of propionic acid were added, and the reaction mixture was stirred under nitrogen. To increase the solubility of 4-bromobenzaldehyde, the reaction mixture was heated to 80 °C at which point the aldehyde was fully dissolved. Freshly distilled pyrrole (0.7 mL; 10 mmol) was then added to the mixture and allowed to stir for 4 h under reflux. Reaction mixture was brought to room temperature, and the reaction flask was then placed in the freezer overnight to aid precipitation of the porphyrin. The crude product was repeatedly chromatographed on silica gel. The purest compound was obtained by recrystallization in methanol. Yield: 3.87g (50%). Mp > 300 °C. ¹H NMR (500 MHz, CDCl₃, 298 K, δ [ppm]) –2.86 (s, 2H, NH), 7.94 (d, J = 7.5 Hz, 4H, Ph-Br), 8.10 (d, J = 7.5 Hz, 4H, Ph-Br), 8.18 (d, J = 10 Hz, 4H, pyridyl-H), 8.88 (m, 8H, β -H Py), 9.07 (d, J = 10 Hz, 4H, pyridyl-H). UV–vis (CH₂Cl₂, λ [nm], 298 K): 418 nm, 514 nm, 547 nm, 588 nm, 645 nm. MALDI-TOF MS (m/z): 775.399 (calcd for C₄₂H₂₆Br₂N₆ exact mass, 774.520). Anal. Calcd for C₄₂H₂₆Br₂N₆: C, 65.13; H, 3.38; N, 10.85. Found: C, 65.14; H, 3.30; N, 10.72.

5,10-Bis(4-aminobiphenyl)-15,20-bis(4-pyridyl)porphyrin (4). A Schlenk tube was charged with 5,20-bis(4-bromophenyl)-10,15-di(pyridin-4-yl)porphyrin (0.054g, 0.07 mmol), 4-(4,4,5,5-tetramethyl-1,3,2-dioxaborolan-2-yl)aniline (0.092g, 0.042 mmol), K₃PO₄ (0.089g, 0.42 mmol), and Pd(PPh₃)₄ (8 mg, 0.07 mmol) under nitrogen atmosphere. Dioxane (5 mL) and deionized water (0.1 mL) were added, and the resulting mixture was refluxed for 24 h, brought to room temperature, and filtered through Celite in a sintered funnel. It was washed several times with DCM, and the filtrate was evaporated in vacuum. The crude product obtained upon evaporation of solvent was

purified by silica gel column chromatography (100–200 mesh) using ethyl acetate/dichloromethane (20:80, v/v) as an eluent. Yield 44.6 mg (80%). Mp > 300 °C. ¹H NMR (500 MHz, CDCl₃, 298 K, δ [ppm]) –2.76 (s, 2H, NH), 3.75 (s, 4H, NH₂), 6.88 (d, 2H, J = 8.5 Hz, β-H Py), 7.72 (d, 2H, J = 8.5 Hz, β-H Py), 7.91 (d, 4H, J = 7.5 Hz, Ph-H), 8.17 (d, 4H, J = 5.5 Hz, pyridyl-H), 8.20 (d, 4H, J = 8 Hz, Ph-H), 8.81 (d, 4H, J = 4 Hz, Ph-H), 8.84 (s, 2H, β-H Py), 8.97 (s, 2H, β-H Py), 9.01 (d, 4H, J = 4.5 Hz, Ph-H), 9.03 (d, 4H, J = 5 Hz, pyridyl-H). UV–vis (CH₂Cl₂, λ [nm], 298 K): 420 nm, 515 nm, 553 nm, 592 nm, 645 nm. MALDI-TOF MS (*m/z*): 798.820 (calcd for C₅₄H₃₈N₈ exact mass, 798.322). Anal. Calcd for C₅₄H₃₈N₈: C, 81.18; H, 4.79; N, 14.03. Found: C, 81.14; H, 4.16; N, 14.12.

5,15-Bis(4-bromophenyl)-10,20-di(4-pyridyl)porphyrin (5). By use of a general method, 2,2'-((4-bromophenyl)methylene)bis(1H-pyrrole) (0.5 g, 1.66 mmol) and 4-pyridinecarboxaldehyde (0.171g, 1.6 mmol) were taken in a round-bottom flask, and 40 mL of propionic acid was added to it. The reaction mixture was then stirred under nitrogen at 298 K for 90 min. Thereafter, the reaction mixture was refluxed under nitrogen for 90 min, brought to room temperature, and left overnight for precipitation at room temperature. The precipitate was poured into sintered funnel and washed several times with methanol. The crude product thus obtained was vacuum-dried followed by repeated silica gel column chromatography. The purest compound was obtained by recrystallization from methanol. Yield 620 mg (50%). Mp > 300 °C. ¹H NMR (500 MHz, CDCl₃, 298 K, δ [ppm]) –2.85 (s, 2H, NH), 7.9 (d, J = 8 Hz, 4H, Ph-Br), 8.10 (d, J = 7.5 Hz, 4H, Ph-Br), 8.18 (d, J = 5.5 Hz, 4H, pyridyl-H), 8.85 (br, 4H, β-H Py), 8.90 (br, 4H, β-H Py), 9.07 (d, J = 5 Hz, 4H, pyridyl-H). UV–vis (CH₂Cl₂, λ [nm], 298 K): 417 nm, 513 nm, 548 nm, 590 nm, 644 nm. MALDI-TOF MS (*m/z*): 772.425 (calcd for C₄₂H₂₆Br₂N₆ exact mass, 772.059). Anal. Calcd for C₄₂H₂₆Br₂N₆: C, 65.13; H, 3.38; N, 10.85. Found: C, 65.24; H, 3.40; N, 10.72.

5,15-Bis(4-bromophenyl)-10,20-bis(4-phenylpyridyl)porphyrin (6). By use of a general method, 2,2'-((4-bromophenyl)methylene)bis(1H-pyrrole) (0.5 g, 1.66 mmol) and 4-(pyridin-4-yl)benzaldehyde (0.304g, 1.6 mmol) were taken in a round-bottom flask and 40 mL of propionic acid was added. The reaction mixture was then stirred under nitrogen at 298 K for 90 min. Thereafter, the reaction mixture was refluxed under nitrogen for 90 min, brought to room temperature, and left overnight for precipitation. The precipitate was poured into sintered funnel and washed with methanol. The crude product left on the sintered funnel was then dried in vacuum. The crude product was purified by silica gel column chromatography (100–200 mesh) using ethyl acetate/dichloromethane (10:90, v/v) as an eluent. Yield: 296 mg (20%). Mp > 300 °C. ¹H NMR (500 MHz, CDCl₃, 298 K, δ [ppm]) –2.81 (s, 2H, NH), 8.91 (br, 4H, pyridyl-H), 8.87 (br, 2H, Py-β-H), 8.85 (br, 4H, pyridyl-H), 8.34 (d, J = 7.5 Hz, 2H, Py-β-H), 8.09 (m, 8H, 4-bromo Ph, Ph), 8.05 (d, J = 7.5 Hz, 2H, Py-β-H), 7.92 (m, 8H, 4-bromo Ph, Ph), 7.86 (d, J = 5.5 Hz, 2H, Py-β-H), UV–vis (CH₂Cl₂, λ [nm], 298 K): 418 nm, 514 nm, 550 nm, 592 nm, 647 nm. MALDI-TOF MS (*m/z*): 925.670 (calcd for C₅₄H₃₄Br₂N₆ exact mass, 924.121). Anal. Calcd for C₅₄H₃₄Br₂N₆: C, 69.99; H, 3.70; N, 9.07. Found: C, 69.94; H, 3.64; N, 9.02.

5-(4-Bromophenyl)-10,15,20-tri(4-pyridyl)porphyrin (7). By use of a general method, 4-pyridinecarboxaldehyde (1.605g, 15 mmol), 4-bromobenzaldehyde (0.925g, 5 mmol), and 50 mL of propionic acid were added and the reaction mixture was magnetically stirred. Freshly distilled pyrrole (1.4 mL; 20 mmol) was then added to the mixture, the temperature then brought to reflux and allowed to stir for 4 h at reflux. After allowing the reaction mixture to cool to room temperature, the reaction flask was placed in the freezer overnight to aid precipitation of the porphyrin. The reaction mixture was then vacuum filtered using a sintered funnel, and a dark purple solid was collected, washed with 5 × 50 mL of DCM, washed with methanol, and dried overnight. The solid was purified by silica gel column chromatography. Yield 2.08 g (15%). Mp > 300 °C. ¹H NMR (500 MHz, CDCl₃, 298 K, δ [ppm]) 9.06 (d, J = 5 Hz, 6H, pyridyl-H), 8.90 (d, J = 4.5 Hz, 2H, β-H Py), 8.86 (s, 4H, β-H Py), 8.83 (d, J = 4.5 Hz, 2H, β-H Py), 8.17 (d, J = 5 Hz, 6H, pyridyl-H), 8.07 (d, J = 8 Hz, 2H, phenyl-H), 7.92 (d, J = 8 Hz, 2H, phenyl-H). UV–vis (CH₂Cl₂, λ

[nm], 298 K): 416 nm, 512 nm, 547 nm, 588 nm, 643 nm. MALDI-TOF MS (*m/z*): 696.658 (calcd for C₄₁H₂₆BrN₇ exact mass, 696.612). Anal. Calcd for C₄₁H₂₆BrN₇: C, 70.69; H, 3.76; N, 14.08. Found: C, 69.70; H, 3.86; N, 14.19.

5,10-Bis(4-carboxyphenyl)-15,20-bis(4-dimethylaminophenyl)porphyrin (8). By use of a general method, 4-(dimethylamino)benzaldehyde (0.745g, 5 mmol), 4-formylbenzoic acid (0.75g, 5 mmol), and 50 mL of propionic acid were added and the reaction mixture was stirred under nitrogen. To increase the solubility of 4-formylbenzoic acid, the reaction mixture was heated to 80 °C at which point the aldehyde fully dissolved. Freshly distilled pyrrole (0.7 mL; 10 mmol) was then added to the reaction mixture and allowed to stir for 4 h under reflux. After allowing the reaction mixture to cool to room temperature, the reaction flask was placed in the freezer overnight to aid precipitation of the porphyrin. The precipitate was vacuum filtered through a sintered funnel, and a dark purple solid so collected was washed with methanol and dried. The solid residue was purified over silica gel chromatography and recrystallized from methanol. Yield: 1.57g (20%). Mp > 300 °C. ¹H NMR (500 MHz, DMSO-*d*₆, 298 K, δ [ppm]) 12.85 (2H, br, -COOH), 8.96 (br, 4H, carboxyPh-CH), 8.82 (br, 6H, carboxyPh-CH and Py-β-CH), 8.38 (d, J = 7.5 Hz, 4H, *N,N*-dimethyl Ph), 8.33 (d, J = 7.5 Hz, 4H, *N,N*-dimethyl Ph), 8.03 (d, J = 7.5 Hz, 2H, Py-β-CH), 7.95 (s, 2H, Py-β-CH), 7.16 (d, J = 8 Hz, 2H, Py-β-CH), 2.89 (s, 12H, Me), –2.84 (br, 2H, NH). UV–vis (CH₂Cl₂, λ [nm], 298 K): 414 nm, 516 nm, 557 nm, 594 nm, 652 nm. MALDI-TOF MS (*m/z*): 788.681 (calcd for C₅₀H₄₀N₆O₄ exact mass, 788.311). Anal. Calcd for C₅₀H₄₀N₆O₄: C, 76.12; H, 5.11; N, 10.65. Found: C, 76.14; H, 5.16; N, 10.62.

5-(4-Carboxyphenyl)-10,15,20-tri(4-dimethylaminophenyl)porphyrin (9). By use of a general method, 4-(dimethylamino)benzaldehyde (2.23g, 15 mmol) and 4-formylbenzoic acid (0.75g, 5 mmol) were added to 50 mL of propionic acid, and the reaction mixture was magnetically stirred. Freshly distilled pyrrole (1.4 mL; 20 mmol) was then added to the mixture, the temperature then brought to reflux and allowed to stir for 4 h at reflux. After allowing the reaction mixture to cool to room temperature, the reaction flask was placed in the freezer overnight to aid precipitation of the porphyrin. The reaction mixture was then vacuum filtered using a sintered funnel, and a dark purple solid was collected, washed with 5 × 50 mL of DCM, washed with methanol, and dried overnight. The solid residue was purified over silica gel chromatography using 30% EtOAc–CH₂Cl₂. Yield 3.1 g (20%). Mp > 300 °C. ¹H NMR (500 MHz, CDCl₃, 298 K, δ [ppm]) 12.85 (1H, br, -COOH), 8.92 (br, 2H, carboxyPh-CH), 8.75 (br, 2H, carboxyPh-CH), 8.57 (s, 4H, Py-β-CH), 8.42 (br, 6H, *N,N*-dimethyl Ph), 8.28 (br, 6H, *N,N*-dimethyl Ph), 8.06 (d, J = 7 Hz, 2H, Py-β-CH), 7.10 (d, J = 7 Hz, 2H, Py-β-CH), 3.32 (s, 18H, Me), –2.70 (br, 2H, NH). UV–vis (CH₂Cl₂, λ [nm], 298 K): 417 nm, 519 nm, 561 nm, 598 nm, 655 nm. MALDI-TOF MS (*m/z*): 787.918 (calcd for C₅₁H₄₅N₇O₂ exact mass, 787.363). Anal. Calcd for C₅₁H₄₅N₇O₂: C, 77.74; H, 5.76; N, 12.44. Found: C, 77.80; H, 5.81; N, 12.41.

5,10,15,20-Tetra(4-pyridyl)porphyrin (10). By use of a general method, 1.07 g (10 mmol) of 4-pyridinecarboxaldehyde and 50 mL of propionic acid were added and the reaction mixture was magnetically stirred. Freshly distilled pyrrole (0.7 mL; 10 mmol) was then added to the mixture, the temperature then brought to reflux and allowed to stir for 2 h at reflux. After allowing the reaction mixture to cool to room temperature, the reaction flask was placed in the freezer overnight to aid precipitation of the porphyrin. The reaction mixture was then vacuum filtered using a sintered funnel, and a dark purple solid was collected, washed with 5 × 50 mL of DCM, washed with methanol, and dried overnight to give 5,10,15,20-tetra(4-pyridyl)porphyrin. Yield 2.472 g (20%). Mp > 300 °C. ¹H NMR (500 MHz, CDCl₃, 298 K, δ [ppm]) 8.94 (d, J = 5 Hz, 8H, pyridyl-H), 8.79 (b, 8H, pyrrole β-H), 8.16 (d, J = 5 Hz, 8H, pyridyl-H), –2.99 (b, 2H, pyrrole NH). UV–vis (CH₂Cl₂, λ [nm], 298 K): 415 nm, 511 nm, 545 nm, 587 nm, 642 nm. MALDI-TOF MS (*m/z*): 618.629 (calcd for C₄₀H₂₆N₈ exact mass, 618.704). Anal. Calcd for C₄₀H₂₆N₈: C, 77.65; H, 4.24; N, 18.11. Found: C, 77.00; H, 4.16; N, 18.07.

Drug and Antibodies. Camptothecin, proteasomal inhibitor MG132, and *N*-acetyl-L-cysteine (NAC) were purchased from Sigma. Mouse monoclonal anti-human Top1 (C21) antibody, rabbit polyclonal PARP1 antibody, and secondary antibodies horseradish peroxidase conjugated anti-rabbit IgG and anti-mouse IgG were obtained from Santa Cruz Biotechnology (USA). Anti-actin (ACTN05) antibody was from Neo Markers (USA).

Recombinant Human Topoisomerase 1 and Plasmid DNA Relaxation Assay. The recombinant human Top1 was purified from Sf-9 insect cells, infected with the recombinant baculovirus (a kind gift from Prof. James. J. Champoux) as described previously.^{6,13}

The type 1 DNA topoisomerase is assayed by decreased mobility of the relaxed isomers of supercoiled pBS (SK⁺) DNA in 1% agarose gel. The relaxation assay was carried out with recombinant human Top1 or the whole cell extracts of human breast adenocarcinoma (MCF7) cells as source of endogenous Top1, diluted in the relaxation buffer with supercoiled plasmid DNA as described previously.^{6,8,13,38}

Cleavage Assay. Plasmid DNA cleavage assay was carried out as described previously.^{6,8} For equilibrium cleavage assays, 25-mer duplex of oligonucleotide containing a Top1 binding motif was labeled and annealed as described previously.^{13,36,38} Samples were analyzed by 12% sequencing gel electrophoresis, dried, and exposed on PhosphorImager screens and imaged with Typhoon FLA 7000 (GE Healthcare, U.K.).

Cell Culture and Transfection. Human cancerous cell lines like MCF7, HeLa, HCT116, NIH:OVCAR-3, and HEK293 were obtained from the Developmental Therapeutics Program as kind gift from Dr. Yves Pommier (NIH/NCI/USA). TDPI^{+/+} and TDPI^{-/-} primary MEF cells were kind gift from Dr. Cornelius F. Boerkoel (University of British Columbia, Canada) and were cultured as described previously.^{6,36,40,42} Plasmid DNAs were transfected with Lipofectamine 2000 (Invitrogen) according to the manufacturer's protocol.

Photobleaching Experiments. Photobleaching experiments were performed as described formerly^{40–42} using Andor Spinning disk inverted confocal laser-scanning microscope equipped with a 60×/1.42 NA oil-immersion objective (Olympus) and with a CO₂-controlled on-stage heated environmental chamber set to 37 °C. FRAP analyses were carried out with living MCF7 cells ectopically expressing EGFP-human Top1 grown on chamber cover glass (Genetix, India) and drug treated as indicated. For FRAP analysis, a subnuclear spot was bleached for 30 ms by solid-state laser line (488 nm for EGFP) adapted to the fluorescent protein of interest and FRAP curves were generated individually normalized to the prebleach signal as described previously.⁴²

Job Plot and Spectrofluorimetric Binding Assay. The binding stoichiometry for compound **8** with Top1 was determined using the method of continuous variation.^{12,14,43} Briefly, reaction mixtures containing variable Top1 and compound **8** to a final concentration of 1.25 μM were analyzed for quenching of tryptophan fluorescence at 350 nm upon excitation at 295 nm on PerkinElmer LS55 luminescence spectrometer.

Spectrofluorimetric binding assay was carried out as previously described^{12,14,43} where Top1 (200 nM) was incubated with various concentrations of compound **8** (0–11 μM) at 25 °C for 10 min. The equation for determining fraction of binding sites (B) occupied by inhibitor was $B = (F_0 - F)/F_{\max}$, where F_0 is the fluorescence intensity at 350 nm of Top1 alone in the absence of any inhibitors, F is the fluorescence intensity at 350 nm of Top1 in the presence of inhibitor, and F_{\max} is obtained from the plot of $1/(F_0 - F)$ versus $1/[X]$ and by extrapolating $1/[X]$ to zero, where $[X]$ is the concentration of compound **8**. The dissociation constant (K_D) was determined as described previously.¹²

Analysis of Compound 8-DNA Intercalation. The competence of the drug to intercalate into plasmid DNA was determined by Top1 unwinding assay.^{36,44} Assays were performed with 50 fmol of pBluscript (SK+) DNA in the presence or absence of compound **8**, m-AMSA, and etoposide at indicated concentrations. Excess of DNA topoisomerase I was reacted with supercoiled plasmid DNA to generate relaxed DNA for the unwinding assays. The relaxed DNA was purified by proteolytic digestion with proteinase K at 37 °C, followed by phenol/chloroform extraction and ethanol precipitation. The

unwinding assays were carried out at 37 °C for 15 min with independent compounds and were analyzed by 1% agarose gel as described above.

Cell Extracts and Immunoblotting. Preparation of whole cell extracts from MCF7 cells and immunoblotting were carried out as described.^{6,40,41} Immunoreactivity was detected using ECL chemiluminescence reaction (Amersham) under ChemiDoc MP system (Bio-Rad, USA).

Immuno Complex of Enzyme (ICE) Bioassay. In vivo Top1 cleavage complexes (Top1cc) were isolated from MCF7 cells using immuno complex of enzyme (ICE) bioassay technique.⁴⁹ Briefly, 5×10^6 MCF7 cells were treated with drugs and were lysed by DNazol reagent (Invitrogen, USA) in the presence of 0.1% SDS. Genomic DNA was prepared and was briefly sonicated. Varying concentrations of DNA were spotted onto nitrocellulose membrane (Millipore, USA) using a slot-blot vacuum system (Biorad, USA). Immunoblotting was carried out with antihuman Top1 antibodies as described.⁴¹

Measurement of ROS. Intracellular ROS was detected in drug-treated MCF7 cells with or without pretreatment of *N*-acetyl-L-cysteine (NAC) for indicated time as described.^{13,46} Briefly, cells were washed and resuspended in 500 μL of 1× PBS and were loaded with 2 μg/mL of H₂DCFDA (Molecular Probes) for 30 min, and green fluorescence of 2,7-dichlorofluorescein was measured at 515 nm by spectrofluorometer.

Alkaline COMET Assays. To detect the levels of drug-induced DNA breaks, after treatment MCF7 cells were subjected to alkaline comet assays according to the manufacturer's instructions (Trevigen, USA) and comet length was measured and was scored for at least 50 cells. Distributions of comet lengths were compared using the Student's *t*-test as described previously.^{13,40,50}

Immunocytochemistry. Immunofluorescence staining of apoptosis marker phosphatidylserine was performed as described previously.^{40,41} After treatment, MCF7 cells were fixed with 2% paraformaldehyde for 10 min at room temperature and stained with annexin V-FITC antibody (BD, USA), mounted in antifade solution with propidium iodide (Vector Laboratories, USA), and examined under Leica TCS SP8 confocal laser-scanning microscope.

Cell Survival Assay. Cell survival was assessed by 3-(4,5-dimethylthiazol-2-yl)-2,5-diphenyltetrazolium bromide (MTT) assay as discussed previously.⁶ The percent inhibition of viability for each concentration of the compounds was calculated with respect to the control, and IC₅₀ values were estimated.

siRNA Transfection. Transfections were performed as described previously.⁴⁰ In brief, cells (1.5×10^5) were transfected with control siRNA or 40 nM Top1 siRNA (Qiagen) using oligofectamine (Invitrogen) according to the manufacturer's protocol. Time course experiments revealed a maximum suppression of Top1 protein at day 3 after transfection, as analyzed by Western blotting.

■ ASSOCIATED CONTENT

📄 Supporting Information

The Supporting Information is available free of charge on the ACS Publications website at DOI: 10.1021/acs.jmedchem.7b01297.

MALDI-TOF MS, ¹H NMR, and ¹H–¹H 2D COSY spectra and UV–vis data of compounds **1–10** (PDF)
Molecular formula strings (CSV)

■ AUTHOR INFORMATION

Corresponding Authors

*H.R.: e-mail, ichr@iacs.res.in.

*B.B.D.: phone, +91 33 2473 4971, extension 2108; fax, +91 33 2473 2805; e-mail, pcbhd@iacs.res.in.

ORCID

Harapriya Rath: 0000-0002-5507-5275

Benu Brata Das: 0000-0003-2519-7105

Notes

The authors declare no competing financial interest.

ACKNOWLEDGMENTS

We thank Dr. Hemanta K Majumder and Dr. Suwendra N Bhattacharyya, CSIR-Indian Institute of Chemical Biology, India for their help during the study and Mr. Gopal K Manna of IACS for his help with the artwork. The BBD team is supported by Wellcome Trust/DBT India Alliance Intermediate Fellowship (Award IA/I/13/1/500888) and also funded the open access charge. A.G. and K.C.S. are recipients of CSIR-NET-Senior Research Fellowship, India. S.P.C. thanks UGC-CSIR-NET for Junior Research Fellowship. S.K.D., I.R., and N.H. thank IACS for SRF and JRF positions, respectively. H.R. thanks DST-SERB (Grant EMR/2016/004705) for the research grant. B.B.D. is a Wellcome Trust/DBT India Alliance Intermediate Fellow.

REFERENCES

- (1) Champoux, J. J. DNA topoisomerases: structure, function, and mechanism. *Annu. Rev. Biochem.* **2001**, *70*, 369–413.
- (2) Capranico, G.; Marinello, J.; Chillemi, G. Type I DNA topoisomerases. *J. Med. Chem.* **2017**, *60*, 2169–2192.
- (3) Pommier, Y. Drugging topoisomerases: lessons and challenges. *ACS Chem. Biol.* **2013**, *8*, 82–95.
- (4) Pommier, Y. DNA topoisomerase I inhibitors: chemistry, biology, and interfacial inhibition. *Chem. Rev.* **2009**, *109*, 2894–2902.
- (5) Pommier, Y. Topoisomerase I inhibitors: camptothecins and beyond. *Nat. Rev. Cancer* **2006**, *6*, 789–802.
- (6) Majumdar, P.; Bathula, C.; Basu, S. M.; Das, S. K.; Agarwal, R.; Hati, S.; Singh, A.; Sen, S.; Das, B. B. Design, synthesis and evaluation of thiohydantoin derivatives as potent topoisomerase I (top1) inhibitors with anticancer activity. *Eur. J. Med. Chem.* **2015**, *102*, 540–551.
- (7) Nagarajan, M.; Morrell, A.; Antony, S.; Kohlhagen, G.; Agama, K.; Pommier, Y.; Ragazzon, P. A.; Garbett, N. C.; Chaires, J. B.; Hollingshead, M.; Cushman, M. Synthesis and biological evaluation of bisindenoisoquinolines as topoisomerase I inhibitors. *J. Med. Chem.* **2006**, *49*, 5129–5140.
- (8) Cushman, M.; Jayaraman, M.; Vroman, J. A.; Fukunaga, A. K.; Fox, B. M.; Kohlhagen, G.; Strumberg, D.; Pommier, Y. Synthesis of new indeno[1,2-c]isoquinolines: cytotoxic non-camptothecin topoisomerase I inhibitors. *J. Med. Chem.* **2000**, *43*, 3688–3698.
- (9) Pommier, Y.; Sun, Y.; Huang, S. N.; Nitiss, J. L. Roles of eukaryotic topoisomerases in transcription, replication and genomic stability. *Nat. Rev. Mol. Cell Biol.* **2016**, *17*, 703–721.
- (10) Wu, N.; Wu, X. W.; Agama, K.; Pommier, Y.; Du, J.; Li, D.; Gu, L. Q.; Huang, Z. S.; An, L. K. A novel DNA topoisomerase I inhibitor with different mechanism from camptothecin induces G2/M phase cell cycle arrest to K562 cells. *Biochemistry* **2010**, *49*, 10131–10136.
- (11) Yu, L. M.; Zhang, X. R.; Li, X. B.; Yang, Y.; Wei, H. Y.; He, X. X.; Gu, L. Q.; Huang, Z. S.; Pommier, Y.; An, L. K. Synthesis and biological evaluation of 6-substituted indolizinoquinolinediones as catalytic DNA topoisomerase I inhibitors. *Eur. J. Med. Chem.* **2015**, *101*, 525–533.
- (12) Chowdhury, S.; Mukherjee, T.; Sengupta, S.; Chowdhury, S. R.; Mukhopadhyay, S.; Majumder, H. K. Novel betulin derivatives as antileishmanial agents with mode of action targeting type IB DNA topoisomerase. *Mol. Pharmacol.* **2011**, *80*, 694–703.
- (13) Ganguly, A.; Das, B.; Roy, A.; Sen, N.; Dasgupta, S. B.; Mukhopadhyay, S.; Majumder, H. K. Betulinic acid, a catalytic inhibitor of topoisomerase I, inhibits reactive oxygen species-mediated apoptotic topoisomerase I-DNA cleavable complex formation in prostate cancer cells but does not affect the process of cell death. *Cancer Res.* **2007**, *67*, 11848–11858.
- (14) Saha, S.; Acharya, C.; Pal, U.; Chowdhury, S. R.; Sarkar, K.; Maiti, N. C.; Jaisankar, P.; Majumder, H. K. A novel spirooxindole derivative inhibits the growth of *Leishmania donovani* parasites both in vitro and in vivo by targeting type IB topoisomerase. *Antimicrob. Agents Chemother.* **2016**, *60*, 6281–6293.
- (15) Sordet, O.; Khan, Q. A.; Plo, I.; Pourquier, P.; Urasaki, Y.; Yoshida, A.; Antony, S.; Kohlhagen, G.; Solary, E.; Sapparbaev, M.; Laval, J.; Pommier, Y. Apoptotic topoisomerase I-DNA complexes induced by staurosporine-mediated oxygen radicals. *J. Biol. Chem.* **2004**, *279*, 50499–50504.
- (16) Sordet, O.; Goldman, A.; Pommier, Y. Topoisomerase II and tubulin inhibitors both induce the formation of apoptotic topoisomerase I cleavage complexes. *Mol. Cancer Ther.* **2006**, *5*, 3139–3144.
- (17) Sen, N.; Banerjee, B.; Das, B. B.; Ganguly, A.; Sen, T.; Pramanik, S.; Mukhopadhyay, S.; Majumder, H. K. Apoptosis is induced in leishmanial cells by a novel protein kinase inhibitor withaferin A and is facilitated by apoptotic topoisomerase I-DNA complex. *Cell Death Differ.* **2007**, *14*, 358–367.
- (18) Sordet, O.; Goldman, A.; Redon, C.; Solier, S.; Rao, V. A.; Pommier, Y. Topoisomerase I requirement for death receptor-induced apoptotic nuclear fission. *J. Biol. Chem.* **2008**, *283*, 23200–23208.
- (19) Teo, R. D.; Hwang, J. Y.; Termini, J.; Gross, Z.; Gray, H. B. Fighting cancer with corroles. *Chem. Rev.* **2017**, *117*, 2711–2729.
- (20) Zou, Q.; Abbas, M.; Zhao, L.; Li, S.; Shen, G.; Yan, X. Biological photothermal nanodots based on self-assembly of peptide-porphyrin conjugates for antitumor therapy. *J. Am. Chem. Soc.* **2017**, *139*, 1921–1927.
- (21) Karunakaran, S. C.; Ramaiah, D.; Schulz, I.; Epe, B. Study of the mode and efficiency of DNA binding in the damage induced by photoactivated water soluble porphyrins. *Photochem. Photobiol.* **2013**, *89*, 1100–1105.
- (22) Munson, B. R.; Fiel, R. J. DNA intercalation and photosensitization by cationic meso substituted porphyrins. *Nucleic Acids Res.* **1992**, *20*, 1315–1319.
- (23) Shuai, L.; Wang, S.; Zhang, L.; Fu, B.; Zhou, X. Cationic porphyrins and analogues as new DNA topoisomerase I and II inhibitors. *Chem. Biodiversity* **2009**, *6*, 827–837.
- (24) Zhai, B.; Shuai, L.; Yang, L.; Weng, X.; Wu, L.; Wang, S.; Tian, T.; Wu, X.; Zhou, X.; Zheng, C. Octa-substituted anionic porphyrins: topoisomerase I inhibition and tumor cell apoptosis induction. *Bioconjugate Chem.* **2008**, *19*, 1535–1542.
- (25) Adler, A. D.; Longo, F. R.; Finarelli, J. D.; Goldmacher, J.; Assour, J.; Korsakoff, L. A simplified synthesis for meso-tetraphenylporphine. *J. Org. Chem.* **1967**, *32*, 476–476.
- (26) Harada, A.; Yamaguchi, H.; Okamoto, K.; Fukushima, H.; Shiotsuki, K.; Kamachi, M. Control of photoinduced electron transfer from zinc-porphyrin to methyl viologen by supramolecular formation between monoclonal antibody and zinc-porphyrin. *Photochem. Photobiol.* **1999**, *70*, 298–302.
- (27) Fouad, F. S.; Crasto, C. F.; Lin, Y.; Jones, G. B. Photoactivated enediynes: targeted chimeras which undergo photo-bergman cyclization. *Tetrahedron Lett.* **2004**, *45*, 7753–7756.
- (28) Ikeda, T.; Shinkai, S.; Sada, K.; Takeuchi, M. A preliminary step toward molecular spring driven by cooperative guest binding. *Tetrahedron Lett.* **2009**, *50*, 2006–2009.
- (29) Smith, M. W.; Lawton, L. G.; Checkoff, J. Tetrapyrrolyl porphyrin derivatives of group 13 metals. *Synth. React. Inorg. Met.-Org. Chem.* **1993**, *23*, 639–651.
- (30) Adler, A. D.; Sklar, L.; Longo, F. R.; Finarelli, J. D.; Finarelli, M. G. A mechanistic study of the synthesis of meso-tetraphenylporphyrin. *J. Heterocycl. Chem.* **1968**, *5*, 669–678.
- (31) Zhang, X.-X.; Wayland, B. B. Rhodium(II) porphyrin bimetallic complexes: preparation and enhanced reactivity with CH4 and H2. *J. Am. Chem. Soc.* **1994**, *116*, 7897–7898.
- (32) DiMaggio, S. G.; Lin, V. S. Y.; Therien, M. J. Catalytic conversion of simple haloporphyrins into alkyl-, aryl-, pyridyl-, and vinyl-substituted porphyrins. *J. Am. Chem. Soc.* **1993**, *115*, 2513–2515.
- (33) Hyslop, A. G.; Therien, M. J. Synthesis of porphyrin-spacer-quinone compounds via metal-mediated cross-coupling: new systems for probing the relative magnitudes of axial and equatorial electronic

coupling at the porphyrin macrocycle in thermal and photoactivated electron transfer reactions. *Inorg. Chim. Acta* **1998**, *275*, 427–434.

(34) Nowak-Król, A.; Koszarna, B.; Yoo, S. Y.; Chromiński, J.; Węclawski, M. K.; Lee, C.-H.; Gryko, D. T. Synthesis of trans-A2B2-porphyrins bearing phenylethynyl substituents. *J. Org. Chem.* **2011**, *76*, 2627–2634.

(35) Ravikanth, M.; Strachan, J.-P.; Li, F.; Lindsey, J. S. Trans-substituted porphyrin building blocks bearing iodo and ethynyl groups for applications in bioorganic and materials chemistry. *Tetrahedron* **1998**, *54*, 7721–7734.

(36) Das, B. B.; Sen, N.; Roy, A.; Dasgupta, S. B.; Ganguly, A.; Mohanta, B. C.; Dinda, B.; Majumder, H. K. Differential induction of *Leishmania donovani* bi-subunit topoisomerase I-DNA cleavage complex by selected flavones and camptothecin: activity of flavones against camptothecin-resistant topoisomerase I. *Nucleic Acids Res.* **2006**, *34*, 1121–1132.

(37) Gentry, A. C.; Juul, S.; Veigaard, C.; Knudsen, B. R.; Osheroff, N. The geometry of DNA supercoils modulates the DNA cleavage activity of human topoisomerase I. *Nucleic Acids Res.* **2011**, *39*, 1014–1022.

(38) Das, B. B.; Sen, N.; Dasgupta, S. B.; Ganguly, A.; Majumder, H. K. N-terminal region of the large subunit of *Leishmania donovani* bisubunit topoisomerase I is involved in DNA relaxation and interaction with the smaller subunit. *J. Biol. Chem.* **2005**, *280*, 16335–16344.

(39) Marchand, C.; Huang, S. Y.; Dexheimer, T. S.; Lea, W. A.; Mott, B. T.; Chergui, A.; Naumova, A.; Stephen, A. G.; Rosenthal, A. S.; Rai, G.; Murai, J.; Gao, R.; Maloney, D. J.; Jadhav, A.; Jorgensen, W. L.; Simeonov, A.; Pommier, Y. Biochemical assays for the discovery of TDP1 inhibitors. *Mol. Cancer Ther.* **2014**, *13*, 2116–2126.

(40) Das, B. B.; Antony, S.; Gupta, S.; Dexheimer, T. S.; Redon, C. E.; Garfield, S.; Shiloh, Y.; Pommier, Y. Optimal function of the DNA repair enzyme TDP1 requires its phosphorylation by ATM and/or DNA-PK. *EMBO J.* **2009**, *28*, 3667–3680.

(41) Das, B. B.; Huang, S. Y.; Murai, J.; Rehman, I.; Ame, J. C.; Sengupta, S.; Das, S. K.; Majumdar, P.; Zhang, H.; Biard, D.; Majumder, H. K.; Schreiber, V.; Pommier, Y. PARP1-TDP1 coupling for the repair of topoisomerase I-induced DNA damage. *Nucleic Acids Res.* **2014**, *42*, 4435–4449.

(42) Das, S. K.; Rehman, I.; Ghosh, A.; Sengupta, S.; Majumdar, P.; Jana, B.; Das, B. B. Poly(ADP-ribose) polymers regulate DNA topoisomerase I (Top1) nuclear dynamics and camptothecin sensitivity in living cells. *Nucleic Acids Res.* **2016**, *44*, 8363–8375.

(43) Huang, C. Y. Determination of binding stoichiometry by the continuous variation method: the Job plot. *Methods Enzymol.* **1982**, *87*, 509–525.

(44) Chen, G. L.; Yang, L.; Rowe, T. C.; Halligan, B. D.; Tewey, K. M.; Liu, L. F. Nonintercalative antitumor drugs interfere with the breakage-reunion reaction of mammalian DNA topoisomerase II. *J. Biol. Chem.* **1984**, *259*, 13560–13566.

(45) Pommier, Y.; Huang, S. Y.; Gao, R.; Das, B. B.; Murai, J.; Marchand, C. Tyrosyl-DNA-phosphodiesterases (TDP1 and TDP2). *DNA Repair* **2014**, *19*, 114–129.

(46) Sen, N.; Das, B. B.; Ganguly, A.; Mukherjee, T.; Tripathi, G.; Bandyopadhyay, S.; Rakshit, S.; Sen, T.; Majumder, H. K. Camptothecin induced mitochondrial dysfunction leading to programmed cell death in unicellular hemoflagellate *Leishmania donovani*. *Cell Death Differ.* **2004**, *11*, 924–936.

(47) Soldani, C.; Scovassi, A. I. Poly(ADP-ribose) polymerase-1 cleavage during apoptosis: an update. *Apoptosis* **2002**, *7*, 321–328.

(48) Hirano, R.; Interthal, H.; Huang, C.; Nakamura, T.; Deguchi, K.; Choi, K.; Bhattacharjee, M. B.; Arimura, K.; Umehara, F.; Izumo, S.; Northrop, J. L.; Salih, M. A.; Inoue, K.; Armstrong, D. L.; Champoux, J. J.; Takashima, H.; Boerkoel, C. F. Spinocerebellar ataxia with axonal neuropathy: consequence of a TDP1 recessive neomorphic mutation? *EMBO J.* **2007**, *26*, 4732–4743.

(49) Regairaz, M.; Zhang, Y. W.; Fu, H.; Agama, K. K.; Tata, N.; Agrawal, S.; Aladjem, M. I.; Pommier, Y. Mus81-mediated DNA

cleavage resolves replication forks stalled by topoisomerase I-DNA complexes. *J. Cell Biol.* **2011**, *195*, 739–749.

(50) El-Khamisy, S. F.; Saifi, G. M.; Weinfeld, M.; Johansson, F.; Helleday, T.; Lupski, J. R.; Caldecott, K. W. Defective DNA single-strand break repair in spinocerebellar ataxia with axonal neuropathy-1. *Nature* **2005**, *434*, 108–113.

Cite this: *Dalton Trans.*, 2018, **47**, 6557

A novel metallogel based approach to synthesize (Mn, Cu) doped ZnS quantum dots and labeling of MCF-7 cancer cells†

Soumya Bhowal,^{id}*^a Arijit Ghosh,^b Srijita Paul Chowdhuri,^b Raju Mondal*^a and Benu Brata Das*^b

The present study aims to formulate a common synthetic strategy for preparing quantum dots (QDs) in a greener way by using combination of popular methods, *viz.* a colloidal method with suitable capping agent and low molecular weight gel based synthesis. Pyridine dicarboxylic acid (PDC) in presence of $AlCl_3$ forms a stable metallogel, which serves as an excellent medium for selective ZnS QD synthesis. The aromatic pyridine moiety, well known for being a capping agent, indeed plays its part in the run up to QD synthesis. To the best of our knowledge, this is the first example of a metallogel based doped ZnS QD synthesis. Altering the doping material and its composition changes the properties of the QDs, but herein we also tried to establish how these changes affect the gel morphology and stability of both gel and QDs. We further demonstrate, by using live cell confocal microscopy, the delivery of QDs Cu ZnS and MnZnS nanomaterials in the nucleus and the cytoplasm of human breast cancer cells (MCF7), implicating the use of metallogel based QDs for bio-imaging and bio-labeling.

Received 13th October 2017,

Accepted 12th April 2018

DOI: 10.1039/c7dt03864j

rsc.li/dalton

Introduction

Although they have been known for a long time, supramolecular gels, as a new branch of nanoscale smart materials, have started to draw attention only recently. Gel materials with unique ability to immobilize solvent or guest molecules inside three-dimensional cross-linked networks have emerged,^{1–8} *inter alia*, as a promising platform for synthesizing semiconductor nanoparticles including quantum dots (QD).^{15,44} Among the QDs, Cd based QDs such as CdS, CdSe or CdTe have been extensively studied owing to their wide range of applications.⁴⁷ However, Cd based QDs have a severe shortcoming of inherent toxicity.⁹ Naturally, non-toxic QDs such as ZnS, along with paramagnetic transition metal dopant, have drawn considerable attention due to their improved opto-

electronic and imaging properties.^{10–12} Gel-based synthesis of QDs is of current interest and has several advantages over other conventional methods. Using gel-based techniques, it is far easier to control and tune the size and shape of the QDs.^{13–16} It is noteworthy that the size and shape remain the main determinant of the quality and efficiency of QDs.^{17,18} Furthermore, difficulties in separating QDs from the conventional synthetic media usually bring unwanted interferences and often limit their meaningful application. Moreover, the heterogeneous nature of the gels facilitates the slow and controlled release of QDs from the gel matrix, most of the time. These advantages of the gel-based approach have been successfully exploited by many researchers in recent times leading to a surge in a wide range of QDs using various gelator molecules.^{13–16} Notwithstanding these successes, metallogels, another class of metal-containing supramolecular gels,²² as a platform for QD generation, have remained largely unexplored, with hardly any reports in the literature. The benefits of introducing metal in a gel system are twofold. First, metal–ligand co-ordination bonds present in metallogels impart extra stability and porosity.^{23,24} Second, with judicious selection of the gelator and metallogel, materials can be tailored to display various physicochemical properties that are exclusively metal specific such as catalytic, spectroscopic and redox properties.^{19–21} However, most QDs are basically metal containing nanoparticles. This brings the unique challenge of separating a selective set of metals for generating the nano-

^aDepartment of Inorganic Chemistry, Indian Association for the Cultivation of Science, Raja S. C. Mullick Road, Kolkata-700032, India. E-mail: icsb8@iacs.res.in, icrm@iacs.res.in

^bDepartment of Biological Chemistry, Indian Association for the Cultivation of Science, Raja S. C. Mullick Road, Kolkata-700032, India. E-mail: pcbbd@iacs.res.in

† Electronic supplementary information (ESI) available: UV-Vis spectra of ligand and gel, UV and PL curve of the undoped ZnS incubated gel. XPS of the gel, FT-IR data of ligand, gel, xerogel, doped ZnS incubated gel, doped ZnS incubated xerogel, DLS curves showing intensity *vs.* size and ζ -potential curve, EDS, SEM images of the gel and some images of the self-healing property of the gel. See DOI: 10.1039/c7dt03864j

particles out from the rest of the metals used in gel network formation. Moreover, irrespective of the synthesis route, majority of the metallo-gels hosting the QD synthesis can get polluted with excess precursors, which also react with gel precursors in the medium, making the gel unstable.

One important link here is the capping agent. Capping agents are generally a special class of organic molecules used in QD synthesis to prevent particle overgrowth or agglomeration.^{25,33,48} Fitted with metal coordinating sites, the molecules form a hedge around the metal nanoparticles with weak coordination bonds. Basically, these molecules can be envisaged to have two major functional components. The *inner part* coordinates with QDs to provide stability as well as help in preserving their vital structural characteristics. The *outer part* does not have any link to QD synthesis, but barricades the pocket engulfing the QDs.²⁵ This contrasting nature of the *outer* and *inner* functional parts of a capping agent forms the basis of our bottom-up synthesis of metallo-gel based QDs. The idea is to use a gel containing a sufficient porous network that contains two functional groups with distinctly different activity: (a) form the metallo-gel that functions as the *outer part* by selectively coordinating to a specific metal and preferably form a co-ordination network that will hold the solvents and QD precursors, thus creating a hostile environment for the nanoparticles to form; and (b) form the *inner* coordinating site that remains an innocuous bystander during gel formation, but once the QDs are formed, becomes active and co-ordinates itself to the metal core of the nanoparticle surface.

We report herein the successful execution of the above mentioned method with the synthesis of ZnS (Mn, Cu) QDs in Aluminium-pyridine dicarboxylic acid (Al-PDC) based metallo-gels (Fig. 1). The aluminium based metallo-gel as well as the QDs were characterized by different microscopic (FESEM, TEM) techniques and diffraction methods. The porosity of the gel was established by BET measurement. Furthermore, the optical properties of Cu and Mn doped ZnS QDs (Cu:ZnS, Mn:ZnS) were investigated. It was found that the percentage of dopant affects the photoluminescence properties and nanoparticle

growth and the presence of the nanoparticles affects the gel stability thermally and mechanically. TGA and rheological studies were performed to obtain the difference in gel morphology between the pristine gel and the doped counterpart. Powder XRD was performed on both the xerogel of the Al-PDC gel and nanoparticle doped Al-PDC gel to obtain the crystalline nature of the gels. Finally, cell labeling was performed under a fluorescence microscope with our gel based nanocrystals. Our study was not only limited to understanding the credibility of our gel based QDs, but also studying the overall changes in gel morphology and optical properties that occur due to nanoparticle incorporation, and exploring as well as establishing the labeling properties shown by the fluorescent gel based QDs.

Experimental

Materials

All the starting materials were of reagent grade and used as received from the commercial suppliers. FT-IR data was collected from Nicolet MAGNA-IR 750. UV-Visible spectra were obtained using a PerkinElmer Lambda 950 UV/vis instrument. PXRD patterns were studied on a Bruker D8 ADVANCE instrument using Cu-K α ($\lambda = 1.5406 \text{ \AA}$). Gas adsorption, surface area and pore size distribution were determined using a Micromeritics ASAP 2020 surface area analyzer. Microscopic techniques were performed on a JMS-6700F for recording field emission scanning electron microscopy (FESEM) images and JEOL JEM 2010 high-resolution microscope instrument for recording TEM images. Dynamic light scattering (DLS) and the ζ -potential of the sample were collected by using a NanoZS90 (Malvern) instrument with water as solvent. Rheological data was collected by using an Anton Paar MCR 102 Rheometer. A PerkinElmer 2400 Series-II CHN analyser was used to perform the elemental analysis. Dulbecco's modified Eagle's medium (DMEM) was purchased from Sigma-Aldrich. Fluorescence images of cells were captured by an Olympus IX 81 microscope using Image-Pro Plus 7.0 software.

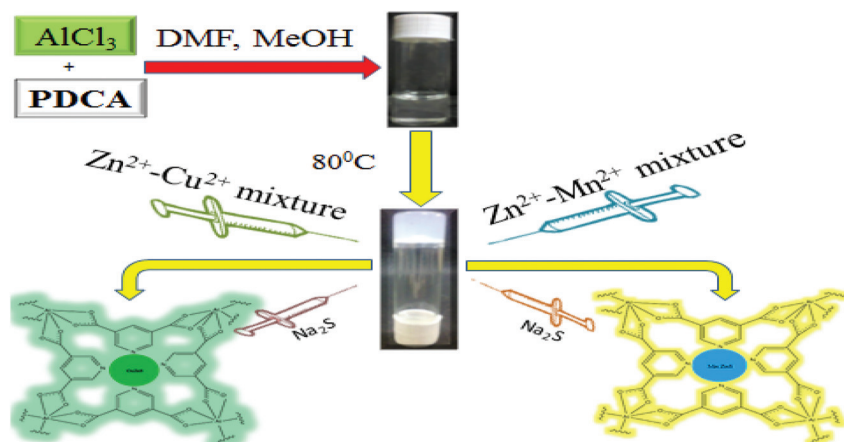


Fig. 1 Schematic representation of reaction and possible gel network-QD interaction.

Synthesis of Al-PDC gel and xerogel

Under solvothermal conditions, AlCl_3 and 3,5-pyridine dicarboxylic acid was taken in 1 wt% (1 : 1 ratio) in a vial and DMF–methanol solvent mixture was added in equal amounts (450 μL); the solution was mixed and heated for 8 hours at 80 °C to obtain the Al-PDC gel. **FT-IR (KBr, cm^{-1}):** 3456 (br), 2934 (m), 2360 (w), 1668 (vs), 1498 (m), 1439 (s), 1388 (s), 1251 (m), 1101 (s), 657 (s).

The xerogel can be synthesized by vacuum drying or open air drying the Al-PDC gel. Applying moderate heat on the gel for faster drying was avoided, so that the nanocrystals in the gel do not agglomerate to obtain QD incorporated gels. **FT-IR (KBr, cm^{-1}):** 3410 (br), 2784 (w), 2360 (w), 1616 (s), 1453 (m), 1414 (s), 1146 (w), 650 (br). **Elemental analysis (%):** C 35.82, H 4.90, N 9.27.

Synthesis of gel incorporated Mn and Cu doped ZnS

We introduced different percentages of Mn and Cu (from 1–10%) with respect to the Zn salts to see which composition gives the best optical property after incubation in the gel. Among these compounds, 2–4% Mn^{2+} incubated gel and 1–2% Cu^{2+} incubated gel give an intense luminescence when irradiated with UV light (365 nm). The optical properties were further characterized by UV-Vis spectroscopy and photoluminescence spectroscopy. For Mn:ZnS, compositions such as 2–4% give characteristic luminescence, but above 4% composition, no special luminescent feature from the gels can be observed. For Cu, only 1–2% Cu:ZnS gel shows luminescence; above this composition none of the gels show any optical property. The synthetic methods of the compositions mentioned above are shown below.

For Mn:ZnS, 5 mL of 0.1 mM $\text{Zn}(\text{OAc})_2$ and 100, 150 and 200 μL of 0.1 mM $\text{Mn}(\text{OAc})_2 \cdot 4\text{H}_2\text{O}$ were mixed to obtain 2%, 3%, and 4% Mn^{2+} – Zn^{2+} solution, respectively. Also, 0.1 mM $\text{Na}_2\text{S} \cdot 9\text{H}_2\text{O}$ solution were prepared. Then, around 50 μL of these solutions were injected into the gels, in sequence. The gel was then sonicated for 5 min and left undisturbed for 24 hours at room temperature to grow QDs inside the gel.

Elemental analysis (%)

C 19.42, H 2.21, N 5.22.

For Cu:ZnS, 50 and 100 μL of 0.1 mM $\text{Cu}(\text{OAc})_2$ in 5 mL of 0.1 mM $\text{Zn}(\text{OAc})_2$ was taken to obtain 1% and 2% solution, respectively, and 50 μL of these solutions were injected into the gels, followed by addition of 50 μL of 0.1 mM $\text{Na}_2\text{S} \cdot 9\text{H}_2\text{O}$. The gels were then sonicated for 15 min and left undisturbed for 48 hours for the QDs to grow.

Elemental analysis (%)

C 18.47, H 1.54, N 4.64.

FT-IR (of both gel imbedded QDs) (KBr, cm^{-1})

3423 (br), 3031(br), 2784 (m), 2451 (w), 2360 (w), 1616 (vs), 1460 (s), 1375 (s), 1289 (w), 1146 (w), 1022 (m), 775 (m), 722 (w), 611 (br) (Fig. S5, ESI[†]).

Biological studies

Cell culture

Cell cultures were maintained at 37 °C under 5% CO_2 in Dulbecco's modified Eagle's medium, containing 10% fetal calf serum (Life Technologies, Rockville, MD, USA). The human breast cancer cells (MCF7) were obtained from the Developmental Therapeutics Program (NCI, NIH/USA).

Live-cell confocal microscopy

Live-cell imaging was carried out using a confocal laser-scanning microscope (Leica TCS SP8) with a UV-laser and 63 \times /1.4 NA oil objective equipped with a heated environmental chamber set to 37 °C with an optimal CO_2 facility. Briefly, MCF7 cells seeded on a cover glass bottom dish (Genetix, Biotech Asia Pvt. Ltd) were incubated with compounds Cu:ZnS and Mn:ZnS separately for 3 h. Nuclei were subsequently stained with Hoechst 33342 (Blue) (Sigma). This was followed by live cell confocal microscopy. Images were collected and processed using the Leica software and sized in Adobe Photoshop 7.0.

Cell survival assay

MCF7 cells (6×10^3) were seeded in 96-well plates (BD Biosciences, USA) and treated with compounds Cu:ZnS and Mn:ZnS at the indicated concentrations. After 72 h-treatment, cell survival was assessed by performing the 3-(4,5-dimethylthiazol-2-yl)-2,5-diphenyltetrazolium bromide (MTT) assay. Briefly, the cells were washed with 1 \times PBS and treated with MTT reagent (Sigma) for 3 h at 37 °C and the resulting formazan was dissolved in 100 μL of dimethyl sulfoxide. The plates were analyzed on Molecular Devices SpectraMax M2 Microplate Reader at 570 nm. The percent inhibition of viability for each concentration of the compounds was calculated with respect to the control. The Data are represented as mean values \pm s.e.m. for three independent experiments.

Results and discussion

The aim of this study was to develop an improved, greener method of synthesizing metallogel based QDs without external heating and most importantly, exploit an unprecedented “in-built” hostile gel environment containing solvents (DMF, MeOH) and a metallogel network that can nurture the QDs. When we tried to synthesize Al-MOF with isophthalic acid, we experienced an Al-isophthalate gel formation in the presence of the above-mentioned solvents. This observation, coupled with the fact that pyridine contains an aromatic nitrogen that has lower chances of co-ordinating with an Al^{3+} ion compared to carboxylic acid oxygen, lead us to believe that PDC, which contains both isophthalic and pyridine moieties in a similar relative spatial disposition, can be used for the dual purposes of gelation and a capping agent.²⁷ The trivalent Al ion, being a hard center, is expected to co-ordinate with carboxylate oxygen atoms,³⁰ thus leaving pyridine nitrogen free. In this study, we focused on the gel synthesized in a 1:1 molar ratio.

Nevertheless, the gelation between AlCl_3 and PDC can also occur in 2 : 1, 1 : 2, and 1 : 3 metal to ligand molar ratio. Since our study demands the insertion of various salts (such as $\text{Zn}(\text{OAc})_2$, $\text{Mn}(\text{OAc})_2$, $\text{Cu}(\text{OAc})_2$, and Na_2S), to prevent unnecessary reactions between the QD precursors with excess gel precursors, the 1 : 1 molar ratio was considered the best option for nanocrystal generation. Our literature survey revealed that in most cases, the nanocrystals were synthesized with excessive heating and in the presence of various organic substances that can cap the nanocrystals.⁴¹ However, the gel based technique is mostly a one pot synthesis route, which does not involve any of the abovementioned conditions.^{26,50} This way our synthetic procedure is greener than the abovementioned methods.

Basic characterization of the metallogel was carried out by UV-Vis, IR and Elemental analysis. The microscopic techniques such as scanning electron microscopy (SEM) and transmission electron microscopy (TEM) were carried out to determine the morphology of the metallogel. The micrographs from both the techniques reveal the presence of an extensive entangled intertwined network made by the self-assembly of nanofibers of infinite lengths and an average diameter of 100 nm. Formation of such a cross-linked network is highly relevant to the present study because of inherent microporous skeleton of the gels, which again can be attributed to Al-carboxylate coordination bond formation. Hardness of the gel was determined by rheological studies. The gel shows quite good stability against stress or sonication. Using this fact, we synthesized the QDs by first adding the precursors and then sonicating the gel to spread the precursors homogeneously all over the gel. The gel does not show any sol-gel transformation. Further corroboration comes from XPS data, showing the peak for $2p_{3/2}$ at around 75.6 eV and for 2s at 117.84 eV (Fig. S4, ESI†), corresponding to the peaks of Al^{3+} with slight deviation.²⁸ The as-formed metallogel shows excellent self-healing properties. This is an essential prerequisite for reintegrating the locally damaged gel network after injection and subsequent homogeneous dispersion of the QD precursor. For homogeneous dispersion of the precursor, the gel network needs to be porous.

The surface area of the metallogel was measured by preparing a xerogel and studying N_2 adsorption at 77 K with BET

(Brunauer–Emmett–Teller) analysis. The BET surface area was measured to be $40.687 \text{ m}^2 \text{ g}^{-1}$ and the Langmuir surface area was $58.858 \text{ m}^2 \text{ g}^{-1}$. The metallogel shows a reasonably high gas intake of 74 cc g^{-1} of N_2 with a typical type-II isotherm (Fig. 2). Most importantly, the gel matrix does indeed turn out to be nanoporous, with the pore diameters in tune with that of the nanoparticles of QDs. The average pore size is equal to 237.855 \AA or 23.785 nm , which makes our metallogel perfectly suitable to host *in situ* generated QDs of comparable diameters. Having confirmed the presence of the requisite pores inside the network, the precursors were then injected inside the metallogel to validate its utility as a medium for QD synthesis.

The FTIR data in this case shows the interaction between the metal and the gelator. IR data was recorded in the wave number range of $400\text{--}4000 \text{ cm}^{-1}$ for both nanoparticle based gels to determine the difference created because of the formation of nanocrystals, which gives a true insight into the QD-gel interaction. Two strong peaks at around $1616\text{--}1668$ and $1460\text{--}1498 \text{ cm}^{-1}$ can be assigned to the symmetric and asymmetric stretching frequency of the carboxylic group (COO^-) of PDC. The peak at around $700\text{--}600 \text{ cm}^{-1}$ denotes the metal-oxygen stretching. For nanoparticle based gels, there are two peaks at $775, 722 \text{ cm}^{-1}$, which can be assigned to metal-pyridine nitrogen stretching. Also, the peak at 1022 cm^{-1} may arise due to S-O-C stretching for the nanoparticle based gel. Apart from these peaks, there are not many differences seen between the peaks of the Al-PDC gel and the nanoparticle doped counterpart. The broad band at around $3500\text{--}3400 \text{ cm}^{-1}$ arises from O-H stretching from solvents. The peaks at around $2900\text{--}3100$ denote aromatic C-H stretching. The peak at $1380\text{--}1250 \text{ cm}^{-1}$ is ascribed to aromatic C=N stretching. The peaks at $1022, 775,$ and 722 cm^{-1} are the most important peaks, which represent the QD formation in the gel (Fig. S5, ESI†).

In this gel based approach we first synthesized the undoped ZnS QDs, but no special optical property was found. However, when the QDs were doped with paramagnetic metal salts, such as Mn and Cu complexes, the optical property enhanced considerably.^{35,39,40,49} Also, a considerable red shift in the luminescence exhibited by the gel was observed.

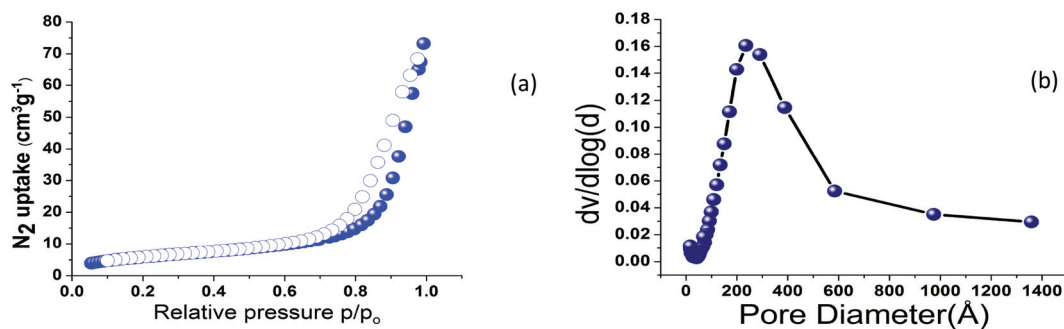


Fig. 2 BET data of the gel, (a) represents the type-II isotherm of Al-PDC gel where the sphere shows the adsorption and open circle shows the desorption curve and (b) represents the pore diameter distribution.

Subsequently, the doped metalgels were characterized using microscopic, diffraction and spectroscopic techniques. The formation of metal nanoparticles inside the doped metalgel was indeed confirmed by the microscopic techniques (TEM). In addition, compared to the highly entangled fibrillar network of Al-PDC gel, the appearance of nanoparticles for the doped samples corroborates the QDs formation (Fig. 3).

The diameter of the QDs is directly proportional to the amount of doping metal introduced into the gel system. A simple ZnS nanoparticle was found to be around 2–3 nm in diameter. Introducing 2–3% Mn does not change the diameter

abruptly, but as the amount rises to 4%, the diameters of the nanoparticles varied in the range of 2.5–4 nm. In case of the Cu doped gel, the 1% Cu gel has a nanocrystal diameter ranging from 5–8 nm. In 2% Cu, the diameter is in the range of 6–12 nm. The Cu:ZnS QDs are found to contain greater average diameter than the Mn:ZnS QDs. It can be seen that the amount of doping materials tunes the nanoparticle size. Moreover, selected area electron diffraction (SAED) (Fig. 3) performed on these nanoparticles revealed the individual particles to be crystalline in nature compared to the amorphous undoped Al-PDC gel.

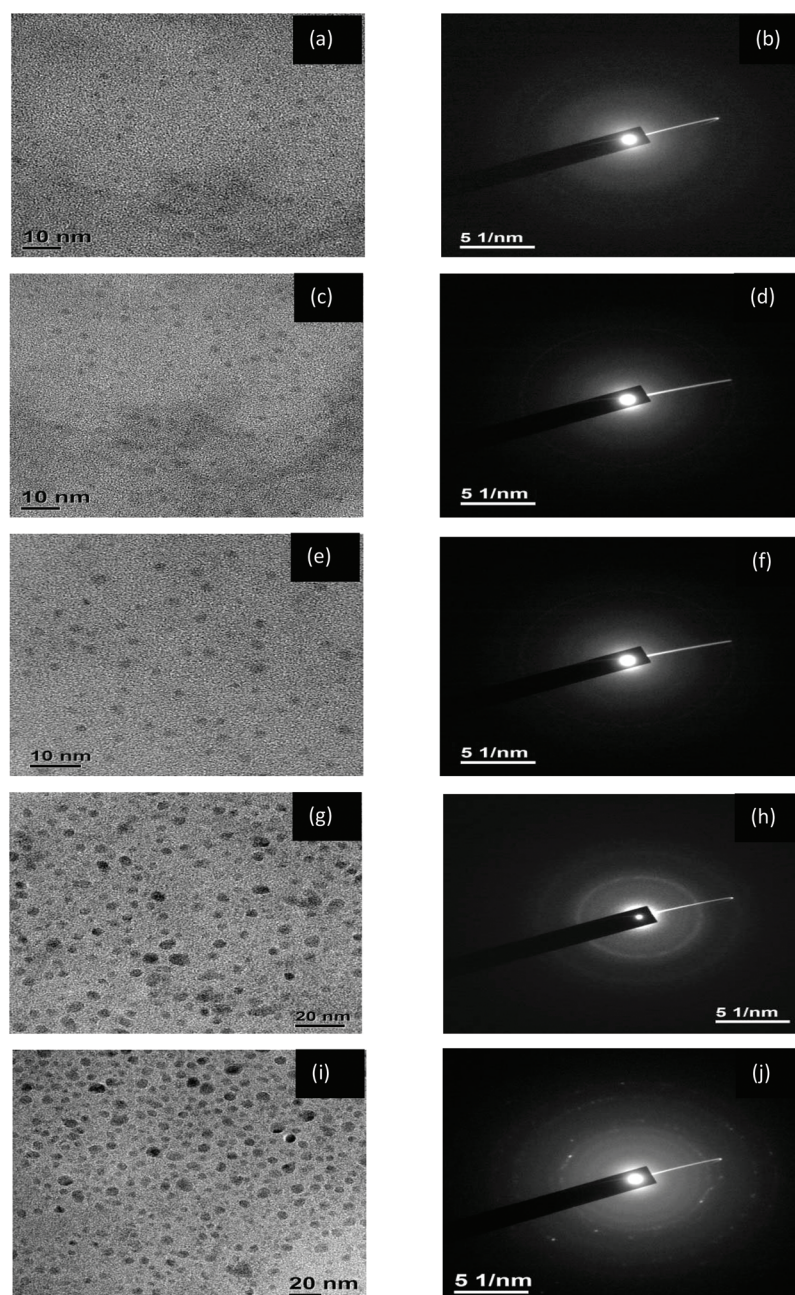


Fig. 3 TEM and SAED pictures of (a), (b) 2% Mn:ZnS, (c), (d) 3% Mn:ZnS, (e), (f) 4% Mn:ZnS, (g), (h) 1% Cu:ZnS, (i), (j) 2% Cu:ZnS respectively.

Incorporation of doping material from lower to higher concentrations result in the introduction of more diffraction patterns, proving the generation of higher crystallinity with QD size. Introduction of dopant-dependent micro-crystallinity is clearly evident from the powder XRD patterns. A comparative depiction of the diffraction patterns for doped and undoped Al-PDC gel places this in perspective (Fig. 4(c)). The PXRD of the Al-PDC xerogel reveals the amorphous nature of the material, with the absence of peaks. The overlay of PXRD patterns, recorded after addition of QD precursors, shows the emergence of some broad peaks with relatively higher intensity compared to the PXRD pattern of the bare Al-PDC xerogel. A literature survey shows that these peaks are corresponding to the (111), (220), (311) planes, which suggests a zinc blend structure for the nanocrystals.³¹ The nanocrystals contain low lattice parameters, which broadens the peaks of the PXRD. This clearly argues in favor of an increase in crystallinity in the gel medium, which in turn, can be attributed to the formation of nanocrystals of $\text{Cu}^{2+}:\text{ZnS}$ and $\text{Mn}^{2+}:\text{ZnS}$ QDs. Also, there are some small sharp peaks, which indicate the presence of bulk crystalline material formed during xerogel formation. These peaks may indicate the presence of impurities (such as ZnO, MnO, and CuO) formed due to the oxidation of precursors, the agglomeration of nanoparticles due to evaporation of solvent or the influence of gel hardening.³²

Furthermore, dynamic light scattering (DLS) was performed to get an accurate idea about the nanoparticle size.

The results are presented in two types of graphs: intensity vs. size and number vs. size. The intensity vs. size curve pro-

vides a comparative picture of gel and nanocrystal size (ESI, Fig. S6†). The size of the gel is much higher than that of the nanocrystals (around 1000 nm). In contrast, the number vs. size plot shows a sheer dominance of QD nanocrystals over the gel. The Mn:ZnS QDs have an average particle size of 2–6 nm with an average ζ -potential of 9.40. The Cu:ZnS QDs have an average particle size of 13–21 nm with an average ζ -potential of 16.5. Through DLS, the hydrodynamic diameter of the ZnS QDs were measured, so the particle size in this case was somewhat higher than that of the QD cores measured from the TEM images. The particle size of the nanocrystals determined by both TEM and DLS proves the fact that the gel can cap nanocrystals having diameters less than the gel's average pore size (<23 nm) (see Fig. 2 and 3).

The optical properties of QDs were characterized by photoluminescence (PL) and UV-Vis spectroscopy. The UV-Vis adsorption spectra of the free ligand and Al-PDC gel show a peak at around 290 nm. When Mn:ZnS (4%) precursors were incubated, there is a second short hump at around 362 nm and for Cu:ZnS (2%), it can be seen at around 425 nm. The UV-Vis spectra of other lower compositions gave an even less intense and shorter hump in the abovementioned wavelengths (Fig. 6(a) and (b)). Appearances of such peaks in the UV-visible spectra are a hallmark of the QD nanoparticles and are consistent with the literature.^{29,36,38} Also, the red shift in the absorbance spectra from Mn:ZnS to Cu:ZnS indicates the growth of the QDs. This theory is also supported by the TEM and DLS results.

Luminescence from nanocrystals provides a very convenient and useful way to monitor their formation when the samples

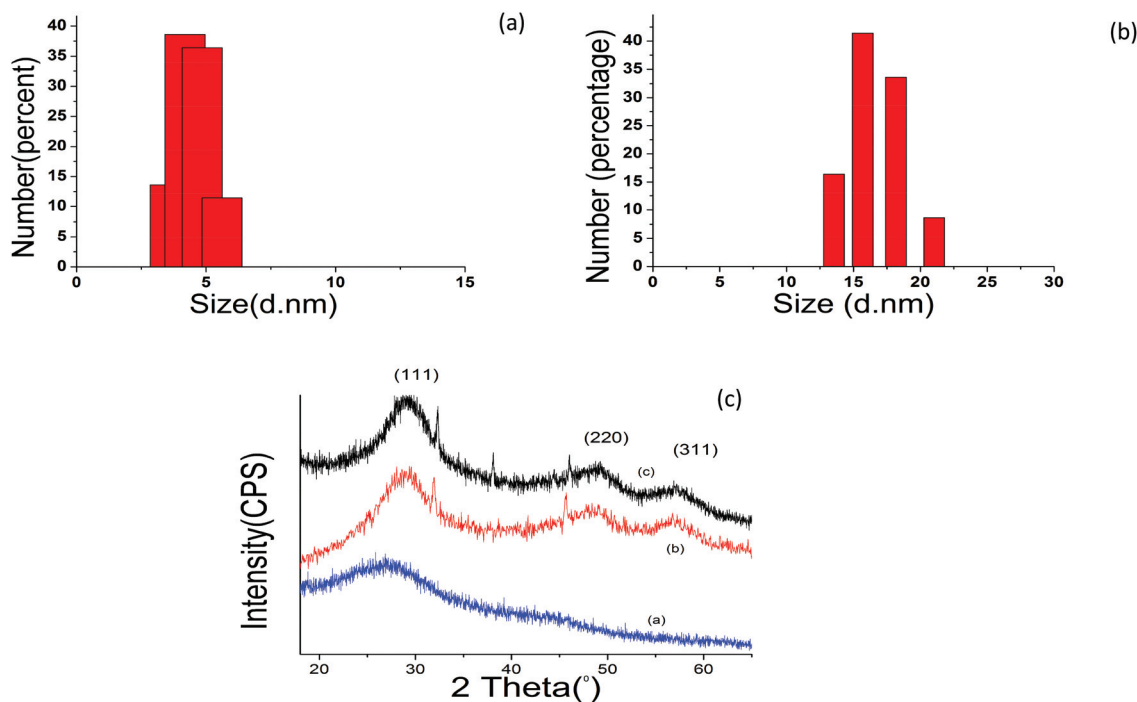


Fig. 4 (a) Represents DLS number vs. size of Mn:ZnS, (b) represents DLS number vs. size of Cu:ZnS (c) comparative depiction of PXRD curves of (a) Al-PDC xerogel, (b) Cu:ZnS containing xerogel (c) Mn:ZnS containing xerogel.

are subjected to UV light ($\lambda = 365$ nm) irradiation. Herein, the percentage of doping metal, such as Mn^{2+} and Cu^{2+} , has a crucial role in determining the luminescence of the gel. ZnS containing gel with 2% and 3% Mn^{2+} gives a light blue colour, while 4% Mn^{2+} gives yellow luminescence. The difference between 2% and 3% Mn^{2+} doped gel is nominal to the naked eye. The 1% Cu^{2+} doping gives a bluish green colour, while 2% Cu^{2+} in the gel containing ZnS shows an intense green luminescence. The Al-PDC gel shows a deep violet colour when irradiated with UV light. No significant change in colour was observed when only the ZnS precursors were added. The change in colour of the doped gel signifies the entrance of the energy levels of the doped metals in the ZnS energy levels. As the amount of doping metal increases, the size of the QDs also increases, which is supported by the TEM results and luminescence nature of the gel.

Further inspection was performed by recording the photoluminescence (PL) spectra of the gels. The UV-Vis humps are seen to have very low intensity, which corroborates the fact that the amount of precursors added into the gel and the amount of QDs formed are very less in quantity. The PL spectrum of the Al-PDC gel shows a wide emission peak at about 359 nm, with an excitation wavelength of 260 nm. Addition of Mn^{2+} in different percentages (2–4%) shows a variety of peaks in PL spectrum. The PL spectrum of 2% Mn^{2+} :ZnS shows a peak at around 479 nm, while that of 3% Mn^{2+} :ZnS shows two peaks situated at 479 nm and 586 nm, with a higher intensity than the previous gel. The 4% Mn^{2+} :ZnS has the dominant peak at 586 nm, but the peak at 479 has almost vanished. For Cu^{2+} doping, both the 1% and 2% doped gel shows two peaks at around 492 nm and 532 nm. The peaks of 2% Mn^{2+} :ZnS show higher intensity with the peak at 532 nm, rising up to be the dominant peak (Fig. 6).

The corresponding schematic emission mechanism, along with the fluorescence energy levels for ZnS QDs, is presented in Fig. 5. The energy gap between conduction and valence band is 3.9 eV.²⁹ However, an additional lower energy state near the conduction band appears because of the defects of the S^{2-} ion in the ZnS. As a result, upon UV light excitation, the transition does not take place directly from conduction to valence bands. Instead, the entire transition involves a two-step process. Initially, there is a transition from the conduction band to the lower energy S^{2-} defect band and subsequently, another transition from this ZnS defect band to the valence band. The latter transition, which appeared at 410 nm in the PL spectrum, can be attributed to the intense deep blue luminescence of the ZnS doped gel materials.

Moreover, Mn and Cu dopants function as an emissive trap, modifying the PL of ZnS QDs. Significant changes occurred in the energy level landscape for Cu^{2+} :ZnS doped and Mn^{2+} :ZnS doped QDs with the introduction of ${}^4\text{T}_1$, ${}^6\text{A}_1$ energy levels³⁴ for high spin Mn^{2+} and for Cu^{2+} ${}^2\text{T}_2$ and ${}^2\text{E}$ energy levels within the band gap. Both of these energy states of doped metals lie between the valence and conduction band as well as in the S^{2-} defect level of the host. As a result, the electron shows ISC (internal system crossing) from the higher energy ZnS lattice to

the triplet states (${}^4\text{T}_1$, ${}^2\text{T}_2$) of transition metals prior to the transition to its ground states (${}^6\text{A}_1$, ${}^2\text{E}$).^{31,37} With a low concentration of both Mn^{2+} (2%) and Cu^{2+} (1%), the presence of bluish luminescence indicates the fact that the transition from ${}^4\text{T}_1$ to the ZnS valence band for Mn^{2+} and ${}^2\text{T}_2$ to the ZnS valence band for Cu^{2+} dominate, which are situated at 479 nm and 490 nm, respectively. However, with an increase in concentration, the energy levels of both of these materials' ground states and the triplet states of doping material enter into the ZnS band gap as trap states. Thus, for higher concentrations of Mn^{2+} and Cu^{2+} , the ${}^4\text{T}_1$ to ${}^6\text{A}_1$ and ${}^2\text{T}_2$ to ${}^2\text{E}$ electron transitions dominate. The emitted wavelength for the transition from the Mn^{2+} excited state (${}^4\text{T}_1$) to the Mn^{2+} ground state (${}^6\text{A}_1$) in the case of Mn^{2+} :ZnS doped QDs appear with emission maxima at 586 nm. Although the PL for the 3% gel shows the presence of both of the emission peaks, ${}^4\text{T}_1$ to ${}^6\text{A}_1$ at 586 nm and ${}^4\text{T}_1$ to ZnS valence band at 479 nm, the 479 nm peak has higher intensity. Moreover, the 4% Mn:ZnS shows ${}^4\text{T}_1$ to ${}^6\text{A}_1$ peak with highest peak intensity, but the ${}^4\text{T}_1$ to ZnS valence band peak almost vanishes. Interestingly, for Cu^{2+} :ZnS doped QDs, the 1% gel shows two peaks with almost same intensity at around 490 nm and 532 nm, while the 2% gel has the ${}^2\text{T}_2$ to ${}^2\text{E}$ transition at 532 nm peak with the higher intensity. Hence, a greener luminescence can be seen from the gel. The absorption and emission wavelength maximum is shown in Table 1.

The fluorescence quantum yield (QY) was calculated using a reference standard method. Here we used Quinine Sulphate in 0.5 M H_2SO_4 for Mn:ZnS and Rhodamine 6G in ethanol for Cu:ZnS as reference solutions. Then, QY was calculated according to the equation below.

$$\phi_s = \phi_R \times \frac{P_s}{P_R} \times \frac{A_R}{A_s} \times \left[\frac{\eta_s}{\eta_R} \right]^2$$

Here, ϕ_s , P_s , A_s and η_s are the photoluminescence QY, integral photoluminescence intensity, absorbance at the excitation wavelength and refractive index of the solvent in which the gel based QD samples are taken (DMF), respectively. Also ϕ_R , P_R , A_R and η_R are the photoluminescence QY, integral photoluminescence intensity, absorbance value at excitation wavelength and refractive index of solvent in which the quinine sulphate is taken, respectively. The calculated QY for gel based Mn:ZnS and Cu:ZnS is 0.2571 (or 25.71%) and 0.2867 (or 28.67%), respectively. According to the literature,^{31,33} the QY determined in this study is almost comparable to the QY of QDs synthesized by the hydrothermal or colloidal methods.

The rheological data (Fig. 7) shows a significant change in viscosity between the Al-PDC gel and the nanoparticle doped gels. Synthesis of QDs in the gel changes the gel stability to an enormous extent. Usually for gels, or in this case metallogels, the dynamic storage modulus or elastic modulus (G') has greater magnitude than the loss modulus or viscosity modulus (G''). In this case, the measurement of the dynamic stress sweep was performed in a range of 0–1000 Pa. The resultant curve shows that the elastic modulus has an almost 10 times greater value than the loss modulus, which effectively rep-

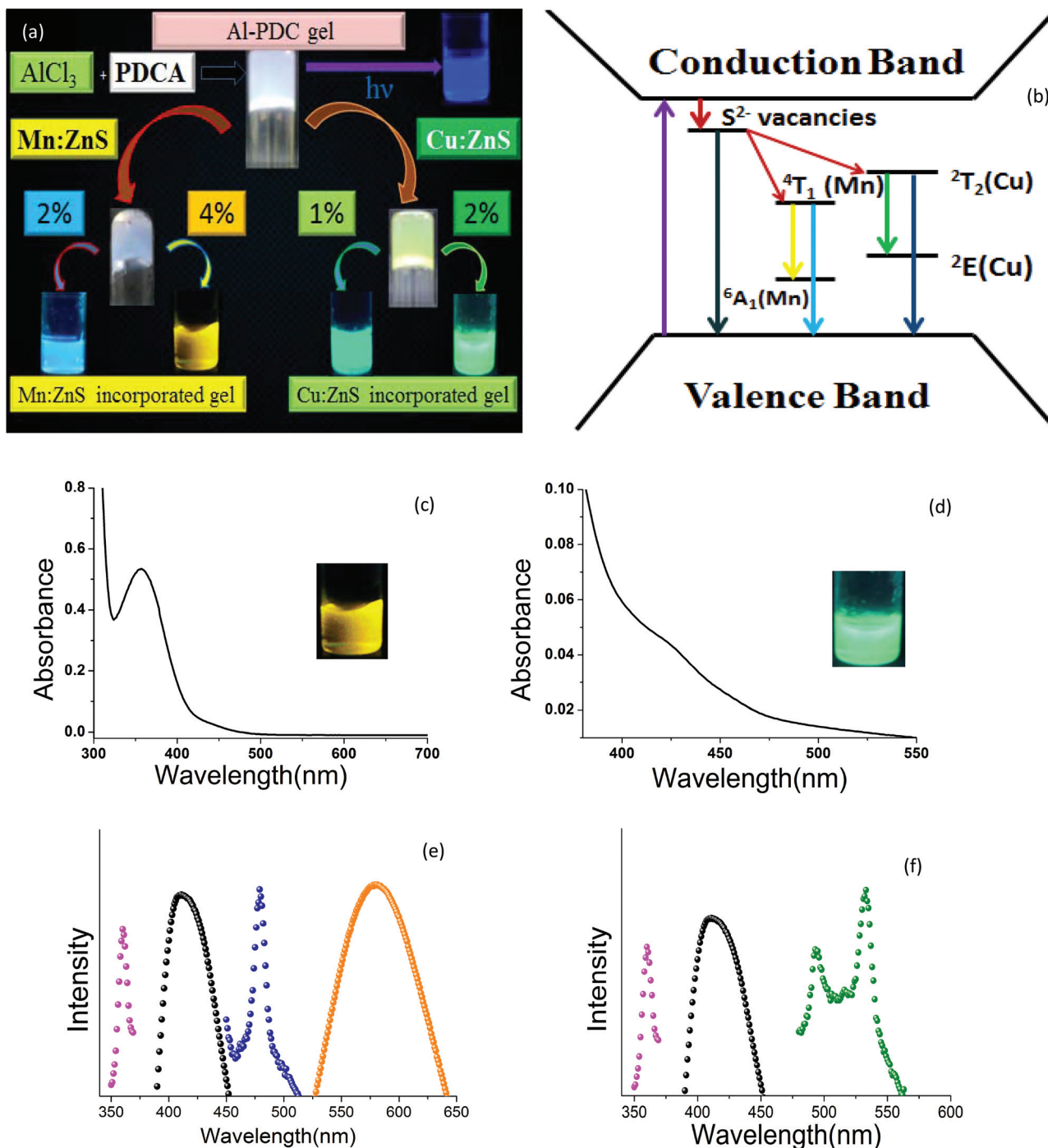


Fig. 5 (a) Schematic representation of the synthesis of Al-PDC based QDs, (b) schematic representation of the electronic transition occurring in the doped ZnS QDs, (c), (d) UV-Vis spectra of Mn:ZnS and Cu:ZnS, (e), (f) overall PL spectra of Mn:ZnS and Cu:ZnS incubated Al-PDC gel respectively.

resents the gelatinous condition of the compound. The yield stress was determined to be 138 Pa for the undoped gel, around 572 Pa for the 4% Mn:ZnS and around 576 Pa for 2% Cu:ZnS. The yield stress for the QD based gel has been found to be higher than that for the undoped gel, which indicates that the gel becomes harder after the incubation of the QD precursors.

Significant change was also observed in their thermal stability and is evident from their TGA plots. The TGA plot of the Al-PDC xerogel shows an initial weight loss of 22% up to 100 °C, corresponding to the loss of solvent, after which the compound was stable up to 220 °C. The presence of doped nanoparticles introduces extra stability in the network. This is manifested in the TGA, since doped gels show an appreciable

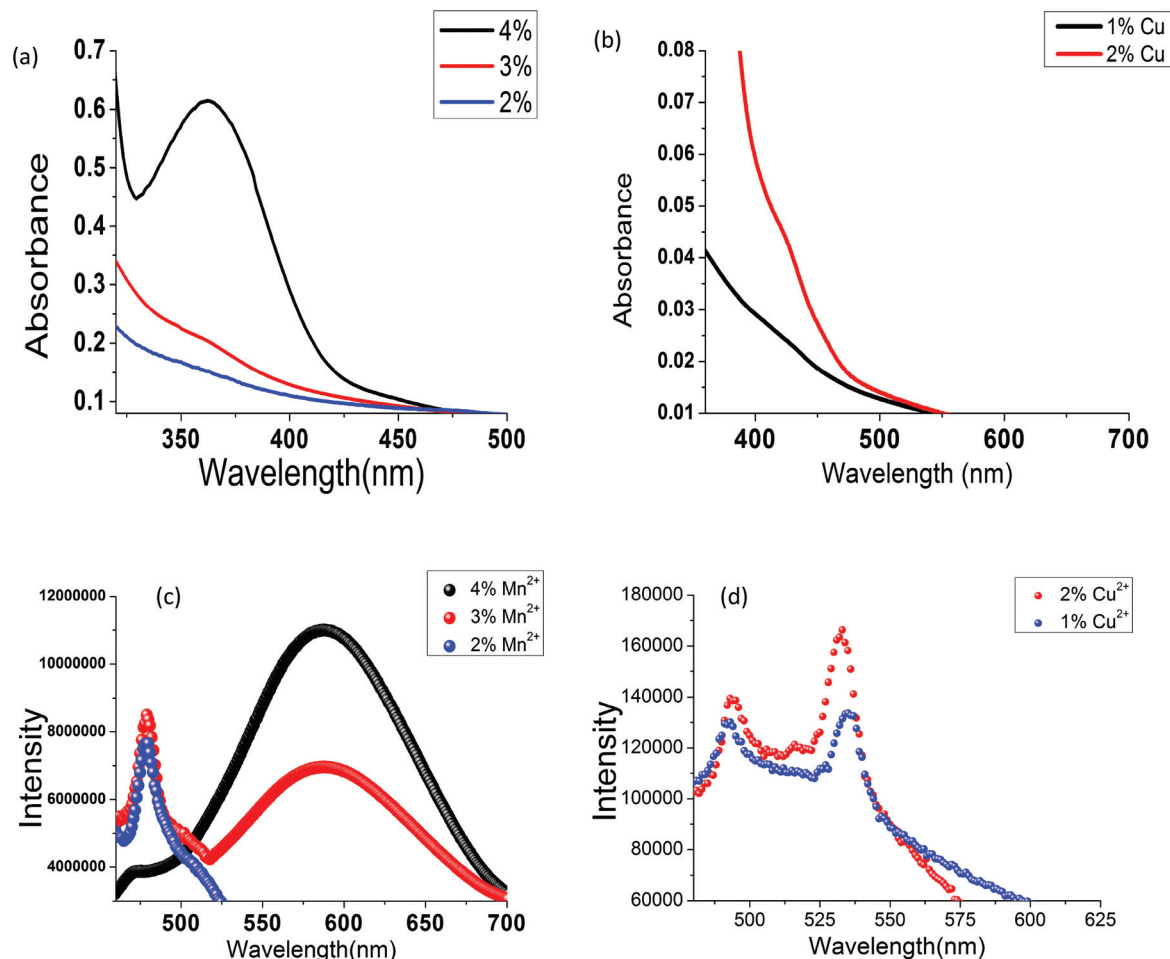


Fig. 6 Comparative depiction of (a), (b) UV-VIS curves of Mn:ZnS and Cu:ZnS, (c), (d) photoluminescence curves of Mn:ZnS and Cu:ZnS respectively in different concentrations.

mass loss of 30% until ~ 400 °C (Fig. 7(c)). The graphs also show that the leftover mass of the QD based gel is more than that of the undoped xerogel due to the presence of ZnO, MnO, and CuO. This extra stability in the doped QDs could be attributed to the presence of the pyridine group ($-C_5H_3N$), which coordinates to the metal nanoparticles while forming the hedge around them. This secondary co-ordination strengthens the gel network and as a result, induces extra thermal and mechanical stability in the doped materials.

The stability of the QDs was checked in different pH solutions. The solutions were made up in the range of pH 4–11, in which the 2 mg of xerogel containing QDs (4% Mn:ZnS, 2% Cu:ZnS) were added. Next, for each of the solutions, photoluminescence data was collected to obtain a comparative depiction of the stability. From the data, it can be seen that at around pH 8–9, the Mn:ZnS QD gives the most intense luminescence curve. Moreover, for the Cu:ZnS QD two types of phenomenon can be seen: a steady increase in the intensity of the peak at 492 nm with pH and the decrease in the intensity of the peak at 532 nm at higher pH (pH-11). However, the intensity of the peak at 532 nm rises until pH 10 (ESI†). In the

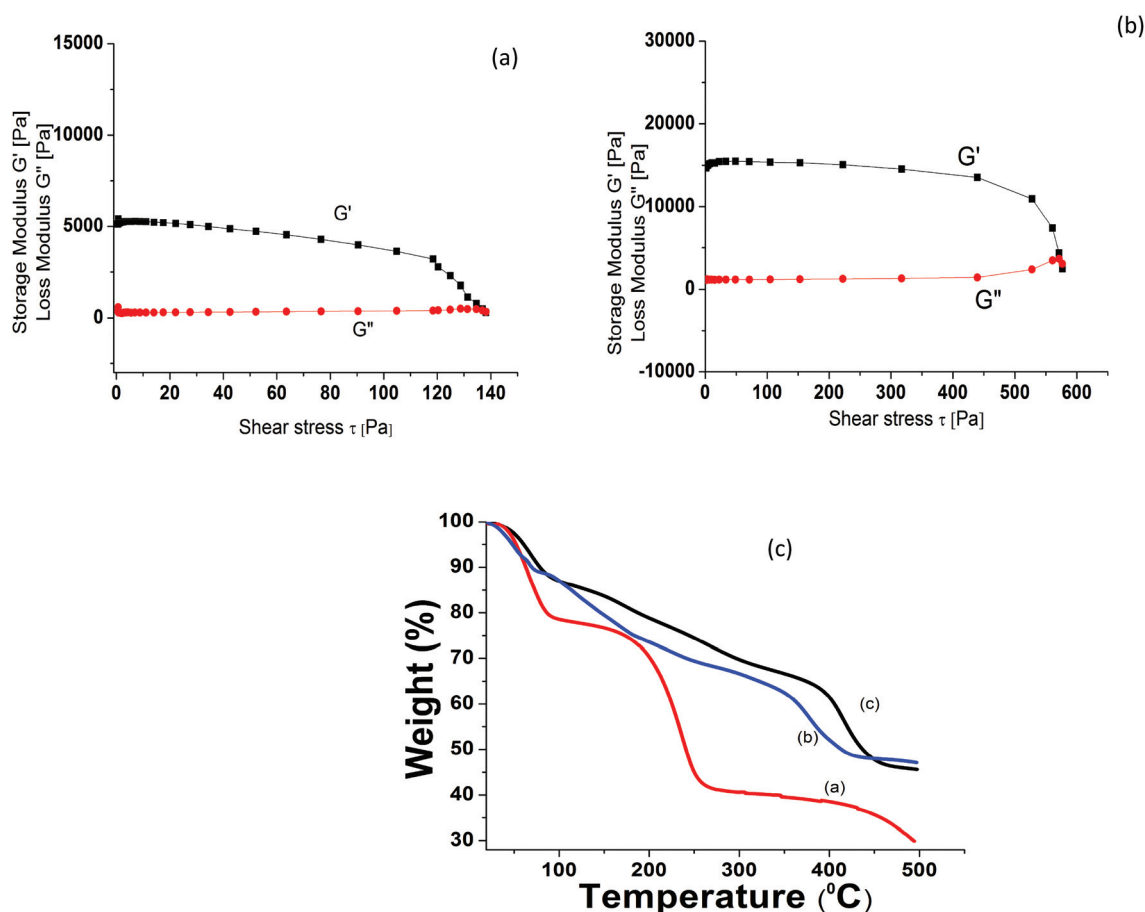
acidic solutions, the intensity of the QDs were found to be the lowest. This could be reasoned as follows: in the acidic solution, the pyridine substituent of the ligands, which successfully capped the QDs, become protonated and thus, the pyridine N-QD bond becomes weaker and consequently decrease the luminescence. By increasing the pH, the pyridine becomes deprotonated and luminescence becomes more intense. Moreover, at higher pH, the intensity of the PL decreases. The reason could be that in an excessively basic solution, the QDs start to dissociate. From this data, it can be said that the QDs are stable around pH 8–10. This also shows the fact that the xerogel successfully retains the QDs.

Biological results and discussion

QDs being stable fluorescent nanomaterials can easily be used for labeling live cells. In fact, ZnS QDs have been used for bio-labeling before.^{42,43} However, to our knowledge, for the first time, gel based ZnS QDs have been used for labeling cancer cells. The samples were prepared by first synthesizing the

Table 1 The absorption, excitation, and emission wavelength of gel and gel based quantum dots with various compositions of QD precursor

Gels	Composition	Absorbance (nm)	Excitation (nm)	Emission (nm)
Al-PDC gel	Gel precursors in 1 : 1 ratio of metal and ligand	270	260	359
Mn:ZnS in Al-PDC gel	2% Mn ²⁺	362	330	410
	3% Mn ²⁺	362	360	410, 479
	4% Mn ²⁺	362	330	410
			360	410, 479, 586
Cu:ZnS in Al-PDC gel	1% Cu ²⁺	425	330	410
	2% Cu ²⁺	425	360	410, 492, 532
			330	410
			360	410, 492, 532

**Fig. 7** Rheological curve of (a) undoped gel, (b) QD based gel, (c) thermal gravimetric analysis curves of (a) xerogel, (b) Mn:ZnS doped gel, (c) Cu:ZnS doped gel.

xerogel. First, we prepared the xerogel of 1 wt% gel, which contained around 10 μM QDs. Then, it was dispersed into 1 mL DMSO. Through sonication, the pores were cleansed with DMSO, while the nanoparticles come out of the gel network to the solvent. After 10–15 minutes the gel network sediments below the solution. At this point, about 100–500 μL solution was drawn from each sample for labelling and other tests. Fig. 8A shows that both the Cu:ZnS and Mn:ZnS nanoparticles were cell permeable when incubated with human breast

cancer cells (MCF7) for 4 h and analysed under live cell confocal microscopy.^{45,46} Our data also indicate that the fluorescent nanomaterials were delivered into the cytoplasm and also incorporated into the nucleus, as indicated by the colocalization with the nuclear marker Hoechst 33342 (blue channel, left panel) in the MCF7 cancer cells. The enlarged images in Fig. 8A demonstrate that the nanomaterial CuZnS forms distinct punctuate staining in the nucleus, which is plausibly localised in the nucleolus. Under similar conditions,

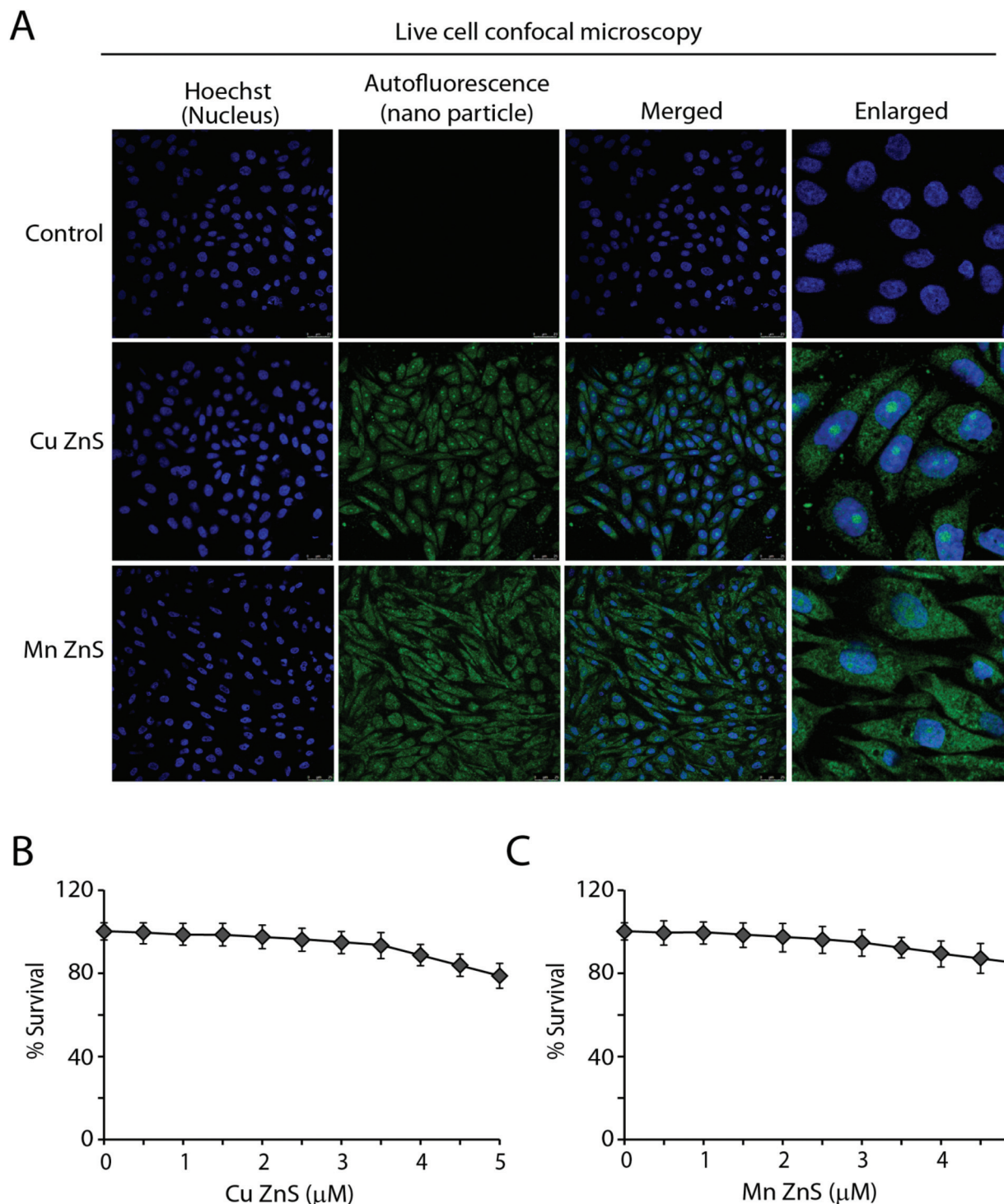


Fig. 8 Live cell laser confocal microscopy showing delivery of compounds Cu:ZnS (green) and Mn:ZnS (green) in the nucleus and the cytoplasm of human breast cancer cells (MCF7). (A) Representative confocal images showing localization of Cu:ZnS (5 μ M) and Mn:ZnS (5 μ M) in human breast adenocarcinoma (MCF7) cells as monitored by intrinsic fluorescence of the drugs (green channel, middle panel) and co-stained with Hoechst 33342 (blue channel, left panel) to detect the nucleus. Right panel shows the merged and enlarged images. (B and C) Cell survival assay with compounds Cu:ZnS and Mn:ZnS reveals no apparent cytotoxicity. (B) Survival curves of MCF7 cells treated with Cu:ZnS for 72 h. Cell viability was determined by MTT assays. Error bars represent standard deviation ($n \geq 3$). (C) Survival curves of MCF7 cells treated with Mn:ZnS for 72 h. Cell viability was determined by MTT assays. Error bars represent standard deviation ($n \geq 3$).

both the nanomaterials (Cu:ZnS and Mn:ZnS) were relatively less toxic in the MCF breast cancer cells (Fig. 8B). Collectively, our data indicate that both the nanomaterials (Cu:ZnS and Mn:ZnS) could be effectively used for labelling live cancer cells.

Conclusions

In summary, we developed a novel metallogel based approach to synthesize QDs. To the best of our knowledge, this is the first example of a metallogel based synthesis of doped ZnS QDs. In this study, we have proved the fact that the size of the nano particles depends on the average pore size of the gel and becomes tunable with the amount of doping material. The novelty of our system lies in the fact that we have successfully established that the presence of nano-materials does strengthen the gel mechanically and increase the thermal stability. Furthermore, the metallogel based QDs can also be treated as a potential agent for labeling cancer cells. Both the QDs do not show any cytotoxicity, so the cells did not deteriorate during the labeling experiment. More such metallogels are being synthesized in our lab, which could open up new avenues in QD research by not only acting as a two-in-one system, but also as a general synthetic method.

Conflicts of interest

There is no conflict of interest.

Acknowledgements

RM gratefully acknowledges Science and Engineering research Board (SERB) (Project No. SB/EMEQ-301/2014) India, for financial assistance. The BBD team is supported by Wellcome Trust/DBT India Alliance Intermediate Fellowship (Award IA/I/13/1/500888). S. B. and S. P. C. thanks University Grants Commission (UGC), India for a Junior Research Fellowship. A. G. is a recipient of CSIR-NET Senior Research Fellowship, India. S. B. also acknowledges Mr Suman Pal and Mr Saptarsi Mondal of IACS Kolkata and Mr Subrata Mondal of IIT Guwahati for various help and support.







References

- C. D. Jones and J. W. Steed, *Chem. Soc. Rev.*, 2016, **45**, 6546–6596.
- L. A. Estroff and A. D. Hamilton, *Chem. Rev.*, 2004, **104**, 1201–1218.
- J. W. Steed, *Chem. Commun.*, 2011, **47**, 1379–1383.
- P. Sutar and T. K. Maji, *Chem. Commun.*, 2016, **52**, 8055–8074.
- N. M. Sangeetha and U. Maitra, *Chem. Soc. Rev.*, 2005, **34**, 821–836.
- J. Zhou, X. W. Du, Y. Gao, J. F. Shi and B. Xu, *J. Am. Chem. Soc.*, 2014, **136**, 2970–2973.
- A. Harada, R. Kobayashi, Y. Takashima, A. Hashidzume and H. Yamaguchi, *Nat. Chem.*, 2011, **3**, 34–37.
- X. Yu, L. Chen, M. Zhang and T. Yi, *Chem. Soc. Rev.*, 2014, **43**, 5346–5371.
- R. Schneider, C. Wolpert, H. Guilloteau, L. Balan, J. Lambert and C. Merlin, *Nanotechnology*, 2009, **20**, 225101.
- S. C. Erwin, L. Zu, M. I. Haftel, A. L. Efros, T. A. Kennedy and D. J. Norris, *Nature*, 2005, **436**, 91–94.
- D. J. Norris, A. L. Efros and S. C. Erwin, *Science*, 2008, **319**, 1776–1779.
- N. S. Karan, D. D. Sarma, R. M. Kadam and N. Pradhan, *J. Phys. Chem. Lett.*, 2010, **1**, 2863–2866.
- P. D. Wadhavane, R. E. Galian, M. A. Izquierdo, J. A. Sigalat, F. Galindo, L. Schmidt, M. I. Burguete, J. P. Prieto and S. V. Luis, *J. Am. Chem. Soc.*, 2012, **134**, 20554–20563.
- S. Chatterjee and U. Maitra, *Phys. Chem. Chem. Phys.*, 2017, **19**, 17726–17734.
- G. Palui, J. Nanda, S. Ray and A. Banerjee, *Chem. – Eur. J.*, 2009, **15**, 6902–6909.
- X. H. Yan, Y. Cui, Q. He, K. W. Wang and J. B. Li, *Chem. Mater.*, 2008, **20**, 1522–1526.
- V. H. Grassian, *J. Phys. Chem. C*, 2008, **112**, 18303–18313.
- S. Sarkar, D. Banerjee, U. K. Ghorai, N. S. Das and K. K. Chattopadhyay, *J. Lumin.*, 2016, **178**, 314–323.
- Q. Wei and S. L. James, *Chem. Commun.*, 2005, **12**, 1555–1556.
- J. Huang, L. He, J. Zhang, L. Chen and C. Y. Su, *J. Mol. Catal. A: Chem.*, 2010, **317**, 97–103.
- S. Sarkar, S. Dutta, P. Baire and T. Pal, *Langmuir*, 2014, **30**, 7833–7841.
- G. Yu, X. Yan, C. Han and F. Huang, *Chem. Soc. Rev.*, 2013, **42**, 6697–6722.
- P. Dastidar, *Chem. Soc. Rev.*, 2008, **37**, 2699–2715.
- M. O. M. Piepenbrock, G. O. Lloyd, N. Clarke and J. W. Steed, *Chem. Rev.*, 2010, **110**, 1960–2004.
- X. Quek, R. Pestman, R. A. Van Santen and E. J. M. Hensen, *ChemCatChem*, 2013, **5**, 3148–3155.
- X. He, Li Gao and N. Ma, *Sci. Rep.*, 2013, **3**, 2825.
- M. Singhal, J. K. Sharma, H. C. Jeon, T. W. Kang and S. Kumar, *J. Mater. Sci.: Mater. Electron.*, 2016, **27**, 3003–3010.
- F. Cordier and E. Ollivier, *Surf. Interface Anal.*, 1995, **23**, 601–608.
- S. Ummartyotin, N. Bunnak, J. Juntaro, M. Sain and H. Manuspiya, *Solid State Sci.*, 2012, **14**, 299–304.
- A. Mahmood, W. Xia, N. Mahmood, Q. Wang and R. Zou, *Sci. Rep.*, 2015, **5**, 10556.
- J. Choi, S. Yoon, F. S. Kim and N. Kim, *J. Alloys Compd.*, 2016, **617**, 360–365.
- D. J. Abdallah, S. A. Sirchio and R. G. Weiss, *Langmuir*, 2000, **16**, 7558–7561.
- T. Gan, N. Zhao, G. Yin, M. Tu, J. Liu and W. Liu, *New J. Chem.*, 2017, **41**, 13425–13434.

- 34 Y. M. Miao, Q. Yang, J. Z. Lv and G. Q. Yan, *New J. Chem.*, 2017, **41**, 14882–14889.
- 35 W. Zhang, Y. Li, H. Zhang, X. Zhou and X. Zhong, *Inorg. Chem.*, 2011, **50**, 10432–10438.
- 36 B. B. Srivastava, S. Jana, N. S. Karan, S. Paria, N. R. Jana, D. D. Sarma and N. Pradhan, *J. Phys. Chem. Lett.*, 2010, **1**, 1454–1458.
- 37 R. N. Bhargava, D. Gallagher, X. Hong and A. Nurmikko, *Phys. Rev. Lett.*, 1994, **72**, 416–419.
- 38 B. B. Srivastava, S. Jana and N. Pradhan, *J. Am. Chem. Soc.*, 2011, **133**, 1007–1015.
- 39 J. Zheng, W. Ji, X. Wang, M. Ikezawa, P. Jing, X. Liu, H. Li, J. Zhao and Y. Masumoto, *J. Phys. Chem. C*, 2010, **114**, 15331–15336.
- 40 V. A. Vlaskin, N. Janssen, J. van Rijssel, R. Beaulac and D. R. Gamelin, *Nano Lett.*, 2010, **10**, 3670–3674.
- 41 Z. Deng, L. Tong, M. Flores, Su Lin, J. X. Cheng, H. Yan and Y. Liu, *J. Am. Chem. Soc.*, 2011, **133**, 5389–5396.
- 42 N. Yin, L. Liu, P. Li and S. Zhao, *Luminescence*, 2018, 1–6, DOI: 10.1002/bio.3456.
- 43 H. S. Raghuram, S. Pradeep, S. Dash, R. Chowdhury and S. Mazumder, *Bull. Mater. Sci.*, 2016, **39**, 405–413.
- 44 S. Chatterjee, B. Kuppan and U. Maitra, *Dalton Trans.*, 2018, **47**, 2522–2530.
- 45 S. K. Das, I. Rehman, A. Ghosh, S. Sengupta, P. Majumdar, B. Jana and B. B. Das, *Nucleic Acids Res.*, 2016, **44**, 8363–8375.
- 46 S. K. Das, A. Ghosh, S. P. Chowdhuri, N. Halder, I. Rehman, S. Sengupta, K. C. Sahoo, H. Rath and B. B. Das, *J. Med. Chem.*, 2018, **61**, 804–817.
- 47 J. L. Yu, J. Su, J. Zhang, X. T. Wei and A. L. Guo, *RSC Adv.*, 2017, **7**, 17819–17823.
- 48 J. Q. Zhuang, X. D. Zhang, G. Wang, D. M. Li, W. S. Yang and T. J. Li, *J. Mater. Chem.*, 2003, **13**, 1853–1857.
- 49 J. T. Zhu, S. L. Mei, W. Yang, G. L. Zhang, Q. H. Chen, W. L. Zhang and R. Q. Guo, *J. Colloid Interface Sci.*, 2017, **506**, 27–35.
- 50 S. Saha, G. Das, J. Thote and R. Banerjee, *J. Am. Chem. Soc.*, 2014, **136**, 14845–14851.

Cite this: *Dalton Trans.*, 2021, **50**, 3593

Lanthanide clusters of phenanthroline containing a pyridine–pyrazole based ligand: magnetism and cell imaging†

Avik De, ^a Sukhen Bala,^b Sayan Saha,^a Krishna Sundar Das,^a Sohel Akhtar, ^a Amit Adhikary, ^a Arijit Ghosh,^c Guo-Zhang Huang, ^b Srijita Paul Chowdhuri,^c Benu Brata Das,^c Ming-Liang Tong ^b and Raju Mondal ^{*a}

In this contribution, we report the synthesis, characterization and luminescence–magnetic properties of Ln-clusters (Ln = Gd³⁺, Eu³⁺ and Tb³⁺) using a new pyridine–pyrazole functionalized ligand fitted with a chromophoric phenanthroline backbone. The unorthodox N-rich ligand forms isostructural trinuclear lanthanide complexes with a topology that closely resembles two interdigitating hairpins. The clusters crystallize in chiral space groups and also exhibit chirality for bulk samples, which were further confirmed using solid state CD spectra. Magnetic studies on the complexes reveal their interesting features while the Gd cluster shows a significant cryogenic magnetic cooling behaviour with a moderately high magnetic entropy change of $-23.42 \text{ J kg}^{-1} \text{ K}^{-1}$ at 7 T and 2 K. On the other hand, Eu and Tb complexes exhibit interesting fluorescence properties. The compounds were subsequently used as fluorescent probes for the imaging of human breast adenocarcinoma (MCF7) cells. Live cell confocal microscopy images show that the complexes penetrate beyond the usual cytoplasm region and can be useful in imaging the nucleus region of MCF7 cells.

Received 3rd December 2020,
Accepted 4th February 2021

DOI: 10.1039/d0dt04122j

rsc.li/dalton

Introduction

There is practically no substitution for lanthanide (Ln) based functional materials in sight for generating sophisticated high-end appliances.^{1–5} Lanthanide ions can simultaneously act as magnetic moment carriers, intrinsic Lewis acidic sites and photoluminescent centres.^{6–13} Owing to their unique mutually inclusive magnetic, catalytic and optical features, Ln based materials have naturally attained an indispensable position in our modern society.^{14–21} Their presence encompasses numerous applications in a wide range of fields including cutting-edge defense technologies, high-tech computer or mobile hardware, hybrid vehicles, wind turbines, optical display devices, and life-saving biomedical applications such as bio-

sensing, bioimaging and scanning.^{22–36} Interestingly, while at a first glance the underlying materials properties may look widely different from each other but at the core there exists unity amid diversity. All these properties primarily arise from the encrypted chemical features of either a specific lanthanide ion/cluster or a particular functional group of the organic ligand through a metal–ligand coordination mode.

There has been persistent research into the development of multifunctional materials through cumulating various properties of lanthanides or organic functionalities in a single system.^{37–44} The idea works on the utilization of the pre-acquired inorganic chemistry knowledge of a particular Ln ion/cluster, a particular organic functional group or metal–ligand coordination mode by grafting it to a functional material for multipurpose use.^{45–49} Clearly, the optimization of the system by choosing a suitable Ln centre or modulating the organic part of the ligands or imparting a specific metal–ligand environment holds the key to success.^{50–54} One such popular target is luminescent–magnetic materials, resulting from the culmination of two distinctly different yet Ln-specific properties: luminescence and magnetism.^{55–60}

Among the lanthanide-magnetism topics, an important aspect would be magnetic refrigeration based on the magneto-caloric effect (MCE).^{61–63} The Gd³⁺ ion, with its large spin-only magnetic moment ($S = 7/2$), weak superexchange interactions

^aSchool of Chemical Sciences, Indian Association for the Cultivation of Science, 2A & 2B, Raja S. C. Mullick Road, Jadavpur, Kolkata 700032, India.
E-mail: icrm@iacs.res.in

^bKey Laboratory of Bioinorganic and Synthetic Chemistry of Ministry of Education, School of Chemistry, Sun Yat-Sen University, Guangzhou 510275, P. R. China

^cLaboratory of Molecular Biology, School of Biological Sciences, Indian Association for the Cultivation of Science, 2A & 2B, Raja S. C. Mullick Road, Jadavpur, Kolkata 700032, India

† Electronic supplementary information (ESI) available. CCDC 2047785–2047787. For ESI and crystallographic data in CIF or other electronic format see DOI: 10.1039/d0dt04122j

and quenched orbital momentum driven reversible change in temperature with changing magnetic field, is considered as the most promising metal ion for ultralow cryogenic technology.^{64–66} Indeed, the majority of the complexes reported for MCE studies are composed of Gd^{3+} ions.^{67–71}

The optical features of Ln are however completely different from those of other metals. Because of the origin of the parity-forbidden f-f transition, the energy absorption of the Ln ion is low which results in very weak luminescence.⁷² However, the desired luminescence effect from Ln-complexes can be extracted using the so-called process “luminescence sensitization” or the “antenna effect”, where a highly absorbing chromophoric part attached to the ligand plays the pivotal role.^{73–80} The three-step processes essentially use ligand chromophores for light absorption followed by transferring the energy to the lanthanide ion which subsequently emits the light in the form of luminescence with all its advantageous characteristic features, while bypassing the shortcomings such as a low quantum yield of individual Ln ions. Another interesting aspect of sensitized luminescence is the precise emission with a specific colour.^{81,82} For example, irrespective of the excitation energy, Eu^{3+} and Tb^{3+} always fluoresce from the resonance levels 5D_0 ($17\,250\text{ cm}^{-1}$) and 5D_4 ($20\,430\text{ cm}^{-1}$), respectively.^{83,84} Such unique luminescence behaviour has enabled the use of Ln-complexes as useful probes for cellular sensing and imaging.^{85–92} Of course, to be an effective probe for sensing internalization into cells is an important issue. This is exactly where the Ln-complexes of low nuclearity with nanoscale dimensions have shown great promise for a number of biomedical applications.^{93–95}

Designing of a ligand is another important aspect of magnetism and luminescence from a lanthanide cluster.^{96–98} Both the properties are extremely sensitive to even tiny distortions of the local coordination geometry of the individual Ln centres as well as their ligand mediated assembly and the final structural topology.^{99–101} In the context of luminescent–magnetic material design, ligand design should aim at including coordi-

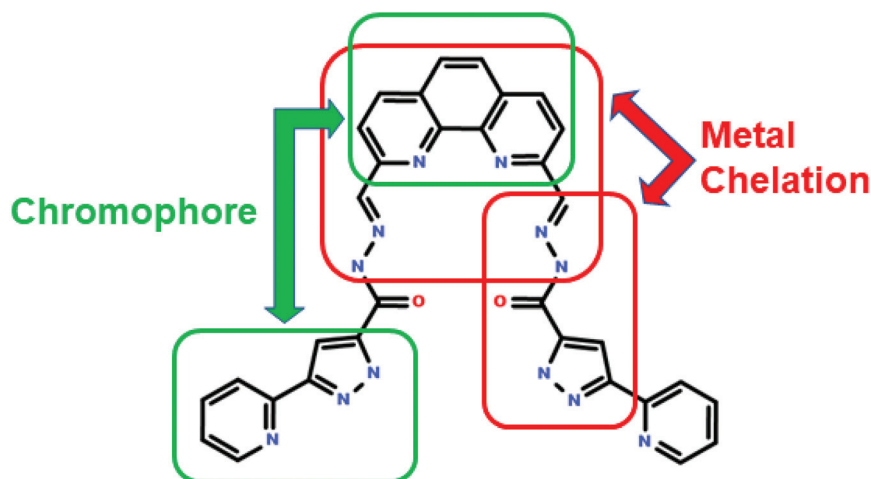
nating functional groups that provide the all-important coordination geometry along with the bridging modes between paramagnetic Ln centres and a grafted organic chromophore.^{102–106} Previous results from our group show that pyridine–pyrazole based ligands are highly effective at forming cages and clusters with both transition metals and lanthanides.^{107–110} The ligand systems are non-conventionally fitted with soft N-rich functional groups but are highly effective at generating Ln-based cages and clusters with various sizes, shapes and nuclearity. Most of these clusters exhibited the potential of good magnetic materials but showed weak fluorescence properties due to the absence of effective chromophores. Naturally, a robust strategy would be to modify the ligand system with the introduction of a chromophoric group, while keeping the design fundamentals of magnetic materials intact.

Herein, we report three luminescent-magnetic Ln-clusters ($Ln = Gd^{3+}$, Eu^{3+} and Tb^{3+}) using a new pyridine–pyrazole functionalized ligand fitted with a chromophoric phenanthroline backbone, 3-(2-pyridyl)-*N*-[(*E*)-[9-[(*E*)-[3-(2-pyridyl)-1*H*-pyrazole-5-carbonyl]hydrazono]methyl]-1,10-phenanthrolin-2-yl]methyleneamino]-1*H*-pyrazole-5-carboxamide (**Phen**). Interestingly, all three complexes crystallize with a chiral space group, and they were spectroscopically further studied using solid state circular dichroism (CD). The magnetic properties of the Tb-complex and Gd-complex were investigated which reveals an interesting magnetocaloric effect for the latter. The fluorescence properties of the Eu and Tb clusters were highly encouraging and further used for the imaging of human breast adenocarcinoma (MCF7) cells with no apparent cytotoxicity.

Results and discussions

Ligand design and synthesis

In a nutshell, the current ligand designing principle demands a fusion of two compatible functional moieties capable of



Scheme 1 Structure of the ligand (**Phen**).

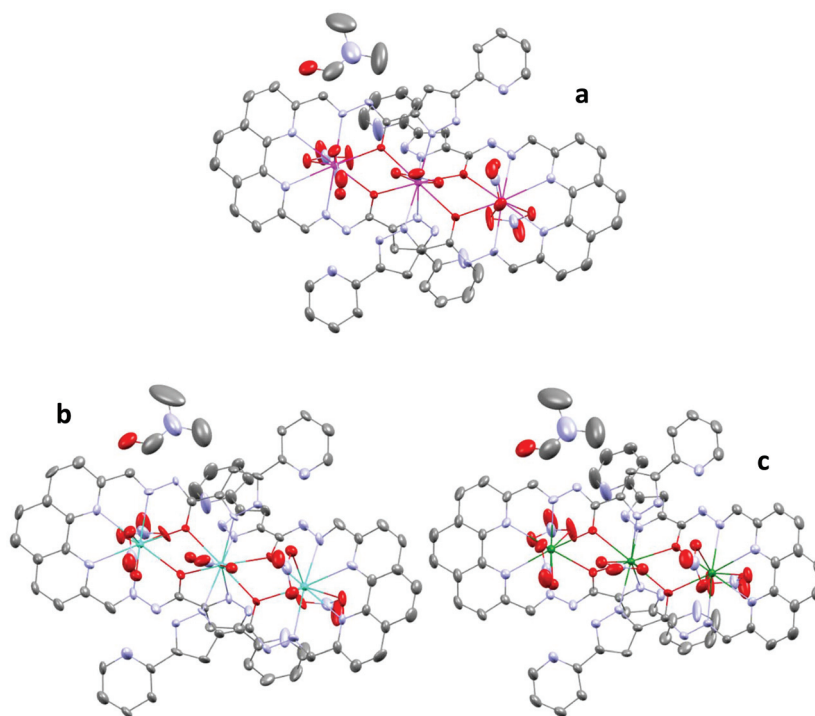


Fig. 1 Crystal structures (ellipsoid with 50% probability) of (a) **Phen-Gd**, (b) **Phen-Tb**, and (c) **Phen-Eu** (grey: C, red: O, cyan: N, magenta: Gd, light green: Tb, and green: Eu).

inducing mutually inclusive magnetic and luminescence features simultaneously in the system. Our previous ligand systems, fitted with a prototype pyridyl-pyrazolyl carbohydrazone functionality containing multiple coordinating sites, have been extremely beneficial for bridging the Ln centres and thereby facilitating the ferromagnetic or antiferromagnetic interactions. In the present work, we have modified the ligand by introducing a 1,10-phenanthroline unit as a dual-purpose chelating backbone-cum-chromophore (Scheme 1). The 1,10-phenanthroline moiety with an extended delocalized rigid structure will not only enhance the fluorescence intensity by an antenna effect but also contain a chelating unit which will ultimately help bring additional coordinating sites near the Ln ions.

The ligand (**Phen**) can be prepared in good yield following a typical Schiff base condensation reaction between 3-(pyridin-2-yl)-1*H*-pyrazole-5-carbohydrazone and 1,10-phenanthroline-2,9-dicarbaldehyde (Scheme S1[†]). All the lanthanide complexes with a general formula of $[\text{Ln}^{\text{III}}_3(\text{Phen})_2(\text{NO}_3)_5]$ (**Phen-Ln**, where Ln = Gd³⁺, Tb³⁺ and Eu³⁺) were synthesized in excellent crystalline form simply by refluxing **Phen** with the nitrate salts of the individual lanthanides. Reasonably good diffraction quality single crystals of the complexes were obtained after a few days from the undisturbed cooled solution and structural studies were carried out using X-ray single-crystal diffraction data. All the complexes were also routinely characterized by FT-IR spectroscopy, elemental analysis and mass spectroscopy.

Descriptions of molecular structures

The **Phen-Ln** complexes are isostructural in nature (Fig. 1). Therefore, only the **Phen-Gd** complex is used for the structural description in this work. The molecular structures along with the coordination environment of the individual lanthanide ions, crystallographic table and selected bond lengths and angles are separately reported in the ESI.[†]

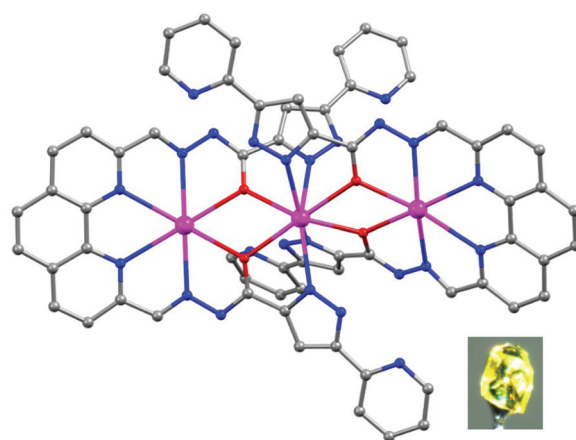


Fig. 2 Crystal structure of **Phen-Gd** (nitrate, solvent molecules and hydrogen atoms are omitted for clarity); the inset shows the picture of the crystal of **Phen-Gd**. All the three complexes show the same type of crystal & crystal structure (magenta: Gd, red: O, blue: N, and grey: C).

The single crystal X-ray structure of **Phen-Gd** reveals that it crystallizes in the orthorhombic $Fdd2$ space group (Table S6†). The asymmetric unit of the structure consists of half of the $[\text{Gd}^{\text{III}}_3(\text{Phen})_2(\text{NO}_3)_5]$ unit and a DMF molecule as the solvent of crystallization. The ligand (**Phen**) adopts a two-prong pendent orientation where the phenanthroline part acts as the pendent and the pyridine-pyrazole part constitutes each prong (Fig. 2). The ligand adopts some interesting hairpin like orientation wherein two inner walls house the array of the coordinating sites of the pyridyl-pyrazolyl units facing each other. Subsequently, two **Phen** molecules undergo interdigitation engulfing three Gd atoms, two of them (**Gd2**) being buried deep inside the trough regions and with the help of four

μ -amide oxygen atoms bridging the third one (**Gd1**), which resides in the intersecting region. The Gd ions are arranged in a linear fashion in the resultant trinuclear unit with an intermetallic distance of 4.184(5) Å. Finally, all five nitrate ions adopt a bidentate chelating mode. One such nitrate group binds to the middle Gd atom, whereas two nitrate groups bind to each of the other two Gd atoms from top and bottom (Fig. 3a and b).

For the trinuclear core, comprising the Gd–O bond lengths, Gd–O–Gd angles, and Gd...Gd separations, the geometric parameters with Gd–O bonds vary from 2.402(5) to 2.511(6) Å, the Gd–O–Gd angles span from 116.08(17)° to 118.79(19)°, and the Gd...Gd separation is 4.184(5) Å (Fig. 3c). The peripheral Gd–N

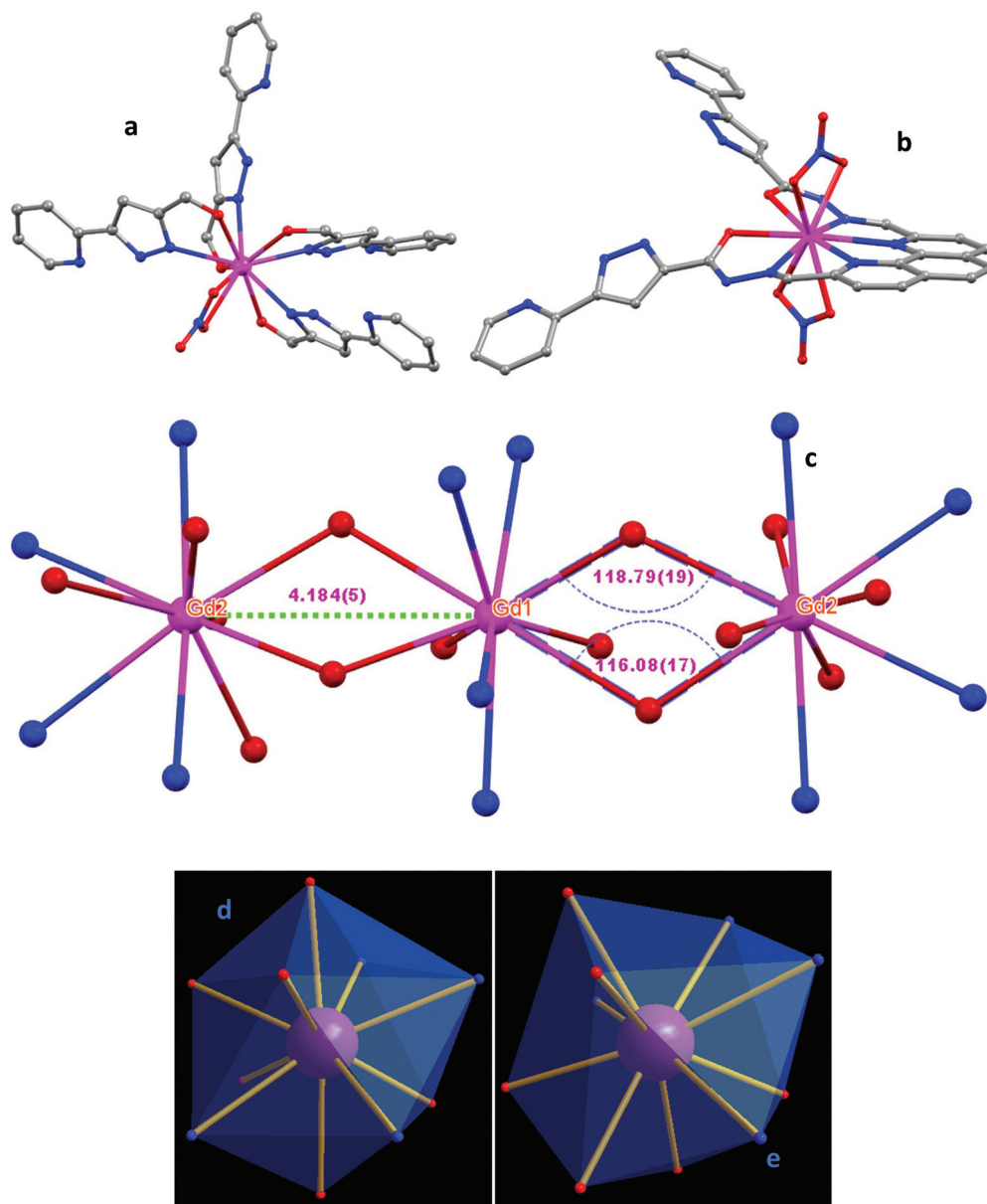


Fig. 3 Coordination environments around the (a) Gd1 and (b) Gd2 centers, (c) trinuclear Gd3 core with coordination motifs; coordination geometry observed around the metal centres in **Phen-Gd**, (d) bicapped square antiprism (for Gd1) and (e) tetradecahedron (for Gd2).

bond lengths are found to lie in the range from 2.550(6) to 2.650(6) Å and are in agreement with the literature. The selective bond lengths and angles are listed in Table S3.†

For **Phen-Tb**, the Tb–O bond lengths vary from 2.384(9) to 2.493(12) Å, the Tb–N bond lengths are found to lie in a range from 2.525(10) to 2.630(11) Å and the Tb–O–Tb angles span from 116.5(3)° to 119.4(4)° (Table S4†). For **Phen-Eu** (Fig. S16†), the Eu–O bond lengths vary from 2.413(5) to 2.527(6) Å, the Eu–N bond lengths are found to lie in a range from 2.557(6) to 2.653(6) Å and the Eu–O–Eu angles span from 115.75(17)° to 118.62(19)° (Table S5†). The value of the distance between two adjacent lanthanide units (Eu–Eu is 4.189(5) Å; Tb–Tb is 4.182(5) Å) is also close to the value for Gd.

SHAPE analysis

The crystal structures exhibit two distinctly different local coordination environments around the Ln centers. While both the metal centres adopt the GdN₄O₆ coordination motif their coordinating sites and local geometries are different. From the continuous shape measure (CShM) values^{111,112} for the Gd1 & Gd2 centers of **Phen-Gd**, we found that the central Gd ion (Gd1) has a geometry closer to a bicapped square antiprism (JBCSAPR-10). On the other hand, the terminal Gd ions (Gd2) adopt a nearly tetradecahedral (2:6:2) (TD-10) geometry (Fig. 3d and e). The list of potential coordination polyhedra of the 10-coordinate metal centers and Continuous Shape Measure (CShM) values for each Ln ion are given in Table S7.† The CShM value of Gd1 for the bicapped square antiprism is 3.45375, which is the lowest among all the possible geometries of a 10-coordinate metal center. Similarly, the CShM value of Gd2 for the tetradecahedron is 1.50029, which is the lowest among all the possible geometries. The Gd1 and Gd2 centers of the complex show D_{4d} and C_{2v} symmetry, respectively. The bicapped square antiprism has 16 triangular faces and 24 edges, whereas the tetradecahedron possesses 22 edges and layers in a ratio of 2:6:2. This geometry has 12 triangular and 2 square faces. For both the centers the geometries are slightly distorted.

As all the three **Phen-Ln** complexes are isostructural in nature, the geometries of the metal centers of the other two complexes are also similar to that of **Phen-Gd**. For **Phen-Tb**, the central Tb (Tb1) and terminal Tb ions (Tb2) favor the bicapped square antiprism geometry (the CShM value is 3.45684) and tetradecahedral (2:6:2) (TD-10) geometry (the CShM value is 1.45976), respectively (Fig. S14†).

Similarly, for **Phen-Eu** the central Eu (Eu1) and terminal Eu ions (Eu2) favor the bicapped square antiprism geometry (the CShM value is 3.52737) and tetradecahedral (2:6:2) (TD-10) geometry (the CShM value is 1.42902), respectively (Fig. S15†).

Circular dichroism (CD) spectra

The crystal structures or more specifically the space groups of the **Phen-Ln** crystals invoke an interesting topic of inorganic chemistry, chirality. Although often overlooked, chirality remains one of the most important properties of traditional inorganic complexes.^{113–116} The popular technique for the syn-

thesis of a chiral complex molecule is the use of a chiral ligand as a precursor. Recent reports show that spontaneous resolution can also be a key technique to impart chirality in a metal complex or cluster.^{117–121} The complexes of the present study crystallize in a chiral *Fdd2* space group with corroborating Flack parameter values of 0.082(9) and 0.144(16) for **Phen-Eu** and **Phen-Tb**, respectively. This prompts us to confirm the presence of chirality in bulk samples with the help of solid-state circular dichroism (CD) spectroscopy using diffused reflectance techniques on KBr pellets of the crystalline powder samples. As illustrated in Fig. 4, the signal obtained in the CD spectra for **Phen-Eu** is better pronounced than that of **Phen-Tb**. The signals for **Phen-Eu** appear at 240, 397, and 295 nm, whereas for **Phen-Tb** the signals appear at 247, 402, 515, 299, and 471 nm. CD measurements were performed with different batches of the samples. In all the cases, more or less similar spectra were obtained, which confirms the enantiomeric purity of the samples.

Magnetic studies

Considering the fact that the primary aim of this study was to generate magnetic–luminescent Ln complexes, we carried out magnetic studies using the resultant cluster complexes. Accordingly, the solid state direct current magnetic susceptibility data of the polycrystalline samples of **Phen-Gd** and **Phen-Tb** were collected in a temperature range of 2–300 K under a magnetic field of 0.1 T and are shown in the $\chi_m T$ (χ_m = molar magnetic susceptibility) vs. T (temperature) plot. The room temperature (300 K) $\chi_m T$ values of **Phen-Gd** and **Phen-Tb** are 23.39 and 35.26 cm³ K mol⁻¹, respectively, which are very close to the calculated values for the three isolated Gd³⁺ and Tb³⁺ ions. The observed values of the three non-interacting Gd³⁺ (⁸S_{7/2}, $g = 2$) and Tb³⁺ ions (⁷F₆, $g = 3/2$) are 23.62 and 35.43 cm³ K mol⁻¹, respectively. With decreasing temperature, the $\chi_m T$ value for **Phen-Gd** decreases slowly up to 30 K (22.79 cm³ K mol⁻¹) and below this temperature the $\chi_m T$ value increases rapidly at low temperature which is due to the ferro-

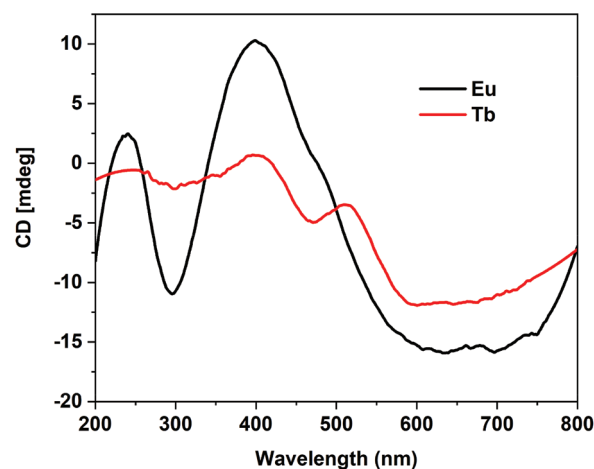


Fig. 4 CD spectra of **Phen-Eu** and **Phen-Tb**.

magnetic interaction between the neighboring Gd^{3+} ions (Fig. 5a) and reaches the value of 25.49 at 2 K. But for **Phen-Tb**, with decreasing temperature, the $\chi_{\text{m}}T$ value decreases slowly and below 50 K the $\chi_{\text{m}}T$ value rapidly decreases which is due to the antiferromagnetic interaction between the neighboring Tb^{3+} ions (Fig. 5c).

Moreover, the data were fitted using the Curie-Weiss equation, $\chi_{\text{M}} = C/(T - \theta)$, where C is the Curie constant and θ is the Curie-Weiss constant (Fig. 5d and e). The fitting of the $1/\chi_{\text{M}}$ vs. T (T more than 100 K) plot gives us the value of $C =$

23.64 $\text{cm}^3 \text{mol}^{-1} \text{K}$ and $\theta = -3.47 \text{K}$ and this C value is close to the room temperature $\chi_{\text{M}}T$ value of 23.39 $\text{cm}^3 \text{mol}^{-1} \text{K}$. The negative θ value further confirms the antiferromagnetic interactions between the adjacent metal centers at higher temperature, whereas at low temperature **Phen-Gd** showed ferromagnetic interactions among the neighboring Gd centers. But in the case of **Phen-Tb**, fitting of the Curie-Weiss equation gives us $C = 15.28 \text{cm}^3 \text{mol}^{-1} \text{K}$ and $\theta = -0.431 \text{K}$ and this negative and low θ value suggests weak antiferromagnetic interactions between adjacent Tb centers.

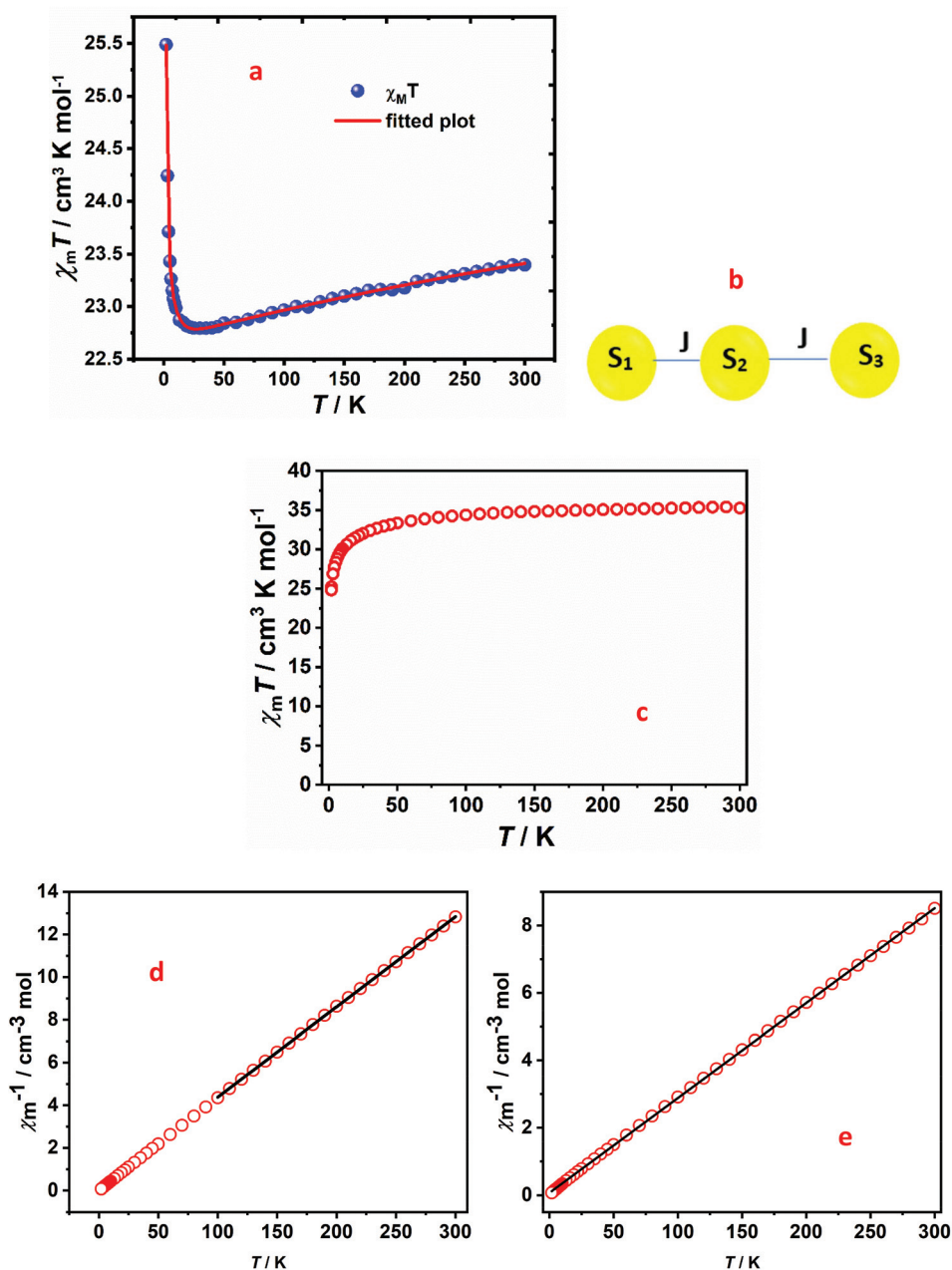


Fig. 5 $\chi_{\text{M}}T$ vs. T plot for (a) Phen-Gd, (b) model used for the fitting of the plot, $\chi_{\text{M}}T$ vs. T plot for (c) Phen-Tb, and $1/\chi_{\text{M}}$ vs. T plot for (d) Phen-Gd and (e) Phen-Tb (straight line for fitting using the Curie-Weiss equation).

For further confirmation of the magneto-structural correlation, the data were fitted (Fig. 5a and b) using the Hamiltonian given below:

$$H = -J(S_1S_2 + S_2S_3) - g\mu_B H \sum_{i=1}^3 S_i$$

where H is the Hamiltonian, J signifies the magnetic coupling constant and S signifies the spin of the metal center. From the best fitting data, we calculated $J = +3.82(2) \text{ cm}^{-1}$ and $g = 2.0$. The low positive value of J represents the weak ferromagnetic interaction among the neighbouring Gd centres.

Gadolinium based coordination compounds are one of the key compounds that are used as molecular magnetic refriger-

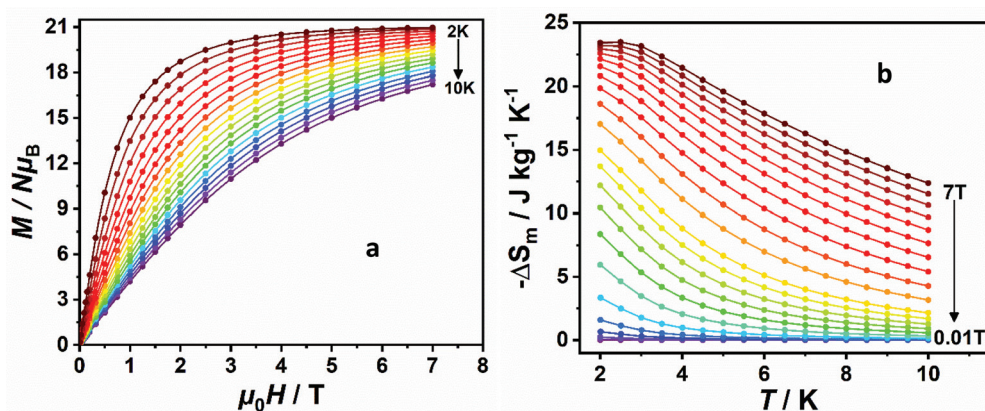


Fig. 6 (a) Field dependent isothermal magnetization and (b) temperature dependencies (2 to 10 K) of the magnetic entropy change ($-\Delta S_m$) for Phen-Gd as obtained from the magnetization data.

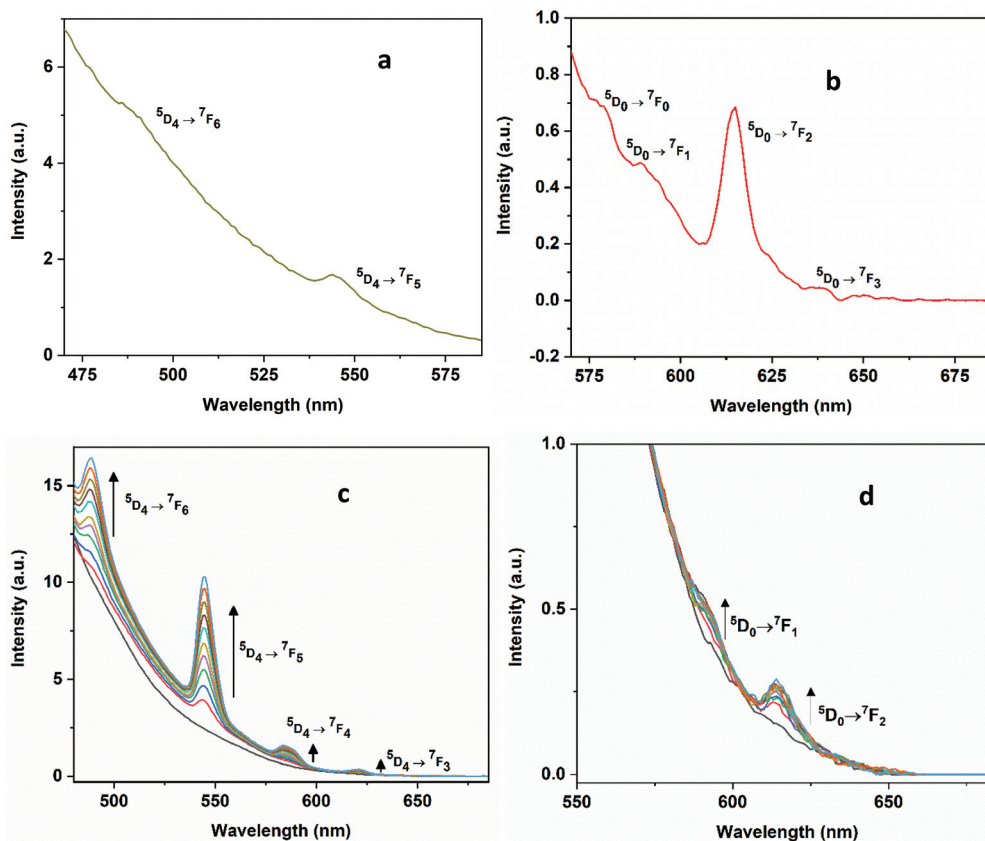


Fig. 7 Fluorescence spectra of (a) Phen-Tb and (b) Phen-Eu, and fluorescence titration spectra for (c) Tb and (d) Eu (the excitation wavelength is 350 nm for every case).

ants and exhibit the magnetocaloric effect (MCE) because of their marginal magnetic anisotropy and large spin ($S = 7/2$). In addition to that, because of the effective shielding of the 4f orbitals of Gd^{III} , the metal-metal magnetic exchange interactions are very weak, which can also increase the MCE value. The magnetic entropy change (ΔS_m) is a vital parameter which reveals the magnitude of the MCE. Considering the abovementioned fact, we have explored our **Phen-Gd** compound as a molecular magnetic refrigerant which exhibits the magnetocaloric effect.

The isothermal field-dependent magnetization data of **Phen-Gd** were obtained and at a higher magnetic field, the magnetization value tends to saturate. At a 7 T magnetic field and 2 K temperature the magnetization value reaches $20.96 N\mu_B$ which is close to the saturation value of $21 N\mu_B$ for the three isolated Gd^{3+} ions ($g = 2$) (Fig. 6a). From the magnetization data the magnetic entropy change values are calculated using the Maxwell relationship:

$$\Delta S_m = \int \left[\frac{\delta M(T, H)}{\delta T} \right]_H dH$$

The obtained ΔS_m values at different temperatures and magnetic fields were plotted. The values of ΔS_m increase with an

increase in the magnetic field and a decrease in temperature. The maximum value of the entropy change ($-\Delta S_m$) is $23.42 J kg^{-1} K^{-1}$ at 7 T and 2 K (Fig. 6b) which is comparable with those of some reported Gd^{III} complexes.^{122–136} The theoretical entropy change value is calculated from the equation:

$$\begin{aligned} -\Delta S_m &= nR \ln(2S + 1) \\ &= 51.865 J mol^{-1} K^{-1} \\ &= 24.22 J kg^{-1} K^{-1} \end{aligned}$$

the value is slightly higher than the experimental value as there is a weak anti-ferromagnetic interaction present among the nearest Gd^{3+} centers. This result suggests that our **Phen-Gd** compound can act as a promising molecular magnetic refrigerant in low temperature applications.

Photoluminescence properties

The magnetic properties of **Phen-Lns** are highly encouraging and naturally prompt us to explore our second target feature, luminescence. Accordingly, the optical properties of the Tb and Eu clusters are characterized by photoluminescence spec-

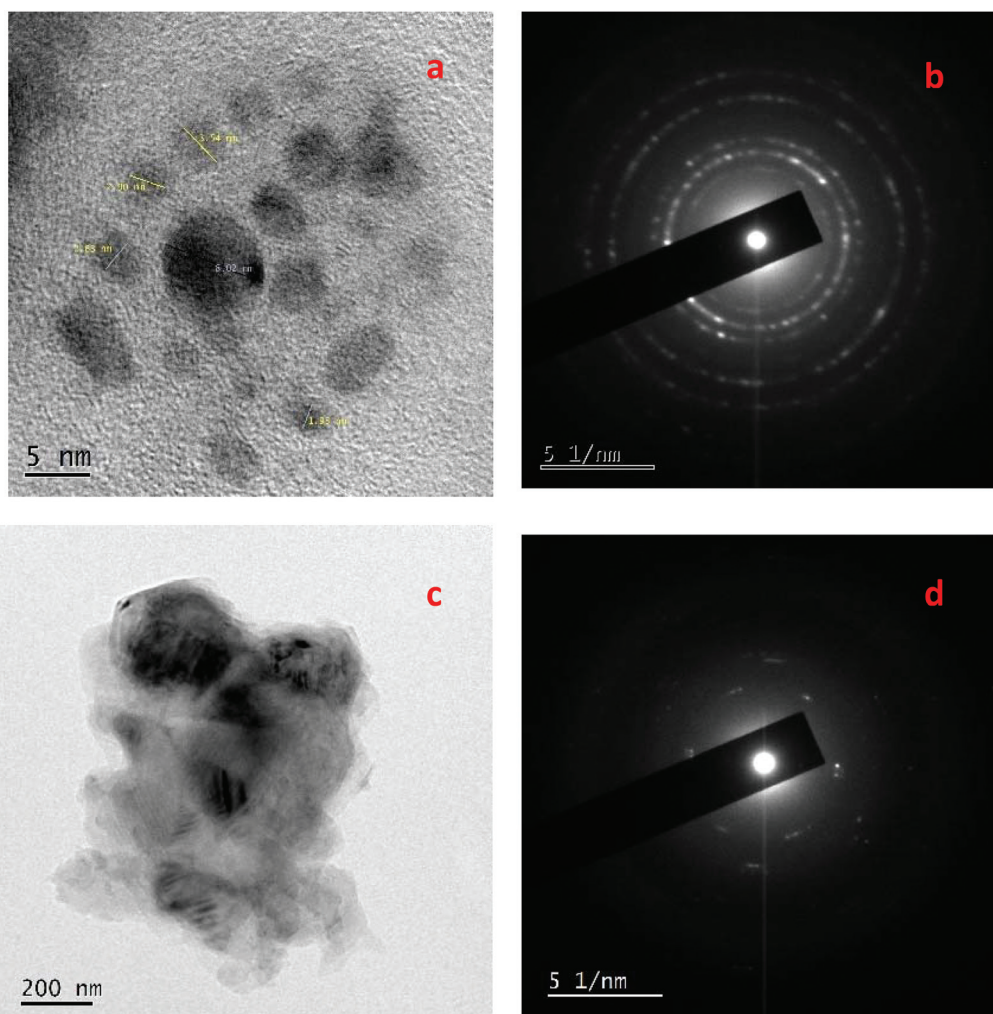


Fig. 8 TEM images of the nanoparticles of (a) **Phen-Tb** and (c) **Phen-Eu**, and SAED pattern data of (b) **Phen-Tb** and (d) **Phen-Eu**.

troscopy. The requisite solutions were prepared by mixing 1 mg of the powder sample of the respective **Phen-Ln** (Ln = Eu³⁺ and Tb³⁺) with 1 mL of DMSO solvent and then sonicated for a few minutes. The resultant yellow-colored solutions were irradiated with a light of 350 nm. As illustrated in Fig. 7a and b, the emission spectra show the characteristic peaks for the Eu and Tb complexes. For **Phen-Tb** two peaks are visible at around 490 nm and 544 nm resulting from the electronic transition of ⁵D₄-⁷F₆ and ⁵D₄-⁷F₅, respectively. On the other hand, the **Phen-Eu** spectrum reveals four peaks at 578 nm, 589 nm, 615 nm and 639 nm, which can be assigned to the electronic transitions of ⁵D₀-⁷F₀, ⁵D₀-⁷F₁, ⁵D₀-⁷F₂, and ⁵D₀-⁷F₃, respectively. The observed distinctive photoluminescence features can be attributed to the presence of chromophores such as phenanthroline. The ligand (without any metals) shows a hump like emission signal at around 400 nm which is totally different in nature from the emission signals responsible for the lanthanide complex of the ligand. We have also performed the titration of the ligand solution with lanthanide salt solutions which shows that with an increase in the salt concentration the peaks for the lanthanide increase (Fig. 7c and d).

Bio-imaging applications

The luminescent nature and low-nuclearity crystal structures led us to believe that **Phen-Tb** and **Phen-Eu** would be ideal candidates for bio-imaging applications. However, in order to have any meaningful bio-imaging applications, the materials have to fulfill certain preconditions, such as dimensions, particle size, and purity. For example, the probe needs to be of sufficiently smaller size for internalization into cells. First and foremost,

the phase purity of the samples was confirmed using the powder X-ray diffraction data which show excellent matching with the simulated pattern generated from the corresponding single crystal X-ray diffraction structure (Fig. S6 and S7†). On the other hand, considering the fact that the size of a common human cell is much smaller than that of our bulk crystals of lanthanide clusters, we had to make crystalline nanoparticles using a step-down procedure. We made powders of **Phen-Eu** and **Phen-Tb** by manually grinding their crystals using a mortar and pestle. Then a solution was prepared by mixing 1 mg of powders with 1 mL of DMSO and then sonicated for 10 minutes. A yellow-colored clear solution was obtained for both the samples. Then the solutions were filtered using 0.22 μm syringe filter paper to remove all the unwanted bigger sized particles. DLS, TEM & ESI-MS were performed with the filtrate. The DLS results (Fig. S10 and S11†) and TEM image (Fig. 8a and c) show that the particle size of **Phen-Eu** is around 200 nm, whereas the particle size of **Phen-Tb** is much smaller (<5 nm). Furthermore, the SAED data from TEM show the crystallinity of the nanoparticles in both the cases (Fig. 8b and c). Another important issue is the stability of the complexes in solution that would be used for cell imaging. The ESI-MS data (Fig. S9†) reveal the fragmented mass of the complexes which confirms the stability of the complex in solution, which has been subsequently used for cell imaging studies (Fig. 9).

Cellular imaging

Having confirmed the fulfillment of the preconditions of crystalline nanoscale sized photoluminescent materials, the potential of the **Phen-Eu** and **Phen-Tb** solutions for biomedical

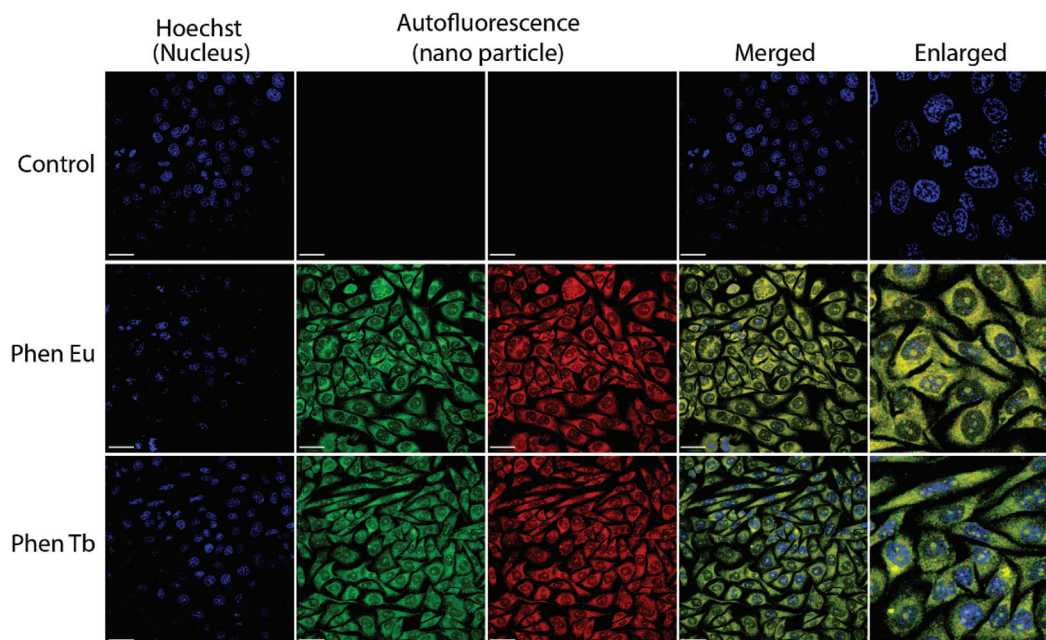


Fig. 9 Live cell confocal microscopy showing the delivery of compounds **Phen-Eu** (red) and **Phen-Tb** (green) in the nucleus and cytoplasm. Representative confocal images showing the localization of **Phen-Eu** (30 μM) and **Phen-Tb** (30 μM) in human breast adenocarcinoma (MCF7) cells as monitored by the intrinsic fluorescence of the drugs (**Phen-Eu**: both green and red channels, middle panel, and **Phen-Tb**: both green and red channels, middle panel) and with Hoechst 33342 (the blue channel, left panel) used as a nuclear marker. The right panel shows merged images.

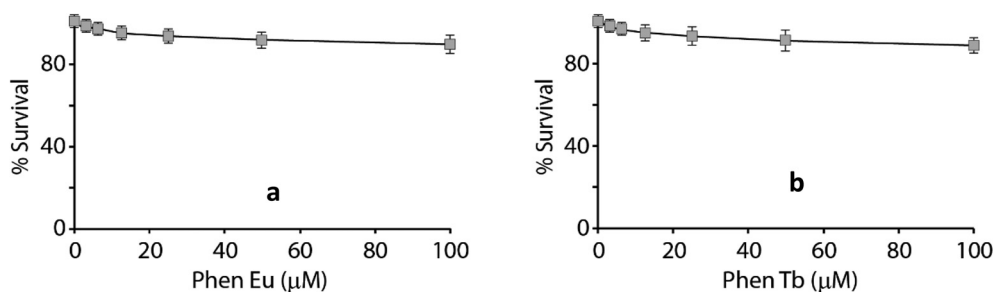


Fig. 10 Cell survival assay with compounds **Phen-Eu** and **Phen-Tb** reveals no apparent cytotoxicity. (a) Survival curves of the MCF7 cells treated with **Phen-Eu** for 72 h. Cell viability was determined by MTT assays. Error bars represent the standard deviation ($n \geq 3$). (b) Survival curves of the MCF7 cells treated with **Phen-Tb** for 72 h. Cell viability was determined by MTT assays. Error bars represent the standard deviation ($n \geq 3$).

applications was explored. One such important and topical biomedical application of stable crystalline fluorescent particles would be the labeling of live cells. In the present context, we use **Phen-Eu** and **Phen-Tb** for the live cell labeling of human breast adenocarcinoma (MCF7) cells. First and foremost, any possible cytotoxic effects of our complexes were assessed with the help of standard cell cytotoxicity (MTT) assay experiments. None of the complexes exert any adverse effects on the cells and enhance the prospect of **Phen-Eu** and **Phen-Tb** as effective probes for the labelling of cancer cells. Further confirmation comes from corroborating survival rates of *ca.* 90%, determined from the survival curves of the MCF7 cells after treatment with **Phen-Eu** and **Phen-Tb** for 72 h (Fig. 10). The optimal results were obtained when the experiments were carried out with a diluted 30 μM concentration of the **Phen-Eu** and **Phen-Tb** solutions. The experimental microscopy images collected and analysed using a live cell confocal microscope were beyond our expectation. In excellent agreement with the HRTEM and DLS results, the sizes of the **Phen-Eu** and **Phen-Tb** complexes were indeed of sufficiently nanoscale dimensions to achieve cell-permeability and as such they easily pass through the cell membrane during the incubation period of 4 hours. Usually the conventional cellular sensing, internalization of probes into cells, proceeds only up to cytoplasm. In the present case, the images clearly show that both the probes go beyond the conventional limit to penetrate through the nuclear membrane and enter into the nucleus of the cells. Localization into the nucleus can be confirmed by using nuclear marker Hoechst 33342 (blue channel, left panel), simultaneously. Furthermore, the enlarged images of the cells unequivocally confirm the localization of our complexes in the nucleolus, and hence prove the importance of using these complexes for biomedical applications.

Conclusions

The aim of the work presented herein was to generate multi-functional lanthanide complexes using a newly synthesized pyridyl-pyrazolyl-based ligand containing a chromophoric 1,10-phenanthroline backbone. Accordingly, we have successfully synthesized three lanthanide complexes with $\{\text{Gd}^{\text{III}}_3\}$,

$\{\text{Tb}^{\text{III}}_3\}$ and $\{\text{Eu}^{\text{III}}_3\}$ cores. The complexes are isostructural and exhibit a topology that closely resembles two interdigitating hairpins. The clusters crystallize in chiral space groups and also exhibit chirality for bulk samples, which were further confirmed using the solid state CD spectra. The magnetic measurement of the Gd cluster reveals a significant cryogenic magnetic refrigeration with a moderately high magnetic entropy change of $-23.42 \text{ J kg}^{-1} \text{ K}^{-1}$ at 7 T and 2 K. The introduction of a 1,10-phenanthroline moiety, on the other hand, made a huge impact on the fluorescence properties of the Eu and Tb complexes. With no apparent cytotoxic adverse effects, the complexes were subsequently used for the imaging of human breast adenocarcinoma (MCF7) cells. The live cell confocal microscopy images show that the complexes penetrate beyond the usual cytoplasm region and can be useful in imaging the nucleus region of MCF7 cells.

Experimental

General materials and methods

Materials. All reagents and solvents were purchased from commercial sources & used without further purification. FTIR spectra were obtained on a Nicolet MAGNA-IR 750 spectrometer with the samples prepared as KBr pellets. Elemental analysis was performed with a PerkinElmer 2400 Series-II CHN analyzer. UV-visible spectroscopy was performed using a PerkinElmer Lambda 950 UV-vis instrument. Magnetic data of the crystalline samples were collected using Quantum Design MPMS (Evercool, 7 T). ^1H NMR analysis was performed with a Bruker spectrometer operating at 400 MHz using a deuterated dimethyl sulfoxide solvent. The photoluminescence measurements were performed with a Horiba Jobin Yvon Fluoromax-3 spectrometer using steady-state 450 W Xe lamps as the excitation source, and the excitation of the samples was performed in the UV region at 350 nm. Mass spectra were recorded on a Q-ToF Micro YA263 high resolution (Waters Corporation) mass spectrometer by positive ion mode electrospray ionization and the spectra were collected in methanol. Powder X-ray diffraction data at room temperature were collected using a Rigaku Smart lab X-ray diffractometer. Dynamic light scattering experiments were performed using a Malvern particle size ana-

lyzer (Model No. ZEN 3690 ZETASIZER NANO ZS 90 version 7.03), and transmission electron microscopy was performed using a Jeol JEM 2010 HRTEM.

Single crystal X-ray diffraction. Crystal data were collected at 100 K using a Bruker D8 VENTURE Microfocus diffractometer equipped with a PHOTON II detector, with Mo K α radiation ($\lambda = 0.71073 \text{ \AA}$), controlled by the APEX3 (v2017.3-0) software package and processed using SAINT. Raw data were integrated and corrected for Lorentz and polarization effects using the Bruker APEX III program suite. The structures were solved by direct methods in SHELXS and refined by full-matrix least squares on F^2 in SHELXL. Crystallographic data are summarized in Table S6.†

Live-cell confocal microscopy. Live-cell imaging was carried out using a confocal laser-scanning microscope (Leica TCS SP8) with a UV-laser and 63 \times /1.4 NA oil objective equipped with a heated environmental chamber set to 37 °C with optimal CO₂ facility. Briefly, MCF7 cells seeded on a cover glass bottom dish (Genetix, Biotech Asia Pvt. Ltd) were incubated with the compounds **Phen-Eu** and **Phen-Tb** separately for 6 h. The nuclei were subsequently stained with Hoechst 33342 (Blue) (Sigma). This was followed by live cell confocal microscopy. Images were collected and processed using the Leica software and sized in Adobe Photoshop 7.0.¹³⁷

Cell survival assay. MCF7 cells (6×10^3) were seeded in 96-well plates (BD Biosciences, USA) and treated with the compounds **Phen-Eu** and **Phen-Tb** at the indicated concentrations. After 72 h of treatment, cell survival was assessed by the 3-(4,5-dimethylthiazol-2-yl)-2,5-diphenyltetrazolium bromide (MTT) assay. Briefly, the cells were washed with 1 \times PBS and treated with the MTT reagent (Sigma) for 3 h at 37 °C and the resulting formazan was dissolved in 100 μ l of dimethyl sulfoxide. The plates were analyzed using a Molecular Devices SpectraMax M2 microplate reader at 570 nm. The percent inhibition of viability for each concentration of the compounds was calculated with respect to the control. Data represent the mean values \pm s.e.m. for three independent experiments.¹³⁷

Synthesis of 1,10-phenanthroline-2,9-dicarbaldehyde. 1,10-Phenanthroline-2,9-dicarbaldehyde was synthesized following a previously reported procedure.¹³⁸ A mixture of 15 mL of 1,4-dioxane & 1 mL of water was added to 0.56 g (5 mmol) of selenium dioxide. Then the mixture was stirred & heated to reflux at 100 °C in a double neck round bottom flask. A separate clear solution was prepared by adding 0.5 g (2.4 mmol) of 2,9-dimethyl-1,10-phenanthroline to 10 mL of 1,4-dioxane & mixed well. Then this solution was added dropwise to the previously refluxed mixture. After that the total mixture was further refluxed for 2 more hours. Then the mixture was filtered under hot conditions & the filtrate was left to cool. A yellow needle shaped product was obtained after cooling and washing with warm 1,4-dioxane (yield-80.1%).

Synthesis of 3-(2-pyridyl)-N-[(E)-[9-[(E)-[3-(2-pyridyl)-1H-pyrazole-5-carbonyl]hydrazono] methyl]-1,10-phenanthroline-2-yl] methyleneamino]-1H-pyrazole-5-carboxamide (Phen). The crude yellow colored compound (1,10-phenanthroline-2,9-dicarbaldehyde) previously synthesized was used for this process. 3-(2-Pyridyl)-N-[(E)-[9-[(E)-[3-(2-pyridyl)-1H-pyrazole-5-

carbonyl]hydrazono]methyl]-1,10-phenanthroline-2-yl]methyleneamino]-1H-pyrazole-5-carboxamide (**Phen**) was synthesized by the condensation reaction between 3-(pyridin-2-yl)-1H-pyrazole-5-carbohydrazide and 1,10-phenanthroline-2,9-dicarbaldehyde. To a mixture of 1.18 g of 1,10-phenanthroline-2,9-dicarbaldehyde and 2.03 g of 3-(pyridin-2-yl)-1H-pyrazole-5-carbohydrazide, 40 mL of ethanol was added and then refluxed at 80 °C for 8 hours (yield: 67%). Anal. calcd (found) for C₃₂H₂₂N₁₂O₂ (%): C, 63.44 (64.85); H, 3.76 (3.24); N, 27.73 (28.62), ¹H NMR spectra/ δ (ppm) (400 MHz, DMSO-d₆): 14.268 (s, 2H, pz NH), 12.421 (s, 2H, amide NH), 9.7 (d, 2H, amide NH), 8.944 (dd, 2H, pyH), 8.634 (m, 4H, aromatic H & non-aromatic CH), 8.413 (d, 2H, aromatic H), 8.158 (m, 4H, aromatic H), 7.947 (td, 2H, aromatic H), 7.524 (s, 2H, pz CH), IR (400–4000 cm⁻¹): 3379w, 3230m, 3049m, 1670vs, 1618s, 1597s, 1543s, 1497s, 1396s, 1310s, 1234m, 1159s, 1067s, 999s, 854s, 787s. ESI-MS m/z (M + H): 608.22.

Synthesis of complex Phen-Eu ([Eu^{III}₃(Phen)₂(NO₃)₅]). **Phen** (0.121 g, 0.2 mmol) and Eu (NO₃)₃·6H₂O (0.134 g, 0.3 mmol) were dissolved in a solvent mixture containing 15 mL of DMF and 10 mL of methanol. The mixture was stirred for half an hour and then refluxed in an oil bath at 80 °C for 8 hours. After cooling the mixture to room temperature, the greenish yellow solution was filtered and kept undisturbed for crystallization. After 7 days, light greenish yellow colored octahedron shaped X-ray diffraction quality single crystals were obtained. The crystals were washed with methanol and dried. (Yield-86%) Anal. calcd (found) for C₇₀H₅₈Eu₃N₃₁O₂₁ (%): C, 39.55 (39.28); H, 2.73 (2.25); N, 20.43 (19.80). IR (400–4000 cm⁻¹): 3431w, 3227m, 2924s, 1664vs 1610s, 1526s, 1448s, 1384s, 1302s, 1194m, 1014s, 903s, 791s.

Synthesis of complex Phen-Tb ([Tb^{III}₃(Phen)₂(NO₃)₅]). **Phen-Tb** was synthesized using a similar procedure to that of **Phen-Eu**. The only difference is that here Tb(NO₃)₃·5H₂O (0.131 g, 0.3 mmol) was used instead of Eu(NO₃)₃·6H₂O. (Yield-75%) Anal. calcd (found) for C₇₀H₅₆Tb₃N₃₁O₂₁ (%): C, 39.19 (39.12); H, 2.61 (2.29); N, 20.25 (19.65). IR (400–4000 cm⁻¹): 3421w, 3224m, 2924s, 1664vs, 1612m, 1526m, 1448s, 1385s, 1304s, 1194s, 1014s, 903s, 791s.

Synthesis of complex Phen-Gd ([Gd^{III}₃(Phen)₂(NO₃)₅]). **Phen-Gd** was synthesized using a similar procedure to that of **Phen-Eu**. The only difference is that here Gd(NO₃)₃·6H₂O (0.135g, 0.3mmol) was used instead of Eu(NO₃)₃·6H₂O. (Yield-71%) Anal. calcd (found) for C₇₀H₅₈Gd₃N₃₁O₂₁ (%): C, 39.27 (39.14); H, 2.71 (2.12); N, 20.29 (19.68). IR (400–4000 cm⁻¹): 3431w, 3231m, 1664vs, 1604m, 1529s, 1447s, 1385s, 1304s, 1194m, 1014s, 905s, 791s.

Conflicts of interest

There are no conflicts to declare.

Acknowledgements

A. D. and K. S. D. are thankful to the Department of Science and Technology (DST), India for the INSPIRE fellowship. S. S.

and S. P. C. are supported by the UGC Senior Research Fellowship, India. S. A. is supported by the CSIR Senior Research Fellowship, India. R. M. gratefully acknowledges the Department of Science and Technology (DST), India, for financial assistance under the Empowerment and Equity Opportunities for Excellence in Science Programme (Project No. EEQ/2018/000194).

References

- 1 R. W. McCallum, L. H. Lewis, R. Skomski, M. J. Kramer and I. E. Anderson, Practical Aspects of Modern and Future Permanent Magnets, *Annu. Rev. Mater. Res.*, 2014, **44**, 451–477.
- 2 Y. Zhang, W. Wei, G. K. Das and T. T. Yang Tan, Engineering lanthanide-based materials for nanomedicine, *J. Photochem. Photobiol., C*, 2014, **20**, 71–96.
- 3 K. H. Thompson and C. Orvig, Editorial: Lanthanide compounds for therapeutic and diagnostic applications, *Chem. Soc. Rev.*, 2006, **35**, 499–499.
- 4 R. D. Teo, J. Termini and H. B. Gray, Lanthanides: Applications in Cancer Diagnosis and Therapy, *J. Med. Chem.*, 2016, **59**, 6012–6024.
- 5 E. Y. Pikalova, A. A. Murashkina, V. I. Maragou, A. K. Demin, V. N. Strekalovsky and P. E. Tsiakaras, CeO₂ based materials doped with lanthanides for applications in intermediate temperature electrochemical devices, *Int. J. Hydrogen Energy*, 2011, **36**, 6175–6183.
- 6 Y. Cui, B. Chen and G. Qian, Lanthanide metal-organic frameworks for luminescent sensing and light-emitting applications, *Coord. Chem. Rev.*, 2014, **273–274**, 76–86.
- 7 J. Long, Y. Guari, R. A. S. Ferreira, L. D. Carlos and J. Larionova, Recent advances in luminescent lanthanide based Single-Molecule Magnets, *Coord. Chem. Rev.*, 2018, **363**, 57–70.
- 8 L. Ungur, S.-Y. Lin, J. Tang and L. F. Chibotaru, Single-molecule toroids in Ising-type lanthanide molecular clusters, *Chem. Soc. Rev.*, 2014, **43**, 6894–6905.
- 9 S. Aime, D. D. Castelli, S. G. Crich, E. Gianolio and E. Terreno, Pushing the Sensitivity Envelope of Lanthanide-Based Magnetic Resonance Imaging (MRI) Contrast Agents for Molecular Imaging Applications, *Acc. Chem. Res.*, 2009, **42**, 822–831.
- 10 M. Bottrill, L. Kwok and N. J. Long, Lanthanides in magnetic resonance imaging, *Chem. Soc. Rev.*, 2006, **35**, 557–571.
- 11 S. Harada, S. Nakashima, S. Sekino, W. Oishi and A. Nishida, Optically Active Helical Lanthanide Complexes: Storable Chiral Lewis Acidic Catalysts for Enantioselective Diels–Alder Reaction of Siloxydienes, *Chem. – Asian J.*, 2020, **15**, 483–486.
- 12 K. Mikami, M. Terada and H. Matsuzawa, “Asymmetric” Catalysis by Lanthanide Complexes, *Angew. Chem., Int. Ed.*, 2002, **41**, 3554–3572.
- 13 J. Rocha, L. D. Carlos, F. A. A. Paz and D. Ananias, Luminescent multifunctional lanthanides-based metal-organic frameworks, *Chem. Soc. Rev.*, 2011, **40**, 926–940.
- 14 T. C. Jenks, A. N. W. Kuda-Wedagedara, M. D. Bailey, C. L. Ward and M. J. Allen, Spectroscopic and Electrochemical Trends in Divalent Lanthanides through Modulation of Coordination Environment, *Inorg. Chem.*, 2020, **59**, 2613–2620.
- 15 T. V. Dubinina, K. V. Paramonova, S. A. Trashin, N. E. Borisova, L. G. Tomilova and N. S. Zefirov, Novel near-IR absorbing phenyl-substituted phthalocyanine complexes of lanthanide(III): synthesis and spectral and electrochemical properties, *Dalton Trans.*, 2014, **43**, 2799–2809.
- 16 J. Jianzhuang, R. C. W. Liu, T. C. W. Mak, T. W. Dominic Chan and D. K. P. Ng, Synthesis, spectroscopic and electrochemical properties of substituted bis(phthalocyaninato)lanthanide(III) complexes, *Polyhedron*, 1997, **16**, 515–520.
- 17 G. Pan, X. Bai, D. Yang, X. Chen, P. Jing, S. Qu, L. Zhang, D. Zhou, J. Zhu, W. Xu, B. Dong and H. Song, Doping Lanthanide into Perovskite Nanocrystals: Highly Improved and Expanded Optical Properties, *Nano Lett.*, 2017, **17**, 8005–8011.
- 18 A. Nadort, J. Zhao and E. M. Goldys, Lanthanide upconversion luminescence at the nanoscale: fundamentals and optical properties, *Nanoscale*, 2016, **8**, 13099–13130.
- 19 L. Charbonnière, R. Ziessel, M. Guardigli, A. Roda, N. Sabbatini and M. Cesario, Lanthanide Tags for Time-Resolved Luminescence Microscopy Displaying Improved Stability and Optical Properties, *J. Am. Chem. Soc.*, 2001, **123**, 2436–2437.
- 20 Y.-G. Huang, F.-L. Jiang and M.-C. Hong, Magnetic lanthanide-transition-metal organic-inorganic hybrid materials: From discrete clusters to extended frameworks, *Coord. Chem. Rev.*, 2009, **253**, 2814–2834.
- 21 J. Feng and H. Zhang, Hybrid materials based on lanthanide organic complexes: a review, *Chem. Soc. Rev.*, 2013, **42**, 387–410.
- 22 Y. Ning, M. Zhu and J.-L. Zhang, Near-infrared (NIR) lanthanide molecular probes for bioimaging and biosensing, *Coord. Chem. Rev.*, 2019, **399**, 213028.
- 23 Y. Fan and F. Zhang, A New Generation of NIR-II Probes: Lanthanide-Based Nanocrystals for Bioimaging and Biosensing, *Adv. Opt. Mater.*, 2019, **7**, 1801417.
- 24 Y. Huang, D. Coman, M. M. Ali and F. Hyder, Lanthanide ion (III) complexes of 1,4,7,10-tetraazacyclododecane-1,4,7,10-tetraaminophosphonate for dual biosensing of pH with chemical exchange saturation transfer (CEST) and biosensor imaging of redundant deviation in shifts (BIRDS), *Contrast Media Mol. Imaging*, 2015, **10**, 51–58.
- 25 S. Aime, M. Botta, M. Fasano and E. Terreno, Lanthanide (III) chelates for NMR biomedical applications, *Chem. Soc. Rev.*, 1998, **27**, 19–29.
- 26 A. Roca-Sabio, M. Regueiro-Figueroa, D. Esteban-Gómez, A. de Blas, T. Rodríguez-Blas and C. Platas-Iglesias,

- Density functional dependence of molecular geometries in lanthanide(III) complexes relevant to bioanalytical and biomedical applications, *Comput. Theor. Chem.*, 2012, **999**, 93–104.
- 27 L.-L. Li, R. Zhang, L. Yin, K. Zheng, W. Qin, P. R. Selvin and Y. Lu, Biomimetic Surface Engineering of Lanthanide-Doped Upconversion Nanoparticles as Versatile Bioprobes, *Angew. Chem., Int. Ed.*, 2012, **51**, 6121–6125.
- 28 K. Zhao, J. Sun, F. Wang, A. Song, K. Liu and H. Zhang, Lanthanide-Based Photothermal Materials: Fabrication and Biomedical Applications, *ACS Appl. Bio Mater.*, 2020, **3**, 3975–3986.
- 29 Y. Hasegawa and T. Nakanishi, Luminescent lanthanide coordination polymers for photonic applications, *RSC Adv.*, 2015, **5**, 338–353.
- 30 J.-C. G. Bünzli and C. Piguet, Taking advantage of luminescent lanthanide ions, *Chem. Soc. Rev.*, 2005, **34**, 1048–1077.
- 31 N. C. Martinez-Gomez, H. N. Vu and E. Skovran, Lanthanide Chemistry: From Coordination in Chemical Complexes Shaping Our Technology to Coordination in Enzymes Shaping Bacterial Metabolism, *Inorg. Chem.*, 2016, **55**, 10083–10089.
- 32 J. Dixon, Energy storage for electric vehicles, *2010 IEEE International Conference on Industrial Technology*, 2010.
- 33 M. Oshitani, M. Watada, K. Shodai and M. Kodama, Effect of Lanthanide Oxide Additives on the High-Temperature Charge Acceptance Characteristics of Pasted Nickel Electrodes, *J. Electrochem. Soc.*, 2001, **148**, A67.
- 34 F. T. Edelmann, Lanthanide amidinates and guanidinates in catalysis and materials science: a continuing success story, *Chem. Soc. Rev.*, 2012, **41**, 7657–7672.
- 35 A. Rogalski and K. Chrzanowski, Infrared devices and techniques, *Opto-Electron. Rev.*, 2002, **10**, 111–136.
- 36 C. D. S. Brites, S. Balabhadra and L. D. Carlos, Lanthanide-Based Thermometers: At the Cutting-Edge of Luminescence Thermometry, *Adv. Opt. Mater.*, 2019, **7**, 1801239.
- 37 X. Li, H.-L. Sun, X.-S. Wu, X. Qiu and M. Du, Unique (3,12)-Connected Porous Lanthanide–Organic Frameworks Based on Ln₄O₄ Clusters: Synthesis, Crystal Structures, Luminescence, and Magnetism, *Inorg. Chem.*, 2010, **49**, 1865–1871.
- 38 A. Rossin, G. Giambastiani, M. Peruzzini and R. Sessoli, Amine-Templated Polymeric Lanthanide Formates: Synthesis, Characterization, and Applications in Luminescence and Magnetism, *Inorg. Chem.*, 2012, **51**, 6962–6968.
- 39 P. Bag, C. K. Rastogi, S. Biswas, S. Sivakumar, V. Mereacre and V. Chandrasekhar, Homodinuclear lanthanide {Ln₂} (Ln=Gd, Tb, Dy, Eu) complexes prepared from an o-vanillin based ligand: luminescence and single-molecule magnetism behavior, *Dalton Trans.*, 2015, **44**, 4328–4340.
- 40 X.-f. Huang, J.-x. Ma and W.-s. Liu, Lanthanide Metalloligand Strategy toward d–f Heterometallic Metal–Organic Frameworks: Magnetism and Symmetric-Dependent Luminescent Properties, *Inorg. Chem.*, 2014, **53**, 5922–5930.
- 41 R. Fu, S. Hu and X. Wu, New 3D Lanthanide Phosphonates: Syntheses, Crystal Structure, Thermal Stability, Luminescence, and Magnetism, *Cryst. Growth Des.*, 2014, **14**, 6197–6204.
- 42 S. Su, W. Chen, C. Qin, S. Song, Z. Guo, G. Li, X. Song, M. Zhu, S. Wang, Z. Hao and H. Zhang, Lanthanide Anionic Metal–Organic Frameworks Containing Semirigid Tetracarboxylate Ligands: Structure, Photoluminescence, and Magnetism, *Cryst. Growth Des.*, 2012, **12**, 1808–1815.
- 43 J.-W. Zhang, X.-M. Kan, B.-Q. Liu, G.-C. Liu, A.-X. Tian and X.-L. Wang, Systematic Investigation of Reaction-Time Dependence of Three Series of Copper–Lanthanide/Lanthanide Coordination Polymers: Syntheses, Structures, Photoluminescence, and Magnetism, *Chem. – Eur. J.*, 2015, **21**, 16219–16228.
- 44 H.-Y. Wong, W. T. K. Chan and G.-L. Law, Assembly of Lanthanide(III) Cubanes and Dimers with Single-Molecule Magnetism and Photoluminescence, *Inorg. Chem.*, 2018, **57**, 6893–6902.
- 45 A. Pindwal, K. Yan, S. Patnaik, B. M. Schmidt, A. Ellern, I. I. Slowing, C. Bae and A. D. Sadow, Homoleptic Trivalent Tris(alkyl) Rare Earth Compounds, *J. Am. Chem. Soc.*, 2017, **139**, 16862–16874.
- 46 J. Dreiser, Molecular lanthanide single-ion magnets: from bulk to submonolayers, *J. Phys.: Condens. Matter*, 2015, **27**, 183203.
- 47 R. Bruno, J. Vallejo, N. Marino, G. De Munno, J. Krzystek, J. Cano, E. Pardo and D. Armentano, Cytosine Nucleobase Ligand: A Suitable Choice for Modulating Magnetic Anisotropy in Tetrahedrally Coordinated Mononuclear Co^{II} Compounds, *Inorg. Chem.*, 2017, **56**, 1857–1864.
- 48 D. Gatteschi, R. Sessoli and L. Sorace, in *Handbook on the Physics and Chemistry of Rare Earths*, ed. J.-C. G. Bünzli and V. K. Pecharsky, Elsevier, 2016, vol. 50, pp. 91–139.
- 49 E. Baa, G. M. Watkins, R. W. Krause and D. N. Tantoh, Current Trend in Synthesis, Post-Synthetic Modifications and Biological Applications of Nanometal–Organic Frameworks (NMOFs), *Chin. J. Chem.*, 2019, **37**, 378–404.
- 50 D. E. Barry, D. F. Caffrey and T. Gunnlaugsson, Lanthanide-directed synthesis of luminescent self-assembly supramolecular structures and mechanically bonded systems from acyclic coordinating organic ligands, *Chem. Soc. Rev.*, 2016, **45**, 3244–3274.
- 51 M. Kumar, L.-H. Wu, M. Kariem, A. Franconetti, H. N. Sheikh, S.-J. Liu, S. C. Sahoo and A. Frontera, A Series of Lanthanide-Based Metal–Organic Frameworks Derived from Furan-2,5-dicarboxylate and Glutarate: Structure-Corroborated Density Functional Theory Study, Magnetocaloric Effect, Slow Relaxation of Magnetization, and Luminescent Properties, *Inorg. Chem.*, 2019, **58**, 7760–7774.
- 52 F. T. Edelmann, Lanthanide amidinates and guanidinates: from laboratory curiosities to efficient homogeneous cata-

- lysts and precursors for rare-earth oxide thin films, *Chem. Soc. Rev.*, 2009, **38**, 2253–2268.
- 53 Y. Zhang, B. Ali, J. Wu, M. Guo, Y. Yu, Z. Liu and J. Tang, Construction of Metallosupramolecular Coordination Complexes: From Lanthanide Helicates to Octahedral Cages Showing Single-Molecule Magnet Behavior, *Inorg. Chem.*, 2019, **58**, 3167–3174.
- 54 H. Kaur, S. Sundriyal, V. Pachauri, S. Ingebrandt, K.-H. Kim, A. L. Sharma and A. Deep, Luminescent metal-organic frameworks and their composites: Potential future materials for organic light emitting displays, *Coord. Chem. Rev.*, 2019, **401**, 213077.
- 55 M. Skwierczyńska, M. Runowski, S. Goderski, J. Szczytko, J. Rybusiński, P. Kulpiński and S. Lis, Luminescent-Magnetic Cellulose Fibers, Modified with Lanthanide-Doped Core/Shell Nanostructures, *ACS Omega*, 2018, **3**, 10383–10390.
- 56 L.-R. Lin, H.-H. Tang, Y.-G. Wang, X. Wang, X.-M. Fang and L.-H. Ma, Functionalized Lanthanide(III) Complexes Constructed from Azobenzene Derivative and β -Diketone Ligands: Luminescent, Magnetic, and Reversible Trans-to-Cis Photoisomerization Properties, *Inorg. Chem.*, 2017, **56**, 3889–3900.
- 57 M. Runowski and S. Lis, Synthesis, surface modification/decoration of luminescent-magnetic core/shell nanomaterials, based on the lanthanide doped fluorides ($\text{Fe}_3\text{O}_4/\text{SiO}_2/\text{NH}_2/\text{PAA}/\text{LnF}_3$), *J. Lumin.*, 2016, **170**, 484–490.
- 58 X.-L. Li, C.-L. Chen, H.-P. Xiao, A.-L. Wang, C.-M. Liu, X. Zheng, L.-J. Gao, X.-G. Yang and S.-M. Fang, Luminescent, magnetic and ferroelectric properties of noncentrosymmetric chain-like complexes composed of nine-coordinate lanthanide ions, *Dalton Trans.*, 2013, **42**, 15317–15325.
- 59 W. Huang, D. Wu, P. Zhou, W. Yan, D. Guo, C. Duan and Q. Meng, Luminescent and Magnetic Properties of Lanthanide-Thiophene-2,5-dicarboxylate Hybrid Materials, *Cryst. Growth Des.*, 2009, **9**, 1361–1369.
- 60 J.-H. Jia, Q.-W. Li, Y.-C. Chen, J.-L. Liu and M.-L. Tong, Luminescent single-molecule magnets based on lanthanides: Design strategies, recent advances and magneto-luminescent studies, *Coord. Chem. Rev.*, 2019, **378**, 365–381.
- 61 J. Romero Gómez, R. Ferreira Garcia, A. De Miguel Catoira and M. Romero Gómez, Magnetocaloric effect: A review of the thermodynamic cycles in magnetic refrigeration, *Renewable Sustainable Energy Rev.*, 2013, **17**, 74–82.
- 62 V. K. Pecharsky and K. A. Gschneidner Jr., Magnetocaloric effect and magnetic refrigeration, *J. Magn. Magn. Mater.*, 1999, **200**, 44–56.
- 63 V. K. Pecharsky and K. A. Gschneidner Jr., Tunable magnetic regenerator alloys with a giant magnetocaloric effect for magnetic refrigeration from ~ 20 to ~ 290 K, *Appl. Phys. Lett.*, 1997, **70**, 3299–3301.
- 64 L.-X. Chang, G. Xiong, L. Wang, P. Cheng and B. Zhao, A 24-Gd nanocapsule with a large magnetocaloric effect, *Chem. Commun.*, 2013, **49**, 1055–1057.
- 65 E. Cremades, S. Gómez-Coca, D. Aravena, S. Alvarez and E. Ruiz, Theoretical Study of Exchange Coupling in 3d-Gd Complexes: Large Magnetocaloric Effect Systems, *J. Am. Chem. Soc.*, 2012, **134**, 10532–10542.
- 66 J. Du, Q. Zheng, Y. B. Li, Q. Zhang, D. Li and Z. D. Zhang, Large magnetocaloric effect and enhanced magnetic refrigeration in ternary Gd-based bulk metallic glasses, *J. Appl. Phys.*, 2008, **103**, 023918.
- 67 J.-M. Jia, S.-J. Liu, Y. Cui, S.-D. Han, T.-L. Hu and X.-H. Bu, 3D Gd^{III} Complex Containing Gd_{16} Macrocycles Exhibiting Large Magnetocaloric Effect, *Cryst. Growth Des.*, 2013, **13**, 4631–4634.
- 68 Y.-Z. Zheng, M. Evangelisti and R. E. P. Winpenney, Co-Gd phosphonate complexes as magnetic refrigerants, *Chem. Sci.*, 2011, **2**, 99–102.
- 69 J.-B. Peng, Q.-C. Zhang, X.-J. Kong, Y.-Z. Zheng, Y.-P. Ren, L.-S. Long, R.-B. Huang, L.-S. Zheng and Z. Zheng, High-Nuclearity 3d–4f Clusters as Enhanced Magnetic Coolers and Molecular Magnets, *J. Am. Chem. Soc.*, 2012, **134**, 3314–3317.
- 70 T. Rajeshkumar, R. Jose, P. R. Remya and G. Rajaraman, Theoretical Studies on Trinuclear $\{\text{Mn}^{\text{III}}_2\text{Gd}^{\text{III}}\}$ and Tetranuclear $\{\text{Mn}^{\text{III}}_2\text{Gd}^{\text{III}}_2\}$ Clusters: Magnetic Exchange, Mechanism of Magnetic Coupling, Magnetocaloric Effect, and Magneto-Structural Correlations, *Inorg. Chem.*, 2019, **58**, 11927–11940.
- 71 J.-Z. Qiu, L.-F. Wang, Y.-C. Chen, Z.-M. Zhang, Q.-W. Li and M.-L. Tong, Magnetocaloric Properties of Heterometallic 3d–Gd Complexes Based on the $[\text{Gd}(\text{oda})_3]^{3-}$ Metalloligand, *Chem. – Eur. J.*, 2016, **22**, 802–808.
- 72 E. Soini, T. Lövgren and C. B. Reimer, Time-Resolved Fluorescence of Lanthanide Probes and Applications in Biotechnology, *CRC Crit. Rev. Anal. Chem.*, 1987, **18**, 105–154.
- 73 J. D. Einkauf, J. M. Clark, A. Paulive, G. P. Tanner and D. T. de Lill, A General Model of Sensitized Luminescence in Lanthanide-Based Coordination Polymers and Metal-Organic Framework Materials, *Inorg. Chem.*, 2017, **56**, 5544–5552.
- 74 R. J. Abergel, A. D'Aléo, C. Ng Pak Leung, D. K. Shuh and K. N. Raymond, Using the Antenna Effect as a Spectroscopic Tool: Photophysics and Solution Thermodynamics of the Model Luminescent Hydroxypyridonate Complex $[\text{Eu}^{\text{III}}(3,4,3\text{-LI}(1,2\text{-HOPO}))]^-$, *Inorg. Chem.*, 2009, **48**, 10868–10870.
- 75 V. Vicinelli, P. Ceroni, M. Maestri, V. Balzani, M. Gorka and F. Vögtle, Luminescent Lanthanide Ions Hosted in a Fluorescent Polylysine Dendrimer. Antenna-Like Sensitization of Visible and Near-Infrared Emission, *J. Am. Chem. Soc.*, 2002, **124**, 6461–6468.
- 76 M. B. Coban, A. Amjad, M. Aygun and H. Kara, Sensitization of Ho^{III} and Sm^{III} luminescence by efficient energy transfer from antenna ligands: Magnetic, visible and NIR photoluminescence properties of Gd^{III} , Ho^{III} and

- Sm^{III} coordination polymers, *Inorg. Chim. Acta*, 2017, **455**, 25–33.
- 77 H. Uh and S. Petoud, Novel antennae for the sensitization of near infrared luminescent lanthanide cations, *C. R. Chim.*, 2010, **13**, 668–680.
- 78 F. Pointillart, T. Cauchy, O. Maury, Y. Le Gal, S. Golhen, O. Cador and L. Ouahab, Tetrathiafulvalene-amido-2-pyridine-N-oxide as Efficient Charge-Transfer Antenna Ligand for the Sensitization of Yb^{III} Luminescence in a Series of Lanthanide Paramagnetic Coordination Complexes, *Chem. – Eur. J.*, 2010, **16**, 11926–11941.
- 79 W.-S. Lo, J. Zhang, W.-T. Wong and G.-L. Law, Highly Luminescent Sm^{III} Complexes with Intraligand Charge-Transfer Sensitization and the Effect of Solvent Polarity on Their Luminescent Properties, *Inorg. Chem.*, 2015, **54**, 3725–3727.
- 80 M. B. Coban, C. Kocak, H. Kara, M. Aygun and A. Amjad, Magnetic properties and sensitized visible and NIR luminescence of Dy^{III} and Eu^{III} coordination polymers by energy transfer antenna ligands, *Mol. Cryst. Liq. Cryst.*, 2017, **648**, 202–215.
- 81 J. Andres and A.-S. Chauvin, Colorimetry of Luminescent Lanthanide Complexes, *Molecules*, 2020, **25**, 4022.
- 82 L. Armelao, S. Quici, F. Barigelletti, G. Rsi, G. Bottaro, M. Cavazzini and E. Tondello, Design of luminescent lanthanide complexes: From molecules to highly efficient photo-emitting materials, *Coord. Chem. Rev.*, 2010, **254**, 487–505.
- 83 X.-F. Qiao, H.-Y. Zhang and B. Yan, Photoactive binary and ternary lanthanide (Eu³⁺, Tb³⁺, Nd³⁺) hybrids with p-tert-butylcalix[4]arene derived Si–O linkages and polymers, *Dalton Trans.*, 2010, **39**, 8882–8892.
- 84 C. D. Geddes, *Rev. Fluoresc.* 2016, Springer, 2017.
- 85 M. Liu, Z. Ye, C. Xin and J. Yuan, Development of a ratiometric time-resolved luminescence sensor for pH based on lanthanide complexes, *Anal. Chim. Acta*, 2013, **761**, 149–156.
- 86 E. J. New, D. Parker, D. G. Smith and J. W. Walton, Development of responsive lanthanide probes for cellular applications, *Curr. Opin. Chem. Biol.*, 2010, **14**, 238–246.
- 87 R. Zhang and J. Yuan, Responsive Metal Complex Probes for Time-Gated Luminescence Biosensing and Imaging, *Acc. Chem. Res.*, 2020, **53**, 1316–1329.
- 88 X. Liu, B. Song, H. Ma, Z. Tang and J. Yuan, Development of a mitochondria targetable ratiometric time-gated luminescence probe for biothiols based on lanthanide complexes, *J. Mater. Chem. B*, 2018, **6**, 1844–1851.
- 89 S. Pandya, J. Yu and D. Parker, Engineering emissive europium and terbium complexes for molecular imaging and sensing, *Dalton Trans.*, 2006, 2757–2766.
- 90 M. P. Coogan and V. Fernández-Moreira, Progress with, and prospects for, metal complexes in cell imaging, *Chem. Commun.*, 2014, **50**, 384–399.
- 91 T. Terai and T. Nagano, Fluorescent probes for bioimaging applications, *Curr. Opin. Chem. Biol.*, 2008, **12**, 515–521.
- 92 A. Jana, B. J. Crowston, J. R. Shewring, L. K. McKenzie, H. E. Bryant, S. W. Botchway, A. D. Ward, A. J. Amoroso, E. Baggaley and M. D. Ward, Heteronuclear Ir(III)–Ln(III) Luminescent Complexes: Small-Molecule Probes for Dual Modal Imaging and Oxygen Sensing, *Inorg. Chem.*, 2016, **55**, 5623–5633.
- 93 X. Yang, S. Wang, D. Schipper, L. Zhang, Z. Li, S. Huang, D. Yuan, Z. Chen, A. J. Gnanam, J. W. Hall, T. L. King, E. Que, Y. Dieye, J. Vadivelu, K. A. Brown and R. A. Jones, Self-assembly of high-nuclearity lanthanide-based nano-clusters for potential bioimaging applications, *Nanoscale*, 2016, **8**, 11123–11129.
- 94 R. A. Jones, A. J. Gnanam, J. F. Arambula, J. N. Jones, J. Swaminathan, X. Yang, D. Schipper, J. W. Hall, L. J. DePue, Y. Dieye, J. Vadivelu, D. J. Chandler, E. M. Marcotte, J. L. Sessler, L. I. R. Ehrlich and K. A. Brown, Lanthanide nano-drums: a new class of molecular nanoparticles for potential biomedical applications, *Faraday Discuss.*, 2014, **175**, 241–255.
- 95 A. Casini, B. Woods and M. Wenzel, The Promise of Self-Assembled 3D Supramolecular Coordination Complexes for Biomedical Applications, *Inorg. Chem.*, 2017, **56**, 14715–14729.
- 96 Z. Zheng, Ligand-controlled self-assembly of polynuclear lanthanide–oxo/hydroxo complexes: from synthetic serendipity to rational supramolecular design, *Chem. Commun.*, 2001, 2521–2529.
- 97 R. Chen, Z.-F. Hong, Y.-R. Zhao, H. Zheng, G.-J. Li, Q.-C. Zhang, X.-J. Kong, L.-S. Long and L.-S. Zheng, Ligand-Dependent Luminescence Properties of Lanthanide–Titanium Oxo Clusters, *Inorg. Chem.*, 2019, **58**, 15008–15012.
- 98 Z.-Y. Du, H.-B. Xu and J.-G. Mao, Rational Design of 0D, 1D, and 3D Open Frameworks Based on Tetranuclear Lanthanide(III) Sulfonate–Phosphonate Clusters, *Inorg. Chem.*, 2006, **45**, 9780–9788.
- 99 V. Chandrasekhar, P. Bag, M. Speldrich, J. van Leusen and P. Kögerler, Synthesis, Structure, and Magnetic Properties of a New Family of Tetra-nuclear {Mn₂^{III}Ln₂} (Ln=Dy, Gd, Tb, Ho) Clusters With an Arch-Type Topology: Single-Molecule Magnetism Behavior in the Dysprosium and Terbium Analogues, *Inorg. Chem.*, 2013, **52**, 5035–5044.
- 100 M.-S. Liu, Q.-Y. Yu, Y.-P. Cai, C.-Y. Su, X.-M. Lin, X.-X. Zhou and J.-W. Cai, One-, Two-, and Three-Dimensional Lanthanide Complexes Constructed from Pyridine-2,6-dicarboxylic Acid and Oxalic Acid Ligands, *Cryst. Growth Des.*, 2008, **8**, 4083–4091.
- 101 M. Pan, W.-M. Liao, S.-Y. Yin, S.-S. Sun and C.-Y. Su, Single-Phase White-Light-Emitting and Photoluminescent Color-Tuning Coordination Assemblies, *Chem. Rev.*, 2018, **118**, 8889–8935.
- 102 L. D. Carlos, R. A. S. Ferreira, V. d. Z. Bermudez and S. J. L. Ribeiro, Lanthanide-Containing Light-Emitting Organic–Inorganic Hybrids: A Bet on the Future, *Adv. Mater.*, 2009, **21**, 509–534.

- 103 L. Götzke, G. Schaper, J. März, P. Kaden, N. Huittinen, T. Stumpf, K. K. K. Kammerlander, E. Brunner, P. Hahn, A. Mehnert, B. Kersting, T. Henle, L. F. Lindoy, G. Zanoni and J. J. Weigand, Coordination chemistry of f-block metal ions with ligands bearing bio-relevant functional groups, *Coord. Chem. Rev.*, 2019, **386**, 267–309.
- 104 J.-C. G. Bünzli and C. Piguet, Lanthanide-Containing Molecular and Supramolecular Polymetallic Functional Assemblies, *Chem. Rev.*, 2002, **102**, 1897–1928.
- 105 P. Escribano, B. Julián-López, J. Planelles-Aragó, E. Cordoncillo, B. Viana and C. Sanchez, Photonic and nanobiophotonic properties of luminescent lanthanide-doped hybrid organic–inorganic materials, *J. Mater. Chem.*, 2008, **18**, 23–40.
- 106 K. Binnemans, Lanthanide-Based Luminescent Hybrid Materials, *Chem. Rev.*, 2009, **109**, 4283–4374.
- 107 S. Bala, A. Adhikary, S. Bhattacharya, M. S. Bishwas, P. Poddar and R. Mondal, Ln₈ (Ln=Gd, Ho, Er, Yb) Butterfly Core-Exhibiting Magnetocaloric Effect and Field-Induced SMM Behavior for Er Analogue, *ChemistrySelect*, 2017, **2**, 11341–11345.
- 108 S. Bala, M. S. Bishwas, B. Pramanik, S. Khanra, K. M. Fromm, P. Poddar and R. Mondal, Construction of Polynuclear Lanthanide (Ln=Dy^{III}, Tb^{III}, and Nd^{III}) Cage Complexes Using Pyridine–Pyrazole-Based Ligands: Versatile Molecular Topologies and SMM Behavior, *Inorg. Chem.*, 2015, **54**, 8197–8206.
- 109 S. Bala, A. Goswami, S. Sengupta, S. Ganguly, S. Bhattacharya, S. Khanra and R. Mondal, Metal-Directed Formation of Molecular Helix, Cage, and Grid Using an Asymmetric Pyridine–Pyrazole Based Bis-Chelating Ligand and Properties, *Cryst. Growth Des.*, 2013, **13**, 5068–5075.
- 110 S. Bala, A. De, A. Adhikary, S. Saha, S. Akhtar, K. S. Das, M.-L. Tong and R. Mondal, Influence of Semirigidity and Diverse Binding Modes of an Asymmetric Pyridine–pyrazole Based Bis-Chelating Ligand in Controlling Molecular Architectures and Their Properties, *Cryst. Growth Des.*, 2020, **20**, 5698–5708.
- 111 S. Alvarez, P. Alemany, D. Casanova, J. Cirera, M. Lluell and D. Avnir, Shape maps and polyhedral interconversion paths in transition metal chemistry, *Coord. Chem. Rev.*, 2005, **249**, 1693–1708.
- 112 D. Casanova, M. Lluell, P. Alemany and S. Alvarez, The Rich Stereochemistry of Eight-Vertex Polyhedra: A Continuous Shape Measures Study, *Chem. – Eur. J.*, 2005, **11**, 1479–1494.
- 113 H. Amouri and M. Gruselle, *Chirality in transition metal chemistry: molecules, supramolecular assemblies and materials*, John Wiley & Sons, 2008.
- 114 M. A. Masood, E. J. Enemark and T. D. P. Stack, Ligand Self-Recognition in the Self-Assembly of a $[\{\text{Cu}(\text{L})\}_2]^{2+}$ Complex: The Role of Chirality, *Angew. Chem., Int. Ed.*, 1998, **37**, 928–932.
- 115 O. Mamula and A. von Zelewsky, Supramolecular coordination compounds with chiral pyridine and polypyridine ligands derived from terpenes, *Coord. Chem. Rev.*, 2003, **242**, 87–95.
- 116 K. Biradha, C. Seward and M. J. Zaworotko, Helical Coordination Polymers with Large Chiral Cavities, *Angew. Chem., Int. Ed.*, 1999, **38**, 492–495.
- 117 X.-J. Kong, Y. Wu, L.-S. Long, L.-S. Zheng and Z. Zheng, A Chiral 60-Metal Sodalite Cage Featuring 24 Vertex-Sharing $[\text{Er}_4(\mu_3\text{-OH})_4]$ Cubanes, *J. Am. Chem. Soc.*, 2009, **131**, 6918–6919.
- 118 M. Alajarin, C. López-Leonardo, A. Vidal, J. Berná and J. W. Steed, Helical Sense Bias Induced by Point Chirality in Cage Compounds, *Angew. Chem., Int. Ed.*, 2002, **41**, 1205–1208.
- 119 V. Steinmetz, F. Couty and O. R. P. David, One-step synthesis of chiral cages, *Chem. Commun.*, 2009, 343–345.
- 120 F. Li, T. Li, X. Li, X. Li, Y. Wang and R. Cao, Synthesis of Chiral Coordination Polymers by Spontaneous Resolution, *Cryst. Growth Des.*, 2006, **6**, 1458–1462.
- 121 L. H. Sommer and J. McLick, Stereochemistry of asymmetric silicon. XI. Optical rotatory dispersion and circular dichroism of. α -NpPhMeSi* X [optically active. α -naphthyl (phenyl)(methyl) silyl] compounds, *J. Am. Chem. Soc.*, 1969, **91**, 2001–2010.
- 122 W.-W. Kuang, L.-L. Zhu, L.-C. Li and P.-P. Yang, Synthesis, Crystal Structure, and Magnetic Properties of a Family of Undecanuclear $[\text{Cu}^{\text{II}}_9\text{Ln}^{\text{III}}_2]$ Nanoclusters, *Eur. J. Inorg. Chem.*, 2015, 2245–2253.
- 123 J.-L. Liu, Y.-C. Chen, Q.-W. Li, S. Gómez-Coca, D. Aravena, E. Ruiz, W.-Q. Lin, J.-D. Lenga and M.-L. Tong, Two 3d–4f nanomagnets formed via a two-step in situ reaction of picolinaldehyde, *Chem. Commun.*, 2013, **49**, 6549–6551.
- 124 C. Meseguer, S. Titos-Padilla, M. M. Hanninen, R. Navarrete, A. J. Mota, M. Evangelisti, J. Ruiz and E. Colacio, Single-Molecule Magnet Behavior and Magnetocaloric Effect in Ferromagnetically Coupled Ln^{III}-Ni^{II}-Ni^{II}-Ln^{III} (Ln^{III}=Dy^{III} and Gd^{III})Linear Complexes, *Inorg. Chem.*, 2014, **53**, 12092–12099.
- 125 J. W. Sharples, Y.-Z. Zheng, F. Tuna, E. J. L. McInnes and D. Collison, Lanthanide discs chill well and relax slowly, *Chem. Commun.*, 2011, **47**, 7650–7652.
- 126 J. A. Sheikh, A. Adhikary and S. Konar, Magnetic refrigeration and slow magnetic relaxation in tetranuclear lanthanide cages (Ln=Gd, Dy) with in situ ligand transformation, *New J. Chem.*, 2014, **38**, 3006–3014.
- 127 S.-J. Liu, J.-P. Zhao, J. Tao, J.-M. Jia, S.-D. Han, Y. Li, Y.-C. Chen and X.-H. Bu, An Unprecedented Decanuclear Gd^{III} Cluster for Magnetic Refrigeration, *Inorg. Chem.*, 2013, **52**, 9163–9165.
- 128 A. Adhikary, J. A. Sheikh, S. Biswas and S. Konar, Synthesis, crystal structure and study of magnetocaloric effect and single molecular magnetic behaviour in discrete lanthanide complexes, *Dalton Trans.*, 2014, **43**, 9334–9343.
- 129 S. K. Gupta, S. K. Langley, K. Sharma, K. S. Murray and R. Murugavel, Pentanuclear Lanthanide Mono-organopho-

- sphates: Synthesis, Structure, and Magnetism, *Inorg. Chem.*, 2017, **56**, 3946–3960.
- 130 W.-M. Wang, H.-X. Zhang, S.-Y. Wang, H.-Y. Shen, H.-L. Gao, J.-Z. Cui and B. Zhao, Ligand Field Affected Single-Molecule Magnet Behavior of Lanthanide(III) Dinuclear Complexes with an 8-Hydroxyquinoline Schiff Base Derivative as Bridging Ligand, *Inorg. Chem.*, 2015, **54**, 10610–10622.
- 131 W.-M. Wang, L.-Y. He, X.-X. Wang, Y. Shi, Z.-L. Wu and J.-Z. Cui, Linear-shaped Ln^{III}4 and Ln^{III}6 clusters constructed by a polydentate Schiff base ligand and a β -diketone co-ligand: structures, fluorescence properties, magnetic refrigeration and single-molecule magnet behavior, *Dalton Trans.*, 2019, **48**, 16744–16755.
- 132 W.-M. Wang, X.-Z. Li, L. Zhang, J.-L. Chen, J.-H. Wang, Z.-L. Wu and J.-Z. Cui, A series of [2 \times 2] square grid Ln^{III}4 clusters: a large magnetocaloric effect and single-molecule-magnet behavior, *New J. Chem.*, 2019, **43**, 7419–7426.
- 133 W.-M. Wang, R.-X. Yue, Y. Gao, M.-J. Wang, S.-S. Hao, Y. Shi, X.-M. Kang and Z.-L. Wu, Large magnetocaloric effect and remarkable single-molecule-magnet behavior in triangle-assembled Ln^{III}6 clusters, *New J. Chem.*, 2019, **43**, 16639–16646.
- 134 W.-M. Wang, T.-T. Zhang, D. Wang and J.-Z. Cui, Structures and magnetic properties of novel Ln(III)-based pentanuclear clusters: magnetic refrigeration and single-molecule magnet behavior, *New J. Chem.*, 2020, **44**, 19351–19359.
- 135 W.-M. Wang, M.-J. Wang, S.-S. Hao, Q.-Y. Shen, M.-L. Wang, Q.-L. Liu, X.-F. Guan, X.-T. Zhang and Z.-L. Wu, 'Windmill'-shaped Ln^{III}4 (Ln^{III}=Gd and Dy) clusters: magnetocaloric effect and single-molecule-magnet behavior, *New J. Chem.*, 2020, **44**, 4631–4638.
- 136 W.-M. Wang, C.-L. Xue, R.-Y. Jing, X. Ma, L.-N. Yang, S.-C. Luo and Z.-L. Wu, Two hexanuclear lanthanide Ln^{III}6 clusters featuring remarkable magnetocaloric effect and slow magnetic relaxation behavior, *New J. Chem.*, 2020, **44**, 18025–18030.
- 137 A. Ghosh, S. Bhattacharjee, S. P. Chowdhuri, A. Mallick, I. Rehman, S. Basu and B. B. Das, SCAN1-TDP1 trapping on mitochondrial DNA promotes mitochondrial dysfunction and mitophagy, *Sci. Adv.*, 2019, **5**, eaax9778.
- 138 C.-L. Xiao, C.-Z. Wang, L.-Y. Yuan, B. Li, H. He, S. Wang, Y.-L. Zhao, Z.-F. Chai and W.-Q. Shi, Excellent Selectivity for Actinides with a Tetradentate 2,9-Diamide-1,10-Phenanthroline Ligand in Highly Acidic Solution: A Hard-Soft Donor Combined Strategy, *Inorg. Chem.*, 2014, **53**, 1712–1720.

Srijita Paul Chowdhuri
12.05.2023